

The inside story of the
CDC's data debacle p. 394

Upcycling the most common
plastic waste pp. 400 & 437

Heart complications
from COVID-19 p. 408

Science

\$15
23 OCTOBER 2020
sciencemag.org

AAAS

OLD FRIENDS

Aging chimps have strong social bonds pp. 403 & 473

CONTENTS

23 OCTOBER 2020 • VOLUME 370 • ISSUE 6515



NEWS

IN BRIEF

386 News at a glance

IN DEPTH

388 Global trial eliminates drugs, pivots to new ones

Definitive results on remdesivir and interferon demonstrate power of massive WHO study *By K. Kupferschmidt*

389 First vaccine may stymie hunt for better ones

Should trials keep using placebos once an approved vaccine exists? *By J. Cohen*

PODCAST

391 Nature journals ink open-access deal

German pact has costs of €9500 per published article *By J. Brinard*

391 Census needs review, panel says

Statisticians call for evaluation of quality of 2020 U.S. count *By J. Mervis*

392 In new strategy, Wellcome Trust takes on global health concerns

Giant philanthropy will focus on infectious disease, mental health, and the health effects of global warming *By K. Kupferschmidt*

393 Troubles escalate at Ecuador's young research university

Dozens of professors depart from Yachay Tech amid conflicts that could scuttle its move toward independence *By L. Wessel and R. Pérez Ortega*

FEATURES

394 Undermining CDC

Deborah Birx, President Donald Trump's COVID-19 coordinator, helped shake the foundation of a premier public health agency *By C. Piller*

396 How CDC foundered

By C. Piller

INSIGHTS

PERSPECTIVES

400 Creating value from plastic waste

Polyethylene can be upcycled into alkylaromatic compounds for the production of detergents *By B. M. Weckhuysen*

REPORT p. 437; PODCAST

402 Forming a mucus barrier along the colon

Optimal barrier function requires both proximal colon- and distal colon-derived mucus

By G. M. H. Birchenough and M. E. V. Johansson

REPORT p. 467

403 The upside of aging

Chimpanzees, like humans, place a higher value on positive social relationships as they grow older

By J. Silk

REPORT p. 473

404 Susceptibility to severe COVID-19

Genetic variants and autoantibodies that suppress antiviral immunity are linked to severe COVID-19

By D. B. Beck and I. Aksentijevich

RESEARCH ARTICLES pp. 422 & 423

406 The engines of SARS-CoV-2 spread

Fighting SARS-CoV-2 requires a clear framework for understanding epidemic spread *By E. C. Lee et al.*

408 COVID-19 can affect the heart

COVID-19 has a spectrum of potential heart manifestations with diverse mechanisms *By E. J. Topol*

410 Joseph H. Connell (1923–2020)

Innovative experimental ecologist *By W. W. Murdoch and W. P. Sousa*

POLICY FORUM

411 Set ambitious goals for biodiversity and sustainability

Multiple, coordinated goals and holistic actions are critical *By S. Díaz et al.*

BOOKS ET AL.

414 The disruption of divisions

Psychological stress is a pervasive aspect of border life, argues a journalist *By M. Diaz-Barriga and M. E. Dorsey*

415 A case for “we” in an “I” country

An eerily similar era gave way to social progress in the United States—will it happen again? *By J. A. Morone*



LETTERS

416 Narwhals require targeted conservation

By M. P. Heide-Jørgensen et al.

416 Wildfire debate needs science, not politics

By A. B. Leverkus et al.

417 “Forest mismanagement” misleads

By M. W. Schwartz et al.

RESEARCH

IN BRIEF

418 From *Science* and other journals

REVIEW

421 Oxygen sensing

Oxygen-sensing mechanisms across eukaryotic kingdoms and their roles in complex multicellularity

E. U. Hammarlund et al.

REVIEW SUMMARY; FOR FULL TEXT:

DX.DOI.ORG/10.1126/SCIENCE.ABA3512

RESEARCH ARTICLES

Coronavirus**422** Inborn errors of type I IFN immunity in patients with life-threatening COVID-19
Q. Zhang et al.

RESEARCH ARTICLE SUMMARY;

FOR FULL TEXT:

DX.DOI.ORG/10.1126/SCIENCE.ABD4570

423 Autoantibodies against type I IFNs in patients with life-threatening COVID-19
P. Bastard et al.

RESEARCH ARTICLE SUMMARY;

FOR FULL TEXT:

DX.DOI.ORG/10.1126/SCIENCE.ABD4585

PERSPECTIVE p. 404

424 Framework materials

Design of higher valency in covalent organic frameworks C. Gropp et al.

RESEARCH ARTICLE SUMMARY; FOR FULL TEXT:

DX.DOI.ORG/10.1126/SCIENCE.ABD6406

425 Geochemistry

Deep abiotic weathering of pyrite X. Gu et al.

RESEARCH ARTICLE SUMMARY; FOR FULL TEXT:

DX.DOI.ORG/10.1126/SCIENCE.ABB8092

426 Coronavirus

De novo design of picomolar SARS-CoV-2 miniprotein inhibitors L. Cao et al.

431 Neurodevelopment

Orderly compartmental mapping of premotor inhibition in the developing zebrafish spinal cord S. Kishore et al.

REPORTS

437 Polymer chemistry

Polyethylene upcycling to long-chain alkylaromatics by tandem hydrogenolysis/aromatization F. Zhang et al.

PERSPECTIVE p. 400

442 Nanomaterials

Supertwisted spirals of layered materials enabled by growth on non-Euclidean surfaces Y. Zhao et al.

446 Atmospheric oxygen

Triple iron isotope constraints on the role of ocean iron sinks in early atmospheric oxygenation A. W. Heard et al.

Structural biology**450** Structural basis of nucleosome-dependent cGAS inhibition
J. A. Boyer et al.**455** Structural basis for the inhibition of cGAS by nucleosomes T. Kujirai et al.**459 Display technology**Metasurface-driven OLED displays beyond 10,000 pixels per inch
W.-J. Joo et al.**463 Developmental biology**Lineage analysis reveals an endodermal contribution to the vertebrate pituitary
P. Fabian et al.**467 Microbiota**

Proximal colon-derived O-glycosylated mucus encapsulates and modulates the microbiota K. Bergstrom et al.

PERSPECTIVE p. 402

473 Sociality

Social selectivity in aging wild chimpanzees A. G. Rosati et al.

PERSPECTIVE p. 403

476 Adaptation

Experimental evolution makes microbes more cooperative with their local host genotype R. T. Batstone et al.

DEPARTMENTS

383 EditorialSaving the poor and vulnerable
By Sir Ian L. Boyd**385 Editorial**Science, politics, and public health
By William Roper**494 Working Life**Mentorship at a distance
By Naomi A. Rankin et al.

ON THE COVER

Lanjo, a 25-year-old male chimpanzee living in the Kanyawara community in Kibale National Park, Uganda. Long-term observations show that wild chimpanzees, like humans, increasingly prioritize strong, mutual social bonds and



positive social interactions during the aging process. Social selectivity in our close relatives reveals the evolutionary roots of successful social aging. See pages 403 and 473. Photo: Suzi Eszterhas/Minden Pictures

Science Staff382
 AAAS Meeting Program479
 Science Careers490

SCIENCE (ISSN 0036-8075) is published weekly on Friday, except last week in December, by the American Association for the Advancement of Science, 1200 New York Avenue, NW, Washington, DC 20005. Periodicals mail postage (publication No. 484460) paid at Washington, DC, and additional mailing offices. Copyright © 2020 by the American Association for the Advancement of Science. The title SCIENCE is a registered trademark of the AAAS. Domestic individual membership, including subscription (12 months): \$165 (\$74 allocated to subscription). Domestic institutional subscription (51 issues): \$2148; Foreign postage extra: Air assist delivery: \$98. First class, airmail, student, and emeritus rates on request. Canadian rates with GST available upon request. GST #R125488122. Publications Mail Agreement Number 1069624. Printed in the U.S.A.
Change of address: Allow 4 weeks, giving old and new addresses and 8-digit account number. **Postmaster:** Send change of address to AAAS, P.O. Box 96178, Washington, DC 20090-6178. **Single-copy sales:** \$15 each plus shipping and handling available from backissues.science.org; bulk rate on request. **Authorization to reproduce** material for internal or personal use under circumstances not falling within the fair use provisions of the Copyright Act can be obtained through the Copyright Clearance Center (CCC), www.copyright.com. The identification code for Science is 0036-8075. Science is indexed in the Reader's Guide to Periodical Literature and in several specialized indexes.

Editor-in-Chief Holden Thorp, hthorp@aaas.org

Executive Editor Monica M. Bradford

Editors, Research Valda Vinson, Jake S. Yeston Editor, Insights Lisa D. Chong

DEPUTY EDITORS Julia Fahrenkamp-Uppenbrink (UK), Stella M. Hurlley (UK), Phillip D. Szuromi, Sacha Vignieri **SR. EDITORIAL FELLOW** Andrew M. Sugden (UK) **SR. EDITORS** Gemma Alderton (UK), Caroline Ash (UK), Brent Grocholski, Pamela J. Hines, Di Jiang, Marc S. Lavine (Canada), Ian S. Osborne (UK), Beverly A. Purnell, L. Bryan Ray, H. Jesse Smith, Keith T. Smith (UK), Jelena Stajic, Peter Stern (UK), Valerie B. Thompson, Brad Wible, Laura M. Zahn **ASSOCIATE EDITORS** Michael A. Funk, Priscilla N. Kelly, Tage S. Rai, Seth Thomas Scanlon (UK), Yury V. Suleymanov **LETTERS EDITOR** Jennifer Sills **LEAD CONTENT PRODUCTION EDITORS** Harry Jach, Lauren Kmec **CONTENT PRODUCTION EDITORS** Amelia Beyna, Jeffrey E. Cook, Chris Filatreau, Julia Katris, Nida Masulis, Suzanne M. White **SR. EDITORIAL COORDINATORS** Carolyn Kyle, Beverly Shields **EDITORIAL COORDINATORS** Aneera Dobbins, Joi S. Granger, Jeffrey Hearn, Lisa Johnson, Maryrose Madrid, Ope Martins, Shannon McMahon, Jerry Richardson, Hilary Stewart (UK), Alana Warnke, Alice Whaley (UK), Anita Wynn **PUBLICATIONS ASSISTANTS** Jeremy Dow, Alexander Kief, Ronnel Navas, Brian White **EXECUTIVE ASSISTANT** Jessica Slater **ASI DIRECTOR, OPERATIONS** Janet Clements (UK) **ASI SR. OFFICE ADMINISTRATOR** Jessica Waldoock (UK)

News Editor Tim Appenzeller

NEWS MANAGING EDITOR John Travis **INTERNATIONAL EDITOR** Martin Enserink **DEPUTY NEWS EDITORS** Elizabeth Culotta, Lila Guterman, David Grimm, Eric Hand (Europe), David Malakoff **SR. CORRESPONDENTS** Daniel Clerly (UK), Jon Cohen, Jeffrey Mervis, Elizabeth Pennisi **ASSOCIATE EDITORS** Jeffrey Brinard, Catherine Maticic **NEWS REPORTERS** Adrian Cho, Jennifer Couzin-Frankel, Jocelyn Kaiser, Kelly Servick, Robert F. Service, Erik Stokstad, Paul Voosen, Meredith Wadman **INTERNS** Lucy Hicks, Cathleen O'Grady **CONTRIBUTING CORRESPONDENTS** Warren Cornwall, Ann Gibbons, Mara Hvistendahl, Sam Kean, Eli Kintisch, Kai Kupferschmidt (Berlin), Andrew Lawler, Mitch Leslie, Eliot Marshall, Virginia Morell, Dennis Normile (Shanghai), Elisabeth Pain (Careers), Charles Piller, Michael Price, Tania Rabesandratana (Barcelona), Joshua Sokol, Emily Underwood, Gretchen Vogel (Berlin), Lizzie Wade (Mexico City) **CAREERS** Donisha Adams, Rachel Bernstein (Editor), Katie Langin (Associate Editor) **COPY EDITORS** Julia Cole (Senior Copy Editor), Cyra Master (Copy Chief) **ADMINISTRATIVE SUPPORT** Meagan Weiland

Creative Director Beth Rakouskas

DESIGN MANAGING EDITOR Marcy Atarod **GRAPHICS MANAGING EDITOR** Alberto Cuadra **PHOTOGRAPHY MANAGING EDITOR** William Douthitt **WEB CONTENT STRATEGY MANAGER** Kara Estelle-Powers **DESIGN EDITOR** Chrystal Smith **DESIGNER** Christina Aycock **GRAPHICS EDITOR** Nirja Desai **INTERACTIVE GRAPHICS EDITOR** Xing Liu **SENIOR SCIENTIFIC ILLUSTRATORS** Valerie Altounian, Chris Bickel **SCIENTIFIC ILLUSTRATOR** Alice Kitterman **SENIOR GRAPHICS SPECIALISTS** Holly Bishop, Nathalie Cary **SENIOR PHOTO EDITOR** Emily Petersen **PHOTO EDITOR** Kaitlyn Dolan **WEB DESIGNER** Jennie Pajerowski

Chief Executive Officer and Executive Publisher Sudip Parikh

Publisher, Science Family of Journals Bill Moran

DIRECTOR, BUSINESS SYSTEMS AND FINANCIAL ANALYSIS Randy Yi **DIRECTOR, BUSINESS OPERATIONS & ANALYSIS** Eric Knott **DIRECTOR OF ANALYTICS** Enrique Gonzales **MANAGER, BUSINESS OPERATIONS** Jessica Tierney **SENIOR BUSINESS ANALYST** Cory Lipman, Meron Kebede **FINANCIAL ANALYST** Alexander Lee **ADVERTISING SYSTEM ADMINISTRATOR** Tina Burks **SENIOR SALES COORDINATOR** Shirley Young **DIGITAL/PRINT STRATEGY MANAGER** Jason Hillman **QUALITY TECHNICAL MANAGER** Marcus Spiegler **ASSISTANT MANAGER DIGITAL/PRINT** Rebecca Doshi **SENIOR CONTENT SPECIALISTS** Steve Forrester, Jacob Hedrick, Antoinette Hodal, Lori Murphy **PRODUCTION SPECIALIST** Kristin Wowk **DIGITAL PRODUCTION MANAGER** Lisa Stanford **CONTENT SPECIALIST** Kimberley Oster **ADVERTISING PRODUCTION OPERATIONS MANAGER** Deborah Tompkins **DESIGNER, CUSTOM PUBLISHING** Jeremy Huntsinger **SR. TRAFFIC ASSOCIATE** Christine Hall **SPECIAL PROJECTS ASSOCIATE** Sarah Dhre

ASSOCIATE DIRECTOR, BUSINESS DEVELOPMENT Justin Sawyers **GLOBAL MARKETING MANAGER** Allison Pritchard **DIGITAL MARKETING MANAGER** Aimee Aponte **JOURNALS MARKETING MANAGER** Shawana Arnold **MARKETING ASSOCIATES** Tori Velasquez, Mike Romano, Ashley Hylton **DIGITAL MARKETING SPECIALIST** Asleigh Rojanavongse **SENIOR DESIGNER** Kim Huynh

DIRECTOR AND SENIOR EDITOR, CUSTOM PUBLISHING Sean Sanders **ASSISTANT EDITOR, CUSTOM PUBLISHING** Jackie Oberst

DIRECTOR, PRODUCT & PUBLISHING DEVELOPMENT Chris Reid **DIRECTOR, BUSINESS STRATEGY AND PORTFOLIO MANAGEMENT** Sarah Whalen **ASSOCIATE DIRECTOR, PRODUCT MANAGEMENT** Kris Bishop **PRODUCT DEVELOPMENT MANAGER** Scott Chernoff **PUBLISHING TECHNOLOGY MANAGER** Michael Di Natale **SR. PRODUCT ASSOCIATE** Robert Koepke **SPJ ASSOCIATE** Samantha Bruno Fuller

DIRECTOR, INSTITUTIONAL LICENSING Iquo Edim **ASSOCIATE DIRECTOR, RESEARCH & DEVELOPMENT** Elisabeth Leonard **MARKETING MANAGER** Kess Knight **SENIOR INSTITUTIONAL LICENSING MANAGER** Ryan Rexroth **INSTITUTIONAL LICENSING MANAGER** Marco Castellani **MANAGER, AGENT RELATIONS & CUSTOMER SUCCESS** Judy Lillibridge **SENIOR OPERATIONS ANALYST** Lana Guz **FULFILLMENT COORDINATOR** Melody Stringer **SALES COORDINATOR** Josh Haverlock

DIRECTOR, GLOBAL SALES Tracy Holmes **US EAST COAST AND MID WEST SALES** Stephanie O'Connor **US WEST COAST SALES** Lynne Stickrod **US SALES MANAGER, SCIENCE CAREERS** Claudia Paulsen-Young **US SALES REP, SCIENCE CAREERS** Tracy Anderson **ASSOCIATE DIRECTOR, ROW** Roger Gonçalves **SALES REP, ROW** Sarah Lelarge **SALES ADMIN ASSISTANT, ROW** Bryony Cousins **DIRECTOR OF GLOBAL COLLABORATION AND ACADEMIC PUBLISHING RELATIONS** Asia Xiaoying Chu **ASSOCIATE DIRECTOR, INTERNATIONAL COLLABORATION** Grace Yao **SALES MANAGER** Danny Zhao **MARKETING MANAGER** Kilo Lan ASCA CORPORATION, JAPAN Kaoru Sasaki (Tokyo), Miyuki Tani (Osaka) **COLLABORATION/CUSTOM PUBLICATIONS/JAPAN** Adarsh Sandhu

DIRECTOR, COPYRIGHT, LICENSING AND SPECIAL PROJECTS Emilie David **RIGHTS AND LICENSING COORDINATOR** Jessica Adams **RIGHTS AND PERMISSIONS ASSOCIATE** Elizabeth Sandler **CONTRACTS AND LICENSING ASSOCIATE** Lili Catlett

MAIN HEADQUARTERS

Science/AAAS
1200 New York Ave. NW
Washington, DC 20005

SCIENCE INTERNATIONAL

Clarendon House
Clarendon Road
Cambridge, CB2 8FH, UK

SCIENCE CHINA

Room 1004, Culture Square
No. 59 Zhongguancun St.
Haidian District, Beijing, 100872

SCIENCE JAPAN

ASCA Corporation
Sibaura TY Bldg. 4F, 1-14-5
Shibaura Minato-ku
Tokyo, 108-0073 Japan

EDITORIAL

science_editors@aaas.org

NEWS

science_news@aaas.org

INFORMATION FOR AUTHORS

sciencemag.org/authors/

science-information-authors

REPRINTS AND PERMISSIONS

sciencemag.org/help/

reprints-and-permissions

MEDIA CONTACTS

scipak@aaas.org

MULTIMEDIA CONTACTS

SciencePodcast@aaas.org

ScienceVideo@aaas.org

INSTITUTIONAL SALES

AND SITE LICENSES

sciencemag.org/librarian

PRODUCT ADVERTISING

& CUSTOM PUBLISHING

advertising.sciencemag.org/

products-services

science_advertising@aaas.org

CLASSIFIED ADVERTISING

advertising.sciencemag.org/

science-careers

advertise@sciencecareers.org

JOB POSTING CUSTOMER SERVICE

employers.sciencemag.org

support@sciencecareers.org

MEMBERSHIP AND INDIVIDUAL

SUBSCRIPTIONS

sciencemag.org/subscriptions

MEMBER BENEFITS

aaas.org/membercentral

AAAS BOARD OF DIRECTORS

CHAIR Steven Chu

PRESIDENT Claire M. Fraser

PRESIDENT-ELECT Susan G. Amara

TREASURER Carolyn N. Ainslie

CHIEF EXECUTIVE OFFICER

Sudip Parikh

BOARD Cynthia M. Beall

Rosina M. Bierbaum

Ann Bostrom

Stephen P.A. Fodor

S. James Gates, Jr.

Laura H. Greene

Kaye Husbands Fealing

Maria M. Klawe

Robert B. Millard

Alonda Nelson

William D. Provine

BOARD OF REVIEWING EDITORS (Statistics board members indicated with \$)

Adriano Aguzzi, U. Hospital Zurich

Takuzo Aida, U. of Tokyo

Leslie Aiello,

Wenner-Gren Foundation

Deji Akinwande, UT Austin

Judith Allen, U. of Manchester

Marcella Alsan, Harvard U.

Sebastian Amigorena,

Institut Curie

James Analytis, UC Berkeley

Trevor Archer, NIEHS, NIH

Paola Arlotta, Harvard U.

Johan Auwerx, EPFL

David Awschalom, U. of Chicago

Clare Baker, U. of Cambridge

Nenad Ban, ETH Zurich

Franz Bauer,

Pontificia U. Católica de Chile

Ray H. Baughman,

U. of Texas at Dallas

Carlo Beenakker, Leiden U.

Yasmine Belkaid, NIAID, NIH

Philip Benfey, Duke U.

Gabriele Bergers, VIB

Kiros T. Berhane, Columbia U.

Bradley Bernstein,

Mass. General Hospital

Joseph J. Berry, NREL

Alessandra Biffi,

Harvard Med. School

Peer Bork, EMBL

Chris Bowler,

École Normale Supérieure

Ian Boyd, U. of St. Andrews

Emily Brodsky, UC Santa Cruz

Ron Brookmeyer, UCLA (\$)

Christian Büchel, UKE Hamburg

Dennis Burton, Scripps Res.

Carter Tribley Butts, UC Irvine

György Buzsáki,

New York U. School of Med.

Blanche Capel, Duke U.

Annamarie Carlton, UC Irvine

Nick Chater, U. of Warwick

M. Keith Chen, UCLA

Zhiqian Chen,

UT Southwestern Med. Ctr.

Ib Chorkendorff, Denmark TU

James J. Collins, MIT

Robert Cook-Deegan,

Arizona State U.

Alan Cowman,

Walter & Eliza Hall Inst.

Carolyn Coyne, U. of Pittsburgh

Roberta Croce, VU Amsterdam

Ismaila Dabo, Penn State U.

Jeff L. Dangl, U. of North Carolina

Chiara Daraio, Caltech

Nicolas Dauphas,

U. of Chicago

Christian Davenport,

U. of Michigan

Frans de Waal, Emory U.

Claude Desplan, New York U.

Sandra Diaz,

U. Nacional de Córdoba

Ulrike Diebold, TU Wien

Hong Ding, Inst. of Physics, CAS

Dennis Discher, U. of Penn.

Jennifer A. Doudna, UC Berkeley

Raissa M. D'Souza, UC Davis

Bruce Dunn, UCLA

William Dunphy, Caltech

Christopher Dye, U. of Oxford

Scott Edwards, Harvard U.

Todd Ehlers, U. of Tübingen

Jennifer Eliseeff,

Johns Hopkins U.

Tim Elston, U. of North Carolina

Andrea Encalada,

U. San Francisco de Quito

Nader Engheta, U. of Penn.

Karen Ersche, U. of Cambridge

Beate Escher,

IFZ & U. of Tübingen

Barry Everitt, U. of Cambridge

Vanessa Ezenwa, U. of Georgia

Michael Feuer,

The George Washington U.

Toren Finkel,

U. of Pittsburgh Med. Ctr.

Gwenn Flowers, Simon Fraser U.

Peter Fratzl,

Max Planck Inst. Potsdam

Elaine Fuchs, Rockefeller U.

Eileen Furlong, EMBL

Jay Gallagher, U. of Wisconsin

Daniel Geschwind, UCLA

Karl-Heinz Glassmeier,

TU Braunschweig

Ramon Gonzalez,

U. of South Florida

Sandra González-Bailón,

U. of Penn

Elizabeth Grove, U. of Chicago

Nicolas Gruber, ETH Zurich

Hua Guo, U. of New Mexico

Kip Guy,

U. of Kentucky College of Pharmacy

Salk Inst. for Biological Studies

Christian Haass,

Ludwig Maximilians U.

Sharon Hammes-Schiffer,

Yale U.

Wolf-Dietrich Hardt, ETH Zurich

Louise Harra, U. College London

Jian He, Clemson U.

Carl-Philipp Heisenberg,

IST Austria

Ykä Helariutta, U. of Cambridge

Janet G. Hering, Eawag

Hans Hilgenkamp, U. of Twente

Kai-Uwe Hinrichs, U. of Bremen

Deirdre Hollingsworth,

U. of Oxford

Lora Hooper,

UT Southwestern Med. Ctr.

Fred Hughson, Princeton U.

Randall Hulet, Rice U.

Auke Ijspeert, EPFL

Akiko Iwasaki, Yale U.

Stephen Jackson,

USGS and U. of Arizona

Erich Jarvis, Rockefeller U.

Kai Johnson, IST Austria

Peter Jonas, EPFL

Matt Kaeblerlein,

U. of Washington

William Kaelin Jr.,

Dana-Farber Cancer Inst.

Daniel Kammen, UC Berkeley

V. Naray Kim, Seoul Nat. U.

Robert Kingston,

Harvard Med. School

Nancy Knowlton,

Smithsonian Institution

Etienne Koechlin,

École Normale Supérieure

Alex L. Kolodkin,

Johns Hopkins U.

Julia Krupic, U. of Cambridge

Thomas Langer,

Max Planck Inst. Cologne

Mitchell A. Lazar, U. of Penn.

Saving the poor and vulnerable

Right now, warm surface water is moving into the western Pacific Ocean in the form of a “La Niña.” It is a sentinel for a complex set of connections that drive weather patterns from the Horn of Africa to Botswana and normally presages drought in East Africa. This event soon will be ringing alarm bells within the World Food Programme (WFP). Even as this United Nations–led agency celebrates its well-deserved award of the 2020 Nobel Peace Prize, the relentless challenge of preventing hunger marches on.

Why a Nobel Prize for the WFP, and why now? Last year, the WFP assisted nearly 100 million people in 88 countries. It is the safety net for those who fall off the edge of existence. It is the humanitarian end of the response to solving the problem of food insecurity. Its Nobel Prize reminds us all of the moral hazard in imagining that the poor and vulnerable are somebody else’s problem.

The work of the WFP is the consequence of failure. It has been around since 1961 and has been the global coordinator of nationally based efforts to avert catastrophes with food aid. If it has struggled at times, this is largely because of the debilitating nexus of war, corruption, climate change, and famine. Despite decades of effort to alleviate hunger, the latest estimate is that about 11% of people on the planet (about 820 million people) are suffering chronic undernourishment. This rises to nearly a quarter of all people in sub-Saharan Africa, and hunger is on the rise in Africa. Progress at reducing undernourishment has stalled despite gains through the 1990s and 2000s.

At this time, when a global pandemic is forcing the rich of the world to adjust their lives—often in minor ways compared with the starving and dispossessed—the Nobel Committee is challenging humanity to act with moral courage and selflessness. Even in good times, the richest of the world are hardly overflowing with generosity. The Group of Seven (G7) nations typically spend less than \$8 per person per year to support the work of the WFP (the annual WFP contribution from a country divided by the population of that country). When we think of all the other things that nations spend money on—from defense to their own

social welfare—do we really get our priorities right? Added to this, many of the countries with the greatest food security problems are debt peons of wealthier nations, often generating the cash to pay off some of these debts in food exports. What is given in generosity in one hand is taken back with the other and, in some places, wealthy nations even supply the weapons to perpetuate wars, which undermine the work of the WFP. Climate change, a product largely of the accrual of capital wealth by rich nations, just adds to the asymmetry of stress. The developing world suffers the most from the negative impacts of climate change.

American philosopher John Rawls saw that addressing the needs of the poor and vulnerable is about more than money—it is mostly about creating conditions under which liberty and opportunity can thrive. Under Rawls’s schema, the “America First” slogan of today seems particularly aversive. Aid that promotes the gap between rich and poor and sustains a “know thy place” message to the recipients is aid with heavy conditions. It was U.S. President Dwight Eisenhower who asked for the WFP to be established, but the current incumbent of that office has hardly shown such leadership. Nations must act together and act globally. Perhaps the Nobel Committee’s choice was

also a poke in the eye for Donald Trump and his tribe.

At least within the scientific community, there is a helping hand because of rapid progress in embedding expertise in fields such as agro-climatology within countries most vulnerable to poverty and hunger. By making its voice heard, science can lead by example. The various national food aid agencies that are coordinated through the WFP are increasingly informed by forecasting of climatic challenges to food production, for instance. The resilience that must be built into some of the poorest countries will not come from loans from wealthy and populous countries, which may have a food deficit of their own, or institutions like the International Monetary Fund. It will be built upon self-confident people using open and shared scientific knowledge to pull themselves out of their misery.

—Sir Ian L. Boyd



Sir Ian L. Boyd

is a professor of biology at the University of St Andrews, Fife, Scotland, UK, and chairman of the UK Research Integrity Office. He is the former chief scientific adviser to the United Kingdom Government on food and environment. ilb@st-andrews.ac.uk

“...the World Food Programme... is the safety net for those who fall off the edge of existence.”

Science, politics, and public health

There is an idea on the part of scientists that politics is dirty, and a companion idea on the part of politicians that science, by its continual qualifications and revisions, is, if not irrelevant, then at least out of touch with the constraints of a democracy: What seems optimal from the perspective of science may be impossible to implement in the political arena.

The events of the past several months regarding the coronavirus disease 2019 (COVID-19) pandemic make it apparent that for public health to continue to improve the lives of everyone, we must find ways to overcome this mutual distrust.

When I was director of the U.S. Centers for Disease Control and Prevention (CDC) from 1990 to mid-1993—an appointee of the George H. W. Bush administration—the nation and the world were facing a major and growing public health crisis: increasing disease and death from HIV/AIDS. The AIDS epidemic had been raging for a decade, and the scientific and biomedical communities were staunchly advancing our understanding of the disease and its prevention and treatment, at the individual and the population level. There were still many unknowns about HIV/AIDS, and the uncertainties about how to tackle it effectively, both medically and socially, made policy-making fraught with challenges.

Among those challenges was the fact that the disease particularly hit marginalized groups in the population. There were major controversies about the safety of the blood supply, about condom distribution and needle exchange programs, and about how to deal with HIV-infected health care workers.

The biomedical community felt that science and scientists should be making the decisions regarding public health—in other words, “getting politics out of public health.” Policy-makers said that these decisions should not be left to unelected public health experts.

Many of those same sentiments are being voiced today, during the COVID-19 pandemic. What’s worse now is that many in Washington, DC, and around the country seem to scorn even the idea of scientific experts. The fact is that each group needs the other—science without politics is impotent, and politics without science is subject to whim and caprice.

In previous decades, the CDC’s role in national and global public health was vital. There were very substantial infectious disease threats—emerging and reemerging—plus growing noninfectious disease challenges, including cancer, heart disease, obesity, tobacco use, environmental and occupational issues, and the mounting problems of injury and violence. Each of these had complicated overlays of science and politics, and included complex economic and cultural impacts.

And yet, it is as true today as it was then that the CDC and the other U.S. public health agencies are not infallible. That is especially true regarding new diseases, those without an existing body of knowledge. Early pronouncements often need to be revisited, and frequently revised, as new discoveries are made.

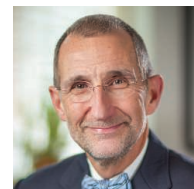
This year, the CDC has been off the mark more than once and has had to reverse its recommendations. But the solution to this reality is not to belittle and tear down this hugely important agency, but rather to continue the quest for more and better scientific knowledge, and to be willing to implement those insights. But there have been repeated reports of political folks pushing the CDC to alter their scientific judgments to fit a political agenda.

Politicians should use the product of the scientific process to make careful policy and to design programs that benefit the public’s health. And scientists should avoid being drawn into the political fray and being used to try to influence elections. Calling for this mutual respect and joint involvement in the public health process may seem naïve—especially in the wake of the recent scientific problems at the CDC, and also at a time of hyperpolitical division and unprecedented election-year chaos.

As a first step, we must recognize the legitimate roles that science and politics must have in our public health processes. And then with real transparency and accountability, we should vigorously debate how best to meet the challenges before us.

Every American—whether scientist or layperson, whether Republican, Democrat, or Independent—has a stake in getting this science–politics balance right. It is far too important for game playing.

—William Roper



William L. Roper

served as the director of the U.S. Centers for Disease Control and Prevention from 1990 to 1993. He was dean of the School of Medicine at the University of North Carolina (UNC)—Chapel Hill and chief executive officer of the UNC Health Care System and then interim president of the UNC System.

“...many...
seem to
scorn even
the idea
of scientific
experts.”

“Most funny to us was the censorship of ‘bone,’ which, after all, [is] the main thing we work with.”

Paleontologist Thomas Holtz, in *The New York Times*, about words that screening software removed from chats at last week’s online meeting of the Society of Vertebrate Paleontology.

IN BRIEF

Edited by **Jeffrey Brainard**

A dust storm in Spearman, Texas, in 2018.

CLIMATE SCIENCE

Rising storms stir fears of Dust Bowl 2.0

Dust storms on the U.S. Great Plains have become more common over the past 20 years, and a tipping point leading to conditions like those of the 1930s-era Dust Bowl may soon arrive, researchers have concluded. A study last week in *Geophysical Research Letters* says more frequent droughts driven by climate change and an expansion of croplands in the region have doubled levels of wind-blown dust since 2000. The findings are based on data

from NASA satellites that measure atmospheric haze caused by smoke and dust, corroborated by ground-level dust sensors. The storms not only remove soil nutrients and decrease agricultural productivity, but also threaten human health: The dust contains ultrafine particles that can cause lung and heart disease. Ironically, dust levels are growing fastest in areas downwind from grasslands plowed up to plant corn to make biofuels—an effort meant to help the environment.

FDA OKs first Ebola treatment

PUBLIC HEALTH | The U.S. Food and Drug Administration last week became the first regulatory body to approve a treatment for Ebola. The treatment is a mix of monoclonal antibodies made by Regeneron. The three antibodies in the cocktail target different regions of a surface protein on the Ebola virus that help it infect cells. The treatment, given as a single infusion, reduced mortality in a study that compared four treatments during an Ebola outbreak in the Democratic Republic of the Congo. The 681-person trial, which ran

from November 2018 to August 2019, found 34% of patients who received the cocktail died within 28 days, compared with 51% of the people in the group that received the least effective treatment. Regeneron is providing the antibodies to the country for free to help it combat an ongoing outbreak.

U.S. funds new reactor designs

NUCLEAR ENERGY | The Department of Energy (DOE) announced last week it will fund two innovative new nuclear reactors that aim to be safer and cheaper than conventional power reactors. In a

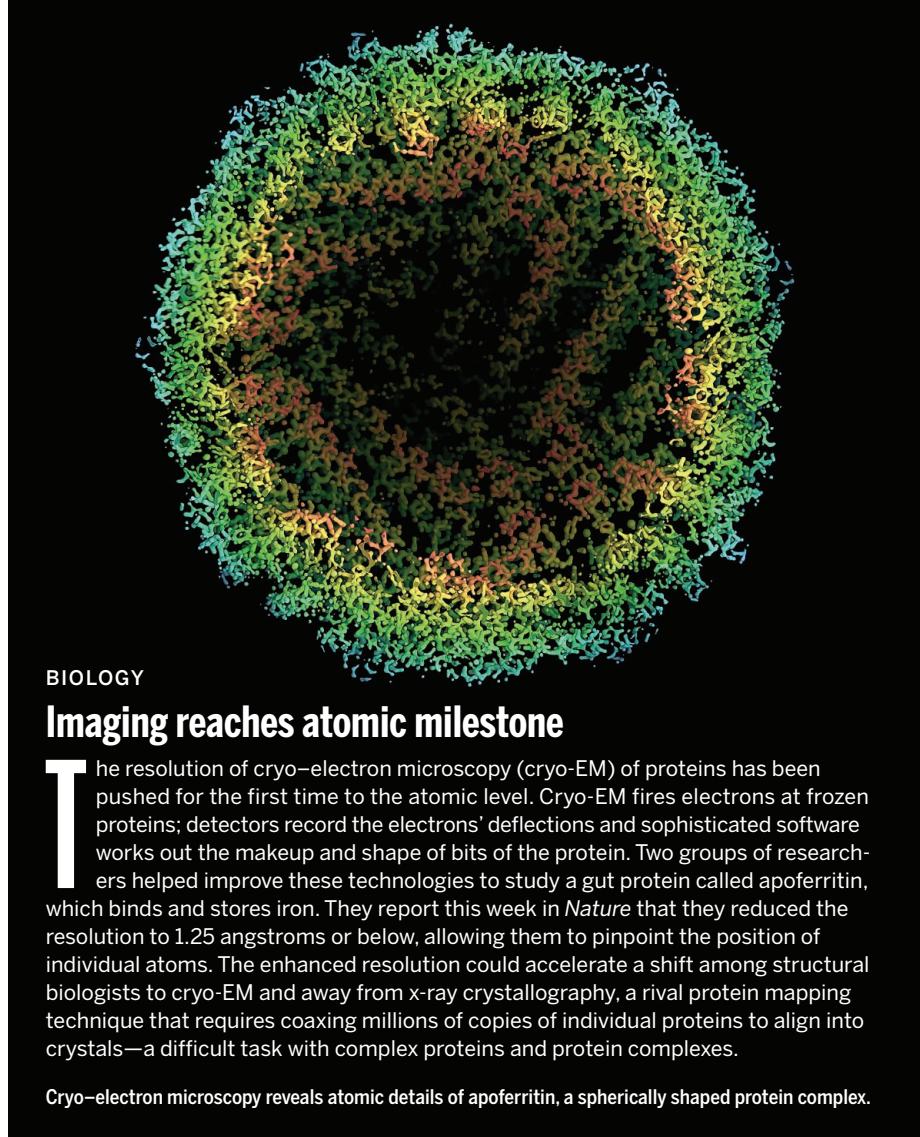
conventional reactor, pressurized water cools the uranium fuel and ferries heat to an external steam generator. In contrast, the Sodium reactor from TerraPower and GE Hitachi would use molten sodium metal as the coolant. The sodium would not need to be pressurized, reducing the reactor’s complexity. The second design, the Xe-100 from X-Energy, would use pressurized helium gas to cool its fuel, which would be packaged in unmelttable, tennis ball-size spheres of graphite. Each project will receive \$80 million this year and could get a total of \$4 billion over 7 years from DOE—if private partners pony up an equal amount.

Millions of lab animals missing

PUBLICATIONS | Most animals used in biomedical experiments are not accounted for in published papers, a first-of-its-kind study suggests. Worldwide, millions of animals may be missing from articles, say authors of the analysis in *BMJ Open Science*. They compared the more than 5500 animals mentioned in applications to oversight boards at University Medical Center Utrecht in 2008–09 with the numbers mentioned in papers resulting from those projects. Small animals, including mice, rats, and rabbits—which made up 90% of the total—were most often missing in action. Only 23% of them showed up in publications, versus 52% of sheep, dogs, and pigs. Scientists surveyed blamed factors including animal studies that go unpublished because they lack statistical significance. One solution: In 2018, researchers launched the first online registry, preclinicaltrials.eu, in which animal research protocols can be registered and tracked.

In India, nostrums for COVID-19

PUBLIC HEALTH | India's health ministry has begun to recommend traditional remedies for people afflicted by the country's burgeoning COVID-19 epidemic, dismaying many doctors and scientists. On 6 October, health minister Harsh Vardhan endorsed new treatment guidelines based on Ayurveda, India's millennia-old medicine system, that includes therapies such as clarified butter applied inside the nostrils; a hot concoction of pepper, ginger, and other herbs; and a patented herbal formulation called Ayush-64. Because no trials have shown any of the therapies to be effective, Vardhan is "inflicting a fraud on the nation and gullible patients by calling placebos as drugs," the Indian Medical Association wrote in a press release. The push for Ayurveda is in line with the Hindu nationalist government's mission to revive traditional medicine. With 7.5 million COVID-19 cases and more than



BIOLOGY

Imaging reaches atomic milestone

The resolution of cryo-electron microscopy (cryo-EM) of proteins has been pushed for the first time to the atomic level. Cryo-EM fires electrons at frozen proteins; detectors record the electrons' deflections and sophisticated software works out the makeup and shape of bits of the protein. Two groups of researchers helped improve these technologies to study a gut protein called apoferritin, which binds and stores iron. They report this week in *Nature* that they reduced the resolution to 1.25 angstroms or below, allowing them to pinpoint the position of individual atoms. The enhanced resolution could accelerate a shift among structural biologists to cryo-EM and away from x-ray crystallography, a rival protein mapping technique that requires coaxing millions of copies of individual proteins to align into crystals—a difficult task with complex proteins and protein complexes.

Cryo-electron microscopy reveals atomic details of apoferritin, a spherically shaped protein complex.

115,000 deaths, India may soon replace the United States as the hardest hit country.

Ironclad beetle takes the pressure

PHYSIOLOGY | A beetle little larger than a grain of rice has a body so tough it survived being run over by a car—a finding that could be used to build superstrong parts for bicycles, cars, and even airplanes, researchers say. The toughness of the diabolical ironclad beetle (*Phloeodes diabolicus*), native to the western United States, stems

from the unusual design of its outer wing cover, which has seams like joined jigsaw puzzle pieces, the authors report this week in *Nature*. The insect can withstand crushing forces equivalent to 39,000 times its body weight—about four times more than the strongest humans exert when squeezing it between the thumb and forefinger. Jesus Rivera of the University of California, Riverside, and his co-authors filmed the beetle's car encounter, and the video can be seen at scim.ag/ironcladbeetle.

Pandemic delays cancer tests

BIOMEDICINE | Cancer screenings plummeted during the first months of the coronavirus pandemic as medical offices closed and patients canceled visits, presaging a rise in U.S. cancer deaths, according to *The Wall Street Journal*. The newspaper compiled data from oncology offices, labs, health insurers, and other sources. Some screening visits rebounded by September, but even a few months' delay can mean cancers are detected at a larger, deadlier stage.

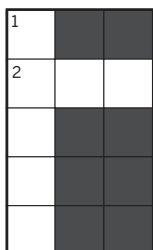
CROSSWORD

A political puzzle

1. Who's the obscure health adviser President Donald Trump put on the map?

2. What three letters explain a fight over astronomy in Hawaii?

If mixing science and politics doesn't make you cross, try your hand at the first News from *Science* crossword puzzle, part of our election 2020 coverage. The interactive version, at scim.ag/crossword, includes 44 clues and a print option.





IN DEPTH

COVID-19 patients in Mar del Plata, Argentina, one of 30 countries taking part in Solidarity.

COVID-19

Global trial eliminates drugs, pivots to new ones

Definitive results on remdesivir and interferon demonstrate power of massive WHO study

By Kai Kupferschmidt

When U.S. patients began to fall sick with COVID-19 earlier this year, Louis Staudt and Wyndham Wilson had an idea for how to help them. The two doctors at the National Cancer Institute had shown that acalabrutinib, a drug they helped develop for some types of lymphomas, has the side effect of dampening part of the immune response. Given the damage the immune reaction to SARS-CoV-2 creates in severely sick patients, acalabrutinib might have a positive effect, Staudt and Wilson reasoned.

Now, their idea is about to be tested in one of the world's largest studies of COVID-19 therapies: the Solidarity trial, organized by the World Health Organization (WHO). That's not because the drug holds so much promise—the evidence it might work is scant—but because Solidarity researchers have crossed more promising drugs off their list and are ready to try something new.

On 15 October, WHO released Solidarity's preliminary results for drugs that had raised earlier hopes—and they're a disappointment. The trial confirmed previous studies showing the antimalarial drug hy-

droxychloroquine and the HIV drugs lopinavir and ritonavir don't reduce mortality. It also dashed hopes for the much-touted antiviral remdesivir (given to U.S. President Donald Trump) and for interferon beta, part of the body's natural defense against viruses. "The take-home from this is that the cavalry is not coming," says Ilan Schwartz, an infectious disease researcher at the University of Alberta, Edmonton.

But the results also demonstrated the power of the trial itself, which has enrolled more than 11,000 patients in 30 countries, to quickly sort through available drugs. "It's disappointing that none of the four have come out and shown a difference in mortality, but it does show why you need big trials," says Jeremy Farrar, director of the Wellcome Trust. WHO now plans to use this machinery, which enlists 2000 patients every month, to test additional "repurposed" drugs such as acalabrutinib, as well as therapies designed for COVID-19.

NOTHING PARTICULARLY PROMISING

Designed in a hurry in March, Solidarity initially included the four seemingly promising treatments. But WHO decided to drop hydroxychloroquine and ritonavir/lopinavir from the study after the United Kingdom's

large Recovery trial showed in June that they did not increase survival, and continued with remdesivir and interferon beta. Now, the WHO study has delivered its verdict, which is under review at *The New England Journal of Medicine (NEJM)* and released as a preprint on medRxiv.

An earlier, U.S. trial in more than 1000 patients published in *NEJM* on 8 October indicated that remdesivir shortened the median recovery time for survivors from 15 days to 10 days, although it did not reduce mortality. Two smaller trials found few significant benefits. The U.S. Food and Drug Administration granted the drug an emergency use authorization (EUA) in May for severe COVID-19 patients and later expanded it to include all patients.

Now, the Solidarity trial is reporting that 11% of 2743 hospitalized patients who received the drug died, versus 11.2% in a control group—a difference that could have arisen by chance. When the researchers pooled their data with those from the three other trials, they found a slight reduction in mortality that wasn't statistically significant either. "This absolutely excludes the suggestion that remdesivir can prevent a substantial fraction of all deaths," the researchers write. The study also did not find that the

drug delayed the need for ventilation or that it sped up recovery, although recovery time was harder to analyze because patients on study drugs had to stay in the hospital longer to complete their course.

Jason Pogue, a researcher at the University of Michigan College of Pharmacy, says he had hoped for a mortality benefit based on some suggestive data in a subset of patients in the U.S. trial. Now, Pogue says, “If your question to me is whether I think it still deserves an EUA status, I actually don’t.”

But the drug’s manufacturer, Gilead Sciences, which agreed to the study design and donated the drug, is casting doubt on the results. The study was not placebo-controlled; to keep it simple, patients in the control group just received the standard of care in their country. There was also “significant heterogeneity in trial adoption, implementation, controls and patient populations,” Gilead says in a statement.

But the lack of a placebo is less of a concern when looking at “hard” outcomes such as mortality, Schwartz says. “For an endpoint like death the fact that the trial is unblinded is going to have a meager if any effect,” he says. And Pogue says the diversity in patient populations is one of Solidarity’s strengths: “I actually think that makes the study more robust [and] more reflective of everybody.”

Solidarity’s results for interferon beta are even more disappointing, says cardiologist Eric Topol, who heads the Scripps Research Translational Institute. Mortality among 2050 people who received that drug (either alone or in combination with lopinavir/ritonavir) was 11.9%, versus 10.5% in the control group. Prior studies have suggested interferon can only help if given early in the course of disease, however. “So I think that’s still an open question,” Topol says.

Solidarity has now dropped interferon beta from the study. The remdesivir arm will continue “to get more precise evidence,” says John-Arne Røttingen, CEO of the Research Council of Norway, who heads the executive group of Solidarity’s steering committee. But the treatment landscape now looks bleak, Schwartz says: “There’s really not a lot out there that looks to be particularly promising.”

HOPES FOR NEW DRUGS

The hopes for acalabrutinib rest on assumptions about its mechanism of action and experience in 19 very ill COVID-19 patients treated off-label so far. Five of those died, Staudt and colleagues reported in June in *Science Immunology*, but most patients’ oxygen levels quickly improved. (The authors included instructions for

mixing acalabrutinib with degassed Coca-Cola because it needs to be dissolved in acid: “Do not use other sodas, Diet Coke or Coke Zero,” they warned.)

Solidarity picked acalabrutinib in part because it’s plentiful. “This is a drug that is easy to synthesize and we have in stock,” says José Baselga, head of oncology at the manufacturer, AstraZeneca, which is running its own phase II trials in COVID-19 patients. Solidarity plans to start to give it to patients in the next few days.

Acalabrutinib might suppress damaging immune responses in much the same way as tocilizumab, a drug for rheumatoid arthritis and other autoimmune diseases that inhibits the signaling molecule interleukin-6 (IL-6). Tocilizumab has been tested against COVID-19 with mixed results and is now part of the Recovery trial, which might produce a definitive answer soon.

Acalabrutinib inhibits a different enzyme, however: Bruton’s tyrosine kinase (BTK). Staudt believes BTK sits at the center of the pathway that triggers immune cells in the lung to induce a so-called cytokine storm in COVID-19 patients. IL-6 inhibitors essentially cut off a branch of this response, he says, whereas “BTK inhibitors are cutting down the entire tree.”

Acalabrutinib may be one of the last repurposed drugs to be tested in large numbers of hospitalized COVID-19 patients. Targeted therapies such as monoclonal antibodies and new antivirals are seen as more promising, and some are starting to become available for large-scale testing. The Recovery trial now includes a combination of two monoclonal antibodies from Regeneron (another experimental therapy given to Trump). Another phase III trial in the United States, now on hold after it was paused on 13 October over a safety concern, is testing an antibody cocktail from Eli Lilly.

Solidarity, which is still expanding to new countries, could yield definitive results about any new therapy within a few months. It and Recovery “have set the standard of the scale that’s required in order to give you clear answers,” Farrar says.

Its global scope has another advantage, says Ana Maria Henao Restrepo, who heads WHO’s Research and Development Group. When the more than 1300 participating doctors see the results in *NEJM*, they will think: “I’ve contributed to that and I understand why that drug works or doesn’t work. I know, I trust it,” she says. “That is different from some Northern Hemisphere group publishing, and they say: ‘Somewhere in a rich country they did a trial and now we all have to believe the results.’” ■

COVID-19

First vaccine may stymie hunt for better ones

Should trials keep using placebos once an approved vaccine exists?

By Jon Cohen

Success in the push to find a COVID-19 vaccine at record-breaking speed could hand the world a new problem. The first vaccine to cross the finish line might be only marginally effective, yet ethicists warn it could disrupt ongoing studies of good—or even great—candidates in the wings.

In all likelihood, the U.S. Food and Drug Administration (FDA) or other regulators will issue the first approval or emergency use authorization (EUA) for one COVID-19 vaccine while clinical trials for many other candidates are still underway or in the planning. At that point, ongoing studies of any candidate—including that first one—arguably could become ethically bound to offer the vaccine with proven efficacy to everyone in a placebo group. “It’s a very vexing issue,” says Christine Grady, who heads the bioethics department at the National Institutes of Health (NIH) Clinical Center, which organized a “grand rounds” webinar on the challenges earlier this month.

“What’s really important is that the science does continue,” says Seth Berkley, who helps run the COVID-19 Vaccine Global Access Facility, an international effort to develop and manufacture a portfolio of COVID-19 vaccines. Berkley, who also heads the advocacy group Gavi, the Vaccine Alliance, predicts the world will need multiple vaccines against the pandemic coronavirus SARS-CoV-2. Not only might some work better than others, but factors such as cost or side effects mean some might offer benefits to specific groups, such as the elderly, pregnant women, or people in low-income countries.

According to the World Health Organization, 44 COVID-19 vaccine candidates were in clinical trials as of 19 October. Ten are in phase III trials, in which tens

Science’s
COVID-19
reporting is
supported by the
Pulitzer Center
and the
Heising-Simons
Foundation.

of thousands of participants randomly and blindly receive either the candidate or a placebo while their health is closely monitored. If efficacy signals surface along the way, vaccinemakers could seek EUAs before a trial's planned end date (see graphic, below). The EUA guidance issued by FDA stipulates that a candidate only needs to achieve 50% efficacy at preventing symptomatic COVID-19 and, as an added measure of safety, have had 2 months pass after roughly half the participants have received their final dose. (Russia and China have granted early approval for various vaccines but without any evidence of efficacy.)

Participants in the NIH webinar agreed that the first EUA for a COVID-19 vaccine will change the landscape for phase III trials, including the one for the permitted vaccine. Should people in the placebo group immediately receive that vaccine, or should the

says if early results for a COVID-19 vaccine candidate lead to an EUA, participants in that trial would have a right to know whether they had received a worthless placebo or a vaccine that potentially could help them. "It's a benefit that people in the trial should have access to," she contends.

Millum counters that the benefit to society of continuing a blinded trial can outweigh the risk to participants who receive the placebo. If the chance that a person in the trial would be exposed to SARS-CoV-2 is relatively low, he said at the webinar, then continuing the blinded study "could then be justified" in light of the need "to gather socially valuable information." This is especially true, he added, given that the world will likely benefit from having more than one COVID-19 vaccine, both because of the needs of different populations and so that supply can meet demand.

candidate be compared to the newly permitted product instead of a placebo. Such studies, known as a noninferiority or superiority trial, are slower and more costly than placebo-controlled trials. If a trial is already underway—especially if it is close to fully enrolled—investigators could explain to participants the value to society of continuing the blinded study. They might choose to stick with it, she says, especially if they were given this promise: "Whenever this trial is finished, we will give you the vaccine that's the most effective."

If the first proven vaccine only offers a modest benefit, Grady adds, participants may be more willing to continue in a blinded study, hoping to receive what might turn out to be a better vaccine. Many people in vaccine trials also have strong altruistic motives for participating, she notes. And if the first validated COVID-19 vaccine is scarce, the incentive to leave the trial may be lower. "If it's not available, it's not available," Grady says.

If an EUA or a full approval does disrupt vaccine trials, Berkley says, "bridging" studies could fill the gap. Researchers may identify immune factors that correlate with protection by the approved vaccine and then pivot efficacy trials to assessing whether other candidates trigger a similar response, avoiding a placebo comparison. (Researchers would have to inform potential participants that a proven vaccine existed, but they would not face the more serious ethical dilemma that a placebo presents.) Those correlates of protection might be enough proof of efficacy for an EUA or full approval of a COVID-19 vaccine. It's the same practice used to approve each year's influenza vaccine.

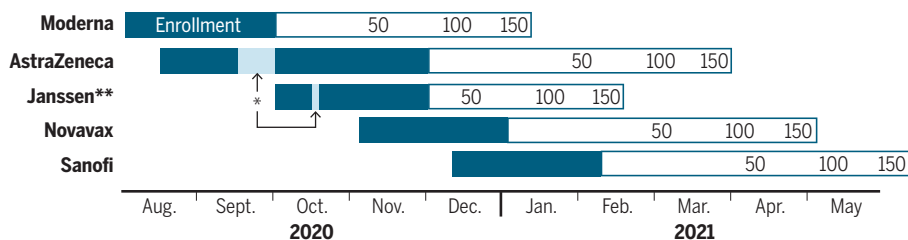
Bridging studies are also used after a vaccine proves itself in an efficacy trial to show that it works in different populations. "That's what's so beautiful about having the correlate of immunity and an understanding of the vaccine," Berkley says.

The telltale sign of efficacy for a COVID-19 vaccine, researchers suspect, will be antibodies that "neutralize" the spike, the surface protein of SARS-CoV-2, preventing the virus from infecting cells. If trials find that a certain level of these neutralizing antibodies does correlate with protection against infection or severe disease, it can serve as a benchmark for comparing vaccines in development to proven ones. "I think that's the way it will ultimately get done," Berkley says.

With an early vaccine approval possible by the end of the year, Grady says she's glad to see discussion of its possible unintended consequences. "This is something that everybody needs to be talking about." ■

Trials interrupted?

The placebo-controlled efficacy trials sponsored by Operation Warp Speed, the U.S. COVID-19 vaccine effort, plan to examine their data as different numbers of participants (roughly 50, 100, 150) develop disease symptoms or other "events." The interim data could lead to an early approval, complicating further vaccine testing.



*Concerning side effects led to a "hold" of the AstraZeneca trial on 8 September and a "temporary pause" on 13 October for the Janssen study.

**The Janssen vaccine candidate, unlike others shown, is given in one dose not two.

blinded trial continue, to make sure that the early benefits pan out over a longer period? Continuing the trial could also reveal rare side effects or shed light on the vaccine's efficacy in the elderly versus young adults.

And should ongoing phase III trials of other vaccines also replace their placebo with the vaccine that just showed efficacy? Will participants in those other trials drop out en masse? Will people refuse to even join new trials, reasoning that they can get a vaccine that already works to some extent?

For such questions, Grady says, the ethical equation "boils down to a fairly simple calculus": the individual versus the societal value. During the webinar, philosopher Joseph Millum framed the issue as "fundamental" to all clinical research. "Clinical research is ethically challenging because it exposes participants to risks for the benefit of others," said Millum, who works with Grady at the NIH Clinical Center.

Scientists and ethicists don't always solve the simple calculus the same way. Grady

Stanford University epidemiologist Steven Goodman agreed, stressing that vaccine studies differ "dramatically" from treatment trials, which aim to help people who have a disease. "If someone asked me whether a therapy for a serious disease should first be given to people participating in the control arms of the clinical trial testing that therapy," Goodman reasoned, "I would say, 'absolutely, yes.'" But people receiving a placebo in a vaccine trial don't need it the way sick people need a treatment, he argued. A widely used vaccine, he noted, can create "herd" immunity by reducing spread of a virus in a community. "If everyone around you has gotten a highly effective vaccine, you don't need it," Goodman said. "That shows that you don't have a problem that needs treating, but the population does."

Gaming out the impact of an EUA on other COVID-19 vaccine trials is even more complicated, Grady says. If a trial of a different candidate has yet to start, ethical considerations may demand that the

SCIENTIFIC PUBLISHING

Nature journals ink open-access deal

German pact has costs of €9500 per published article

By Jeffrey Brainard

A prominent publisher of selective subscription journals has stepped up its commitment to open access. This week, the Nature family of journals said it has struck a deal that will allow scientists at research institutions across Germany to publish papers in *Nature* and its 54 sister journals that are immediately free to read. Most of those journals have traditionally had paywalls, although they do allow authors to deposit articles in free public repositories such as PubMed 6 months after publication.

The deal, known as a transformative agreement, comes as research funders in Europe are pushing to demolish journal paywalls and redirect money spent on subscriptions to supporting open access. Many open-access journals support their operations by charging authors a processing fee, often more than \$2000 per paper. The Nature deal is different. Starting in January 2021, institutions can pay an annual fee that allows their scientists to publish an unlimited number of research articles in the journals that will be free to all readers. The fee will also include access to other types of Nature content, including the review articles that appear in 21 journals, that currently require a subscription to read.

Even if all 120 institutes in Germany that now subscribe to Nature's titles sign up, the publisher estimates their authors will publish no more than 400 papers per year in its journals. That would be about 3.5% of all articles published in *Nature* and its sister journals.

The fee each institution pays will be based in part on Nature's calculation that it will cost €9500 (\$11,200) to publish each open-access paper. Some institutions could end up spending more than they do now on Nature subscriptions, the publisher noted. It also said that Springer Nature, Nature's parent company, plans to roll out other ways for "authors around the world" to publish open-access articles in its journals. ■



Activists urge New York City residents to fill out the 2020 census.

DEMOGRAPHY

Census needs review, panel says

Statisticians call for evaluation of quality of 2020 U.S. count

By Jeffrey Mervis

An expert panel last week called for an independent group of researchers to pore over the billions of bits of information collected by a truncated 2020 U.S. census and report publicly on whether the Census Bureau has met its goal of "counting everyone once, and only once, and in the right place."

The report, from a task force of the American Statistical Association (ASA), was prompted by what ASA regards as unprecedented political interference by President Donald Trump's administration in the \$15 billion head count conducted by the nation's top statistical agency. "We are doing our best to support the Census Bureau because they have been put in a very difficult situation," says ASA President Rob Santos, who co-chaired the task force, which includes three former Census directors. "They don't have full control of their operations." Recent reports from two government watchdog agencies have voiced similar concerns.

The twist is the latest in the troubled 2020 census, which went live on 1 April after 10 years of planning. The COVID-19 pandemic delayed field operations, originally set to end on 31 July, and prompted the Trump administration to request additional time. But the White House later reversed course and announced it would seek an earlier end to field operations; it

also said it needed only three rather than 5 months to crunch the data.

Civil rights groups and local officials sued, fearing that truncated fieldwork would miss a disproportionate number of residents from minority, immigrant, and low-income communities. But last week a Supreme Court ruling enabled the Census Bureau to end operations on 15 October.

The groups had also pushed to extend by 4 months, to April 2021, the deadline for sending the president the final tally, which is used to determine how many seats each state gets in the 435-seat House of Representatives. But the administration has stuck to a 31 December deadline, creating what the task force fears is a formula for disaster.

The Census Bureau has "eliminated many quality-control steps," it asserts, and the agency's "current plan for quality assessment is unknown." The census "is a chain of many, many operations, and it is only as strong as its weakest link," says Nancy Potok, co-chair of the task force and a former deputy Census director.

Statisticians are also concerned about political meddling. Trump has ordered the agency to find ways to subtract undocumented residents from the count—a task that many legal scholars say is illegal and most data experts say is impossible (*Science*, 7 August, p. 611). And the recent arrival of three high-level political appointees at the traditionally nonpartisan agency has raised concerns that they will try to influ-

ence the analysis in order to give Republicans an advantage in House apportionment.

Commerce Secretary Wilbur Ross, whose department includes the Census Bureau, has downplayed those concerns. Last week, he said the census has met its goals because “99.9% of housing units have been accounted for.” But Potok calls that “a meaningless number” that can’t be used to measure data quality. For example, fieldworkers might have marked an address as counted even if they repeatedly failed to obtain any information from residents, or gleaned only incomplete information from “proxies”—for example, a neighbor or landlord.

“Ross says it’s possible [to have a quality census despite a truncated schedule],” Santos says. But internal government emails that have been made public as part of ongoing litigation “say that he’s living in a fantasy world,” he adds. “It’s sophistry.”

The task force report lists many indicators that the Census Bureau—and outside evaluators—could use to determine how close it has come to a complete count. They include the percentage of addresses enumerated by proxy, for example, or how much it relied on data already in government files to fill out a resident’s demographic profile, which are also less reliable than self-responses.

Statisticians could look, as well, at the percentage of records that lack a full name or date of birth, the number of duplicate enumerations, and how much information is being imputed. (Imputation means making an educated guess about the demographic characteristics of occupants based on indirect information, such as the type of housing unit or characteristics of the neighborhood.) Such data are readily available and accessible because this year’s census is the first in which field operations were conducted electronically.

This week, Census officials released data on the percentage of addresses enumerated by proxy and by using administrative data. Potok calls it “a good first step” but says researchers still need to assess the results at the smallest unit, covering a few city blocks.

What the outside experts learn could affect how Census Director Steven Dillingham presents the final tally. “He could tell the president he cannot submit a count, or that he doesn’t believe the numbers are accurate,” Potok says. “Or he could say that we’ve identified problems with the count that Congress might want to look into.”

Santos doesn’t think those scenarios are likely because they would require Ross’s support. But he says the task force wanted to “send a message” about the value of using an independent assessment “to restore public confidence in the 2020 census.” ■

RESEARCH FUNDING

In new strategy, Wellcome Trust takes on global health concerns

Giant philanthropy will focus on infectious disease, mental health, and the health effects of global warming

By Kai Kupferschmidt

One of the world’s largest non-governmental funders of science, the Wellcome Trust, is enlarging its focus to include goal-oriented, as well as basic, research. The London-based philanthropy, which spends more than £1 billion per year, said this week it will boost funding for research on infectious diseases, the health effects of global warming, and mental health. The new strategy moves it closer to philanthropies such as the Bill & Melinda Gates Foundation, which focuses on global health challenges. “It’s a big shift,” says Jeremy Farrar, an infectious disease expert who leads the charity. “It’s not just about discovering stuff, it’s also about making sure that changes come to peoples’ lives.”

Wellcome already funds research in infectious disease. But outbreaks are becoming larger, more frequent, and more complex, a Wellcome spokesperson says, and so it will spend more money on researching neglected tropical diseases and pushing for “clinical trials with greater participant diversity.” It also hopes to make an impact in new areas. The spokesperson argues that there has been “little scientific progress in 30 years” on mental health or on the health impacts of global warming, which include the spread of diseases and heat-related sickness and death.

Adding mental health is a big step, says Devi Sridhar, a global health expert at the University of Edinburgh who receives some Wellcome funding and who consulted on a review that led to the new strategy. “We haven’t really seen a charity take on the mental health agenda,” she says.

The strategy is likely to influence other funders because of Wellcome’s importance in the U.K. research system and beyond, says James Wilsdon, a science policy expert

at the University of Sheffield who is partly funded by Wellcome. “In a sense, where Wellcome moves, others quite often follow.”

Wellcome, which has seen its endowment rise to £28 billion (more than the \$22.6 billion of the Howard Hughes Medical Institute and less than the Gates Foundation’s \$50 billion), also plans to spend more money outside the United Kingdom. The trust wants to foster international cooperation as a counterweight to rising nationalism, Farrar says.

Farrar acknowledges that the new strategy is a departure from a focus on curiosity-driven basic research. “There are certain

challenges, where you can’t just leave it to the idiosyncrasies of discovery,” he says. “You have to have a greater sense of mission of where you’re trying to get to.”

He adds, however, that basic research will still be the major beneficiary over the next 3 to 5 years. That’s partly because Wellcome needs to develop expertise in areas like climate change. “The frank truth is we couldn’t put a huge amount of money into that space at

the moment and know quite where to use it,” Farrar says. Given Wellcome’s growing wealth, money for basic research could stay roughly at current levels while spending in the new priority areas ramps up, the Wellcome spokesperson says.

Helga Nowotny, a former president of the European Research Council (ERC), the EU basic research funding organization, says that is good news. As the coronavirus pandemic and climate change press down on society, research focused on urgent problems is in vogue, and often it comes at the expense of basic research. In a July budget deal, for example, European leaders proposed slashing the ERC budget in favor of more applied research. “The tendency to prioritize short-term-oriented research over discovery research has recently increased again,” she says. ■



Wellcome Trust head Jeremy Farrar is pushing for goal-oriented research.



LATIN AMERICA

Troubles escalate at Ecuador's young research university

Dozens of professors depart from Yachay Tech amid conflicts that could scuttle its move toward independence

By **Lindzi Wessel** and **Rodrigo Pérez Ortega**

It was supposed to become Ecuador's dream research university—an international hub for science and higher education, nestled in a new campus in the mountains 2 hours north of Quito. Instead, 6-year-old Yachay Tech University has long been mired in conflicts. Now, Ecuador's economic woes and shifting politics have stirred new turmoil that threatens the university's drive for "independent" status, which would allow it to run its own affairs.

The past year, dozens of professors were fired or left because of salary reductions or alleged mistreatment. The departures have left students struggling to enroll in courses or find thesis advisers, they say. On 13 October, Ecuador's Higher Education Council (CES) ordered the university to file a "clear and accurate report" within 10 days answering complaints and inquiries from two professors and a group of students.

The turmoil comes at a sensitive time. In Ecuador, new universities are established by the government but must go through a process called institutionalization, which includes awarding tenure to some faculty and democratically electing university leadership. Given the current chaos, Yachay

Tech will almost certainly miss the 31 December deadline for doing so, sources say.

Many blame the problems on mathematician Hermann Mena, who became university president in August 2019. "He is breaking everything apart," says Juan Lobos Martin, a Spanish materials scientist who has been at Yachay Tech from its start. "We've lost a lot of professors who have a lot of experience and teach very well." But Mena rejects those criticisms. In an interview with *Science*, he said seven professors were justifiably fired; the others left because of salary cuts he had to make after Ecuador's government slashed Yachay Tech's annual budget by 12%, or \$1.8 million. Administrative staff's salaries, including his own, have been cut as well, Mena says. "Everything we have done has been strictly by law."

Yachay Tech, ranked first in Ecuador for original research output by Nature Index last year, has been beset by conflicts about its course almost from the start in 2014 (*Science*, 28 July 2017, p. 340). Mena is already the eighth president.

Institutionalization has created fresh trouble. As part of the process, the university granted some 55 professors tenure starting in October 2018. But in March 2019, Ecuador's Secretariat of Higher Edu-

Yachay Tech University, launched in 2014, drew faculty from around the world to its brand new campus.

cation, Science, Technology and Innovation (Senescyt) suddenly froze the process after Mena, then a faculty member, and others claimed it was tainted by conflicts of interest. Senescyt ousted the sitting president and elevated Mena to the top job.

Since then, Yachay Tech administrative officials with little or no scientific training have re-evaluated current professors based on their CVs and recent output, university researchers say. Some saw their salary cut by up to 40%. "The process is not transparent," says Si Amar Dahoumane, a former biotechnology researcher at Yachay Tech. "Professors were not involved."

Foreigners, originally the majority of the teaching staff, bore the brunt of the scrutiny. More than 80% of the estimated 44 professors who left Yachay Tech since Mena took office are foreigners, faculty say, and of the few replacement hires, most are Ecuadorians. Computer scientist Israel Pineda, who is Ecuadorian, is dismayed that the university fired its translator and appears to have given up on its ambition to teach in English. "All of our major presence right now is in Spanish," Pineda says.

Some say politics plays a role. Yachay Tech was launched by then-Ecuadorian President Rafael Correa, a leftist who poured money into health and education; the current government appears to take little interest in his legacy, faculty members say. Senescyt's head, Agustín Albán Maldonado, did not respond to multiple interview requests.

It's not clear what will happen if the university misses the 31 December deadline, but some students worry about the university's survival. "Right now, we have many problems and no information from the authorities," says Diana Estefanía López Ramos, a biomedical engineering student and president of the Student Association. Mena's critics hope the CES inquiry will uncover some answers—and push Mena to rethink his decisions.

Mena acknowledges that "it seems that communication has not been the best," and says misinformation is circulating. His team will make key documents public soon, he says, and this week, the university posted a video about the controversies surrounding the tenuring process online. Mena says he still has confidence in the school's future. "The point is that Yachay is not a project anymore, we are a university," he says. "And the idea is to make it sustainable." ■

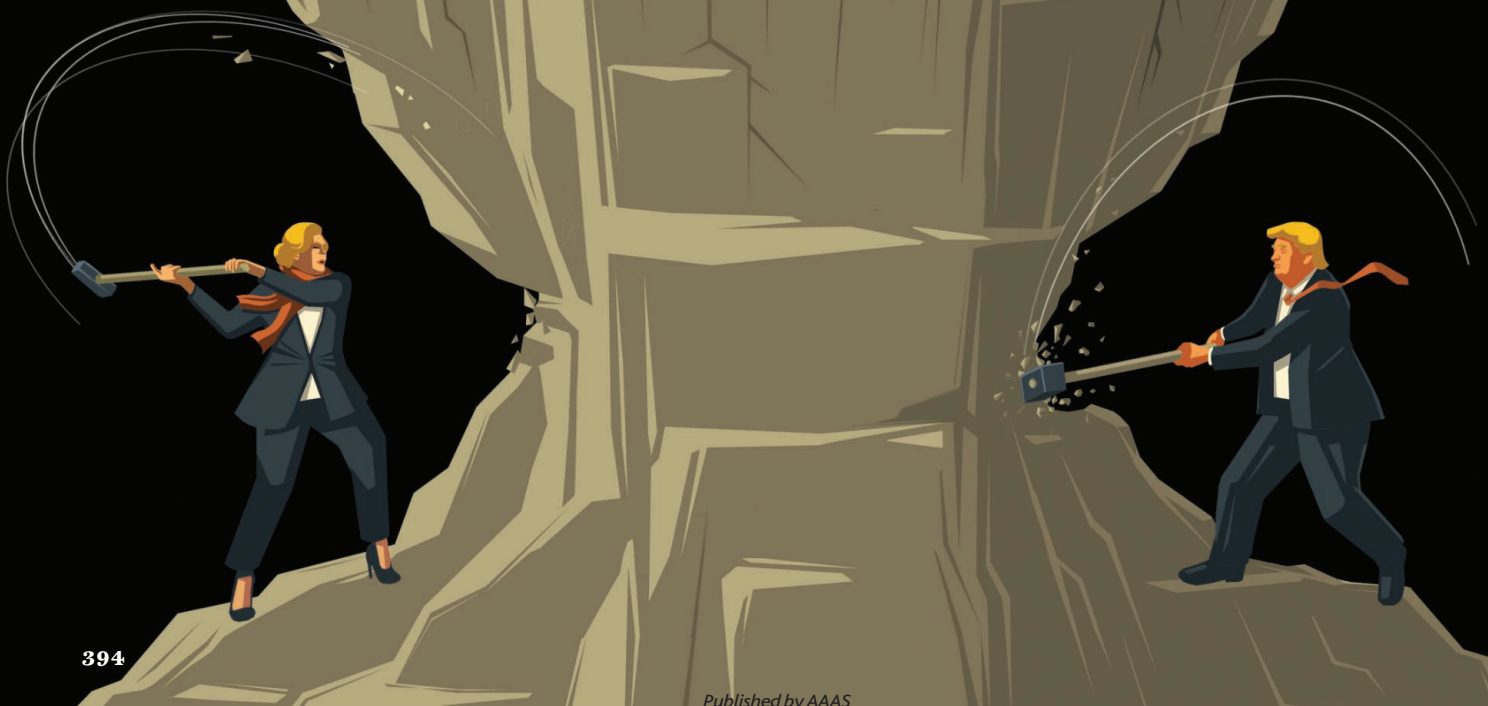
Lindzi Wessel is a journalist in the San Francisco Bay Area. Rodrigo Pérez Ortega is a science journalist in Mexico City.

PHOTO: MEDIOS PÚBLICOS EP/FUCKR CC BY-SA

UNDERMINING CDC

Deborah Birx, President Donald Trump's COVID-19 coordinator, helped shake the foundation of a premier public health agency

By Charles Piller



On the morning of 13 July, more than 20 COVID-19 experts from across the U.S. government assembled in a conference room at the Department of Health and Human Services, steps from the Capitol. The group conferred on how best to gather key data on available beds and supplies of medicine and protective gear from thousands of hospitals. Around the table, masks concealed their expressions, but with COVID-19 cases surging out of control in some parts of the country, their grave mood was unmistakable, say two people who were in the room.

Irum Zaidi, a top aide to White House Coronavirus Task Force Coordinator Deborah Birx, chaired the meeting. Zaidi lifted her mask slightly to be heard and delivered a *fait accompli*: Birx, who was not present, had pulled the plug on the Centers for Disease Control and Prevention's (CDC's) system for collecting hospital data and turned much of the responsibility over to a private contractor, Pittsburgh-based TeleTracking Technologies Inc., a hospital data management company. The reason: CDC had not met Birx's demand that hospitals report 100% of their COVID-19 data every day.

According to two officials in the meeting, one CDC staffer left and immediately began to sob, saying, "I refuse to do this. I cannot work with people like this. It is so toxic." That person soon resigned from the pandemic data team, sources say.

Other CDC staffers considered the decision arbitrary and destructive. "Anyone who knows the data supply chain in the U.S. knows [getting all the data daily] is impossible" during a pandemic, says one high-level expert at CDC. And they considered Birx's imperative unnecessary because staffers with decades of experience could confidently estimate missing numbers from partial data.

"Why are they not listening to us?" a CDC official at the meeting recalls thinking. Several CDC staffers predicted the new data system would fail, with ominous implications. "Birx has been on a monthslong rampage against our data," one texted to a colleague shortly afterward. "Good f---ing luck getting the hospitals to clean up their data and update daily."

When Birx, a physician with a background in HIV/AIDS research, was named coordinator of the task force in February, she was widely praised as a tough, indefatigable manager and a voice of data-driven reason. But some of her actions have undermined the effectiveness of the world's preeminent public

health agency, according to a *Science* investigation. Interviews with nine current CDC employees, several of them senior agency leaders, and 20 former agency leaders and public health experts—as well as a review of more than 100 official emails, memos, and other documents—suggest Birx's hospital data takeover fits a pattern in which she opposed CDC guidance, sometimes promoting President Donald Trump's policies or views against scientific consensus.

The agency's loss of control over hospital data is emblematic of its decline in nine short months. Since the pandemic began, CDC has floundered (see sidebar, p. 396). It has committed unforced errors, such as creating faulty coronavirus tests, and has been squelched amid political interference.



As coordinator of the White House Coronavirus Task Force, Deborah Birx, shown at a March news conference, has been accused of abetting the Trump administration's political interference with CDC.

CDC employees with whom *Science* spoke—who requested anonymity because they fear retaliation—along with other public health leaders, say Birx's actions, abetted by a chaotic White House command structure and weak leadership from CDC Director Robert Redfield, have contributed to what amounts to an existential crisis for the agency. And her disrespect for CDC has sent morale plummeting, senior officials say. During a May task force meeting, *The Washington Post* reported, Birx said: "There is nothing from the CDC that I can trust."

CDC scientists and others say Birx's record echoes her approach as head of the President's Emergency Plan for AIDS Relief (PEPFAR) since 2014. Although that program is widely praised, people who worked on it for

years say her draconian management and unrealistic data demands damaged morale and disrupted fieldwork and patient services.

Through the office of Vice President Mike Pence, who heads the task force, Birx declined to be interviewed or to respond to written questions, including whether the White House pressured her to use TeleTracking's system. (TeleTracking's majority owner, real estate developer Michael Zamagias, has donated to Republican candidates and has ties to Trump businesses through colleagues, according to an NPR report.)

Redfield also declined to be interviewed or to respond to written questions. In a statement, he said: "I will do everything in my power to support [CDC scientists] as I maintain my commitment to lead this agency

grounded in data, science, and public service."

Birx's admirers, including Emory University epidemiologist Carlos del Rio, credit her with sometimes pushing back against antiscientific White House policies. And Anthony Fauci, respected head of the National Institute of Allergy and Infectious Diseases and fellow task force member, has consistently praised Birx as someone who picks her battles to exert positive influence in the long run. He has suggested her recent trips to advise state health leaders have helped reduce COVID-19 cases.

"Birx is in a horribly difficult position," says Nancy Cox, former director of CDC's influenza division, now retired. "She wants to stay in the good graces of the president and the rest of the administration while trying

to do the right thing with respect to public health. Do I view her as a good scientist who gets things done? Yes.”

But Birx’s lack of background in respiratory disease outbreaks has left her with blind spots, as has her management style, Cox says. “Do I view her as someone who is willing to railroad people into doing what she has decided is the right thing to do? Yes. Does she listen real well? Not necessarily. One result was the debacle with the hospital data.”

The interviews and documents obtained by *Science* show Birx replaced a functional, if imperfect, CDC data system—well understood by hospitals and state health departments—with an error-ridden and unreliable filter on hospital needs that sometimes displays nonsensical data, such as negative numbers of beds. Such problems could hamper effective distribution of federal resources during an anticipated fall and winter spike in COVID-19 and flu cases, CDC officials say.

“This is the surreal part of it: They are attempting to replicate something we built over 15 years. And they are failing,” says a high-level CDC official with personal knowledge of the system. “Either Birx isn’t looking at the data, or she’s looking away—because it’s an absolute disaster.”

WHEN TRUMP INSTALLED Birx to coordinate the task force on 27 February, she was widely regarded as a strong choice, even by the president’s critics. Public health scientists hoped her “data driven” discipline, political adroitness, long-standing ties to Redfield, and military bearing—she spent 28 years in the Army—could insulate the pandemic response and CDC against some of Trump’s damaging impulses. Her new role gave her substantial authority over CDC (see organizational chart, p. 398).

At that point, the agency was already struggling. Among other mistakes, CDC had botched the rollout of its initial COVID-19 tests in early February. And the Trump administration had attacked or muzzled agency leaders for speaking basic truths and repeatedly forced CDC to soften its advice.

Birx appeared to have the experience to bolster the agency. She had worked as a fellow in cellular immunology under Fauci and later became lab deputy to Redfield at the Walter Reed Army Institute of Research (WRAIR), where he directed AIDS vaccine research. The pair co-authored numerous scientific papers during the late 1980s and early ’90s. When Redfield was investigated for possible misconduct after presenting overly rosy data on a “vaccine therapy” approach to AIDS treatment at a 1992 Amsterdam conference, Birx defended him to Army investigators. (The investigation found errors but cleared Redfield of misconduct charges.)

Soon after, Redfield retired from the military and Birx assumed his job at WRAIR. She rose to direct the U.S. Military HIV Research Program, then moved to CDC, directing its global AIDS project for 9 years. In 2014, then-President Barack Obama appointed her as global AIDS ambassador and head of the Department of State’s PEPFAR, seen by many people as an exemplary foreign aid program. It is credited with saving millions of lives in the developing world since its founding in 2003 and sharply lowering HIV infection rates among girls and young women, among other achievements.

Birx set out to strengthen PEPFAR data systems and move funds to where they could save the most lives, those familiar with the program say. “PEPFAR had a mandate of doing more with the same budget,” says del Rio, who chairs PEPFAR’s Scientific Advisory Board. Birx succeeded by “squeezing out inefficiencies, and being very data driven,” and by cutting drug costs, he says.

Sten Vermund, dean of the Yale School of Public Health, led PEPFAR programs in Africa under Birx and her predecessor, Eric Goosby. Vermund praises Birx’s “industry and science” and notes that his Mozambique program got more funding under her leadership. Birx also deftly shepherded PEPFAR into the Trump era with no budget cuts, says Amanda Glassman, executive vice president of the Center for Global Development, a Washington, D.C.- and London-based research group.

But Glassman and Vermund also agree that Birx made constant, burdensome, ur-

gent demands for data on HIV/AIDS cases, treatments, and other factors. Vermund says those demands sometimes disrupted services for patients. He describes some of Birx’s data demands as “almost whimsical” and their purposes opaque, calling her leadership style “authoritarian.”

That description is backed by a blistering audit of PEPFAR’s work in four African countries, issued in February by the Department of State’s inspector general (IG). Most of the PEPFAR staff whom auditors interviewed in 2019 said their input was ignored and that program heads, led by Birx, set unachievable benchmarks.

One PEPFAR staffer told auditors that a target for the number of people on antiretroviral therapy in one country was “greater than the number of people living with HIV.” Some staff described PEPFAR management as “autocratic” or “dictatorial.” One said high-level technical staff adopted an approach of “just obey and move on. ... Working in fear and a space where nothing is negotiable.”

Programs that missed data quotas could have their funding cut off, a situation a third staffer described as “a recipe for cooking data.” The data targets “put a lot of pressure on the [local] partners,” a fourth staffer told the IG investigators. “Sometimes, you are not even sure that the numbers are true. Especially when you go to the field and look at the [patient] registers. You cannot verify that they are real patients.” A CDC PEPFAR manager told *Science* that “Countries need the money,” so program staff manipulated data.

How CDC foundered

With stumbles such as flawed COVID-19 tests in February and confusing guidance on aerosol transmission of coronavirus in September, the Centers for Disease Control and Prevention (CDC) has sometimes been its own worst enemy during the pandemic. But the agency’s compromised standing derives mostly from attacks by President Donald Trump and his surrogates, often including Deborah Birx, coordinator of the White House Coronavirus Task Force (see main story, p. 394). The administration has muzzled agency leaders for speaking basic truths, manipulated CDC publications, and forced the agency to replace widely praised guidelines for reopening schools and the economy with weaker ones that sparked confusion and concern among health officials.

CDC Director Robert Redfield has quietly complied with many of the administration’s demands, although recently he has begun to push back. In August, former National Institutes of Health Director Harold Varmus and Rajiv Shah, president of the Rockefeller Foundation, wrote a scathing op-ed in *The New York Times* titled: “It has come to this: Ignore the CDC.”

“A major element of CDC’s success has been its willingness to tell the truth. ... It took decades to build up that public trust, and you can lose it fast,” says Jeffrey Koplan, who led CDC under former Presidents Bill Clinton and George W. Bush.

Recent polls reflect such concerns. In 2015, CDC was viewed favorably by 70% of the public, the highest for any agency measured. But in March, the percentage of the public that held a “great deal” of trust in CDC dropped to 46%. In September, it was only 19%.

CDC insiders say agency morale similarly plummeted. A top agency leader compared its role during the current pandemic to that during the swine flu, when CDC officials led federal public health actions and messaging. “In 2009, we were empowered and responsible,” the official says. “Now, we are disempowered, yet held responsible.” —C.P.

Vermund says his program never falsified data, but “we knew for a fact that others did not necessarily tell the truth, ... [using] exaggerations to make themselves look better.” He says some programs double-counted patients who entered treatment, dropped out, and then returned. “Perverse incentives were created based on the data-driven outcomes.” Despite the pressure, the audit showed, Birx’s data targets were often missed.

Amid the constant distraction of data demands, services to patients sometimes suffered, one staffer told the IG. That problem occurred in many PEPFAR nations, the CDC manager says.

In response to the IG report, Birx promised some reforms and “clearer, transparent dialogue.” She said local PEPFAR teams would set their own targets, although funding would be “adjusted to the presented level of ambition.” Before those actions were fully in place, Trump appointed her to coordinate the Coronavirus Task Force.

Del Rio isn’t surprised that some PEPFAR staff members were unhappy. “She’s a no-bullshit kind of person,” he says. “She’s not running a Montessori school.”

And Glassman notes that many women who attain powerful jobs face extra criticism or get tagged as authoritarian, whereas men with comparable leadership styles are simply accepted. “Is [Birx] getting pounded partially because she’s a woman?” she asks.

But Glassman concedes that despite good intentions, Birx’s style was “a disaster” at PEPFAR. And tying data targets to funding

without verification does invite misreporting, she says. “Her desire to get those results and show them to the world, I think, just overcame everything,” Glassman says.

Now, some CDC staffers say, Birx is applying the PEPFAR playbook to the new pandemic, and the dismantling of CDC’s COVID-19 hospital data system is a consequence.

AGENCY INSIDERS CONCEDE that CDC’s National Healthcare Safety Network (NHSN)—the system used for 15 years to gather crucial data from hospitals—was far from perfect. The network, which collects data from about 37,000 hospitals and other health care facilities, has been underfunded for years. All the same, five times weekly, NHSN reliably produced actionable COVID-19 data such as available hospital beds, intensive care occupancy, and ventilators used, according to CDC sources and internal reports obtained by *Science*. CDC staffers used long-tested statistical algorithms to impute missing data.

When NHSN was shut down for hospital COVID-19 data in July, more than 100 public health and patient advocacy groups, along with scientific and medical societies (including AAAS, which publishes *Science*), warned that the switch could degrade crucial data reporting. Attorneys general for more than 20 states echoed their concerns. (The system still collects COVID-19 data from nursing homes and other data from hospitals.)

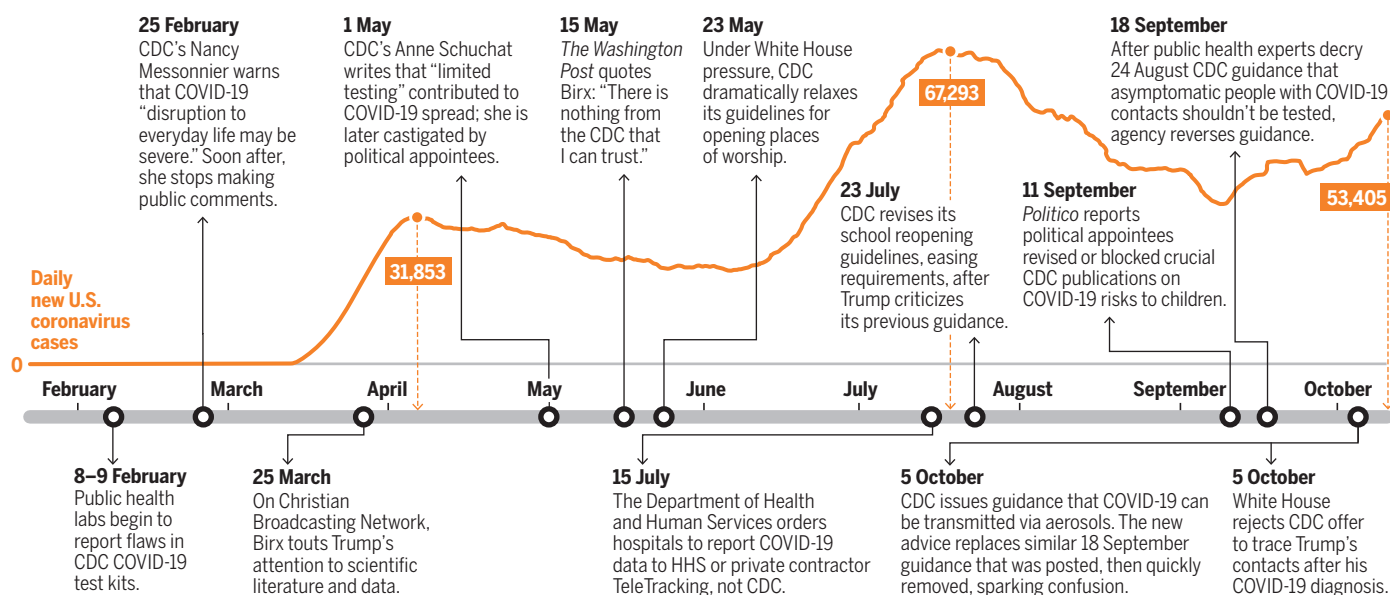
But del Rio says Birx viewed NHSN in a similar light as the data system she inherited

at PEPFAR in 2014—as woefully inadequate. Birx was exasperated, del Rio said, that NHSN could not provide daily, comprehensive data to guide the government’s efforts, for example on supplies of remdesivir, an antiviral medicine given to Trump.

In a spring meeting, Birx seemed fixated on applying the lessons of HIV/AIDS in a small African nation to COVID-19 in the United States, says a CDC official who was present. “Birx was able to get data from every hospital on every case” in Malawi, the official says. “She couldn’t understand why that wasn’t happening in the United States” with COVID-19. Birx didn’t seem to see the difference between a slow-moving HIV outbreak and a raging respiratory pandemic. “[CDC Principal Deputy Director] Anne Schuchat had to say, ‘Debbi, this is not HIV.’ Birx got unhappy with that.”

Birx insisted every hospital update 100% of its data every day, including detailed patient demographics. She added new data categories, such as patient age and supplies of remdesivir. CDC officials told her 100% daily compliance was virtually impossible, but said NHSN statisticians could accurately extrapolate from partial data, providing results “in near real time,” one official says.

Another CDC official charged with responding to Birx’s demands calls her “fixation and fetishization of those daily count numbers” deeply frustrating. Birx’s top assistants accused CDC employees who pushed back of being callous about COVID-19 deaths. The process assumed the tone of a



A crippled response

As more and more Americans have been sickened by the pandemic coronavirus, CDC has often provided confusing or weak public guidance. It made missteps of its own, but also suffered from many instances of political meddling by President Donald Trump, Deborah Birx, and others.

military command structure, the CDC official says: Obey without question. Echoing PEPFAR employees, the official adds that it seemed “designed to make you feel like you are failing every day.”

Birx “doesn’t really understand data,” says James Curran, public health dean at Emory University, who led CDC’s HIV/AIDS unit for 15 years. “I don’t think she’s asking the right questions. It doesn’t mean that the CDC is always right. But you should have a partnership with people.”

Instead, say CDC sources with direct knowledge of the events, Birx’s team made a demand: Immediately collect case data by age, or NHSN would be replaced.

When the switch to TeleTracking was announced, Redfield applauded it as a way

patient records. Some hospital associations and health departments combine data from hospitals into spreadsheets and send them by fax or email to HHS. TeleTracking also offers a web interface for hospitals or their contractors to enter data.

The underlying data tables are updated daily but run 3 to 4 days behind—less efficient than NHSN before it ceased operating. CDC officials and public health experts blame several factors for those problems: Hospitals aren’t used to TeleTracking’s system and the additional data points added work. Also, TeleTracking has long-standing relationships with fewer hospitals than NHSN; such relationships can speed troubleshooting.

In a 7 October written reply to questions, an HHS spokesperson acknowledged the

“filled with inaccuracies, misunderstandings, and errors,” without providing details, and questioned its authenticity.

But *Science* also obtained a report prepared by CDC data experts for use by the agency and Birx’s team dated 19 May, back when TeleTracking and NHSN were both offered as options for data submission. NHSN showed 3% to 6% missing data for items such as COVID-19 bed occupancy and ventilator use. TeleTracking showed 36% to 57% missing data. Those results were mostly unchanged, with significant improvement in only one category, in the 23 September update.

Like NHSN, the HHS system—based on data provided to TeleTracking or reported to HHS directly by the states—estimates missing data, but HHS declined to release details for independent analysis. CDC staffers say the system has other problems; for example, many hospitals share ID numbers, making it difficult to differentiate between each one’s needs. (In an email, TeleTracking wrote that it issues separate IDs for each hospital. But within the HHS system, the ID problem continues, according to a CDC official.) CDC critiques obtained by *Science* and data displayed on the HHS data hub also show the system has consistently reported nonsensical numbers. For example, it showed negative numbers and estimates of occupied hospital beds, as well as more than 15,000 beds for a single California hospital. In nearly 1500 cases, it showed more beds filled than total beds at a hospital.

TeleTracking referred questions to HHS, which said it plans to boost automation to reduce errors. For now, the HHS spokesperson wrote: “HHS made a conscious decision to take a different approach on data collection. ... Rather than reject incorrect data outright, HHS allows it to flow into our system” and then attempts to manually fix detected errors. A CDC data expert calls that “an admission of faulty data practices.”

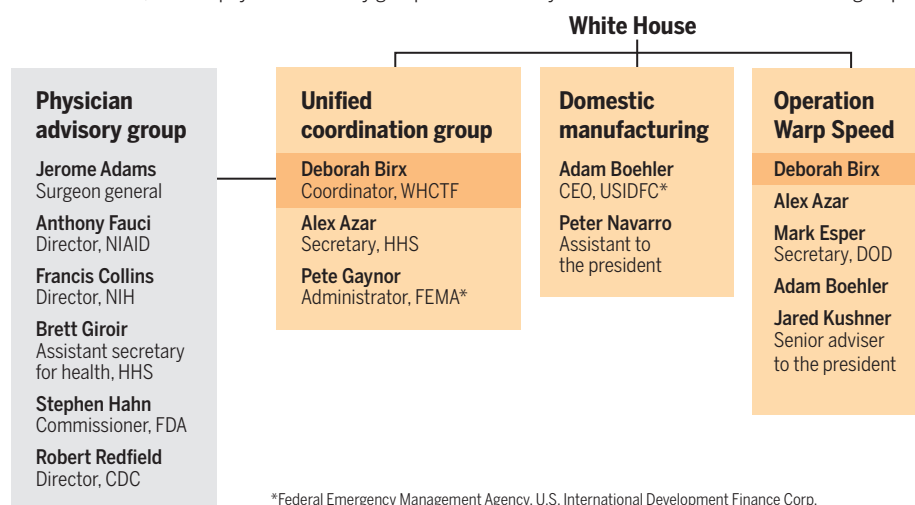
In a 25 September memo from Birx to HHS Secretary Alex Azar, obtained by *Science*, Birx gave up on elements of the daily 100% compliance rule that had motivated the switch to TeleTracking. For example, she instead asked that inventories of supplies, such as personal protective equipment, be provided weekly because more frequent reporting had proved infeasible.

During the 6 October press briefing, Birx said the moves “ensure that we are not adding additional burden” for hospitals. The key is “valid and timely data,” she said.

But in that same briefing, Birx and Centers for Medicare & Medicaid Services Administrator Seema Verma announced a new and stringent requirement reminiscent of PEPFAR: Funding will be tied to reporting compliance. Hospitals will be

Power in the pandemic

A “working organization chart,” issued on 31 July and obtained by *Science*, shows Deborah Birx’s central roles in the federal COVID-19 response. She coordinates the White House Coronavirus Task Force and co-chairs two of its three divisions: the unified coordination group, which manages the response from the departments of Health and Human Services (HHS) and Defense (DOD); and Operation Warp Speed, which works with agencies to develop vaccines. The domestic manufacturing group coordinates production of personal protective gear and other needs, and the physician advisory group has an advisory role. Listed individuals co-chair the groups.



to “streamline reporting.” He also tweeted that the decision was made at “working levels” in CDC and didn’t rise to his level. Many people in CDC saw his comments as a betrayal.

BIRX’S IMPERATIVE of 100% of hospital data every day has proved elusive. The Department of Health and Human Services (HHS) data hub for hospital capacity, including inpatient beds occupied overall and by COVID-19 patients, now draws on data collected by TeleTracking, a for-profit company with nearly 400 employees, and on data submitted by state health departments and hospital associations. As with NHSN, nearly all data are collected manually rather than automatically from electronic

time lag but called it “a good practice to provide the most complete dataset” because hospitals might not be able to respond on weekends, for example. But HHS plans to reduce the lag, the spokesperson wrote.

At a 6 October press briefing, Birx said 98% of hospitals were reporting at least weekly and 86% daily. In its reply to *Science*, HHS pegged the daily number at 95%. To achieve that, the bar for “compliance” was set very low, as a single data item during the prior week. A 23 September CDC report, obtained by *Science*, shows that as of that date only about 24% of hospitals reported all requested data, including protective equipment supplies. In five states or territories, not a single hospital provided complete data.

HHS said the 23 September analysis was

disqualified from Medicare and Medicaid reimbursements if they fail to submit required data after being warned of lapses. The memo from Birx to Azar, marked “not releasable to the public,” shows Birx pushed for the change.

The move is “sledgehammer enforcement” that could needlessly divert time and money from patient care, Federation of American Hospitals President and CEO Charles “Chip” Kahn said in a statement.

As at PEPFAR, CDC officials say this requirement could create “perverse incentives” to supply false data. Medicare funding is vital for hospitals, so many are likely to submit the requested numbers regardless of whether they are accurate, say three high-level CDC officials.

HHS cited safeguards against such fraud, including help from state health departments and “systematic logic and error checking.” The department’s IG also identifies fraud aggressively, the spokesperson wrote.

However, the potential long-term impact keeps CDC staffers up at night, one says. “I worry, is this going to damage the whole process of how public health data are collected down the road?”

BIRX ACQUIRED HER OUTSIZE influence over the agency in part because of how power was allocated in the federal pandemic response, CDC staffers say. An organizational chart obtained by *Science*, marked “for official use only,” shows Birx coordinates the task force and co-chairs two key bodies: the unified coordination group, which manages the response from HHS and therefore CDC; and Operation Warp Speed, the vaccine development effort. A physician advisory group, comprising Fauci, Redfield, National Institutes of Health Director Francis Collins, and others—is off to the side. Senior CDC people say those advisers have been reduced to “window dressing,” with little ability to mediate between Birx and CDC.

The hospital data system is perhaps the most calamitous flashpoint in that relationship. But CDC officials say that, in other instances, Birx flouted science and undermined the agency to placate the president. For example, she responded with silence to Trump’s suggestion that injecting disinfectants might cure COVID-19. And according to the nonpartisan FactCheck.org, in March she understated the pandemic’s spread by “misleadingly” portraying states with few cases as “almost 40% of the country,” although those states make up only about 7% of the population.

“Dr. Birx, what the hell are you doing?”

What happened to you? Your HIV colleagues are ashamed,” tweeted Yale AIDS expert Gregg Gonslaves in response.

And she pressured CDC to tone down its guidance on school openings, according to *The New York Times*; it published an email she wrote asking Redfield to take a more permissive approach.

Several CDC leaders say Birx’s distrust and rejection of input from CDC data experts has created enormous animosity. “She calls into question the science of the agency,” says a current senior CDC official. “We’re not perfect ... but in the midst of a crisis, to indicate that one of your chief arms for responding to a very severe pandemic can’t be believed” has been disastrous.

Birx’s supporters say she has done as well

sort for our usual way of operating, whereas that’s the modus operandi for this administration and the White House task force,” the official says. “We need people who think like we do. I’ve heard that stated in multiple instances” by Birx’s top assistants, the official adds. “It’s not scientific.”

Many executives and midcareer professionals who represent the future of the agency plan to leave if Trump wins reelection, several sources say. Public health authorities wonder whether CDC has already passed a tipping point, from which it will struggle to recover no matter who is elected.

The implications of a discredited CDC for the COVID-19 pandemic are grave, says Thomas Frieden, who led the agency un-



CDC Director Robert Redfield, shown at its Atlanta headquarters, has been criticized for failing to robustly defend the agency against political interference.

as anyone can working for Trump. “She can navigate science and politics,” del Rio says. “I don’t think anybody can navigate science and Trump.” Birx has resisted some of Trump’s claims, even persuading Pence to sometimes wear a mask. In August, she described the pandemic to CNN as “extraordinarily widespread,” losing some favor with Trump.

Even critics within CDC give Birx qualified credit. Her consistent push for widespread COVID-19 testing has “gotten crosswise with the White House,” says a top CDC official, who adds: “At her core, she’s a scientist.”

But that official and others also see Birx as a cautionary tale of how an ostensibly well-meaning expert can cause great harm by working in the style of the Trump administration. “Bullying and threatening is a last re-

der Obama. If the public doesn’t trust government guidance to take vaccines when available, he says, the pandemic could rage indefinitely. “Breaking that trust could cost our economy—and American lives.”

Senior career executives at another beleaguered agency, the Food and Drug Administration, recently called for preservation of their scientific independence in a *USA Today* editorial. At CDC, leaders below Redfield are talking privately about whether to take a similar public stand against the destruction of their agency by the Trump administration. One says: “The longer we don’t speak out, the harder it will be to regain our credibility.” ■

This story was supported by the Science Fund for Investigative Journalism.

Polyethylene waste, such as grocery bags, is of low value for recycling. “Upcycling” to more valuable products could save it from landfills.



PERSPECTIVES

POLYMER CHEMISTRY

Creating value from plastic waste

Polyethylene can be upcycled into alkylaromatic compounds for the production of detergents

By **Bert M. Weckhuysen**

Plastic waste presents a number of environmental problems (1–3). Although only a small fraction of it enters rivers, lakes, and oceans, it can be transformed there into micro- and nano-plastics that are harmful to aquatic organisms. When plastic waste is buried in landfills or incinerated, it generates heat and carbon dioxide. However, plastic waste also offers great opportunities if its economic value can be increased substantially through upcycling processes that convert it into more valuable chemical products. On page 437 of this issue, Zhang *et al.* (4) report on an upcycling process that converts polyethylene

(often used for packaging and grocery bags) into long-chain alkylaromatics that can be sulfonated to make biodegradable surfactants. This process operates at a moderate reaction temperature, does not need any solvent or added hydrogen, and produces only a small amount of light-gas by-products such as methane.

Chemical recycling has emerged as a promising technology to valorize waste plastics (5, 6). Plastics can be gasified into hydrogen and carbon monoxide (synthesis gas) as a feedstock for fuel production. Pyrolysis and solvolytic routes can convert polymers back into monomers and oligomers that, after purification, can be repolymerized. Unfortunately, the low cost of virgin monomer from fossil carbon-based feedstocks and the lack of regulatory incentives often make chemical recycling commercially unattractive.

One way to overcome this economic hurdle is to convert waste plastics into value-added materials or chemicals. Several approaches have been explored, which include the use of waste plastic to make battery electrodes or photovoltaics films (7, 8). With regard to the upcycling of polyethylene, Bäckström *et al.* recently reported on the selective conversion of high-density polyethylene (HDPE) waste into succinic, glutaric, and adipic acid, which could be converted into plasticizers for polylactic acid (PLA) processing (9).

Zhang *et al.* present an innovative catalytic process in which two chemical reactions, hydrogenolysis and aromatization, are combined. They produce long-chain alkylaromatics from a low-molecular-weight polyethylene model compound for plastic waste with a commonly used heterogeneous catalyst, platinum (Pt) nanoparticles dis-

Inorganic Chemistry and Catalysis, Debye Institute for Nanomaterials Science, Utrecht University, 3584 CG Utrecht, Netherlands. Email: b.m.weckhuysen.uu.nl

PHOTO: VCHAL/ISTOCK.COM

persed on an alumina (Al_2O_3) support (see the figure). An essential step is the in situ synthesis of hydrogen through the dehydroaromatization reaction of shorter hydrocarbon chains, which leads to the formation of aromatic compounds. These chains can be made from longer hydrocarbon chains through a hydrogenolysis reaction that requires hydrogen as reactant.

A delicate balance between these two catalytic reactions must be maintained to avoid the unnecessary production of less valuable gases, such as methane, ethane, and propane, as well as carbon (coke) deposits that may lead to catalyst deactivation. Fine-tuning was realized by opting for a moderate reaction temperature (280°C), because higher reaction temperatures (e.g., 330°C) led to production of gases and volatile hydro-

plete mechanism, including proper reaction kinetics, of this upcycling process. For example, they noted that a higher amount of hydrogen formed than was anticipated, and also observed a wider range of aromatics. Notwithstanding, the authors noted a competition between adsorbed polyethylene chains and alkylaromatics on the platinum surfaces, in that alkylaromatics adsorb more strongly than polyethylene. The higher temperatures needed to desorb these products also enhanced hydrogenolysis activity and led to a larger fraction of light gases in the outlet stream.

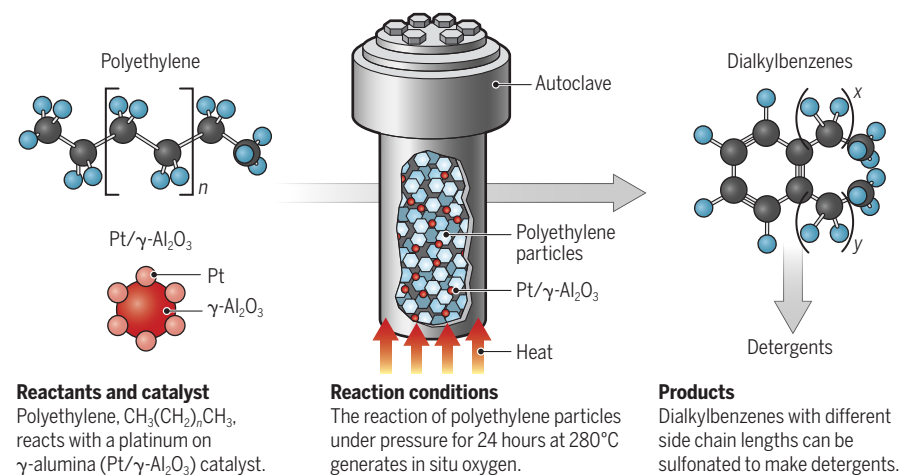
The acid sites of the Al_2O_3 support also play a role in these reactions. This acidity may promote competing processes, such as β -scission reactions, but very little of the expected light olefin products was detected.

(10, 11). The catalyst performance could be largely maintained, and the observed decreases in activity could be correlated with a lower Pt surface area. Although these metals, such as chromium, titanium, and zirconium, are present in only small amounts in plastic waste, they can influence both the activity and selectivity of the Pt catalyst. The chosen Pt/ Al_2O_3 catalyst can be further optimized and made more resistant to coking and metal deactivation. Cheaper alternatives based on non-noble metals, as well as other support oxides with different acid-base properties, should also be explored.

Zhang *et al.* have developed a promising tandem catalysis route to convert plastic waste into valuable chemical building blocks, from which daily life products can be manufactured (4). Several other tandem combinations are possible, although some of them may require solvents to separate the product ionic or oxygenated compounds from the plastic waste mixture. These new plastic-solvent-process combinations will unlock potential methods for dealing with real-world plastic waste that may contain plasticizers, inks, and dyes, or are mixed with other polymers. Most likely each type of plastic will require a specific chemical conversion process to be upcycled (5). When this can be realized, non-fossil-based plastics may become more economically attractive as carbon atoms can be recycled and chemical functionality can be reintroduced in a high-value product. These developments will pave the way toward a circular plastics economy, in which plastic is not considered waste but rather a valuable raw material (12). ■

From plastic waste to detergents

Zhang *et al.* upconverted polyethylene waste into aromatic compounds that could be used to make more valuable products such as detergents.



carbons. The partial pressure of hydrogen was high enough to realize hydrogenolysis but low enough to avoid hydrogenation of the valuable alkylaromatics formed.

The authors also used a low-density polyethylene (LDPE) plastic bag as well as a HDPE water-bottle cap to explore their upcycling process for treating actual plastic waste. Although the catalytic yields were somewhat lower than for the conversion of the low-molecular-weight polyethylene model compound, these experiments indicated that polymer density and degree of branching did not largely influence the developed tandem hydrogenolysis-aromatization process. The authors' upcycling process produced long-chain alkylaromatics and alkylnaphthenates with an average number of ~30 carbon atoms and in a yield of ~80% by weight.

Despite their experimental efforts, Zhang *et al.* were not yet able to develop a com-

Shorter or longer contact times between feedstock and catalyst material will affect the carbon and hydrogen transfer reactions taking place on the Pt surface. More characterization studies, including labeling experiments in combination with advanced product analysis, are needed to elucidate the different reaction pathways, which can be taken by various catalyst systems. This knowledge should lead to the selective production of aromatics (benzene, toluene, and xylene) to make polymers (such as polystyrene, polyurethane, and polyester), cyclohexanes (a component of jet and gasoline fuels), or alkylaromatics (used to make detergents and lubricants).

Zhang *et al.* also performed catalyst stability tests by performing three consecutive runs with the Pt/ Al_2O_3 catalyst. This experiment sought to clarify the long-term effect of trapped metal polymerization catalysts

REFERENCES AND NOTES

1. D. Cressey, *Nature* **536**, 263 (2016).
2. G. Lopez, M. Artetxe, M. Amutio, J. Bilbao, M. Olazar, *Renew. Sustain. Energy Rev.* **73**, 346 (2017).
3. A. Rahimi, J. M. Garcia, *Nat. Rev. Chem.* **1**, 0046 (2017).
4. F. Zhang *et al.*, *Science* **370**, 437 (2020).
5. I. Vollmer *et al.*, *Angew. Chem. Int. Ed.* **59**, 15402 (2020).
6. G. W. Coates, Y. D. Y. L. Getzler, *Nat. Rev. Mater.* **5**, 501 (2020).
7. P. J. Kim, H. D. Fontecha, K. Kim, V. G. Pol, *ACS Appl. Mater. Interfaces* **10**, 14827 (2018).
8. D. Choi, J. S. Yeo, H. I. Joh, S. Lee, *ACS Sustain. Chem. Eng.* **6**, 12463 (2018).
9. E. Backström, K. Odelius, M. Hakkarainen, *ACS Sustain. Chem. Eng.* **7**, 11004 (2019).
10. M. P. McDaniel, *Adv. Catal.* **53**, 123 (2010).
11. M. Stürzel, S. Mihan, R. Mülhaupt, *Chem. Rev.* **116**, 1398 (2016).
12. J. B. Zimmerman, P. T. Anastas, H. C. Erythropel, W. Leitner, *Science* **367**, 397 (2020).

ACKNOWLEDGMENTS

B.M.W. is supported by the Netherlands Organization for Scientific Research (NWO) in the frame of a Gravitation Program, MCEC (Netherlands Center for Multiscale Catalytic Energy Conversion), as well as from the Advanced Research Center (ARC) Chemical Buildings Blocks Consortium (CBBC), a public-private research consortium in the Netherlands.

10.1126/science.abe3873

PHYSIOLOGY

Forming a mucus barrier along the colon

Optimal barrier function requires both proximal colon- and distal colon-derived mucus

By **George M. H. Birchenough** and
Malin E. V. Johansson

The intestine is exposed to numerous hazards and is heavily colonized by microorganisms. This requires a balanced protective system, which includes secreted mucus layers that play an important role in keeping luminal contents, including bacteria, separated from the epithelium (1). Intestinal mucus contains many different proteins, and the densely O-glycosylated mucin 2 (MUC2) is the core molecule (2, 3). Colonic mucus defects that allow bacteria to reach the epithelium have been associated with colitis (4). On page 467 of this issue, Bergstrom *et al.* (5) expand our understanding of the colonic mucus system by showing that mucus from proximal colonic regions contributes extensively to forming the protective barrier in the distal colon. This work highlights the role of the colonic tissue as a whole in driving mucus barrier formation and indicates the potential for regionally targeted therapeutic interventions in intestinal disease.

Mucus coating on distal colonic fecal material has been previously observed (6), but Bergstrom *et al.* used glycan-specific lectin staining of fixed whole mouse colons to differentiate between differently O-glycosylated mucus originating from proximal and distal colonic regions. They found that proximal colon-derived mucus primarily encapsulates fecal pellets as they form and is further strengthened by a secondary encapsulation of mucus produced in the distal colon. Thus, mucus from both regions is associated with the excreted pellet. The authors showed that regions between pellets normally harbor relatively low numbers of bacteria compared with mucus-encapsulated pellets. Inducing mucus defects in the proximal or distal colon of mice increased the bacterial load in areas between pellets. This enhanced contact between uncontained bacteria and the epithelium led to inflammation that was most pronounced in the distal colon. Simultaneous disruption of the proximal- and distal-derived mucus resulted in se-

vere loss of barrier function, highlighting the need for cooperation between proximal and distal mucus production in maintaining the protective barrier.

It should be noted that analysis of mucus in fixed tissue sections is challenging because secreted mucus is highly hydrated and shrinks upon exposure to chemical fixatives. In addition, secreted mucus is rarely preserved in fixed intestinal tissue that does not contain fecal material. Indeed, analysis of mucus in live tissue demonstrates that it forms a continuous attached layer on the epithelium throughout the intestine (7–9). This attached mucus contains several com-

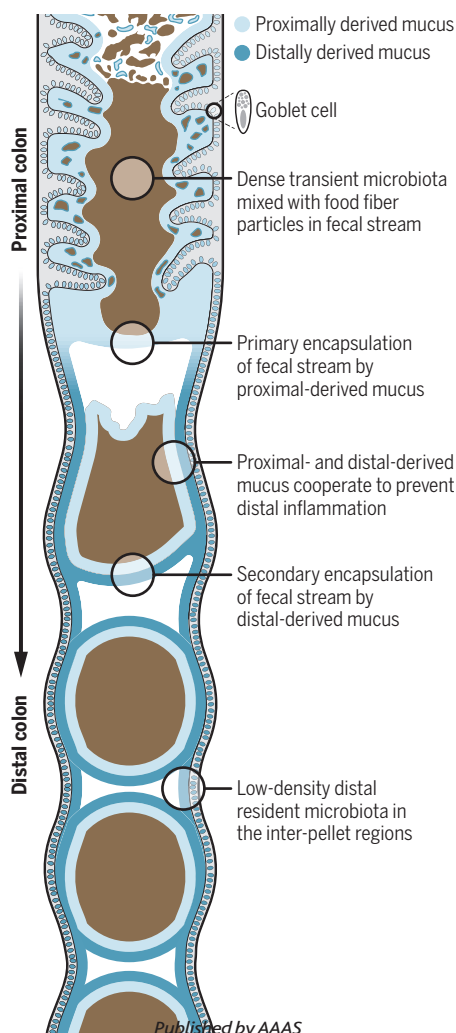
ponents that restrict direct bacterial contact as part of its protective properties (9, 10). By combining our current understanding of the mucus system with the findings of Bergstrom *et al.*, it is likely that the *in vivo* mucus barrier comprises an attached mucus layer that covers the epithelium as a local barrier, which is detached gradually and thereby continuously added to the passing fecal pellets (see the figure).

With regard to microbiota-mucus interactions, Bergstrom *et al.* found that formation of the proximal-derived, but not the distal-derived, mucus layer was dependent on bacterial colonization. This effect was not mediated by inflammasomes (innate immune signaling complexes that can play a role in microbe-dependent mucus secretion), suggesting a mechanism different from the fast mucus secretory response to bacteria mediated by microbe-sensing sentinel goblet cells within the colonic epithelium (11). The proximal mucus also had marked effects on microbiota composition and metabolism. Mucus alterations in the proximal colon would likely have effects on the mucus niche-associated resident microbiota that are found in the folds of the proximal colon and are thought to have a more intimate relationship with the host than the transient microbiota (12). The high load of propagating bacteria in the proximal colon combined with mucus and bacteria from the small intestine and cecum make up the bulk of the fecal pellets in mice. However, there are also mucus-associated bacteria along the length of the intestine that differ in composition from the bulk material found in the fecal stream (13).

Bergstrom *et al.* and others (6) have noted the paucity of bacteria in the inter-pellet regions in histological sections; however, live imaging and quantitative and qualitative microbiota characterization have indicated the presence of a robust bacterial community that is dominated by mucus specialists (e.g., *Mucispirillum*) (9). This mucus-associated community likely represents the distal colonic equivalent of the resident microbiota in the proximal colon, and it probably undergoes interactions with host tissues distinct from those between the encapsulated pellet microbiota and host tissues. Loss of the distinction between mucus-associated and encapsulated bacteria may be associated with disease.

The mucus barrier

Continuous colonic mucus barrier formation along the proximal-distal axis is required for effective barrier function and results in the formation of distinct microbial niche environments.



Department of Medical Biochemistry, Institute of Biomedicine, University of Gothenburg, Sweden.
Email: malin.johansson@medkem.gu.se

The mucus barrier is a critical defensive system that inhibits the interaction of pathogens with the intestinal epithelium. However, many specialized intestinal pathogens have evolved mechanisms that allow them to penetrate the mucus barrier and initiate mucosal infections (14). The study of Bergstrom *et al.* raises questions about the spatiotemporal pathogenesis of these infections. For example, does an intestinal pathogen that infects the distal colon first have to escape mucus encapsulation in the proximal colon? Or must separate strategies be employed to penetrate proximally and distally derived mucus barriers that have distinct properties?

Bergstrom *et al.* also detected mucus layer coating of excreted fecal material in both baboons and humans (5). The colonic regional origin of the mucus in these samples was not determined; however, it is possible that an analogous continual mucus encapsulation process is active in humans. It is also possible that differences in function, motility, total transit time, and luminal consistency could result in more species-specific solutions to protect the epithelium. In humans, the relatively long exposure to the fecal material and its much higher water content likely give rise to different demands for the mucosal surface. Similarly, mucus secreted in the more proximal elements of the human intestine is exposed to the degradative action of bacteria for a longer period than in mice. In this context, locally produced mucus protection in the human distal colon could be even more crucial for health. Further investigation of how the mucus system works throughout the colon in humans is critical to provide targeted aid to the increasing number of people with intestinal disorders. ■

REFERENCES AND NOTES

1. M. E. Johansson *et al.*, *Proc. Natl. Acad. Sci. U.S.A.* **105**, 15064 (2008).
2. A. M. Rodríguez-Piñero *et al.*, *Am. J. Physiol. Gastrointest. Liver Physiol.* **305**, G348 (2013).
3. S. van der Post *et al.*, *Gut* **68**, 2142 (2019).
4. M. E. Johansson *et al.*, *Gut* **63**, 281 (2014).
5. K. Bergstrom *et al.*, *Science* **370**, 467 (2020).
6. J. B. J. Kamphuis, M. Mercier-Bonin, H. Eutamène, V. Theodorou, *Sci. Rep.* **7**, 8527 (2017).
7. C. Atuma, V. Strugala, A. Allen, L. Holm, *Am. J. Physiol. Gastrointest. Liver Physiol.* **280**, G922 (2001).
8. A. Ermund, A. Schütte, M. E. V. Johansson, J. K. Gustafsson, G. C. Hansson, *Am. J. Physiol. Gastrointest. Liver Physiol.* **305**, G341 (2013).
9. J. H. Bergström *et al.*, *Proc. Natl. Acad. Sci. U.S.A.* **113**, 13833 (2016).
10. E. E. L. Nyström *et al.*, *EBioMedicine* **33**, 134 (2018).
11. G. M. Birchenough, E. E. L. Nyström, M. E. V. Johansson, G. C. Hansson, *Science* **352**, 1535 (2016).
12. G. M. Nava, T. S. Stappenbeck, *Gut Microbes* **2**, 99 (2011).
13. B. Chassaing, A. T. Gewirtz, *Cell. Mol. Gastroenterol. Hepatol.* **7**, 157 (2018).
14. E. C. Martens, M. Neumann, M. S. Desai, *Nat. Rev. Microbiol.* **16**, 457 (2018).

10.1126/science.abe7194

SOCIAL PSYCHOLOGY

The upside of aging

Chimpanzees, like humans, place a higher value on positive social relationships as they grow older

By Joan Silk

A primary goal of science is to produce robust and generalizable theories of empirical phenomena. For psychologists, the phenomena of interest are the human mind and behavior. Both the robustness and generalizability of psychological theories have come into question over the past decade. Experimental findings from some of the most widely known theories in social psychology could not be reproduced, provoking what is sometimes called the replication crisis (1). Moreover, results derived from studies of Western, educated, industrialized, rich, and democratic (WEIRD) societies do not always generalize to a more diverse range of human societies (2). Comparative studies of humans and other species can reveal which psychological theories generalize to other species and which apply only to humans. On page 473 of this issue, Rosati *et al.* (3) use comparative data to assess the tenets of one prominent theory in social psychology.

Socioemotional selectivity theory (SST) posits that humans become progressively more aware of their mortality, and this awareness prompts us to place a greater priority on positive social relationships as we grow older (4). People in several—mainly WEIRD—societies show this pattern (4). If these effects are linked to a conscious awareness of the passage of time and knowledge of our own mortality, the pattern should not generalize to other species that do not have a similarly sophisticated concept of time or the capacity to anticipate future events. To test this prediction, Rosati *et al.* examined age-related changes in relationship quality among male chimpanzees (*Pan troglodytes*).

Chimpanzees live in large communities that include multiple adult males, multiple adult females, and immature offspring. Communities regularly split into temporary subgroups (parties) that travel and forage independently within the group's home range (5). Throughout their lives, males remain in the communities in which they are born, whereas the majority of females disperse to new communities when they reach sexual maturity. Chimpanzees have very long life

spans. Males reach adulthood at about 15 years of age, and some males live into their sixties (6). Cooperation among males plays an important role in chimpanzee life. They groom one another, form alliances against rivals, hunt together, share meat, and collectively patrol the boundaries of their territories (5). Males rely on strategic alliances to attain and maintain high rank in their groups, and high rank enhances individual fitness (7). They also have strong affinities for particular partners, and close bonds among males can last for a decade or more (8).

Rosati *et al.* drew on an extraordinary dataset that included behavioral and demographic information collected over a 20-year period on a group of chimpanzees in the Kibale National Park of Uganda. Their sample included 21 males ranging from 15 to 58 years

“...the patterns that socioemotional selectivity theory was created to explain...might not depend on...conscious awareness of mortality.”

of age. For each year, the authors created an association index that was based on the number of times each male was in close proximity to each of the other males in the community while they were in the same party. A male's “friends” were those for whom the value of the association index exceeded the mean + 0.25 standard deviation of its association indices with all partners. In some cases a male's friendship was not reciprocated. This procedure produced three categories: mutual friends, one-sided friends, and nonfriends.

The authors found that old males have significantly more mutual friendships and fewer one-sided friendships than younger males. Thus, a 40-year-old male has on average three times as many mutual friendships and one-third as many one-sided friendships as a 15-year-old male. Investment of males in their social bonds also changes as they age. Males over the age of 35 selectively groom males with whom they have mutual friendships, and grooming is more equita-

School of Human Evolution and Social Change, Arizona State University, Tempe, AZ 85287, USA. Email: joan.silk@asu.edu

bly balanced among males that have mutual friendships than among pairs of males who have one-sided friendships or males that are not friends at all. Also, rates of aggression in males decline with age, and this effect is independent of male dominance rank.

Rosati *et al.* provide convincing evidence that male chimpanzees behave much like humans do as we age, and this pattern might exist in other primates as well (9, 10). Thus, the patterns that SST was created to explain appear to generalize beyond our own species and might not depend on having a well-developed concept of time or conscious awareness of mortality. Rosati *et al.* speculated that the patterns in chimpanzees might be influenced by age-related shifts in emotional reactivity (that is, the tendency to experience frequent and intense emotional arousal). Similar mechanisms could operate in humans and be amplified by events that prompt us to contemplate our own mortality.

Similar patterns of age-related changes in social strategies in humans, chimpanzees, and other primates might be the product of evolutionary forces that shape life-history strategies. As individuals pass the age of sexual maturity, their reproductive value steadily declines. This might affect payoffs derived from alternative behavioral strategies. For example, the benefits derived from risky behaviors, such as challenging the top-ranking male for control of the group, are higher for young males than for old ones (11). This is reflected in a decline in risk-taking behavior with increasing age in humans (12) and other species. For example, the preference of European starlings for risky choices declines as a function of their telomere length, a biological measure of aging (13). An evolutionary perspective can provide valuable insights into how natural selection shapes human social behavioral strategies as we grow old. ■

REFERENCES AND NOTES

1. Open Science Collaboration, *Perspect. Psychol. Sci.* **7**, 657 (2012).
2. J. Henrich, S. J. Heine, A. Norenzayan, *Behav. Brain Sci.* **33**, 61 (2010).
3. A. G. Rosati *et al.*, *Science* **370**, 473 (2020).
4. L. L. Carstensen, D. M. Isaacowitz, S. T. Charles, *Am. Psychol.* **54**, 165 (1999).
5. M. N. Muller, J. C. Mitani, *Adv. Stud. Behav.* **35**, 275 (2005).
6. B. M. Wood, D. P. Watts, J. C. Mitani, K. E. Langergraber, *J. Hum. Evol.* **105**, 41 (2017).
7. I. C. Gilby *et al.*, *Behav. Ecol. Sociobiol.* **67**, 373 (2013).
8. J. C. Mitani, *Anim. Behav.* **77**, 633 (2009).
9. L. Almeling, K. Hammerschmidt, H. Sennhenn-Reulen, A. M. Freund, J. Fischer, *Curr. Biol.* **26**, 1744 (2016).
10. A. G. Rosati, A. M. Arre, M. L. Platt, L. R. Santos, *Behav. Ecol. Sociobiol.* **72**, 163 (2018).
11. A. I. Houston, T. W. Fawcett, D. E. Mappress, J. M. McNamara, *Evol. Hum. Behav.* **35**, 502 (2014).
12. D. J. Paulsen, M. L. Platt, S. A. Huettel, E. M. Brannon, *Front. Psychol.* **3**, 313 (2012).
13. C. Andrews *et al.*, *Behav. Ecol.* **29**, 589 (2018).

10.1126/science.abe9110

CORONAVIRUS

Susceptibility to severe COVID-19

Genetic variants and autoantibodies that suppress antiviral immunity are linked to severe COVID-19

By David B. Beck and Ivona Aksentijevich

The coronavirus disease 2019 (COVID-19) pandemic has led to unprecedented changes in all aspects of our lives and has placed biomedical research at the forefront. One of the many pressing questions surrounding severe acute respiratory syndrome coronavirus 2 (SARS-CoV-2) infections is identifying the determinants of the clinical spectrum, from people with asymptomatic disease to patients with severe COVID-19. Up to 40% of infections may be asymptomatic, suggesting that a large proportion of people may be protected from disease (1). On the other end of the spectrum is severe disease, with an overall estimated fatality rate near 1% (2). On pages 422 and 424 of this issue, Zhang *et al.* (3) and Bastard *et al.* (4), respectively, report analyses of >1600 patients infected with SARS-CoV-2 from >15 countries to identify endogenous factors that determine susceptibility to severe COVID-19.

Many studies have focused on characterizing the heterogeneity of COVID-19 in terms of demographics, with clear evidence of higher mortality in men and older individuals. The adaptive immune system, including both B and T cells, has recently been recognized to play a critical role in providing preexisting immunity to SARS-CoV-2 (5–7). These studies have highlighted mechanisms that protect against severe symptoms but have not revealed factors that predispose to mortality. Consequently, acquired immune responses to prior infections may account for a large percentage of the variability in disease presentation, although questions remain about additional determinants of disease, such as preexisting comorbidities. Host genetic risk factors have also emerged as a potential explanation for clinical heterogeneity and additionally offer the potential for understanding molecular pathways for tailored therapeutic intervention.

Small-scale studies have implicated the type I interferon (IFN) pathway as protective against SARS-CoV-2 (8, 9). The type I IFN pathway plays a crucial role in mediating innate immune responses to viral infec-

tions. This family of cytokines is comprised of 13 IFN- α subtypes, IFN- β , IFN- ω , IFN- κ , and IFN- ϵ , which all signal through the heterodimeric IFN I receptor, composed of IFN- α/β receptor 1 (IFNAR1) and IFNAR2 (see the figure). In host cells, type I IFNs are expressed at low amounts, poised to combat infections. Upon infection, they are rapidly produced by immune cells, such as macrophages and dendritic cells, to limit the spread of pathogens. In addition, type I IFNs induce the expression of several hundred interferon stimulated genes that can further limit pathogen replication through various mechanisms. However, this typically protective immune response can, when overactivated, lead to autoimmune diseases. Conversely, loss-of-function variants in genes encoding members of the type I IFN pathway lead to severe immunodeficiencies characterized by life-threatening viral infections. Recently, multiple studies demonstrated that impaired type I IFN responses may be a hallmark of severe COVID-19 (10–12), but why this pathway was suppressed remained unclear.

Zhang *et al.* report a large genetic sequencing effort to define host risk factors to SARS-CoV-2 infection, analyzing exome or genome sequences from 659 patients with severe COVID-19 for rare pathogenic variants that could be associated with life-threatening disease. The authors focused on the type I IFN pathway and analyzed 13 candidate genes that have previously been linked with susceptibility to other viral infections. Deleterious variants that can impair gene function were identified in 3.5% (23/659) of cases. Defects in type I IFN gene expression and protein levels were recapitulated in patient cells harboring these variants, demonstrating recurrent diminished activity of this pathway in severe disease. SARS-CoV-2 viral loads were higher in patients' immune cells than in cells from healthy donors (who were infection-negative and seronegative for SARS-CoV-2), demonstrating an inability to properly clear the virus. Together, these data implicate the importance of type I IFN signaling in defense against SARS-CoV-2 infection and suggest that inherited deleterious variants explain a subset of severe COVID-19.

Bastard *et al.* identified neutralizing autoantibodies as another potential cause of severe COVID-19. Autoantibodies recognize and thereby may inhibit host proteins; they

Inflammatory Disease Section, National Human Genome Research Institute, National Institutes of Health, Bethesda, MD 20892, USA. Email: aksentii@mail.nih.gov

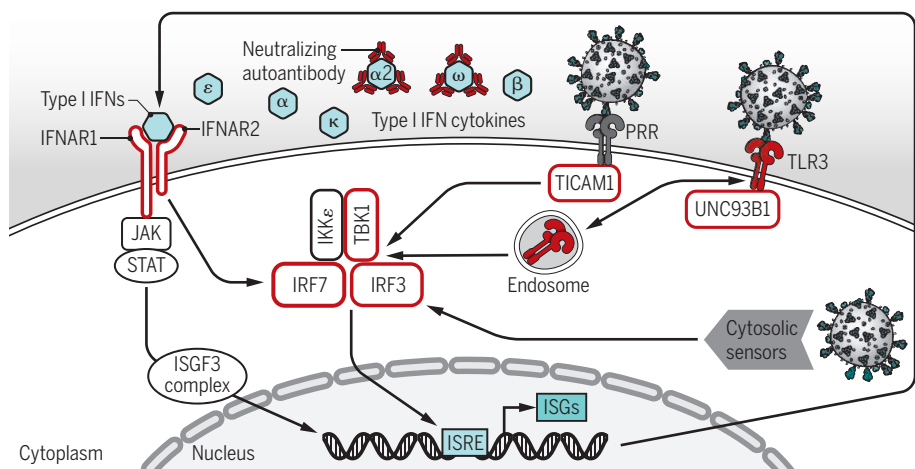
are a hallmark of many autoimmune diseases and are thought to be a contributor to autoimmune pathophysiology. Neutralizing autoantibodies against type I IFNs, mostly IFN- α 2 and IFN- ω , were found in up to 13.7% (135/987) of patients with life-threatening COVID-19 and were shown to neutralize activation of the pathway in vitro. By contrast, these autoantibodies were not present in 663 patients with asymptomatic or mild COVID-19 and were only found in 0.33% (4/1227) healthy individuals not exposed to SARS-CoV-2. The presence of neutralizing autoantibodies correlated with low serum IFN- α concentrations. Autoantibodies against type I IFNs were also detected in blood samples of some patients obtained before SARS-CoV-2 infection, indicating that their production

autoantibodies is not always understood (13). Studying the mechanisms of acquired immunodeficiency, perhaps related to sex and aging, could help reduce infectious disease morbidity and mortality.

Type I IFN concentrations are tightly regulated, with several rare monogenic autoimmune-inflammatory and immunodeficiency disorders caused by either too much or too little interferon production, respectively. Healthy people may have impaired type I IFN responses owing to inherited loss-of-function variants in genes encoding components of the type I IFN signaling cascade but remain clinically silent until they encounter particular viruses or other microbes (8). This may be the case in severe COVID-19 patients who have no prior history of clinical immunodeficiency.

Viral sensing by the type I interferon pathway

Viral particles are sensed by various PRRs, including cytosolic sensors. Type I IFNs are potent antiviral cytokines produced by innate immune cells. They bind a specific cell-surface receptor and signal through the JAK-STAT pathway to induce expression of ISGs that encode other antiviral proteins and various transcription factors. Subsets of patients with severe COVID-19 have loss-of-function genetic variants in several members of the type I IFN pathway (red) or neutralizing autoantibodies against type I IFNs, specifically IFN- α 2 and IFN- ω .



COVID-19, coronavirus disease 2019; IFN, interferon; IFNAR, type I IFN receptor; ISG, IFN-stimulated gene; IKK ϵ , inhibitor of nuclear factor κ B kinase subunit ϵ ; ISRE, IFN-stimulated response element; IRF, IFN-regulatory factor; JAK, Janus kinase; PRR, pattern recognition receptor; STAT, signal transducer and activator of transcription; TBK1, TANK-binding kinase 1; TICAM1, TIR domain-containing adapter molecule 1; TLR, Toll-like receptor.

was not triggered by the virus in those patients. Notably, inactivating autoantibodies were identified primarily in males (94%) and may be a cause of the higher male-specific disease mortalities.

By analyzing patients with severe COVID-19, these two studies provide evidence that type I IFNs are protective against COVID-19 and that limiting this response through either gene mutations or autoantibodies leads to severe disease. Autoantibodies against other proinflammatory cytokines—including type II IFN (IFN- γ), interleukin-6 (IL-6), IL-17A, and IL-17F—have been reported in healthy individuals, patients with autoimmune diseases, and other opportunistic infections, although the function of these

Collectively, this work has important therapeutic implications. Inhaled IFN- β and systemic antiviral therapies are being studied for COVID-19 in clinical trials (14). The studies of Zhang *et al.* and Bastard *et al.* offer a potential avenue for identifying people who are at risk of developing life-threatening SARS-CoV-2 infection, primarily older men, by a presymptomatic screening of their blood samples for type I IFN autoantibodies. Identification of such patients may also be important to avoid potential therapeutic use of their convalescent plasma (which will contain the cytokine-neutralizing autoantibodies) in ongoing clinical trials. Furthermore, recombinant IFN- β treatment may not benefit patients with neutralizing autoantibod-

ies, whereas it may work well for patients who carry loss-of-function variants in type I IFN genes, other than *IFNAR1* or *IFNAR2*. In patients with autoantibodies, treatment with IFN- β may be beneficial because neutralizing autoantibodies against this cytokine appear to be less common (4, 14). Findings from these studies have paved the way for precision medicine and personalized treatment strategies for COVID-19.

What remains unknown are the contributions of genetic variation outside of the type I IFN pathway for defense against SARS-CoV-2 infection. Additionally, although Zhang *et al.* focused on rare germline variation, the roles of common single-nucleotide polymorphisms (SNPs) and acquired somatic mutations in immune cells, which accumulate with age, need to be investigated. Further comprehensive genetic studies could also help provide insights into the potential contribution of deleterious variation in the severe SARS-CoV-2-associated multisystem inflammatory syndrome in children (15). Although the studies of Zhang *et al.* and Bastard *et al.* illuminate the importance of pathways responsible for clearing infections, it is also possible that proinflammatory variants may either reduce or enhance disease severity. Why some patients who carry pathogenic variants in innate immune genes, such as IFN-related genes, remain asymptomatic until their exposure to a specific pathogen is likely explained by the presence of other genetic modifying alleles or epigenetic factors. Unbiased genomic studies can answer some of these questions; however, they need to be expanded to larger and more diverse populations (beyond mostly European descent) to meaningfully address the susceptibility to SARS-CoV-2 and other potentially pandemic viral infections. Ultimately, through collaborative efforts, biomedical research should and will help combat spread of the virus by identifying people at risk with rapid diagnostic tests and facilitating new targeted therapies. ■

REFERENCES AND NOTES

1. D. P. Oran, E. J. Topol, *Ann. Intern. Med.* **173**, 362 (2020).
2. D. M. Morens, A. S. Fauci, *Cell* **182**, 1077 (2020).
3. Q. Zhang *et al.*, *Science* **370**, eabd4570 (2020).
4. P. Bastard *et al.*, *Science* **370**, eabd4585 (2020).
5. A. Grifoni *et al.*, *Cell* **181**, 1489 (2020).
6. C. Kreer *et al.*, *Cell* **182**, 843 (2020).
7. A. Sette, S. Crotty, *Nat. Rev. Immunol.* **20**, 457 (2020).
8. C. I. van der Made *et al.*, *JAMA* **324**, 663 (2020).
9. M. LoPresti *et al.*, *Am. J. Hum. Genet.* **107**, 381 (2020).
10. J. Hadjadj *et al.*, *Science* **369**, 718 (2020).
11. P. S. Arunachalam *et al.*, *Science* **369**, 1210 (2020).
12. J. S. Lee, E. C. Shin, *Nat. Rev. Immunol.* **20**, 585 (2020).
13. C.-L. Ku *et al.*, *Hum. Genet.* **139**, 783 (2020).
14. E. Davoudi-Monfared *et al.*, *Antimicrob. Agents Chemother.* **64**, e01061 (2020).
15. C. Gruber *et al.*, *Cell* **10.1016/j.cell.2020.09.034** (2020).

ACKNOWLEDGMENTS

We thank D. Kastner and E. Beck for helpful discussions.

10.1126/science.abe7591

VIEWPOINT: COVID-19

The engines of SARS-CoV-2 spread

Fighting SARS-CoV-2 requires a clear framework for understanding epidemic spread

By **Elizabeth C. Lee**^{1,2}, **Nikolas I. Wada**²,
M. Kate Grabowski^{1,2,3}, **Emily S. Gurley**^{1,2},
Justin Lessler^{1,2}

Severe acute respiratory syndrome coronavirus 2 (SARS-CoV-2) has spread rapidly across the globe, causing epidemics that range from quickly controlled local outbreaks (such as New Zealand) to large ongoing epidemics infecting millions (such as the United States). A tremendous volume of scientific literature has followed, as has vigorous debate about poorly understood facets of the disease, including the relative importance of various routes of transmission, the roles of asymptomatic and presymptomatic infections, and the susceptibility and transmissibility of specific age groups. This discussion may create the impression that our understanding of transmission is frequently overturned. Although our knowledge of SARS-CoV-2 transmission is constantly deepening in important ways, the fundamental engines that drive the pandemic are well established and provide a framework for interpreting this new information.

The majority of SARS-CoV-2 infections likely occur within households and other residential settings (such as nursing homes). This is because most individuals live with other people, and household contacts include many forms of close, high-intensity, and long-duration interaction. Both early contact tracing studies and a large study of more than 59,000 case contacts in South Korea found household contacts to be greater than six times more likely to be infected with SARS-CoV-2 than other close contacts (1, 2). Household contacts accounted for 57% of identified secondary infections in the South Korean study, despite exhaustive tracking of community contacts. Globally, the proportion of cases attributable to household transmission will vary because of multiple factors, including household size. Contact studies suggest that 17 to 38% of contacts occur in households, implying that 46 to 66% of transmission is household-based (using the standard formula for attributable fraction) (3).

This is consistent with household contact being a key driver of transmission for other respiratory viruses.

Even among close contacts within households, there are considerable heterogeneities in transmission risk. Spouses of index cases are more than twice as likely to be infected as other adult household members, and symptomatic index cases may be more likely to transmit the virus (4). Moreover, older age is associated with increased susceptibility to infection, increased transmissibility, and severe disease (4). Older members may face extra risk in multigenerational households if younger members have unavoidable work or school obligations, although young children may be less susceptible to infection and transmit the virus less readily (4).

Just as in households, those who live in congregate residences such as prisons, worker dormitories, and long-term care facilities have intense, long-duration, close contact. There are more potential contacts in these settings, which are often among older age groups. The confluence of these factors can lead to high infection rates in outbreaks (attack rate); for example, 66% of residents were infected in a homeless shelter, 62% in a nursing home, and 80% in a prison dormitory (5, 6). Even when residents rarely leave, these facilities are highly connected to communities through workers and guests.

Although transmission may be easiest and most frequent in households and congregate residences, community transmission connects these settings and is, therefore, essential to sustain the epidemic, even if it directly causes fewer cases. Inevitably, “community contacts” include a heterogeneous mix of interactions. The probability that any of these interactions results in transmission stems from a complex interplay of pathogen attributes, host characteristics, timing, and setting. Hence, the properties of community transmission are difficult to measure, and this is where much of the remaining debate around SARS-CoV-2 transmission occurs.

A crucial factor in community transmission is that infected individuals not experiencing symptoms can transmit SARS-CoV-2. Infectiousness may peak before symptom onset (7). Viral loads appear to be similar between asymptomatic and symptomatic patients (8), although the implications for infectiousness are unclear. People experiencing symptoms may self-isolate or seek medi-

cal care, but those with no or mild symptoms may continue to circulate in the community. Because of this, those without severe symptoms have the potential to be “superspreaders” and may have an outsized influence on maintaining the epidemic.

Superspreading events, in which one person infects many, are often as much the result of setting as host characteristics. Apparent superspreading events of SARS-CoV-2 have occurred during choir practice (9), in department stores, at church events, and in health care settings (5). These are all settings where one individual can have many close contacts over a short period of time. Transmission can also be amplified if multiple subsequent infections occur in rapid succession, and outbreaks with high attack rates have occurred in close-contact settings such as schools (14%), meat processing plants (36%), and churches (38%) (5, 10).

Both superspreading events and transmission-amplifying settings are part of a more general phenomenon: overdispersion in transmission. Overdispersion means that there is more variation than expected if cases exhibit homogeneity in transmissibility and number of contacts; hence, a small number of individuals are responsible for the majority of infections. This phenomenon has been described for diseases as diverse as measles, influenza, and pneumonic plague (11). For SARS-CoV-2, studies suggest that ~10% of cases cause 80% of infections (1). Overdispersion is characterized by a large number of people who infect no one, and most people who do transmit infect a low-to-moderate number of individuals. Large superspreading events (such as those infecting 10 or more people) are likely quite rare, although they are far more likely to be detected and reported.

Such events have driven much of the debate around the relative importance of different modes of transmission. In household settings, contacts are so long and intense that it matters little whether large droplets, fomites (contaminated surfaces), or aerosolized particles are driving spread; all have ample opportunity. In community settings, where there is greater variety in the nature of infectious contacts, these distinctions become more important, particularly because they affect policy. Aerosolization of fecal matter caused one of the largest superspreading events of the 2003 SARS-CoV

¹Department of Epidemiology, Johns Hopkins Bloomberg School of Public Health, Baltimore, MD, USA. ²Johns Hopkins Novel Coronavirus Research Compendium, Johns Hopkins Bloomberg School of Public Health, Baltimore, MD, USA. ³Department of Pathology, Johns Hopkins School of Medicine, Baltimore, MD, USA. Email: justin@jhu.edu

epidemic (12), and aerosolizing medical procedures facilitate the spread of coronaviruses (12, 13). Several SARS-CoV-2 transmission events suggest that aerosolized viral particles may play a role in transmission in everyday settings. Although the frequency of aerosolized transmission is uncertain, extended close contact and sharing of spaces poses the greatest risk. It is also difficult to generalize the importance of different modes of transmission across settings because their relative contributions can be modified by environmental conditions. For example, low-absolute humidity environments are associated with influenza virus transmission in temperate regions, probably because these conditions facilitate small droplet spread, yet influenza outbreaks are still common in tropical regions, with fomites potentially playing a larger role (14).

A mode of transmission need not be frequent to be important, and regardless of the cause, overdispersion has considerable implications. First, overdispersion means that most infected individuals who enter a community will not transmit, so many introductions may occur before an epidemic takes hold; likewise, overdispersion also increases the probability of disease extinction as the epidemic recedes and fewer people are infected (11). When large transmission events do occur, epidemics can expand rapidly, but as the epidemic grows, overdispersion will matter less to the trajectory until incidence decreases and case counts are low again. Second, overdispersion gives transmission networks “scale-free” properties, in which connectivity in the network is dominated by a few highly connected nodes. Compared with networks with more evenly distributed connections, the connectivity of scale-free networks is less sensitive to random node removal but more susceptible to targeting of highly connected nodes (11).

If transmission is highly overdispersed, broad and untargeted interventions may be less effective than expected, whereas interventions targeted at settings conducive to superspreading (such as mass gatherings and hospitals) may have an outsized effect. Although some determinants of overdispersion may not be amenable to targeted interventions, others related to occupation or setting could be. For example, rapidly improved infection control procedures within health care facilities played a critical role in containing the nascent SARS-CoV pandemic of 2003.

Intercity, interregional, and international

spread are also essential to sustain the pandemic, even if long-distance transmission events are rare (see the figure). Only a small number of such long-distance connections are needed to create a “small world” network in which only a few infection events can transmit the virus between any two individuals worldwide. This is one reason why early travel bans could not stop the global spread of SARS-CoV-2, although they may have slowed the pandemic. However, travel restrictions can work: Extreme measures in China played an important part in achieving domestic suppression of the virus.

could have large effects even if they offer only modest protection. Conversely, control measures at larger spatial scales (for example, interregional) must be widely implemented and highly effective to contain the virus. Indeed, few nations have managed to curb infection without stay-at-home orders and business closures, particularly after community transmission is prevalent.

The impact of accumulated SARS-CoV-2 immunity on transmission will vary across spatial scales. Any immunity conferred by infection or vaccination mitigates transmission in households or communities in near-direct

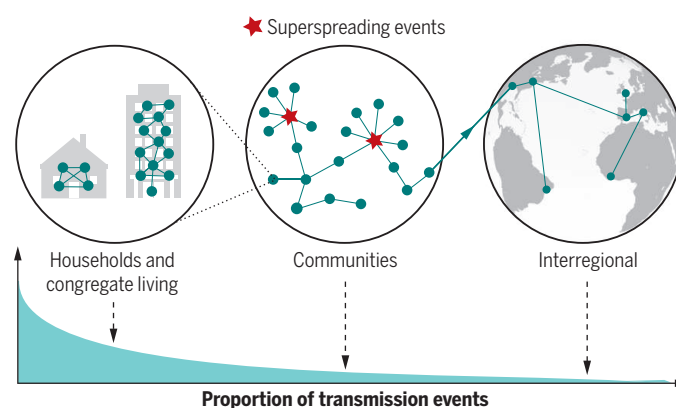
proportion to the number of potential infectees that become immune, plus ancillary benefits due to herd immunity. However, because of overdispersion and small-world network properties, the ability for the virus to spread between communities is less sensitive to accumulating immunity. If even a few regions exist with a sufficient proportion of susceptible individuals to support viral spread, SARS-CoV-2 can continue to circulate in humans.

More is learned about SARS-CoV-2 transmission every day, and important uncertainties remain. The relative risk of transmission in different community settings, such as restaurants and retail stores, is still unclear, as is the impact of mitigation measures in these contexts. It is

still unknown how seasonality and heterogeneities in the population distribution and duration of immunity will affect future transmission dynamics. Filling these and other knowledge gaps will clarify how the engines of transmission interact to drive the pandemic—and how best to fight back. ■

SARS-CoV-2 spread across spatial scales

Severe acute respiratory syndrome coronavirus 2 (SARS-CoV-2) is mostly transmitted within households and household-like settings. A decreasing proportion of transmission events take place at increasing spatial scales, but these events become more critical for sustaining the pandemic.



Phylogenetic data provide some insight into global connectivity and the scale at which intercommunity mixing is most relevant to spread. Major SARS-CoV-2 clades are present in all global regions. Within the United States, where interstate travel continued during lockdowns, the mix of viral lineages was similar across states (15). This suggests that viral lineages spread quickly throughout the country and that reintroductions are highly probable should an area achieve local elimination of the virus.

The engines of the SARS-CoV-2 pandemic—household and residential settings, community, and long-distance transmission—have important implications for control. Moving from international to household scales, the burdens of interventions are shared by more people; there are few international travelers, but nearly everyone lives in households and communities. Measures to reduce household spread may appear particularly challenging, but because they directly affect so many, they need not be perfect. Household mask use and partitioning of home spaces, isolation or quarantine outside the home, and, in the future, household provision of preventive drugs

REFERENCES AND NOTES

1. Q. Bi et al., *Lancet Infect. Dis.* **20**, 911 (2020).
2. Y. J. Park et al., *Emerg. Infect. Dis.* **26**, 10 (2020).
3. J. M. Read et al., *Proc. Biol. Sci.* **281**, 1785 (2014).
4. Z. J. Madewell et al., *medRxiv* 2020.07.29.20164590 [Preprint] 1 August 2020.
5. Q. J. Leclerc et al., *Dataset*, Figshare (2020).
6. H. Njuguna et al., *MMWR Morb. Mortal. Wkly. Rep.* **69**, 26 (2020).
7. X. He et al., *Nat. Med.* **26**, 672 (2020).
8. S. Lee et al., *JAMA Intern. Med.* **10**, 1001/jamainternmed.2020.3862 (2020).
9. L. Hamner et al., *MMWR Morb. Mortal. Wkly. Rep.* **69**, 19 (2020).
10. C. Stein-Zamir et al., *Euro Surveill.* **25**, 29 (2020).
11. J. O. Lloyd-Smith et al., *Nature* **438**, 355 (2005).
12. B. Gamage et al., *Am. J. Infect. Control* **33**, 114 (2005).
13. D. A. T. Cummings et al., *Clin. Infect. Dis.* **ciaa900** (2020).
14. S. Paynter, *Epidemiol. Infect.* **143**, 1110 (2015).
15. J. Hadfield et al., *Bioinformatics* **34**, 4121 (2018).

ACKNOWLEDGMENTS

E.C.L. and N.I.W. contributed equally to this article.

10.1126/science.abd8755

VIEWPOINT: COVID-19

COVID-19 can affect the heart

COVID-19 has a spectrum of potential heart manifestations with diverse mechanisms

By **Eric J. Topol**

The family of seven known human coronaviruses are known for their impact on the respiratory tract, not the heart. However, the most recent coronavirus, severe acute respiratory syndrome coronavirus 2 (SARS-CoV-2), has marked tropism for the heart and can lead to myocarditis (inflammation of the heart), necrosis of its cells, mimicking of a heart attack, arrhythmias, and acute or protracted heart failure (muscle dysfunction). These complications, which at times are the only features of coronavirus disease 2019 (COVID-19) clinical presentation, have occurred even in cases with mild symptoms and in people who did not experience any symptoms. Recent findings of heart involvement in young athletes, including sudden death, have raised concerns about the current limits of our knowledge and potentially high risk and occult prevalence of COVID-19 heart manifestations.

The four “common cold” human coronaviruses—HCoV-229E, HCoV-NL63, HCoV-OC43, and HCoV-HKU1—have not been associated with heart abnormalities. There were isolated reports of patients with Middle East respiratory syndrome (MERS; caused by MERS-CoV) with myocarditis and a limited number of case series of cardiac disease in patients with SARS (caused by SARS-CoV) (1). Therefore, a distinct feature of SARS-CoV-2 is its more extensive cardiac involvement, which may also be a consequence of the pandemic and the exposure of tens of millions of people to the virus.

What appears to structurally differentiate SARS-CoV-2 from SARS is a furin polybasic site that, when cleaved, broadens the types of cells (tropism) that the virus can infect (2). The virus targets the angiotensin-converting enzyme 2 (ACE2) receptor throughout the body, facilitating cell entry by way of its spike protein, along with the cooperation of the cellular serine protease transmembrane protease serine 2 (TMPRSS2), heparan sulfate, and other proteases (3). The heart is one of the many organs with high expression of ACE2. Moreover, the affinity of SARS-CoV-2 to ACE2 is significantly greater than that

of SARS (4). The tropism to other organs beyond the lungs has been studied from autopsy specimens: SARS-CoV-2 genomic RNA was highest in the lungs, but the heart, kidney, and liver also showed substantial amounts, and copies of the virus were detected in the heart from 16 of 22 patients who died (5). In an autopsy series of 39 patients dying from COVID-19, the virus was not detectable in the myocardium in 38% of patients, whereas 31% had a high viral load above 1000 copies in the heart (6).

Accordingly, SARS-CoV-2 infection can damage the heart both directly and indirectly (see the figure). SARS-CoV-2 exhibited a striking ability to infect cardiomyocytes derived from induced pluripotent stem cells (iPSCs) in vitro, leading to a distinctive pattern of heart muscle cell fragmentation, with “complete dissolution of the contrac-

“...why do certain individuals have a propensity for heart involvement after SARS-CoV-2 infection?”

tile machinery” (7). Some of these findings were verified from patient autopsy specimens. In another iPSC study, SARS-CoV-2 infection led to apoptosis and cessation of beating within 72 hours of exposure (8). Besides directly infecting heart muscle cells, viral entry has been documented in the endothelial cells that line the blood vessels to the heart and multiple vascular beds. A secondary immune response to the infected heart and endothelial cells (endothelitis) is just one dimension of many potential indirect effects. These include dysregulation of the renin-angiotensin-aldosterone system that modulates blood pressure, and activation of a proinflammatory response involving platelets, neutrophils, macrophages, and lymphocytes, with release of cytokines and a prothrombotic state. A propensity for clotting, both in the microvasculature and large vessels, has been reported in multiple autopsy series and in young COVID-19 patients with strokes.

There is a diverse spectrum of cardiovascular manifestations, ranging from limited necrosis of heart cells (causing in-

jury), to myocarditis, to cardiogenic shock (an often fatal inability to pump sufficient blood). Cardiac injury, as reflected by concentrations of troponin (a cardiac muscle-specific enzyme) in the blood, is common with COVID-19, occurring in at least one in five hospitalized patients and more than half of those with preexisting heart conditions. Such myocardial injury is a risk factor for in-hospital mortality, and troponin concentration correlates with risk of mortality. Furthermore, patients with higher troponin amounts have markers of increased inflammation [including C-reactive protein, interleukin-6 (IL-6), ferritin, lactate dehydrogenase (LDH), and high neutrophil count] and heart dysfunction (amino-terminal pro-B-type natriuretic peptide) (9).

More worrisome than the pattern of limited injury is myocarditis: diffuse inflammation of the heart, usually representing a variable admixture of injury and the inflammatory response to the injury that can extend throughout the three layers of the human heart to the pericardium (which surrounds the heart). Unlike SARS-associated myocarditis, which did not exhibit lymphocyte infiltration, this immune and inflammatory response is a typical finding at autopsy after SARS-CoV-2 infections. Involvement of myocytes, which orchestrate electrical conduction, can result in conduction block and malignant ventricular arrhythmias, both of which can lead to cardiac arrest.

Along with such in-hospital arrhythmias, there have been reports of increased out-of-hospital cardiac arrest and sudden death in multiple geographic regions of high COVID-19 spread, such as the 77% increase in Lombardy, Italy, compared with the prior year (10). There have been many reports of myocarditis simulating a heart attack, owing to the cluster of chest pain symptoms, an abnormal electrocardiogram, and increased cardiac-specific enzymes in the blood, even in patients as young as a 16-year-old boy. When there is extensive and diffuse heart muscle damage, heart failure, acute cor pulmonale (right heart failure and possible pulmonary emboli), and cardiogenic shock can occur.

COVID-19-associated heart dysfunction can also be attributed to other pathways, including Takotsubo syndrome (also called stress cardiomyopathy), ischemia from endothelitis and related atherosclerotic plaque rupture with thrombosis, and the multisystem inflammatory syndrome of children (MIS-C). The underlying mechanism of stress cardiomyopathy is poorly understood but has markedly increased during the pandemic. MIS-C is thought to be immune-mediated and manifests with a spectrum of cardiovascular features, including vasculitis,

coronary artery aneurysms, and cardiogenic shock. This syndrome is not exclusive to children because the same clinical features have been the subject of case reports in adults, such as in a 45-year-old man (17).

Recent series of COVID-19 patients undergoing magnetic resonance imaging (MRI) or echocardiography of the heart have provided some new insights about cardiac involvement (12–14). In a cohort of 100 patients recovered from COVID-19, 78 had cardiac abnormalities, including 12 of 18 patients without any symptoms, and 60 had ongoing myocardial inflammation, which is consistent with myocarditis (12). The majority of more than 1200 patients in a large prospective cohort with COVID-19

time course of resolution or persistence of any organ abnormalities after SARS-CoV-2 infection has not yet been reported. With a high proportion of silent infections despite concurrent evidence of internal organ damage, there is a fundamental and large hole in our knowledge base.

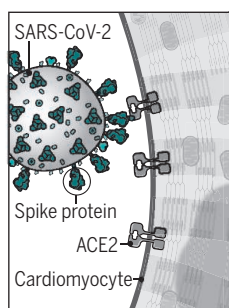
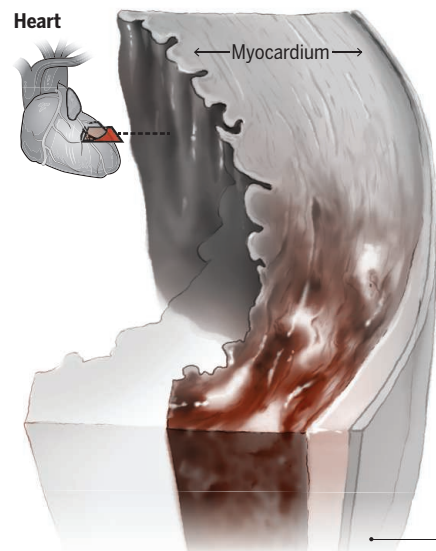
In contrast to people without symptoms, there is a substantial proportion of people who suffer a long-standing, often debilitating illness, called long-COVID. Typical symptoms include fatigue, difficulty in breathing, chest pain, and abnormal heart rhythm. An immunologic basis is likely but has yet to be determined. Nor have such patients undergone systematic cardiovascular assessment for possible myocarditis or

with one of major league baseball's top pitchers. Collectively, these young, healthy individuals had mild COVID-19 but were subsequently found to have unsuspected cardiac pathology. This same demographic group—young and healthy—are the most common to lack symptoms after SARS-CoV-2 infections, which raises the question of how many athletes have occult cardiac disease? Systematic assessment of athletes who test positive for SARS-CoV-2, irrespective of symptoms, with suitable controls through some form of cardiac imaging and arrhythmia screening seems prudent until more is understood.

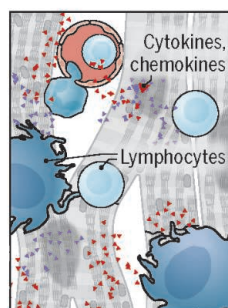
The most intriguing question that arises is why do certain individuals have a propensity for heart involvement after SARS-CoV-2 infection? Once recognized a few months into the pandemic, the expectation was that cardiac involvement would chiefly occur in patients with severe COVID-19. Clearly, it is more common than anticipated, but the true incidence is unknown. It is vital to determine what drives this pathogenesis. Whether it represents an individual's inflammatory response, an autoimmune phenomenon, or some other explanation needs to be clarified. Beyond preventing SARS-CoV-2 infections, the goal of averting cardiovascular involvement is paramount. The marked heterogeneity of COVID-19, ranging from lack of symptoms to fatality, is poorly understood. A newly emerged virus, widely circulating throughout the human population, with a panoply of disease manifestations, all too often occult, has made this especially daunting to unravel. ■

Damaging the heart

Severe acute respiratory syndrome coronavirus 2 (SARS-CoV-2) infection has the potential to directly and indirectly induce cardiac damage.



SARS-CoV-2 can **directly** infect cardiomyocytes, attaching to angiotensin-converting enzyme 2 (ACE2) through its spike protein and entering the cells by fusing viral and cellular membranes.



SARS-CoV-2 infection can **indirectly** damage cardiomyocytes through systemic inflammatory responses and diminished blood supply (e.g., from blood clots and endothelitis, not shown).

Complications

Damaged cardiomyocytes, necrosis, and cardiogenic shock can result from direct and/or indirect effects of SARS-CoV-2 infection. This can lead to scarring and thinning of the myocardium, myocarditis, cardiomyopathy, arrhythmias, and potentially cardiac arrest.

had echocardiographic abnormalities (13). This raises concerns about whether there is far more prevalent heart involvement than has been anticipated, especially because at least 30 to 40% of SARS-CoV-2 infections occur without symptoms. Such individuals may have underlying cardiac pathology.

To date, there have been four small series of asymptomatic individuals with bona fide infections who underwent chest computed tomography (CT) scans to determine whether there were lung abnormalities consistent with COVID-19. Indeed, half of the asymptomatic people showed lung CT features that were seen in patients with symptoms. But so far, there have been minimal cardiac imaging studies in people who test positive for SARS-CoV-2 or are seropositive but without symptoms. Furthermore, the

other heart abnormalities, such as fibrosis, which could account for some of the enduring symptoms. It would not be surprising in the future for patients to present with cardiomyopathy of unknown etiology and test positive for SARS-CoV-2 antibodies. However, attributing such cardiomyopathy to the virus may be difficult given the high prevalence of infections, and ultimately a biopsy might be necessary to identify virus particles to support causality.

Cardiac involvement in athletes has further elevated the concerns. A 27-year-old professional basketball player, recovered from COVID-19, experienced sudden death during training. Several college athletes have been found to have myocarditis (14), including 4 of 26 (15%) in a prospective study from Ohio State University (15), along

REFERENCES AND NOTES

1. T. Y. Xiong, S. Redwood, B. Prendergast, M. Chen, *Eur. Heart J.* **41**, 1798 (2020).
2. N. J. Matheson, P. J. Lehner, *Science* **369**, 510 (2020).
3. F. Hikmet et al., *Mol. Syst. Biol.* **16**, e9610 (2020).
4. A. Gupta et al., *Nat. Med.* **26**, 1017 (2020).
5. V. G. Puelles et al., *N. Engl. J. Med.* **383**, 590 (2020).
6. D. Lindner et al., *JAMA Cardiol.* 10.1001/jamacardio.2020.3551 (2020).
7. J. A. Perez-Bermejo et al., *bioRxiv* 265561, (2020).
8. A. Sharma et al., *Cell Rep. Med.* 10.1016/j.xcrm.2020.100052 (2020).
9. R. O. Bonow, G. C. Fonarow, P. T. O'Gara, C. W. Yancy, *JAMA Cardiol.* **5**, 751 (2020).
10. E. Baldi et al., *Lombardia CaRe Researchers, N. Engl. J. Med.* **383**, 496 (2020).
11. S. Shaigany et al., *Lancet* **396**, e8 (2020).
12. V. O. D. Puntmann et al., *JAMA Cardiol.* 10.1001/jamacardio.2020.3557 (2020).
13. M. R. Dweck et al., *Eur. Heart J.* **21**, 949 10.1093/ehjci/jeaa178 (2020).
14. L. Huang et al., *JACC Cardiovasc. Imaging* S1936-878X(20)30403-4 (2020).
15. S. Rajpal et al., *JAMA Cardiol.* 10.1001/jamacardio.2020.4916 (2020).

ACKNOWLEDGMENTS

E.J.T. is supported by National Institutes of Health grant UL1 TR001114.

Published online 23 September 2020

10.1126/science.abe2813

RETROSPECTIVE

Joseph H. Connell (1923–2020)

Innovative experimental ecologist

By William W. Murdoch¹ and Wayne P. Sousa²

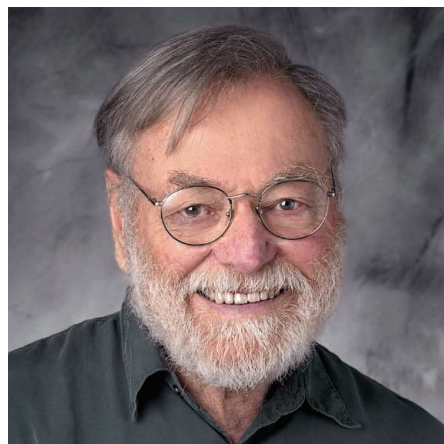
Joseph (“Joe”) H. Connell, a hugely creative ecologist, died on 1 September at the age of 96. Joe had a knack for devising simple yet rigorous ways to uncover the mechanisms behind the patterns and dynamics in natural communities. Perhaps the most influential experimental ecologist of his generation, he articulated theories explaining natural phenomena such as the maintenance of biological diversity.

Joe was born on 5 October 1923 in Gary, Indiana. After Pearl Harbor, in 1941, he enlisted in the U.S. Army Air Corps. He was sent to the University of Chicago for training in meteorology and then stationed in the Azores from 1943 to 1945 flying weather survey missions. In 1946, he completed his B.S. in meteorology at the University of Chicago, followed by an M.A. in zoology at the University of California, Berkeley, in 1953 and a Ph.D. at the University of Glasgow, United Kingdom, in 1956 under zoologist Charles Maurice Yonge. Postdoctoral research at Woods Hole Oceanographic Institution, Massachusetts, preceded his hiring in 1958 as an assistant professor by the University of California, Santa Barbara (UCSB), where he remained for the rest of his career.

Joe’s groundbreaking early research led the transition of ecology from a largely descriptive to an experimental science. He addressed a ubiquitous pattern in nature: One species often abruptly replaces another along continuously changing physical gradients, such as up mountainsides. His Ph.D. research on the island of Cumbrae in Scotland investigated factors controlling such a pattern in the distribution of adults of two barnacle species in the intertidal zone on the rocky seashore. Joe conjectured that this zonation was maintained by physical competition between the barnacles for space rather than by different tolerances to physical stresses along the intertidal gradient. First, he showed that the distributions of newly settled larvae of both species overlapped broadly across the intertidal zone. He then confirmed his interspecific competition hypothesis by removing the larger, faster-growing species from small rep-

licated plots on the mid- to low shore where it predominated; in contrast to controls, the smaller, slower-growing species in these plots survived to adulthood well outside the upper zone where its adults typically occur.

In his early Pacific coast research on San Juan Island, Washington, Joe examined two different intertidal barnacle species. Here, three species of predatory snails reduced the density of barnacles and precluded interspecific competition between them for space. Whereas larvae of the smaller species settled over much of the shore, adults were restricted to a refuge zone high on the shore, where predators were scarce. Adults of the larger barnacle species could grow large enough to be invulnerable to the snail predators, so they coexisted with snails on the mid- to low shore.



These simple yet revolutionary experiments were among the first to demonstrate the roles of interspecific competition, predation, and refuges in structuring natural communities. They are featured in every ecology textbook and have galvanized ecologists to investigate ecological patterns and processes through field experiments. They also foreshadowed extensive future investigations of the interaction between competition and predation.

At UCSB, Joe’s interests turned to the immensely diverse tropical coral reefs and rainforests of Australia. He wondered how so many potentially competing species could coexist in habitats that had long been presumed to be environmentally stable. To answer this question, Joe established multiple permanent plots in forest and reef sites, where he monitored, over decades, the demography and in-

teractions of marked or photographed individuals. Two major hypotheses emerged from these pioneering studies. The first was that recurrent disturbances can maintain species diversity by preventing local competition from progressing to completion. Joe demonstrated this by recording cyclone-induced damage and recovery on the Great Barrier Reef. The second hypothesis, elaborated for rainforests but potentially relevant to all assemblages of sessile organisms, posited that when seeds and seedlings of a particular species are locally abundant, host-specific enemies (such as herbivores and pathogens) preferentially thin those dense patches. By following the fates of individual seedlings for decades, Joe and colleagues verified this pattern of compensatory seedling mortality: Rarer species are favored over common ones, thereby helping maintain diversity.

In addition to his innovative empirical studies, Joe made enormous conceptual contributions to ecology. He wrote synthetic reviews evaluating published research on key ecological themes, and in doing so he influenced thinking on mechanisms maintaining species diversity, the role of recruitment in “open” systems, and the mechanisms causing successional changes in communities through time. The myriad honors and awards bestowed upon Joe included the Guggenheim Fellowship (twice), the Ecological Society of America’s George Mercer and Eminent Ecologist awards, fellowship in the American Academy of Arts and Sciences, and membership in the Australian Academy of Science.

We both came to UCSB because Joe was there: W.W.M. in 1965 as a colleague and W.P.S. in 1973 as a graduate student. Joe was a wonderful senior colleague and adviser—supportive and never domineering. He was modest, without guile, irreverent, and hilarious. Antiauthority and antiestablishment, he was skeptical of general theories, especially if they were his own or had become dogma, until he found strong evidence or produced it himself. Joe was widely adored by his many graduate students and postdocs. As one of them observed, he enjoyed being questioned rather than worshipped and having his theories tested rather than hyped.

Joe brought to science a mind uncluttered by orthodoxy, a deep curiosity about how nature works, and a rich imagination for finding ways to satisfy that curiosity. He tackled each problem in the way that seemed to him most obvious and straightforward, yet his approaches were often surprisingly original. His research expanded our understanding of virtually all the major biological processes thought to control natural communities and inspired legions of ecologists to follow in his footsteps. ■

10.1126/science.abe8992

¹Emeritus Professor of Ecology, University of California, Santa Barbara, CA, USA. ²Department of Integrative Biology, University of California, Berkeley, CA, USA. Email: wwmurdoch@ucsb.edu

BIODIVERSITY

Set ambitious goals for biodiversity and sustainability

Multiple, coordinated goals and holistic actions are critical

By Sandra Díaz, Noelia Zafra-Calvo, Andy Purvis, Peter H. Verburg, David Obura, Paul Leadley, Rebecca Chaplin-Kramer, Luc De Meester, Ehsan Dulloo, Berta Martín-López, M. Rebecca Shaw, Piero Visconti, Wendy Broadgate, Michael W. Bruford, Neil D. Burgess, Jeannine Cavender-Bares, Fabrice DeClerck, José María Fernández-Palacios, Lucas A. Garibaldi, Samantha L. L. Hill, Forest Isbell, Colin K. Khoury, Cornelia B. Krug, Jianguo Liu, Martine Maron, Philip J. K. McGowan, Henrique M. Pereira, Victoria Reyes-García, Juan Rocha, Carlo Rondinini, Lynne Shannon, Yunne-Jai Shin, Paul V. R. Snelgrove, Eva M. Spehn, Bernardo Strassburg, Suneetha M. Subramanian, Joshua J. Tewksbury, James E. M. Watson, Amy E. Zanne

Global biodiversity policy is at a crossroads. Recent global assessments of living nature (1, 2) and climate (3) show worsening trends and a rapidly narrowing window for action. The Convention on Biological Diversity (CBD) has recently announced that none of the 20 Aichi targets for biodiversity it set in 2010 has been reached and only six have been partially achieved (4). Against this backdrop, nations are now negotiating the next generation of the CBD's global goals [see supplementary materials (SM)], due for adoption in 2021, which will frame actions of governments and other actors for decades to come. In response to the goals proposed in the draft post-2020 Global Biodiversity Framework (GBF) made public by the CBD (5), we urge negotiators to consider three points that are critical if the agreed goals are to stabilize or reverse nature's decline. First, multiple goals are required because of nature's complexity, with different facets—genes, populations, species, deep evolutionary history, ecosystems, and their contributions to people—having markedly different geographic distributions and responses to human drivers. Second, interlinkages among these facets mean that goals must be defined and developed holistically rather than in isolation, with potential to advance multiple goals simultaneously and minimize trade-offs between them. Third, only the highest level of ambition in setting each goal, and implementing all goals in an integrated manner, will give a realistic chance of stopping—and beginning to reverse—biodiversity loss by 2050.

Achieving this will require prompt and concerted measures to address the causes of

biodiversity loss (6), meaning that implementation will be crucial. The draft GBF (5) has advanced conceptually relative to its predecessor by highlighting the importance of outcome-oriented goals (i.e., what we want the state of nature to be in 2050 in terms of, for example, species extinction rates or ecosystem area and integrity). These outcome goals link the broad aspirational vision ("living in harmony with nature"; see SM) to the concrete actions needed to achieve it. The outcome goals—operationalized by more specific targets and assessed using indicators—provide a compass for directing actions and a way of checking their results; for example, whether meeting a set of action-based targets (e.g., designating X% of Earth's surface as protected areas) delivers on a desired outcome (e.g., "no net loss in the area and integrity of natural ecosystems") needed to realize the aspirational vision. It is more important than ever that the necessary outcomes are incorporated in the GBF and that they adequately cover the distinct facets of nature, are sufficiently ambitious, and are grounded in the best knowledge available.

Various proposals for the new CBD outcome goals have focused on individual facets of nature, such as ecosystems (7), species (8), or genetic diversity (9). What has been missing is a unified view on how these facets relate to each other in setting goals to achieve the CBD's 2050 vision. To address this gap, we surveyed, evaluated, and discussed published proposals of goals for ecosystems, species, genetic diversity, and nature's contributions to people (NCP) in relation to the empirical and theoretical knowledge in the scientific literature. Our evaluation addresses whether proposed goals encompass, are consistent with, or are opposed to each other; whether they are sufficiently ambitious such that meeting

them will indeed curb and reverse biodiversity trends; and whether they contain all the elements needed to make them difficult to "game" (i.e., avoid making substantial contributions by exploiting weaknesses in wording) (see SM for details on our analysis).

DISTINCT GOALS

As the failure to achieve the CBD's single 2010 goal—to substantially reduce the rate of biodiversity loss—shows, having an "apex" goal does not guarantee success. Whereas the mission of the United Nations Framework Convention on Climate Change (UNFCCC) focuses on one main outcome—preventing dangerous climate change, for which one goal and indicator (well below 2°C) provide a reasonable proxy for the others—CBD's vision and mission have three components that are distinct, complementary, and often trade off with each other: conserving nature, using it sustainably, and (though we do not consider this component here) sharing its benefits equitably. The nature conservation component is itself complex because biodiversity includes variation in life at all levels, from genes to ecosystems. Recognizing this, the proposed formulation of the GBF (5) (see SM) started by proposing separate goals that explicitly covered ecosystems, species, genetic diversity, and the contributions to people derived from them. Whether this structure is retained, or the necessary outcomes for these facets are instead subsumed into more overarching goals, our analysis (see SM) shows that all these facets need to be addressed explicitly because of how they interrelate. If the facets were nested into one another like Russian dolls, or at least nearly so, then a single concise goal that specifies one number about the most encompassing facet could cover all of them. However, although the facets of nature are deeply interlinked, they are far from neatly nested and represent instead a "minimum set" (10, 11). As a result, there is no single goal based on any one facet that would, if realized, guarantee by itself that the necessary outcome for the other facets would be achieved (12, 13).

Another reason for having multiple goals is "Goodhart's law": Whenever a measure becomes a policy goal itself, it ceases to be a good measure of the true state of the system because it can be "gamed" (14). For example, incentives would favor actions to enhance the targeted metric irrespective of effects on the rest of nature. Given nature's multidimensionality, this approach would cause inefficient use of resources at best and possibly promote perverse outcomes (14). If the CBD enshrined an "apex" goal focusing on a single facet of nature, other facets may be relegated to the back seat. By incentivizing holistic actions, a framework with multiple

See supplementary materials for author affiliations.
Email: sandra.diaz@unc.edu.ar

Sustainability at the crossroads

Columns show different facets of nature and their contributions to people (NCP). Each cell shows a potential goal (in bold) at a particular level of ambition in attaining it and some consequences of reaching it, including effects on the other facets of nature and NCP. Only the scenario in green would contribute substantially to “bending the curve” of biodiversity loss. See supplementary materials for further details.

GOALS			
ECOSYSTEMS	SPECIES	GENES	NATURE'S CONTRIBUTIONS TO PEOPLE
LOW AMBITION – DECLINE			
Lax “no net loss” <ul style="list-style-type: none"> Critical ecosystems lost “Natural” ecosystems lose integrity and function Unchecked extinction and loss of genetic diversity Ecosystems less able to provide resilient flows of NCP 	Stabilize extinction rate and average abundance <ul style="list-style-type: none"> Continued rapid extinction of species and populations Many ecosystems altered by, e.g., loss of megafauna Threatened species lose adaptability 	50% conserved <ul style="list-style-type: none"> Critical ecosystems cannot adjust to climate change Many species can no longer adapt and die out Crops and livestock more vulnerable to pests and diseases, causing famines 	Few NCP secured <ul style="list-style-type: none"> Critical ecosystems cannot adjust to climate change Many species can no longer adapt and die out Crops and livestock more vulnerable to pests and diseases, causing famines
MEDIUM AMBITION – UNCERTAIN FUTURE			
Strict “no net loss” <ul style="list-style-type: none"> “Natural” and “managed” ecosystems keep functioning and delivering NCP Critical ecosystems stabilized Species currently with too little habitat will go extinct 	Reduce extinction rate and stop rare species declines <ul style="list-style-type: none"> Many species saved Large or specialist species may still go extinct Many ecosystems lose functions delivered by particular groups of species 	75% conserved <ul style="list-style-type: none"> Most species can adapt Ecosystem adaptability safeguards many NCP, but others are diminished Many species at risk from reduced adaptability to climate change 	Some NCP secured <ul style="list-style-type: none"> Some NCP secured but critical shortfalls in many Ongoing deterioration of “natural” and “managed” ecosystems and species that deliver NCP Climate risks remain
HIGH AMBITION – ROAD TO RECOVERY			
Strict “no net loss” and targeted protection and restoration <ul style="list-style-type: none"> Net increase in “natural” ecosystem area and integrity Large numbers of species and much genetic diversity saved NCP flow from “natural” and “managed” ecosystems secured 	Minimal loss of species and populations <ul style="list-style-type: none"> Stabilizes species abundance, including particular groups delivering ecosystem functions and NCP Safeguards the “tree of life” Saves culturally important species 	90% conserved <ul style="list-style-type: none"> Resilient ecosystems Safeguards adaptability of most of rare species Crops, livestock, and their wild relatives can adapt to pests, diseases, and climate change 	Broad range of NCP secured <ul style="list-style-type: none"> Food, water, health, and climate security for the most vulnerable people More resilient “natural” and “managed” ecosystems Nature-based solutions reduce climate risk

goals reduces the risk that the goals could be achieved without also achieving the overarching vision that they were intended to serve.

HOLISTIC ACTIONS

The interdependence of ecosystems, species, genetic diversity, and NCP offers the opportunity to design policies and actions that contribute to multiple goals simultaneously. This offers the possibility for mutually reinforcing goals, in which progress toward one goal also advances the others, even though each facet of nature will also require targeted actions to address its specificities (see SM). For example, restoring ecosystems that are species-rich, have many endemics, and store large amounts of carbon, such as tropical peatlands, contributes toward all goals. The downside of this interdependence is that failure to achieve one goal will likely undermine others in a negative mutually reinforcing cycle: Ongoing loss of area and integrity of tropical peatlands leads to global extinctions and reduces options for climate mitigation; climate change then causes further loss of ecosystems, species, populations, genetic diversity, and NCP (see SM).

Although the scientific and management communities have been long aware of interactions among biodiversity goals and targets,

these linkages have not been sufficiently operationalized (17). We highlight the need for the connectedness, partial dependence, and imperfect nesting of nature's facets to be built right from the start in the design of outcome goals, targets, indicators, and actions. In addition to addressing different facets of nature, goals must be set across the whole gradient from “natural” to “managed” ecosystems, attending to the specificities of these different landscapes (see SM).

NEED TO AIM HIGH

Holistically designed goals on ecosystems, species, genetic diversity, and NCP are necessary to achieve the 2050 vision; whether they are sufficient will depend on the level of ambition that these goals reflect. Even perfect implementation cannot make up for outcome goals set too low or too narrowly at the start. Different levels of ambition are, for example, whether the curve of biodiversity loss will bend (high ambition) or merely flatten (low), or whether no net loss of ecosystems is specified with a lax (low) or strict (high) criterion for replaceability (see SM). The interdependence among facets of nature means that missing a goal for one facet risks also missing goals related to other facets, whereas achieving each goal at a sufficient ambition

level can contribute to reaching the others. Our synthesis of the evidence (see the figure, and SM) illustrates that the CBD's 2050 vision is feasible only by aiming high with each of the goals. Lower levels of ambition will deliver inadequate outcomes, including loss in area and integrity of ecosystems, more global extinctions, reduced abundance and performance of many important species, loss of genetic diversity, and reduced benefits to people. This would not only compromise the objectives of the CBD but also undermine progress toward most of the United Nations Sustainable Development Goals and the Paris Climate Agreement (1). The stakes are high.

MULTIPLE GOALS, ONE VISION

Our arguments for setting multiple goals do not mean that there is no place for a compelling and unifying overarching vision. Collective action over more than a century offers a clear lesson: To gain political traction, any unifying vision needs to be a rallying cry—broad, normative, inspirational, and aspirational. The CBD process has already set such clear vision: “living in harmony with nature.” The goals underpinning the vision, by contrast, need to be unambiguous and strongly based on the best available knowledge to make it possible to derive SMART (specific,

measurable, assignable, realistic, time-related) operational targets (15) from them.

In sum, one compelling overarching vision, buttressed by facet-specific goals that are mutually reinforcing, scientifically traceable, and individually traceable, will deliver the overarching vision more reliably than any single-facet goal. Using a single-facet goal as the only flagship of global biodiversity policy is analogous to using blood pressure or body mass index as the sole surrogate for the vision of “vibrant health”: simple but risky.

COP15 AND BEYOND

The main challenge ahead lies not in the number of goals but rather in making them happen. However many goals are in the GBF, their specific wording and the supporting framework of targets and indicators will be equally influential on global policy. This wording will be decided by the governments

at the 15th Conference of the Parties (COP15) of the CBD in 2021. We summarize critical elements emerging from our analysis that we hope delegates will consider when establishing the GBF, intended to help maximize positive impacts of each goal and minimize perverse interpretations (see the box).

We have deliberately focused on how the different facets of nature and their contributions to people should look in 2030 and 2050 to achieve the CBD 2050 vision (with 2030 seen as reflecting crucial “stepping stones” in the right direction toward 2050). We have not evaluated the economic and political consequences of the proposed goals nor the governance and distributional challenges of their implementation. In the case of NCP, we focused on their generation rather than on how they are accessed to meet actual needs and therefore result (or not) in people’s good quality of life. Implementing

actions to achieve these outcomes without considering social and political issues would be a recipe for further failure. We thus provide just one piece of the formidable puzzle that must be resolved. But it is an essential piece: what could be effective from the biological perspective, provided that the right actions are implemented and all relevant actors are involved in pursuing them. Actions to implement these goals will need to tackle the indirect socioeconomic drivers (and underlying value systems) at the root of nature’s decline as well as the direct proximal drivers on which conservation has mostly focused to date (1). Only then will the 2050 vision have a chance. We exhort the parties to be ambitious in setting their goals, and holistic in their actions afterward, to transition to a better and fairer future for all life on Earth. ■

REFERENCES AND NOTES

1. Intergovernmental Science-Policy Platform on Biodiversity and Ecosystem Services (IPBES), “The global assessment report on biodiversity and ecosystem services: Summary for policymakers,” S. Díaz *et al.*, Eds. (IPBES secretariat, Bonn, 2019).
2. S. Díaz *et al.*, *Science* **366**, eaax3100 (2019).
3. Intergovernmental Panel on Climate Change (IPCC), “Special report on climate change, desertification, land degradation, sustainable land management, food security, and greenhouse gas fluxes in terrestrial ecosystems,” A. Arneth *et al.*, Eds. (IPCC, London, 2019).
4. CBD, “Global biodiversity outlook 5” (CBD, Montreal, 2020).
5. CBD, “Zero draft of the post-2020 global biodiversity framework,” Version 6, January 2020, updated 17 August 2020 (CBD/POST2020/PREP/2/1, UN Environment Programme, 2020); www.cbd.int/doc/c/3064/749a/0f65ac7f9def86707f4eaeaf/post2020-prep-02-01-en.pdf.
6. D. Leclère *et al.*, *Nature* **585**, 551 (2020).
7. J. E. M. Watson *et al.*, *Nature* **563**, 27 (2018).
8. M. D. A. Rounsevell *et al.*, *Science* **368**, 1193 (2020).
9. L. Laikre *et al.*, *Science* **367**, 1083 (2020).
10. H. M. Pereira, L. M. Navarro, I. S. Martins, *Annu. Rev. Environ. Resour.* **37**, 25 (2012).
11. A. Marques *et al.*, *Basic Appl. Ecol.* **15**, 633 (2014).
12. G. M. Mace *et al.*, *Glob. Environ. Change* **28**, 289 (2014).
13. A. Purvis, *Nat. Ecol. Evol.* **4**, 768 (2020).
14. A. C. Newton, *Conserv. Lett.* **4**, 264 (2011).
15. E. J. Green *et al.*, *Conserv. Biol.* **33**, 1360 (2019).

ACKNOWLEDGMENTS

This article was initiated at a meeting of 63 scientists from 26 countries organized by the Earth Commission in close collaboration with the CBD and Future Earth. Financial support for the meeting, which took place on 28 February to 2 March 2020, was provided by Oak Foundation and Porticus. S. Dobrota, H. Moersberger, and the whole of the Earth Commission Secretariat provided support in the meeting organization. We thank the following contributors to the Report to the CBD Synthesizing the Scientific Evidence to Inform the Development of the Post-2020 Global Framework on Biodiversity, on which this article builds: J. Bascompte, J. Cariño, N. Castañeda-Alvarez, M. Azeredo de Dornelas, S. Hoban, S. Jones, P. Jordano, L. Laikre, N. Maxted, P. Miloslavich, D. Moreno-Mateos, R. Ogden, G. Segelbacher, J.-C. Svenning. We also thank members of the Future Earth GRP EvolveS (formerly bioGENESIS): M. Bellon, L. Colli, F. Forest, M. Johnson, R. Kassen, C. Souffreau, and E. Vázquez-Domínguez. We thank D. Cooper for useful discussions and for advice in the design of the meeting. We thank Georgina M. Mace for discussions about this paper and countless others and for her wonderful and generous leadership, insight, support, and example over many years; we will miss her greatly.

SUPPLEMENTARY MATERIALS

science.sciencemag.org/content/370/6515/411/suppl/DC1

10.1126/science.abe1530

Key considerations for 2050 biodiversity goals

The following key elements are essential for the new post-2020 Convention on Biological Diversity goals. If not fully expressed in the actual goals, they should structure the action targets and indicator framework. To clarify their ambition and enable tracking of legitimate progress, all goals need to have clear reference years (e.g., 2020). For detailed explanations and supporting references, see supplementary materials.

The ecosystems goal should:

- Include clear ambition to halt the (net) loss of “natural” ecosystem area and integrity.
- Expand ecosystem restoration to support no net loss by 2030 relative to 2020, and net gain of 20% of area and integrity of “natural” ecosystems and 20% gain of integrity of “managed” ecosystems by 2050.
- Require strict conditions and limits to compensation, including “like-for-like” (substitution by the same or similar ecosystem as that lost) and no loss of “critical” ecosystems that are rare, vulnerable, or essential for planetary function, or which cannot be restored.
- Recognize that improving the integrity of “managed” ecosystems is key to the continued provision of many of nature’s contributions to people.
- Recognize that outcomes of conservation and restoration activities strongly depend on location and that spatial targeting is essential to achieve synergies with other goals.

The species goal should:

- Have clear ambitions to reduce extinction risk and extinction rate across both threatened and nonthreatened species by 2050, with a focus on threatened species in the short term.
- Focus on retaining and restoring local population abundances and the natural geographical extent of ecological and functional groups that have been depleted, and on conserving evolutionary lineages across the entire “tree of life.”

The genetic diversity goal should:

- Include maintenance of genetic diversity—the raw material for evolutionary processes that support survival and adaptation; population size is not an adequate proxy for this.
- Be set at the highest ambition level (e.g., above 90% of genetic diversity maintained).
- Focus on populations and their adaptive capacity and include wild species and domesticated species and their wild relatives.

The nature’s contributions to people (NCP) goal should:

- Be addressed directly in a goal that recognizes NCP (e.g., food, medicines, clean water, and climate regulation) and avoids conflation with a good quality of life (e.g., food security or access to safe drinking water), which results from other factors as well as from NCP.
- Encompass spatial and other distributional aspects, such as provision from both “natural” and “managed” ecosystems, and inter- and intragenerational equity to ensure benefits to all.



Two individuals embrace in front of the U.S.-Mexico border wall in South Texas in 2016.

BOOKS *et al.*

SOCIAL SCIENCE

The disruption of divisions

Psychological stress is a pervasive aspect of border life, argues a journalist

By Miguel Díaz-Barriga and Margaret E. Dorsey

With the fall of the Berlin Wall in 1989, politicians and pundits heralded a new age: a world without walls. But the celebration was short-lived. Walls, once again the rage, are now part of a global rise in border militarization that, while aimed at keeping undocumented migrants, drug traffickers, and terrorists out, has led to increased violence against, and death among, undocumented migrants and refugees.

A less understood aspect of border fortifications is their impact on the people who live near them, including the citizens they are ostensibly designed to protect. In her new book, *Wall Disease*, journalist Jessica Wapner argues that these impacts include the emergence of an illness first characterized by psychologist Dietfried Müller-Hegemann in the 1970s. Drawing from his observations of a number of East Germans, Müller-Hegemann coined the term “wall disease” to describe a condition experienced by those living near physical barriers whose

symptoms include a sense of social isolation, dejection, and suicidal thoughts.

Wapner argues that wall disease is now a global phenomenon, resulting from the worldwide proliferation of border walls and the increasing poverty and violence found near them. To support her case, she draws on various sources, including firsthand accounts from the U.S.-Mexico border, border studies scholarship, and psychological studies.

The book begins with a visit to Texas, where Wapner learns that the border wall slashes through private property and nature preserves. Here, Wapner recounts her discussions with border resident and anti-border wall activist Reynaldo Anzaldúa about how his family’s relation to their U.S. land has changed now that it falls south of the border wall. “We know we’re going to lose this,” he tells her. “It’s not about the money, it’s about our love of the land.”

Wapner describes the history of international borders, drawing attention to how, until World War I, passports were not needed for travel and highlighting the recent and somewhat arbitrary creation of certain borders, such as the one that di-

vides India and Pakistan, and how these borders have fomented violence. Citing research conducted by border study scholars Reece Jones and Élisabeth Vallet, she explores the dangers associated with living near border walls, including cases in which border agents have killed migrants and incidents of border residents being sprayed with the pesticides used to clear vegetation near walls.

Interspersed throughout these accounts are discussions of how the brain responds to closed spaces, violence, imprisonment, and poverty. Wapner describes, for example, Edvard Moser’s studies on how “border cells” in the brains of rats fire in response to wall-like edges. “When we create a map of our environment, it is rarely a purely physical map,” Moser tells Wapner. “Elements of the map also depend on how important they are to us emotionally.” Wapner also cites research by psychologist Oshin Vartanian, who has found that open spaces are essential for maintaining mental health.

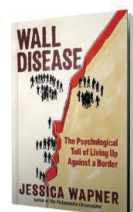
The psychological toll of living near a wall is spreading well beyond physical borders. In many countries, border agents now subscribe to the view that “the border is everywhere.” In southern Texas, for example, there are border patrol checkpoints, where travelers must provide proof of citizenship, as far as 75 miles north of the international boundary with Mexico.

Governments have waived laws, declared states of emergency, eased restrictions on the use of force, and changed rules for search, seizure, and arrest within up to 100 miles of international boundaries. While Wapner’s book does not focus on these political dynamics, we feel that it is important to note that diminishing rights are a key aspect of many border residents’ opposition to walls. Indeed, the psychological effects of being constantly surveilled and having one’s citizenship questioned, along with the fear of potentially having one’s

rights taken away, are all factors deserving of greater study.

Although more journalistic than scholarly, *Wall Disease* is nonetheless an important contribution that raises public awareness about the potential harm caused by border walls. The book is also a clarion call for scientists to develop a broader interdisciplinary understanding of the impacts of such fortifications. ■

10.1126/science.abe0594



Wall Disease
Jessica Wapner
The Experiment,
2020. 128 pp.

The reviewers are at the Department of Sociology and Anthropology, University of Richmond, Richmond, VA 23173, USA, and the authors of *Fencing in Democracy: Border Walls, Necrocitizenship, and the Security State* (Duke Univ. Press, 2020). Email: mdiazbar@richmond.edu

A case for “we” in an “I” country

An eerily similar era gave way to social progress in the United States—will it happen again?

By James A. Morone

In the 1890s, a biracial coalition swept to power in North Carolina, infuriating white supremacists, who primed themselves for the next election. “You are Anglo-Saxons,” shouted former congressman Alfred Moore Waddell to white voters in Wilmington in 1898. “Go to the polls tomorrow, and if you find the Negro out voting, tell him to leave the polls and if he refuses, kill him.” Intimidation and violence defeated the coalition, and the day after the election, militiamen led white mobs through the city’s Black neighborhood, killing, burning, and looting. After the ethnic cleansing, Waddell declared himself mayor and, in doing so, managed something rare in U.S. history—a violent coup (1).

As Robert Putnam and Shaylyn Romney Garrett show in their remarkable new book, *The Upswing*, race relations were not the only phenomenon at low tide then. At the turn of the 20th century, the United States suffered from rampant inequality, vicious partisanship, a torn social fabric, and unabashed egoism. Individuals and corporations lunged ahead, the devil take the hindmost. But from that terrible epoch—eerily similar to today—something admirable sprang up and flour-

ished: six decades of steady, albeit imperfect, social amelioration.

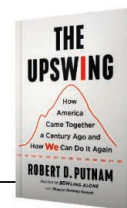
On every imaginable dimension, Putnam and Garrett find a rising communalism. Economic equality soared. Social networks flourished. Solidarity grew. Comity spread. The United States steadily became “a more egalitarian, cooperative, cohesive, and altruistic nation.” In the 1960s, however, the nation tumbled back toward a brash new Gilded Age, marked by ferocious inequality, bare-knuckle partisanship, social fragmentation, and a culture of narcissism. Putnam and Garrett sum up the three epochs as “I–we–I.”

Other social scientists have charted the same bell curve, but perhaps none have packed in so much data across so many dimensions: from income equality and economic mobility, to infant mortality, collaboration in Congress, church membership, social trust, and the list goes on. The authors even note how communally minded parents of the past opted for the familiar when they named their children (e.g., John and Mary) whereas today’s egoists insist on something that stands out (e.g., Jaden and Harper).

But what was it about the 1960s that cracked a sunny community and turned it back into a selfish, snarling, and segregated land? After much searching, the authors declare that “it is fruitless to look for a single cause.” Nonetheless, a powerful potential cause glints through, and the authors seem repeatedly tempted to settle on it.

The Upswing

Robert D. Putnam with
Shaylyn Romney Garrett
Simon and Schuster, 2020.
480 pp.



At the height of the civil rights movement, George Wallace, a fiery segregationist, stunned everyone by riding a crude racial backlash to strong showings in the 1964 primaries. The Republican Party, led by Barry Goldwater (in 1964) and Richard Nixon (in 1968 and 1972), cashed in and began to wink at white privilege. Suddenly, the majority of white people stopped voting for Democrats (who averaged just 39% of the white vote in presidential contests between 1976 and 2016) (2).

Over the past 50 years, the backlash spread from civil rights to welfare policies (“we” do not want to pay for “them”) to immigration (another racialized “them”) and, eventually, to all government action, leading some citizens to question the very idea of good policy, science, and expertise. By the 1990s, the political parties were channeling unprecedented tribal division. Democrats embraced all the so-called minorities, while Republicans spoke to racial anxieties. And just as the temperature was rising, in 2005, the U.S. Census Bureau predicted a majority-minority nation within a generation, further stoking white fear. Putnam and Garrett return to racial tensions in four different chapters, raising the question of whether it was white racial anxiety that shattered the great American “we.” The authors do not go so far as saying yes, but they lay out enough evidence to allow readers to judge for themselves.

Despite painting a bleak portrait of recent U.S. history, every shred of data in *The Upswing* reverberates with the same exhortation: We came together once, and we can do it again. The authors emphasize the role that bold reformers played in imagining a better, more inclusive nation during the 20th century’s long upswing. Their book is an extended call for a new generation to take up the fight. ■

REFERENCES AND NOTES

1. J. A. Morone, *Republic of Wrath: How American Politics Turned Tribal, From George Washington to Donald Trump* (Basic Books, 2020).
2. 1976–2016 voting average computed from the Roper Center’s “How Groups Voted” data (<https://ropercenter.cornell.edu/how%20groups%20voted>).

10.1126/science.abe4421

The reviewer is at the Department of Political Science, Brown University, Providence, RI 02912, USA.
Email: james_morone@brown.edu



Social progress stalled in the United States in the 1960s as racial tensions rose during civil rights protests.

Edited by Jennifer Sills

Narwhals require targeted conservation

Narwhals are one of three highly specialized whale species that are endemic to the Arctic (1). The global narwhal population may number more than 100,000 individuals, but the species persists as a complex, highly divided meta-population, with limited or no exchange between neighboring subpopulations (1). Several narwhal populations in Greenland are suffering from low and declining numbers, and unsustainable hunting is putting the species at risk of local extirpation (1–5). Narwhal conservation requires human activities to be managed at the scale of subpopulations, each of which has its own environmental conditions and exploitation history.

In Melville Bay, the number of narwhals killed by hunters has likely been unsustainable for a decade or more. From 2007 to 2019, the size of the area used by narwhals in Melville Bay has shrunk by 84% from 16,000 to 2600 km² (6). The North Atlantic Marine Mammal Commission (NAMMCO) and the Canada-Greenland Joint Commission on Conservation and Management of Narwhal and Beluga recommended a limit of 280 removals between 2015 and 2019 (2), but the estimated accumulated removal during this period was at least 423 narwhals (7).

In Southeast Greenland, the Scientific Committee of NAMMCO recommended in 2017—and reiterated in 2018—that annual catches should be reduced to fewer than 20 narwhals and that no narwhal should be taken south of 68°N (3, 4). When improved population modeling outputs became available in 2019, the Scientific

Committee changed its recommendation to a moratorium on narwhal hunting throughout Southeast Greenland (5). Even so, the catches from 2017 to 2019 totaled 268 animals (5). The effects of the ongoing overharvesting can be seen in the population composition: a decreased proportion of females, an overrepresentation of old males, and an absence of calves and juveniles (5). The quota for 2020 is set at 58 narwhals (8, 9); this level of harvest could put the long-term existence of the narwhal stocks in Southeast Greenland in jeopardy.

The narwhal is regarded as the most sensitive of all Arctic endemic marine mammals to climate change because of its adaptations to a narrow sea-temperature niche, dependence on sea ice, specialized feeding habits, relatively restricted range, and general sensitivity to ocean noise and other forms of anthropogenic disturbance (1). It is vital for authorities in Greenland to accept scientific advice regarding regional narwhal population declines and take the need for responsible management seriously. Given the extreme site fidelity of narwhals (1), individuals from other populations are unlikely to recolonize localities where the species has been extirpated. The loss of a local narwhal population from a specific fjord system is likely to be permanent.

M. P. Heide-Jørgensen^{1,2*}, E. Garde^{1,2}, R. G. Hansen^{1,2}, O. M. Tervo^{1,2}, Mikkel-Holger S. Sinding³, L. Witting², M. Marcoux⁴, C. Watt⁴, K. M. Kovacs⁵, R. R. Reeves⁶

¹Greenland Institute of Natural Resources, DK-1401 Copenhagen, Denmark. ²Greenland Institute of Natural Resources, DK-3900 Nuuk, Greenland.

³Smurfit Institute of Genetics, Trinity College Dublin, D02 DK07 Dublin, Ireland. ⁴Fisheries and Oceans Canada, Central and Arctic Region, Winnipeg, MB R3T 2N6, Canada. ⁵Norwegian Polar Institute, Fram Centre, 9296 Tromsø, Norway. ⁶International Union for Conservation of Nature Species Survival Commission Cetacean Specialist Group, Okapi Wildlife Associates, Hudson, QC J0P 1H0, Canada.

*Corresponding author. Email: mhj@ghsd.dk

REFERENCES AND NOTES

1. R. C. Hobbs *et al.*, *Mar. Fish. Rev.* **81**, 1 (2019).
2. NAMMCO, "Report of the 22nd Scientific Committee meeting" (2015).
3. NAMMCO, "Report of the 24th Scientific Committee meeting" (2017).
4. NAMMCO, 2018, "Report of the 25th Scientific Committee meeting" (2018).
5. NAMMCO, "Report of the 26th Scientific Committee meeting" (2019).
6. R. G. Hansen *et al.*, "Trends in abundance and distribution of narwhals (*Monodon monoceros*) on the summering grounds in Inglefield Bredning and Melville Bay, Greenland from 2007–2019" (NAMMCO–JCNB Joint Working Group on Narwhals and Belugas, 2020).
7. Government of Greenland, "Recommendations, quotas, and catches for the most important species" (2020); <https://naalakkersuisut.gl/da/Naalakkersuisut/Departement/Fiskeri-Fangst-og-Landbrug/Fangst-og-jagtafdelingen/Kvoter-og-andre-begraensninger> [in Danish].
8. Government of Greenland, "2020 quotas for belugas and narwhals" (2020); https://naalakkersuisut.gl/da/Naalakkersuisut/Nyheder/2020/01/0301_Qilalugartassiusutit [in Danish].
9. Government of Greenland, Press release 15/6/2020 from the Department of Fisheries, Hunting and Agriculture, Journal number 2020-1593, File 13998768 (2020) [in Danish].

10.1126/science.abe7105

Wildfire debate needs science, not politics

The causes of unprecedented wildfires and their impacts on all forested continents are increasingly the subject of discussion. Proper understanding and management of wildfires are crucial to safeguard human lives and to achieve the United Nations' target of "halting and reversing the degradation of ecosystems worldwide" (1). However, the insights obtained from scientific research are largely off the public radar compared with the lighthearted, but often biased, opinions of politicians [e.g., (2, 3)]. This is wrongly giving the public the impression

that we understand little about wildfires and that intensifying wildfire regimes are a surprise. Decades of research, especially after major wildfires such as the 1988 Yellowstone fires (4) and 2009 southern Australian wildfires (5, 6), have created a vast body of knowledge that politicians are disregarding in favor of opinions. To address these increasingly destructive wildfires, the public debate and resulting policy response must be based on science.

Historically, neglecting the role of fire in ecosystems and as a positive driver of biodiversity has produced policies that lead to more fire and ecosystem degradation. Widespread fire suppression has produced landscapes with high fuel loads that exacerbate future fires (4). Removing burnt trees in the name of restoration has impaired the recovery of ecosystem functions and biodiversity (7). Creating even-aged, monospecific conifer plantations for silviculture has increased fire spread and imperiled regeneration potential (8).

There is considerable scientific consensus on the importance of fire for ecosystems, species evolution, and society (9), as well as on the feedbacks between human land use, changes in wildfire regimes, ecosystem responses, and impacts on human society (4, 5, 10). We have also learned that climate change interacts with wildfires in multiple ways, for instance by extending the fire season and increasing the frequency of dry years (11). Recent wildfires in Australia, California, and South America exemplify how protracted drought magnifies fire propagation and intensity, leads to fire spreading to nonflammable ecosystems, increases smoke that impairs human health, and undermines the capacity of ecosystems to recover (10, 12). Scientific research has promoted policies for a healthier coexistence with fire [e.g., (4, 5, 10)], including the use of prescribed fire to simulate natural processes and the creation of heterogeneous landscapes in restoration programs to enhance regeneration in case of fire.

Wildfires and droughts will likely transform landscapes and our relationships with them. Whereas research generates knowledge and helps identify new policies to deal with wildfires, recent public debates politicize their causes and consequences by blaming political opponents. These distracting arguments risk setting back the policy advances that have already been made. We advocate a stronger scientific platform to inform public debates about wildfires. Greater promotion of science can improve understanding and

management of the ecosystems that face intensifying fire regimes globally.

Alexandro B. Leverkus^{1,2*}, Simon Thorn³,

David B. Lindenmayer⁴, Juli G. Pausas⁵

¹Departamento de Ecología, Facultad de Ciencias, Universidad de Granada, 18071, Granada. ²Laboratorio de Ecología, Instituto Interuniversitario de Investigación del Sistema Tierra en Andalucía (IISTA), Universidad de Granada, 18006, Granada, Spain. ³Field Station Fabrikschleibach, Department of Animal Ecology and Tropical Biology, Biocenter, Universität Würzburg, 97070 Würzburg, Germany. ⁴Fenner School of Environment and Society, Australian National University, Canberra, ACT 2601, Australia. ⁵Centro de Investigaciones sobre Desertificación (CIDE-CSIC), 46113 Montcada, Valencia, Spain. *Corresponding author. Email: leverkus@ugr.es

REFERENCES AND NOTES

1. J. Fischer *et al.*, *Trends Ecol. Evol.* doi.org/10.1016/j.tree.2020.08.018 (2020).
2. P. Baker *et al.*, "As Trump again rejects science, Biden calls him a climate arsonist," *The New York Times* (2020).
3. H. McKay, "Climate change or poor policy? As Australia's wildfires see some relief, blame game ascends," *Fox News* (2020).
4. M. G. Turner *et al.*, *Front. Ecol. Environ.* **1**, 351 (2003).
5. M. A. Moritz *et al.*, *Nature* **515**, 58 (2014).
6. C. Taylor *et al.*, *Conserv. Lett.* **7**, 355 (2014).
7. A. B. Leverkus *et al.*, *Front. Ecol. Environ.* **18**, 391 (2020).
8. J. R. Thompson *et al.*, *Proc. Natl. Acad. Sci. U.S.A.* **104**, 10743 (2007).
9. J. G. Pausas, J. E. Keeley, *Front. Ecol. Environ.* **17**, 289 (2019).
10. B. A. Wintle *et al.*, *Trends Ecol. Evol.* **35**, 753 (2020).
11. A. L. Westerling *et al.*, *Science* **313**, 940 (2006).
12. N. J. Enright *et al.*, *Front. Ecol. Environ.* **13**, 265 (2015).

10.1126/science.abf1326

"Forest mismanagement" misleads

Politicians (1) and journalists (2) have attributed the increased size and intensity of U.S. western wildfires to "forest mismanagement," an ambiguous term that implicates resource managers. To reduce the risk of damage from wildfires, we must understand the constraints on responsible forest management and work to overcome them.

Resource managers face a range of obstacles to science-based solutions to extreme wildfire. Harvesting trees remains both ecologically problematic and socially unpopular (3). Removing dense, small, low-value trees requires economic subsidies (4). Biomass production struggles to become economically viable (5). Let-burn wildfire policies carry risks (6). Intentionally set, prescribed fires face regulatory hurdles from smoke-generated pollution (6). Increasing any active management option faces economic, social, and regulatory barriers.

In addition, wildfire is not just a conifer forest issue. Most of California's largest and most damaging wildfires have been in regions dominated by non-forested habitats (7) and lacking in commercial timber operations (5, 8). Attributing recent wildfires to

"forest mismanagement" fails to acknowledge the limits of forest resource managers in addressing the full range of fires.

Meanwhile, U.S. public land management agencies are budget starved. Appropriated Forest Service budgets over the past 25 years have shifted from proactive forest management to reactive fire operations (9). To empower resource managers to implement evidence-based policies, legislators must provide agencies with funds to support management actions at sufficient scales.

The state of California and the U.S. Forest Service recently made progress by signing a memorandum of understanding that would expand forest treatments to 1,000,000 acres/year (10). However, successfully addressing wildfires will require rethinking our social responses to forest management. We may have to embrace increased timber operations, accept more smoke, and modify built communities to tolerate fire as a natural ecosystem process. Labeling a complicated decision-making process as "forest mismanagement" oversimplifies, obfuscates, and politicizes an issue that we cannot afford to misunderstand.

Mark W. Schwartz^{1*}, James H. Thorne¹,

Brandon M Collins², Peter A. Stine³

¹Department of Environmental Science & Policy, University of California, Davis, Davis, CA 95616, USA. ²Center for Fire Research and Outreach, University of California, Berkeley, Berkeley, CA 94720, USA. ³Retired, Pacific Southwest Research Station, U.S. Department of Agriculture Forest Service, Richmond, CA 94804, USA.

*Corresponding author.

Email: mwschwartz@ucdavis.edu

REFERENCES AND NOTES

1. R. Ayesh, "Oregon governor: Wildfires are result of climate change and forest mismanagement," *Axios* (2020).
2. "California's disastrous forest mismanagement," *National Review* (2020).
3. T. A. Spies *et al.*, *Tech. Coords.*, "Synthesis of science to inform land management within the Northwest Forest Plan area," Gen. Tech. Rep. PNW-GTR-966 [U.S. Department of Agriculture (USDA), Forest Service, Pacific Northwest Research Station, 2018].
4. D. Calkin, K. Gebert, *West. J. Appl. For.* **21**, 217 (2006).
5. C. P. McIver *et al.*, "California's forest products industry and timber harvest, 2012," Gen. Tech. Rep. PNW-GTR-908 (USDA, Forest Service, Pacific Northwest Research Station, 2015).
6. D. Schweizer *et al.*, in *Extreme Weather Events and Human Health*, R. Akhtar, Ed. (Springer International Publishing, 2020), pp. 41–58.
7. A. D. Syphard, J. E. Keeley, *Int. J. Wildl. Fire* **29**, 595 (2020).
8. USDA Forest Service Resource Bulletin PNW, no. 35 (1970).
9. USDA Forest Service, "The rising cost of wildfire operations, effects on the Forest Service's non-fire work" (2015).
10. State of California, "Agreement for Shared Stewardship of California's Forest and Rangelands Between the State of California and the USDA, Forest Service Pacific Southwest Region" (2020); www.gov.ca.gov/wp-content/uploads/2020/08/8.12.20-CA-Shared-Stewardship-MOU.pdf.

COMPETING INTERESTS

P.A.S. is a part-time employee of the National Older Workers Career Center, which is part of the Agriculture Conservation Experienced Services Program at the Natural Resources Conservation Services under USDA. He is working on a project funded by the Forest Service.

10.1126/science.abe9647

RESEARCH

IN SCIENCE JOURNALS

Edited by Michael Funk

ANIMAL ROBOTS

Trot on the wild side

Legged robots can access spaces that wheeled robots cannot. Lee *et al.* developed a robust locomotion controller that uses deep reinforcement learning to teach a quadrupedal robot how to navigate unseen and unstructured environments without the need for external sensors, relying solely on proprioception. The trained quadruped was deployed in various outdoor settings to demonstrate that it could traverse a range of challenging terrain: deformable surfaces such as mud and snow, dynamic footholds such as rubble, and impediments such as thick vegetation and flowing water. —MML

Sci. Robot. 5, eabc5986 (2020).

Integrating proprioceptive feedback allows a quadrupedal robot to navigate challenging terrain, such as a gravel-strewn alpine road.



DISPLAY TECHNOLOGY

Metasurface-based microdisplays

Organic light-emitting diodes (OLEDs) have found wide application in high-resolution, large-area televisions and the handheld displays of smartphones and tablets. With the screen located some distance from the eye, the typical number of pixels per inch is in the region of hundreds. For near-eye microdisplays—for example, in virtual and augmented reality applications—the required pixel density runs to several thousand pixels per inch and cannot be met by present display technologies. Joo *et al.* developed a full-color, high-brightness OLED design based on an engineered metasurface

as a tunable back-reflector. An ultrahigh density of 10,000 pixels per inch readily meets the requirements for the next-generation microdisplays that can be fabricated on glasses or contact lenses. —ISO

Science, this issue p. 459

DEVELOPMENTAL BIOLOGY

Origins of the pituitary gland

Placodes are specializations of the head ectoderm that are considered the source of many vertebrate novelties, including the nose, lens, ear, and hormone-producing portion of the pituitary. However, the presence of a pituitary-like structure in nonvertebrate chordates, derived instead from the endoderm, had suggested that

the pituitary may predate placodes. Fabian *et al.* performed lineage tracing, time-lapse imaging, and single-cell messenger RNA sequencing to show that both endodermal and ectodermal cells can generate hormone-producing cells of the zebrafish pituitary. These experiments support

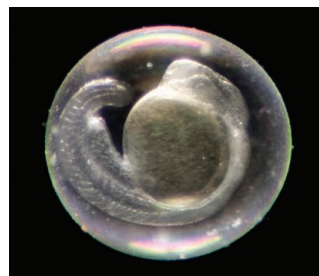
that the vertebrate pituitary arises through interactions of an ancestral endodermal protopituitary with newly evolved placodal ectoderm. —BAP

Science, this issue p. 463

NEURODEGENERATION

Detecting toxic protein

Spinocerebellar ataxia type 3 (SCA3) is a neurodegenerative disorder caused by CAG trinucleotide repeat expansion in the ataxin-3 gene (*ATXN3*). Reducing the toxic polyglutamine ATXN3 protein might be an effective strategy for treating the disease, and identification of pharmacodynamic markers would facilitate the assessment of potential therapies. Prudencio *et al.* showed that the toxic protein could be detected in cerebrospinal fluid



Light microscopy image of a zebrafish embryo 24 hours postfertilization, at which point specialized neural structures have begun to form

from patients, was associated with clinical features, and could be used to assess treatment response. Moreover, the authors identified a single-nucleotide polymorphism in the *ATXN3* gene associated with CAG-expanded alleles. The results could improve the development of new therapies and the evaluation of treatment efficacy. —MM
Sci. Transl. Med. **12**, eabb7086 (2020).

ATMOSPHERIC OXYGEN The iron did it

What factors controlled the accumulation of atmospheric oxygen gas (O_2) early in the history of Earth? Heard *et al.* used high-precision iron isotopic measurements of Archean-Paleoproterozoic sediments, with ages between 3.8 billion and 2.3 billion years ago, and laboratory data about synthetic pyrites to show that pyrite, or iron sulfide, burial could have resulted in net O_2 export. These reactions therefore may have contributed to early episodes of transient oxygenation before the Great Oxidation Event that began about 2.4 billion years ago. —HJS

Science, this issue p. 446

NEURODEVELOPMENT Spinal circuit development

Motor neuron circuits in the zebrafish spinal cord support both the rapid evasion response and the leisurely swimming response. Kishore *et al.* now follow the development of inhibitory interneurons as these circuits are assembled in the larva. Interneurons generated early in development drive different sorts of circuits and synapse onto different subcellular sections of the motor neurons than interneurons generated later in development. Thus, both rapid evasion and slower swimming are supported by the same cellular components assembled in different ways. The authors suggest that development follows an opportunistic rule in which interneurons synapse onto what is available to

them at that moment in development. —PJH

Science, this issue p. 431

NANOMATERIALS Using curves to make twists

The growth of layered materials on flat substrates usually occurs in stacked layers, although defects or a lattice mismatch can induce strains that distort the shape of subsequent layers. However, these effects are usually small and can be uncontrolled. Zhao *et al.* now demonstrate the possibility of synthesizing multilayers of two-dimensional materials with certain twists between the layers induced by the presence of screw dislocations in combination with curved substrate surfaces. Different twist angles are achieved by varying the amount of nonplanarity and the character (conical or hyperbolic) of the surface. —MSL

Science, this issue p. 442

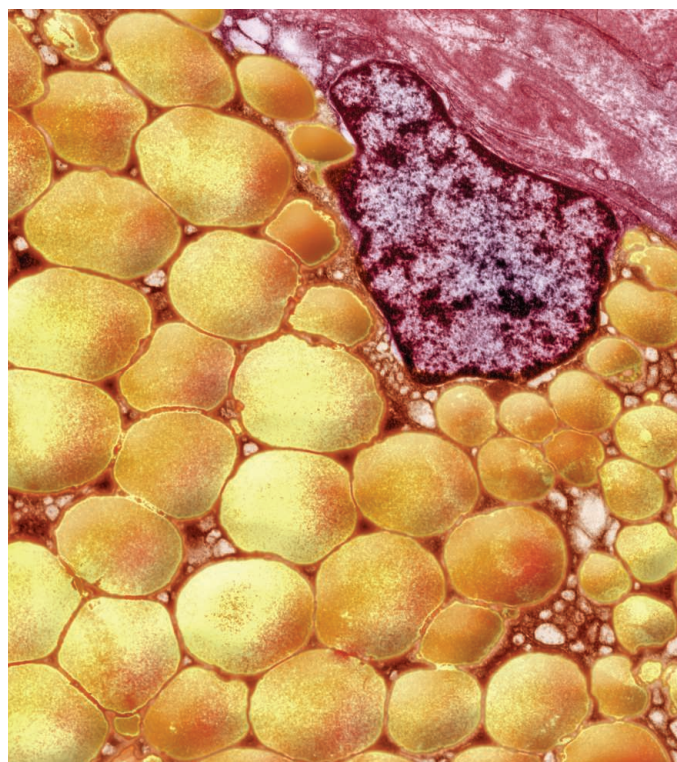
STRUCTURAL BIOLOGY Saving a host cell from itself

A fundamental mammalian defense mechanism against pathogens and damaged cellular DNA is to recognize DNA fragments in the cytosol and trigger an inflammatory response. The cyclic guanosine monophosphate–adenosine monophosphate synthase (cGAS) that recognizes cytosolic DNA is also found in the nucleus, but here its activity is suppressed by tethering to chromatin. Two papers now report cryo–electron microscopy structures of cGAS bound to the nucleosome core particle (NCP). Kujirai *et al.* observed a structure with two cGAS molecules bridging two NCPs, whereas Boyer *et al.* observed cGAS bound to a single nucleosome. Together, these structures show how cGAS is prevented from autoreactivity toward host DNA. —VV

Science, this issue p. 455, p. 450

IN OTHER JOURNALS

Edited by **Caroline Ash**
and **Jesse Smith**



METABOLISM

Obesity and inflammation

Obesity is associated with chronic inflammation, which can trigger other diseases such as atherosclerosis, type 2 diabetes, and even cancer. There appears to be a genetic component to excess fat accumulation, and studies suggest that inflammatory gene variants may contribute. Karunakaran *et al.* found that single-nucleotide polymorphisms in the human receptor-interacting serine/threonine-protein kinase 1 gene (*RIPK1*) increase its expression and are causally associated with obesity. RIPK1 is a key regulator of inflammatory responses and cell death. Silencing of *Ripk1* in mice on a high-fat diet reduced fat mass, body weight, and inflammatory responses in adipose tissue. This suggests that RIPK1-mediated inflammation (and possibly other functions) contribute to obesity and that RIPK1 could be a therapeutic target. —GKA
Nat. Metab. 10.1038/s42255-020-00279-2 (2020).

Accumulation of fat cells (shown in yellow in this micrograph) may be promoted by gene variants linked to inflammation.

DEVELOPMENT Moving heart elements and cells

Transposable elements comprise a large percentage of the human genome, with the endogenous retrovirus

(ERV) subclass representing more than 8%. Using human pluripotent stem cell–derived cardiomyocytes and bioengineered micropatterning to recapitulate cardiogenesis, Wilson *et al.* found evidence that the primate-specific ERV MER41



FOREST DECLINE

A century of pollution in the boreal forest

The environs of Norilsk, in northern Siberia, are among the most heavily polluted in the world as a result of the effects of decades of heavy metal production and sulfur dioxide emissions. Kirdyanov *et al.* reveal the extent of pollutant effects on the boreal forests of the region through a study of tree-ring patterns in larch and spruce from sites along a 200-kilometer transect on either side of Norilsk. Their results document tree growth rates before the onset of industrialization in the region in the 1930s and show the trajectory of subsequent decline in growth rates that eventually led to dieback of entire forest stands. These effects fit into a wider picture of increasing pollution from multiple sources across the wider boreal and arctic region. —AMS
Ecol. Lett. 10.1111/ele.13611 (2020).

Hundreds of square kilometers of forest around the industrial zone of Norilsk, Siberia, are experiencing severe dieback among larch trees as a result of pollution since the 1930s.

is involved in primate heart development. A MER41-derived long noncoding RNA called BANCER is exclusively expressed in the fetal heart. When BANCER is eliminated, cardiomyocyte migration is disrupted. The cardiogenic transcription factor TBX5 and Hippo signaling factors TEAD4/YAP1 bind to a BANCER enhancer during fetal development. A related analysis in mouse shows that heart size increases with embryo BANCER knock-in. —BAP

Dev. Cell **54**, 694 (2020).

STRUCTURAL BIOLOGY
Organized but dynamic

An isoform of tropomyosin called Tm1-I/C is required for germ cell maturation in *Drosophila*. This isoform has a low-complexity domain at its carboxy terminus that facilitates assembly into intermediate filaments. The isolated tail domain assembles into polymers that have amyloid-like cross- β structures, but whereas amyloid fibers are extremely stable, these structures are dynamic. Sysoev *et al.* labeled the tail domain in the context of

assembled filaments and used solid-state nuclear magnetic resonance spectroscopy to study its conformation. They again observed the dynamic cross- β structure involving the same sequence as in the isolated tail domain, whereas more than half of the tail remained disordered. There may be other cases in which sequence-specific labile interactions drive the assembly of low-complexity domains to achieve dynamic cellular organization. —VV

Proc. Natl. Acad. Sci. U.S.A. **117**, 23510 (2020).

PHYSICS
Looking for charge order

At low temperatures, ions in some one-dimensional (1D) crystal lattices are predicted to transition into a chain of dimers. The resulting charge order has been observed in quasi-1D solids consisting of ionic chains with weak interchain interactions. Aiming to find out whether this transition occurs in purely 1D systems, Yang *et al.* synthesized nanowires of Mo_6Se_6 from monolayers of the transition metal dichalcogenide

MoSe_2 . This resulted in two types of nanowires: those attached along the edges of MoSe_2 and those connecting adjacent MoSe_2 flakes. Scanning tunneling spectroscopy revealed coherent charge order in the former, but not the latter, type. The loss of coherence might be caused by the formation of polaronic quasiparticles in the 1D system. —JS

Phys. Rev. X **10**, 031061 (2020).

IRON UPTAKE
Siderophore piracy

Both free-living and pathogenic microbes face iron restriction and have developed chemical and biological innovations to liberate and sequester iron. Studying the bacterial pathogen *Pseudomonas aeruginosa*, Normant *et al.* found that two siderophores produced by other bacteria, nocardamine and desferrioxamine B, could induce expression of a transporter, FoxA, which was involved in their uptake. Surprisingly, desferrioxamine B could also support growth in a FoxA deletion strain, perhaps through import by an as-yet-unknown transporter.

Understanding siderophore piracy will help inform development of siderophore-mimicking antimicrobials. —MAF

ACS Chem. Biol. 10.1021/acscchembio.0c00535 (2020).

ORGANIC CHEMISTRY
Asymmetric catalysis goes nonclassical

The structure of the norbornyl cation was the subject of fierce debate in the latter half of the 20th century. The controversy hinged on whether a positive charge left behind by a departed substituent could be shared between two carbon centers in a three-center bonding arrangement or whether two more classical structures with isolated charges were rapidly interconverting. Ultimately, the shared, nonclassical model won out, but Properzi *et al.* turned to a different challenge—steering a new substituent to just one of the carbons. Their enveloping imidodiphosphorimidate catalyst proved up to the task. —JSY

Nat. Chem. 10.1038/s41557-020-00558-1 (2020).

ALSO IN SCIENCE JOURNALS

Edited by Michael Funk

CORONAVIRUS

Understanding epidemic spread

The global spread of severe acute respiratory syndrome coronavirus 2 (SARS-CoV-2) infection has caused both quickly controlled outbreaks and large ongoing epidemics. These varied outcomes have prompted much investigation into how the virus is transmitted and what the key engines of viral spread are. In a Perspective, Lee *et al.* discuss the main pillars of SARS-CoV-2 spread, including household and residential settings, community and superspreading events, and interregional transmission. Understanding how to prevent transmission in these situations as well as the importance of these different settings in the pattern of epidemic spread should help to improve and focus mitigation measures and control the pandemic. —GKA

Science, this issue p. 406

CORONAVIRUS

Damaging the heart

Severe acute respiratory syndrome coronavirus 2 (SARS-CoV-2) is largely considered a respiratory virus, but evidence is emerging that it can also affect the heart. In a Perspective, Topol discusses the indirect and direct effects that the virus can have on the heart. Direct effects range from mild injury to inflammation and shock, which can lead to arrhythmia and possibly cardiac arrest. SARS-CoV-2 also has vascular effects that can indirectly affect heart function, as can systemic inflammation. Heart damage does not seem to correlate with the severity of disease, so more assessment of heart function in people infected with SARS-CoV-2 is needed to understand the frequency and what determines whether someone will develop cardiac pathology. —GKA

Science, this issue p. 408

ARCHAEOLOGY

New insights into Clovis-era archaeology

Defined by a distinctive projectile point style, Clovis was once thought to be the earliest archaeological culture in North America. Although new finds throughout the Americas have overturned that hypothesis, questions remain about its origins, relationships to other cultures, and disappearance. Waters *et al.* obtained 32 high-precision radiocarbon dates from 10 Clovis archaeological sites and determined that the age of these sites spanned from 13,050 to 12,750 calibrated radiocarbon years before the present. These dates confirm that Clovis was a contemporary of at least three other distinctive archaeological cultures, a finding that complicates current models of the peopling of the Americas. The new dates also show that Clovis technology disappeared coincident with the extinction of large mammals such as mammoth, mastodon, and others. —MSA

Sci. Adv. 10.1126/sciadv.aaz0455 (2020).

NATURAL KILLER CELLS

Liver NK cells with antigen specificity

Natural killer (NK) cells are heterogeneous innate effector cells, with some NK subsets displaying features of adaptive immunity, including memory and antigen specificity. Because liver NK cells are enriched for adaptive NK cells, Stary *et al.* used RNA sequencing and flow cytometry of human liver NK cells to search for correlations between NK cell phenotypes and their capacity to carry out adaptive effector functions. A distinct subset of liver NK cells expressed a cytotoxicity-associated gene program and exhibited antigen-specific killing of autologous target cells pulsed with viral antigens or metal

allergens. Identification of this human hepatic NK subset is an advance in the ongoing quest to understand the molecular basis for antigen-specific recognition by adaptive NK cells. —IRW

Sci. Immunol. 5, eaba6232 (2020).

STRUCTURAL BIOLOGY

Protected by dimerization

Ubiquitination is critical for mitotic exit and requires the E2 ubiquitin-conjugating enzyme UBE2S, which can autoubiquitinate and promote its own turnover. Liess *et al.* found that dimerization of UBE2S prevented its autoubiquitination and kept this protein in an inactive state (see the Focus by Bremm). Human cells that expressed wild-type UBE2S were able to exit from drug-induced mitotic arrest, unlike those expressing the dimerization-defective form of UBE2S. Thus, UBE2S may dimerize to prevent its turnover in noncycling cells and ensure its availability for future mitotic cycles. —WW

Sci. Signal. 13, eaba8208, eabd9892 (2020).

CORONAVIRUS

The genetics underlying severe COVID-19

The immune system is complex and involves many genes, including those that encode cytokines known as interferons (IFNs). Individuals that lack specific IFNs can be more susceptible to infectious diseases. Furthermore, the autoantibody system dampens IFN response to prevent damage from pathogen-induced inflammation. Two studies now examine the likelihood that genetics affects the risk of severe coronavirus disease 2019 (COVID-19) through components of this system (see the Perspective by Beck and Aksentijevich). Q. Zhang *et al.* used a candidate gene approach and identified patients with severe COVID-19 who have

mutations in genes involved in the regulation of type I and III IFN immunity. They found enrichment of these genes in patients and conclude that genetics may determine the clinical course of the infection. Bastard *et al.* identified individuals with high titers of neutralizing autoantibodies against type I IFN- α 2 and IFN- ω in about 10% of patients with severe COVID-19 pneumonia. These autoantibodies were not found either in infected people who were asymptomatic or had milder phenotype or in healthy individuals. Together, these studies identify a means by which individuals at highest risk of life-threatening COVID-19 can be identified. —LMZ

Science, this issue p. 422, p. 423; see also p. 404

FRAMEWORK MATERIALS

Higher-valency ligands for COFs

Metal-organic frameworks (MOFs) have exhibited more extensive connectivity (valency) and topological diversity than covalent organic frameworks (COFs), mainly because MOF linkers can connect from 3 to 24 discrete units or even infinity for one-dimensional rods. For COFs, linkers generally have a valency of 3 or 4 that reflect the valency of organic carbon. Gropp *et al.* created cubane-like linkers from 1,4-boronophenylphosphonic acid that could condense to make COFs with a valency of 8 or, by adding acid, could form large, single crystals with an infinite-rod topology. —PDS

Science, this issue p. 424

GEOCHEMISTRY

Getting rid of fool's gold

Pyrite, also called fool's gold, is an iron sulfide mineral that is very commonly found in rock but is almost nonexistent in sediments today. Pyrite oxidizes quickly and is a major source of sulfur to the ocean, but it

is also a proxy for the oxygen content historically in Earth's atmosphere. Gu *et al.* conducted a set of detailed observations of the pyrite oxidation process in a shale unit. The authors found that erosion tied to fracturing is just as important as the oxygen content for the dissolution process. They developed a model that helps determine the conditions in Earth's past for which pyrite might have been stable and the role of microorganisms in the oxidation process. —BG

Science, this issue p. 425

CORONAVIRUS

Miniproteins against SARS-CoV-2

Severe acute respiratory syndrome coronavirus 2 (SARS-CoV-2) is decorated with spikes, and viral entry into cells is initiated when these spikes bind to the host angiotensin-converting enzyme 2 (ACE2) receptor. Many monoclonal antibody therapies in development target the spike proteins. Cao *et al.* designed small, stable proteins that bind tightly to the spike and block it from binding to ACE2. The best designs bind with very high affinity and prevent SARS-CoV-2 infection of mammalian Vero E6 cells. Cryo-electron microscopy shows that the structures of the two most potent inhibitors are nearly identical to the computational models. Unlike antibodies, the miniproteins do not require expression in mammalian cells, and their small size and high stability may allow formulation for direct delivery to the nasal or respiratory system. —VV

Science, this issue p. 426

POLYMER CHEMISTRY

A new future for polyethylene

Most current plastic recycling involves chopping up the waste and repurposing it in materials with less stringent engineering requirements than the original application. Chemical decomposition at the molecular

level could, in principle, lead to higher-value products. However, the carbon-carbon bonds in polyethylene, the most common plastic, tend to resist such approaches without exposure to high-pressure hydrogen. F. Zhang *et al.* now report that a platinum/alumina catalyst can transform waste polyethylene directly into long-chain alkylbenzenes, a feedstock for detergent manufacture, with no need for external hydrogen (see the Perspective by Weckhuysen). —JSY

Science, this issue p. 437;
see also p. 400

ADAPTATION

Microbial selection drives adaptation

Many legumes have a host-symbiote relationship with nitrogen-fixing bacteria, or rhizobia, that provides a benefit to both the plant and the microbe. Batstone *et al.* experimentally evolved the association between five legume accessions and different bacterial isolates. Rather than observe selection by the host for bacterial associations (host choice), mutations accumulated within a bacterial plasmid and increased the strength of the mutualism. Thus, local and recent associations between bacterial strains and plant genotypes are due to selection for bacterial adaptation. —LMZ

Science, this issue p. 476

OXYGEN SENSING

Origins and evolution of hypoxia response

In our current oxygen-rich atmosphere, the ability of eukaryotic cells to sense variation in oxygen concentrations is essential for adapting to low-oxygen conditions. However, Earth's atmosphere has not always contained such high oxygen concentrations. Hammarlund *et al.* discuss oxygen-sensing systems across both plants and animals and argue that the systems are functionally convergent and that

their emergence in an initially hypoxic environment shaped how they operate today. —SNV

Science, this issue p. 421

MICROBIOTA

So much more to mucus

Mammals accommodate a dense community of metabolically active microorganisms in their gut. This is not a passive relationship, and host and microbe have antagonistic as well as mutualistic responses to each other. Using a whole-colon imaging method in mice, Bergstrom *et al.* looked at the role of colonic mucus in segregating the microbiota from host cells during elimination of feces (see the Perspective by Birchenough and Johansson). Host goblet cells synthesize two forms of mucin that differ in branched chain O-glycosylation and the site of production in the colon. A "thick" mucus in the proximal, ascending colon wraps the microbiota to form fecal pellets. Transit along the distal, descending colon is lubricated by "thin" mucus that transiently links with the thick mucus. Normal mucus encapsulation prevents inflammation and hyperplasia and thus is important for maintenance of a healthy gut. —CA

Science, this issue p. 467;
see also p. 402

SOCIALITY

Old chimp friends

As humans age, we prioritize established positive friendships over the new, but risky, socializing we do when we are young. It has been hypothesized that this shift may come as our own sense of mortality kicks in. Rosati *et al.* analyzed a rare, long-term dataset on social bonds among male chimpanzees and found a very similar focus on old and positive friendships (see the Perspective by Silk). Though there is evidence of some sense of time among nonhuman animals, it seems unlikely that they have the same impending sense of mortality that we experience; thus, these results suggest that

a different, and deeper, mechanism may be at play. —SNV

Science, this issue p. 473;
see also p. 403

REVIEW SUMMARY

OXYGEN SENSING

Oxygen-sensing mechanisms across eukaryotic kingdoms and their roles in complex multicellularity

Emma U. Hammarlund^{*†}, Emily Flashman, Sofie Mohlin, Francesco Licausi^{*†}

BACKGROUND: Animals and land plants are the most diverse complex multicellular life-forms on Earth, and their success intricately links a capacity for adhering cells to perform different tasks at different times. The performance of cell tasks, however, can be both dependent on and challenged by oxygen. Oxygen acts as the final electron acceptor for aerobic respiration but also participates in reactions to generate metabolites and structural macromolecules; recently, oxygen also has come to the fore for its signaling role in developmental programs in animals and plants. Today, the relative oxygen concentration within multicellular organisms integrates information about cell position, metabolic state, and environmental conditions. For the rise of complex life, the capacity to link oxygen perception to transcriptional responses would have allowed organisms to attune cell fates to fluctuations in oxygen availability and metabolic needs in a spatiotemporal manner.

ADVANCES: Recent discoveries of oxygen-sensing mechanisms in different eukaryotic kingdoms allow us to compare molecular strategies dedicated to this task and the outputs that these produce. Remarkably, higher plants and ani-

mals converged, from a functional perspective, to recruit dioxygenase enzymes to posttranslationally modify transcriptional regulators for proteasomal degradation at the relatively “normoxic” conditions. In this way, transcriptional responses can be repressed at higher oxygen levels (which is context dependent) but are specifically elicited under hypoxia. The mitigation of the effects of prolonged hypoxia is also similar in animals and plants: reduction of metabolic rate, avoidance of toxicity of anaerobic by-products, and prevention of cell injury upon reoxygenation. Recent geological and phylogenetic investigations allow us to reconstruct the origin of such molecular switches in the eukaryotic clade and compare it with the development of organ-grade multicellularity. The results support the perspective that oxygen-consuming enzymes evolved sensory functions depending on the contingent requirements imposed by the environment and developmental programs. Considering that these sensing machineries evolved at a time (in the Neoproterozoic and early Paleozoic eras) when atmospheric oxygen concentrations were substantially lower than today, and in marine settings where redox is prone to vary, they may have played a major

role in guiding development and homeostasis in response to endogenous oxygen dynamics. The broad scope of oxygen sensing and response machineries for multicellular success is further highlighted when hijacked during tumorigenesis to support uncontrolled growth in a variety of conditions and stresses.

OUTLOOK: The broad role of oxygen-sensing systems in the survival and evolution of complex multicellular life requires further exploration, including into the commonality and conservation of the oxygen-sensing machineries. That higher plants and animals adopted alternative solutions to direct their primary hypoxia responses, despite their ancestors likely being equipped with the same enzymatic repertoire, may describe differences in their respective environmental, cellular, and organismal features and histories. Broadly, by shifting focus from exploring oxygen-sensing mechanisms as primarily a response to oxygen shortage for aerobic respiration, we can potentially reveal previously unidentified ways in which these systems can be manipulated for clinical and agricultural benefit. By such an approach, we will gain further insight to their broad scope and the challenges that multicellular life is exposed to, today as in geologic history. ■

The list of author affiliations is available in the full article online.

^{*}These authors contributed equally to this work.

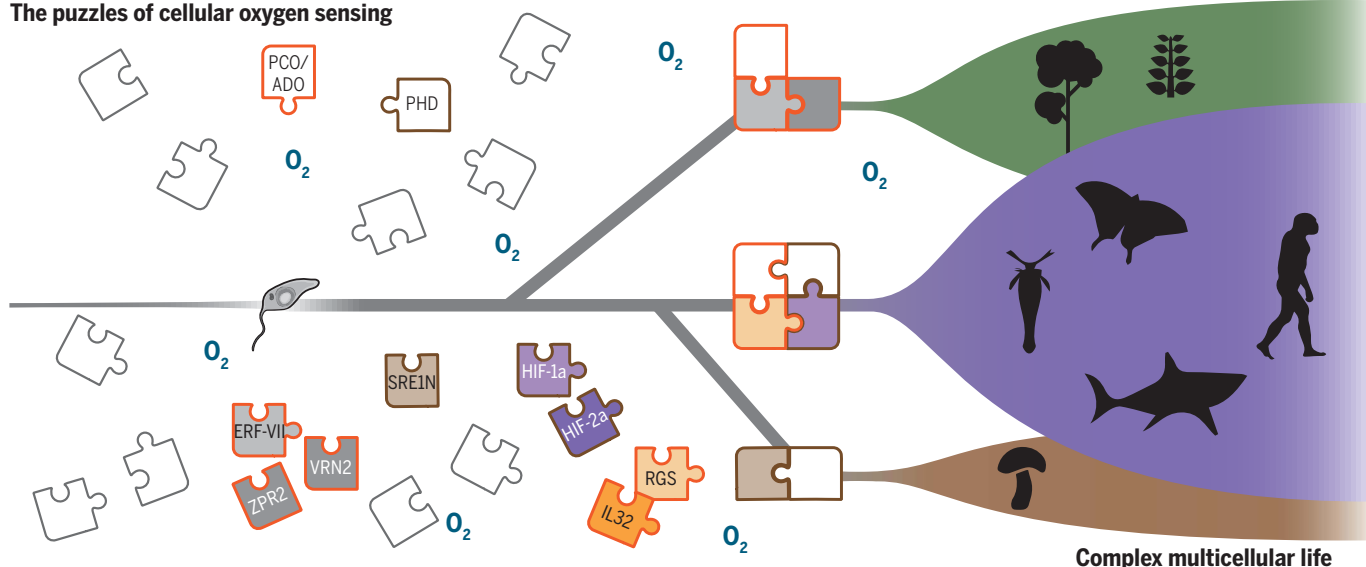
[†]Corresponding author. Email: emma.hammarlund@med.lu.se

(E.U.H.); francesco.licausi@plants.ox.ac.uk (F.L.)

Cite this article as E. U. Hammarlund et al., *Science* **370**, eaba3512 (2020). DOI: 10.1126/science.aba3512

S READ THE FULL ARTICLE AT
<https://doi.org/10.1126/science.aba3512>

The puzzles of cellular oxygen sensing



Eukaryotic kingdoms convergently recruited dioxygenases to sense fluctuations in ambient oxygen and to respond under hypoxia. Oxygen sensing allows cells to attune their metabolism and fate to spatiotemporal requirements, a critical component in complex multicellularity. The basal oxygen-sensing mechanisms use alternative targets in plants, fungi, and animals—kingdoms that alone demonstrate the capacity to form tissues of different complexities.

REVIEW

OXYGEN SENSING

Oxygen-sensing mechanisms across eukaryotic kingdoms and their roles in complex multicellularity

Emma U. Hammarlund^{1,2,3,*†}, Emily Flashman⁴, Sofie Mohlin^{1,5}, Francesco Licausi^{6,7,8,*†}

Oxygen-sensing mechanisms of eukaryotic multicellular organisms coordinate hypoxic cellular responses in a spatiotemporal manner. Although this capacity partly allows animals and plants to acutely adapt to oxygen deprivation, its functional and historical roots in hypoxia emphasize a broader evolutionary role. For multicellular life-forms that persist in settings with variable oxygen concentrations, the capacity to perceive and modulate responses in and between cells is pivotal. Animals and higher plants represent the most complex life-forms that ever diversified on Earth, and their oxygen-sensing mechanisms demonstrate convergent evolution from a functional perspective. Exploring oxygen-sensing mechanisms across eukaryotic kingdoms can inform us on biological innovations to harness ever-changing oxygen availability at the dawn of complex life and its utilization for their organismal development.

The rise of Earth's most complex and sizable life-forms—animals and land plants—remains enigmatic. Out of all of life's diversity, only animals and land plants have multiple organs such as a brain and lungs or roots and leaves. Animals and plants therefore represent two distinctly successful versions of complex multicellularity, but the inferred causes for their success are opposing. Although the rise of animals is commonly explained as a result of environmental change (increased oxygen) that unleashed the full potential of biological innovations (1, 2), the rise of plants is explained with biological innovations unleashing a capacity to live with environmental change (for example, in aquatic or terrestrial environments) (3). However, recent and transdisciplinary insights demonstrate that animals and land plants share a particularly versatile capacity to perceive and respond to fluctuating oxygen conditions (4, 5). Here, we propose that the acquisition of the capacity to perceive and respond to the variable presence of oxygen must have been central to the rise of complex life. To evaluate this hypothesis, we consider two worlds in parallel, and bridge their information: the modern world, in which an oxygen-sensing capacity provides key functions to animals and plants, and the

historic one, in which neither oxygen-sensing mechanisms nor complex multicellular organisms were yet fully in place.

Free oxygen profoundly affects eukaryotic cells. On the one hand, molecular oxygen acts as a terminal electron acceptor that yields unprecedented energy during aerobic respiration and builds metabolites. On the other hand, reactive chemical species that contain oxygen can change the configuration and function of nucleic acids, sugars, lipids, proteins, and metabolites. The paramount impact that fluctuating oxygen availability has for cell function and constitution makes the capacity to perceive oxygen vitally important for any eukaryotic organism, especially when the organism is multicellular. Complex multicellular organisms are defined by their persistent three-dimensional organization, in which adhering cells can perform different tasks of labor at different times (6–8). Cell clustering per se represents a state that buffers environmental chemical fluctuations and stabilizes internal gradients. However, internal oxygen gradients also change dynamically as a function of cell respiration. Cells will therefore experience different oxygen availability depending on both their spatial and temporal (spatiotemporal) position. These fluctuations in dynamic internal oxygen gradients combined with oxygen's power to affect cell functions therefore make the capacity to perceive oxygen an adaptation with considerable but yet underappreciated scope. If the capacity to sense oxygen is combined with specific responses to different oxygen concentrations, it would also facilitate spatiotemporal induction of different cellular functions.

Oxygen sensing is the ability by which modern organisms detect changes in the amount of oxygen within and between cells, coupled to a context-dependent response. As of today,

oxygen sensing is commonly described as the acute response to oxygen concentrations below the respiratory requirements (hypoxia) of the host. This allows tissue homeostasis when, for example, a muscle experiences oxygen depletion during a fast run or when a root's access to oxygen is blocked by waterlogging. However, although the necessity of an acute response to hypoxia makes sense to us humans, as obligate aerobes, the normalcy of hypoxia offers another perspective: Oxygen levels below the ambient concentration can be argued to be normal for certain tissues in plants (9) and most tissues in animals (10–12). Hypoxia also prevailed globally at the time in Earth history when oxygen sensing evolved, with atmospheric oxygen concentrations presumably below ~5% (13, 14). The hypoxia-response machineries reach beyond coping with hypoxia to coordinate different cell fates (future identities and tasks) in accordance with—and despite—oxygen availability and fluctuations.

Here, we present a broad look at oxygen-sensing mechanisms across eukaryotic kingdoms and time, to place their role within the context of evolving complex multicellularity (Box 1). We describe the rarity of complex multicellularity over the history of life, the prevalence of fluctuating environmental oxygen conditions, and the necessity to perceive these fluctuations. We then review the different known oxygen-sensing mechanisms and their roles for modern forms of multicellularity, discussing the conceptual gaps that present opportunities to explore the hierarchical order, evolution, and impacts of cellular oxygen sensing.

The historic arena: Hypoxic, variable, and largely devoid of multicellularity

Complex multicellular organisms are rare in the long history of life when compared with the diversity of unicellular organisms. The diversity of unicellular prokaryotes (Archaea and Bacteria) and eukaryotes (protists in the broad sense, including Protozoa, Chromista, and Archezoa) is estimated to supersede the collective phylogenetic diversity of animals, plants, and fungi by at least an order of magnitude (15, 16). The degree of organismal complexity can also be compared by the diversity of cell types that make up tissues. With that view, vascular plants and particularly animals are by far more complex than all other known organisms (17–19). Simple multicellularity is an aggregation of cells where spatiotemporal coordination of labor is lacking, and this has evolved independently multiple times (20). Complex multicellularity, however, has diversified only six times across geologic history: three within the plant kingdom (red algae, brown algae, and land plants), twice in the kingdom of fungi, and once as the animal kingdom (7). Out of these events, only animals and land plants (Embryophyta) form organ

¹Translational Cancer Research, Department of Laboratory Medicine, Lund University, Scheelevägen 8, 223 81 Lund, Sweden.

²Nordic Center for Earth Evolution, University of Southern Denmark, Campusvej 55, 5230 Odense M, Denmark.

³Department of Geology, Lund University, Sölvegatan 12, 223 62 Lund, Sweden.

⁴Chemistry Research Laboratory, University of Oxford, Mansfield Road, Oxford OX1 3TA, UK.

⁵Division of Pediatrics, Department of Clinical Sciences, Lund University, 221 00 Lund, Sweden.

⁶Department of Plant Sciences, University of Oxford, South Parks Road, Oxford OX1 3RB, UK.

⁷PlantLab, Institute of Life Sciences, Scuola Superiore, Sant'Anna, 56124 Pisa, Italy.

⁸Department of Biology, University of Pisa, Pisa, Italy.

*These authors contributed equally to this work.

†Corresponding author. Email: emma.hammarlund@med.lu.se

(E.U.H.); francesco.licausi@plants.ox.ac.uk (F.L.)

Box 1. Glossary.

Cell fate: The future identity of a cell (or its daughter cells) and the accompanying phenotype or task to perform within its tissue and context.

Enzymatic proteolysis: Breakdown of proteins into peptides by the action of proteases, often organized in complexes, such as the proteasome. In cells, proteolysis is often directed by cascades of posttranslational modifications, including ubiquitination, that label a protein for degradation.

Enzymes: Proteins that can catalyze a chemical reaction (biocatalyst) and thus offer a kinetic potential to chemical reactions. Oxygen-dependent enzymes discussed in this review include 2-OG-dependent dioxygenases, thiol dioxygenases, PCOs, and ADO.

Fe(II)/2-oxoglutarate (2-OG)-dependent dioxygenase: Oxidoreductase enzymes that catalyze incorporation of oxygen atoms into a variety of substrates. 2-oxoglutarate is concomitantly converted to succinate and CO₂.

Thiol dioxygenases: Fe(II)-dependent enzymes that catalyze the oxygen-dependent oxidation of free thiols (-SH) to sulfinic acid (-SO₂H).

Plant cysteine oxidases (PCOs): A group of thiol dioxygenases that catalyze dioxygenation of cysteinyl (Cys) residues at the N termini of substrate proteins, such as the ERF-VII TFs.

2-Aminoethanethiol dioxygenase (ADO): A thiol dioxygenase that regulates stability of N-terminal Cys-initiating proteins IL32 and RGS4 and -5 in humans through Cys dioxygenation and the N-degron pathway.

Eukaryotic kingdoms: Protista, Plantae, Animalia (Metazoa), and Fungi.

Eumetazoa: A basal animal clade and sister group to Porifera (sponges). Eumetazoans have either radial (for example, cnidaria) or bilateral symmetry (invertebrates or vertebrates).

Hypoxia-response machinery: Cellular system that consists of one component that perceives a decrease in oxygen availability (such as an enzyme) and one that induces a response (such as a TF) to trigger cellular adaptation.

Oxygen sensing: The ability to detect changes in the amount of oxygen and mount an adaptive response.

Redox: Chemical reactions in which the oxidation states of atoms change.

Stemness: Cell ability of self-renewal through division and differentiation into specialized cell types.

Spatiotemporal division of cell fate: When cells in an organ perform different functions at the same time in a coordinated manner.

Transcription factor (TF): A protein that controls the rate of transcription of genetic information from DNA to mRNA. They bind to DNA in a sequence-specific manner. The main TFs discussed in this Review are HIFs and ERF-VIIs.

Hypoxia inducible factors (HIFs): Members of the basic helix-loop-helix (bHLH) family, consisting of an α subunit and a β unit (ARNT). Generally, the HIFs are constitutively expressed, but their α subunit is degraded via Fe(II)/2-OG-dependent oxygenases in the presence of oxygen.

Group VII ethylene response factors (ERF-VIIs): Cys-initiating members of the ERF/APETALA2 (ERF/AP2) family. Some ERF-VIIs are constitutively expressed but degraded through the activity of PCOs in the presence of oxygen.

Viridiplantae: Green plants, consisting of the clades Chlorophyta and Streptophyta, under which land plants (Embryophyta) and vascular plants (Tracheophyta) are subdivisions. A subdivision of vascular plants is flowering plants (angiosperms).

systems. Although the ages of the first or last common eukaryotic ancestor as well as when eukaryotic kingdoms diverged are debated, the diversification of eukaryotes is considered late by most. Records of molecular clock estimates and microfossils suggest that it took at least a billion years before the diversification of the animal and plant (Viridiplantae and Streptophyta) kingdoms began some 0.8 billion years (Ga) ago in the Cryogenian Period (21, 22). Thereafter, animal diversity “exploded” in the Cambrian and Ordovician periods (0.54 to 0.44 Ma ago), which was also when land plants (Embryophyta) and vascular plants (Tracheophyta) originated (Fig. 1) (3, 21). Thus, organ-grade complex multicellularity evolved only twice, both relatively late in Earth history.

The rarity of successful transitions from unicellular eukaryotes to complex multicellular life suggests that cellular and environmental components necessary to facilitate persistent and complex multicellularity are difficult to align. One environmental component, and proposed cause for the rise of animal diversity in particular, is how environments would have become permissive through the inferred increase in free oxygen (1, 2, 23). However, the increased ability to sense fluctuations of free oxygen can also be inferred as a biological component and cause of the rise of diversity of animals as well as in plants.

Free oxygen began to build up in the atmosphere about halfway through Earth's 4.6-Ga history, instigated by the cyanobacterial ca-

capacity for oxidative photosynthesis. The signs of free atmospheric oxygen are visible in the rock record at ~2.45 Ga ago, through indirect geochemical evidence (24). Before this, however, free oxygen was produced and seemingly present in marine shallow (shelf) settings (25) at the trace concentrations that allow biosynthesis of steroids (26). After this, and for more than the following 2 Ga, atmospheric oxygen concentrations were likely predominantly as low as what oceanographers call severely hypoxic (<2%) or hypoxic [<5 to 7%, albeit this is context dependent (27)] (14). Over the Cambrian and Ordovician periods, when animals diversified and vascular plants originated, geochemical reconstructions estimate that the atmosphere had 2 to 5% or, at most, 10% oxygen (13, 14, 28, 29). Not until ~150 Ma after the rise of animals and plants, in the Silurian or Devonian periods, did global oxygenation approach modern levels (Fig. 1) (30). Thus, conditions at the time when animals and plants and their oxygen-sensing mechanisms originated and diversified can be considered hypoxic by today's standards.

Variability of oxygen concentrations is a physical imperative on Earth's surface. Even today, when the atmosphere is richly oxygenated (21% O₂), oxygen levels vary dramatically both in soil and within the ocean. Respiration of biomass may consume oxygen faster than it is replenished, whether in soil or water (in water, gas diffusion is four orders of magnitude slower than in air). Animals and green plants evolved in the ocean, where production and respiration of biomass together with physical mixing, such as from winds and waves, result in constantly variable environmental oxygen conditions. The long history of oxygen fluctuations in shallow marine niches would have posed a ceaseless challenge to nascent multicellular organisms with limited capacity to perceive and respond to these variations. Thus, both the challenges and opportunities for eukaryotic life to intermittently encounter free oxygen attributes an evolutionary importance to the cellular mechanisms that perceive it. Before the development of cellular mechanisms to perceive and to orchestrate organismal responses to changes in oxygen conditions, complex multicellular life would have struggled to sustain in niches with fluctuating conditions on Earth's surface (31).

The past and present of oxygen sensing

Oxygen sensing acts as a transducer of hypoxic signaling, which is best illustrated by the primary hypoxia-response machineries in plants and animals. These machineries function through the action of oxygen-dependent enzymes that repress the operation of transcription factors (TFs). In an oxygen-dependent reaction, these enzymes catalyze a posttranslational modification of the TF that reduces its stability (4, 5). Oxic conditions therefore lead to degradation

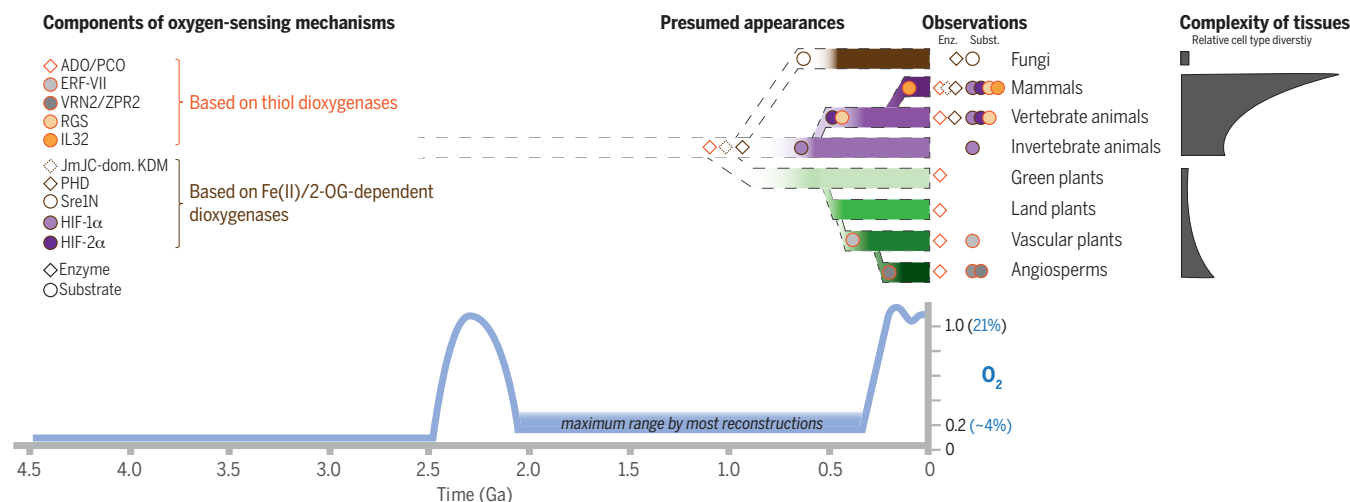


Fig. 1. Increasing complexity of oxygen-sensing mechanisms and the extent of complexity within multicellular organisms over Earth's history of 4.6 Ga. Enzymes (diamonds) and substrates (circles) form components of oxygen-sensing mechanisms, based on thiol dioxygenases (orange outlines) and Fe(II)/2-OG-dependent dioxygenases (brown outlines). We depict the presumed appearance of the oxygen-sensing components during the divergence of the eukaryotic animal, plant, and fungi kingdoms (dashed lineages). We depict the onset of the respective diversifications of fungi (Basidiomycota and Ascomycota) with differentiated tissues (brown) (138); invertebrate animals, vertebrates, and mammals (purple) (23); and green, land, and vascular plants (green) (3). Observations of enzymes (Enz.) and substrates (Subst.) for each group of organisms include when found in sequences, when determined to have an oxygen-

sensing role, or both. Complexity of tissues for each group of organisms is represented by their maximum number of different cell types (diversity) (6, 17, 19). Reconstructions of atmospheric oxygen levels in the past, which constrain ranges of min-max oxygenation, agree upon a maximum oxygenation of ~0.2 of modern levels (<~4% oxygen) for the Mesoproterozoic Era (1.6 to 1.0 Ga ago) and Neoproterozoic Era (1.0 to 0.6 Ga ago) (thick blue field) (14, 139). The maximum oxygenation of ~4% is presumed for the time interval when eukaryotic kingdoms diversified (0.8 to 0.5 Ga ago) (21, 22), meaning that the evolution of oxygen-sensing mechanisms is rooted in hypoxic conditions. Geochemical indications and modeling efforts indicate that high atmospheric oxygen concentrations, as today, persisted at 2.5 to 2.0 Ga ago and then from 0.4 Ga ago (the Devonian Period) onward (13, 14, 24, 28, 30, 139).

of these TFs and, hence, inactivity of the hypoxic responses. In hypoxic conditions, however, reduced activity of the oxygen-sensing enzymes allows stabilization of the TFs, which direct the response to hypoxia by up-regulating a suite of genes that trigger adaptation. Enzymes are particularly suited to act as sensors because their rate of activity is proportional to the amount of substrate available—they can elicit a graded response to oxygen.

Sensing through Fe(II)/2-OG-dependent oxygenases

The first identified and most characterized hypoxia-response machinery is the system of hypoxia-inducible factors (HIFs) in animals, the discovery of which was recognized with the 2019 Nobel Prize in Physiology or Medicine (32). HIFs are heterodimers that consist of α subunits and the aryl hydrocarbon receptor nuclear translocator (ARNT), or β subunit. HIF- α subunits are stabilized at hypoxia, leading to the transcription of hundreds of genes that promote adaptive responses. In physiologically oxic conditions, however, the oxygen-dependent prolyl hydroxylase (PHD) enzymes catalyze hydroxylation of specific prolyl residues in HIF- α proteins that enable their recognition by ubiquitin ligase complexes [commonly the von Hippel Lindau (VHL) pro-

tein] and subsequent degradation through the proteasome (33). A second hydroxylase enzyme [factor-inhibiting HIF (FIH)] catalyzes hydroxylation of an asparagine (Asn) residue in HIF- α to reduce the transactivation capacity of HIFs. The PHDs and FIH are Fe(II), 2-oxoglutarate (2-OG), and oxygen-dependent enzymes, whose rate of activity is sensitive to oxygen availability, particularly the PHDs (34–36). This means that even a small decrease in oxygen availability can potentially result in a reduction in HIF hydroxylation to enable HIF stabilization and activation of its transcriptional response (Fig. 2). Although PHD-like enzymes are conserved even in bacteria (37) and fill an oxygen-dependent regulatory role in yeast (38), their oxygen-sensing function appears refined with the involvement of HIF and the ubiquitin-proteasome system (39). All eumetazoans (animals with bilateral and radial symmetry) except the ctenophores possess the HIF-1 α subunit, whereas only vertebrate animals possess the HIF-2 α subunit (40, 41).

Eukaryotes and prokaryotes involve Fe(II)/2-OG-dependent dioxygenases in a number of important biological functions (42). Although the catalytic rate of all these enzymes depends on oxygen availability, whether or not these enzymes can act as oxygen sensors in the hypoxia-response machinery depends on two

factors: (i) whether the impact of their activity is transduced through their substrates to induce a response and (ii) whether their rate of activity is limited by the range of oxygen concentrations present in the cell. Despite overall conservation of enzyme structure and catalytic mechanism, different Fe(II)/2-OG-dependent dioxygenases are rate-limited by oxygen at different concentrations. The PHDs are rate-limited at relatively high oxygen concentrations. FIH activity can, however, tolerate mild hypoxia for HIF Asn-hydroxylation and even more severe hypoxia for non-HIF substrates (43). Other members of this enzyme family are restricted only at very low oxygen concentrations to initiate an adaptive response at severe hypoxia. For example, ten-eleven translocation (TET) DNA demethylases only lose their activity in severely hypoxic tumors, leading to DNA hypermethylation (44).

A subset of Fe(II)/2-OG-dependent oxygenase enzymes, the Jumonji C (JmJC) domain-containing histone lysine demethylases (KDMs), has been reported to demonstrate an oxygen-sensing role across a broader range of oxygen concentrations. The status of histone methylation can affect chromatin packing and transcriptional responses by regulating access of TFs to promoter regions. Recent studies have connected the oxygen sensitivity of some KDMs with

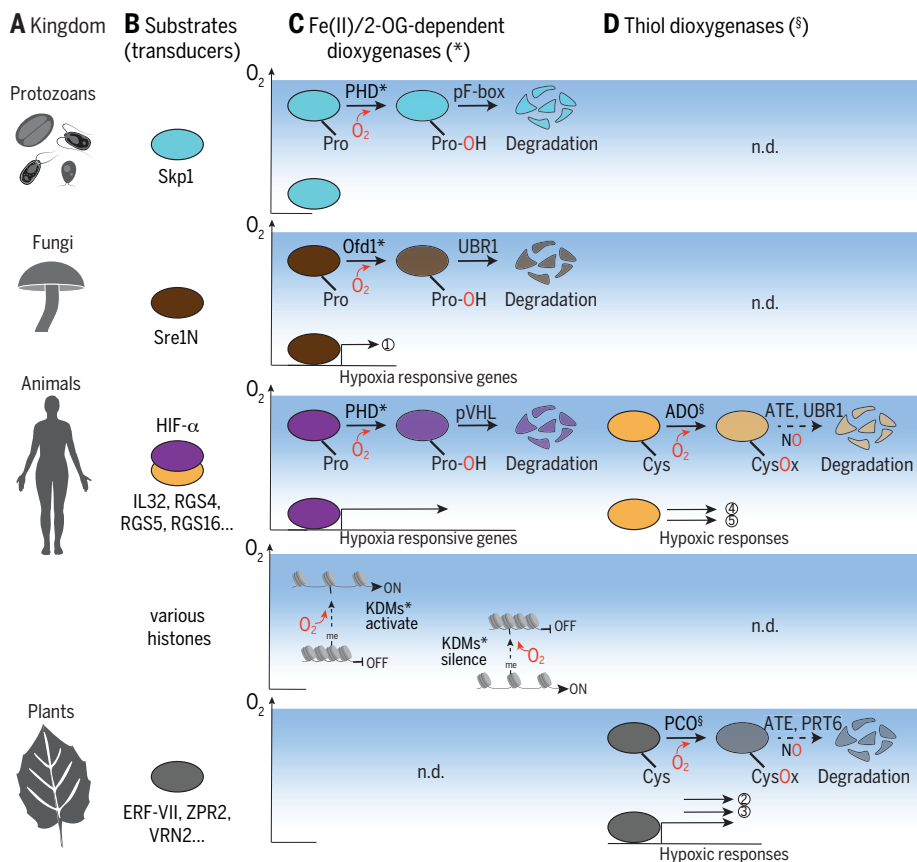


Fig. 2. Direct mechanisms for oxygen sensing and hypoxic signaling. (A) Complex multicellular organisms within the eukaryotic kingdoms. Shown are protozoa, fungi, vascular plants, and animals. (B) The transducers of hypoxia-response machineries. Shown are the Pro-containing proteins that may be hydroxylated and degraded in the presence of oxygen (blue field) or stabilized by hypoxia (white fields): Skp1; sterol regulatory element-binding protein TF (Sre1N) and HIF; or the Cys-initiating proteins ERF-VII, ZPR2, VRN2, IL32, and RGS4 and -5. Histone (de)methylation can be also modulated in an oxygen-dependent manner in eukaryotes. (C) The sensory components based on Fe(II)/2-OG-dependent dioxygenases (*) are PHDs or Ofd1, or JmJC-domain-containing KDMs. (D) The sensory components based on thiol dioxygenases (§) are PCO and ADO. By contrast, proteolysis (involving also proteins such as pF-box, UBR1, ATE, PRT6, and pVHL proteins and NO) and demethylation occur at relatively high oxygen concentrations (blue shading). Cellular responses at hypoxic conditions (hypoxic responses) are context and substrate dependent: (1) When the stabilized protein is a TF (Sre1N, ERF-VII, and HIF- α), hypoxia-responsive genes are induced, and the hypoxia responses are of different scopes (length of black arrows). Also, (2) of the PCO substrates in plants VRN2 regulates chromatin condensation, whereas (3) ZPR2 controls activity of TFs. Of the ADO substrates in animals, (4) RGS4 and -5 control G protein signaling, and (5) IL32 controls inflammation by interacting with an unknown receptor. In animals, demethylation by the JmJC-domain-containing KDMs can both activate and silence gene expression in an oxygen-dependent manner.

altered histone methylation status in hypoxia (45–47). Of these, KDM5A and KDM6A play a role in cell differentiation and fate restriction and have implications for tumorigenesis (48).

In yeast and protozoa, certain Fe(II)/2-OG dioxygenases also play oxygen-sensing roles. In fission yeast, a sterol regulatory element-binding protein TF (Sre1) promotes adaptation to hypoxic conditions, and the activity of Sre1 is controlled by an oxygen-sensitive Fe(II)/2-OG-dependent dioxygenase, Ofd1 (49). This mechanism controls cholesterol synthesis and uptake in yeast (as does its homolog in animals) (50). In protozoa, oxygen-sensing PHDs cat-

alyze hydroxylation of S-phase kinase-associated protein 1 (Skp1), an essential subunit of a ubiquitin-ligase complex. This hydroxylation transduces the oxygen-dependent regulation of different developmental stages in the protozoan life cycle. At these stages, certain oxygen concentrations work as environmental triggers and correspond to concentrations at which the enzymes are rate limited (51, 52). This rate limitation suggests that the oxygen sensitivity of these reactions has been fine-tuned and advantageous during evolution. The function of this oxygen sensitivity is clear from slime molds (Mycetozoa, normally soli-

tary amoebae), for which it facilitates regulation of cells of different differentiation states during the formation of their multicellular fruiting bodies (53).

Prokaryotes also have a variety of Fe(II)/2-OG-dependent oxygenases with a wide range of roles, including in protein translation (37, 54). Broadly, none of these has yet been reported as being highly sensitive to oxygen (except for a thermophilic ribosomal oxygenase under high-temperature conditions) (55). Bacterial oxygen sensing is instead achieved with different mechanisms that involve either conformational change of a DNA-binding protein upon oxygen binding or phosphorylation cascades that result in transcriptional up-regulation in hypoxia. Bacterial oxygen sensing is described in detail in several reviews [for example, (56)].

Sensing through thiol dioxygenases and the Arg branch of the N-degron pathway

Vascular plants exploit a different hypoxia-response machinery, albeit with features in common with the HIF system of eumetazoans. With these, constitutively expressed TFs belonging to the group VII of the ethylene response factor family (ERF-VIIs) are stabilized in hypoxia to enable transcription of a suite of genes that promote adaptive responses (57, 58). In physiologically oxic settings, the ERF-VIIs are degraded via the Arg/N-degron pathway, a process of degradation signaling in which the identity at the N terminus of a protein dictates its stability (59, 60). Plant cysteine oxidases (PCOs) catalyze dioxygenation of cysteinyl (Cys) residues at N termini (Nt) of the ERF-VII TFs (61, 62), which are subsequently arginylated by arginyl-transferases (ATEs) and then presumably recognized by the ubiquitin ligase proteolysis 6 (PRT6) (63). Basal nitric oxide (NO) levels are also required for this process (64). This recognition leads to the degradation of the ERF-VIIs. So, in plants, PCOs act as sensors, whereas the ERF-VIIs transduce the hypoxic signal into a response.

PCOs are Fe(II)-dependent thiol dioxygenases whose rate of activity with respect to ERF-VII oxidation is sensitive to oxygen availability (65), similar to the metazoan PHDs involved in HIF regulation. Apparently, these two hypoxia-response mechanisms have evolved separately but fulfill similar roles. Unlike the HIF hydroxylases, for which activity toward non-HIF substrates is uncertain (66), the PCOs appear to have multiple substrates, including little zipper protein 2 (ZPR2) and vernalization 2 (VRN2) (57, 67). There are therefore several “response” components controlled by the oxygen-sensing PCOs. This means that a hypoxic response can be transduced through several pathways, depending on the cellular context. Although the degree of oxygen sensitivity of the PCOs toward these and other alternative

substrates is yet unreported, the hypoxia dependence of this function is clear. ERF-VIIs first appeared in vascular plants, and ZPR2 and VRN2 became Cys-initiating proteins in flowering plants (angiosperms) (68, 69). On the other hand, the enzymatic asset of the Arg/N-degron pathway and PCOs required to operate oxygen-dependent degradation of Nt-Cys-degrons can be traced back to unicellular eukaryotic ancestors of plants and animals (69). Thus, it can be hypothesized that other Cys-initiating proteins control the hypoxia response in lower plants. In this perspective, the identification and characterization of Cys-initiating TFs is of particular interest.

Intriguingly from an evolutionary perspective, a human homolog of the PCOs, the enzyme 2-aminoethanethiol dioxygenase (ADO), was recently identified as regulating the stability of certain N-terminal Cys-initiating proteins in humans [interleukin-32 (IL32) and regulator of G protein signaling 4 and 5 (RGS4/5)] through the Arg/N-degron pathway (70). ADO acts as a separate human oxygen sensor by means of an equivalent mechanism to that of the PCOs in plants. ADO activity toward RGS4/5 is particularly oxygen sensitive, with a rate dependence close to that of the PHDs (36). So far, no Nt-Cys-degron TF has been identified as an ADO substrate; thus, the response component of this machinery does not amplify the transduction of the hypoxic signal similarly to HIF or ERF-VIIs. Nevertheless, the commonality in oxygen-dependent proteolysis (degradation) mediated by thiol-dioxygenases in plants and animals is striking and may suggest the existence of an ancestral mechanism in early eukaryotes.

These observations hint at both convergence and divergence of oxygen-sensing machineries in complex multicellular eukaryotes. On the one hand, both metazoans and vascular plants converged to the aerobic degradation of constitutively expressed transcriptional regulators. The key sensory dioxygenases and protein substrates differ, but the proteostatic logic that enables the activation of adaptive responses is very similar. On the other hand, the presence of both enzymes in the plant and animal kingdoms indicate a preference toward either system, possibly to accommodate specific developmental, physiologic, or metabolic requirements. In the evolutionary perspective of oxygen perception, it is remarkable that plant and animal species share few conserved mechanisms when compared with the high diversity displayed in bacteria, archaea, and fungi (56, 71).

The power of hypoxia-response machineries

The roles of oxygen-sensing mechanisms have been explored at the cellular, individual, and evolutionary levels, often under the assumption that hypoxia is a “stress.” Here, however,

we evaluate whether the adaptations provided by oxygen sensing allow cells and individuals to cope with fluctuations and internal gradients in oxygen availability on both temporal and evolutionary time scales. We also consider their capacity for spatiotemporal coordination of cell labor and fates.

Guarding against oxygen fluctuations—homeostasis

Oxygen concentrations perpetually fluctuate in Earth’s surface environments as a function of consumption, diffusion, and resupply. Similarly, oxygen concentrations fluctuate within and outside of organisms, tissue, and cells. When oxygen concentrations are temporarily lower than the organism’s respiratory requirements, responses act to maintain homeostasis through reversal or mitigation. Homeostatic responses to hypoxia typically involve mRNA reprogramming, which represses energetically expensive pathways and up-regulates those associated with adaptation or avoidance (72–74).

Temporal oxygen deficit for metabolic reactions requires activation of alternative pathways that minimize oxygen consumption (75, 76) but also may induce the activity of essential enzymes that use oxygen as a substrate (77, 78). When severe hypoxia shifts sugar metabolism toward substrate-level phosphorylation at the expense of the oxidative pathway, this is achieved by facilitating carbon entry into the glycolytic pathway (74), putting on the brakes to pyruvate channeling into the tricarboxylic acid (TCA) cycle and redirecting it to fermentative reduction. Albeit different in eukaryotic kingdoms, these ancillary reactions sustain the carbon flux through glycolysis by the regeneration of oxidized nicotinamide adenine dinucleotide (NAD⁺) and, concomitantly, prevent the inhibition of glycolysis by its own products. The majority of animals as well as some fungi reduce pyruvate to lactate by means of hypoxia-inducible lactate dehydrogenase (LDH) (79), whereas yeasts rely exclusively on alcohol fermentation by means of a two-reaction pathway that decarboxylates pyruvate and reduces the resulting acetaldehyde (80). In Viridiplantae, both metabolic strategies of reducing pyruvate, either from LDH or through alcohol fermentation, are activated under hypoxia, with additional contribution of formate, hydrogen, acetate, and alanine synthetic pathways (81, 82). Higher plants evolved toward a preference for ethanol fermentation because lactic acid deprotonation contributes to cytosolic acidosis and thus jeopardizes cellular functioning and integrity. Removal of fermentative products is also facilitated in the animal and plant kingdoms—for example, with the up-regulation of lactate exporters (83, 84). In contrast to lower species in which fermentation appears controlled by substrate availability or posttranslational regulation, genes coding for enzymes and trans-

porters involved in this metabolic adaptation to hypoxia are found incorporated in the main hypoxia response in metazoans and higher plants (74, 76). From this perspective, transcriptional regulation of the genes coding for this metabolic adaptation is a recent acquisition, concomitant to the increase in developmental complexity in both kingdoms. Thus, convergence toward this regulation seems to offer an ecological advantage for complex multicellular systems to cope with the temporal offset between metabolic requirements and oxygen availability (Fig. 3).

Counteracting hypoxia through reoxygenation is also activated in animal and plant tissues. In most vertebrates, for example, this is attained through the local generation of new blood vessels (angiogenesis) and of synthesis of erythrocytes that carry oxygenated hemoglobin (85). Plants, instead, lack a dedicated oxygen distribution system, and thus certain species that are adapted to flooding acquired the ability to form hollow paths along stems and roots (aerenchyma) for unrestricted gas diffusion from above-water organs to submerged tissues (86). When the whole plant is underwater, rapid growth of stems and leaves can be deployed for emergence and ensure oxygen acquisition (87). Neither aerenchyma formation nor the elongation of organs are controlled by oxygen availability directly but rather through the gas hormone ethylene, whose synthesis is enhanced by submergence (88, 89).

Fluctuations in oxygen are concomitant with fluctuations in reactive oxygen species (ROS) and reactive nitrogen species (RNS). A burst of hydrogen peroxide (H₂O₂) and NO has been reported to occur in animal and plant cells when these are challenged by severe oxygen deficiency (90–93). Additional and more severe ROS accumulation is also expected as normoxic conditions are restored. Genes regulated by HIFs and ERF-VII in animals and plants, respectively, code for scavengers of both ROS and NO, as well as enzymes involved in redox homeostasis, such as glutathione peroxidase, superoxide dismutase, glutathione *S*-transferases, and thio-redoxins (94, 95). In turn, ROS and NO contribute to HIF and ERF-VII regulation at the transcriptional and posttranslational level in animal and plant cells, respectively (64, 96).

Although strategies to reverse the effects of short-term hypoxia are kingdom specific (reoxygenation), mitigation of the effects of prolonged hypoxia can be related to similar strategies in animals and plants: reduction of the metabolic rate, avoiding toxicity of anaerobic by-products, and preventing cell injuries upon reoxygenation. Oxygen-sensing machineries assist animals and plants in these strategies to cope with the imbalances that fluctuating oxygen availability causes to the cellular environment. Collectively, these systems contribute to the ability of multicellular organisms to maintain homeostasis.

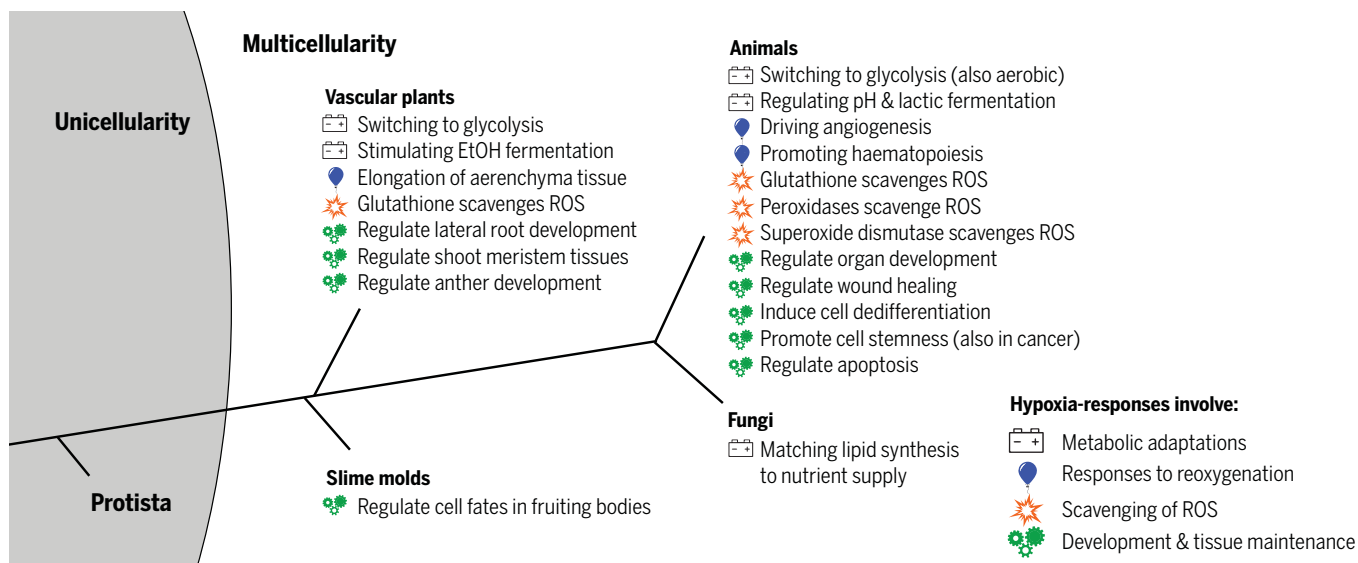


Fig. 3. Roles that hypoxia-response machineries appear to be involved in across eukaryotic kingdoms. Also shown are representative roles listed as related to mediation of metabolism (battery), oxygen resupply (balloon), scavenging of ROS (explosion), or development and tissue maintenance (cogs).

A capacity to modulate cell fate

The importance of oxygen availability and gradients for cells to multiply and differentiate has been recognized for a long time, and so has the cellular capacity to sense these. A wide range of oxygen concentrations have been measured across plant and animal organs and observed to vary throughout developmental stages (68, 97). Mammalian embryogenesis occurs mainly at low oxygen concentration, and several types of stem and progenitor cells are embedded in hypoxic niches, where oxygen gradients drive their differentiation (98). Similarly in plants, the proliferative tissues responsible for producing new organs, the meristems, have also been shown to be embedded in hypoxic niches (67). Furthermore, detrimental cell growth hijacks the oxygen-sensing machinery and may induce cellular responses contrary to what oxygen gradients would dictate. In solid tumors, the uncontrolled proliferation of cells and their active metabolism often exceed the delivery capacity of the surrounding blood vessels, limiting oxygen availability (99). It is now 30 years since the discovery that the HIF system enables and supports tumorigenesis (100, 101). Similarly in higher plants, tumor-like tissues, such as calli or galls, experience oxygen limitations, and ERF-VIIs support the metabolism and proliferation of highly dividing and undifferentiated cells (102, 103).

Clues from cancer: Uncoordinated formation of multicellularity

The cancer field has put more emphasis on HIFs than has any other field, owing to the contribution of these factors to the success of tumor multicellularity. HIF- α is produced and degraded in the cytoplasm and, when stabilized for long enough, translocates to the nu-

cleus. Localization and functions for the HIF- α subunits, however, appear to differ (104). In the case of HIF-1 α , nondegraded protein is more or less exclusively present in the nucleus. Its activity is rather uniform by how it induces target gene expression in response to hypoxia in virtually any cell. That HIF-1 α plays a reliable role in the immediate cellular response to hypoxia argues for its seminal role as an adaptation to acute oxygen fluctuations. HIF-2 α , however, displays cytoplasmic in addition to nuclear localization (105–107). Insight from tumor multicellularity demonstrates that functions of HIF- α subunits do not always overlap. Whereas the HIF-1 α subunit, which is specific to all eumetazoans except ctenophores, can be regarded as a fast response to metabolic alterations, the vertebrate-specific HIF-2 α subunit is demonstrated to contribute to the success of tumors by modulating cell fate. Albeit that HIF-2 α also plays a modest role in metabolic regulation, its main functions are regulation of cell fate, cell immaturity (stemness), and metastasis and to establish a hypoxia-mimicking phenotype in oxygenated milieus (pseudohypoxic niches) (108–111).

The pseudohypoxic phenotype is a consequence of HIF-2 α accumulation in normoxic tumor cells, including such with the capacity to self-renew (a stem cell trait typically associated with hypoxia). Some of these HIF-2 α -expressing cells are located in perivascular niches, despite their access to oxygen in these areas (107, 112). This phenomenon is particularly well studied in the cancer forms glioblastoma and neuroblastoma (107, 112), for which there are no correlations between HIF-1 α expression and outcome, whereas expression of HIF-2 α predicts poor prognosis and distal metastasis. It is not the collected expression

itself that falls out as a predictor but rather the presence of this small fraction of HIF-2 α -positive perivascular tumor cells. These constitute a rare cell type within the tumor that coexpresses several stem cell markers, strengthening HIF-2 α as a promoter of stemness. The link between the pseudohypoxic phenotype, stemness, and the formation of tumor multicellularity is also supported by how mutations in *EPAS1* (encoding HIF-2 α) directly induce tumor formation (113). As an example of the complexity of this protein, a HIF-2-specific inhibitor, PT2385 (114), which prevents ARNT binding and transactivation capacity, does not affect downstream transcription, cell proliferation, or in vivo tumor growth in neuroblastoma (105, 115, 116). In glioma, HIF-2 α localizes to extranuclear polysomes to promote translation of a large but distinct set of proteins (117). These and other data suggest that the HIF-2 α protein displays additional, although as yet mainly unknown, functions. We thus know that HIF-2 α is expressed in the cytoplasm in addition to the nucleus. HIF-2 α has ARNT-independent functions, and it is plausible that it forms complexes with proteins other than ARNT to initiate transcription. In addition, HIF-2 α might form protein complexes in the cytoplasm to promote translation, stabilization, and secretion of proteins important for stemness, pseudohypoxic phenotypes, and tumor cell metastasis. In essence, HIF-2 α appears to mediate a hypoxic or nonhypoxic cellular response—that associates with cell stemness [for example, (118)]—independently of surrounding oxygen concentrations.

Clues from coordinated multicellular development

Developmental pathways are affected by the hypoxic transcriptional regulators in both animals

and plants. These regulators act as switches or “pacemakers” of stem cell proliferation and differentiation.

During animal development, HIF-1 α and its binding partner ARNT are ubiquitously expressed, whereas HIF-2 α expression is more tissue- and time-restricted (119, 120). Among invertebrate animals, hypoxia and subsequent HIF-1 α accumulation are associated with growth and stem cell proliferation during development in fruit flies and mosquitos (121, 122). In vertebrates, HIF-1 α is ubiquitously expressed throughout development, and homozygous deletion is lethal (123, 124). HIF-1 α and HIF-2 α are demonstrated to promote the generation of new blood vessels and branching of existing ones. However, *EPAS1* appears to have evolved before the downstream *erythropoietin* (EPO) gene, a promoter of increased systemic oxygen carrying capacity, and now, HIF-2 α directly promotes erythrocyte differentiation from bone marrow progenitors (125). During development, expression of HIF-2 α is temporally and spatially restricted. Endothelial cells display high expression of HIF-2 α continuously, whereas cells of the developing sympathetic nervous system (SNS) express HIF-2 α mRNA and protein during discrete periods of mammalian development (120, 126, 127). The central roles by which the animal-specific HIFs regulate hypoxic cell functions is suggested to have facilitated primitive animals to cope, and fully access, oxic niches during evolution (41).

In higher plants, developmental processes are intertwined with the activity of at least three classes of transcriptional regulators characterized by an exposed N-terminal cysteine, which is regulated by the oxygen-dependent branch of the N-degron pathway. First, ERF-VIIs have been shown to repress opening of the protective hypocotyl hook and cotyledon greening as well as to antagonize hormone signaling in the root for timely shaping of its architecture (128, 129). Second, ZPR2 binds and inactivates homeodomain III-type TFs, regulators of meristem maintenance and new organ formation (67). Third, VRN2 is assembled into the polycomb repressive complex 2 (PRC2) that represses gene expression through histone methylation (57). One of the best characterized targets of this complex is the *FLOWERING LOCUS C* gene, a repressor of the transition toward reproductive development in *Arabidopsis*.

Epigenetic control of developmental pathways through histone methylation in both kingdoms is also controlled in part by oxygen-dependent KDMs. Although recent reports confirmed the hypoxia sensitivity of members of this protein family in human cells, with consequences for differentiation in several cell line model systems (45, 46, 48, 130), this has not yet been explored in plants. However, several JmjC-domain-containing KDM proteins have

been shown to control aspects of plant development in *Arabidopsis*, including germination, flowering, and callus formation (131).

Oxygen-sensing machineries as adaptations for nascent multicellularity

In all kingdoms of life, enzymes that detoxify ROS are ubiquitously present, which indicates that their evolution predated photosynthetic oxygenation (132). ROS can be locally produced by abiotic photolysis on a largely anoxic planet, according to geochemical and geophysical studies of both Earth and Mars (133). Continuous scavenging of ROS through enzymatic or metabolic assets, however, is likely to be costly for cells. Instead, the acquisition of mechanisms for perception and response would be of higher gain. This perception and response would engage detoxification only when oxygen and ROS levels exceeded a danger threshold and thus be metabolically cheaper. The multitude of oxygen-sensing strategies in prokaryotes and eukaryotes probably reflects adaptation to environmental niches distinguished by oxygen dynamics, in addition to the regulation of specific metabolic needs (56). The acquisition of mechanisms for ROS perception and scavenging would have pioneered the utilization of free oxygen as a resource. With a control of ROS detoxification, oxygen-sensing machineries could also be co-opted to express oxygen-requiring genes when this substrate is available and conversely suppress them in favor of anaerobic strategies in case of hypoxia.

The convergent evolution in complex eukaryotes toward selective proteolysis of transcriptional regulators that control hypoxia responses suggests the superiority of this strategy over others that use free oxygen. In all cases considered, the recruitment of specific transcriptional regulators by way of oxygen-dependent regulatory pathways occurred long after the “invention” of oxygen-consuming enzymes that operate on amino acid residues (40). These enzymes could have evolved from their original metabolic function toward a role as sensors. In turn, the transcriptional regulators acquired the specific residues that are substrates of the sensor enzyme in strategic positions to subdue the kinetics of the reaction to physiologically relevant oxygen levels. To constitutively synthesize transcriptional regulators is also costly, but the cost can be balanced by the advantage of rapid activation once degradation is inhibited. By contrast, bacteria exploit posttranslational regulation that is faster and less energy demanding, such as phosphorylation or dimerization (56). This type of regulation, however, is not as effective or can possibly not guarantee a sufficient level of specificity. The oxygen-sensing systems in plants and animals are fine-tuned through several layers of modification, although they all seem

to be subordinated to the proteolytic system. For example, whereas most translated HIF- α proteins are proteasomally degraded in oxic conditions through PHD- or VHL-mediated ubiquitination, a second layer of HIF regulation is driven by FIH, which catalyzes oxygen-dependent asparagine hydroxylation of HIF- α . This second layer prevents the interaction between HIF- α and transcriptional activators. That FIH hydroxylates the asparagine motif less efficiently on HIF-2 α than on HIF-1 α could be one molecular explanation as to why HIF-2 α is stabilized at higher oxygen concentrations (43, 134). Essentially, although the road to proteolysis can be retarded or distinctly coupled to interval oxygen concentrations, the oxygen-sensing machineries across eukaryotic kingdoms master the route along which proteins are degraded by oxygen.

The commonality between organisms that exploited selective proteolysis as a solution to oxygen sensing resides in their complex multicellularity. Remarkably, HIF- α and ERF-VII and the regulatory proteins involved in their oxygen-dependent regulation are, at the outset, expressed and subsequently degraded. This hints at the need for a unified system to perceive and interpret oxygen gradients that are unavoidably generated throughout growth and development. As compared with diffusible signal molecules produced endogenously, such as hormones, molecular oxygen provides a faster and more direct connection to the metabolic needs of aerobic cells. Within a persistent three-dimensional organization in which respiration and transport regulate the mass balance of oxygen, cells are continuously exposed to variable oxygen concentrations, depending on their position in space and time. The multiple layers of oxygen perception and response demonstrate a capacity by which this variability is recorded and translated during growth, development, and activities of daily living in the eukaryotic kingdoms with complex multicellularity. This capacity appears more restricted in protozoa and fungi that also demonstrate both lower phenotypic and cell type diversity than those of animals or vascular plants. In all cases, however, the oxygen-sensing mechanisms contribute to the spatiotemporal induction of cellular functions, which is one of the defining features of complex multicellular life (Fig. 4) (6–8).

Conceptual gaps

The role of oxygen sensing for complex multicellular life and evolution appears crucial, but conceptual gaps remain on several layers. On the biomolecular and cellular level, for example, the presence of Nt-Cys-degron TFs that are ADO substrates could inform us about the most ancestral of oxygen-sensing strategies. Also, the existence of parallel oxygen-sensing strategies based on 2-OG-dependent oxygenases, such as KDMs, remain to be investigated

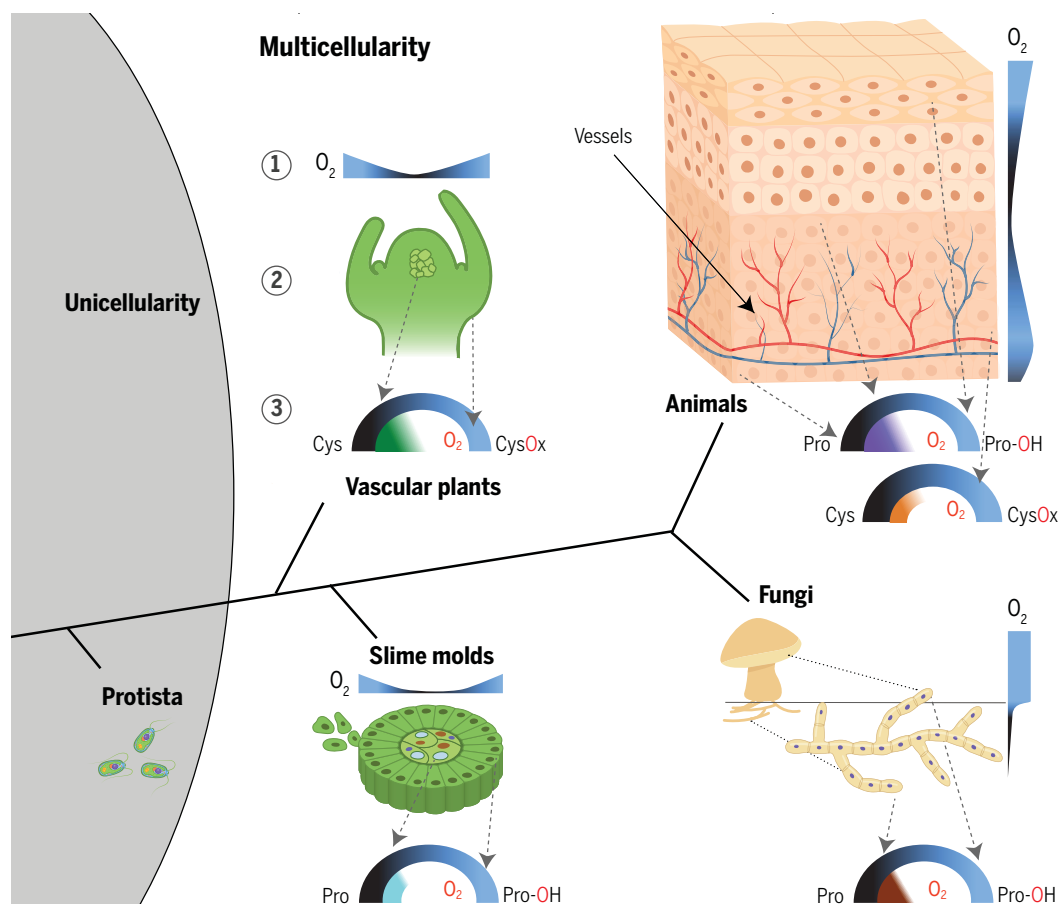


Fig. 4. Oxygen-sensing mechanisms across the eukaryotic kingdoms.

Complex multicellularity converged to the recruitment of enzymatic control of the stability of regulatory proteins at specific endogenous oxygen concentrations (depicted for animals). (1) Endogenous oxygen gradients and (2) the spatial position of perceiving cells are stylized, with (3) a dial depicting the sensing (outer half circle) and response (inner half circle). In the dial, proteins are labeled as oxidized (Pro-OH/CysOx) at oxic conditions (blue) or nonoxidized

(Cys/Pro) at hypoxia (black). The inner half circle of the dial represents the stabilization of a protein (half halo) or as a TF (pie chart; color coding and substrates are as in Fig. 2). Thiol-dioxygenases stabilize TFs in green plants (Viridiplantae), and 2-OG-dependent dioxygenases stabilize TFs in animals (Eumetazoa and Cnidaria) and Fungi. Protein stabilization (not TFs) is also regulated by thiol-dioxygenases in mammals and by 2-OG-oxygenases in slime molds.

in plants and fungi (64, 135). The involvement of NO in the hypoxic signaling also deserves special attention. In animal cells, NO and RNS affect HIF expression, stability, and activity in a complex manner, depending on local concentrations and cellular milieu (96). Moreover, the Arg/N-degron pathway has been shown to act as a sensing mechanism to detect low NO levels both in animals and plants, although the response elicited by such conditions only marginally overlaps with those to hypoxia (136). The proteolytic element(s) positively affected by NO remains to be identified but seems to lie elsewhere than thiol-dioxygenase activity (136). Future efforts will likely shed light on defining the contribution of this signaling molecule to oxygen sensing in plants, animals, and their ancestors.

On the evolutionary level, the commonality in oxygen-sensing mechanisms between the plant and animal kingdoms is striking, but land plants and animals adopted alternative solutions to direct their primary hypoxia re-

sponses, even though their ancestors were likely equipped with the same repertoire of dioxygenases. The acquisition of oxygen-sensing function may be associated with a reduction in oxygen affinity that matches variations in oxygen concentration occurring in the cells and tissues. These variations are in turn determined by environmental, ecological, and organismal features, such as metabolic rates and anatomy. Thus, fundamental differences in internal and external characteristics could have driven the distinct selection of biochemical pathways to direct selective proteolysis in these two systems—but what are these defining characteristics, and what trade-offs followed with the different systems? Even for most modern multicellular organisms, we lack information on endogenous oxygen gradients and their fluctuations. However, many enzymes use oxygen as a cofactor but appear not to contribute to oxygen-sensing machineries. This suggests that either their oxygen-sensing potential is unexplored or their function is to catalyze other

specific reactions, irrespective of the environment. Nevertheless, constraining the details and hierarchical order of oxygen-sensing systems will allow investigations of whether components were shared by a common ancestor or shared after the divergence of the respective kingdoms.

Last, expanding our understanding of the evolution of oxygen sensing, by learning from geological history, will allow identification of opportunities for further beneficial manipulation of these systems for both clinical and agricultural purposes. Already, synthetic biology approaches that involve interchange of regulatory modules between organisms from different kingdoms constitute an innovative strategy to adapt oxygen sensitivity and the magnitude of response machineries (137). For example, transfer of oxygen-sensing components from plant to yeast has contributed to defining features of these systems and could readily help to develop drugs that interfere with their functioning (136). We advocate a

shift in focus, away from exploring oxygen sensing as primarily a response to oxygen shortage for aerobic respiration and toward considering it as a mechanism that enables multicellularity to cope with and even use fluctuations in oxygen concentrations. We predict that this will reward us with new perspectives on the broad scope of oxygen-sensing mechanisms and the challenges that multicellular life is exposed to, today as in geologic history.

REFERENCES AND NOTES

- J. R. Nursall, Oxygen as a prerequisite to the origin of the Metazoa. *Nature* **183**, 1170–1172 (1959). doi: [10.1038/1831170b0](#)
- L. V. Berkner, L. C. Marshall, On the origin and rise of oxygen concentration in the Earth's atmosphere. *J. Atmos. Sci.* **22**, 225–261 (1965). doi: [10.1175/1520-0469\(1965\)022<0225:OTOARO>2.0.CO;2](#)
- J. L. Morris *et al.*, The timescale of early land plant evolution. *Proc. Natl. Acad. Sci. U.S.A.* **115**, E2274–E2283 (2018). doi: [10.1073/pnas.1719588115](#); pmid: [29463716](#)
- F. Licausi, B. Giuntoli, P. Perata, Similar and yet different: Oxygen sensing in animals and plants. *Trends Plant Sci.* **25**, 6–9 (2020). doi: [10.1016/j.tplants.2019.10.013](#); pmid: [31780335](#)
- D. J. Gibbs, M. J. Holdsworth, Every breath you take: New insights into plant and animal oxygen sensing. *Cell* **180**, 22–24 (2020). doi: [10.1016/j.cell.2019.10.043](#); pmid: [31785834](#)
- D. Arendt *et al.*, The origin and evolution of cell types. *Nat. Rev. Genet.* **17**, 744–757 (2016). doi: [10.1038/nrg.2016.127](#); pmid: [27818507](#)
- A. Seb  Pedr  s, B. M. Degan, I. Ruiz-Trillo, The origin of Metazoa: A unicellular perspective. *Nat. Rev. Genet.* **18**, 498–512 (2017). doi: [10.1038/nrg.2017.21](#); pmid: [28479598](#)
- R. K. Grosberg, R. R. Strathmann, The evolution of multicellularity: A minor major transition? *Annu. Rev. Ecol. Syst.* **38**, 621–654 (2007). doi: [10.1146/annurev.ecolsys.36.102403.114735](#)
- J. T. van Dongen, F. Licausi, Oxygen sensing and signaling. *Annu. Rev. Plant Biol.* **66**, 345–367 (2015). doi: [10.1146/annurev-arplant-043014-114813](#); pmid: [25580837](#)
- J.-C. Massabuau, From low arterial- to low tissue-oxygenation strategy: An evolutionary theory. *Resp. Physiol.* **128**, 249–261 (2001). doi: [10.1016/s0034-5687\(01\)00305-x](#); pmid: [11718757](#)
- W. S. Webster, D. Abela, The effect of hypoxia in development. *Birth Defects Res. C. Embryo Today* **81**, 215–228 (2007). doi: [10.1002/bdrc.20102](#); pmid: [17963271](#)
- S. R. McKeown, Defining normoxia, physioxia and hypoxia in tumours-implications for treatment response. *Br. J. Radiol.* **87**, 20130676 (2014). doi: [10.1259/bjr.20130676](#); pmid: [24588669](#)
- N. M. Bergman, T. M. Lenton, A. J. Watson, COPSE: A new model of biogeochemical cycling over Phanerozoic time. *Am. J. Sci.* **304**, 397–437 (2004). doi: [10.2475/ajs.304.5.397](#)
- D. E. Canfield, in *Treatise on Geochemistry*, K. Turekian, H. Holland, Eds. (Elsevier Science, 2014), pp. 197–216.
- W. B. Whitman, D. C. Coleman, W. J. Wiebe, Prokaryotes: The unseen majority. *Proc. Natl. Acad. Sci. U.S.A.* **95**, 6578–6583 (1998). doi: [10.1073/pnas.95.12.6578](#); pmid: [9618454](#)
- International Union for Conservation of Nature (IUCN), “The World Conservation Union. Red List of Threatened Species 2014.3. Summary Statistics for Globally Threatened Species. Table 1: Numbers of threatened species by major groups of organisms (1996–2014)” (IUCN, 2014).
- J. W. Valentine, A. G. Collins, C. P. Meyer, Morphological complexity increase in Metazoans. *Paleobiology* **20**, 131–142 (1994). doi: [10.1017/S0094837300012641](#)
- L. E. Graham, M. E. Cook, J. S. Busse, The origin of plants: Body plan changes contributing to a major evolutionary radiation. *Proc. Natl. Acad. Sci. U.S.A.* **97**, 4535–4540 (2000). doi: [10.1073/pnas.97.9.4535](#); pmid: [10781058](#)
- G. Bell, A. O. Mooers, Size and complexity among multicellular organisms. *Biol. J. Linn. Soc. Lond.* **60**, 345–363 (2008). doi: [10.1111/j.1095-8312.1997.tb01500.x](#)
- A. H. Knoll, The multiple origins of complex multicellularity. *Annu. Rev. Earth Planet. Sci.* **39**, 217–239 (2011). doi: [10.1146/annurev.earth.031208.100209](#)
- S. M. Porter, The fossil record of early eukaryotic diversification. *The Paleontologic. Soc. Pap.* **10**, 35–50 (2004). doi: [10.1017/S1089332600002321](#)
- N. J. Butterfield, Early evolution of the Eukaryota. *Palaeontology* **58**, 5–17 (2015). doi: [10.1111/pala.12139](#)
- A. H. Knoll, S. B. Carroll, Early animal evolution: Emerging views from comparative biology and geology. *Science* **284**, 2129–2137 (1999). doi: [10.1126/science.284.5423.2129](#); pmid: [10381872](#)
- J. Farquhar, H. Bao, M. Thieme, Atmospheric influence of Earth's earliest sulfur cycle. *Science* **289**, 756–759 (2000). doi: [10.1126/science.289.5480.756](#); pmid: [10926533](#)
- B. Kendall *et al.*, Pervasive oxygenation along late Archaean ocean margins. *Nat. Geosci.* **3**, 647–652 (2010). doi: [10.1038/ngeo942](#)
- J. R. Waldbauer, D. K. Newman, R. E. Summons, Microaerobic steroid biosynthesis and the molecular fossil record of Archaean life. *Proc. Natl. Acad. Sci. U.S.A.* **108**, 13409–13414 (2011). doi: [10.1073/pnas.1104160108](#); pmid: [21825157](#)
- E. A. Sperling, A. H. Knoll, P. R. Girguis, The ecological physiology of Earth's second oxygen revolution. *Annu. Rev. Ecol. Syst.* **46**, 215–235 (2015). doi: [10.1146/annurev.ecolsys.110512-135808](#)
- T. W. Dahl *et al.*, Devonian rise in atmospheric oxygen correlated to the radiations of terrestrial plants and large predatory fish. *Proc. Natl. Acad. Sci. U.S.A.* **107**, 17911–17915 (2010). pmid: [20884852](#)
- A. J. Krause *et al.*, Stepwise oxygenation of the Paleozoic atmosphere. *Nat. Commun.* **9**, 4081 (2018). pmid: [30287825](#)
- T. M. Lenton *et al.*, Earliest land plants created modern levels of atmospheric oxygen. *Proc. Natl. Acad. Sci. U.S.A.* **113**, 9704–9709 (2016). doi: [10.1073/pnas.1604787113](#); pmid: [27528678](#)
- E. Hammarlund, Harnessing hypoxia as an evolutionary driver of complex multicellularity. *Interface Focus* **10**, 20190101 (2019). doi: [10.1098/rsfs.2019.0101](#); pmid: [32642048](#)
- An award to oxygen sensing. *Nat. Biomed. Eng.* **3**, 843–844 (2019). pmid: [31628432](#)
- W. G. J. Kaelin Jr., P. J. Ratcliffe, Oxygen sensing by metazoans: The central role of the HIF hydroxylase pathway. *Mol. Cell* **30**, 393–402 (2008). pmid: [18498744](#)
- A. C. Epstein *et al.*, *C. elegans* EGL-9 and mammalian homologs define a family of dioxygenases that regulate HIF by prolyl hydroxylation. *Cell* **107**, 43–54 (2001). pmid: [11595184](#)
- M. Hirsil  , P. K  iv  nen, V. G  nzler, K. I. Kivirikko, J. Myllyharju, Characterization of the human prolyl 4-hydroxylases that modify the hypoxia-inducible factor. *J. Biol. Chem.* **278**, 30772–30780 (2003). pmid: [12788921](#)
- H. Tarhonskaya *et al.*, Investigating the contribution of the active site environment to the slow reaction of hypoxia-inducible factor prolyl hydroxylase domain 2 with oxygen. *Biochem. J.* **463**, 363–372 (2014). pmid: [25120187](#)
- J. S. Scotti *et al.*, Human oxygen sensing may have origins in prokaryotic elongation factor Tu prolyl-hydroxylation. *Proc. Natl. Acad. Sci. U.S.A.* **111**, 13331–13336 (2014). pmid: [25197067](#)
- C. Loenarz *et al.*, Hydroxylation of the eukaryotic ribosomal decoding center affects translational accuracy. *Proc. Natl. Acad. Sci. U.S.A.* **111**, 4019–4024 (2014). pmid: [24550462](#)
- C. Loenarz *et al.*, The hypoxia-inducible transcription factor pathway regulates oxygen sensing in the simplest animal, *Trichoplax adhaerens*. *EMBO Rep.* **12**, 63–70 (2011). pmid: [21109780](#)
- K. T. Rytk  nen, T. A. Williams, G. M. Renshaw, C. R. Primmer, M. Nikinmaa, Molecular evolution of the metazoan PHD-HIF oxygen-sensing system. *Mol. Biol. Evol.* **28**, 1913–1926 (2011). pmid: [21228399](#)
- E. U. Hammarlund, K. von Stedingk, S. P  hlman, Refined control of cell stemness allowed animal evolution in the oxic realm. *Nat. Ecol. Evol.* **2**, 220–228 (2018). pmid: [29348641](#)
- M. S. Islam, T. M. Leissing, R. Chowdhury, R. J. Hopkinson, C. J. Schofield, 2-Oxoglutarate-dependent oxygenases. *Annu. Rev. Biochem.* **87**, 585–620 (2018). pmid: [29494239](#)
- H. Tarhonskaya *et al.*, Kinetic investigations of the role of factor inhibiting hypoxia-inducible factor (FIH) as an oxygen sensor. *J. Biol. Chem.* **290**, 19726–19742 (2015). pmid: [26112411](#)
- B. Thienpont *et al.*, Tumour hypoxia causes DNA hypermethylation by reducing TET activity. *Nature* **537**, 63–68 (2016). pmid: [27533040](#)
- M. Batie *et al.*, Hypoxia induces rapid changes to histone methylation and reprograms chromatin. *Science* **363**, 1222–1226 (2019). pmid: [30872526](#)
- R. L. Hancock, K. Dunne, L. J. Walport, E. Flashman, A. Kawamura, Epigenetic regulation by histone demethylases in hypoxia. *Epigenomics* **7**, 791–811 (2015). pmid: [25832587](#)
- R. L. Hancock, N. Masson, K. Dunne, E. Flashman, A. Kawamura, The activity of JmJc histone lysine demethylase KDMA4 is highly sensitive to oxygen concentrations. *ACS Chem. Biol.* **12**, 1011–1019 (2017). doi: [10.1021/acscchembio.6b00958](#); pmid: [28051298](#)
- A. A. Chakraborty *et al.*, Histone demethylase KDMA6 directly senses oxygen to control chromatin and cell fate. *Science* **363**, 1217–1222 (2019). doi: [10.1126/science.aaw1026](#); pmid: [30872525](#)
- B. T. Hughes, P. J. Espenshade, Oxygen-regulated degradation of fission yeast SREBP by Otd1, a prolyl hydroxylase family member. *EMBO J.* **27**, 1491–1501 (2008). doi: [10.1038/emboj.2008.83](#); pmid: [18418381](#)
- P. J. Espenshade, A. L. Hughes, Regulation of sterol synthesis in eukaryotes. *Annu. Rev. Genet.* **41**, 401–427 (2007). doi: [10.1146/annurev.genet.41.110306.130315](#); pmid: [17666007](#)
- T. Liu *et al.*, Biochemical and biophysical analyses of hypoxia sensing prolyl hydroxylases from *Dictyostelium discoideum* and *Toxoplasma gondii*. *J. Biol. Chem.* (2020). doi: [10.1074/jbc.RA120.013998](#)
- Y. Xu, Z. A. Wang, R. S. Green, C. M. West, Role of the Skp1 prolyl-hydroxylation/glycosylation pathway in oxygen dependent submerged development of *Dictyostelium*. *BMC Dev. Biol.* **12**, 31 (2012). doi: [10.1186/1471-213X-12-31](#); pmid: [23098648](#)
- D. J. Dickinson, W. J. Nelson, W. I. Weis, A polarized epithelium organized by β - and α -catenin predates cadherin and metazoan origins. *Science* **331**, 1336–1339 (2011). doi: [10.1126/science.1199633](#); pmid: [21393547](#)
- R. Chowdhury *et al.*, Ribosomal oxygenases are structurally conserved from prokaryotes to humans. *Nature* **510**, 422–426 (2014). doi: [10.1038/nature13263](#); pmid: [24814345](#)
- R. Sekirnik *et al.*, YcF_{DM} is a thermophilic oxygen-dependent ribosomal protein μ L16 oxygenase. *Extremophiles* **22**, 553–562 (2018). doi: [10.1007/s00792-018-1016-9](#); pmid: [29523972](#)
- C. Y. Taabazuing, J. A. Hangasky, M. J. Knapp, Oxygen sensing strategies in mammals and bacteria. *J. Inorg. Biochem.* **133**, 63–72 (2014). doi: [10.1016/j.jinorgbio.2013.12.010](#); pmid: [24468676](#)
- D. J. Gibbs *et al.*, Oxygen-dependent proteolysis regulates the stability of angiosperm polycorn repressive complex 2 subunit VERNALIZATION 2. *Nat. Commun.* **9**, 5438 (2018). doi: [10.1038/s41467-018-07875-7](#); pmid: [30575749](#)
- F. Licausi *et al.*, Oxygen sensing in plants is mediated by an N-end rule pathway for protein destabilization. *Nature* **479**, 419–422 (2011). doi: [10.1038/nature10536](#); pmid: [22020282](#)
- A. Varshavsky, N-degron and C-degron pathways of protein degradation. *Proc. Natl. Acad. Sci. U.S.A.* **116**, 358–366 (2019). doi: [10.1073/pnas.1816596116](#); pmid: [30622213](#)
- A. Bachmair, D. Finley, A. Varshavsky, In vivo half-life of a protein is a function of its amino-terminal residue. *Science* **234**, 179–186 (1986). doi: [10.1126/science.3018930](#); pmid: [3018930](#)
- D. A. Weits *et al.*, Plant cysteine oxidases control the oxygen-dependent branch of the N-end rule pathway. *Nat. Commun.* **5**, 3425 (2014). doi: [10.1038/ncomms4425](#); pmid: [24599061](#)
- M. D. White *et al.*, Plant cysteine oxidases are dioxygenases that directly enable arginyl transferase-catalysed arginylation of N-end rule targets. *Nat. Commun.* **8**, 14690 (2017). doi: [10.1038/ncomms14690](#); pmid: [28332493](#)
- N. Dissmeyer, Conditional protein function via N-degron pathway-mediated proteostasis in stress physiology. *Annu. Rev. Plant Biol.* **70**, 83–117 (2019). doi: [10.1146/annurev-arplant-050718-095937](#); pmid: [30892918](#)
- D. J. Gibbs *et al.*, Nitric oxide sensing in plants is mediated by proteolytic control of group VII ERF transcription factors. *Mol. Cell* **53**, 369–379 (2014). doi: [10.1016/j.molcel.2013.12.020](#); pmid: [24462115](#)
- M. D. White, J. J. A. G. Kamps, S. East, L. J. Taylor Kearney, E. Flashman, The plant cysteine oxidases from *Arabidopsis thaliana* are kinetically tailored to act as oxygen sensors. *J. Biol. Chem.* **293**, 11786–11795 (2018). doi: [10.1074/jbc.RA118.003496](#); pmid: [29848548](#)
- M. E. Cockman *et al.*, Lack of activity of recombinant HIF prolyl hydroxylases (PHDs) on reported non-HIF substrates. *eLife* **8**, e46490 (2019). doi: [10.7554/eLife.46490](#); pmid: [31500697](#)

67. D. A. Weits *et al.*, An apical hypoxic niche sets the pace of shoot meristem activity. *Nature* **569**, 714–717 (2019). doi: [10.1038/s41586-019-1203-6](#); pmid: [31092919](#)
68. D. A. Weits, J. T. van Dongen, F. Licausi, Molecular oxygen as a signaling component in plant development. *New Phytol.* **164**, 2424 (2020). doi: [10.1111/nph.16424](#); pmid: [31943217](#)
69. M. J. Holdsworth, D. J. Gibbs, Comparative biology of oxygen sensing in plants and animals. *Curr. Biol.* **30**, R362–R369 (2020). doi: [10.1016/j.cub.2020.03.021](#); pmid: [32315638](#)
70. N. Masson *et al.*, Conserved N-terminal cysteine dioxygenases transduce responses to hypoxia in animals and plants. *Science* **365**, 65–69 (2019). doi: [10.1126/science.aaw0112](#); pmid: [31273118](#)
71. N. Grahl, R. A. Cramer Jr., Regulation of hypoxia adaptation: An overlooked virulence attribute of pathogenic fungi? *Med. Mycol.* **48**, 1–15 (2010). doi: [10.1093/3693780902947342](#); pmid: [19462332](#)
72. U. Lendahl, K. L. Lee, H. Yang, L. Poellinger, Generating specificity and diversity in the transcriptional response to hypoxia. *Nat. Rev. Genet.* **10**, 821–832 (2009). doi: [10.1038/nrg2665](#); pmid: [19884889](#)
73. R. Tian *et al.*, Adaptive evolution of energy metabolism-related genes in hypoxia-tolerant mammals. *Front. Genet.* **8**, 205–205 (2017). doi: [10.3389/fgene.2017.02025](#); pmid: [29270192](#)
74. A. Mustroph *et al.*, Cross-kingdom comparison of transcriptomic adjustments to low-oxygen stress highlights conserved and plant-specific responses. *Plant Physiol.* **152**, 1484–1500 (2010). doi: [10.1104/pp.109.151845](#); pmid: [20097791](#)
75. T. N. Seagroves *et al.*, Transcription factor HIF-1 is a necessary mediator of the pasteur effect in mammalian cells. *Mol. Cell. Biol.* **21**, 3436–3444 (2001). doi: [10.1128/MCB.21.10.3436-3444.2001](#); pmid: [11313469](#)
76. L. T. Bui *et al.*, Conservation of ethanol fermentation and its regulation in land plants. *J. Exp. Bot.* **70**, 1815–1827 (2019). doi: [10.1093/jxb/erz052](#); pmid: [30861072](#)
77. J. Klinkenberg *et al.*, Two fatty acid desaturases, STEAROYL-ACYL CARRIER PROTEIN Δ9-DESATURASE6 and FATTY ACID DESATURASE3, are involved in drought and hypoxia stress signaling in Arabidopsis crown galls. *Plant Physiol.* **164**, 570–583 (2014). doi: [10.1104/pp.113.230326](#); pmid: [24368335](#)
78. P. J. Lee *et al.*, Hypoxia-inducible factor-1 mediates transcriptional activation of the heme oxygenase-1 gene in response to hypoxia. *J. Biol. Chem.* **272**, 5375–5381 (1997). doi: [10.1074/jbc.272.9.5375](#); pmid: [9038135](#)
79. K. G. Alberti, The biochemical consequences of hypoxia. *J. Clin. Pathol. Suppl. (R Coll. Pathol.)* **11**, 14–20 (1977). doi: [10.1136/jcp.s3.11.14](#); pmid: [198434](#)
80. S. Dashko, N. Zhou, C. Compagno, J. Piškur, Why, when, and how did yeast evolve alcoholic fermentation? *FEMS Yeast Res.* **14**, 826–832 (2014). doi: [10.1111/1567-1364.12161](#); pmid: [24824836](#)
81. C. António *et al.*, Regulation of primary metabolism in response to low oxygen availability as revealed by carbon and nitrogen isotope redistribution. *Plant Physiol.* **170**, 43–56 (2016). doi: [10.1104/pp.15.00266](#); pmid: [26553649](#)
82. W. Yang, C. Catalanotti, T. M. Wittkopp, M. C. Posewitz, A. R. Grossman, Algae after dark: Mechanisms to cope with anoxic/hypoxic conditions. *Plant J.* **82**, 481–503 (2015). doi: [10.1111/tpj.12823](#); pmid: [25752440](#)
83. W.-G. Choi, D. M. Roberts, Arabidopsis NIP2;1, a major intrinsic protein transporter of lactic acid induced by anoxic stress. *J. Biol. Chem.* **282**, 24209–24218 (2007). doi: [10.1074/jbc.M700982200](#); pmid: [17584741](#)
84. M. S. Ullah, A. J. Davies, A. P. Halestrap, The plasma membrane lactate transporter MCT4, but not MCT1, is up-regulated by hypoxia through a HIF-1α-dependent mechanism. *J. Biol. Chem.* **281**, 9030–9037 (2006). doi: [10.1074/jbc.M511397200](#); pmid: [16452478](#)
85. B. L. Krock, N. Skuli, M. C. Simon, Hypoxia-induced angiogenesis: Good and evil. *Genes Cancer* **2**, 1117–1133 (2011). doi: [10.1177/1947601911423654](#); pmid: [22866203](#)
86. T. Yamauchi, S. Shimamura, M. Nakazono, T. Mochizuki, Aerenchyma formation in crop species: A review. *Field Crops Res.* **152**, 8–16 (2013). doi: [10.1016/j.fcr.2012.12.008](#)
87. Y. Hattori *et al.*, The ethylene response factors SNORKEL1 and SNORKEL2 allow rice to adapt to deep water. *Nature* **460**, 1026–1030 (2009). doi: [10.1038/nature08258](#); pmid: [19693083](#)
88. C. He, S. A. Finlayson, M. C. Drew, W. R. Jordan, P. W. Morgan, Ethylene biosynthesis during aerenchyma formation in roots of maize subjected to mechanical impedance and hypoxia. *Plant Physiol.* **112**, 1679–1685 (1996). doi: [10.1104/pp.112.4.1679](#); pmid: [12226471](#)
89. E. Cohen, H. Kende, In vivo 1-aminocyclopropane-1-carboxylate synthase activity in internodes of deepwater rice: Enhancement by submergence and low oxygen levels. *Plant Physiol.* **84**, 282–286 (1987). doi: [10.1104/pp.84.2.282](#); pmid: [16665431](#)
90. C. Pucciariello, S. Parlanti, V. Banti, G. Novi, P. Perata, Reactive oxygen species-driven transcription in Arabidopsis under oxygen deprivation. *Plant Physiol.* **159**, 184–196 (2012). doi: [10.1104/pp.111.191122](#); pmid: [22415514](#)
91. R. Chen *et al.*, Reactive oxygen species formation in the brain at different oxygen levels: The role of hypoxia inducible factors. *Front. Cell Dev. Biol.* **6**, 132 (2018). doi: [10.3389/fcell.2018.00132](#); pmid: [30364203](#)
92. K. J. Gupta *et al.*, The role of nitrite and nitric oxide under low oxygen conditions in plants. *New Phytol.* **225**, 1143–1151 (2020). doi: [10.1111/nph.15969](#); pmid: [31144317](#)
93. A. Galkin, A. Higgins, S. Moncada, Nitric oxide and hypoxia. *Essays Biochem.* **43**, 29–42 (2007). doi: [10.1042/bse0430029](#); pmid: [17705791](#)
94. V. L. Dengler, M. Galbraith, J. M. Espinosa, Transcriptional regulation by hypoxia inducible factors. *Crit. Rev. Biochem. Mol. Biol.* **49**, 1–15 (2014). doi: [10.3109/10409238.2013.838205](#); pmid: [24099156](#)
95. B. Giuntoli *et al.*, Age-dependent regulation of ERF-VII transcription factor activity in Arabidopsis thaliana. *Plant Cell Environ.* **40**, 2333–2346 (2017). doi: [10.1111/pce.13037](#); pmid: [28741696](#)
96. M. Hendrickson, P. R., Crosstalk between nitric oxide and hypoxia-inducible factor signaling pathways: An update. *Res. Rep. Biochem.* **5**, 147–161 (2015).
97. M. Zaidi, F. Fu, D. Cojocari, T. D. McKee, B. G. Wouters, Quantitative visualization of hypoxia and proliferation gradients within histological tissue sections. *Front. Bioeng. Biotechnol.* **7**, 397 (2019). doi: [10.3389/fbioe.2019.00397](#); pmid: [31867322](#)
98. M. C. Simon, B. Keith, The role of oxygen availability in embryonic development and stem cell function. *Nat. Rev. Mol. Cell Biol.* **9**, 285–296 (2008). doi: [10.1038/nrm2354](#); pmid: [18285802](#)
99. B. Muz, P. de la Puente, F. Azab, A. K. Azab, The role of hypoxia in cancer progression, angiogenesis, metastasis, and resistance to therapy. *Hypoxia (Auckl.)* **3**, 83–92 (2015). doi: [10.2147/HP.S93413](#); pmid: [27774485](#)
100. G. L. Semenza, S. T. Koury, M. K. Neifelt, J. D. Gearhart, S. E. Antonarakis, Cell-type-specific and hypoxia-inducible expression of the human erythropoietin gene in transgenic mice. *Proc. Natl. Acad. Sci. U.S.A.* **88**, 8725–8729 (1991). doi: [10.1073/pnas.88.19.8725](#); pmid: [1924331](#)
101. C. W. Pugh, C. C. Tan, R. W. Jones, P. J. Ratcliffe, Functional analysis of an oxygen-regulated transcriptional enhancer lying 3' to the mouse erythropoietin gene. *Proc. Natl. Acad. Sci. U.S.A.* **88**, 10553–10557 (1991). doi: [10.1073/pnas.88.23.10553](#); pmid: [1961720](#)
102. L. Kerpen, L. Niccolini, F. Licausi, J. T. van Dongen, D. A. Weits, Hypoxic conditions in crown galls induce plant anaerobic responses that support tumor proliferation. *Front. Plant Sci.* **10**, 56 (2019). doi: [10.3389/fpls.2019.00056](#); pmid: [30804956](#)
103. A. Gravot *et al.*, Hypoxia response in Arabidopsis roots infected by *Plasmiodiophora brassicae* supports the development of clubroot. *BMC Plant Biol.* **16**, 251 (2016). doi: [10.1186/s12870-016-0941-y](#); pmid: [27835985](#)
104. B. Keith, R. S. Johnson, M. C. Simon, HIF1α and HIF2α: Sibling rivalry in hypoxic tumour growth and progression. *Nat. Rev. Cancer* **12**, 9–22 (2011). doi: [10.1038/nrc3183](#); pmid: [21669972](#)
105. C. U. Persson *et al.*, ARNT-dependent HIF-2 transcriptional activity is not sufficient to regulate downstream target genes in neuroblastoma. *Exp. Cell Res.* **388**, 111845 (2020). doi: [10.1016/j.yexcr.2020.111845](#); pmid: [31945318](#)
106. L. Holmquist-Mengelbier *et al.*, Recruitment of HIF-1α and HIF-2α to common target genes is differentially regulated in neuroblastoma: HIF-2α promotes an aggressive phenotype. *Cancer Cell* **10**, 413–423 (2006). doi: [10.1016/j.ccr.2006.08.026](#); pmid: [17097563](#)
107. Z. Li *et al.*, Hypoxia-inducible factors regulate tumorigenic capacity of glioma stem cells. *Cancer Cell* **15**, 501–513 (2009). doi: [10.1016/j.ccr.2009.03.018](#); pmid: [19477429](#)
108. K. L. Covello *et al.*, HIF-2α regulates Oct-4: Effects of hypoxia on stem cell function, embryonic development, and tumor growth. *Genes Dev.* **20**, 557–570 (2006). doi: [10.1101/gad.1399906](#); pmid: [16510872](#)
109. B. Das *et al.*, HIF-2α suppresses p53 to enhance the stemness and regenerative potential of human embryonic stem cells. *Stem Cells* **30**, 1685–1695 (2012). doi: [10.1002/stem.1142](#); pmid: [22689594](#)
110. S. Mohlin, C. Wigerup, A. Jögi, S. Pahlman, Hypoxia, pseudohypoxia and cellular differentiation. *Exp. Cell Res.* **356**, 192–196 (2017). doi: [10.1016/j.yexcr.2017.03.007](#); pmid: [28284840](#)
111. I. Comino-Méndez *et al.*, Tumoral EPAS1 (HIF2A) mutations explain sporadic pheochromocytoma and paraganglioma in the absence of erythrocytosis. *Hum. Mol. Genet.* **22**, 2169–2176 (2013). doi: [10.1093/hmg/ddt069](#); pmid: [23418310](#)
112. A. Pietras *et al.*, High levels of HIF-2α highlight an immature neural crest-like neuroblastoma cell cohort located in a perivascular niche. *J. Pathol.* **214**, 482–488 (2008). doi: [10.1002/path.2304](#); pmid: [18189331](#)
113. Z. Zhuang *et al.*, Somatic HIF2A gain-of-function mutations in paraganglioma with polycythemia. *N. Engl. J. Med.* **367**, 922–930 (2012). doi: [10.1056/NEJMoal205119](#); pmid: [22931260](#)
114. T. H. Scheuermann *et al.*, Allosteric inhibition of hypoxia inducible factor-2 with small molecules. *Nat. Chem. Biol.* **9**, 271–276 (2013). doi: [10.1038/nchembio.1185](#); pmid: [23434853](#)
115. I. Westerlund *et al.*, Combined epigenetic and differentiation-based treatment inhibits neuroblastoma tumor growth and links HIF2α to tumor suppression. *Proc. Natl. Acad. Sci. U.S.A.* **114**, E6137–E6146 (2017). doi: [10.1073/pnas.1700655114](#); pmid: [28696319](#)
116. S. Mohlin, K. von Stedingk, A. Pietras, S. Pahlman, No reason to reconsider HIF-2 as an oncogene in neuroblastoma and other cancer forms. *Proc. Natl. Acad. Sci. U.S.A.* **114**, E10856–E10858 (2017). doi: [10.1073/pnas.1716644115](#); pmid: [29233939](#)
117. J. Uniaque *et al.*, An oxygen-regulated switch in the protein synthesis machinery. *Nature* **486**, 126–129 (2012). doi: [10.1038/nature11055](#); pmid: [22678294](#)
118. C. U. Niklasson *et al.*, Hypoxia inducible factor-2α importance for migration, proliferation, and self-renewal of trunk neural crest cells. *Dev. Dynam.* (2020). doi: [10.1002/dvdy.253](#)
119. H. Tian, R. E. Hammer, A. M. Matsumoto, D. W. Russell, S. L. McKnight, The hypoxia-responsive transcription factor EPAS1 is essential for catecholamine homeostasis and protection against heart failure during embryonic development. *Genes Dev.* **12**, 3320–3324 (1998). doi: [10.1101/gad.12.21.3320](#); pmid: [9808618](#)
120. S. Jain, E. Maltepe, M. M. Lu, C. Simon, C. A. Bradfield, Expression of ARNT, ARNT2, HIF1α, HIF2α and Ah receptor mRNAs in the developing mouse. *Mech. Dev.* **73**, 117–123 (1998). doi: [10.1016/S0925-4773\(98\)00038-0](#); pmid: [9545558](#)
121. L. Gregory, P. J. Came, S. Brown, Stem cell regulation by JAK/STAT signaling in Drosophila. *Semin. Cell Dev. Biol.* **19**, 407–413 (2008). doi: [10.1016/j.semcdb.2008.06.003](#); pmid: [18603010](#)
122. L. Valzania, K. L. Coon, K. J. Vogel, M. R. Brown, M. R. Strand, Hypoxia-induced transcription factor signaling is essential for larval growth of the mosquito *Aedes aegypti*. *Proc. Natl. Acad. Sci. U.S.A.* **115**, 457–465 (2018). doi: [10.1073/pnas.1719063115](#); pmid: [29298915](#)
123. N. V. Iyer *et al.*, Cellular and developmental control of O₂ homeostasis by hypoxia-inducible factor 1α. *Genes Dev.* **12**, 149–162 (1998). doi: [10.1101/gad.12.2.149](#); pmid: [9436976](#)
124. H. E. Ryan, J. Lo, R. S. Johnson, HIF-1α is required for solid tumor formation and embryonic vascularization. *EMBO J.* **17**, 3005–3015 (1998). doi: [10.1093/emboj/17.11.3005](#); pmid: [9606183](#)
125. V. H. Haase, Regulation of erythropoiesis by hypoxia-inducible factors. *Blood Rev.* **27**, 41–53 (2013). doi: [10.1016/j.blre.2012.12.003](#); pmid: [23291219](#)
126. A. Jögi *et al.*, Hypoxia alters gene expression in human neuroblastoma cells toward an immature and neural crest-like phenotype. *Proc. Natl. Acad. Sci. U.S.A.* **99**, 7021–7026 (2002). doi: [10.1073/pnas.102601999](#); pmid: [12011461](#)
127. S. Mohlin, A. Hamidian, S. Pahlman, HIF2A and IGF2 expression correlates in human neuroblastoma cells and normal immature sympathetic neuroblasts. *Neoplasia* **15**, 328–334 (2013). doi: [10.1593/neo.121706](#); pmid: [23479510](#)
128. M. Abbas *et al.*, Oxygen sensing coordinates photomorphogenesis to facilitate seedling survival. *Curr. Biol.* **25**, 1483–1488 (2015). doi: [10.1016/j.cub.2015.03.060](#); pmid: [25981794](#)
129. V. Shukla *et al.*, Endogenous hypoxia in lateral root primordia controls root architecture by antagonizing auxin signaling in Arabidopsis. *Mol. Plant* **12**, 538–551 (2019). doi: [10.1016/j.molp.2019.01.007](#); pmid: [30641154](#)

130. A. Shmakova, M. Batie, J. Druker, S. Rocha, Chromatin and oxygen sensing in the context of JmjC histone demethylases. *Biochem. J.* **462**, 385–395 (2014). doi: [10.1042/BJ20140754](https://doi.org/10.1042/BJ20140754); pmid: [25145438](https://pubmed.ncbi.nlm.nih.gov/25145438/)
131. Y. Huang, D. Chen, C. Liu, W. Shen, Y. Ruan, Evolution and conservation of JmjC domain proteins in the green lineage. *Mol. Genet. Genomics* **291**, 33–49 (2016). doi: [10.1007/s00438-015-1089-4](https://doi.org/10.1007/s00438-015-1089-4); pmid: [26152513](https://pubmed.ncbi.nlm.nih.gov/26152513/)
132. R. Siauciunaite, N. S. Foulkes, V. Calabrò, D. Vallone, Evolution shapes the gene expression response to oxidative stress. *Int. J. Mol. Sci.* **20**, 3040 (2019). doi: [10.3390/ijms20123040](https://doi.org/10.3390/ijms20123040); pmid: [31234431](https://pubmed.ncbi.nlm.nih.gov/31234431/)
133. I. Slesak, H. Slesak, J. Kruk, Oxygen and hydrogen peroxide in the early evolution of life on earth: In silico comparative analysis of biochemical pathways. *Astrobiology* **12**, 775–784 (2012). doi: [10.1089/ast.2011.0704](https://doi.org/10.1089/ast.2011.0704); pmid: [22970865](https://pubmed.ncbi.nlm.nih.gov/22970865/)
134. C. P. Bracken *et al.*, Cell-specific regulation of hypoxia-inducible factor (HIF)-1 α and HIF-2 α stabilization and transactivation in a graded oxygen environment. *J. Biol. Chem.* **281**, 22575–22585 (2006). doi: [10.1074/jbc.M600288200](https://doi.org/10.1074/jbc.M600288200); pmid: [16760477](https://pubmed.ncbi.nlm.nih.gov/16760477/)
135. R.-G. Hu *et al.*, The N-end rule pathway as a nitric oxide sensor controlling the levels of multiple regulators. *Nature* **437**, 981–986 (2005). doi: [10.1038/nature04027](https://doi.org/10.1038/nature04027); pmid: [16222293](https://pubmed.ncbi.nlm.nih.gov/16222293/)
136. M. L. Puerta *et al.*, A Ratiometric Sensor Based on Plant N-Terminal Degrons Able to Report Oxygen Dynamics in *Saccharomyces cerevisiae*. *J. Mol. Biol.* **431**, 2810–2820 (2019). doi: [10.1016/j.jmb.2019.05.023](https://doi.org/10.1016/j.jmb.2019.05.023); pmid: [31125566](https://pubmed.ncbi.nlm.nih.gov/31125566/)
137. F. Licausi, B. Giuntoli, Synthetic biology of hypoxia. *New Phytol.* nph.16441 (2020). doi: [10.1111/nph.16441](https://doi.org/10.1111/nph.16441); pmid: [31960974](https://pubmed.ncbi.nlm.nih.gov/31960974/)
138. J. E. Stajich *et al.*, The fungi. *Curr. Biol.* **19**, R840–R845 (2009). doi: [10.1016/j.cub.2009.07.004](https://doi.org/10.1016/j.cub.2009.07.004); pmid: [19788875](https://pubmed.ncbi.nlm.nih.gov/19788875/)
139. L. R. Kump, The rise of atmospheric oxygen. *Nature* **451**, 277–278 (2008). doi: [10.1038/nature06587](https://doi.org/10.1038/nature06587); pmid: [18202642](https://pubmed.ncbi.nlm.nih.gov/18202642/)

ACKNOWLEDGMENTS

The authors thank K. Pienta and S. Pählman for essential and constructive discussions. We apologize to those whose work we were not able to cite because of space limitations but acknowledge the contributions you have made to the field. **Funding:** This work was supported by the European Research Foundation Starting Grant 949538 (E.U.H.), the Swedish Research Council (E.U.H.), the Crafoord Foundation (E.U.H. and S.M.), The Villum Foundation grant 16518 (E.U.H.), the Swedish Cancer Society (S.M.), the Swedish Childhood Cancer Fund (S.M.), the Engineering and Physical Sciences Research Council (E.F.), the European Research Council (E.F.), and the Italian Ministry of University and Research (F.L.). **Author contributions:** E.U.H. and F.L. conceptualized the Review, and E.U.H., E.F., S.M., and F.L. wrote the paper. **Competing interests:** The authors declare no competing interests.

10.1126/science.aba3512

RESEARCH ARTICLE SUMMARY

CORONAVIRUS

Inborn errors of type I IFN immunity in patients with life-threatening COVID-19

Qian Zhang *et al.*

INTRODUCTION: Clinical outcomes of human severe acute respiratory syndrome coronavirus 2 (SARS-CoV-2) infection range from silent infection to lethal coronavirus disease 2019 (COVID-19). Epidemiological studies have identified three risk factors for severe disease: being male, being elderly, and having other medical conditions. However, interindividual clinical variability remains huge in each demographic category. Discovering the root cause and detailed molecular, cellular, and tissue- and body-level mechanisms underlying life-threatening COVID-19 is of the utmost biological and medical importance.

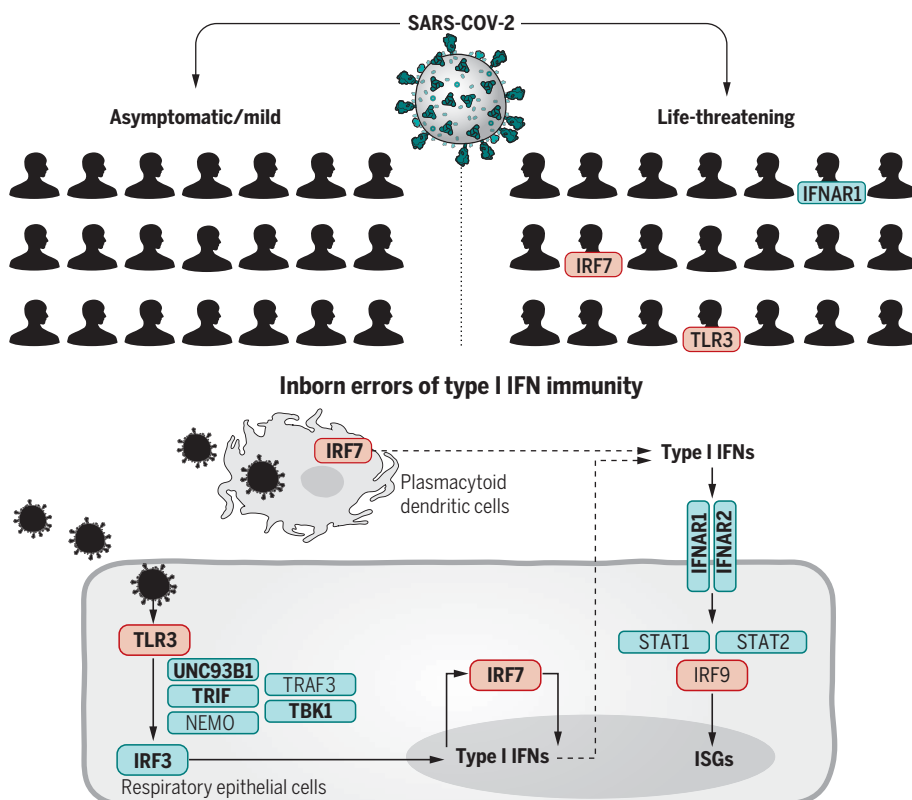
RATIONALE: We established the COVID Human Genetic Effort (www.covidhge.com) to test

the general hypothesis that life-threatening COVID-19 in some or most patients may be caused by monogenic inborn errors of immunity to SARS-CoV-2 with incomplete or complete penetrance. We sequenced the exome or genome of 659 patients of various ancestries with life-threatening COVID-19 pneumonia and 534 subjects with asymptomatic or benign infection. We tested the specific hypothesis that inborn errors of Toll-like receptor 3 (TLR3)- and interferon regulatory factor 7 (IRF7)-dependent type I interferon (IFN) immunity that underlie life-threatening influenza pneumonia also underlie life-threatening COVID-19 pneumonia. We considered three loci identified as mutated in patients with life-threatening influenza: *TLR3*, *IRF7*, and *IRF9*. We also con-

sidered 10 loci mutated in patients with other viral illnesses but directly connected to the three core genes conferring influenza susceptibility: *TICAM1/TRIF*, *UNC93B1*, *TRAF3*, *TBK1*, *IRF3*, and *NEMO/IKBKG* from the TLR3-dependent type I IFN induction pathway, and *IFNAR1*, *IFNAR2*, *STAT1*, and *STAT2* from the IRF7- and IRF9-dependent type I IFN amplification pathway. Finally, we considered various modes of inheritance at these 13 loci.

RESULTS: We found an enrichment in variants predicted to be loss-of-function (pLOF), with a minor allele frequency <0.001, at the 13 candidate loci in the 659 patients with life-threatening COVID-19 pneumonia relative to the 534 subjects with asymptomatic or benign infection ($P = 0.01$). Experimental tests for all 118 rare nonsynonymous variants (including both pLOF and other variants) of these 13 genes found in patients with critical disease identified 23 patients (3.5%), aged 17 to 77 years, carrying 24 deleterious variants of eight genes. These variants underlie autosomal-recessive (AR) deficiencies (*IRF7* and *IFNAR1*) and autosomal-dominant (AD) deficiencies (*TLR3*, *UNC93B1*, *TICAM1*, *TBK1*, *IRF3*, *IRF7*, *IFNAR1*, and *IFNAR2*) in four and 19 patients, respectively. These patients had never been hospitalized for other life-threatening viral illness. Plasmacytoid dendritic cells from IRF7-deficient patients produced no type I IFN on infection with SARS-CoV-2, and *TLR3*^{-/-}, *TLR3*^{+/-}, *IRF7*^{-/-}, and *IFNAR1*^{-/-} fibroblasts were susceptible to SARS-CoV-2 infection in vitro.

CONCLUSION: At least 3.5% of patients with life-threatening COVID-19 pneumonia had known (AR *IRF7* and *IFNAR1* deficiencies or AD *TLR3*, *TICAM1*, *TBK1*, and *IRF3* deficiencies) or new (AD *UNC93B1*, *IRF7*, *IFNAR1*, and *IFNAR2* deficiencies) genetic defects at eight of the 13 candidate loci involved in the TLR3- and IRF7-dependent induction and amplification of type I IFNs. This discovery reveals essential roles for both the double-stranded RNA sensor TLR3 and type I IFN cell-intrinsic immunity in the control of SARS-CoV-2 infection. Type I IFN administration may be of therapeutic benefit in selected patients, at least early in the course of SARS-CoV-2 infection. ■



Inborn errors of TLR3- and IRF7-dependent type I IFN production and amplification underlie life-threatening COVID-19 pneumonia. Molecules in red are encoded by core genes, deleterious variants of which underlie critical influenza pneumonia with incomplete penetrance, and deleterious variants of genes encoding biochemically related molecules in blue underlie other viral illnesses. Molecules represented in bold are encoded by genes with variants that also underlie critical COVID-19 pneumonia.

The full author list and the list of affiliations is available in the full article online.

Corresponding author: Jean-Laurent Casanova (casanova@rockefeller.edu)

This is an open-access article distributed under the terms of the Creative Commons Attribution license (<https://creativecommons.org/licenses/by/4.0/>), which permits unrestricted use, distribution, and reproduction in any medium, provided the original work is properly cited. Cite this article as Q. Zhang *et al.*, *Science* 370, eabd4570 (2020). DOI: 10.1126/science.abd4570

READ THE FULL ARTICLE AT
<https://doi.org/10.1126/science.abd4570>

RESEARCH ARTICLE

CORONAVIRUS

Inborn errors of type I IFN immunity in patients with life-threatening COVID-19

Qian Zhang¹, Paul Bastard^{2,3*}, Zhiyong Liu^{1*}, Jérémie Le Pen^{4*}, Marcela Moncada-Velez^{1*}, Jie Chen^{1*}, Masato Ogishi^{1*}, Ira K. D. Sabli^{5*}, Stephanie Hodeib^{5*}, Cecilia Korol^{2*}, Jérémie Rosain^{2,3*}, Kaya Bilguvar^{6*}, Junqiang Ye^{7*}, Alexandre Bolze^{8*}, Benedetta Bigio^{1*}, Rui Yang^{1*}, Andrés Augusto Arias^{1,9,10*}, Qinhua Zhou^{1*}, Yu Zhang^{11,12*}, Fanny Onodi¹³, Sarantis Korniotis¹³, Léa Karpf¹³, Quentin Philippot^{2,3}, Marwa Chbihi^{2,3}, Lucie Bonnet-Madin¹⁴, Karim Dorgham¹⁵, Nikaia Smith¹⁶, William M. Schneider⁴, Brandon S. Razoogy⁴, Hans-Heinrich Hoffmann⁴, Eleftherios Michailidis⁴, Leen Moens¹⁷, Ji Eun Han¹, Lazaro Lorenzo^{2,3}, Lucy Bizien^{2,3}, Philip Meade¹⁸, Anna-Lena Neehus^{2,3}, Aileen Camille Ugurbil¹, Aurélien Corneau¹⁹, Gaspard Kerner^{2,3}, Peng Zhang¹, Franck Rapaport¹, Yoann Seeleuthner^{2,3}, Jeremy Manry^{2,3}, Cecile Masson²⁰, Yohann Schmitt²⁰, Agatha Schlüter²¹, Tom Le Voyer^{2,3}, Taushif Khan²², Juan Li¹, Jacques Fellay^{23,24,25}, Lucie Roussel²⁶, Mohammad Shahrooei^{27,28}, Mohammed F. Alosaimi²⁹, Davood Mansouri^{30,31,32}, Haya Al-Saud³³, Fahd Al-Mulla³⁴, Feras Almourfi³³, Saleh Zaid Al-Muhsen³⁵, Fahad Alsouhime²⁹, Saeed Al Turki^{36,37}, Rana Hasanato²⁹, Diederik van de Beek³⁸, Andrea Biondi³⁹, Laura Rachele Bettini³⁹, Mariella D'Angio³⁹, Paolo Bonfanti⁴⁰, Luisa Imberti⁴¹, Alessandra Sottini⁴¹, Simone Paghera⁴¹, Eugenia Quiros-Roldan⁴², Camillo Rossi⁴³, Andrew J. Oler⁴⁴, Miranda F. Tompkins⁴⁵, Camille Alba⁴⁵, Isabelle Vandermoot⁴⁶, Jean-Christophe Goffard⁴⁷, Guillaume Smits⁴⁶, Isabelle Migeotte⁴⁸, Filomeen Haerynck⁴⁹, Pere Soler-Palacin⁵⁰, Andrea Martin-Nalda⁵⁰, Roger Colobran⁵¹, Pierre-Emmanuel Morange⁵², Sevgi Keles⁵³, Fatma Çölkesen⁵⁴, Tayfun Ozelcik⁵⁵, Kadriye Kart Yasar⁵⁶, Sevtap Senoglu⁵⁶, Şemsi Nur Karabela⁵⁶, Carlos Rodríguez-Gallego^{57,58}, Giuseppe Novelli⁵⁹, Sami Hraiech⁶⁰, Yacine Tandjaoui-Lambiotte^{61,62}, Xavier Duval^{63,64}, Cédric Lauouenan^{63,64,65}, COVID-STORM Clinicians†, COVID Clinicians†, Imagine COVID Group†, French COVID Cohort Study Group†, CoV-Contact Cohort†, Amsterdam UMC Covid-19 Biobank†, COVID Human Genetic Effort†, NIAID-USUHS/TAGC COVID Immunity Group†, Andrew L. Snow⁶⁶, Clifton L. Dalgard^{45,67}, Joshua D. Milner⁶⁸, Donald C. Vinh²⁶, Trine H. Mogensen^{69,70}, Nico Marr^{22,71}, András N. Spaan^{1,72}, Bertrand Boisson^{1,2,3}, Stéphanie Boisson-Dupuis^{1,2,3}, Jacinta Bustamante^{1,2,3,73}, Anne Puel^{1,2,3}, Michael J. Ciancanelli^{1,74}, Isabelle Meyts^{17,75}, Tom Maniatis^{7,76}, Vassili Soumelis^{13,77}, Ali Amara¹⁴, Michel Nussenzweig^{78,79}, Adolfo García-Sastre^{18,80,81,82}, Florian Kramer¹⁸, Aurora Pujol²¹, Darragh Duffy¹⁶, Richard P. Lifton^{83,84,85}†, Shen-Ying Zhang^{1,2,3}†, Guy Gorochov¹⁵†, Vivien Béziat^{1,2,3}†, Emmanuelle Jouanguy^{1,2,3}†, Vanessa Sancho-Shimizu⁵†, Charles M. Rice⁴†, Laurent Abel^{1,2,3}†, Luigi D. Notarangelo^{11,12}§, Aurélie Cobat^{1,2,3}§, Helen C. Su^{11,12}§, Jean-Laurent Casanova^{1,2,3,79,86}§¶

Clinical outcome upon infection with severe acute respiratory syndrome coronavirus 2 (SARS-CoV-2) ranges from silent infection to lethal coronavirus disease 2019 (COVID-19). We have found an enrichment in rare variants predicted to be loss-of-function (LOF) at the 13 human loci known to govern Toll-like receptor 3 (TLR3)- and interferon regulatory factor 7 (IRF7)-dependent type I interferon (IFN) immunity to influenza virus in 659 patients with life-threatening COVID-19 pneumonia relative to 534 subjects with asymptomatic or benign infection. By testing these and other rare variants at these 13 loci, we experimentally defined LOF variants underlying autosomal-recessive or autosomal-dominant deficiencies in 23 patients (3.5%) 17 to 77 years of age. We show that human fibroblasts with mutations affecting this circuit are vulnerable to SARS-CoV-2. Inborn errors of TLR3- and IRF7-dependent type I IFN immunity can underlie life-threatening COVID-19 pneumonia in patients with no prior severe infection.

Severe acute respiratory syndrome coronavirus 2 (SARS-CoV-2) has already claimed at least 1 million lives, has been detected in at least 20 million people, and has probably infected at least another 200 million. The clinical manifestations range from silent infection to lethal disease, with an infection fatality rate of 0.1 to 0.9%. Three epidemiological factors increase the risk of severity: (i) increasing age, decade by decade, after the age of 50, (ii) being male,

and (iii) having various underlying medical conditions (1). However, even taking these factors into account, there is immense inter-individual clinical variability in each demographic category considered. Following on from our human genetic studies of other severe infectious diseases (2, 3), we established the COVID Human Genetic Effort (<https://www.covidhge.com>) to test the general hypothesis that in some patients, life-threatening coronavirus disease 2019 (COVID-19) may be

caused by monogenic inborn errors of immunity to SARS-CoV-2 with incomplete or complete penetrance (4). We enrolled 659 patients (74.5% men and 25.5% women, 13.9% of whom died) of various ancestries between 1 month and 99 years of age (Fig. 1A). These patients were hospitalized for life-threatening pneumonia caused by SARS-CoV-2 (critical COVID-19). We sequenced their whole genome ($N = 364$) or exome ($N = 295$), and principal component analysis (PCA) on these data confirmed their ancestries (Fig. 1B).

Candidate variants at 13 human loci that govern immunity to influenza virus

We first tested the specific hypothesis that inborn errors of Toll-like receptor 3 (TLR3)- and interferon regulatory factor 7 (IRF7)-dependent type I interferon (IFN) immunity, which underlie life-threatening influenza pneumonia, may also underlie life-threatening COVID-19 pneumonia (5) (Fig. 2). We considered three loci previously shown to be mutated in patients with critical influenza pneumonia: *TLR3* (6), *IRF7* (7), and *IRF9* (8). We also considered 10 loci mutated in patients with other viral illnesses but directly connected to the three core genes conferring influenza susceptibility: *TICAM1/TRIF* (9), *UNC93B1* (10), *TRAF3* (11), *TBK1* (12), *IRF3* (13), and *NEMO/IKBKG* (14) in the TLR3-dependent type I IFN induction pathway, and *IFNAR1* (15), *IFNAR2* (16), *STAT1* (17), and *STAT2* (18) in the IRF7- and IRF9-dependent type I IFN amplification pathway. We collected both monoallelic and biallelic nonsynonymous variants with a minor allele frequency (MAF) <0.001 at all 13 loci. Twelve of the 13 candidate loci are autosomal, whereas *NEMO* is X-linked. For the latter gene, we considered only a recessive model (19). Autosomal-dominant (AD) inheritance has not been proven for six of the 12 autosomal loci (*UNC93B1*, *IRF7*, *IFNAR1*, *IFNAR2*, *STAT2*, and *IRF9*). Nevertheless, we considered heterozygous variants because none of the patients enrolled had been hospitalized for critical viral infections before COVID-19, raising the possibility that any underlying genetic defects that they might have display a lower penetrance for influenza and other viral illnesses than for COVID-19, which is triggered by a more virulent virus.

Enrichment of variants predicted to be LOF at the influenza susceptibility loci

We found four unrelated patients with biallelic variants of *IRF7* or *IFNAR1* (Table 1 and table S1). We also found 113 patients carrying 113 monoallelic variants at 12 loci: *TLR3* ($N = 7$ patients/7 variants), *UNC93B1* ($N = 10/9$), *TICAM1* ($N = 17/15$), *TRAF3* ($N = 6/6$), *TBK1* ($N = 12/11$), *IRF3* ($N = 5/5$), *IRF7* ($N = 20/13$), *IFNAR1* ($N = 14/13$), *IFNAR2* ($N = 17/15$), *STAT1* ($N = 4/4$), *STAT2* ($N = 11/11$), and *IRF9* ($N = 4/4$). We detected no copy number variation

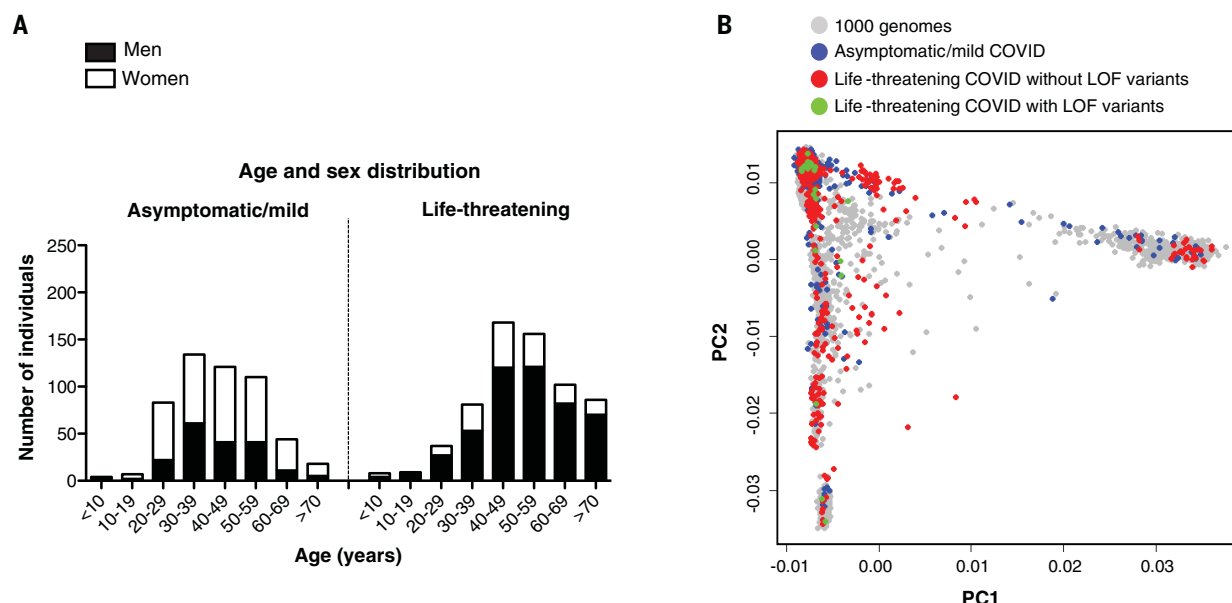


Fig. 1. Demographic and genetic data for the COVID-19 cohort. (A) Age and sex distribution of patients with life-threatening COVID-19. (B) PCA of patient (with or without LOF variants in the 13 candidate genes) and control cohorts (patients with mild or asymptomatic disease and individuals from the 1000 Genomes Project).

¹St. Giles Laboratory of Human Genetics of Infectious Diseases, Rockefeller Branch, The Rockefeller University, New York, NY, USA. ²Laboratory of Human Genetics of Infectious Diseases, Necker Branch, INSERM U1163, Necker Hospital for Sick Children, Paris, France. ³University of Paris, Imagine Institute, Paris, France. ⁴Laboratory of Virology and Infectious Disease, The Rockefeller University, New York, NY, USA. ⁵Department of Paediatric Infectious Diseases & Virology, Imperial College London, London, UK. ⁶Yale Center for Genome Analysis and Department of Genetics, Yale School of Medicine, New Haven, CT, USA. ⁷Zukerman Mind Brain Behavior Institute, Columbia University, New York, NY, USA. ⁸Helix, San Mateo, CA, USA. ⁹Primary Immunodeficiencies Group, University of Antioquia UdeA, Medellín, Colombia. ¹⁰School of Microbiology, University of Antioquia UdeA, Medellín, Colombia. ¹¹Laboratory of Clinical Immunology and Microbiology, Division of Intramural Research, NIAID, NIH, Bethesda, MD, USA. ¹²NIAID Clinical Genomics Program, NIH, Bethesda, MD, USA. ¹³Université de Paris, Institut de Recherche Saint-Louis, INSERM U976, Hôpital Saint-Louis, Paris, France. ¹⁴Laboratory of Genomes & Cell Biology of Disease, INSERM U944, CNRS UMR 7212, Université de Paris, Institut de Recherche Saint-Louis, Hôpital Saint-Louis, Paris, France. ¹⁵Sorbonne Université, Inserm, Centre d'Immunologie et des Maladies Infectieuses-Paris (CIMI PARIS), Assistance Publique-Hôpitaux de Paris (AP-HP) Hôpital Pitié-Salpêtrière, Paris, France. ¹⁶Translational Immunology Lab, Institut Pasteur, Paris, France. ¹⁷Laboratory for Inborn Errors of Immunity, Department of Microbiology, Immunology and Transplantation, Department of Pediatrics, University Hospitals Leuven, KU Leuven, Leuven, Belgium. ¹⁸Department of Microbiology, Icahn School of Medicine at Mount Sinai, New York, NY, USA. ¹⁹Sorbonne Université, UMS037, PASS, Plateforme de Cytométrie de la Pitié-Salpêtrière CyPS, Paris, France. ²⁰Bioinformatics Platform, Structure Fédérative de Recherche Necker, INSERM UMR1163, Université de Paris, Imagine Institute, Paris, France. ²¹Neurometabolic Diseases Laboratory, IDIBELL-Hospital Duran i Reynals, CIBERER U759, and Catalan Institution of Research and Advanced Studies (ICREA), Barcelona, Spain. ²²Department of Immunology, Research Branch, Sidra Medicine, Doha, Qatar. ²³School of Life sciences, Ecole Polytechnique Fédérale de Lausanne, Lausanne, Switzerland. ²⁴Precision Medicine Unit, Lausanne University Hospital and University of Lausanne, Lausanne, Switzerland. ²⁵Swiss Institute of Bioinformatics, Lausanne, Switzerland. ²⁶Infectious Disease Susceptibility Program, Research Institute, McGill University Health Centre, Montréal, Québec, Canada. ²⁷Specialized Immunology Laboratory of Dr. Shahrooei, Sina Medical Complex, Ahvaz, Iran. ²⁸Department of Microbiology and Immunology, Clinical and Diagnostic Immunology, KU Leuven, Leuven, Belgium. ²⁹Department of Pathology and Laboratory Medicine, College of Medicine, King Saud University, Riyadh, Saudi Arabia. ³⁰Department of Clinical Immunology and Infectious Diseases, National Research Institute of Tuberculosis and Lung Diseases, Shahid Beheshti University of Medical Sciences, Tehran, Iran. ³¹The Clinical Tuberculosis and Epidemiology Research Center, National Research Institute of Tuberculosis and Lung Diseases (NRITLD), Masih Daneshvari Hospital, Shahid Beheshti, University of Medical Sciences, Tehran, Iran. ³²Pediatric Respiratory Diseases Research Center, National Research Institute of Tuberculosis and Lung Diseases, Shahid Beheshti, Iran. ³³National Center of Genomics Technology, King Abdulaziz City for Science and Technology, Riyadh, Saudi Arabia. ³⁴Dasman Diabetes Institute, Department of Genetics and Bioinformatics, Kuwait. ³⁵Immunology Research Laboratory, Department of Pediatrics, College of Medicine and King Saud University Medical City, King Saud University, Riyadh, Saudi Arabia. ³⁶Translational Pathology, Department of Pathology and Laboratory Medicine, King Abdulaziz Medical City, Misery of National Guard Health Affairs, Riyadh, Saudi Arabia. ³⁷Cancer & Blood Research, King Abdullah International Medical Research Center, Riyadh, Saudi Arabia. ³⁸Amsterdam UMC, Department of Neurology, Amsterdam Neuroscience, Amsterdam, Netherlands. ³⁹Pediatric Department and Centro Tettamanti-European Reference Network PaedCan, EuroBloodNet, MetabERN-University of Milano-Bicocca-Fondazione MBBM-Ospedale, San Gerardo, Monza, Italy. ⁴⁰Department of Infectious Diseases, San Gerardo Hospital-University of Milano-Bicocca, Monza, Italy. ⁴¹CREA Laboratory, Diagnostic Laboratory, ASST Spedali Civili di Brescia, Brescia, Italy. ⁴²Department of Infectious and Tropical Diseases, University of Brescia and ASST Spedali di Brescia, Brescia, Italy. ⁴³Chief Medical Officer, ASST Spedali Civili di Brescia, Brescia, Italy. ⁴⁴Bioinformatics and Computational Biosciences Branch, Office of Cyber Infrastructure and Computational Biology, NIAID, NIH, Bethesda, MD, USA. ⁴⁵PRIMER, Uniformed Services University of the Health Sciences, Bethesda, MD, USA. ⁴⁶Center of Human Genetics, Hôpital Erasme, Université Libre de Bruxelles, Brussels, Belgium. ⁴⁷Department of Internal Medicine, Hôpital Erasme, Université Libre de Bruxelles, Brussels, Belgium. ⁴⁸Fonds de la Recherche Scientifique (FNRS) and Center of Human Genetics, Hôpital Erasme, Université Libre de Bruxelles, Brussels, Belgium. ⁴⁹Department of Paediatric Immunology and Pulmonology, Centre for Primary Immunodeficiency Ghent (CPIG), PID Research Lab, Jeffrey Modell Diagnosis and Research Centre, Ghent University Hospital, Ghent, Belgium. ⁵⁰Pediatric Infectious Diseases and Immunodeficiencies Unit, Hospital Universitari Vall d'Hebron, Vall d'Hebron Research Institute, Vall d'Hebron Barcelona Hospital Campus, Universitat Autònoma de Barcelona (UAB), Barcelona, Catalonia, Spain. ⁵¹Immunology Division, Genetics Department, Hospital Universitari Vall d'Hebron, Vall d'Hebron Research Institute, Vall d'Hebron Barcelona Hospital Campus, UAB, Barcelona, Catalonia, Spain. ⁵²Aix Marseille Univ, INSERM, INRAE, C2VN, CHU Timone, Marseille, France. ⁵³Necmettin Erbakan University, Meram Medical Faculty, Division of Pediatric Allergy and Immunology, Konya, Turkey. ⁵⁴Department of Infectious Diseases and Clinical Microbiology, Konya Training and Research Hospital, Konya, Turkey. ⁵⁵Department of Molecular Biology and Genetics, Bilkent University, Bilkent-Ankara, Turkey. ⁵⁶Departments of Infectious Diseases and Clinical Microbiology, Bakirkoy Dr. Sadi Konuk Training and Research Hospital, University of Health Sciences, Istanbul, Turkey. ⁵⁷Department of Immunology, Hospital Universitario de G.C. Dr. Negrín, Canarian Health System, Las Palmas de Gran Canaria, Spain. ⁵⁸University Fernando Pessoa Canarias, Las Palmas de Gran Canaria, Spain. ⁵⁹Department of Biomedicine and Prevention, University of Rome "Tor Vergata", Rome, Italy. ⁶⁰Intensive Care Unit, AP-HM, Marseille, France. ⁶¹Avicenne Hospital Intensive Care Unit, APHP, Bobigny, INSERM U1272 Hypoxia & Lung, Paris, France. ⁶²PH Réanimation CHU Avicenne, Bobigny, INSERM U1272 Hypoxie & Poumon, Paris, France. ⁶³Université de Paris, IAME UMR-S 1137, INSERM, Paris, France. ⁶⁴Inserm CIC 1425, Paris, France. ⁶⁵AP-HP, Département Épidémiologie Biostatistiques et Recherche Clinique, Hôpital Bichat, Paris, France. ⁶⁶Department of Pharmacology & Molecular Therapeutics, Uniformed Services University of the Health Sciences, Bethesda, MD, USA. ⁶⁷Department of Anatomy, Physiology & Genetics, Uniformed Services University of the Health Sciences, Bethesda, MD, USA. ⁶⁸Division of Pediatric Allergy, Immunology and Rheumatology, Columbia University, New York, USA. ⁶⁹Department of Infectious Diseases, Aarhus University Hospital, Skejby, Denmark. ⁷⁰Department of Biomedicine, Aarhus University, Aarhus, Denmark. ⁷¹College of Health and Life Sciences, Hamad Bin Khalifa University, Doha, Qatar. ⁷²Department of Medical Microbiology, Utrecht UMC, Utrecht, Netherlands. ⁷³Study Center for Primary Immunodeficiencies, Necker Hospital for Sick Children, Paris, France. ⁷⁴Turnstone Biologics, New York, NY, USA. ⁷⁵Department of Pediatrics, University Hospitals Leuven, KU Leuven, Leuven, Belgium. ⁷⁶New York Genome Center, New York, NY, USA. ⁷⁷AP-HP, Hôpital Saint-Louis, Laboratoire d'Immunologie, Paris, France. ⁷⁸Laboratory of Molecular Immunology, Rockefeller University, New York, NY, USA. ⁷⁹Howard Hughes Medical Institute, New York, NY, USA. ⁸⁰Department of Medicine, Division of Infectious Diseases, Icahn School of Medicine at Mount Sinai, New York, NY, USA. ⁸¹Global Health and Emerging Pathogens Institute, Icahn School of Medicine at Mount Sinai, New York, NY, USA. ⁸²The Tisch Cancer Institute, Icahn School of Medicine at Mount Sinai, New York, NY, USA. ⁸³Laboratory of Genetics and Genomics, The Rockefeller University, New York, NY, USA. ⁸⁴Department of Genetics, Yale University School of Medicine, New Haven, CT, USA. ⁸⁵Yale Center for Genome Analysis, Yale School of Medicine, New Haven, CT, USA. ⁸⁶Pediatric Hematology and Immunology Unit, Necker Hospital for Sick Children, AP-HP, Paris, France.

*These authors contributed equally to this work.

†All collaborators and their affiliations appear at the end of this paper.

‡These authors contributed equally to this work.

§These authors contributed equally to this work.

¶Corresponding author. Email: casanova@rockefeller.edu

for these 13 genes. Unexpectedly, one of these variants has been reported in patients with life-threatening influenza pneumonia (*TLR3* p.Pro554Ser) (6, 20) and another was shown to be both deleterious and dominant-negative

(*IFNAR1* p.Pro335del) (21). Nine of the 118 biallelic or monoallelic variants were predicted to be LOF (pLOF), whereas the remaining 109 were missense or in-frame indels (table S1). In a sample of 534 controls with asymptomatic

or mild SARS-CoV-2 infection, we found only one heterozygous pLOF variation with a MAF <0.001 at the 13 loci (*IRF7* p.Leu99fs). A PCA-adjusted burden test on the 12 autosomal loci revealed significant enrichment in pLOF variants in patients relative to controls [$P = 0.01$; odds ratio (OR) = 8.28; 95% confidence interval (CI) = 1.04 to 65.64] under an AD mode of inheritance. The same analysis performed on synonymous variants with a MAF <0.001 was not significant ($P = 0.19$), indicating that our ethnicity-adjusted burden test was well calibrated.

Experimentally deleterious alleles at the influenza susceptibility loci in 3.5% of patients

We tested these 118 variants experimentally in ad hoc overexpression systems. We found that 24 variants of eight genes were deleterious (including all the pLOF variants) because they were loss-of-expression, LOF, or severely hypomorphic: *TLR3* ($N = 4$ variants), *UNC93B1* ($N = 1$), *TICAM1* ($N = 3$), *TBK1* ($N = 2$), *IRF3* ($N = 2$), *IRF7* ($N = 8$), *IFNAR1* ($N = 3$), and *IFNAR2* ($N = 1$) (table S1, Fig. 3, and figs. S1 to S8). Consistently, heterozygous LOF variants of *IRF3* and *IRF7* were reported in single patients with life-threatening influenza pneumonia (22, 23). The remaining 94 variants were biochemically neutral. Twenty-three patients carried these 24 deleterious variants, resulting in four autosomal-recessive (AR) deficiencies (homozygosity or compound heterozygosity

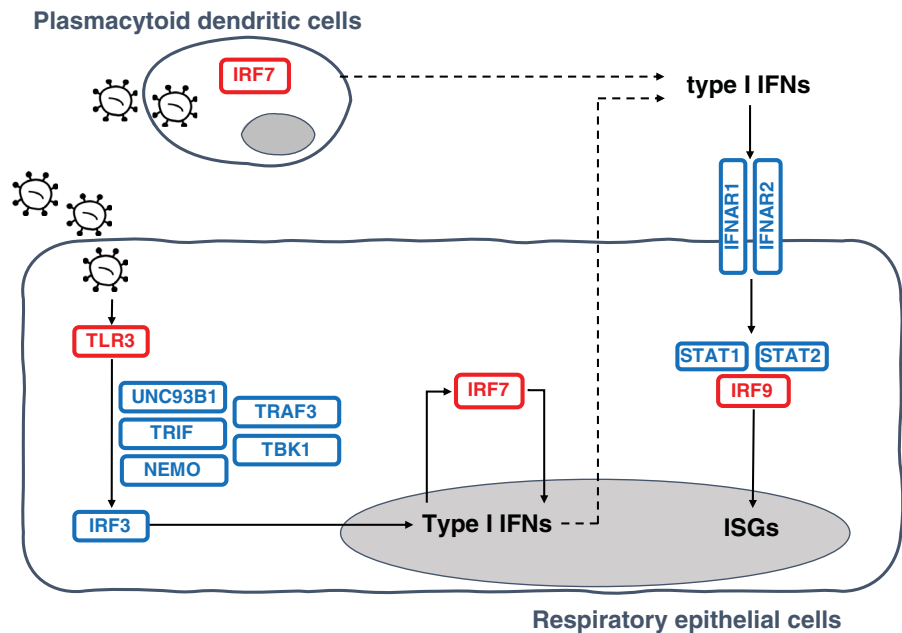


Fig. 2. Illustration of TLR3- and IRF7-dependent type I IFN production and amplification circuit. Molecules in red are encoded by core genes, deleterious variants of which underlie critical influenza pneumonia with incomplete penetrance; deleterious variants of genes encoding biochemically related molecules in blue underlie other viral illnesses. Type I IFNs also induce themselves. ISGs, interferon-stimulated genes.

Table 1. Disease-causing variants identified in patients with life-threatening COVID-19.							
Gene	Inheritance	Genetic form	Genotype	Gender	Age [years]	Ancestry/residence	Outcome
<i>TLR3</i>	AD	Known	p.Ser339fs/WT	M	40	Spain	Survived
<i>TLR3</i>	AD	Known	p.Pro554Ser/WT	M	68	Italy	Survived
<i>TLR3</i>	AD	Known	p.Trp769*/WT	M	77	Italy	Survived
<i>TLR3</i>	AD	Known	p.Met870Val/WT	M	56	Colombia/Spain	Survived
<i>UNC93B1</i>	AD	New	p.Glu96*/WT	M	48	Venezuela/Spain	Survived
<i>TICAM1</i>	AD	Known	p.Thr41le/WT	M	49	Italy	Survived
<i>TICAM1</i>	AD	Known	p.Ser60Cys/WT	F	61	Vietnam/France	Survived
<i>TICAM1</i>	AD	Known	p.Gln392Lys/WT	F	71	Italy	Deceased
<i>TBK1</i>	AD	Known	p.Phe24Ser/WT	F	46	Venezuela/Spain	Survived
<i>TBK1</i>	AD	Known	p.Arg308*/WT	M	17	Turkey	Survived
<i>IRF3</i>	AD	Known	p.Glu49del/WT	F	23	Bolivia/Spain	Survived
<i>IRF3</i>	AD	Known	p.Asn146Lys/WT	F	60	Italy	Survived
<i>IRF7</i>	AR	Known	p.Pro364fs/p.Pro364fs	F	49	Italy/Belgium	Survived
<i>IRF7</i>	AR	Known	p.Met371Val/p.Asp117Asn	M	50	Turkey	Survived
<i>IRF7</i>	AD	New	p.Arg7fs/WT	M	60	Italy	Survived
<i>IRF7</i>	AD	New	p.Gln185*/WT	M	44	France	Survived
<i>IRF7</i>	AD	New	p.Pro246fs/WT	M	41	Spain	Survived
<i>IRF7</i>	AD	New	p.Arg369Gln/WT	M	69	Italy	Survived
<i>IRF7</i>	AD	New	p.Phe95Ser/WT	M	37	Turkey	Survived
<i>IFNAR1</i>	AR	Known	p.Trp73Cys/Trp73Cys	M	38	Turkey	Survived
<i>IFNAR1</i>	AR	Known	p.Ser422Arg/Ser422Arg	M	26	Pakistan/Saudi Arabia	Deceased
<i>IFNAR1</i>	AD	New	p.Pro335del/WT	F	23	China/Italy	Survived
<i>IFNAR2</i>	AD	New	p.Glu140fs/WT	F	54	Belgium	Survived

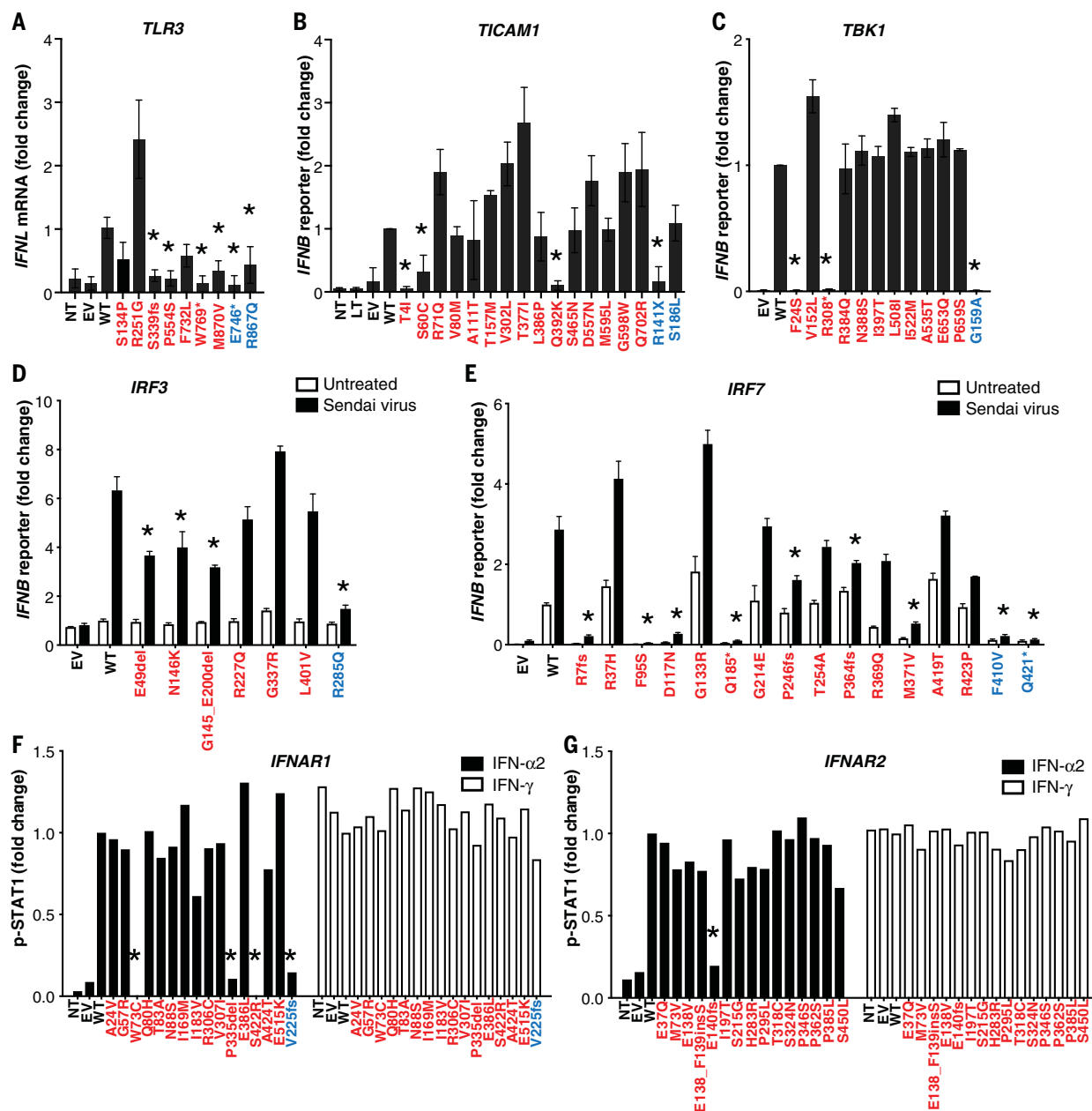


Fig. 3. Impact of TLR3, TICAM1, TBK1, IRF3, IRF7, IFNAR1, and IFNAR2

variants on type I IFN signaling. (A) TLR3-deficient P2.1 fibrosarcoma cells were stably transfected with plasmids expressing WT or mutant forms of *TLR3*, and *IFNL1* mRNA levels were determined by reverse transcription quantitative PCR. *IFNL1* mRNA levels were expressed relative to the housekeeping gene *GUS* and then normalized. *IFNL1* was undetectable in unstimulated cells. The differences between variants and WT were tested using one-way ANOVA (* $P < 0.05$). (B) TICAM1-deficient SV40-Fib cells were transiently transfected with WT or mutant forms of *TICAM1*, together with an IFN- β luciferase reporter and a constitutively expressed reporter. Normalized luciferase induction was measured 24 hours after transfection. The differences between variants and WT were tested using one-way ANOVA (* $P < 0.05$). (C) HEK293T cells were transiently transfected with WT and mutant forms of *TBK1*, together with an IFN- β luciferase reporter and a constitutively expressed reporter. Normalized luciferase activity was measured 24 hours after transfection. The differences between variants and WT were tested using one-way ANOVA (* $P < 0.05$). (D) IRF3-deficient HEK293T cells were transiently transfected with WT and mutant forms of *IRF3*, together with an IFN- β

luciferase reporter and a constitutively expressed reporter. Cells were either left untreated or infected with Sendai virus for 24 hours before the normalized measurement of luciferase activity. The differences between variants and WT were evaluated using two-way ANOVA (* $P < 0.05$). (E) HEK293T cells were transiently transfected with WT and mutant forms of *IRF7*, together with an IFN- β luciferase reporter and a constitutively expressed reporter. Cells were either left untreated or infected with Sendai virus for 24 hours before the normalized measurement of luciferase activity. The differences between variants and WT were tested using two-way ANOVA (* $P < 0.05$). (F and G) IFNAR1- or IFNAR2-deficient SV40-Fib cells were transiently transfected with WT or mutant forms of *IFNAR1* for 36 hours, and either left untreated or stimulated with IFN- $\alpha 2$ or IFN- γ . Fluorescence-activated cell sorting (FACS) staining with anti-p-STAT1 antibody and the z-score of the MFI were assessed. Asterisks indicate variants with MFI < 50% of WT. Variants in red were identified in COVID-19 patients. Variants in blue are known deleterious variants and served as negative controls. EV, empty vector; LT, lipofectamine. Three technical repeats were performed for (A) to (E). Means and SD are shown in the columns and horizontal bars when appropriate.

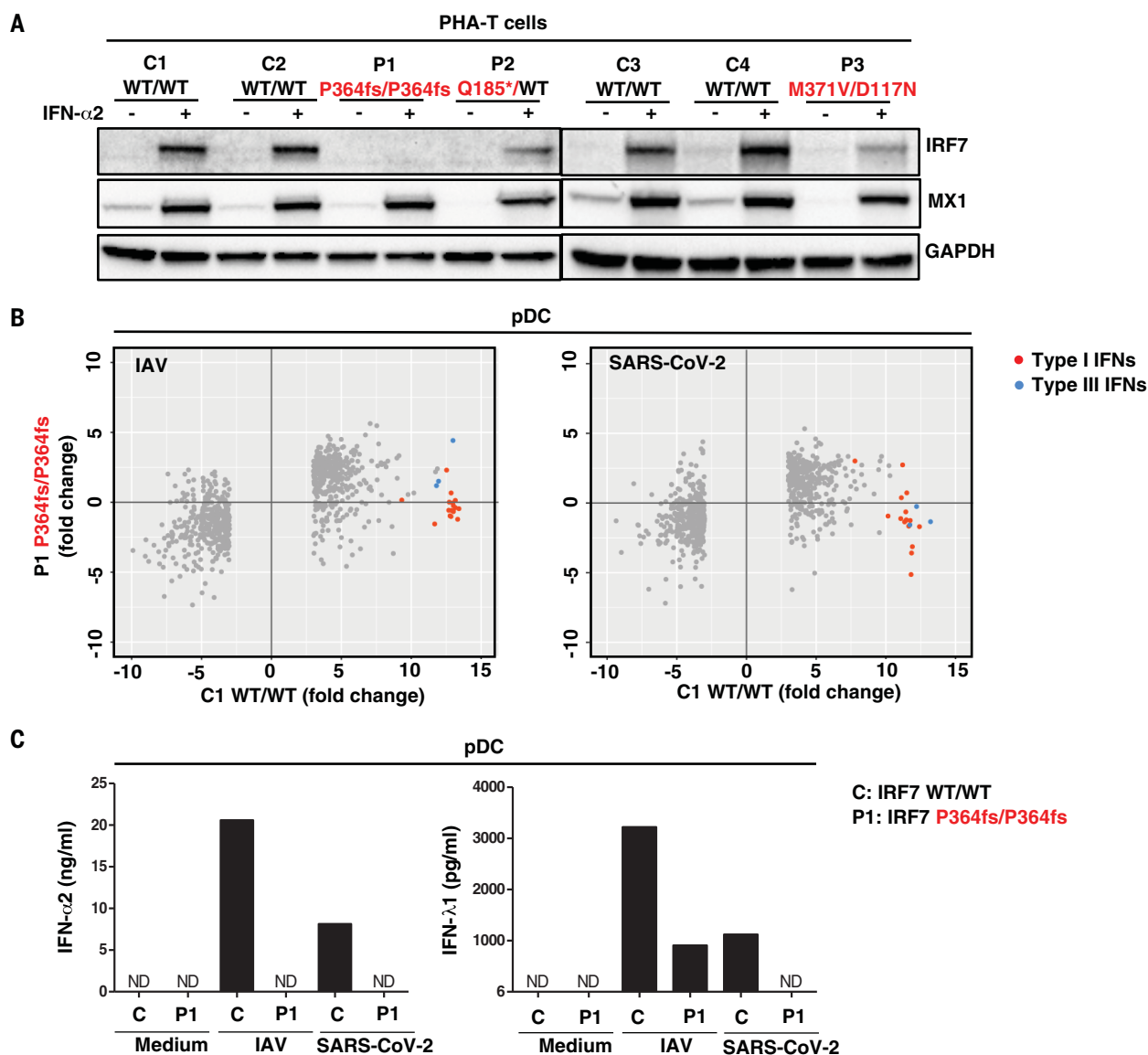


Fig. 4. Type I IFN responses in patient cells defective for IRF7. (A) Levels of the IRF7 protein in PHA-T cells from two patients with AR IRF7 deficiency (P1 and P3), one patient with AD IRF7 deficiency (P2), and four healthy donors (C1 to C4). Cells were either left untreated or stimulated with IFN- α 2 for 24 hours, and protein levels were measured by Western blotting. MX1 was used as a positive control for IFN- α 2 treatment. (B) pDCs isolated from an AR IRF7-deficient patient (P1) and a healthy donor (C1) were either left untreated or

infected with influenza A virus (IAV) or SARS-CoV-2, and RNA-seq was performed. Genes with expression >2.5-fold higher or lower in C1 after infection are plotted as the fold change in expression. Red dots are type I IFN genes; blue dots are type III IFN genes. (C) pDCs isolated from healthy donor C and IRF7-deficient patient (P1) were either left untreated (Medium) or infected with IAV or SARS-CoV-2, and the production of IFN- α 2 and IFN- λ 1 was measured by CBA and ELISA, respectively, on the supernatant. ND, not detected.

for IRF7; homozygosity for *IFNAR1*) and 19 AD deficiencies. These 23 patients did not carry candidate variants at the other 417 loci known to underlie inborn errors of immunity (table S2) (24–26). These findings suggest that at least 23 (3.5%) unrelated patients of the 659 patients tested suffered from a deficiency at one of eight loci among the 13 tested: four patients with a known AR disorder (*IRF7* or *IFNAR1*) (7, 15), 11 with a known AD disorder (*TLR3*, *TICAM1*, *TBK1*, or *IRF3*) (6, 9, 12, 13, 20), and eight with a previously unknown AD genetic disorder (*UNC93B1*, *IRF7*, *IFNAR1*, or *IFNAR2*).

Impaired TLR3- and IRF7-dependent type I immunity in patient cells in vitro

We tested cells from patients with selected genotypes and showed that PHA-driven T cell blasts (PHA-T cells) from patients with AR or AD IRF7 deficiency had low levels of IRF7 expression (Fig. 4A). We then isolated circulating plasmacytoid dendritic cells (pDCs) from a patient with AR IRF7 deficiency (fig. S9A) (7). These cells were present in normal proportions (fig. S9B), but they did not produce any detectable type I or III IFNs in response to SARS-CoV-2, as analyzed by cytometric bead

array (CBA), enzyme-linked immunosorbent assay (ELISA), and RNA sequencing (RNA-seq) (Fig. 4, B and C). We also showed that PHA-T cells from a patient with AR IFN- α / β receptor 1 (*IFNAR1*) deficiency had impaired *IFNAR1* expression and responses to IFN- α 2 or IFN- β , and that the patient's SV40-transformed fibroblast (SV40-Fib) cells did not respond to IFN- α 2 or IFN- β (Fig. 5). We then infected *TLR3*^{-/-}, *TLR3*^{+/-}, *IRF7*^{-/-} SV40-Fib cells, and *IRF7*^{-/-} SV40-Fib cells rescued with wild-type (WT) *IRF7*; *IFNAR1*^{-/-} SV40-Fib cells, and *IFNAR1*^{-/-} SV40-Fib cells rescued with WT

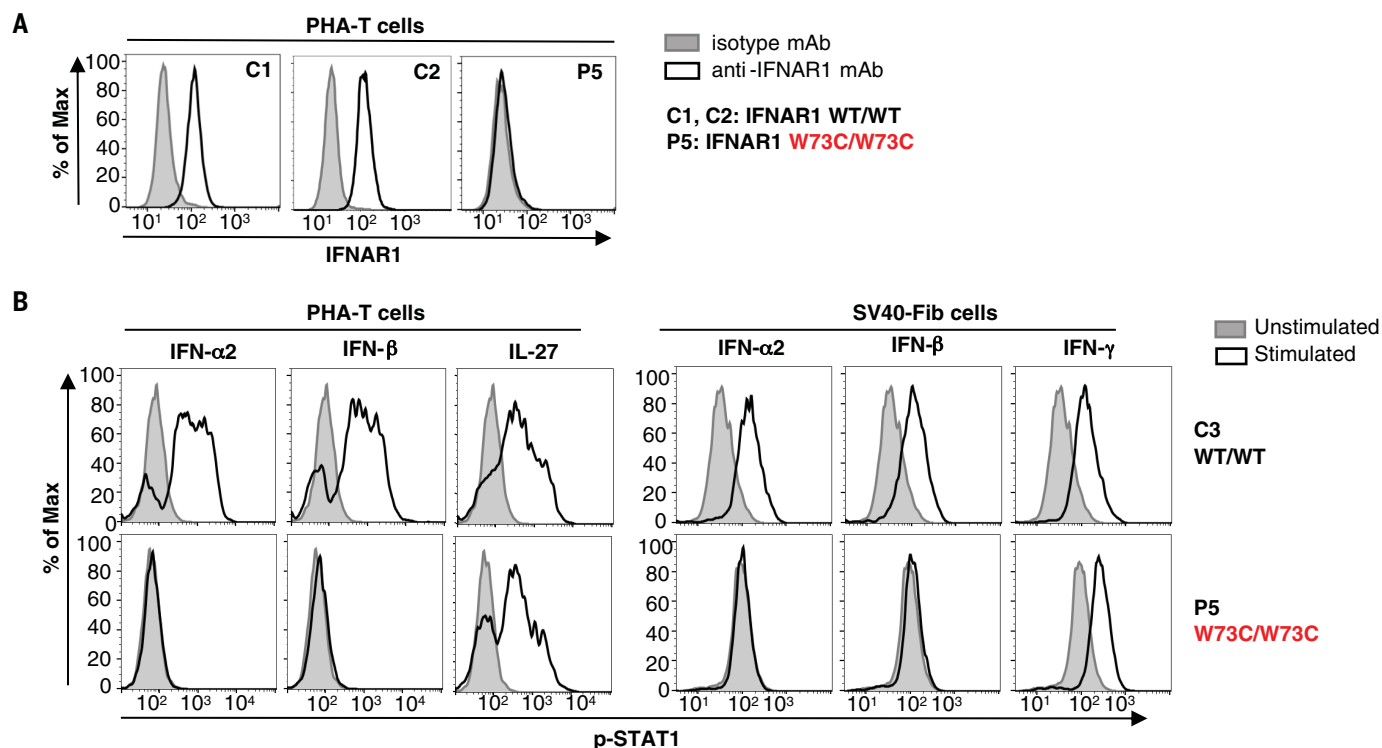


Fig. 5. Type I IFN responses in patient cells defective for IFNAR1. (A) FACS staining of IFNAR1 on the surface of PHA-T cells from a patient with AR IFNAR1 deficiency (P5) and healthy donors (C1 and C2). (B) PHA-T cells and SV40-Fib from a patient with AR IFNAR1 deficiency (P5) and a healthy donor (C3) were stimulated with IFN- α 2 or IFN- β , and p-STAT1 levels were determined by FACS. Interleukin-27 stimulation served as a positive control on PHA-T cells, whereas IFN- γ stimulation served as a positive control on SV40-Fib cells.

IFNAR1, all of which were previously transduced with angiotensin-converting enzyme 2 (ACE2) and transmembrane protease, serine 2 (TMPRSS2). SARS-CoV-2 infection levels were higher in mutant cells than in cells from healthy donors, and transduction of WT *IRF7* or *IFNAR1* rescued their defects (Fig. 6). Collectively, these findings showed that AR *IRF7* deficiency impaired the production of type I IFN by pDCs stimulated with SARS-CoV-2, whereas AR and AD deficiencies of TLR3 or AR deficiency of IFNAR1 impaired fibroblast-intrinsic type I IFN immunity to SARS-CoV2. They also suggest that heterozygosity for LOF variations at the other five mutated loci also underlie life-threatening COVID-19.

Impaired production of type I IFNs in patients in vivo

We tested whether these genotypes impaired the production of type I IFN in vivo during the course of SARS-CoV-2 infection. We measured the levels of the 13 types of IFN- α in the blood of patients during the acute phase of COVID-19. We found that 10 of the 23 patients with mutations for whom samples were available (one with AR *IRF7* deficiency, four with AD *IRF7* deficiency, one with AD TLR3 deficiency, two with AD TBK1 deficiency, one with AR IFNAR1 deficiency, and one with AD TICAM1 deficiency) had serum IFN- α levels <1 pg/ml

(Fig. 7). By contrast, previously published cohorts of patients hospitalized with unexplained, severe COVID-19 had various serum IFN- α levels, significantly higher than our 10 patients [one-way analysis of variance (ANOVA), $P = 1.4 \times 10^{-7}$; Fig. 7] (27, 28). Another 29 patients from our cohort displaying auto-antibodies (auto-Abs) against type I IFNs, reported in an accompanying paper, had undetectable levels of serum IFN- α (29). Moreover, none of the 23 patients with LOF mutations of the eight genes had detectable auto-Abs against type I IFNs (29), strongly suggesting that the two mechanisms of disease are similar but independent. Excluding patients with auto-Abs against type I IFN from the burden test of pLOF variants at the 12 autosomal loci strengthened the association signal ($P = 0.007$; OR = 8.97; 95% CI = 1.13 to 71.09).

Inborn errors of TLR3- and IRF7-dependent type I immunity underlie critical COVID-19

Collectively, our data suggest that at least 23 of the 659 patients with life-threatening COVID-19 pneumonia studied had known (six disorders) or new (four disorders) genetic defects at eight loci involved in the TLR3- and IRF7-dependent induction and amplification of type I IFNs. This discovery reveals the essential role of both the double-stranded RNA sensor TLR3 and type I IFN cell-intrinsic immunity in the

control of SARS-CoV-2 infection in the lungs, consistent with their previously documented roles in pulmonary immunity to influenza virus (5–8). These genotypes were silent until infection with SARS-CoV-2. The most thought-provoking examples are the AR deficiencies of *IRF7* and *IFNAR1*. AR *IRF7* deficiency was diagnosed in two individuals aged 49 and 50 years, and AR *IFNAR1* deficiency was diagnosed in two individuals aged 26 and 38 years, and none of the four patients had a prior history of life-threatening infections (Table 1). One patient with *IRF7* deficiency was tested and was seropositive for several common viruses, including various influenza A and B viruses (figs. S10 and S11). These genetic defects therefore display incomplete penetrance for influenza respiratory distress and only manifested clinically upon infection with the more virulent SARS-CoV-2.

Conclusion

The AR form of *IFNAR1* deficiency highlights the importance of type I IFN production relative to type III IFN production, which is also impaired by defects of TLR3, *IRF7*, and *IRF9* (5). This conclusion is also supported by our accompanying report of neutralizing auto-Abs against type I IFNs, but not type III IFNs, in other patients with life-threatening COVID-19 pneumonia (29). Inborn errors of TLR3- and

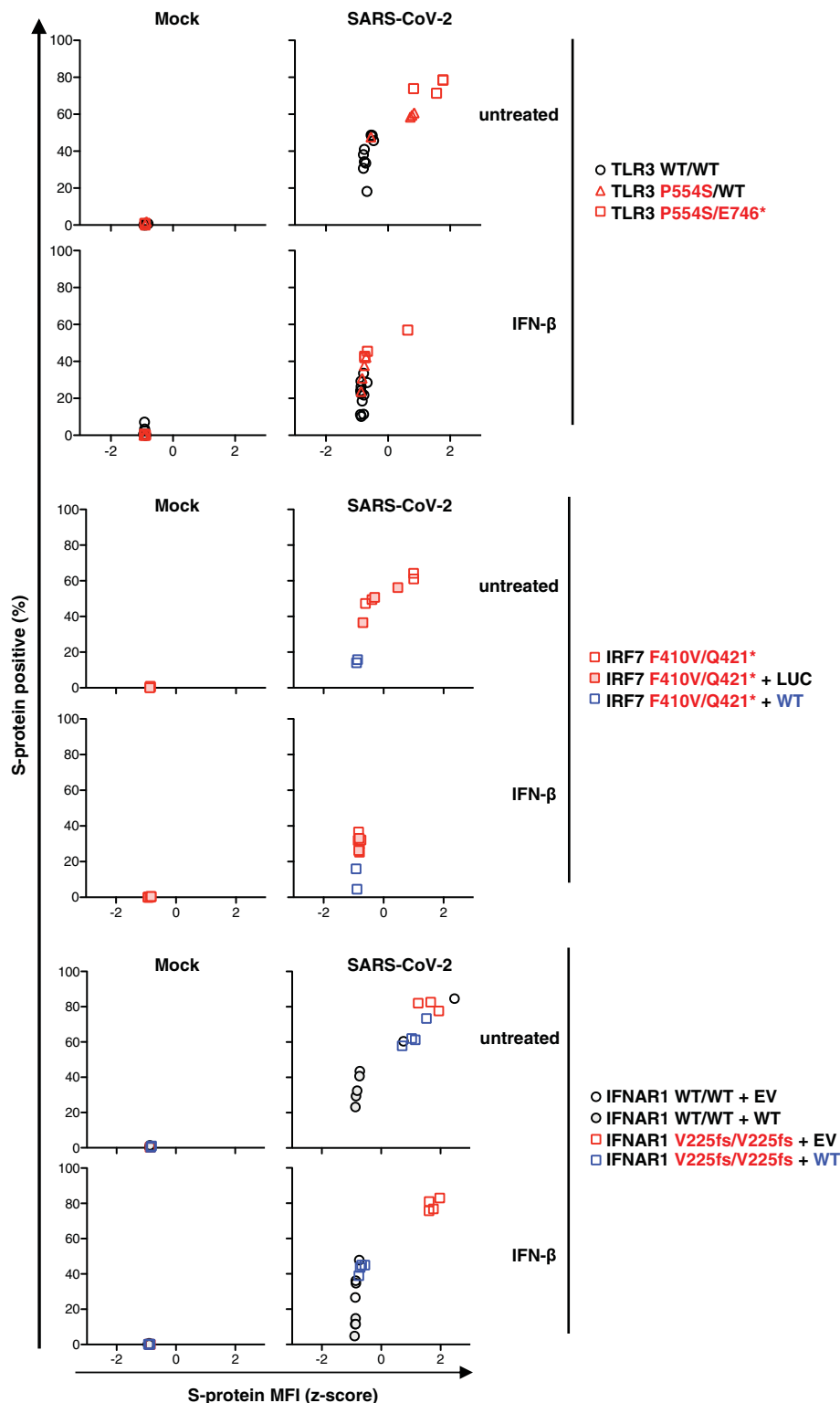


Fig. 6. Cell-intrinsic type I IFN response to SARS-CoV-2. SV40-Fib cells of TLR3^{-/-}, TLR3^{+/-}, IRF7^{-/-}, and IRF7^{+/-} SV40-Fib cells rescued with WT IRF7; IFNAR1^{-/-} SV40-Fib cells, and IFNAR1^{+/-} SV40-Fib cells rescued with WT IFNAR1 were transduced with ACE2 and TMPRSS2 and then either left untreated or treated with IFN-β for 4 hours. Cells were then infected with SARS-CoV-2 (MOI = 0.5). After staining, ACE2 and viral S-protein levels were measured by high-content microscopy with gating on ACE2⁺ cells. IRF7-deficient SV40-Fib cells were previously transduced with either WT IRF7 or negative control (Luc). IFNAR1-deficient cells were previously transduced with either WT IFNAR1 or empty vector (EV).

IRF7-dependent type I IFN immunity at eight loci were found in as many as 23 patients (3.5%) of various ages (17 to 77 years) and ancestries (various nationalities from Asia, Europe, Latin America, and the Middle East) and in patients of both sexes (Table 1). Our findings suggest that there may be mutations in other type I IFN-related genes in other patients with life-threatening COVID-19 pneumonia. They also suggest that the administration of type I IFN may be of therapeutic benefit in selected patients, at least early in the course of SARS-CoV-2 infection.

Methods

Patients

We included in this study 659 patients with life-threatening COVID-19 pneumonia, defined as patients with pneumonia who developed critical disease, whether pulmonary with mechanical ventilation (CPAP, BIPAP, intubation, hi-flow oxygen), septic shock, or with any other organ damage requiring admission to the intensive care unit. Patients who developed Kawasaki-like syndrome were excluded. The age of the patients ranged from 0.1 to 99 years, with a mean age of 51.8 years (SD 15.9 years), and 25.5% of the patients were female. As controls, we enrolled 534 individuals infected with SARS-CoV-2 based on a positive polymerase chain reaction (PCR) and/or serological test and/or the presence of typical symptoms such as anosmia or ageusia after exposure to a confirmed COVID-19 case, who remained asymptomatic or developed mild, self-healing, ambulatory disease.

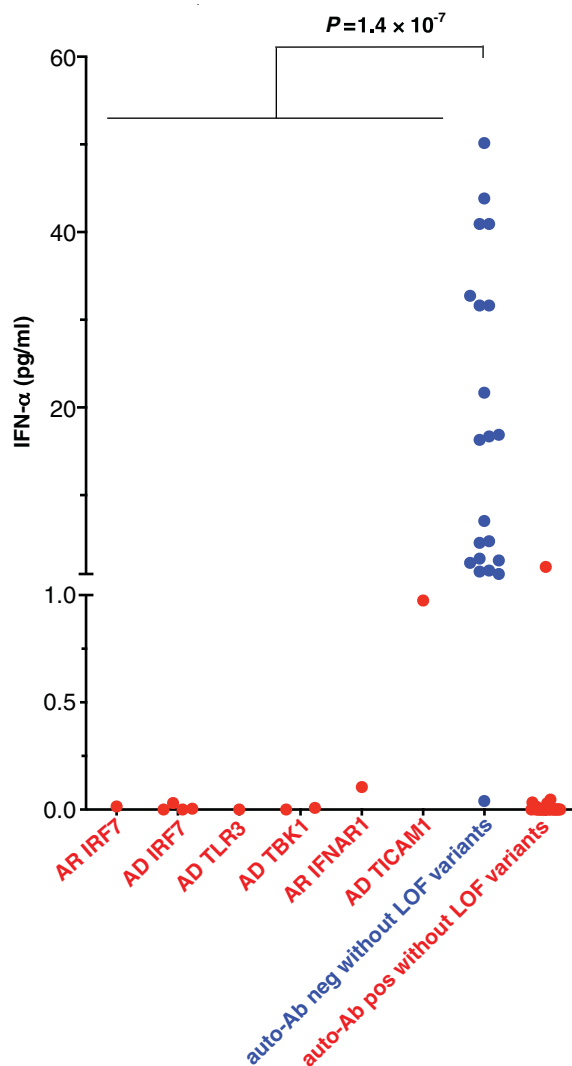
Next-generation sequencing

Genomic DNA was extracted from whole blood. For the 1193 patients and controls included, the whole exome ($N = 687$) or whole genome ($N = 506$) was sequenced. We used the Genome Analysis Software Kit (GATK) (version 3.4-46 or 4) best-practice pipeline to analyze our whole-exome-sequencing data (30). We aligned the reads obtained with the human reference genome (hg19) using the maximum exact matches algorithm in Burrows-Wheeler Aligner software (31). PCR duplicates were removed with Picard tools (<http://broadinstitute.github.io/picard/>). The GATK base quality score recalibrator was applied to correct sequencing artifacts.

All of the variants were manually curated using Integrative Genomics Viewer (IGV) and confirmed to affect the main functional protein isoform by checking the protein sequence before inclusion in further analyses. The main functional protein isoforms were TLR3 (NM_003265), UNC93B1 (NM_030930.4), TICAM1 (NM_182919), TRAF3 (NM_145725.2), TBK1 (NM_013254.4), IRF3 (NM_001571), IRF7 (NM_001572.5), IFNAR1 (NM_000629.3), IFNAR2 (NM_001289125.3), STAT1 (NM_007315.4), STAT2

Fig. 7. In vivo type I IFN responses to SARS-CoV-2 infections.

Plasma levels of 13 IFN- α were measured by Simoa. Auto-Ab(+) without LOF variants indicates COVID-19 patients with neutralizing anti-IFN- α auto-Abs in our accompanying report (29). *P* values indicated were evaluated using one-way ANOVA.



(NM_005419.4), and IRF9 (NM_006084.5). The analysis of IKBKG was customized to unmask the duplicated region in IKBKG using a specific pipeline previously described (32). We searched the next-generation-sequencing data for deletions in the 13 genes of interest using both the HMZDelFinder (33) and CANOES (34) algorithms.

Statistical analysis

We performed an enrichment analysis on our cohort of 659 patients with life-threatening COVID-19 pneumonia and 534 SARS-CoV2-infected controls, focusing on 12 autosomal IFN-related genes. We considered variants that were pLOF with a MAF <0.001 (gnomAD version 2.1.1) after experimentally demonstrating that all of the pLOF variants seen in the cases were actually LOF. We compared the proportion of individuals carrying at least one pLOF variant of the 12 autosomal genes in cases and controls by means of logistic regression with the likelihood ratio test. We ac-

counted for the ethnic heterogeneity of the cohorts by including the first three principal components of the PCA in the logistic regression model. PC adjustment is a common and efficient strategy for accounting for different ancestries of patients and controls in the study of rare variants (35–38). We checked that our adjusted burden test was well calibrated by also performing an analysis of enrichment in rare (MAF <0.001) synonymous variants of the 12 genes. PCA was performed with Plink version 1.9 software on whole-exome- and whole-genome-sequencing data and the 1000 Genomes (1kG) Project phase 3 public database as a reference, using 27,480 exonic variants with a MAF >0.01 and a call rate >0.99. The OR was also estimated by logistic regression and adjusted for ethnic heterogeneity.

Reporter assays

Cell lines or SV40-Fib cells with known defects were transiently or stably transfected with WT, mutant variants, IFN- β or ISRE-*firefly*

luciferase reporter, and pRL-TK-*Renilla* luciferase reporter. Reporter activity was measured with the Dual-Luciferase Reporter Assay System (Promega) according to the manufacturer's instructions. *Firefly* luciferase activity was normalized against *Renilla* luciferase activity and expressed as a fold change. TRAF3-deficient human embryonic kidney (HEK) 293T cells were kindly provided by M. Romanelli (39).

pDC activation by SARS-CoV-2 and cytokine production

pDCs from an IRF7^{-/-} patient and a healthy donor matched for age and sex were cultured in the presence of medium alone, influenza virus (A/PR/8/34, 2 μ g/ml; Charles River Laboratories), or the SARS-CoV-2 primary strain 220_95 (GISAID accession ID: EPI_ISL_469284) at a multiplicity of infection (MOI) of 2. After 12 hours of culture, pDC supernatant was collected for cytokine quantification. IFN- α 2 levels were measured using CBA analysis (BD Biosciences) in accordance with the manufacturer's protocol using a 20 pg/ml detection limit. IFN- λ 1 secretion was measured in an ELISA (R&D Systems, DuoSet DY7246), in accordance with the manufacturer's instructions.

SARS-CoV-2 infection in patient SV40-Fib

To make patient-derived fibroblasts permissive to SARS-CoV-2 infection, we delivered human ACE2 and TMPRSS2 cDNA to cells by lentivirus transduction using a modified SCRPSY vector (GenBank ID: KT368137.1). SARS-CoV-2 strain USA-WA1/2020 was obtained from BEI Resources. ACE2/TMPRSS2-transduced cells were either left untreated or treated with 500 U/ml IFN- β (11415-1, PBL Assay Science) 4 hours before infection. Cells were infected with SARS-CoV-2 (MOI = 0.5) for 1 hour at 37°C. After 24 hours of infection, cells were fixed and taken out of the BSL3 for staining.

After fixation, cells were stained with SARS-CoV-2 and ACE2 primary antibodies (0.5 and 1 μ g/ml, respectively). Primary antibodies were as follows: for SARS-CoV-2, human monoclonal anti-spike-SARS-CoV-2 C121 antibody (40), and for ACE2, mouse monoclonal Alexa Fluor 488-conjugated antibody (FAB9332G-100UG, R&D Systems). Images were acquired with an ImageXpress Micro XLS microscope (Molecular Devices) using the 4 \times objective. MetaXpress software (Molecular Devices) was used to obtain single-cell mean fluorescence intensity (MFI) values.

Data analysis on single-cell MFI values was done in the R environment (version 4.0.2). ACE2/TMPRSS2-transduced cells were classified as ACE2 positive when the ACE2 log MFI was superior to the log mean MFI of mock-transduced cells plus 2.5 SDs. We excluded all wells with <150 ACE2-positive cells before SARS-CoV-2 scoring. ACE2-expressing cells were classified SARS-CoV-2 positive when the fluorescence intensity value was superior to

the MFI of mock-infected cells plus 4 SDs. The median SARS-CoV-2 MFI and percentage SARS-CoV-2-positive cells were calculated for each well (independent infection).

Single-molecule array (Simoa) IFN- α digital ELISA

Serum IFN- α concentrations were determined using Simoa technology, with reagents and procedures obtained from Quanterix Corporation (Quanterix SimoaTM IFN α Reagent Kit, Lexington, MA, USA). According to the manufacturer's instructions, the working dilutions were 1:2 for all sera in working volumes of 170 μ l.

REFERENCES AND NOTES

- D. M. Morens, A. S. Fauci, Emerging pandemic diseases: How we got to COVID-19. *Cell* **182**, 1077–1092 (2020). doi: [10.1016/j.cell.2020.08.021](https://doi.org/10.1016/j.cell.2020.08.021); pmid: [32846157](https://pubmed.ncbi.nlm.nih.gov/32846157/)
- J. L. Casanova, L. Abel, Lethal Infectious Diseases as Inborn Errors of Immunity: Toward a Synthesis of the Germ and Genetic Theories. *Annu. Rev. Pathol.* (2020). pmid: [32289233](https://pubmed.ncbi.nlm.nih.gov/32289233/)
- J. L. Casanova, L. Abel, The human genetic determinism of life-threatening infectious diseases: Genetic heterogeneity and physiological homogeneity? *Hum. Genet.* **139**, 681–694 (2020). doi: [10.1007/s00439-020-02184-w](https://doi.org/10.1007/s00439-020-02184-w); pmid: [32462426](https://pubmed.ncbi.nlm.nih.gov/32462426/)
- J. L. Casanova, H. C. Su, COVID Human Genetic Effort, A global effort to define the human genetics of protective immunity to SARS-CoV-2 infection. *Cell* **181**, 1194–1199 (2020). doi: [10.1016/j.cell.2020.05.016](https://doi.org/10.1016/j.cell.2020.05.016); pmid: [32405102](https://pubmed.ncbi.nlm.nih.gov/32405102/)
- Q. Zhang, Human genetics of life-threatening influenza pneumonitis. *Hum. Genet.* **139**, 941–948 (2020). doi: [10.1007/s00439-019-02108-3](https://doi.org/10.1007/s00439-019-02108-3); pmid: [32025908](https://pubmed.ncbi.nlm.nih.gov/32025908/)
- H. K. Lim *et al.*, Severe influenza pneumonitis in children with inherited TLR3 deficiency. *J. Exp. Med.* **216**, 2038–2056 (2019). doi: [10.1084/jem.20181621](https://doi.org/10.1084/jem.20181621); pmid: [31217193](https://pubmed.ncbi.nlm.nih.gov/31217193/)
- M. J. Ciancanelli *et al.*, Life-threatening influenza and impaired interferon amplification in human IRF7 deficiency. *Science* **348**, 448–453 (2015). doi: [10.1126/science.1283446](https://doi.org/10.1126/science.1283446); pmid: [25814066](https://pubmed.ncbi.nlm.nih.gov/25814066/)
- N. Hernandez *et al.*, Life-threatening influenza pneumonitis in a child with inherited IRF9 deficiency. *J. Exp. Med.* **215**, 2567–2585 (2018). doi: [10.1084/jem.20180628](https://doi.org/10.1084/jem.20180628); pmid: [30143481](https://pubmed.ncbi.nlm.nih.gov/30143481/)
- V. Sancho-Shimizu *et al.*, Herpes simplex encephalitis in children with autosomal recessive and dominant TRIF deficiency. *J. Clin. Invest.* **121**, 4889–4902 (2011). doi: [10.1172/JCI59259](https://doi.org/10.1172/JCI59259); pmid: [22105173](https://pubmed.ncbi.nlm.nih.gov/22105173/)
- A. Casrouge *et al.*, Herpes simplex virus encephalitis in human UNC-93B deficiency. *Science* **314**, 308–312 (2006). doi: [10.1126/science.1128346](https://doi.org/10.1126/science.1128346); pmid: [16973841](https://pubmed.ncbi.nlm.nih.gov/16973841/)
- R. Pérez de Diego *et al.*, Human TRAF3 adaptor molecule deficiency leads to impaired Toll-like receptor 3 response and susceptibility to herpes simplex encephalitis. *Immunity* **33**, 400–411 (2010). doi: [10.1016/j.immuni.2010.08.014](https://doi.org/10.1016/j.immuni.2010.08.014); pmid: [20832341](https://pubmed.ncbi.nlm.nih.gov/20832341/)
- M. Herman *et al.*, Heterozygous TBK1 mutations impair TLR3 immunity and underlie herpes simplex encephalitis of childhood. *J. Exp. Med.* **209**, 1567–1582 (2012). doi: [10.1084/jem.20111316](https://doi.org/10.1084/jem.20111316); pmid: [22851595](https://pubmed.ncbi.nlm.nih.gov/22851595/)
- L. L. Andersen *et al.*, Functional IRF3 deficiency in a patient with herpes simplex encephalitis. *J. Exp. Med.* **212**, 1371–1379 (2015). doi: [10.1084/jem.20142274](https://doi.org/10.1084/jem.20142274); pmid: [26216125](https://pubmed.ncbi.nlm.nih.gov/26216125/)
- M. Audry *et al.*, NEMO is a key component of NF- κ B- and IRF3-dependent TLR3-mediated immunity to herpes simplex virus. *J. Allergy Clin. Immunol.* **128**, 610–617.e4 (2011). doi: [10.1016/j.jaci.2011.04.059](https://doi.org/10.1016/j.jaci.2011.04.059); pmid: [21272947](https://pubmed.ncbi.nlm.nih.gov/21272947/)
- N. Hernandez *et al.*, Inherited IFNAR1 deficiency in otherwise healthy patients with adverse reaction to measles and yellow fever live vaccines. *J. Exp. Med.* **216**, 2057–2070 (2019). doi: [10.1084/jem.20182295](https://doi.org/10.1084/jem.20182295); pmid: [31270247](https://pubmed.ncbi.nlm.nih.gov/31270247/)
- C. J. Duncan *et al.*, Human IFNAR2 deficiency: Lessons for antiviral immunity. *Sci. Transl. Med.* **7**, 307ra154 (2015). doi: [10.1126/scitranslmed.aac4227](https://doi.org/10.1126/scitranslmed.aac4227); pmid: [26424569](https://pubmed.ncbi.nlm.nih.gov/26424569/)
- S. Dupuis *et al.*, Impaired response to interferon- α /beta and lethal viral disease in human STAT1 deficiency. *Nat. Genet.* **33**, 388–391 (2003). doi: [10.1038/ng1097](https://doi.org/10.1038/ng1097); pmid: [12590259](https://pubmed.ncbi.nlm.nih.gov/12590259/)
- S. Hambleton *et al.*, STAT2 deficiency and susceptibility to viral illness in humans. *Proc. Natl. Acad. Sci. U.S.A.* **110**, 3053–3058 (2013). doi: [10.1073/pnas.1220098110](https://doi.org/10.1073/pnas.1220098110); pmid: [23391734](https://pubmed.ncbi.nlm.nih.gov/23391734/)
- R. Döflinger *et al.*, X-linked anhidrotic ectodermal dysplasia with immunodeficiency is caused by impaired NF- κ B signaling. *Nat. Genet.* **27**, 277–285 (2001). doi: [10.1038/85837](https://doi.org/10.1038/85837); pmid: [11242109](https://pubmed.ncbi.nlm.nih.gov/11242109/)
- S. Y. Zhang *et al.*, TLR3 deficiency in patients with herpes simplex encephalitis. *Science* **317**, 1522–1527 (2007). doi: [10.1126/science.1139522](https://doi.org/10.1126/science.1139522); pmid: [17872438](https://pubmed.ncbi.nlm.nih.gov/17872438/)
- G. Zhang *et al.*, A proline deletion in IFNAR1 impairs IFN- γ signaling and underlies increased resistance to tuberculosis in humans. *Nat. Commun.* **9**, 85 (2018). doi: [10.1038/s41467-017-02611-z](https://doi.org/10.1038/s41467-017-02611-z); pmid: [29311663](https://pubmed.ncbi.nlm.nih.gov/29311663/)
- M. M. Thomsen *et al.*, Identification of an IRF3 variant and defective antiviral interferon responses in a patient with severe influenza. *Eur. J. Immunol.* **49**, 2111–2114 (2019). doi: [10.1002/eji.201848083](https://doi.org/10.1002/eji.201848083); pmid: [31250433](https://pubmed.ncbi.nlm.nih.gov/31250433/)
- M. M. Thomsen *et al.*, Defective interferon priming and impaired antiviral responses in a patient with an IRF7 variant and severe influenza. *Med. Microbiol. Immunol. (Berl.)* **208**, 869–876 (2019). doi: [10.1007/s00430-019-00623-8](https://doi.org/10.1007/s00430-019-00623-8); pmid: [31172279](https://pubmed.ncbi.nlm.nih.gov/31172279/)
- S. G. Tangye *et al.*, Human inborn errors of immunity: 2019 update on the classification from the International Union of Immunological Societies Expert Committee. *J. Clin. Immunol.* **40**, 24–64 (2020). doi: [10.1007/s10875-019-00737-x](https://doi.org/10.1007/s10875-019-00737-x); pmid: [31953710](https://pubmed.ncbi.nlm.nih.gov/31953710/)
- A. Bousfiha *et al.*, Human Inborn Errors of Immunity: 2019 Update of the IUIS Phenotypical Classification. *J. Clin. Immunol.* **40**, 66–81 (2020). doi: [10.1007/s10875-020-00758-x](https://doi.org/10.1007/s10875-020-00758-x); pmid: [32048120](https://pubmed.ncbi.nlm.nih.gov/32048120/)
- L. D. Notarangelo, R. Bacchetta, J.-L. Casanova, H. C. Su, Human inborn errors of immunity: An expanding universe. *Sci. Immunol.* **5**, eabb1662 (2020). doi: [10.1126/sciimmunol.abb1662](https://doi.org/10.1126/sciimmunol.abb1662); pmid: [32651211](https://pubmed.ncbi.nlm.nih.gov/32651211/)
- J. Hadjadj *et al.*, Impaired type I interferon activity and inflammatory responses in severe COVID-19 patients. *Science* **369**, 718–724 (2020). doi: [10.1126/science.abc6027](https://doi.org/10.1126/science.abc6027); pmid: [32661059](https://pubmed.ncbi.nlm.nih.gov/32661059/)
- S. Trouillet-Assant *et al.*, Type I IFN immunoprofiling in COVID-19 patients. *J. Allergy Clin. Immunol.* **146**, 206–208.e2 (2020). doi: [10.1016/j.jaci.2020.04.029](https://doi.org/10.1016/j.jaci.2020.04.029); pmid: [32360285](https://pubmed.ncbi.nlm.nih.gov/32360285/)
- P. Bastard *et al.*, Auto-antibodies against type I IFNs in patients with life-threatening COVID-19. *Science* **10.1126/science.abc4585** (2020).
- M. A. DePristo *et al.*, A framework for variation discovery and genotyping using next-generation DNA sequencing data. *Nat. Genet.* **43**, 491–498 (2011). doi: [10.1038/ng.806](https://doi.org/10.1038/ng.806); pmid: [21478889](https://pubmed.ncbi.nlm.nih.gov/21478889/)
- H. Li, R. Durbin, Fast and accurate short read alignment with Burrows-Wheeler transform. *Bioinformatics* **25**, 1754–1760 (2009). doi: [10.1093/bioinformatics/btp324](https://doi.org/10.1093/bioinformatics/btp324); pmid: [19451168](https://pubmed.ncbi.nlm.nih.gov/19451168/)
- B. Boisson *et al.*, Rescue of recurrent deep intronic mutation underlying cell type-dependent quantitative NEMO deficiency. *J. Clin. Invest.* **129**, 583–597 (2019). doi: [10.1172/JCI124011](https://doi.org/10.1172/JCI124011); pmid: [30422821](https://pubmed.ncbi.nlm.nih.gov/30422821/)
- T. Gambin *et al.*, Homozygous and hemizygous CNV detection from exome sequencing data in a Mendelian disease cohort. *Nucleic Acids Res.* **45**, 1633–1648 (2017). pmid: [27980096](https://pubmed.ncbi.nlm.nih.gov/27980096/)
- D. Backenroth *et al.*, CANOES: Detecting rare copy number variants from whole exome sequencing data. *Nucleic Acids Res.* **42**, e97 (2014). doi: [10.1093/nar/gku345](https://doi.org/10.1093/nar/gku345); pmid: [24771342](https://pubmed.ncbi.nlm.nih.gov/24771342/)
- M. Bouaziz, J. Mullaert, B. Bigio, Y. Seeluthner, J.-L. Casanova, A. Alcais, L. Abel, A. Cobat, Controlling for human population stratification in rare variant association studies. *bioRxiv* 969477 [Preprint]. 28 February 2020. doi: [10.1101/2020.02.28.969477](https://doi.org/10.1101/2020.02.28.969477)
- E. Persyn, R. Redon, L. Bellanger, C. Dina, The impact of a fine-scale population stratification on rare variant association test results. *PLOS ONE* **13**, e0207677 (2018). doi: [10.1371/journal.pone.0207677](https://doi.org/10.1371/journal.pone.0207677); pmid: [30521541](https://pubmed.ncbi.nlm.nih.gov/30521541/)
- Y. Zhang, X. Shen, W. Pan, Adjusting for population stratification in a fine scale with principal components and sequencing data. *Genet. Epidemiol.* **37**, 787–801 (2013). doi: [10.1002/gepi.21764](https://doi.org/10.1002/gepi.21764); pmid: [24123217](https://pubmed.ncbi.nlm.nih.gov/24123217/)
- S. Boisson-Dupuis *et al.*, Tuberculosis and impaired IL-23-dependent IFN- γ immunity in humans homozygous for a common TYK2 missense variant. *Sci. Immunol.* **3**, eaau8714 (2018). doi: [10.1126/sciimmunol.aau8714](https://doi.org/10.1126/sciimmunol.aau8714); pmid: [30578352](https://pubmed.ncbi.nlm.nih.gov/30578352/)
- S. Fochi *et al.*, TRAF3 Is Required for NF- κ B Pathway Activation Mediated by HTLV Tax Proteins. *Front. Microbiol.* **10**, 1302 (2019). doi: [10.3389/fmicb.2019.01302](https://doi.org/10.3389/fmicb.2019.01302); pmid: [31244811](https://pubmed.ncbi.nlm.nih.gov/31244811/)
- D. F. Robbiani *et al.*, Convergent antibody responses to SARS-CoV-2 in convalescent individuals. *Nature* **584**, 437–442 (2020). doi: [10.1038/s41586-020-2456-9](https://doi.org/10.1038/s41586-020-2456-9); pmid: [32553588](https://pubmed.ncbi.nlm.nih.gov/32553588/)
- Q. Zhang, P. Bastard, Z. Liu, J. Le Pen, M. Moncada-Velez, J. Chen, M. Ogishi, I. K. D. Sabli, S. Hodeib, C. Korol, J. Rosain, K. Bilguvar, J. Ye, A. Bolze, B. Bigio, R. Yang, A. Augusto Arias Sierra, Q. Zhou, Y. Zhang, F. Onodi, S. Korniotis, L. Karpf, Q. Philippot, M. Chihli, L. Bonnet-Madin, K. Dorgham, N. Smith, W. M. Schneider, B. S. Razooky, H.-H. Hoffmann, E. Michailidis, L. Moens, J. E. Han, L. Lorenzo, L. Bizio, P. Meade, A.-L. Neehus, A. C. Ugurbil, A. Corneau, G. Kerner, P. Zhang, F. Rapaport, Y. Seeluthner, J. Manry, C. Masson, Y. Schmitt, A. Schlüter, T. Le Voyer, T. Khan, J. Li, J. Fellay, L. Roussel, M. Shahrooei, M. F. Alosaimi, D. Mansouri, H. Al-Saud, F. Al-Mulla, F. Almourfi, S. Z. Al-Muhsen, F. Alshome, S. Al Turki, R. Hasanato, D. van de Beek, A. Biondi, L. R. Bettini, M. D'Angio, P. Bonfanti, L. Impert, A. Sottini, S. Paghera, E. Quiros-Roldan, C. Rossi, A. J. Oler, M. F. Tompkins, C. Alba, I. Vandernoot, J.-C. Goffard, G. Smits, I. Migeotte, F. Haerynk, P. Soler-Palacin, A. Martin-Nalda, R. Colobran, P.-E. Morange, S. Koles, F. Çölkens, T. Özcelik, K. K. Yasar, S. Senoglu, Ş. N. Karabela, C. Rodríguez-Gallego, G. Novelli, S. Hraiech, Y. Tandjaoui-Lambiotte, X. Duval, C. Laouenan, COVID-STORM Clinicians, COVID Clinicians, Imagine COVID Group, French COVID Cohort Study Group, CoV-Contact Cohort, Amsterdam UMC Covid-19 Biobank, COVID Human Genetic Effort, NIAID-USUHS/TAGC COVID Immunity Group, A. L. Snow, C. L. Dalgard, J. Milner, D. C. Vinh, T. H. Mogensen, N. Marr, A. N. Spaan, B. Boisson, S. Boisson-Dupuis, J. Bustamante, A. Puel, M. Ciancanelli, I. Meyts, T. Maniatis, V. Soumelis, A. Amara, M. Nussenzweig, A. Garcia-Sastre, F. Krammer, A. Pujol, D. Duffy, L. Lifton, S.-Y. Zhang, G. Gorochov, V. Béziat, E. Jouanguy, V. Sancho-Shimizu, C. M. Rice, L. Abel, L. D. Notarangelo, A. Cobat, H. C. Su, J.-L. Casanova, Detailed genotype counts for all coding variants for: Inborn errors of type I IFN immunity in patients with life-threatening COVID-19. *Dryad* (2020). doi: [10.5061/dryad.8pk0p2nkk](https://doi.org/10.5061/dryad.8pk0p2nkk)

ACKNOWLEDGMENTS

We thank the patients, their families, and healthy donors for placing their trust in us; Y. Nemirovskaya, D. Papandrea, M. Woollet, D. Liu, C. Rivalain, and C. Patissier for administrative assistance; A. Adeleye, D. Bacikova, E. McGrath Martinez, A. R. Soltis, K. Dobbs, J. Danielson, H. Matthews, and S. Weber for technical and other assistance; M. M. A. Ata and F. Al Ali for their contribution to VirScan experiments; S. Elledge (Brigham and Women's Hospital and Harvard Medical School, Boston, MA) for kindly providing the VirScan phage library used in this study; A. W. Ashbrook, the BSL3 manager of the Rice laboratory assistance; M. Lazzaro, Director of Immigration and Academic Appointments, for assistance; W. Chung, K. Kiryluk, S. O'Byrne, D. Pendrick, J. Williamson, C. Andrews, and M. Disco in the J.M. lab for assistance; M. Andreoni (Tor Vergata, Italy) for his clinical contribution; and A. Novelli (Bambino Gesù Hospital, Italy) for his collaboration. We thank the GEN-COVID multicenter study (<https://sites.google.com/dbm.unisi.it/gen-covid>). This study used the high-performance computational resources of the National Institutes of Health (NIH) HPC Biowulf cluster (<http://hpc.nih.gov>) and the Office of Cyber Infrastructure and Computational Biology (OCICB) High Performance Computing (HPC) cluster at the National Institute of Allergy and Infectious Diseases (NIAID), Bethesda, MD. The opinions and assertions expressed herein are those of the authors and are not to be construed as reflecting the views of the Uniformed Services University of the Health Sciences (USUHS) or the U.S. Department of Defense (DoD). **Funding:** This work was supported by a generous donation from the Fisher Center for Alzheimer's Research Foundation. The Laboratory of Human Genetics of Infectious Diseases is supported by the Howard Hughes Medical Institute, the Rockefeller University, the St. Giles Foundation, the NIH (R01AI088364), the National Center for Advancing Translational Sciences (NCATS), the NIH Clinical and Translational Science Award (CTSA) program (UL1 TR001866), a Fast Grant from Emergent Ventures, Mercatus Center at George Mason University, the Yale Center for Mendelian Genomics and the GSP Coordinating Center funded by the National Human Genome Research Institute (NHGRI) (UM1HG006504 and U24HG008956), the French National Research Agency (ANR) under the "Investments for the Future" program (ANR-10-IAHU-01), the Integrative Biology of Emerging Infectious Diseases Laboratory of Excellence (ANR-10-LABX-62-IBED), the French Foundation for

Medical Research (FRM) (EQU201903007798), the FRM and ANR GENCOVID project, ANRS-COV05, the Square Foundation, Grandir-Fonds de Solidarité pour l'Enfance, the SCOR Corporate Foundation for Science, Institut National de la Santé et de la Recherche Médicale (INSERM), the University of Paris. The French COVID Cohort study group was sponsored by Inserm and supported by the REACTing consortium and by a grant from the French Ministry of Health (PHRC 20-0424). Regione Lombardia, Italy (project "Risposta immune in pazienti con COVID-19 e co-morbidità"), and the Intramural Research Program of the NIAID, NIH. The laboratory of Genomes & Cell Biology of Disease is supported by "Integrative Biology of Emerging Infectious Diseases" (grant no. ANR-10-LABX-62-IBED), the "Fondation pour la Recherche Médicale" (grant FRM-EQU202003010193), the "Agence Nationale de la Recherche" (ANR-FLASH COVID project IDISCOVR cofounded by the "Fondation pour la Recherche Médicale"), University of Paris ("Plan de Soutien Covid-19": RACP20IFR01-COVID-SOUL). I.M. is a senior clinical investigator with the FWO Vlaanderen; I.M. and L.M. are supported by FWO GOC8517N – G0B5120N. The VS team was supported by "Agence Nationale de la Recherche" (ANR-17-CE15-0003, ANR-17-CE15-0003-01) and by Université de Paris "PLAN D'URGENCE COVID19". L.K. was supported by a fellowship from the French Ministry of Research. V.S.-S. is supported by a UKRI Future Leaders Fellowship (MR/S032304/1). S.Z.A.-M. is supported by the Elite Johnsons Program at King Saud University through grant no. PEJP-16-107. The J.M. laboratory is supported by Columbia University COVID biobank and grant no. UL1TR001873. Work in the Laboratory of Virology and Infectious Disease was supported by NIH grants P01AI138398-S1, 2U19AI11825, and R01AI091707-10S1; a George Mason University Fast Grant; and the G. Harold and Leila Y. Mathers Charitable Foundation. J.L.P. is supported by a European Molecular Biology Organization Long-Term Fellowship (ALTF 380-2018). Work at the Neurometabolic Diseases Laboratory received funding from the European Union's Horizon 2020 research and innovation program under grant no. 824110 (EasiGenomics grant no. COVID-19/PID12342) to A.P., and Roche and Illumina Covid Match Funds to M.G.. C.R.G. and colleagues are supported by Instituto de Salud Carlos III (COV20_01333 and COV20_01334), Spanish Ministry of Science and Innovation, with the funding of European Regional Development Fund-European Social Fund -FEDER-FSE; (RTC-2017-6471-1; AEI/FEDER, UE), and Cabildo Insular de Tenerife (CGIEU0000219140 and "Apuestas científicas del ITER para colaborar en la lucha contra la COVID-19"). D.C.V. is supported by the Fonds de la recherche en santé du Québec clinician-scientist scholar program. H.S. is adjunct faculty at the University of Pennsylvania. A.-L.N. was supported by the Foundation Bettencourt Schueller. The Amsterdam UMC Covid-19 Biobank was funded by the Netherlands Organization for Health Research and Development (ZonMw, NWO-vici 91819627), The Corona Research Fund (Amsterdam UMC), Dr. J. C. Vaillantfonds, and Amsterdam UMC. Work on COVID-19 at the A.G.-S. laboratory is partly supported by NIH supplements to grants U19AI123972, U19AI142733, and R35 HL135834, and to contract HHSN272201800048C, by a DoD supplement to grant W81XWH-20-1-0270, by DARPA project HRO011-19-2-0020, by CRIP (Center for Research on Influenza Pathogenesis), a NIAID funded Center of Excellence for Influenza Research and Surveillance (CEIRS, contract HHSN272201400008C), by an NIAID funded Collaborative Influenza Vaccine Innovation Center (SEM-CIVIC, contract 75N93019C00051) and by the generous support of the JPB Foundation, the Open Philanthropy Project (research grant 2020-215611(5384)) and anonymous donors. The Virscan analysis presented in fig. S11 was performed with financial support from Sidra Medicine. J.R.H. is supported by Biomedical Advanced Research and Development Authority under Contract (HHSO10201600031C).

Author contributions: A.G., A.A., A.A.A., A.L.S., A.-L.N., A.C., A.C., A.P., B.B., B.S.R., C.A., C.M., C.K., C.L., C.M.R., C.L.D., D.D., E.M., E.J., F.A., F.A.-M., F.O., F.A., F.K., G.N., G.S., G.G., H.-H.H., H.K.A.S., H.S., I.K.D.S., I.M., J.L.P., J.R., J.E.H., J.C., J.M., J.Y., K.D., K.B., L.A., L.L.-D., L.K., L.M., L.B.-M., L.B., L.N., M.M.-V., M.C., M.O., M.C., M.N., M.F.T., M.S., M.F.A., N.M., N.S., P.B., P.M., Q.Z., Q.Z., Q.P., R.L., R.Y., S.A.T., S.Z.A.-M., S.H., S.K., S.H., S.B.-D., T.K., T.M., T.H.M., V.S.-S., V.S., V.B., W.S., X.D., Y.S., and Z.D. either performed or supervised experiments, generated and analyzed data, and contributed to the manuscript. A.S., A.C.U., A.B., A.O., A.P., B.B., D.V., D.B., F.R., G.K., J.M., P.Z., S.-Y.Z., T.L.-V., Y.S., and Y.Z. performed computational analysis. A.S., A.N.S., A.M.-N., A.B., C.R., D.M., D.C.V., E.Q.-R., F.H., I.M., I.V., J.B., J.-C.G., L.R.B., L.R., L.I., M.D., P.B., P.S.-P., P.-E.M., R.H., R.C., S.K., S.P., T.O., Y.T.-L., K.K., S.S., J.F., and S.N.K. evaluated and recruited patients to COVID and/or control cohorts. Q.Z. and J.-L.C. wrote the manuscript. All authors edited the manuscript. J.-L.C. supervised the project. **Competing interests:**

The authors declare no competing financial interests. J.-L.C. is listed as an inventor on patent application US63/055,155 filed by The Rockefeller University that encompasses aspects of this publication. R.L. is a non-executive director of Roche and its subsidiary Genentech. **Data and materials availability:** Plasma, cells, and genomic DNA are available from J.-L.C. or D.V. under a material transfer agreement with Rockefeller University/Research Institute-McGill University Health Centre. pSCRPSY_TMPRSS2-2A-Neor_ACE2 and Huh-7.5 cells are available upon request from C.R. under a material transfer agreement with The Rockefeller University, or The Rockefeller University and Apath, LLC, respectively. Clinical data, DNA, and other patient samples are available from the Amsterdam UMC Covid-19 Biobank (D.v.d.B.) under a material transfer agreement with Amsterdam UMC. Material and reagents used are almost exclusively commercially available and nonproprietary. Requests for materials derived from human samples may be made available, subject to any underlying restrictions on such samples. J.-L.C. can make material transfer agreements available through The Rockefeller University. Detailed genotype counts for all coding variants in the genes investigated in this manuscript are available at Dryad (41). The whole-genome sequencing datasets used for the analyses, including critical patients and asymptomatic controls described in this manuscript, were deposited in dbGaP under accession number phs002245.v1.p1. All other data are available in the manuscript or the supplementary material. This work is licensed under a Creative Commons Attribution 4.0 International (CC BY 4.0) license, which permits unrestricted use, distribution, and reproduction in any medium, provided the original work is properly cited. To view a copy of this license, visit <https://creativecommons.org/licenses/by/4.0/>. This license does not apply to figures/photos/artwork or other content included in the article that is credited to a third party; obtain authorization from the rights holder before using such material.

COVID-STORM Clinicians Giuseppe Foti¹, Giacomo Bellani¹, Giuseppe Citerio¹, Ernesto Contro¹, Alberto Pesci², Maria Grazia Valsecchi³, Marina Cazzaniga⁴

¹Department of Emergency, Anesthesia and Intensive Care, School of Medicine and Surgery, University of Milano-Bicocca, San Gerardo Hospital, Monza, Italy. ²Department of Pneumology, School of Medicine and Surgery, University of Milano-Bicocca, San Gerardo Hospital, Monza, Italy. ³Center of Bioinformatics and Biostatistics, School of Medicine and Surgery, University of Milano-Bicocca, San Gerardo Hospital, Monza, Italy. ⁴Phase I Research Center, School of Medicine and Surgery, University of Milano-Bicocca, San Gerardo Hospital, Monza, Italy.

COVID Clinicians Jorge Abad¹, Sergio Aguilera-Albesa², Ozge Metin Akcan³, Ilad Alavi Darazam⁴, Juan C. Aldave⁵, Miquel Alfonso Ramos⁶, Seyed Alireza Nadjfi⁷, Gulsum Alkan⁸, Jerome Allardet-Servent⁹, Luis M. Allende¹⁰, Laia Alsina¹¹, Maria-Alexandra Alyanaki¹², Blanca Amador-Borrero¹³, Zahir Amoura¹⁴, Arnau Antolli¹⁵, Sevket Arslan¹⁶, Sophie Assant¹⁷, Terese Auguet¹⁸, Axelle Azot¹⁹, Fanny Bajolle²⁰, Aurélie Baldolli²¹, Maite Ballester²², Hagit Baris Feldman²³, Benoit Barrou²⁴, Alexandra Beurton²⁵, Agurtzane Bilbao²⁶, Geraldine Blanchard-Rohner²⁷, Ignacio Blanco²⁸, Adeline Blandiniere²⁸, Daniel Blazquez-Gamero²⁹, Marketa Bloomfield³⁰, Mireia Bolívar-Prados³¹, Raphael Borie³², Cédric Bosteels³³, Ahmed A. Boussif³⁴, Claire Bouvattier³⁵, Oksana Boyarchuk³⁶, Maria Rita P. Bueno³⁷, Jacinta Bustamante³⁸, Juan José Cáceres Agra³⁸, Semra Calimiri³⁹, Ruggero Capra⁴⁰, Maria Carrabba⁴¹, Carlos Casasnovas⁴², Marion Caseris⁴³, Martin Castelle⁴⁴, Francesco Castelli⁴⁵, Martín Castillo de Vera⁴⁶, Mateus V. Castro³⁷, Emilie Catherineot⁴⁷, Martin Chalumeau⁴⁸, Bruno Charbit⁴⁹, Matthew P. Cheng⁵⁰, Père Clavé³¹, Bonaventura Clotet⁵¹, Anna Codina⁵², Fatih Colkesen⁵³, Fatma Colkesen⁵⁴, Roger Colobran⁵⁵, Cloé Comarmond⁵⁶, David Dalmau⁵⁷, David Ross Darier⁵⁸, Nicolas Dauby⁵⁹, Stéphane Dauge⁶⁰, Loïc de Pontual⁶¹, Amin Dehban⁶², Geoffroy Delplanq⁶³, Alexandre Demoule⁶⁴, Jean-Luc Diehl⁶⁵, Stephanie Dobbelaere⁶⁶, Sophie Durand⁶⁷, Waleed Eldars⁶⁸, Mohamed Elgarni⁶⁹, Marwa H. Elmagdy⁷⁰, Melike Emiroglu⁷¹, Emine Hafize Erdeniz⁷², Selma Erol Aytekin⁷³, Romain Evraud⁷⁴, Recep Evcen⁷⁵, Giovanna Fabio⁴¹, Laurence Faivre⁷⁶, Antonin Falck⁴³, Muriel Fartoukh⁷⁷, Morgane Faure⁷⁸, Miguel Fernandez Arquerio⁷⁹, Carlos Flores⁸⁰, Bruno Francois⁸¹, Victoria Fumaz⁸², Francesca Fusco⁸³, Blanca Garcia Solis⁸⁴, Pascale Gaussem⁸⁵, Juana Gil-Herrera⁸⁶, Laurent Gildardin⁸⁷, Monica Girona Alarcón⁸⁸, Mónica Girona-Alarcón⁸⁸, Jean-Christophe Goffard⁸⁹, Funda Gök⁹⁰, Rafaela González-Montelongo⁹¹, Antoine Guerder⁹², Yahya Gul⁹³, Sukru Nail Guner⁹³, Marta Gut⁹⁴, Jérôme Hadjadj⁹⁵, Filomeen Haerynck⁹⁶, Rabih Halwani⁹⁷, Lennart Hammarström⁹⁸, Nevin Hatipoglu⁹⁹, Elisa Hernandez-Brito¹⁰⁰,

Cathérine Heijmans¹⁰¹, María Soledad Holanda-Peña¹⁰², Juan Pablo Horcajada¹⁰³, Levi Hoste¹⁰⁴, Eric Hoste¹⁰⁵, Sami Hraiech¹⁰⁶, Linda Humbert¹⁰⁷, Alejandro D. Iglesias¹⁰⁸, Antonio Íñigo-Campos⁹¹, Matthieu Jamme¹⁰⁹, María Jesús Arranz¹¹⁰, Iolanda Jordan¹¹¹, Philippe Jorens¹¹², Fikret Kanat¹¹³, Hasan Kapaklı¹¹⁴, Iskender Kara¹¹⁵, Adem Karbuz¹¹⁶, Kadiye Kart Yasa¹¹⁷, Sevgi Keles¹¹⁸, Yasemin Kendir Demirkol¹¹⁹, Adam Klocperk¹²⁰, Zbigniew J. Król¹²¹, Paul Kuentz¹²², Yat Wah M. Kwan¹²³, Jean-Christophe Lagier¹²⁴, Bart N. Lembrechts¹²⁵, Yu-Lung Lu¹²⁵, Fleur Le Bourgeois¹²⁶, Yee-Sin Leo¹²⁶, Rafael Leon Lopez¹²⁷, Daniel Leung¹²⁵, Michael Levin¹²⁸, Michael Levy⁶⁰, Romain Lévy²⁰, Zhi Li⁴⁹, Agnes Linglart¹²⁹, Bart Loeys¹³⁰, José M. Lorenzo-Salazar⁹¹, Céline Louapre¹³¹, Catherine Lubetzki¹³¹, Charles-Edouard Luyt¹³², David C. Lye¹³³, Davood Mansouri¹³⁴, Majid Marjani¹³⁵, Jesus Marquez Pereira¹³⁶, Andrea Martini¹³⁴, David Martinez Pueyo¹³⁷, Javier Martinez-Picado¹³⁸, Iciar Marzana¹⁴⁰, Alexis Mathian¹⁴, Larissa R. B. Matos³⁷, Gail V. Matthews¹⁴¹, Julien Mayaux¹⁴², Jean-Louis Mège¹⁴³, Isabelle Melki¹⁴⁴, Jean-François Meritet¹⁴⁵, Ozge Metin¹⁴⁶, Isabelle Meyts¹⁴⁷, Mehdi Mezidi¹⁴⁸, Isabelle Migeotte¹⁴⁹, Maude Millereux¹⁵⁰, Tristan Mirault¹⁵¹, Clotilde Mircher⁶⁷, Mehdi Mirsaedi¹⁵², Abián Montesdeoca Melián¹⁵³, Antonio Morales Martinez¹⁵⁴, Pierre Morange¹⁵⁵, Clémence Mordacq¹⁰⁷, Guillaume Morelle¹⁵⁶, Stéphane Mouly¹³, Adrián Muñoz-Barrera⁹¹, Leslie Naesens¹⁵⁷, Cyril Nafati¹⁵⁸, João Farela Neves¹⁵⁹, Lisa FP. Ng¹⁶⁰, Yeray Novoa Medina¹⁶¹, Esmeralda Nuñez Cuadros¹⁶², J. Gonzalo Ochoa-Vinyals¹⁶³, Zerrin Orbak¹⁶⁴, Mehdi Oualha²⁰, Tayfun Özçelik¹⁶⁵, Qiang Pan-Hammarström¹⁶⁶, Christophe Parizo¹⁴², Tiffany Pascreau¹⁶⁷, Estela Paz-Artal¹⁶⁸, Sandra Pellegrini⁴⁹, Rebeca Pérez de Diego⁸⁴, Aurélien Philippe¹⁶⁹, Quentin Philipott⁷⁷, Laura Planas-Serra¹⁷⁰, Dominique Ploin¹⁷¹, Julien Poissy¹⁷², Géraldine Poncet¹⁷³, Marie Pouletty¹⁷³, Paul Quenric¹⁴², Didier Raoult¹⁴³, Anne-Sophie Rebillat⁶⁷, Ismail Reissi¹⁷⁴, Pilar Ricart¹⁷⁵, Jean-Christophe Richard¹⁷⁶, Nadia Rivet¹⁷⁷, Jacques G. Rivière¹⁷⁷, Gemma Rocamora Blanch¹⁵, Carlos Rodrigo¹, Carlos Rodriguez-Gallego¹⁷⁸, Agustí Rodríguez-Palmero¹⁷⁹, Carolina Soledad Romero¹⁸⁰, Anya Rothenbuhler¹⁸¹, Flore Rozenberg¹⁸², Maria Yolanda Ruiz del Prado¹⁸³, Joan Sabater Riera¹⁵, Oliver Sanchez¹⁸⁴, Silvia Sánchez-Ramón¹⁸⁵, Agatha Schluter¹⁷⁰, Matthias Schmidt¹⁸⁶, Cyril E. Schweitzer¹⁸⁷, Francesco Scolar¹⁸⁸, Anna Sediva¹⁸⁹, Luis M. Seijo¹⁹⁰, Damien Sene¹³, Sevtap Senoglu¹¹⁷, Mikko R. J. Seppänen¹⁹¹, Alex Serra Illoich¹⁹², Mohammad Shahrroo¹⁹³, Hans Slabbynck¹⁹⁴, David M. Smadja¹⁹⁴, Ali Sobh¹⁹⁵, Xavier Solanich Moreno¹⁹⁶, Jordi Solé-Llomb¹⁹⁶, Catherine Soler¹⁹⁷, Pere Soler-Palacin¹⁹⁷, Yuri Stepanovskiy¹⁹⁸, Annabelle Stoclin¹⁹⁹, Fabio Taccone¹⁴⁹, Yacine Tandjaoui-Lambiotte²⁰⁰, Jean-Luc Taupin²⁰¹, Simon J. Tavernier²⁰², Benjamin Terrier²⁰³, Caroline Thumerelle¹⁰⁷, Gabriele Tomasoni²⁰⁴, Julie Toubiana¹⁴⁸, Josep Trenado Alvarez²⁰⁵, Sophie Trouillet-Assant²⁰⁶, Jesús Troya²⁰⁷, Alessandra Tucci²⁰⁸, Matilde Valeria Ursini¹⁸³, Yurdagül Uzunhan²⁰⁹, Pierre Vabres²¹⁰, Juan Valencia-Den Rym⁸⁴, Eva Van Braeckel¹³³, Stijn Van de Velde²¹², Ana Maria Van Den Ry⁸⁴, Jens Van Praet²¹³, Isabelle Vandernoo²¹⁴, Hulya Vatansev²¹⁵, Valentina Vélez-Santamaría¹⁹⁶, Sébastien Viel¹⁷¹, Cédric Vilain²¹⁶, Marie E. Vilaire¹⁷, Audrey Vincent³⁵, Guillaume Voiriot²¹⁷, Fanny Vuotto¹⁸⁷, Alper Yosunkaya⁹⁰, Barnaby E. Young¹²⁶, Fatih Yucel²¹⁸, Faiez Zannad²¹⁹, Mayana Zatz²²⁰, Alexandre Belot^{220*}

¹University Hospital and Research Institute "Germans Trias i Pujol," Badalona, Spain. ²Navarra Health Service Hospital, Pamplona, Spain. ³Division of Pediatric Infectious Diseases, Necmettin Erbakan University, Meram Medical Faculty, Konya, Turkey. ⁴Department of Infectious Diseases, Lohman Hakim Hospital, Shahid Beheshti University of Medical Sciences, Tehran, Iran. ⁵Hospital Nacional Edgardo Rebagliatti Martins, Lima, Peru. ⁶Parc Sanitari Sant Joan de Déu, Sant Boi de Llobregat, Spain. ⁷Virology Research Center, National Institutes of Tuberculosis and Lung Diseases, Shahid Beheshti University of Medical Sciences, Tehran, Iran. ⁸Division of Pediatric Infectious Diseases, Faculty of Medicine, Selçuk University, Konya, Turkey. ⁹Intensive Care Unit, Hôpital Européen, Marseille, France. ¹⁰Immunology Department, University Hospital 12 de Octubre, Research Institute imas12, and Complutense University, Madrid, Spain. ¹¹Clinical Immunology and Primary Immunodeficiencies Unit, Hospital Sant Joan de Déu, Barcelona, Spain. ¹²Department of Biological Immunology, Necker Hospital for Sick Children, APHP and INEM, Paris, France. ¹³Internal Medicine Department, Hôpital Lariboisière, APHP; Université de Paris, Paris, France. ¹⁴Internal Medicine Department, Pitié-Salpêtrière Hospital, Paris, France. ¹⁵Hospital Universitari de Bellvitge, Barcelona, Spain. ¹⁶Division of Clinical Immunology and Allergy, Necmettin Erbakan University, Meram Medical Faculty, Konya, Turkey. ¹⁷Joint Research Unit, Hospices Civils de Lyon-bio Mérieux, Hospices Civils de Lyon, Lyon Sud Hospital, Lyon, France. ¹⁸Hospital U. de Tarragona Joan XXIII, Universitat Rovira i Virgili (URV), IISPV, Tarragona, Spain. ¹⁹Private practice, Paris, France. ²⁰Necker Hospital for Sick Children, AP-HP, Paris, France. ²¹Department of Infectious

- Diseases, CHU de Caen, Caen, France. ²²Consorcio Hospital General Universitario, Valencia, Spain. ²³The Genetics Institute, Tel Aviv Sourasky Medical Center and Sackler Faculty of Medicine, Tel Aviv University, Tel Aviv, Israel. ²⁴Department of Urology, Nephrology, and Transplantation, APHP-SU, Sorbonne Université, INSERM U 1082, Paris, France. ²⁵Service de Médecine Intensive-Réanimation et Pneumologie, APHP Hôpital Pitié-Salpêtrière, Paris, France. ²⁶Cruces University Hospital, Bizkaia, Spain. ²⁷Paediatric Immunology and Vaccinology Unit, Geneva University Hospitals and Faculty of Medicine, Geneva, Switzerland. ²⁸Hematology, Georges Pompidou Hospital, APHP, Paris, France. ²⁹Pediatric Infectious Diseases Unit, Instituto de Investigación 12 de Octubre imas12, and Hospital Universitario 12 de Octubre, Madrid, Spain. ³⁰Department of Immunology, Motol University Hospital, 2nd Faculty of Medicine, Charles University, Department of Pediatrics, Thomayer's Hospital, 1st Faculty of Medicine, Charles University, Prague, Czech Republic. ³¹Centro de Investigación Biomédica en Red de Enfermedades Hepáticas y Digestivas (Ciberehd), Hospital de Mataró, Consorci Sanitari del Maresme, Mataró, Spain. ³²Service de Pneumologie, Hôpital Bichat, APHP, Paris, France. ³³Department of Pulmonology, Ghent University Hospital, Ghent, Belgium. ³⁴Clinical Immunology Unit, Pediatric Infectious Disease Department, Faculty of Medicine and Pharmacy, Averroes University Hospital, LICIA Laboratoire d'Immunologie Clinique, d'Inflammation et d'Allergie, Hassani li University, Casablanca, Morocco. ³⁵Endocrinology Unit, APHP Hôpitaux Universitaires Paris-Sud, Le Kremlin-Bicêtre, France. ³⁶Department of Children's Diseases and Pediatric Surgery, I. Horbachevsky Ternopil National Medical University, Ternopil, Ukraine. ³⁷Human Genome and Stem-Cell Research Center, University of São Paulo, São Paulo, Brazil. ³⁸Hospital Insular, Las Palmas de Gran Canaria, Spain. ³⁹Division of Critical Care Medicine, Department of Anesthesiology and Reanimation, Konya State Hospital, Konya, Turkey. ⁴⁰MS Center, Spedali Civili, Brescia, Italy. ⁴¹Fondazione IRCCS Ca' Granda Ospedale Maggiore Policlinico, Milan, Italy. ⁴²Bellvitge University Hospital, L'Hospitalet de Llobregat, Barcelona, Spain. ⁴³Hôpital Robert Debré, Paris, France. ⁴⁴Pediatric Immuno-hematology Unit, Necker Enfants Malades Hospital, AP-HP, Paris, France. ⁴⁵Department of Infectious and Tropical Diseases, University of Brescia, ASST Spedali Civili di Brescia, Brescia, Italy. ⁴⁶Doctoral Health Care Center, Canarian Health System, Las Palmas de Gran Canaria, Spain. ⁴⁷Hôpital Foch, Suresnes, France. ⁴⁸Necker Hospital for Sick Children, Paris University, AP-HP, Paris, France. ⁴⁹Pasteur Institute, Paris, France. ⁵⁰McGill University Health Centre, Montreal, Canada. ⁵¹University Hospital and Research Institute "Germans Trias i Pujol," IrsiCaixa AIDS Research Institute, Uvic-UCC, Badalona, Spain. ⁵²Clinical Biochemistry, Pathology, Paediatric Neurology and Molecular Medicine Departments and Biobank, Institut de Recerca Sant Joan de Déu and CIBERER-ISCIII, Espiguas, Spain. ⁵³Division of Clinical Immunology and Allergy, Department of Internal Medicine, Necmettin Erbakan University, Meram Medical Faculty, Konya, Turkey. ⁵⁴Department of Infectious Diseases and Clinical Microbiology, Konya Training and Research Hospital, Konya, Turkey. ⁵⁵Hospital Universitari Vall d'Hebron, Barcelona, Spain. ⁵⁶Pitié-Salpêtrière Hospital, Paris, France. ⁵⁷Fundació Docència i Recerca Mútua Terrassa, Barcelona, Spain; Hospital Universitari Mútua Terrassa, Universitat de Barcelona, Terrassa, Catalonia, Spain. ⁵⁸UNSW Medicine, St. Vincent's Clinical School, and Department of Thoracic Medicine, St. Vincent's Hospital Darlinghurst, Sydney, Australia. ⁵⁹CHU Saint-Pierre, Université Libre de Bruxelles, Brussels, Belgium. ⁶⁰Pediatric Intensive Care Unit, Robert-Debré University Hospital, APHP, Paris, France. ⁶¹Sorbonne Paris Nord, Hôpital Jean Verdier, APHP, Bondy, France. ⁶²Specialized Immunology Laboratory of Dr. Shahrooei, Sina Medical Complex, Ahvaz, Iran. ⁶³Centre de Génétique Humaine, CHU Besançon, Besançon, France. ⁶⁴Sorbonne Université Médecine and APHP Sorbonne Université Site Pitié-Salpêtrière, Paris, France. ⁶⁵Intensive Care Unit, Georges Pompidou Hospital, APHP, Paris, France. ⁶⁶Department of Pneumology, AZ Delta, Roeselare, Belgium. ⁶⁷Institut Jérôme Lejeune, Paris, France. ⁶⁸Department of Microbiology and Immunology, Faculty of Medicine, Mansoura University, Mansoura, Egypt. ⁶⁹Department of Chest, Faculty of Medicine, Mansoura University, Mansoura, Egypt. ⁷⁰Department of Medical Biochemistry and Molecular Biology, Faculty of Medicine, Mansoura University, Mansoura, Egypt. ⁷¹Faculty of Medicine, Division of Pediatric Infectious Diseases, Selcuk University, Konya, Turkey. ⁷²Division of Pediatric Infectious Diseases, Ondokuz Mayıs University, Samsun, Turkey. ⁷³Necmettin Erbakan University, Meram Medical Faculty, Division of Pediatric Allergy and Immunology, Konya, Turkey. ⁷⁴Centre Hospitalier Fleyriat, Bourg-en-Bresse, France. ⁷⁵Division of Clinical Immunology and Allergy, Department of Internal Medicine, Necmettin Erbakan University, Meram Medical Faculty, Konya, Turkey. ⁷⁶Centre de Génétique, CHU Dijon, Dijon, France. ⁷⁷APHF Tenon Hospital, Paris, France. ⁷⁸Sorbonne Universités, UPMC University of Paris, Paris, France. ⁷⁹Department of Clinical Immunology, Hospital Clínico San Carlos, Madrid, Spain. ⁸⁰Genomics Division, Instituto Tecnológico y de Energías Renovables (ITER), Santa Cruz de Tenerife, Spain; CIBER de Enfermedades Respiratorias, Instituto de Salud Carlos III, Madrid, Spain; Research Unit, Hospital Universitario N.S. de Candelaria, Santa Cruz de Tenerife, Spain; Instituto de Tecnologías Biomédicas (ITB), Universidad de La Laguna, San Cristóbal de La Laguna, Spain. ⁸¹CHU Limoges and Inserm CIC 1435 and UMR 1092, Limoges, France. ⁸²Infectious Diseases Unit, Department of Pediatrics, Hospital Sant Joan de Déu, Barcelona, Spain; Institut de Recerca Sant Joan de Déu, Spain; Universitat de Barcelona (UB), Barcelona, Spain. ⁸³Institute of Genetics and Biophysics "Adriano Buzzati-Traverso," IGB-CNR, Naples, Italy. ⁸⁴Laboratory of Immunogenetics of Human Diseases, IdiPAZ Institute for Health Research, La Paz Hospital, Madrid, Spain. ⁸⁵Hematology, APHP, Hôpital Européen Georges Pompidou and Inserm UMR-S1140, Paris, France. ⁸⁶Hospital General Universitario and Instituto de Investigación Sanitaria "Gregorio Marañón," Madrid, Spain. ⁸⁷Bégin military Hospital, Bégin, France. ⁸⁸Pediatric Intensive Care Unit, Hospital Sant Joan de Déu, Barcelona, Spain. ⁸⁹Department of Internal Medicine, Hôpital Erasme, Université Libre de Bruxelles, Brussels, Belgium. ⁹⁰Division of Critical Care Medicine, Department of Anesthesiology and Reanimation, Necmettin Erbakan University, Meram Medical Faculty, Konya, Turkey. ⁹¹Genomics Division, Instituto Tecnológico y de Energías Renovables (ITER), Santa Cruz de Tenerife, Spain. ⁹²Assistance Publique Hôpitaux de Paris, Paris, France. ⁹³Division of Allergy and Immunology, Necmettin Erbakan University, Meram Medical Faculty, Konya, Turkey. ⁹⁴CNAG-CRG, Centre for Genomic Regulation (CRG), Barcelona Institute of Science and Technology (BIST); Universitat Pompeu Fabra (UPF), Barcelona, Spain. ⁹⁵Department of Internal Medicine, National Reference Center for Rare Systemic Autoimmune Diseases, AP-HP, APHP-CUP, Hôpital Cochin, Paris, France. ⁹⁶Ghent University Hospital, Ghent, Belgium. ⁹⁷Sharjah Institute of Medical Research, College of Medicine, University of Sharjah, Sharjah, UAE. ⁹⁸Department of Laboratory Medicine, SE14186, Huddinge, Karolinska Institutet, Stockholm, Sweden. ⁹⁹Pediatric Infectious Diseases Unit, Bakirkoy Dr. Sadi Konuk Training and Research Hospital, University of Health Sciences, Istanbul, Turkey. ¹⁰⁰Department of Immunology, Hospital Universitario de Gran Canaria Dr. Negrín, Canarian Health System, Las Palmas de Gran Canaria, Spain. ¹⁰¹Department of Pediatric Hemato-Oncology, Jolimont Hospital; Department of Pediatric Hemato-Oncology, HUIDEF, Brussels, Belgium. ¹⁰²Intensive Care Unit, Marqués de Valdecilla Hospital, Santander, Spain. ¹⁰³Hospital del Mar, Parc de Salut Mar, Barcelona, Spain. ¹⁰⁴Department of Pediatric Pulmonology and Immunology, Ghent University Hospital, Ghent, Belgium. ¹⁰⁵Department of Intensive Care Unit, Ghent University Hospital, Ghent, Belgium. ¹⁰⁶Intensive Care Unit, APHM, Marseille, France. ¹⁰⁷CHU Lille, Lille, France. ¹⁰⁸Department of Pediatrics, Columbia University, New York, NY, USA. ¹⁰⁹Centre Hospitalier Intercommunal Poissy Saint Germain en Laye, Poissy, France. ¹¹⁰Fundació Docència i Recerca Mútua Terrassa, Terrassa, Spain. ¹¹¹Hospital Sant Joan de Déu, Kids Corona Plattform, Barcelona, Spain. ¹¹²Department of Intensive Care Unit, University Hospital Antwerp, Antwerp, Belgium. ¹¹³Selcuk University, Faculty of Medicine, Chest Diseases Department, Konya, Turkey. ¹¹⁴Division of Allergy and Immunology, Balikesir Ataturk City Hospital, Balikesir, Turkey. ¹¹⁵Division of Critical Care Medicine, Selcuk University, Faculty of Medicine, Konya, Turkey. ¹¹⁶Division of Pediatric Infectious Diseases, Prof. Dr. Cemil Tascioglu City Hospital, Istanbul, Turkey. ¹¹⁷Departments of Infectious Diseases and Clinical Microbiology, Bakirkoy Dr. Sadi Konuk Training and Research Hospital, University of Health Sciences, Istanbul, Turkey. ¹¹⁸Meram Medical Faculty, Necmettin Erbakan University, Meram Medical Faculty, Konya, Turkey. ¹¹⁹Health Sciences University, Umraniye Education and Research Hospital, Istanbul, Turkey. ¹²⁰Department of Immunology, 2nd Faculty of Medicine, Charles University and University Hospital in Motol, Prague, Czech Republic. ¹²¹Central Clinical Hospital of Ministry of the Interior and Administration in Warsaw, Warsaw, Poland. ¹²²Oncobiologie Génétique Bioinformatique, PC Bio, CHU Besançon, Besançon, France. ¹²³Paediatric Infectious Disease Unit, Hospital Authority Infectious Disease Center, Princess Margaret Hospital, Hong Kong (Special Administrative Region), China. ¹²⁴Aix Marseille University, IRD, MEPhi, IHU Méditerranée Infection, Marseille, France. ¹²⁵Department of Paediatrics and Adolescent Medicine, The University of Hong Kong, Hong Kong, China. ¹²⁶National Center for Infectious Diseases, Singapore. ¹²⁷Hospital Universitario Reina Sofia, Cordoba, Spain. ¹²⁸Imperial College, London, UK. ¹²⁹Endocrinology and Diabetes for Children, AP-HP, Bicêtre Paris-Saclay Hospital, Le Kremlin-Bicêtre, France. ¹³⁰Department of Medical Genetics, University Hospital Antwerp, Antwerp, Belgium. ¹³¹Neurology Unit, APHP Pitié-Salpêtrière Hospital, Paris University, Paris, France. ¹³²Intensive Care Unit, APHP Pitié-Salpêtrière Hospital, Paris University, Paris, France. ¹³³National Center for Infectious Diseases; Tan Tock Seng Hospital; Yong Loo Lin School of Medicine; Lee Kong Chian School of Medicine, Singapore. ¹³⁴Department of Clinical Immunology and Infectious Diseases, National Research Institute of Tuberculosis and Lung Diseases, Shahid Beheshti University of Medical Sciences, Tehran, Iran. ¹³⁵Clinical Tuberculosis and Epidemiology Research Center, National Research Institute of Tuberculosis and Lung Diseases (NRITLD), Shahid Beheshti University of Medical Sciences, Tehran, Iran. ¹³⁶Hospital Sant Joan de Déu and University of Barcelona, Barcelona, Spain. ¹³⁷Pediatric Infectious Diseases and Immunodeficiencies Unit, Hospital Universitari Vall d'Hebron, Vall d'Hebron Research Institute, Vall d'Hebron Barcelona Hospital Campus. Universitat Autònoma de Barcelona (UAB), Barcelona, Spain. ¹³⁸Hospital Universitari Mutua de Terrassa, Universitat de Barcelona, Barcelona, Spain. ¹³⁹IrsiCaixa AIDS Research Institute, ICREA, Uvic-UCC, Research Institute "Germans Trias i Pujol," Badalona, Spain. ¹⁴⁰Department of Laboratory, Cruces University Hospital, Barakaldo, Bizkaia, Spain. ¹⁴¹University of New South Wales, New South Wales, Australia. ¹⁴²APHF Pitié-Salpêtrière Hospital, Paris, France. ¹⁴³Aix-Marseille University, APHM, Marseille, France. ¹⁴⁴Robert Debré Hospital, Paris, France. ¹⁴⁵APHF Cohin Hospital, Paris, France. ¹⁴⁶Necmettin Erbakan University Meram Faculty of Medicine Department of Pediatric Infectious Diseases, Konya, Turkey. ¹⁴⁷University Hospitals Leuven, Leuven, Belgium. ¹⁴⁸Hospices Civils de Lyon, Hôpital de la Croix-Rousse, Lyon, France. ¹⁴⁹Hôpital Erasme, Brussels, Belgium. ¹⁵⁰CH Gonesse, Gonesse, France. ¹⁵¹Vascular Medicine, Georges Pompidou Hospital, APHP, Paris, France. ¹⁵²Division of Pulmonary and Critical Care, University of Miami, Miami, FL, USA. ¹⁵³Guanarterm Health Care Center, Canarian Health System, Las Palmas de Gran Canaria, Spain. ¹⁵⁴Regional University Hospital of Málaga, Málaga, Spain. ¹⁵⁵Aix-Marseille Université, Marseille, France. ¹⁵⁶Department of General Paediatrics, Hôpital Bicêtre, AP-HP, University of Paris Saclay, Le Kremlin-Bicêtre, France. ¹⁵⁷Department of Internal Medicine, Ghent University Hospital, Ghent, Belgium. ¹⁵⁸CHU de La Timone, Marseille, France. ¹⁵⁹Centro Hospitalar Universitário de Lisboa Central, Lisbon, Portugal. ¹⁶⁰Infectious Diseases Horizontal Technology Centre, A*STAR, Singapore Immunology Network, A*STAR, Singapore. ¹⁶¹Department of Pediatrics, Complejo Hospitalario Universitario Insular-Materno Infantil, Canarian Health System, Las Palmas de Gran Canaria, Spain. ¹⁶²Regional University Hospital of Málaga, Málaga, Spain. ¹⁶³Hospital Universitario Marqués de Valdecilla, Santander, Spain. ¹⁶⁴Faculty of Medicine, Ataturk University, Erzurum, Turkey. ¹⁶⁵Department of Molecular Biology and Genetics, Bilkent University, Ankara, Turkey. ¹⁶⁶Department of Biosciences and Nutrition, Karolinska Institutet, SE14183, Stockholm, Sweden. ¹⁶⁷L'Hôpital Foch, Suresnes, France. ¹⁶⁸Department of Immunology, Hospital Universitario 12 de Octubre, Instituto de Investigación Sanitaria Hospital 12 de Octubre imas12, Madrid, Spain. ¹⁶⁹APHF Hôpitaux Universitaires Paris-Sud, Le Kremlin-Bicêtre, France. ¹⁷⁰Neurometabolic Diseases Laboratory, IDIBELL-Hospital Duran i Reynals, Barcelona; CIBERER U759, ISCIII, Madrid, Spain. ¹⁷¹Hospices Civils de Lyon, Lyon, France. ¹⁷²Université de Lille, Inserm U1285, CHU Lille, Paris, France. ¹⁷³Département de General Pediatrics, University Hospital Robert Debré, APHP, Paris, France. ¹⁷⁴Necmettin Erbakan University, Konya, Turkey. ¹⁷⁵Germans Trias i Pujol Hospital, Badalona, Spain. ¹⁷⁶Medical Intensive Care Unit, Hôpital de la Croix-Rousse, Hospices Civils de Lyon, Lyon, France. ¹⁷⁷Pediatric Infectious Diseases and Immunodeficiencies Unit, Hospital Universitari Vall d'Hebron, Vall d'Hebron Research Institute, Vall d'Hebron Barcelona Hospital Campus., Barcelona, Spain. ¹⁷⁸Department of Immunology, Hospital Universitario de Gran Canaria Dr. Negrín, Canarian Health System, Las Palmas de Gran Canaria, Spain. ¹⁷⁹University Fernando Pessoa Canarias, Las Palmas de Gran Canaria, Spain. ¹⁷⁹Neurometabolic Diseases Laboratory, IDIBELL-Hospital Duran i Reynals, Barcelona, Spain. ¹⁸⁰Consorcio Hospital General Universitario, Valencia, Spain. ¹⁸¹APHF Hôpitaux Universitaires Paris-Sud, Paris, France. ¹⁸²Virology Unit, Université de Paris, Cohin Hospital, APHP, Paris, France. ¹⁸³Hospital San Pedro, Logroño, Spain. ¹⁸⁴Respiratory Medicine, Georges Pompidou Hospital, APHP, Paris, France. ¹⁸⁵Department of Immunology, Hospital Clínico San Carlos, Madrid, Spain. ¹⁸⁶Service de Médecine Intensive Réanimation, Institut de Cardiologie, Hôpital Pitié-Salpêtrière, Paris, France. ¹⁸⁷CHRU de Nancy, Hôpital d'Enfants, Vandoeuvre, France. ¹⁸⁸Chair of Nephrology, University of Brescia, Brescia, Italy. ¹⁸⁹Department of Immunology, 2nd Faculty of Medicine, Charles University and Motol University Hospital, Prague,

Czech Republic. ¹⁹⁰Clinica Universidad de Navarra, Madrid, Spain. ¹⁹¹HUS Helsinki University Hospital, Children and Adolescents, Rare Disease Center, and Inflammation Center, Adult Immunodeficiency Unit, Majakka, Helsinki, Finland. ¹⁹²Fundació Docència i Recerca Mútua Terrassa, Terrassa, Spain. ¹⁹³Department of Pulmonology, ZNA Middelheim, Antwerp, Belgium. ¹⁹⁴INSERM UMR-S 1140, Biosurgical Research Lab (Carpentier Foundation), Paris University and Hospital Européen Georges Pompidou, Paris, France. ¹⁹⁵Department of Pediatrics, Faculty of Medicine, Mansoura University, Mansoura, Egypt. ¹⁹⁶Critical Care Unit, Hospital Universitario de Gran Canaria Dr. Negrín, Canarian Health System, Las Palmas de Gran Canaria, Spain. ¹⁹⁷CHU de Saint Etienne, Saint-Priest-en-Jarez, France. ¹⁹⁸Shupky National Medical Academy for Postgraduate Education, Kiev, Ukraine. ¹⁹⁹Gustave Roussy Cancer Campus, Villejuif, France. ²⁰⁰Intensive Care Unit, Avicenne Hospital, APHP, Bobigny, France. ²⁰¹Laboratory of Immunology and Histocompatibility, Saint-Louis Hospital, Paris University, Paris, France. ²⁰²Department of Internal Diseases and Pediatrics, Primary Immune Deficiency Research Lab, Centre for Primary Immunodeficiency Ghent, Jeffrey Modell Diagnosis and Research Centre, Ghent University Hospital, Ghent, Belgium. ²⁰³Department of Internal Medicine, Université de Paris, INSERM, U970, PARCC, F-75015, Paris, France. ²⁰⁴First Division of Anesthesiology and Critical Care Medicine, University of Brescia, ASST Spedali Civili di Brescia, Brescia, Italy. ²⁰⁵Intensive Care Department, Hospital Universitari Mutua Terrassa, Universitat Barcelona, Terrassa, Spain. ²⁰⁶Hospices Civils de Lyon, Lyon Sud Hospital, Lyon, France. ²⁰⁷Infanta Leonor University Hospital, Madrid, Spain. ²⁰⁸Hematology Department, ASST Spedali Civili di Brescia, Brescia, Italy. ²⁰⁹Pneumology, Hôpital Avicenne, APHP, INSERM U1272, Université Sorbonne Paris Nord, Bobigny, France. ²¹⁰Dermatology Unit, Laboratoire GAD, INSERM UMR1231 LNC, Université de Bourgogne, Dijon, France. ²¹¹University Hospital of Burgos, Burgos, Spain. ²¹²Intensive Care Unit, M.iddelares Ghent, Ghent, Belgium. ²¹³Department of Nephrology and Infectiology, AZ Sint-Jan Brugge-Oostende AV, Bruges, Belgium. ²¹⁴Center of Human Genetics, Hôpital Erasme, Université Libre de Bruxelles, Brussels, Belgium. ²¹⁵Department of Chest Diseases, Necmettin Erbakan University, Meram Medical Faculty, Konya, Turkey. ²¹⁶CHU de Caen, Caen, France. ²¹⁷Sorbonne Université, Service de Médecine Intensive Réanimation, Hôpital Tenon, Assistance Publique-Hôpitaux de Paris, Paris, France. ²¹⁸General Intensive Care Unit, Konya Training and Research Hospital, Konya, Turkey. ²¹⁹CHU de Nancy, Nancy, France. ²²⁰University of Lyon, CIRI, INSERM U1111, National Referee Centre RAISE, Pediatric Rheumatology, HFME, Hospices Civils de Lyon, Lyon, France.

*Leader of COVID Clinicians.

Imagine COVID Group Christine Bole-Feyssot, Stanislas Lyonnet*, Cécile Masson, Patrick Nitschke, Aurore Pouliet, Yoann Schmitt, Frederic Tores, Mohammed Zahrhate

Imagine Institute, Université de Paris, INSERM UMR 1163, Paris, France.

*Leader of the Imagine COVID Group.

French COVID Cohort Study Group Laurent Abel¹, Claire Andrejak², François Angoulvant³, Delphine Bachelet⁴, Romain Basmaci⁵, Sylvie Behillili⁶, Marine Beluze⁷, Dehbia Benkerrou⁸, Krishna Bhavsar⁴, François Bompard⁹, Lila Bouadma⁴, Maude Bouscambert¹⁰, Mireille Caral¹¹, Minerva Cervantes-Gonzalez¹², Anissa Chair⁴, Alexandra Coelho¹³, Camille Couffignal⁴, Sandrine Couffin-Cadiergues¹⁴, Eric D'Ortenzio¹², Charlene Da Silveira⁴, Marie-Pierre Debray⁴, Dominique Deplanque¹⁵, Diane Descamps¹⁶, Mathilde Desvallées¹⁷, Alpha Diallo¹⁸, Alphonsine Diouf¹³, Céline Dorival¹⁸, François Dubos¹⁹, Xavier Duval⁴, Philippine Eloy⁴, Vincent VE Enouf²⁰, Hélène Esperou²¹, Marina Esposito-Farese⁴, Manuel Etienne²², Nadia Etthaloui⁴, Nathalie Gault⁴, Alexandre Gaymard²³, Jade Ghosn⁴, Tristan Gigante²³, Isabelle Gorenne⁴, Jérémie Guedj²⁴, Alexandre Hochtini¹³, Isabelle Hoffmann⁴, Salma Jaafoura²⁵, Ouifuya Kafifi¹³, Florentia Kaguelidou²⁵, Sabina Kalf⁴, Antoine Khalil⁴, Coralie Khan¹⁷, Cédric Laouénan⁴, Samira Laribi⁴, Minh Le⁴, Quentin Le Hingrat⁴, Soizic Le Mestre¹⁹, Hervé Le Nagard⁴, François-Xavier Lescuré⁴, Yves Lévy²⁶, Claire Levy-Marchal²⁷, Bruno Lina¹⁰, Guillaume Lingas²⁴, Jean Christophe Lucet⁴, Denis Malvy²⁸, Marina Mambert¹³, France Mentre⁴, Noémie Mercier¹⁸, Amira Meziane⁸, Hugo Mouquet²⁰, Jimmy Mullaert⁴, Nadège Neant²⁴, Marion Noret²⁹, Justine Pages³⁰, Aurélie Papadopoulos²¹, Christelle Paul¹⁸, Nathan Pfeiffer-Smadja⁴, Ventzislava Petrov-Sanchez²⁸, Gilles Peytavin⁴, Olivier Picone³¹, Oriane Puchal¹², Manuel Rosa-Calatrava¹⁰, Bénédicte Rossignol²³, Patrick Rossignol³², Carine Roy⁴, Marion Schneider⁴, Caroline Semaille³², Nassima Si Mohammed⁴, Lysa Tagherset⁴, Coralie Tardivon⁴, Marie-Capucine Tellier⁴,

François Téoulé⁸, Olivier Terrier¹⁰, Jean-François Timsit⁴, Théo Trioux⁴, Christelle Tual³³, Sarah Tubiana⁴, Sylvie van der Werf³⁴, Noémie Vanel³⁵, Aurélie Veislingier³³, Benoit Visseaux¹⁶, Aurélie Wiedemann²⁶, Yazdan Yazdanpanah³⁶

¹Inserm UMR 1163, Paris, France. ²CHU Amiens, France. ³Hôpital Necker, Paris, France. ⁴Hôpital Bichat, Paris, France. ⁵Hôpital Louis Mourier, Colombes, France. ⁶Institut Pasteur, Paris, France. ⁷F-CRIN Partners Platform, AP-HP, Université de Paris, Paris, France. ⁸Inserm UMR 1136, Paris, France. ⁹Drugs for Neglected Diseases Initiative, Geneva, Switzerland. ¹⁰Inserm UMR 1111, Lyon, France. ¹¹Inserm Transfert, Paris, France. ¹²REACTing, Paris, France. ¹³Inserm UMR 1018, Paris, France. ¹⁴Inserm, Pôle Recherche Clinique, Paris, France. ¹⁵CIC 1403 Inserm-CHU Lille, Paris, France. ¹⁶Université de Paris, IAME, INSERM UMR 1137, AP-HP, University Hospital Bichat Claude Bernard, Virology, Paris, France. ¹⁷Inserm UMR 1219, Bordeaux, France. ¹⁸ANRS, Paris, France. ¹⁹CHU Lille, Lille, France. ²⁰Pasteur Institute, Paris, France. ²¹Inserm sponsor, Paris, France. ²²CHU Rouen-SMIT, Rouen, France. ²³FCRIN INI-CRCT, Nancy, France. ²⁴Inserm UMR 1137, Paris, France. ²⁵Centre d'Investigation Clinique, Inserm CIC1426, Hôpital Robert Debré, Paris, France. ²⁶Inserm UMR 955, Créteil, France; Vaccine Research Institute (VRI), Paris, France. ²⁷F-CRIN INI-CRCT, Paris, France. ²⁸CHU de Bordeaux-SMIT, Bordeaux, France. ²⁹RENARCI, Annecy, France. ³⁰Hôpital Robert Debré, Paris, France. ³¹Hôpital Louis Mourier-Gynécologie, Colombes, France. ³²University of Lorraine, Plurithematic Clinical Investigation Centre Inserm CIC-P: 1433, Inserm U1116, CHRU Nancy Hopitaux de Brabois, F-CRIN INI-CRCT (Cardiovascular and Renal Clinical Trials), Nancy, France. ³³Inserm CIC-1414, Rennes, France. ³⁴Institut Pasteur, UMR 3569 CNRS, Université de Paris, Paris, France. ³⁵Hôpital la Timone, Marseille, France. ³⁶Bichat-SMIT, Paris, France.

CoV-Contact Cohort Loubna Alavoine¹, Karine K. A. Amat², Sylvie Behillili³, Julia Bielicki⁴, Patricia Bruijning⁵, Charles Burdet⁶, Eric Caumes⁷, Charlotte Charpentier⁸, Bruno Coignard⁹, Yolande Costa¹, Sandrine Couffin-Cadiergues¹⁰, Florence Diamond⁸, Aline Dechanet¹¹, Christelle Delmas¹⁰, Diane Descamps⁸, Xavier Duval¹, Jean-Luc Ecobichon¹, Vincent Enouf³, Hélène Espérou¹⁰, Wahiba Frezouls¹, Nadhira Houhou¹¹, Emila Illic-Habensuss¹, Ouifuya Kafifi¹¹, John Kikoine¹¹, Quentin Le Hingrat³, David Lebeaux¹², Anne Leclercq¹, Jonathan Lehecach¹, Sophie Letrou¹, Bruno Lina³, Jean-Christophe Lucet¹⁴, Denis Malvy¹⁵, Pauline Manchoni¹¹, Milica Mandic¹, Mohamed Meghadecha¹⁶, Justina Motiejunaite¹⁷, Mariama Nourouline¹, Valentine Piquard¹¹, Andreea Postolache¹¹, Caroline Quintin¹, Jade Rexach¹, Layidé Roufai¹⁰, Zaven Terzian¹¹, Michael Thy¹⁸, Sarah Tubiana¹, Sylvie van der Werf³, Valérie Vignali¹, Benoit Visseaux⁸, Yazdan Yazdanpanah¹⁴

¹Centre d'Investigation Clinique, Inserm CIC 1425, Hôpital Bichat Claude Bernard, APHP, Paris, France. ²IMEA Fondation Léon M'Ba, Paris, France. ³Institut Pasteur, UMR 3569 CNRS, Université de Paris, Paris, France. ⁴University of Basel Children's Hospital. ⁵Julius Center for Health Sciences and Primary Care, Utrecht, Netherlands. ⁶Université de Paris, IAME, Inserm UMR 1137, F-75018, Paris, France, Hôpital Bichat Claude Bernard, APHP, Paris, France. ⁷Hôpital Pitié Salpêtrière, APHP, Paris. ⁸Université de Paris, IAME, INSERM UMR 1137, AP-HP, University Hospital Bichat Claude Bernard, Virology, Paris, France. ⁹Santé Publique France, Saint Maurice, France. ¹⁰Pole Recherche Clinique, Inserm, Paris, France. ¹¹Hôpital Bichat Claude Bernard, APHP, Paris, France. ¹²APHP, Paris, France. ¹³Virpath Laboratory, International Center of Research in Infectiology, Lyon University, INSERM U1111, CNRS UMR 5308, ENS, UCBL, Lyon, France. ¹⁴IAME Inserm UMR 1138, Hôpital Bichat Claude Bernard, APHP, Paris, France. ¹⁵Service des Maladies Infectieuses et Tropicales; Groupe Pellegrin-Place Amélie-Raba-Léon, Bordeaux, France. ¹⁶Hôpital Hotel Dieu, APHP, Paris, France. ¹⁷Service des Explorations Fonctionnelles, Hôpital Bichat-Claude Bernard, APHP, Paris, France. ¹⁸Center for Clinical Investigation, Assistance Publique-Hôpitaux de Paris, Bichat-Claude Bernard University Hospital, Paris, France.

Amsterdam UMC Covid-19 Biobank Michiel van Agtmael¹, Anna Geke Algera², Frank van Baarle², Diane Bax³, Martijn Beudel⁴, Harm Jan Bogaard⁵, Marije Bomers¹, Lieuwke Bos², Michela Botta², Justin de Brabander⁶, Godelieve de Bree⁶, Matthijs C. Brouwer⁴, Sanne de Bruin⁷, Marianna Bugiani⁷, Esther Bulle², Osoul Chouchane¹, Alex Coherly⁷, Paul Elbers⁸, Lucas Fleuren², Suzanne Geerlings¹, Bart Geerts⁸, Theo Geijtenbeek⁹, Armand Girbes², Bram Goorhuis¹, Martin P. Grobusch¹, Florianne Hafkamp⁹, Laura Hagens², Jorg Hamann¹⁰, Vanessa Harris¹, Robert Hemke¹, Sabine M. Hermans¹, Leo Heunks¹, Markus W. Hollmann⁸, Janneke Horn², Joppe W. Hovius¹,

Menno D. de Jong¹², Rutger Koning⁴, Niels van Mourik², Jeaninne Nellen¹, Frederique Paulus², Edgar Peters¹, Tom van der Pol¹, Benedikt Preckel¹, Jan M. Prins¹, Jorinde Raasveld², Tom Reijnders¹, Michiel Schinkel¹, Marcus J. Schultz², Alex Schuurman¹³, Kim Sigaloff¹, Marry Smit², Cornelis S. Stijns¹, Willemke Stijlma², Charlotte Teunissen¹⁴, Patrick Thorai², Anissa Tsonas², Marc van der Valk¹, Denise Veelo⁸, Alexander P.J. Vlaai¹⁵, Heder de Vries², Michèle van Vugt¹, W. Joost Wiersinga², Dorien Wouters¹⁶, A. H. (Kees) Zwiderman¹⁷, Diederik van de Beek^{4*}

¹Department of Infectious Diseases, Amsterdam UMC, Amsterdam, Netherlands. ²Department of Intensive Care, Amsterdam UMC, Amsterdam, Netherlands. ³Experimental Immunology, Amsterdam UMC, Amsterdam, Netherlands. ⁴Department of Neurology, Amsterdam UMC, Amsterdam Neuroscience, Amsterdam, Netherlands. ⁵Department of Pulmonology, Amsterdam UMC, Amsterdam, Netherlands. ⁶Department of Infectious Diseases, Amsterdam UMC, Amsterdam, Netherlands. ⁷Department of Pathology, Amsterdam UMC, Amsterdam, Netherlands. ⁸Department of Anesthesiology, Amsterdam UMC, Amsterdam, Netherlands. ⁹Department of Experimental Immunology, Amsterdam UMC, Amsterdam, Netherlands. ¹⁰Amsterdam UMC Biobank Core Facility, Amsterdam UMC, Amsterdam, Netherlands. ¹¹Department of Radiology, Amsterdam UMC, Amsterdam, Netherlands. ¹²Department of Medical Microbiology, Amsterdam UMC, Amsterdam, Netherlands. ¹³Department of Internal Medicine, Amsterdam UMC, Amsterdam, Netherlands. ¹⁴Neurochemical Laboratory, Amsterdam UMC, Amsterdam, Netherlands. ¹⁵Department of Intensive Care, Amsterdam UMC, Amsterdam, Netherlands. ¹⁶Department of Clinical Chemistry, Amsterdam UMC, Amsterdam, Netherlands. ¹⁷Department of Clinical Epidemiology, Biostatistics and Bioinformatics, Amsterdam UMC, Amsterdam, Netherlands. ¹⁸Department of Neurology, Amsterdam UMC, Amsterdam, Netherlands. *Leader of the AMC Consortium.

COVID Human Genetic Effort Laurent Abel¹, Alessandro Aiuti², Saleh Al Muhsen³, Fahd Al-Mulla⁴, Mark S. Anderson⁵, Andrés Augusto Arias⁶, Hagit Baris Feldman⁷, Dusan Bogunovic⁸, Alexandre Bolze⁹, Anastasia Bondarenko¹⁰, Ahmed A. Bousfiha¹¹, Petter Brodin¹², Yenan Bryceon¹², Carlos D. Bustamante¹³, Manish Butte¹⁴, Giorgio Casari¹⁵, Samya Chakravorty¹⁶, John Christodoulou¹⁷, Elizabeth Cirulli³, Antonio Condino-Neto¹⁸, Megan A. Cooper¹⁹, Clifton L. Dalgaard²⁰, Alessia David²¹, Joseph L. DeRisi²², Murkesh Desai²³, Beth A. Drolet²⁴, Sara Espinosa²⁵, Jacques Fellay²⁶, Carlos Flores²⁷, Jose Luis Franco²⁸, Peter K. Gregersen²⁹, Filomene Haerynck³⁰, David Hagin³¹, Rabiha Halwani³², Jim Heath³³, Sarah E. Henrickson³⁴, Elena Hsieh³⁵, Kohsuke Imai³⁶, Yuval Itan⁸, Timokratsi Karamitros³⁷, Kai Kisand³⁸, Cheng-Lung Ku³⁹, Yu-Lung Lau⁴⁰, Yun Ling⁴¹, Carrie L. Lucas⁴², Tom Maniatis⁴³, Davoud Mansouri⁴⁴, Laszlo Marodi⁴⁵, Isabelle Meyts⁴⁶, Joshua Milner⁴⁷, Kristina Mironska⁴⁸, Trine Mogensen⁴⁹, Tomohiro Morio⁵⁰, Lisa FP. Ng⁵¹, Luigi D. Notarangelo⁵², Antonio Novelli⁵³, Giuseppe Novelli⁵⁴, Cliona O'Farrelly⁵⁵, Satoshi Okada⁵⁶, Tayfun Ozelcik⁵⁷, Rebeca Perez de Diego⁵⁸, Anna M. Planas⁵⁹, Carolina Prando⁶⁰, Aurora Pujol⁶¹, Luis Quintana-Murci⁶², Laurent Renia⁶³, Alessandra Renieri⁶⁴, Carlos Rodríguez-Gallego⁶⁵, Vanessa Sancho-Shimizu⁶⁶, Vijay Sankaran⁶⁷, Kelly Schiabor Barrett⁶⁸, Mohammed Shahrooei⁶⁸, Andrew Snow⁶⁹, Pere Soler-Palacin⁷⁰, Andrés N. Spaan⁷¹, Stuart Tangye⁷², Stuart Turvey⁷³, Furkan Uddin⁷⁴, Mohammed J. Uddin⁷², Diederik van de Beek⁷⁶, Sara E. Vazquez⁷⁷, Donald C. Vinh⁷⁸, Horst von Bernuth⁷⁹, Nicole Washington⁸⁰, Pawel Zawadzki⁸⁰, Helen C. Su⁵², Jean-Laurent Casanova⁸¹

¹INSERM U1163, University of Paris, Imagine Institute, Paris, France. ²San Raffaele Telethon Institute for Gene Therapy, IRCCS Ospedale San Raffaele, Milan, Italy. ³King Saud University, Riyadh, Saudi Arabia. ⁴Kuwait University, Kuwait City, Kuwait. ⁵University of California, San Francisco, San Francisco, CA, USA. ⁶Universidad de Antioquia, Group of Primary Immunodeficiencies, Antioquia, Colombia. ⁷The Genetics Institute, Tel Aviv Sourasky Medical Center and Sackler Faculty of Medicine, Tel Aviv University, Tel Aviv, Israel. ⁸Cahn School of Medicine at Mount Sinai, New York, NY, USA. ⁹Helix, San Mateo, CA, USA. ¹⁰Shupky National Medical Academy for Postgraduate Education, Kiev, Ukraine. ¹¹Clinical Immunology Unit, Pediatric Infectious Disease Department, Faculty of Medicine and Pharmacy, Averroes University Hospital; LICIA Laboratoire d'Immunologie Clinique, d'Inflammation et d'Allergie, Hassani II University, Casablanca, Morocco. ¹²Karolinska Institute, Stockholm, Sweden. ¹³Stanford University, Stanford, CA, USA. ¹⁴University of California, Los Angeles, CA, USA. ¹⁵Medical Genetics, IRCCS Ospedale San Raffaele, Milan, Italy. ¹⁶Emory University Department of Pediatrics and Children's Healthcare of Atlanta, Atlanta, GA, USA. ¹⁷Murdoch

Children's Research Institute, Victoria, Australia. ¹⁸University of São Paulo, São Paulo, Brazil. ¹⁹Washington University School of Medicine, St. Louis, MO, USA. ²⁰The American Genome Center; Uniformed Services University of the Health Sciences, Bethesda, MD, USA. ²¹Centre for Bioinformatics and System Biology, Department of Life Sciences, Imperial College London, South Kensington Campus, London, UK. ²²University of California, San Francisco, CA, USA; Chan Zuckerberg Biohub, San Francisco, CA, USA. ²³Bai Jerbai Wadia Hospital for Children, Mumbai, India. ²⁴School of Medicine and Public Health, University of Wisconsin, Madison, WI, USA. ²⁵Instituto Nacional de Pediatría (National Institute of Pediatrics), Mexico City, Mexico. ²⁶Swiss Federal Institute of Technology Lausanne, Lausanne, Switzerland. ²⁷Research Unit, Hospital Universitario Nuestra Señora de Candelaria, Canarian Health System, Santa Cruz de Tenerife, Spain. ²⁸University of Antioquia, Medellín, Colombia. ²⁹Feinstein Institute for Medical Research, Northwell Health USA, Manhasset, NY, USA. ³⁰Department of Paediatric Immunology and Pulmonology, Centre for Primary Immunodeficiency Ghent (CPiG), PID Research Lab, Jeffrey Modell Diagnosis and Research Centre, Ghent University Hospital, Edegem, Belgium. ³¹The Genetics Institute, Tel Aviv Sourasky Medical Center, Tel Aviv, Israel. ³²Sharjah Institute of Medical Research, College of Medicine, University of Sharjah, Sharjah, UAE. ³³Institute for Systems Biology, Seattle, WA, USA. ³⁴Children's Hospital of Philadelphia, Philadelphia, PA, USA. ³⁵Anschutz Medical Campus, Aurora, CO, USA. ³⁶Riken, Tokyo, Japan. ³⁷Hellenic Pasteur Institute, Athens, Greece. ³⁸University of Tartu, Tartu, Estonia. ³⁹Chang Gung University, Taoyuan County, Taiwan. ⁴⁰The University of Hong Kong, Hong Kong, China. ⁴¹Shanghai Public Health Clinical Center, Fudan University, Shanghai, China. ⁴²Yale School of Medicine, New Haven, CT, USA. ⁴³New York Genome Center, New York, NY, USA. ⁴⁴Shahid Beheshti University of Medical Sciences, Tehran, Iran. ⁴⁵Semmelweis University Budapest, Budapest, Hungary. ⁴⁶KU Leuven, Department of Immunology, Microbiology and Transplantation, Leuven, Belgium. ⁴⁷Columbia University Medical Center, New York, NY, USA. ⁴⁸University Clinic for Children's Diseases, Skopje, North Macedonia. ⁴⁹Aarhus University, Aarhus, Denmark. ⁵⁰Tokyo Medical & Dental University Hospital, Tokyo, Japan. ⁵¹Singapore Immunology Network, Singapore. ⁵²National Institute of Allergy and Infectious Diseases, National Institutes of Health, Bethesda, MD, USA. ⁵³Bambino Gesù Children's

Hospital, Rome, Italy. ⁵⁴Department of Biomedicine and Prevention, University of Rome "Tor Vergata", Rome, Italy. ⁵⁵Trinity College, Dublin, Ireland. ⁵⁶Hiroshima University, Hiroshima, Japan. ⁵⁷Bilkent University, Ankara, Turkey. ⁵⁸Laboratory of Immunogenetics of Human Diseases, Innate Immunity Group, IdiPAZ Institute for Health Research, La Paz Hospital, Madrid, Spain. ⁵⁹IBB-CSIC, IDIBAPS, Barcelona, Spain. ⁶⁰Faculdades Pequeno Príncipe e Instituto de Pesquisa Pelé Pequeno Príncipe, Curitiba, Brazil. ⁶¹Neurometabolic Diseases Laboratory, IDIBELL-Hospital Duran I Reynals; Catalan Institution for Research and Advanced Studies (ICREA); CIBERER U759, ISCIII Madrid Spain, Barcelona, Spain. ⁶²Institut Pasteur (CNRS UMR2000) and Collège de France, Paris, France. ⁶³Infectious Diseases Horizontal Technology Center and Singapore Immunology Network, Agency for Science Technology (A*STAR), Singapore. ⁶⁴Medical Genetics, University of Siena, Siena, Italy; Genetica Medica, Azienda Ospedaliero-Universitaria Senese, Italy; GEN-COVID Multicenter Study. ⁶⁵Hospital Universitario de Gran Canaria Dr. Negrín, Canarian Health System, Canary Islands, Spain. ⁶⁶Imperial College London, London, UK. ⁶⁷Boston Children's Hospital, Harvard Medical School, Boston, MA, USA. ⁶⁸Saeed Pathobiology and Genetic Lab, Tehran, Iran. ⁶⁹Uniformed Services University of the Health Sciences, Bethesda, MD, USA. ⁷⁰Hospital Universitari Vall d'Hebron, Barcelona, Spain. ⁷¹University Medical Center Utrecht, Amsterdam, The Netherlands. ⁷²Garvan Institute of Medical Research, Sydney, Australia. ⁷³The University of British Columbia, Vancouver, Canada. ⁷⁴Holy Family Red Crescent Medical College; Centre for Precision Therapeutics, NeuroGen Children's Healthcare; Genetics and Genomic Medicine Centre, NeuroGen Children's Healthcare, Dhaka, Bangladesh. ⁷⁵Mohammed Bin Rashid University of Medicine and Health Sciences, College of Medicine, Dubai, UAE; The Centre for Applied Genomics, Department of Genetics and Genome Biology, The Hospital for Sick Children, Toronto, Ontario, Canada. ⁷⁶Amsterdam UMC, University of Amsterdam, Department of Neurology, Amsterdam Neuroscience, Amsterdam, The Netherlands. ⁷⁷University of California, San Francisco, CA, USA. ⁷⁸McGill University Health Centre, Montreal, Canada. ⁷⁹Charité—Berlin University Hospital Center, Berlin, Germany. ⁸⁰Molecular Biophysics Division, Faculty of Physics, A. Mickiewicz University, Uniwersytetu Poznańskiego 2, Poznań, Poland.

⁸¹Rockefeller University, Howard Hughes Medical Institute, Necker Hospital, New York, NY, USA.

*Leaders of the COVID Human Genetic Effort.

NIAID-USUHS/TAGC COVID Immunity Group Huie Jing^{1,2}, Wesley Tung^{1,2}, Christopher R. Luthers³, Brady M. Bauman³, Samantha Shafer^{2,4}, Lixin Zheng^{2,4}, Zinan Zhang^{2,4}, Satoshi Kubo^{2,4}, Samuel D. Chauvin^{2,4}, Kazuyuki Meguro^{1,2}, Elana Shaw^{1,2}, Michael Lenardo^{2,4}, Justin Lack⁵, Eric Karlins⁶, Daniel M. Hupalo⁷, John Rosenberger⁷, Gauthaman Sukumar⁷, Matthew D. Wilkerson⁷, Xijun Zhang⁷

¹Laboratory of Clinical Immunology and Microbiology, Division of Intramural Research, NIAID, NIH, Bethesda, MD, USA. ²NIAID Clinical Genomics Program, National Institutes of Health, Bethesda, MD, USA. ³Department of Pharmacology & Molecular Therapeutics, Uniformed Services University of the Health Sciences, Bethesda, MD, USA. ⁴Laboratory of Immune System Biology, Division of Intramural Research, NIAID, NIH, Bethesda, MD, USA. ⁵NIAID Collaborative Bioinformatics Resource, Frederick National Laboratory for Cancer Research, Leidos Biomedical Research, Inc., Frederick, MD, USA. ⁶Bioinformatics and Computational Biosciences Branch, Office of Cyber Infrastructure and Computational Biology, NIAID, NIH, Bethesda, MD, USA. ⁷The American Genome Center, Uniformed Services University of the Health Sciences, Bethesda, MD, USA.

SUPPLEMENTARY MATERIALS

science.sciencemag.org/content/370/6515/eabd4570/suppl/DC1

Materials and Methods

Figs. S1 to S11

Tables S1 and S2

References (42 and 43)

MDAR Reproducibility Checklist

[View/request a protocol for this paper from Bio-protocol.](#)

22 June 2020; accepted 16 September 2020

Published online 24 September 2020

10.1126/science.abd4570

RESEARCH ARTICLE SUMMARY

CORONAVIRUS

Autoantibodies against type I IFNs in patients with life-threatening COVID-19

Paul Bastard*† and Lindsey B. Rosen† *et al.*

INTRODUCTION: Interindividual clinical variability is vast in humans infected with severe acute respiratory syndrome coronavirus 2 (SARS-CoV-2), ranging from silent infection to rapid death. Three risk factors for life-threatening coronavirus disease 2019 (COVID-19) pneumonia have been identified—being male, being elderly, or having other medical conditions—but these risk factors cannot explain why critical disease remains relatively rare in any given epidemiological group. Given the rising toll of the COVID-19 pandemic in terms of morbidity and mortality, understanding the causes and mechanisms of life-threatening COVID-19 is crucial.

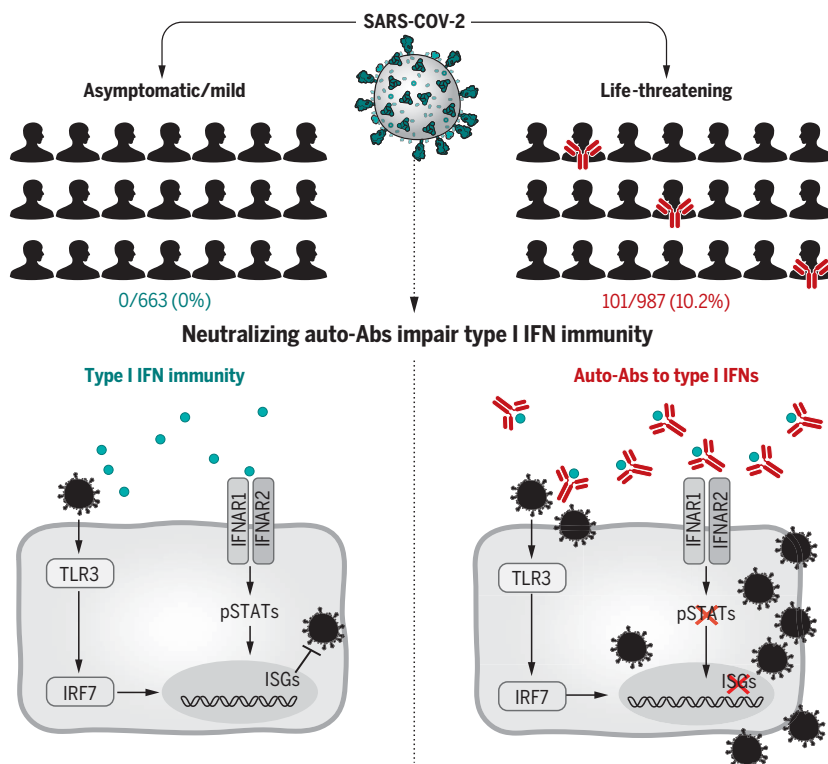
RATIONALE: B cell autoimmune infectious phenocopies of three inborn errors of cyto-

kine immunity exist, in which neutralizing autoantibodies (auto-Abs) against interferon- γ (IFN- γ) (mycobacterial disease), interleukin-6 (IL-6) (staphylococcal disease), and IL-17A and IL-17F (mucocutaneous candidiasis) mimic the clinical phenotypes of germline mutations of the genes that encode the corresponding cytokines or receptors. Human inborn errors of type I IFNs underlie severe viral respiratory diseases. Neutralizing auto-Abs against type I IFNs, which have been found in patients with a few underlying noninfectious conditions, have not been unequivocally shown to underlie severe viral infections. While searching for inborn errors of type I IFN immunity in patients with life-threatening COVID-19 pneumonia, we also tested the hypothesis that neutralizing auto-Abs against type I IFNs

may underlie critical COVID-19. We searched for auto-Abs against type I IFNs in 987 patients hospitalized for life-threatening COVID-19 pneumonia, 663 asymptomatic or mildly affected individuals infected with SARS-CoV-2, and 1227 healthy controls from whom samples were collected before the COVID-19 pandemic.

RESULTS: At least 101 of 987 patients (10.2%) with life-threatening COVID-19 pneumonia had neutralizing immunoglobulin G (IgG) auto-Abs against IFN- ω (13 patients), against the 13 types of IFN- α (36), or against both (52) at the onset of critical disease; a few also had auto-Abs against the other three individual type I IFNs. These auto-Abs neutralize high concentrations of the corresponding type I IFNs, including their ability to block SARS-CoV-2 infection *in vitro*. Moreover, all of the patients tested had low or undetectable serum IFN- α levels during acute disease. These auto-Abs were present before infection in the patients tested and were absent from 663 individuals with asymptomatic or mild SARS-CoV-2 infection ($P < 10^{-16}$). They were present in only 4 of 1227 (0.33%) healthy individuals ($P < 10^{-16}$) before the pandemic. The patients with auto-Abs were 25 to 87 years old (half were over 65) and of various ancestries. Notably, 95 of the 101 patients with auto-Abs were men (94%).

CONCLUSION: A B cell autoimmune phenocopy of inborn errors of type I IFN immunity accounts for life-threatening COVID-19 pneumonia in at least 2.6% of women and 12.5% of men. In these patients, adaptive autoimmunity impairs innate and intrinsic antiviral immunity. These findings provide a first explanation for the excess of men among patients with life-threatening COVID-19 and the increase in risk with age. They also provide a means of identifying individuals at risk of developing life-threatening COVID-19 and ensuring their enrolment in vaccine trials. Finally, they pave the way for prevention and treatment, including plasmapheresis, plasmablast depletion, and recombinant type I IFNs not targeted by the auto-Abs (e.g., IFN- β). ■



Neutralizing auto-Abs to type I IFNs underlie life-threatening COVID-19 pneumonia. We tested the hypothesis that neutralizing auto-Abs against type I IFNs may underlie critical COVID-19 by impairing the binding of type I IFNs to their receptor and the activation of the downstream responsive pathway. Neutralizing auto-Abs are represented in red, and type I IFNs are represented in blue. In these patients, adaptive autoimmunity impairs innate and intrinsic antiviral immunity. ISGs, IFN-stimulated genes; TLR, Toll-like receptor; IFNAR, IFN- α/β receptor; pSTAT, phosphorylated signal transducers and activators of transcription; IRF, interferon regulatory factor.

The full author list and the list of author affiliations is available in the full article online.

*Corresponding authors: Jean-Laurent Casanova (jean-laurent.casanova@rockefeller.edu); Paul Bastard (paul.bastard@institutimagine.org)

†These authors contributed equally to this work. This is an open-access article distributed under the terms of the Creative Commons Attribution license (<https://creativecommons.org/licenses/by/4.0/>), which permits unrestricted use, distribution, and reproduction in any medium, provided the original work is properly cited. Cite this article as P. Bastard *et al.*, *Science* 370, eabd4585 (2020). DOI: 10.1126/science.abd4585

READ THE FULL ARTICLE AT
<https://doi.org/10.1126/science.abd4585>

RESEARCH ARTICLE

CORONAVIRUS

Autoantibodies against type I IFNs in patients with life-threatening COVID-19

Paul Bastard^{1,2,3,*}†, Lindsey B. Rosen⁴†, Qian Zhang³†, Eleftherios Michailidis⁵†, Hans-Heinrich Hoffmann⁵†, Yu Zhang⁴†, Karim Dorgham⁶†, Quentin Philippot^{1,2}†, Jérémie Rosain^{1,2}†, Vivien Béziat^{1,2,3}†, Jérémy Manry^{1,2}, Elana Shaw⁴, Liis Haljasmägi⁷, Pärt Peterson⁷, Lazaro Lorenzo^{1,2}, Lucy Bizien^{1,2}, Sophie Trouillet-Assant^{8,9}, Kerry Dobbs⁴, Adriana Almeida de Jesus⁴, Alexandre Belot^{10,11,12}, Anne Kallaste¹³, Emilie Catherinot¹⁴, Yacine Tandjaoui-Lambiotte¹⁵, Jeremie Le Pen⁵, Gaspard Kerner^{1,2}, Benedetta Bigio³, Yoann Seeleuthner^{1,2}, Rui Yang³, Alexandre Bolze¹⁶, András N. Spaan^{3,17}, Ottavia M. Delmonte⁴, Michael S. Abers⁴, Alessandro Aiuti¹⁸, Giorgio Casari¹⁸, Vito Lampasona¹⁸, Lorenzo Piemonti¹⁸, Fabio Ciceri¹⁸, Kaya Bilguvar¹⁹, Richard P. Lifton^{19,20,21}, Marc Vasse²², David M. Smadja²³, Mélanie Migaud^{1,2}, Jérôme Hadjadj²⁴, Benjamin Terrier²⁵, Darragh Duffy²⁶, Lluís Quintana-Murci^{27,28}, Diederik van de Beek²⁹, Lucie Roussel^{30,31}, Donald C. Vinh^{30,31}, Stuart G. Tangye^{32,33}, Filomeen Haerynck³⁴, David Dalmau³⁵, Javier Martinez-Picado^{36,37,38}, Petter Brodin^{39,40}, Michel C. Nussenzweig^{41,42}, Stéphanie Boisson-Dupuis^{1,2,3}, Carlos Rodríguez-Gallego^{43,44}, Guillaume Vogt⁴⁵, Trine H. Mogensen^{46,47}, Andrew J. Oler⁴⁸, Jingwen Gu⁴⁸, Peter D. Burbelo⁴⁹, Jeffrey I. Cohen⁵⁰, Andrea Biondi⁵¹, Laura Rachele Bettini⁵¹, Mariella D'Angio⁵¹, Paolo Bonfanti⁵², Patrick Rossignol⁵³, Julien Mayaux⁵⁴, Frédéric Rieux-Laucat²⁴, Eystein S. Husebye^{55,56,57}, Francesca Fusco⁵⁸, Matilde Valeria Ursini⁵⁸, Luisa Imberti⁵⁹, Alessandra Sottini⁵⁹, Simone Paghera⁵⁹, Eugenia Quiros-Roldan⁶⁰, Camillo Rossi⁶¹, Riccardo Castagnoli⁶², Daniela Montagna^{63,64}, Amelia Licari⁶², Gian Luigi Marseglia⁶², Xavier Duval^{65,66,67,68,69}, Jade Ghosn^{68,69}, HGID Lab§, NIAID-USUHS Immune Response to COVID Group§, COVID Clinicians§, COVID-STORM Clinicians§, Imagine COVID Group§, French COVID Cohort Study Group§, The Milieu Intérieur Consortium§, CoV-Contact Cohort§, Amsterdam UMC Covid-19 Biobank§, COVID Human Genetic Effort§, John S. Tsang^{70,71}, Raphaela Goldbach-Mansky⁴, Kai Kisand⁷, Michail S. Lionakis⁴, Anne Puel^{1,2,3}, Shen-Ying Zhang^{1,2,3}, Steven M. Holland⁴¶, Guy Gorochoff^{6,72}¶, Emmanuelle Jouanguy^{1,2,3}¶, Charles M. Rice⁵¶, Aurélie Cobat^{1,2,3}¶, Luigi D. Notarangelo⁴¶, Laurent Abel^{1,2,3}¶, Helen C. Su⁴#, Jean-Laurent Casanova^{1,2,3,4,27,3}##

Interindividual clinical variability in the course of severe acute respiratory syndrome coronavirus 2 (SARS-CoV-2) infection is vast. We report that at least 101 of 987 patients with life-threatening coronavirus disease 2019 (COVID-19) pneumonia had neutralizing immunoglobulin G (IgG) autoantibodies (auto-Abs) against interferon- ω (IFN- ω) (13 patients), against the 13 types of IFN- α (36), or against both (52) at the onset of critical disease; a few also had auto-Abs against the other three type I IFNs. The auto-Abs neutralize the ability of the corresponding type I IFNs to block SARS-CoV-2 infection in vitro. These auto-Abs were not found in 663 individuals with asymptomatic or mild SARS-CoV-2 infection and were present in only 4 of 1227 healthy individuals. Patients with auto-Abs were aged 25 to 87 years and 95 of the 101 were men. A B cell autoimmune phenocopy of inborn errors of type I IFN immunity accounts for life-threatening COVID-19 pneumonia in at least 2.6% of women and 12.5% of men.

Myobacteriosis, staphylococcosis, and candidiasis can be driven by monogenic inborn errors of interferon- γ (IFN- γ), interleukin-6 (IL-6), and IL-17A and IL-17F, respectively, or they can be driven by their genetically driven autoimmune phenocopies, with the production of neutralizing autoantibodies (auto-Abs) against these cytokines (1–8). Type I IFNs, first described in 1957, are ubiquitously expressed cytokines that contribute to both innate immunity (through their secretion by plasmacytoid dendritic cells and other leukocytes) and cell-intrinsic immunity (in most if not all cell types) against viral infections (9–13). Their receptors are ubiquitously expressed and trigger the induction of IFN-stimulated genes (ISGs) via phosphorylated STAT1-STAT2-IRF9

trimers (STAT, signal transducers and activators of transcription; IRF, interferon regulatory factor) (14). Neutralizing immunoglobulin G (IgG) auto-Abs against type I IFNs can occur in patients treated with IFN- α 2 or IFN- β (15) and exist in almost all patients with autoimmune polyendocrinopathy syndrome type I (APS-1) (16). They are also seen in women with systemic lupus erythematosus (17).

These patients do not seem to suffer from unusually severe viral infections, although human inborn errors of type I IFNs can underlie severe viral diseases, both respiratory and otherwise (18). In 1984, Ion Gresser described a patient with unexplained auto-Abs against type I IFNs suffering from severe chickenpox and shingles (19, 20). More recently, auto-Abs against type I IFNs have been found in a few

patients with biallelic, hypomorphic *RAG1* or *RAG2* mutations and viral diseases including severe chickenpox and viral pneumonias (21). Our attention was drawn to three patients with APS-1, with known preexisting anti-type I IFN auto-Abs, who had life-threatening coronavirus disease 2019 (COVID-19) pneumonia (22) (see detailed case reports in Methods). While searching for inborn errors of type I IFNs (18, 23), we hypothesized that neutralizing auto-Abs against type I IFNs might also underlie life-threatening COVID-19 pneumonia.

Auto-Abs against IFN- α 2 and/or IFN- ω in patients with critical COVID-19

We searched for auto-Abs against type I IFNs in 987 patients hospitalized for life-threatening COVID-19 pneumonia. We also examined 663 individuals infected with severe acute respiratory syndrome coronavirus 2 (SARS-CoV-2) presenting asymptomatic infection or mild disease and 1227 healthy controls whose samples were collected before the COVID-19 pandemic. Plasma or serum samples were collected from patients with critical COVID-19 during the acute phase of disease. Multiplex particle-based flow cytometry revealed a high fluorescence intensity (FI) (>1500) for IgG auto-Abs against IFN- α 2 and/or IFN- ω in 135 patients (13.7%) with life-threatening COVID-19 (Fig. 1A). We found that 49 of these 135 patients were positive for auto-Abs against both IFN- α 2 and IFN- ω , whereas 45 were positive only for auto-Abs against IFN- α 2, and 41 were positive only for auto-Abs against IFN- ω .

We also performed enzyme-linked immunosorbent assay (ELISA), and the results obtained were consistent with those obtained with Luminex technology (fig. S1A). We found that 11 and 14 of 23 patients tested had low levels of IgM and IgA auto-Abs against IFN- ω and IFN- α 2, respectively (Fig. 1B and fig. S1B). Auto-Abs against type I IFNs were detected in two unrelated patients for whom we had plasma samples obtained before SARS-CoV-2 infection, which indicates that these antibodies were present before SARS-CoV-2 infection and were not triggered by the infection. As a control, we confirmed that all 25 APS-1 patients tested had high levels of auto-Abs against IFN- α 2 and IFN- ω (fig. S1C). Overall, we found that 135 of 987 patients (13.7%) with life-threatening COVID-19 pneumonia had IgG auto-Abs against at least one type I IFN.

The auto-Abs neutralize IFN- α 2 and IFN- ω in vitro

We then tested whether auto-Abs against IFN- α 2 and IFN- ω were neutralizing in vitro. We incubated peripheral blood mononuclear cells (PBMCs) from healthy controls with 10 ng/mL IFN- α 2 or IFN- ω in the presence of plasma from healthy individuals or from patients with auto-Abs. A complete abolition of STAT1 phosphorylation was observed in 101 patients

with auto-Abs against IFN- α 2 and/or IFN- ω (table S1). The antibodies detected were neutralizing against both IFN- α 2 and IFN- ω in 52 of these 101 patients (51%), against only IFN- α 2 in 36 patients (36%), and against only IFN- ω in 13 patients (13%) at the IFN- α 2 and IFN- ω concentrations tested (Fig. 1, C and D). IgG depletion from patients with auto-Abs restored normal pSTAT1 induction after IFN- α 2 and IFN- ω stimulation, whereas the purified IgG fully neutralized this induction (Fig. 1C and fig. S1D). Furthermore, these auto-Abs neutralized high amounts of IFN- α 2 (fig. S1E) and were neutralizing at high dilutions (Fig. 1E and fig. S1F). Notably, 15 patients with life-threatening COVID-19 and auto-Abs against IFN- α 2 and/or IFN- ω also had auto-Abs against other cytokines [IFN- γ , granulocyte-macrophage colony-stimulating factor (GM-CSF), IL-6, IL-10, IL-12p70, IL-22, IL-17A, IL-17F, and/or tumor necrosis factor- β (TNF β)], only three of which (IL-12p70, IL-22, and IL-6) were neutralizing (in four patients) (fig. S2, A to C). Similar proportions were observed in the other cohorts (fig. S2, D to L).

We also analyzed ISG induction after 2 hours of stimulation with IFN- α 2, IFN- β , or IFN- γ in

the presence of plasma from healthy individuals or from patients with auto-Abs. With plasma from eight patients with auto-Abs against IFN- α 2, the induction of ISG CXCL10 was abolished after IFN- α 2 stimulation but maintained after stimulation with IFN- γ (Fig. 1F). We then found that plasma from the five patients with neutralizing auto-Abs neutralized the protective activity of IFN- α 2 in Madin-Darby bovine kidney (MDBK) cells infected with vesicular stomatitis virus (VSV) (table S2). Overall, we found that 101 of 987 patients (10.2%)—including 95 men (94%)—with life-threatening COVID-19 pneumonia had neutralizing IgG auto-Abs against at least one type I IFN. By contrast, auto-Abs were detected in only 4 of 1227 healthy controls (0.33%) (Fisher exact test, $P < 10^{-16}$) and in none of the 663 patients with asymptomatic or mild SARS-CoV-2 infection tested (Fisher exact test, $P < 10^{-16}$).

Auto-Abs against all 13 IFN- α subtypes in patients with auto-Abs to IFN- α 2

We investigated whether patients with neutralizing auto-Abs against IFN- α 2 only or those with neutralizing auto-Abs against IFN- α 2 and IFN- ω also had auto-Abs against the other 15

type I IFNs. ELISA showed that all patients tested ($N = 22$) with auto-Abs against IFN- α 2 also had auto-Abs against all 13 IFN- α subtypes (IFN- α 1, - α 2, - α 4, - α 5, - α 6, - α 7, - α 8, - α 10, - α 13, - α 14, - α 16, - α 17, and - α 21), whereas only 2 of the 22 patients tested had auto-Abs against IFN- β , 1 had auto-Abs against IFN- κ , and 2 had auto-Abs against IFN- ϵ (Fig. 2A). The auto-Abs against IFN- β had neutralizing activity against IFN- β (Fig. 1D). We confirmed that all of the patients had auto-Abs against all 13 subtypes of IFN- α by testing the same samples using luciferase-based immunoprecipitation assay (LIPS) (Fig. 2B). For IFN- β , we also screened the whole cohort in a multiplex assay. We found that 19 of 987 (1.9%) patients had auto-Abs against IFN- β and that all of them were in our cohort of severe COVID-19 individuals with neutralizing auto-Abs against IFN- α and/or IFN- ω . Of these patients with auto-Abs against IFN- β , only two were neutralizing against IFN- β (Fig. 1, D and F).

Ten of the 17 genes encoding type I IFNs (IFN- α 2, - α 5, - α 6, - α 8, - α 13, - α 14, - α 21, - β , - ω , and - κ), have undergone strong negative selection, which suggests that they play an essential role in the general population. By contrast, the

¹Laboratory of Human Genetics of Infectious Diseases, Necker Branch, INSERM U1163, Necker Hospital for Sick Children, Paris, France. ²University of Paris, Imagine Institute, Paris, France.

³St. Giles Laboratory of Human Genetics of Infectious Diseases, Rockefeller Branch, The Rockefeller University, New York, NY, USA. ⁴Laboratory of Clinical Immunology and Microbiology, Division of Intramural Research, National Institute of Allergy and Infectious Diseases (NIAID), National Institutes of Health (NIH), Bethesda, MD, USA. ⁵Laboratory of Virology and Infectious Disease, The Rockefeller University, New York, NY, USA. ⁶Sorbonne Université, INSERM, Centre d'Immunologie et des Maladies Infectieuses, (CIMI-Paris), Paris, France. ⁷Institute of Biomedicine and Translational Medicine, University of Tartu, Tartu, Estonia. ⁸Hospices Civils de Lyon, Lyon Sud Hospital, Pierre-Bénite, France. ⁹International Center of Research in Infectiology, Lyon University, INSERM U1111, CNRS UMR 5308, ENS, UCBL, Lyon, France. ¹⁰International Center of Research in Infectiology, Lyon University, INSERM U1111, CNRS UMR 5308, ENS, UCBL, Lyon, France. ¹¹National Reference Centre for Rheumatic and Autoimmune and Systemic Diseases in Children (RAISE), Lyon, France. ¹²Lyon Immunopathology Federation (LIFE), Hospices Civils de Lyon, Lyon, France. ¹³Internal Medicine Clinic, Tartu University Hospital, Tartu, Estonia. ¹⁴Pneumology Department, Foch Hospital, Suresne, France. ¹⁵Avicenne Hospital, Assistance Publique Hôpitaux de Paris (AP-HP), Bobigny, INSERM U1272 Hypoxia and Lung, Bobigny, France. ¹⁶Helix, San Mateo, CA, USA. ¹⁷Department of Medical Microbiology, University Medical Center Utrecht, Utrecht, Netherlands. ¹⁸IRCCS San Raffaele Hospital and Vita-Salute San Raffaele University, Milan, Italy. ¹⁹Department of Genetics, Yale University School of Medicine, New Haven, CT, USA. ²⁰Yale Center for Genome Analysis, Yale University School of Medicine, New Haven, CT, USA. ²¹Laboratory of Human Genetics and Genomics, The Rockefeller University, New York, NY, USA. ²²Service de Biologie Clinique and UMR-S 1176, Hôpital Foch, Suresnes, France. ²³INSERM UMR-S 1140, Biosurgical Research Laboratory (Carpentier Foundation), Paris University and European Georges Pompidou Hospital, Paris, France. ²⁴Laboratory of Immunogenetics of Pediatric Autoimmune Diseases, INSERM UMR 1163, University of Paris, Imagine Institute, Paris, France. ²⁵Department of Internal Medicine, National Referral Center for Rare Systemic Autoimmune Diseases, Assistance Publique Hôpitaux de Paris-Centre (APHP-CUP), University of Paris, Paris, France. ²⁶Translational Immunology Laboratory, Institut Pasteur, Paris, France. ²⁷Human Evolutionary Genetics Unit, Institut Pasteur, CNRS UMR 2000, 75015, Paris, France. ²⁸Human Genomics and Evolution, Collège de France, Paris, France. ²⁹Amsterdam UMC, University of Amsterdam, Department of Neurology, Amsterdam Neuroscience, Amsterdam, Netherlands. ³⁰Department of Medicine, Division of Infectious Diseases, McGill University Health Centre, Montréal, Québec, Canada. ³¹Infectious Disease Susceptibility Program, Research Institute, McGill University Health Centre, Montréal, Québec, Canada. ³²Garvan Institute of Medical Research, Darlinghurst 2010, NSW, Sydney, Australia. ³³St Vincent's Clinical School, Faculty of Medicine, University of New South Wales Sydney, Darlinghurst 2010, NSW, Australia. ³⁴Department of Paediatric Immunology and Pulmonology, Centre for Primary Immunodeficiency Ghent (CPIG), PID Research Laboratory, Jeffrey Modell Diagnosis and Research Centre, Ghent University Hospital, Ghent, Belgium. ³⁵Infectious Diseases and HIV Service, Hospital Universitari Mutua Terrassa, Universitat de Barcelona, Fundació Docència i Recerca Mutua Terrassa, Terrassa, Barcelona, Catalonia, Spain. ³⁶IrsiCaixa AIDS Research Institute and Institute for Health Science Research Germans Trias i Pujol (IGTP), Badalona, Spain. ³⁷Infectious Diseases and Immunity, Centre for Health and Social Care Research (CESS), Faculty of Medicine, University of Vic-Central University of Catalonia (UVic-UCC), Vic, Spain. ³⁸Catalan Institution for Research and Advanced Studies (ICREA), Barcelona, Spain. ³⁹Science for Life Laboratory, Department of Women's and Children's Health, Karolinska Institutet, Karolinska, Sweden. ⁴⁰Department of Pediatric Rheumatology, Karolinska University Hospital, Karolinska, Sweden. ⁴¹Laboratory of Molecular Immunology, The Rockefeller University, New York, NY, USA. ⁴²Howard Hughes Medical Institute, New York, NY, USA. ⁴³Department of Immunology, Hospital Universitario de Gran Canaria Dr. Negrín, Canarian Health System, Las Palmas de Gran Canaria, Spain. ⁴⁴Department of Clinical Sciences, University Fernando Pessoa Canarias, Las Palmas de Gran Canaria, Spain. ⁴⁵Neglected Human Genetics Laboratory, INSERM, University of Paris, Paris, France. ⁴⁶Department of Infectious Diseases, Aarhus University Hospital, Skejby, Denmark. ⁴⁷Department of Biomedicine, Aarhus University, Aarhus, Denmark. ⁴⁸Bioinformatics and Computational Biosciences Branch, Office of Cyber Infrastructure and Computational Biology, NIAID, NIH, Bethesda, MD, USA. ⁴⁹Division of Intramural Research, National Institute of Dental Craniofacial Research (NIDCR), NIH, Bethesda, MD, USA. ⁵⁰Laboratory of Infectious Diseases, Division of Intramural Research, NIAID, NIH, Bethesda, MD, USA. ⁵¹Pediatric Department and Centro Tettamanti-European Reference Network PaedCan, EuroBloodNet, MetabERN-University of Milano-Bicocca-Fondazione MBBM-Ospedale, San Gerardo, Monza, Italy. ⁵²Department of Infectious Diseases, San Gerardo Hospital - University of Milano-Bicocca, Monza, Italy. ⁵³University of Lorraine, Plurithematic Clinical Investigation Center INSERM CIC-P 1433, INSERM U1116, CHRU Nancy Hôpitaux de Brabois, F-CRIN INI-CRCT (Cardiovascular and Renal Clinical Trialists), Nancy, France. ⁵⁴Intensive Care Unit, Pitié-Salpêtrière Hospital, Paris University, AP-HP, Paris, France. ⁵⁵Department of Clinical Science and K.G. Jebsen Center for Autoimmune Disorders, University of Bergen, Bergen, Norway. ⁵⁶Department of Medicine, Haukeland University Hospital, Bergen, Norway. ⁵⁷Department of Medicine (Solna), Karolinska Institutet, Stockholm, Sweden. ⁵⁸Human Molecular Genetics Laboratory, Institute of Genetics and Biophysics, "A. Buzzati-Traverso" Consiglio Nazionale delle Ricerche, Naples, Italy. ⁵⁹Centro di Ricerca Emato-oncologica AIL (CREA) Laboratory, Diagnostic Department, ASST Spedali Civili di Brescia, Brescia, Italy. ⁶⁰Department of Infectious and Tropical Diseases, University of Brescia and ASST Spedali di Brescia, Brescia, Italy. ⁶¹Direzione Sanitaria, ASST Spedali Civili di Brescia, Brescia, Italy. ⁶²Department of Pediatrics, Fondazione IRCCS Policlinico San Matteo, University of Pavia, Pavia, Italy. ⁶³Laboratory of Immunology and Transplantation, Fondazione IRCCS Policlinico San Matteo, Pavia, Italy. ⁶⁴Department of Clinical, Surgical, Diagnostic and Pediatric Sciences, University of Pavia, Pavia, Italy. ⁶⁵INSERM CIC 1425, Paris, France. ⁶⁶AP-HP, University Hospital of Bichat, Paris, France. ⁶⁷University Paris Diderot, Paris 7, UFR de Médecine-Bichat, Paris, France. ⁶⁸Infection, Antimicrobials, Modelling, Evolution (IAME), INSERM, UMR1137, University of Paris, Paris, France. ⁶⁹AP-HP, Bichat Claude Bernard Hospital, Infectious and Tropical Diseases Department, Paris, France. ⁷⁰Center for Human Immunology, NIH, Bethesda, MD, USA. ⁷¹Multiscale Systems Biology Section, Laboratory of Immune System Biology, NIAID, NIH, Bethesda, MD, USA. ⁷²Département d'Immunologie, AP-HP, Hôpital Pitié-Salpêtrière, Paris, France. ⁷³Pediatric Hematology and Immunology Unit, Necker Hospital for Sick Children, AP-HP, Paris, France.

*Corresponding author. Email: jean-laurent.casanova@rockefeller.edu (J.-L.C.); paul.bastard@institutimagine.org (P.B.)

†These authors contributed equally to this work.

‡These authors contributed equally to this work.

§All collaborators and their affiliations appear at the end of this paper.

¶These authors contributed equally to this work.

#These authors contributed equally to this work.

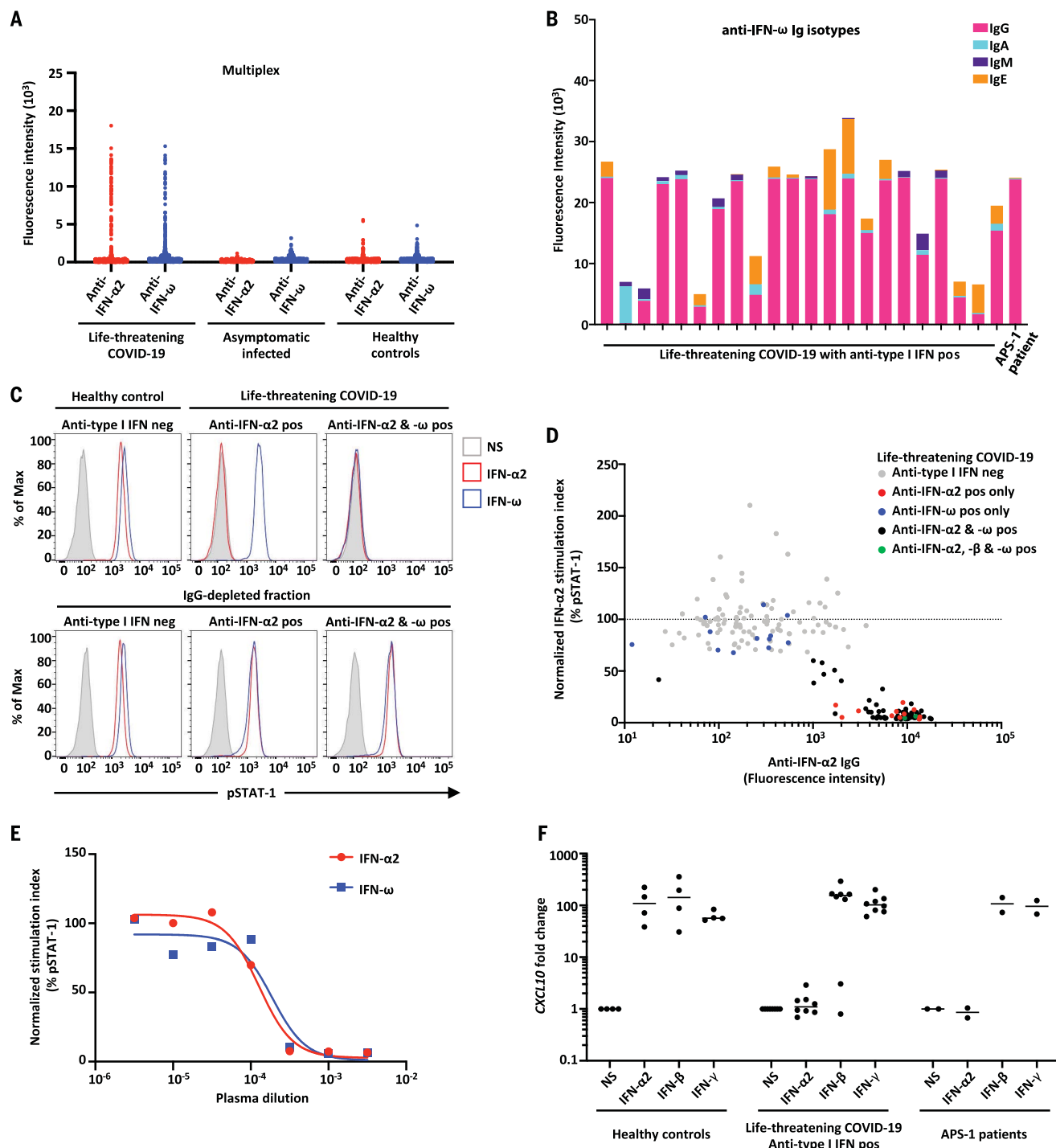


Fig. 1. Neutralizing auto-Abs against IFN- $\alpha 2$ and/or IFN- ω in patients with life-threatening COVID-19. (A) Multiplex particle-based assay for auto-Abs against IFN- $\alpha 2$ and IFN- ω in patients with life-threatening COVID-19 ($N = 782$), in patients with asymptomatic or mild SARS-CoV-2 infection ($N = 443$), and in healthy controls not infected with SARS-CoV-2 ($N = 1160$). (B) Anti-IFN- ω Ig isotypes in 23 patients with life-threatening COVID-19 and auto-Abs to type I IFNs. (C) Representative fluorescence-activated cell sorting (FACS) plots depicting IFN- $\alpha 2$ - or IFN- ω -induced pSTAT1 in healthy control cells (gated on CD14 $^{+}$ monocytes) in the presence of 10% healthy control or anti-IFN- $\alpha 2$ or anti-IFN- ω auto-Abs-containing patient plasma (top panel) or an IgG-depleted plasma fraction (bottom panel). Max, maximum; neg, negative; pos, positive; NS, not stimulated. (D) Plot of anti-IFN- $\alpha 2$ auto-Ab levels against their

neutralization capacity. The stimulation index (stimulated over unstimulated condition) for the plasma from each patient was normalized against that of healthy control plasma from the same experiment. Spearman's rank correlation coefficient = -0.6805 ; $P < 0.0001$. (E) Median inhibitory concentration (IC_{50}) curves representing IFN- $\alpha 2$ - and IFN- ω -induced pSTAT1 levels in healthy donor cells in the presence of serial dilutions of patient plasma. The stimulation index (stimulated over unstimulated condition) for patient plasma was normalized against that of 10% healthy control plasma. IFN- $\alpha 2$: $IC_{50} = 0.016\%$, $R^2 = 0.985$; IFN- ω : $IC_{50} = 0.0353\%$, $R^2 = 0.926$. R^2 , coefficient of determination. (F) Neutralizing effect on CXCL10 induction, after stimulation with IFN- $\alpha 2$, IFN- β , or IFN- γ , in the presence of plasma from healthy controls ($N = 4$), patients with life-threatening COVID-19 and auto-Abs against IFN- $\alpha 2$ ($N = 8$), and APS-1 patients ($N = 2$).

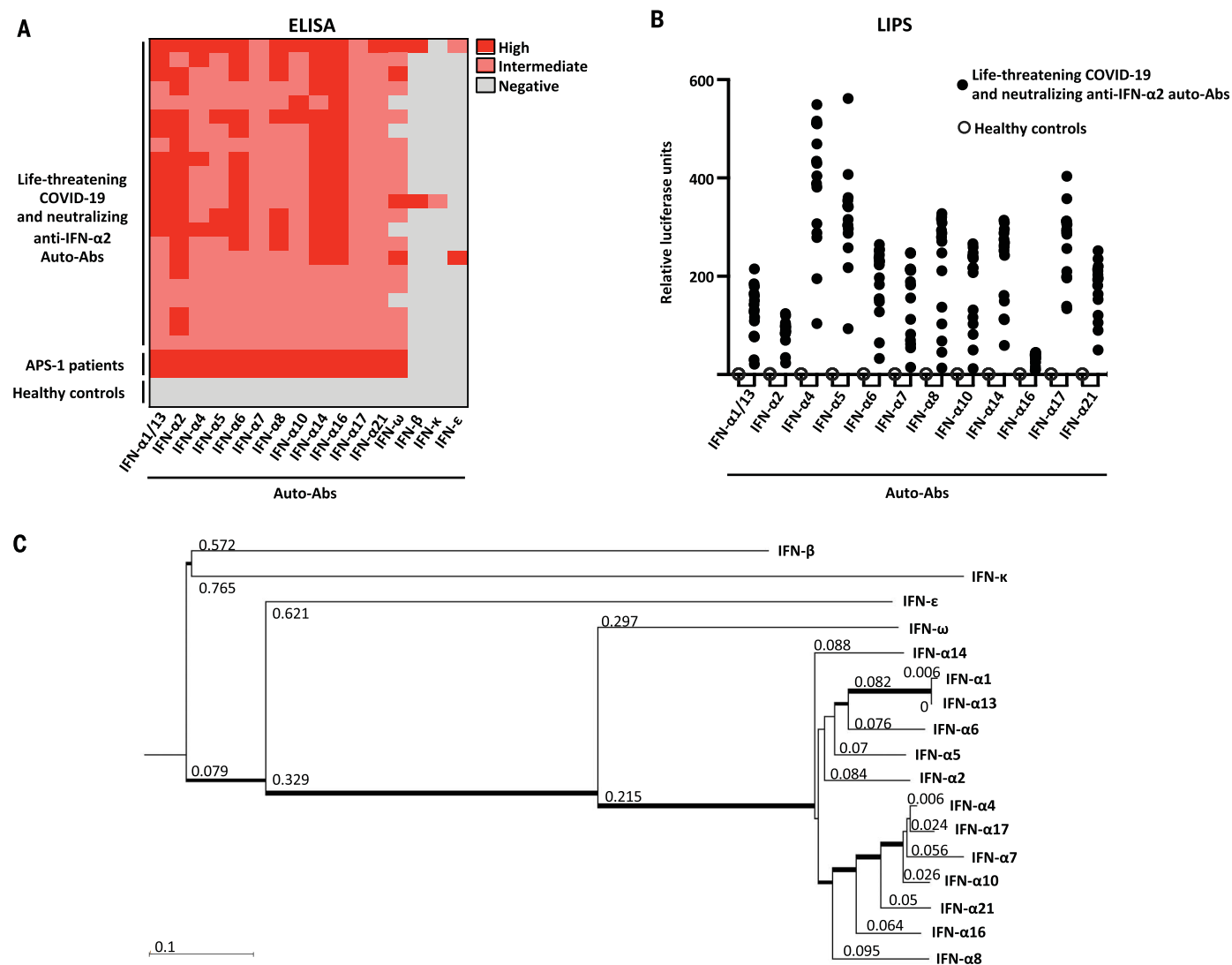


Fig. 2. Auto-Abs against the different type I IFN subtypes. (A) ELISA for auto-Abs against the 13 different IFN-α subtypes, IFN-ω, IFN-β, IFN-κ, and IFN-ε in patients with life-threatening COVID-19 and auto-Abs against IFN-α2 ($N = 22$), APS-1 patients ($N = 2$), and healthy controls ($N = 2$). (B) LIPS for the 12 different IFN-α subtypes tested in patients with auto-Abs against IFN-α2 ($N = 22$) and

healthy controls ($N = 2$). (C) Neighbor-joining phylogenetic tree of the 17 human type I IFN proteins. Horizontal branches are drawn to scale (bottom left, number of substitutions per site). Thinner, intermediate, and thicker internal branches have bootstrap support of <50 , ≥ 50 , and $>80\%$, respectively. The bootstrap value for the branch separating IFN-ω from all IFN-α subtypes is 100%.

other seven IFN loci in the human genome often carry loss-of-function alleles (24). Moreover, the 13 IFN-α subtypes and IFN-ω are more closely related to each other than they are to the other three IFNs (IFN-β, IFN-ε, and IFN-κ), which are structurally and phylogenetically more distant (Fig. 2C). Thus, all patients with neutralizing auto-Abs against IFN-α2 that we tested ($N = 22$) had auto-Abs against all 13 IFN-α subtypes, and 3 of the 22 patients tested (14%) had auto-Abs against 14 or more type I IFNs.

The auto-Abs neutralize IFN-α2 against SARS-CoV-2 in vitro and IFN-α in vivo

Plasma from eight patients with neutralizing auto-Abs against type I IFN also neutralized the ability of IFN-α2 to block the infection of

Huh7.5 cells with SARS-CoV-2 (Fig. 3A). Plasma from two healthy controls or from seven SARS-CoV-2-infected patients without auto-Abs did not block the protective action of IFN-α2 (Fig. 3A and fig. S3A). These data provide compelling evidence that the patients' blood carried sufficiently large amounts of auto-Abs to neutralize the corresponding type I IFNs and block their antiviral activity in vitro, including that against SARS-CoV-2.

We also found that all 41 patients with neutralizing auto-Abs against the 13 types of IFN-α tested had low (one patient) or undetectable (40 patients) levels of the 13 types of IFN-α in their plasma during the course of the disease (Fig. 3B) (25, 26). Type I IFNs may be degraded and/or bound to the corresponding circulating auto-Abs. The presence of circulating neutral-

izing auto-Abs against IFN-α is, therefore, strongly associated with low serum IFN-α levels (Fisher exact test, $P < 10^{-6}$). Consistently in patients with neutralizing auto-Abs against IFN-α2, the baseline levels of type I IFN-dependent transcripts were low, whereas they were normal for nuclear factor κB (NF-κB)-dependent transcripts (Fig. 3C and fig. S3B). Overall, our findings indicate that the auto-Abs against type I IFNs present in patients with life-threatening COVID-19 were neutralizing in vitro and in vivo.

Pronounced excess of men in patients with auto-Abs against type I IFNs

There was a pronounced excess of male patients (95 of 101; 94%) with critical COVID-19 pneumonia and neutralizing auto-Abs against type I

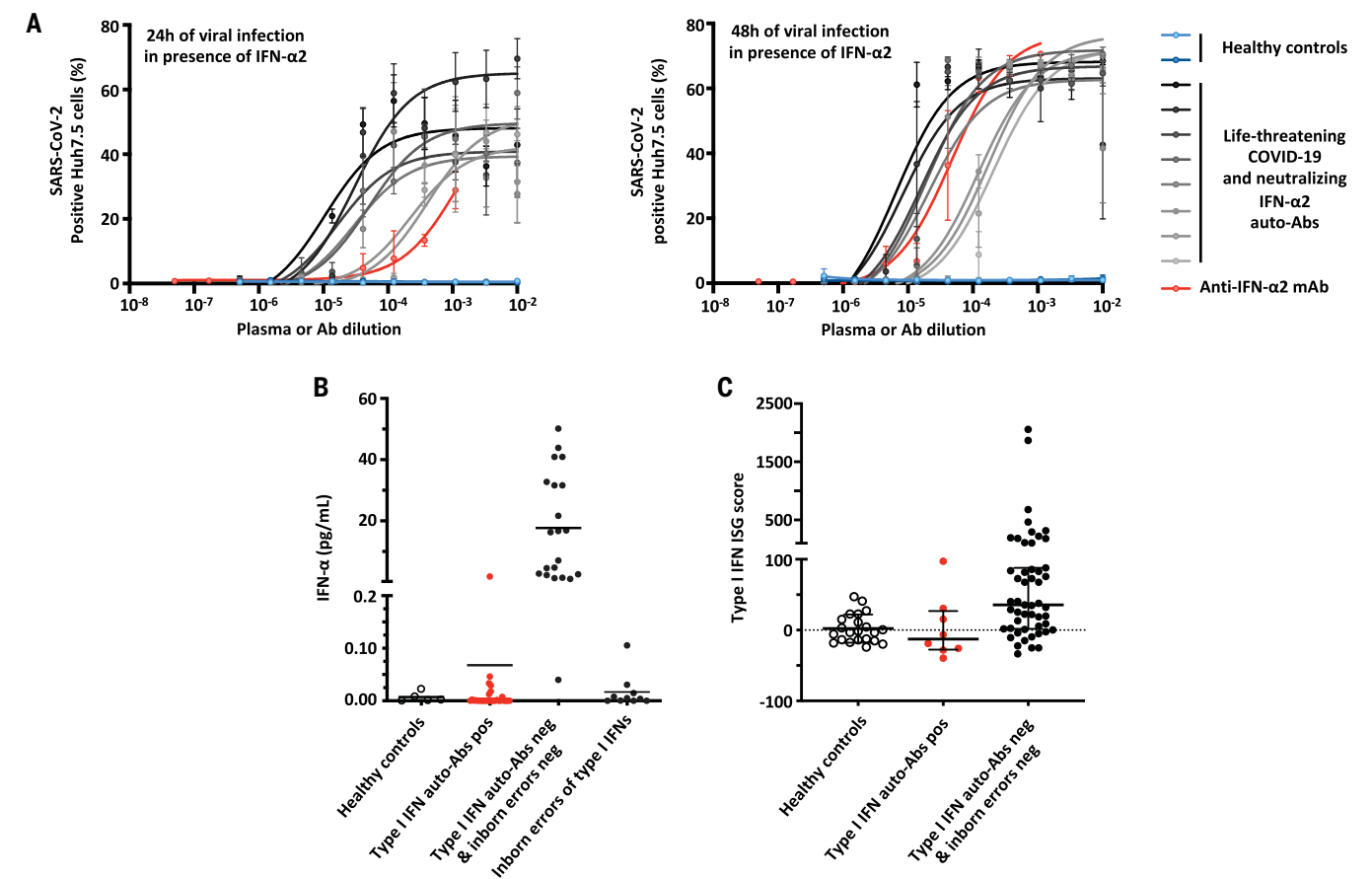


Fig. 3. Enhanced SARS-CoV-2 replication, despite the presence of IFN-α2, in the presence of plasma from patients with auto-Abs against IFN-α2 and low in vivo levels of IFN-α. (A) SARS-CoV-2 replication—measured 24 hours (left) and 48 hours (right) after infection—in Huh7.5 cells treated with IFN-α2 in the presence of plasma from patients with life-threatening COVID-19 and neutralizing auto-Abs against IFN-α2 (*N* = 8); a commercial anti-IFN-α2 antibody; or control plasma (*N* = 2). (B) IFN-α levels in the plasma or serum of patients with neutralizing auto-Abs

(*N* = 41), healthy controls (*N* = 5), COVID-19 patients without auto-Abs (*N* = 21), and patients with life-threatening COVID-19 and loss-of-function (LOF) variants (*N* = 10), as assessed by Simoa ELISA. (C) z-scores for type I IFN gene responses in whole blood of COVID-19 patients with (*N* = 8) or without (*N* = 51) neutralizing auto-Abs, or healthy uninfected controls (*N* = 22). The median ± interquartile range is shown. z-scores were significantly lower for patients with neutralizing auto-Abs compared with patients without auto-Abs (Mann-Whitney test, *P* = 0.01).

Table 1. Sex and age distribution of patients with critical COVID-19 with and without auto-Abs. Ages and sexes of the patients and controls and information about auto-Abs against IFN-α2 and IFN-α, presented by age and sex. Dashes in rightmost column indicate data not available. OR, odds ratio; CI, confidence interval.				
Life-threatening COVID-19	<i>N</i> total	<i>N</i> auto-Abs positive (percentage)	OR [95% CI]	<i>P</i> value*
Sex				
Female	226	6 (2.6%)	1	—
Male	761	95 (12.5%)	5.22 [2.27 – 14.80]	2.5 × 10 ⁻⁶
Age				
<65 years	602	51 (8.5%)	1	—
≥65 years	385	50 (13.0%)	1.61 [1.04 – 2.49]	0.024

**P* values were derived from Fisher's exact test, as implemented in R (<https://cran.r-project.org/>).

IFNs. This proportion of males was higher than that observed in patients with critical COVID-19 without auto-Abs (75%; Fisher exact test, *P* = 2.5 × 10⁻⁶), and the proportion was much higher than that in male patients in the asymptomatic

or pauci-symptomatic cohort (28%; Fisher exact test, *P* < 10⁻⁶) (Table 1, Fig. 4A, and fig. S4A). Further evidence for X-chromosome linkage was provided by the observation that one of the seven women with auto-Abs and life-

threatening COVID-19 had X chromosome-linked incontinentia pigmenti (IP), in which cells activate only a single X chromosome (cells having activated the X chromosome bearing the null mutation in *NEMO* dying in the course of development) (27). The prevalence of auto-Abs against type I IFNs in the general population was estimated at 0.33% (0.015 to 0.67%) in a sample of 1227 healthy individuals—a value much lower than that in patients with life-threatening COVID-19 pneumonia, by a factor of at least 15. The patients with auto-Abs were also slightly older than the rest of our cohort (49.5% of patients positive for auto-Abs were over 65 years of age versus 38% for the rest of the cohort; *P* = 0.024), which suggests that the frequency of circulating anti-type I IFNs auto-Abs increases with age (Table 1 and Fig. 4B). However, auto-Abs were found in patients aged from 25 to 87 years (fig. S4B). Principal components analysis (PCA) was performed on data from

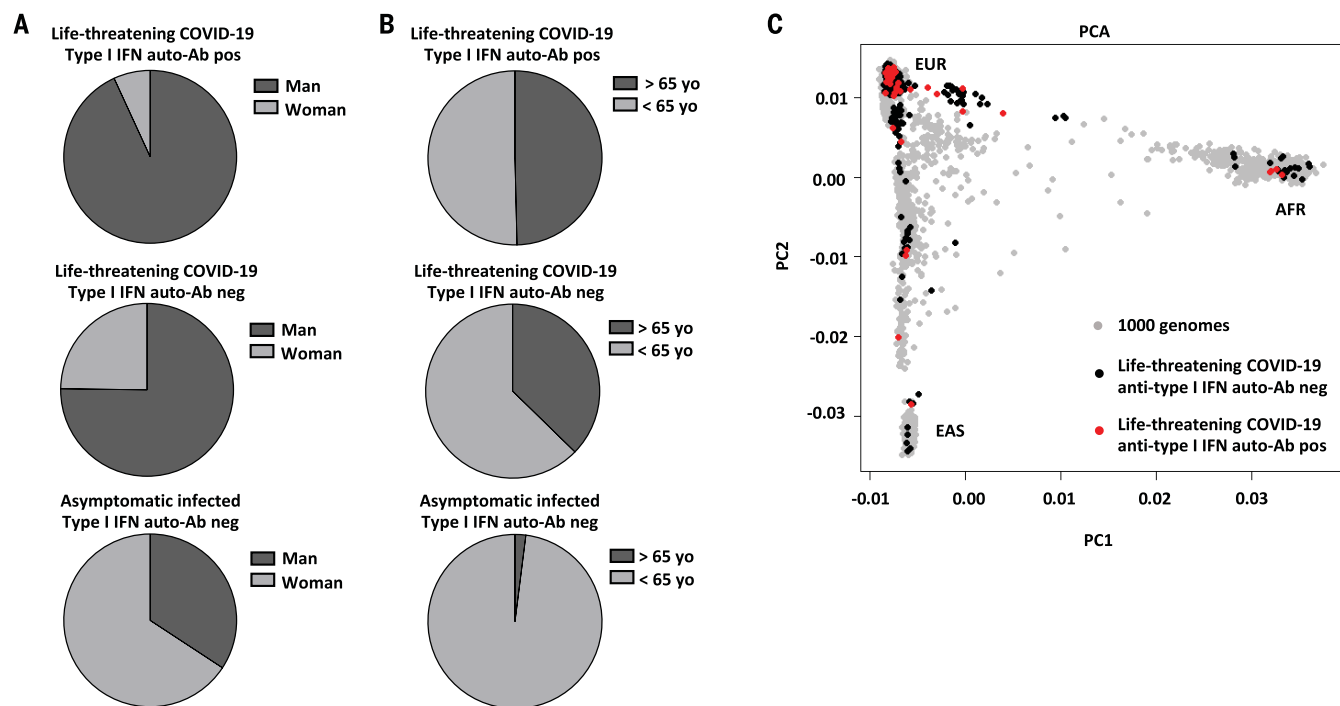


Fig. 4. Demographic and ethnic information about the patients and controls. (A) Gender distribution in patients with life-threatening COVID-19 and auto-Abs to type I IFNs, patients with life-threatening COVID-19 and without auto-Abs to type I IFNs, and individuals with asymptomatic or mild SARS-CoV-2. (B) Age distribution in patients with life-threatening COVID-19

and auto-Abs to type I IFNs, patients with life-threatening COVID-19 and without auto-Abs to type I IFNs, and individuals with asymptomatic or mild SARS-CoV-2. yo, years old. (C) PCA on 49 patients with life-threatening COVID-19 and auto-Abs against type I IFNs. EUR, Europeans; AFR, Africans; EAS, East-Asians.

49 patients: 34 Europeans, 5 North Africans, 4 sub-Saharan Africans, 2 patients from the Middle East, 2 South Asians, 1 East Asian, and 1 South American (Fig. 4C). Large-scale studies will be required to determine the frequency of such auto-Abs in humans of different sexes, ages, and ancestries. Finally, the presence of auto-Abs was associated with a poor outcome, with death occurring in 37 of the 101 patients (36.6%) (table S1).

Neutralizing auto-Abs to type I IFNs are causative of critical COVID-19

There are multiple lines of evidence to suggest that the neutralizing auto-Abs against type I IFNs observed in these 101 patients preceded infection with SARS-CoV-2 and accounted for the severity of disease. First, the two patients for whom testing was performed before COVID-19 were found to have auto-Abs before infection. Second, three patients with APS-1 known to have neutralizing auto-Abs against type I IFN immunity before infection also had life-threatening COVID-19 (22) (supplementary methods). Third, we screened a series of 32 women with IP and found that a quarter of them had auto-Abs against type I IFNs, including one who developed critical COVID-19 (fig. S1C). Fourth, there is a marked bias in favor of men, which suggests that the production of auto-Abs against type I IFNs—whether

driven by germ line or somatic genome—may be X chromosome-linked and therefore pre-existing to infection.

Moreover, IFN- α subtypes were undetectable during acute disease in the blood of patients with auto-Abs against IFN- α , which suggests a preexisting or concomitant biological impact in vivo. It is also unlikely that patients could break self-tolerance and mount high titers of neutralizing IgG auto-Abs against type I IFN within only 1 or even 2 weeks of infection. Finally, inborn errors of type I IFNs underlying life-threatening COVID-19 in other previously healthy adults—including autosomal recessive IFN- α/β receptor subunit 1 (IFNAR1) deficiency—have also been reported in an accompanying paper (18). Collectively, these findings suggest that auto-Abs against type I IFNs are a cause and not a consequence of severe SARS-CoV-2 infection, although their titers and affinity may be enhanced by the SARS-CoV-2-driven induction of type I IFNs. They also provide an explanation for the major sex bias seen in patients with life-threatening COVID-19 and perhaps also for the increase in risk with age.

Conclusion

We report here that at least 10% of patients with life-threatening COVID-19 pneumonia have neutralizing auto-Abs against type I IFNs. With our accompanying description of patients

with inborn errors of type I IFNs and life-threatening COVID-19 (18), this study highlights the crucial role of type I IFNs in protective immunity against SARS-CoV-2. These auto-Abs against type I IFNs were clinically silent until the patients were infected with SARS-CoV-2—a poor inducer of type I IFNs (28)—which suggests that the small amounts of IFNs induced by the virus are important for protection against severe disease. The neutralizing auto-Abs against type I IFNs, like inborn errors of type I IFN production, tip the balance in favor of the virus, which results in devastating disease with insufficient, and even perhaps deleterious, innate and adaptive immune responses.

Our findings have direct clinical implications. First, SARS-CoV-2-infected patients can be screened to identify individuals with auto-Abs at risk of developing life-threatening pneumonia. Such patients recovering from life-threatening COVID-19 should also be excluded from donating convalescent plasma for ongoing clinical trials, or at least they should be tested before their plasma donations are accepted (29). Second, this finding paves the way for preventive or therapeutic intervention, including plasmapheresis, monoclonal Abs depleting plasmablasts, and the specific inhibition of type I IFN-reactive B cells (30). Finally, in this patient group, early treatment with IFN- α is unlikely to be beneficial; however, treatment

with injected or nebulized IFN- β may have beneficial effects, as auto-Abs against IFN- β appear to be rare in patients with auto-Abs against type I IFNs.

Materials and methods

Subjects and samples

We enrolled 987 patients with proven life-threatening (critical) COVID-19, 663 asymptomatic or pauci-symptomatic individuals with proven COVID-19, and 1227 healthy controls in this study. All subjects were recruited following protocols approved by local Institutional Review Boards (IRBs). All protocols followed local ethics recommendations and informed consent was obtained when required.

COVID-19 disease severity was assessed in accordance with the Diagnosis and Treatment Protocol for Novel Coronavirus Pneumonia. The term life-threatening COVID-19 pneumonia describes pneumonia in patients with critical disease, whether pulmonary, with mechanical ventilation [continuous positive airway pressure (CPAP), bilevel positive airway pressure (BIPAP), intubation, or high-flow oxygen], septic shock, or damage to any other organ requiring admission in the intensive care unit (ICU). The individuals with asymptomatic or mild SARS-CoV-2 infection were individuals infected with SARS-CoV-2 who remained asymptomatic or developed mild, self-healing, ambulatory disease with no evidence of pneumonia. The healthy controls were individuals who had not been exposed to SARS-CoV-2.

Plasma and serum samples from the patients and controls were frozen at -20°C immediately after collection. The fluid-phase LIPS assay was used to determine the levels of antibodies against the SARS-CoV-2 nucleoprotein and spike protein, as has been previously described (31).

Detection of anti-cytokine auto-Abs

Multiplex particle-based assay

Serum and plasma samples were screened for auto-Abs against 18 targets in a multiplex particle-based assay, in which magnetic beads with differential fluorescence were covalently coupled to recombinant human proteins. Patients with an FI of >1500 for IFN- $\alpha 2$ or IFN- β or >1000 for IFN- ω were tested for blocking activity, as were patients positive for another cytokine.

ELISA

ELISA was performed as previously described (5). In brief, ELISA plates were coated with recombinant human interferon- α (rhIFN- α) or rhIFN- ω and incubated with 1:50 dilutions of plasma samples from the patients or controls. A similar protocol was used when testing for 12 subtypes of IFN- α .

LIPS

Levels of auto-Abs against IFN- α subtypes were measured with LIPS, as previously described

(32). IFN- $\alpha 1$, IFN- $\alpha 2$, IFN- $\alpha 4$, IFN- $\alpha 5$, IFN- $\alpha 6$, IFN- $\alpha 7$, IFN- $\alpha 8$, IFN- $\alpha 10$, IFN- $\alpha 14$, IFN- $\alpha 16$, IFN- $\alpha 17$, and IFN- $\alpha 21$ sequences were transfected in HEK293 cells, and the IFN- α -luciferase fusion proteins were collected in the tissue culture supernatant. For autoantibody screening, serum samples were incubated with protein G agarose beads, and we then added 2×10^6 luminescence units (LU) of antigen and incubated. Luminescence intensity was measured. The results are expressed in arbitrary units (AU), as a fold-difference relative to the mean of the negative control samples.

Functional evaluation of anti-cytokine auto-Abs

The blocking activity of anti-IFN- α and anti-IFN- ω auto-Abs was determined by assessing STAT1 phosphorylation in healthy control cells after stimulation with the appropriate cytokines in the presence of 10% healthy control or patient serum or plasma.

We demonstrated that the IFN- α and IFN- ω blocking activity observed was due to auto-Abs and not another plasma factor, by depleting IgG from the plasma with a protein G column. Without eluting the IgG, the flow-through fraction (IgG-depleted) was then collected and compared with total plasma in the phospho-STAT1 assay.

The blocking activity of anti-IFN- γ , -GM-CSF, -IFN- $\lambda 1$, -IFN- $\lambda 2$, -IFN- $\lambda 3$, -IL-6, -IL-10, -IL-12p70, -IL-22, -IL-17A, -IL-17F, -TNF α , and -TNF β antibodies was assessed with the assays outlined in table S3, as previously reported (21).

For the neutralization of ISG induction, PBMCs were left unstimulated or were stimulated for 2 hours with 10 ng/mL IFN- α or 10 ng/mL IFN- γ in a final volume of 100 μL . Real-time quantitative polymerase chain reaction (RT-qPCR) analysis was performed with Applied Biosystems Taqman assays for *CXCL10*, and the β -glucuronidase (GUS) housekeeping gene for normalization. Results are expressed according to the $\Delta\Delta\text{Ct}$ method, as described by the manufacturer's kit.

Phylogenetic reconstruction

Protein sequences were aligned with the online version of MAFFT v7.471 software (33), using the L-INS-i strategy (34) and the BLOSUM62 scoring matrix for amino acid substitutions. Phylogenetic tree reconstruction was performed by the neighbor-joining method (35) with the substitution model (36). Low-confidence branches ($<50\%$) are likely to be due to gene conversion events between *IFNA* genes, as previously reported (24, 37). The tree was then visualized (38). Very similar results were obtained with the corresponding DNA sequences (37, 39).

Statistical analysis

Comparison of proportions were performed using a Fisher exact test, as implemented in R

(<https://cran.r-project.org/>). PCA was performed with Plink v1.9 software on whole-exome and whole-genome sequencing data with the 1000 Genomes (1kG) Project phase 3 public database as a reference.

Simoa

Serum IFN- α concentrations were determined with Simoa technology, as previously described (40, 41), with reagents and procedures obtained from the Quanterix Corporation.

VSV assay

The seroneutralization assay was performed as previously described (42). In brief, the incubation of IFN- $\alpha 2$ with MDBK cells protects the cultured cells against the cytopathic effect of VSV. The titer of anti-IFN- α antibodies was defined as the last dilution causing 50% cell death.

SARS-CoV-2 experiment

SARS-CoV-2 strain USA-WA1/2020 was obtained from BEI Resources and amplified in Huh7.5 hepatoma cells at 33°C . Viral titers were measured on Huh7.5 cells in a standard plaque assay. Plasma samples or a commercial anti-IFN- $\alpha 2$ antibody were serially diluted and incubated with 20 pM recombinant IFN- $\alpha 2$ for 1 hour at 37°C (starting concentrations: plasma samples = 1/100 and anti-IFN- $\alpha 2$ antibody = 1/1000). The cell culture medium was then removed and replaced with the plasma- or antibody-IFN- $\alpha 2$ mixture. The plates were incubated overnight, and the plasma- or antibody-IFN- $\alpha 2$ mixture was removed by aspiration. The cells were washed once with phosphate-buffered saline (PBS) to remove potential anti-SARS-CoV-2 neutralizing antibodies, and fresh medium was then added. Cells were then infected with SARS-CoV-2 by directly adding the virus to the wells. Cells infected at a high multiplicity of infection (MOI) were incubated at 37°C for 24 hours, whereas cells infected at a low MOI were incubated at 33°C for 48 hours. The cells were fixed with 7% formaldehyde, stained for SARS-CoV-2 with an anti-N antibody, imaged, and analyzed as previously described (43).

Nanostring

For the NanoString assay, total RNA was extracted from whole blood samples collected in PaxGene tubes. The expression of selected genes was determined by NanoString methods and a 28-gene type I IFN score was calculated (44).

REFERENCES AND NOTES

1. J.-L. Casanova, L. Abel, The human genetic determinism of life-threatening infectious diseases: Genetic heterogeneity and physiological homogeneity? *Hum. Genet.* **139**, 681–694 (2020). doi: [10.1007/s00439-020-02184-w](https://doi.org/10.1007/s00439-020-02184-w); pmid: [32462426](https://pubmed.ncbi.nlm.nih.gov/32462426/)
2. R. Döflinger et al., Autoantibodies to interferon- γ in a patient with selective susceptibility to mycobacterial infection and

- organ-specific autoimmunity. *Clin. Infect. Dis.* **38**, e10–e14 (2004). doi: [10.1086/380453](https://doi.org/10.1086/380453); pmid: [14679469](https://pubmed.ncbi.nlm.nih.gov/14679469/)
3. C. Höflich *et al.*, Naturally occurring anti-IFN- γ autoantibody and severe infections with *Mycobacterium chelonae* and *Burkholderia coccovenans*. *Blood* **103**, 673–675 (2004). doi: [10.1182/blood-2003-04-1065](https://doi.org/10.1182/blood-2003-04-1065); pmid: [12947000](https://pubmed.ncbi.nlm.nih.gov/12947000/)
 4. B. Kampmann *et al.*, Acquired predisposition to mycobacterial disease due to autoantibodies to IFN- γ . *J. Clin. Invest.* **115**, 2480–2488 (2005). doi: [10.1172/JCI19316](https://doi.org/10.1172/JCI19316); pmid: [16127458](https://pubmed.ncbi.nlm.nih.gov/16127458/)
 5. A. Puel *et al.*, Recurrent staphylococcal cellulitis and subcutaneous abscesses in a child with autoantibodies against IL-6. *J. Immunol.* **180**, 647–654 (2008). doi: [10.4049/jimmunol.180.1.647](https://doi.org/10.4049/jimmunol.180.1.647); pmid: [18097067](https://pubmed.ncbi.nlm.nih.gov/18097067/)
 6. A. Puel *et al.*, Autoantibodies against IL-17A, IL-17F, and IL-22 in patients with chronic mucocutaneous candidiasis and autoimmune polyendocrine syndrome type 1. *J. Exp. Med.* **207**, 291–297 (2010). doi: [10.1084/jem.20091983](https://doi.org/10.1084/jem.20091983); pmid: [20123958](https://pubmed.ncbi.nlm.nih.gov/20123958/)
 7. K. Kisand *et al.*, Chronic mucocutaneous candidiasis in APECED or thymoma patients correlates with autoimmunity to Th17-associated cytokines. *J. Exp. Med.* **207**, 299–308 (2010). doi: [10.1084/jem.20091669](https://doi.org/10.1084/jem.20091669); pmid: [20123959](https://pubmed.ncbi.nlm.nih.gov/20123959/)
 8. C.-L. Ku, C.-Y. Chi, H. von Bernuth, R. Doffinger, Autoantibodies against cytokines: Phenocopies of primary immunodeficiencies? *Hum. Genet.* **139**, 783–794 (2020). doi: [10.1007/s00439-020-02180-0](https://doi.org/10.1007/s00439-020-02180-0); pmid: [32419033](https://pubmed.ncbi.nlm.nih.gov/32419033/)
 9. A. Isaacs, J. Lindenmann, Virus interference. I. The interferon. *Proc. R. Soc. Lond. B* **147**, 258–267 (1957). doi: [10.1098/rspb.1957.0048](https://doi.org/10.1098/rspb.1957.0048); pmid: [13465720](https://pubmed.ncbi.nlm.nih.gov/13465720/)
 10. A. Isaacs, J. Lindenmann, R. C. Valentine, Virus interference. II. Some properties of interferon. *Proc. R. Soc. Lond. B* **147**, 268–273 (1957). doi: [10.1098/rspb.1957.0049](https://doi.org/10.1098/rspb.1957.0049); pmid: [13465721](https://pubmed.ncbi.nlm.nih.gov/13465721/)
 11. I. Gresser, Wherefore interferon? *J. Leukoc. Biol.* **61**, 567–574 (1997). doi: [10.1002/jlb.61.5.567](https://doi.org/10.1002/jlb.61.5.567); pmid: [9129205](https://pubmed.ncbi.nlm.nih.gov/9129205/)
 12. H.-H. Hoffmann, W. M. Schneider, C. M. Rice, Interferons and viruses: An evolutionary arms race of molecular interactions. *Trends Immunol.* **36**, 124–138 (2015). doi: [10.1016/j.it.2015.01.004](https://doi.org/10.1016/j.it.2015.01.004); pmid: [25704559](https://pubmed.ncbi.nlm.nih.gov/25704559/)
 13. N. A. de Weerd, J. P. Vivian, S. S. Lim, S. U.-S. Huang, P. J. Hertzog, Structural integrity with functional plasticity: What type I IFN receptor polymorphisms reveal. *J. Leukoc. Biol.* **108**, 909–924 (2020). doi: [10.1002/JLB.2MR0420-152R](https://doi.org/10.1002/JLB.2MR0420-152R)
 14. J. E. Darnell Jr., STATs and gene regulation. *Science* **277**, 1630–1635 (1997). doi: [10.1126/science.277.5332.1630](https://doi.org/10.1126/science.277.5332.1630); pmid: [9287210](https://pubmed.ncbi.nlm.nih.gov/9287210/)
 15. A. Vallbracht, J. Treuner, B. Flehmig, K. E. Joester, D. Niethammer, Interferon-neutralizing antibodies in a patient treated with human fibroblast interferon. *Nature* **289**, 496–497 (1981). doi: [10.1038/289496a0](https://doi.org/10.1038/289496a0); pmid: [6162104](https://pubmed.ncbi.nlm.nih.gov/6162104/)
 16. A. Meager *et al.*, Anti-interferon autoantibodies in autoimmune polyendocrinopathy syndrome type 1. *PLOS Med.* **3**, e289 (2006). doi: [10.1371/journal.pmed.0030289](https://doi.org/10.1371/journal.pmed.0030289); pmid: [16784312](https://pubmed.ncbi.nlm.nih.gov/16784312/)
 17. S. Panem, I. J. Check, D. Henriksen, J. Vilcek, Antibodies to alpha-interferon in a patient with systemic lupus erythematosus. *J. Immunol.* **129**, 1–3 (1982). pmid: [6177744](https://pubmed.ncbi.nlm.nih.gov/6177744/)
 18. Q. Zhang *et al.*, Inborn errors of type I IFN immunity in patients with life-threatening COVID-19. *Science* **370**, eabd4570 (2020). doi: [10.1126/science.abd4570](https://doi.org/10.1126/science.abd4570)
 19. B. Pozzetto, K. E. Mogensén, M. G. Tovey, I. Gresser, Characteristics of autoantibodies to human interferon in a patient with varicella-zoster disease. *J. Infect. Dis.* **150**, 707–713 (1984). doi: [10.1093/infdis/150.5.707](https://doi.org/10.1093/infdis/150.5.707); pmid: [6238105](https://pubmed.ncbi.nlm.nih.gov/6238105/)
 20. J.-L. Casanova, Ion Gresser, *J. Interferon Cytokine Res.* **39**, 317–320 (2019). doi: [10.1089/jir.2018.29015.mem](https://doi.org/10.1089/jir.2018.29015.mem)
 21. J. E. Walter *et al.*, Broad-spectrum antibodies against self-antigens and cytokines in RAG deficiency. *J. Clin. Invest.* **125**, 4135–4148 (2015). doi: [10.1172/JCI80477](https://doi.org/10.1172/JCI80477); pmid: [26457731](https://pubmed.ncbi.nlm.nih.gov/26457731/)
 22. G. Beccuti *et al.*, A COVID-19 pneumonia case report of autoimmune polyendocrine syndrome type 1 in Lombardy, Italy: Letter to the editor. *J. Endocrinol. Invest.* **43**, 1175–1177 (2020). doi: [10.1007/s40618-020-01323-4](https://doi.org/10.1007/s40618-020-01323-4); pmid: [32519200](https://pubmed.ncbi.nlm.nih.gov/32519200/)
 23. J.-L. Casanova, H. C. Su, COVID Human Genetic Effort, A Global Effort to Define the Human Genetics of Protective Immunity to SARS-CoV-2 Infection. *Cell* **181**, 1194–1199 (2020). doi: [10.1016/j.cell.2020.05.016](https://doi.org/10.1016/j.cell.2020.05.016); pmid: [32405102](https://pubmed.ncbi.nlm.nih.gov/32405102/)
 24. J. Manry *et al.*, Evolutionary genetic dissection of human interferons. *J. Exp. Med.* **208**, 2747–2759 (2011). doi: [10.1084/jem.20111680](https://doi.org/10.1084/jem.20111680); pmid: [22162829](https://pubmed.ncbi.nlm.nih.gov/22162829/)
 25. S. Trouillet-Assant *et al.*, Type I IFN immunoprofiling in COVID-19 patients. *J. Allergy Clin. Immunol.* **146**, 206–208.e2 (2020). doi: [10.1016/j.jaci.2020.04.029](https://doi.org/10.1016/j.jaci.2020.04.029); pmid: [32360285](https://pubmed.ncbi.nlm.nih.gov/32360285/)
 26. J. Hadjadj *et al.*, Impaired type I interferon activity and inflammatory responses in severe COVID-19 patients. *Science* **369**, 718–724 (2020). doi: [10.1126/science.abc6027](https://doi.org/10.1126/science.abc6027); pmid: [32661059](https://pubmed.ncbi.nlm.nih.gov/32661059/)
 27. A. Harris, J. Collins, D. Vetrie, C. Cole, M. Bobrow, X. inactivation as a mechanism of selection against lethal alleles: Further investigation of incontinentia pigmenti and X linked lymphoproliferative disease. *J. Med. Genet.* **29**, 608–614 (1992). doi: [10.1136/jmg.29.9.608](https://doi.org/10.1136/jmg.29.9.608); pmid: [1404291](https://pubmed.ncbi.nlm.nih.gov/1404291/)
 28. D. Blanco-Melo *et al.*, Imbalanced Host Response to SARS-CoV-2 Drives Development of COVID-19. *Cell* **181**, 1036–1045.e9 (2020). doi: [10.1016/j.cell.2020.04.026](https://doi.org/10.1016/j.cell.2020.04.026); pmid: [32416070](https://pubmed.ncbi.nlm.nih.gov/32416070/)
 29. S. L. Klein *et al.*, Sex, age, and hospitalization drive antibody responses in a COVID-19 convalescent plasma donor population. *J. Clin. Invest.* **142**, 142004 (2020). doi: [10.1172/JCI142004](https://doi.org/10.1172/JCI142004); pmid: [32764200](https://pubmed.ncbi.nlm.nih.gov/32764200/)
 30. T. T. Wang, J. V. Ravetch, Functional diversification of IgGs through Fc glycosylation. *J. Clin. Invest.* **129**, 3492–3498 (2019). doi: [10.1172/JCI130029](https://doi.org/10.1172/JCI130029); pmid: [31478910](https://pubmed.ncbi.nlm.nih.gov/31478910/)
 31. P. D. Burbelo *et al.*, Sensitivity in Detection of Antibodies to Nucleocapsid and Spike Proteins of Severe Acute Respiratory Syndrome Coronavirus 2 in Patients With Coronavirus Disease 2019. *J. Infect. Dis.* **222**, 206–213 (2020). doi: [10.1093/infdis/jiaa273](https://doi.org/10.1093/infdis/jiaa273); pmid: [32427334](https://pubmed.ncbi.nlm.nih.gov/32427334/)
 32. S. Meyer *et al.*, AIRE-Deficient Patients Harbor Unique High-Affinity Disease-Ameliorating Autoantibodies. *Cell* **166**, 582–595 (2016). doi: [10.1016/j.cell.2016.06.024](https://doi.org/10.1016/j.cell.2016.06.024); pmid: [27426947](https://pubmed.ncbi.nlm.nih.gov/27426947/)
 33. K. Katoh, J. Rozewicki, K. D. Yamada, MAFFT online service: Multiple sequence alignment, interactive sequence choice and visualization. *Brief. Bioinform.* **20**, 1160–1166 (2019). doi: [10.1093/bib/bbx108](https://doi.org/10.1093/bib/bbx108); pmid: [28968734](https://pubmed.ncbi.nlm.nih.gov/28968734/)
 34. K. Katoh, K. Kuma, H. Toh, T. Miyata, MAFFT version 5: Improvement in accuracy of multiple sequence alignment. *Nucleic Acids Res.* **33**, 511–518 (2005). doi: [10.1093/nar/gki198](https://doi.org/10.1093/nar/gki198); pmid: [15661851](https://pubmed.ncbi.nlm.nih.gov/15661851/)
 35. N. Saitou, M. Nei, The neighbor-joining method: A new method for reconstructing phylogenetic trees. *Mol. Biol. Evol.* **4**, 406–425 (1987). doi: [10.1093/oxfordjournals.molbev.a040454](https://doi.org/10.1093/oxfordjournals.molbev.a040454); pmid: [3447015](https://pubmed.ncbi.nlm.nih.gov/3447015/)
 36. D. T. Jones, W. R. Taylor, J. M. Thornton, The rapid generation of mutation data matrices from protein sequences. *Comput. Appl. Biosci.* **8**, 275–282 (1992). doi: [10.1093/bioinformatics/8.3.275](https://doi.org/10.1093/bioinformatics/8.3.275); pmid: [1633570](https://pubmed.ncbi.nlm.nih.gov/1633570/)
 37. C. H. Woelk, S. D. W. Frost, D. D. Richman, P. E. Higley, S. L. Kosakovsky Pond, Evolution of the interferon alpha gene family in eutherian mammals. *Gene* **397**, 38–50 (2007). doi: [10.1016/j.gene.2007.03.018](https://doi.org/10.1016/j.gene.2007.03.018); pmid: [17512142](https://pubmed.ncbi.nlm.nih.gov/17512142/)
 38. M. V. Han, C. M. Zmasek, phyloXML: XML for evolutionary biology and comparative genomics. *BMC Bioinformatics* **10**, 356 (2009). doi: [10.1186/1471-2105-10-356](https://doi.org/10.1186/1471-2105-10-356); pmid: [19860910](https://pubmed.ncbi.nlm.nih.gov/19860910/)
 39. S. Pestka, C. D. Krause, M. R. Walter, Interferons, interferon-like cytokines, and their receptors. *Immunol. Rev.* **202**, 8–32 (2004). doi: [10.1111/j.0105-2896.2004.00204.x](https://doi.org/10.1111/j.0105-2896.2004.00204.x); pmid: [15546383](https://pubmed.ncbi.nlm.nih.gov/15546383/)
 40. D. M. Rissin *et al.*, Single-molecule enzyme-linked immunosorbent assay detects serum proteins at subfemtomolar concentrations. *Nat. Biotechnol.* **28**, 595–599 (2010). doi: [10.1038/nbt.1641](https://doi.org/10.1038/nbt.1641); pmid: [20495550](https://pubmed.ncbi.nlm.nih.gov/20495550/)
 41. A. Mathian *et al.*, Monitoring Disease Activity in Systemic Lupus Erythematosus With Single-Molecule Array Digital Enzyme-Linked Immunosorbent Assay Quantification of Serum Interferon- α . *Arthritis Rheumatol.* **71**, 756–765 (2019). doi: [10.1002/art.40792](https://doi.org/10.1002/art.40792); pmid: [30507062](https://pubmed.ncbi.nlm.nih.gov/30507062/)
 42. P. Lebon, G. Ponsot, J. Aicardi, F. Goutières, M. Arthuis, Early intrathecal synthesis of interferon in herpes encephalitis. *Biomedicine* **31**, 267–271 (1979). pmid: [94549](https://pubmed.ncbi.nlm.nih.gov/94549/)
 43. D. F. Robbiani *et al.*, Convergent antibody responses to SARS-CoV-2 in convalescent individuals. *Nature* **584**, 437–442 (2020). doi: [10.1038/s41586-020-2456-9](https://doi.org/10.1038/s41586-020-2456-9); pmid: [32555388](https://pubmed.ncbi.nlm.nih.gov/32555388/)
 44. H. Kim *et al.*, Development of a Validated Interferon Score Using NanoString Technology. *J. Interferon Cytokine Res.* **38**, 171–185 (2018). doi: [10.1089/jir.2017.0127](https://doi.org/10.1089/jir.2017.0127); pmid: [29638206](https://pubmed.ncbi.nlm.nih.gov/29638206/)
 45. J. P. Ferreira *et al.*, Cohort Profile: Rationale and design of the fourth visit of the STANISLAS cohort: a familial longitudinal population-based cohort from the Nancy region of France. *Int. J. Epidemiol.* **47**, 395–395j (2018). doi: [10.1093/ije/dyx240](https://doi.org/10.1093/ije/dyx240); pmid: [29220499](https://pubmed.ncbi.nlm.nih.gov/29220499/)

ACKNOWLEDGMENTS

We thank the patients, their families, and healthy donors for placing their trust in us. We thank the French Incontinentia pigmenti association for their help and support. We thank Y. Nemirovskaya, D. Papandrea, M. Woollett, D. Liu, C. Rivalain, and C. Patissier for administrative assistance; D. Kapogiannis (National Institute on Aging) for providing healthy donor samples; B. Xirasager, J. Barnett, X. Cheng, S. Weber, J. Danielson, B. Garabedian, and H. Matthews for their assistance in this study. We also thank R. Apps, B. Ryan, and Y. Belkaid of the CHI for their assistance. We thank the CRB-Institut Jérôme Lejeune, CRB-BioLeL, Paris, France, for their assistance. We thank

M. C. García Guerrero; I. Erkiia; E. Grau; M. Massanella from IrsiCaixa AIDS Research Institute, Badalona, Spain; and J. Guitart from the Department of Clinical Genetics, University Hospital Germans Trias i Pujol, Badalona, Spain, for providing samples. We also thank J. Dalmau from IrsiCaixa for assistance. **Funding:** The Laboratory of Human Genetics of Infectious Diseases is supported by the Howard Hughes Medical Institute, The Rockefeller University, the St. Giles Foundation, the National Institutes of Health (NIH) (R01AI088364), the National Center for Advancing Translational Sciences (NCATS), NIH Clinical and Translational Science Award (CTSA) program (UL1 TR001866), a Fast Grant from Emergent Ventures, the Mercatus Center at George Mason University, the Yale Center for Mendelian Genomics and the GSP Coordinating Center funded by the National Human Genome Research Institute (NHGRI) (UMIHG006504 and U24HG008956), the French National Research Agency (ANR) under the Investments for the Future program (ANR-10-IAHU-01), the Integrative Biology of Emerging Infectious Diseases Laboratory of Excellence (ANR-10-LABX-62-IBED), the French Foundation for Medical Research (FRM) (EQU201903007798), the FRM and ANR GENCOV project (ANRS-COV05), the Square Foundation, Grandir – Fonds de solidarité pour l'enfance, the SCOR Corporate Foundation for Science, the Institut National de la Santé et de la Recherche Médicale (INSERM), and the University of Paris. Samples from San Raffaele Hospital were obtained through the Covid-BioB project and by healthcare personnel of San Raffaele Hospital, San Raffaele Telethon Institute for Gene Therapy (SR-TIGET) clinical laboratory and clinical research unit, funded by the Program Project COVID-19 OSR-UniSR and Fondazione Telethon. The French COVID Cohort Study Group was sponsored by INSERM and supported by the REACTing consortium and by a grant from the French Ministry of Health (PHRC 20-0424). The Cov-Contact Cohort was supported by the REACTing consortium, the French Ministry of Health, and the European Commission (RECOVER WP 6). The Milieu Intérieur Consortium was supported by the French Government's Investissement d'Avenir program, Laboratoire d'Excellence Milieu Intérieur grant (ANR-10-LABX-69-01) (primary investigators: L.Q.-M. and D.Du.). The Simoa experiment was supported by the PHRC 20-0375 COVID-19 grant "DIGITAL COVID" (primary investigator: G.G.). S.G.T. is supported by a Leadership 3 Investigator Grant awarded by the National Health and Medical Research Council of Australia and a COVID19 Rapid Response Grant awarded by UNSW Sydney. C.R.-G. and colleagues were supported by the Instituto de Salud Carlos III (COV20_01333 and COV20_01334, Spanish Ministry of Science and Innovation RTC-2017-6471-1; AEI/FEDER, UE) and Cabildo Insular de Tenerife (CGIEU0000219140 and "Apuestas científicas del ITER para colaborar en la lucha contra la COVID-19"). S.T.-A. and A.B. were supported by ANR-20-COVI-0064 (primary investigator: A.Be.). This work is supported by the French Ministry of Health "Programme Hospitalier de Recherche Clinique Inter régional 2013", by the Contrat de Plan Etat-Lorraine and FEDER Lorraine, and by a public grant overseen by the French National Research Agency (ANR) as part of the second Investissements d'Avenir program FIGHT-HF (reference no. ANR-15-RHU-0004) and by the French PIA project "Lorraine Université d'Excellence" (reference no. ANR-15-IDEX-04-LUE) (45); and biobanking is performed by the Biological Resource Center Lorrain BB-0033-00035. This study was supported by the Fonds IMMUNOV, for Innovation in Immunopathology; by a grant from the Agence Nationale de la Recherche (ANR-flash Covid19 "AIROCovid" to F.R.-L.); and by the FAST Foundation (French Friends of Sheba Tel Hashomer Hospital). Work in the Laboratory of Virology and Infectious Disease was supported by NIH grants P01AI138398-S1, 2U19AI111825, and R01AI091707-10S1; a George Mason University Fast Grant; and the G. Harold and Leila Y. Mathers Charitable Foundation. The Amsterdam UMC Covid-19 Biobank was supported by grants from the Amsterdam Corona Research Fund, the Dr. C.J. Vaillant Fund, and the Netherlands Organization for Health Research and Development [ZonMw; NWO-Vici-Grant (grant no. 918-19-627 to D.v.d.B.)]. This work was also supported by the Division of Intramural Research of the National Institute of Dental Craniofacial Research and the National Institute of Allergy and Infectious Diseases, National Institutes of Health, and by Regione Lombardia, Italy (project "Risposta immune in pazienti con COVID-19 e comorbidità"). The opinions and assertions expressed herein are those of the author(s) and do not necessarily reflect the official policy or position of the Uniformed Services University or the Department of Defense. J.H. holds an Institut Imagine M.D.-Ph.D. fellowship from the Fondation Bettencourt Schueller. J.R. is supported by the INSERM Ph.D. program ("poste d'accueil Inserm"). P.B.a. was supported by the French Foundation for Medical Research (FRM, EA20170638020) and the M.D.-Ph.D. program

of the Imagine Institute (with the support of the Fondation Bettencourt-Schueller). We thank the Association "Turner et vous" for their help and support. Sample processing at IrsiCaixa was possible thanks to the crowdfunding initiative YoMeCorono. D.C.V. is supported by the Fonds de la recherche en santé du Québec clinician-scientist scholar program. K.K. was supported by the Estonian Research Council grant PUT1367. We thank the GEN-COVID Multicenter Study (<https://sites.google.com/dbm.unisi.it/gen-covid>). We thank the NIAID Office of Cyber Infrastructure and Computational Biology, Bioinformatics and Computational Biosciences Branch (contract no. HHSN316201300006W/HHSN27200002 to MSC, Inc.), the Operations Engineering Branch for developing the HGRRepo system to enable streamlined access to the data, and the NCI Advanced Biomedical Computational Science (ABCS) for data transformation support. Biomedical Advanced Research and Development Authority was supported under contract no. HHS010201600031C (to J.H.). Financial support was provided by the National Institute of Allergy and Infectious Diseases (NIAID) K08AI135091; the Burroughs Wellcome Fund CAMS; the Clinical Immunology Society; and the American Academy of Allergy, Asthma, and Immunology. **Author contributions:** P.Ba., L.B.R., Q.Z., E.M., H.-H.H., Y.Z., K.Dor., Q.P., J.R., V.B., J.Ma., E.S., L.H., P.P., L.L., L.B., S.T.-A., K.Dob., A.A.d.J., A.Be., L.P., D.D., E.S.H., J.S.T., R.G.-M., K.K., A.P., S.-Y.Z., S.M.H., G.G., E.J., C.M.R., L.D.N., H.C.S., and J.-L.C. performed or provided supervision of experiments, generated and analyzed data, and contributed to the manuscript by providing figures and tables. J.L.P., G.K., B.B., Y.S., R.Y., A.B., K.B., R.P.L., M.M., A.C., and L.A. performed computational analysis of data. P.Ba., A.K., E.C., Y.T.-L., A.N.S., O.M.D., M.S.A., A.A., G.C., V.L., F.C., M.V., D.M.S., J.H., B.T., D.Du., L.Q.-M., D.v.d.B., L.R., D.C.V., S.G.T., F.H., D.Da., T.H.M., P.Br., J.M.-P., M.C.N., S.B.-D., C.R.-G., G.V., A.J.O., J.Gu., P.D.B., J.I.C., A.B., L.R.B., M.D.A., P.Ba., P.R., F.R.-L., F.F., M.V.U., L.I., A.S., S.P., E.Q.-R., C.R., R.C., D.M., A.L., G.L.M., X.D., J.Gh., M.S.L., and G.G. evaluated and recruited patients to COVID and/or control cohorts of patients. P.Ba. and J.-L.C. wrote the manuscript. J.-L.C. supervised the project. All authors edited the manuscript. **Competing interests:** H.C.S. is adjunct faculty at the University of Pennsylvania. J.-L.C. is listed as an inventor on patent application U.S. 63/055,155 filed by The Rockefeller University that encompasses aspects of this publication. R.P.L. is a nonexecutive director of Roche and its subsidiary Genentech. The authors declare no other competing interests. **Data and materials availability:** All data are available in the manuscript or in the supplementary materials. Plasma, cells, and genomic DNA are available from J.-L.C. or D.C.V. under a material transfer agreement with The Rockefeller University and the Research Institute-McGill University Health Centre. HuH7.5 cells are available on request from C.M.R. under a material transfer agreement with The Rockefeller University and Apath, LLC. Materials and reagents used are almost exclusively commercially available and nonproprietary. Requests for materials derived from human samples may be made available, subject to any underlying restrictions on such samples. J.-L.C. can make material transfer agreements available through The Rockefeller University. This work is licensed under a Creative Commons Attribution 4.0 International (CC BY 4.0) license, which permits unrestricted use, distribution, and reproduction in any medium, provided the original work is properly cited. To view a copy of this license, visit <https://creativecommons.org/licenses/by/4.0/>. This license does not apply to figures/photos/artwork or other content included in the article that is credited to a third party; obtain authorization from the rights holder before using such material.

SUPPLEMENTARY MATERIALS

science.sciencemag.org/content/370/6515/eabd4585/suppl/DC1
Supplementary Materials and Methods

Figs. S1 to S4

Tables S1 to S3

Data S1

[View/request a protocol for this paper from Bio-protocol.](#)

HGID Lab Andrés Augusto Arias^{1,3}, Bertrand Boisson^{1,2}, Soraya Bouchier², Jacinta Bustamante^{1,2}, Marwa Chbihi², Jie Chen¹, Maya Chrabieh², Tatiana Kochetkov¹, Tom Le Voyer², Dana Liu¹, Yelena Nemirovskaya², Masato Ogishi¹, Dominick Papandrea², Cécile Patissier², Franck Rapaport¹, Manon Roynard², Natasha Vladikine², Mark Woollett¹, Peng Zhang¹

¹St. Giles Laboratory of Human Genetics of Infectious Diseases, Rockefeller Branch, The Rockefeller University, New York, NY, USA.

²Laboratory of Human Genetics of Infectious Diseases, Necker

Branch, INSERM U1163, Necker Hospital for Sick Children, Paris, France. ³School of Microbiology and Group of Primary Immunodeficiencies, University of Antioquia UdeA, Medellín, Colombia.

NIAID-USUHS Immune Response to COVID Group Anuj Kashyap¹, Li Ding¹, Marita Bosticardo¹, Qinlu Wang², Sebastian Ochoa¹, Hui Liu¹, Samuel D. Chauvin³, Michael Stack¹, Galina Koroleva⁴, Neha Bansal⁵, Clifton L. Dalgard^{6,7}, Andrew L. Snow⁸

¹Laboratory of Clinical Immunology and Microbiology, Division of Intramural Research, NIAID, NIH, Bethesda, MD, USA. ²Bioinformatics and Computational Biosciences Branch, NIAID Office of Cyber Infrastructure and Computational Biology, NIAID, NIH, Bethesda, MD, USA. ³Laboratory of Immune System Biology, Division of Intramural Research, NIAID, NIH, Bethesda, MD, USA. ⁴NIH Center for Human Immunology, NIH, Bethesda, MD, USA. ⁵Multiscale Systems Biology Section, Laboratory of Immune System Biology, NIAID, NIH, Bethesda, MD, USA. ⁶PRIMER, Uniformed Services University of the Health Sciences, Bethesda, MD, USA. ⁷Department of Anatomy, Physiology & Genetics, Uniformed Services University of the Health Sciences, Bethesda, MD, USA. ⁸Department of Pharmacology & Molecular Therapeutics, Uniformed Services University of the Health Sciences, Bethesda, MD, USA.

COVID Clinicians Jorge Abad¹, Sergio Aguilera-Albesa², Ozge Metin Akcan³, Ilad Alavi Darazam⁴, Juan C. Alkan⁵, Miquel Alfonso Ramos⁵, Seyed Alireza Nadi¹, Gulsun Altan⁸, Jerome Allardet-Servent⁹, Luis M. Allende¹⁰, Laia Alsina¹¹, Marie-Alexandra Alyanaki¹², Blanca Amador-Borrero¹³, Zahir Amoura¹⁴, Arnau Antol¹⁵, Sveklet Arslan¹⁶, Sophie Assant¹⁷, Terese Auguet¹⁸, Axelle Azot¹⁹, Fanny Bajolle²⁰, Aurélie Baldoli²¹, Maite Ballester²², Hagit Baris Feldman²³, Benoit Barrou²⁴, Alexandra Beuron²⁵, Agurtzane Bilbao²⁶, Geraldine Blanchard-Rohner²⁷, Ignacio Blanco¹, Adeline Blandinières²⁸, Daniel Blazquez-Garnero²⁹, Marketa Bloomfield³⁰, Mireia Bolivar-Prados³¹, Raphael Borie³², Ahmed A. Boufhi³³, Claire Bouvattier³⁴, Oksana Boyarchuk³⁵, Maria Rita P. Bueno³⁶, Jacinta Bustamante²⁰, Juan José Cáceres Agra³⁷, Semra Calimli³⁸, Ruggero Capra³⁹, Maria Carrabba⁴⁰, Carlos Casanovas⁴¹, Marion Caseris⁴², Martin Castelle⁴³, Francesco Castelli⁴⁴, Martín Castillo de Vera⁴⁵, Mateus V. Castro⁴⁶, Emilie Catherine⁴⁶, Martin Chalumeau⁴⁷, Bruno Charbit⁴⁸, Matthew P. Cheng⁴⁹, Père Clavé⁵¹, Bonaventura Clotet⁵⁰, Anna Codina⁵¹, Fatih Colkesen⁵², Fatma Colkesen⁵³, Roger Colobran⁵⁴, Clóé Comarmond⁵⁵, Angelo G. Corsico⁵⁶, David Dalmau⁵⁷, David Ross Darley⁵⁸, Nicolas Dauby⁵⁹, Stéphane Dager⁶⁰, Loïc de Pontual⁶¹, Amin Dehban⁶², Geoffroy Delplanq⁶³, Alexandre Demoule⁶⁴, Antonio Di Sabatino⁶⁵, Jean-Luc Diehl⁶⁶, Stephanie Dobbela⁶⁷, Sophie Durand⁶⁸, Waleed Eldars⁶⁹, Mohamed Elgamal⁷⁰, Marwa H. Elmagdy⁷¹, Melike Emiroglu⁷², Emine Hafize Erdeniz⁷³, Selma Erol Aytekin⁷⁴, Romain Euvard⁷⁵, Recep Evcen⁷⁶, Giovanna Fabio⁴⁰, Laurence Faivre⁷⁷, Antonin Falck⁴², Muriel Fartoukh⁷⁸, Morgane Faure⁷⁹, Miguel Fernandez Arquer⁸⁰, Carlos Flores⁸¹, Bruno Francois⁸², Victoria Fumadó⁸³, Francesca Fusco⁸⁴, Blanca Garcia Solis⁸⁵, Pascale Gaussem⁸⁶, Juana Gil-Herrera⁸⁷, Laurent Gilardin⁸⁸, Mónica Girona Alarcón⁸⁹, Mónica Girona-Alarcón⁸⁹, Jean-Christophe Goffard⁹⁰, Funda Gök⁹¹, Rafaela González-Montelongo⁹², Antoine Guerdier⁹³, Yahya Gul⁹⁴, Sukru Nail Guner⁹⁴, Marta Gut⁹⁵, Jérôme Hadjad⁹⁶, Filomeen Haerynck⁹⁷, Rabih Halwan⁹⁸, Lennart Hammarström⁹⁹, Nevin Hatipoglu¹⁰⁰, Elisa Hernandez-Brito¹⁰¹, María Soledad Holanda-Peña¹⁰², Juan Pablo Horcajada¹⁰³, Sami Iraiech¹⁰⁴, Linda Humbert¹⁰⁵, Alejandro D. Iglesias¹⁰⁶, Antonio Íñigo-Campos⁹², Matthieu Jamme¹⁰⁷, María Jesús Arranz¹⁰⁸, Iolanda Jordan¹⁰⁹, Fikret Kanat¹¹⁰, Hasan Kapakli¹¹¹, Iskender Kara¹¹², Adem Karbuz¹¹³, Kadriye Kart Yasar¹¹⁴, Sevgi Keles¹¹⁵, Yasemin Kendir Demirkol¹¹⁶, Adam Klocperk¹¹⁷, Zbigniew J. Król¹¹⁸, Paul Kuentz¹¹⁹, Yat Wah M. Kwan¹²⁰, Jean-Christophe Lagier¹²¹, Yu-Lun Lau¹²², Fleur Le Bourgeois⁶⁰, Yee-Sin Leo¹²³, Rafael Leon Lopez¹²⁴, Daniel Leung¹²², Michael Levin¹²⁵, Michael Levy⁶⁰, Romain Lévy²⁰, Zhi Li⁴⁸, Agnes Lingralt¹²⁶, José M. Lorenzo-Salazar⁹², Céline Louapre¹²⁷, Catherine Lubetzki¹²⁷, Charles-Edouard Luyt¹²⁸, David C. Lye¹²⁹, Davood Mansouri¹³⁰, Majid Marjani¹³¹, Jesus Marquez Pereira¹³², Andrea Martin¹³³, David Martínez Pueyo¹³⁴, Javier Martínez-Picado¹³⁵, Iciar Marzana¹³⁶, Alexis Mathian¹⁴, Larissa R. B. Matos³⁶, Gail V. Matthews¹³⁷, Julien Mayaux¹³⁸, Jean-Louis Mége¹³⁹, Isabelle Melki¹⁴⁰, Jean-François Meritet¹⁴¹, Ozge Metin¹⁴², Isabelle Meyts¹⁴³, Mehdi Mezidi¹⁴⁴, Isabelle Migeotte¹⁴⁵, Maude Millereux¹⁴⁶, Tristan Miralet¹⁴⁷, Clotilde Mircher⁶⁸, Mehdi Mirsaedi¹⁴⁸, Abián Montesdeoca Melián¹⁴⁹, Antonio Morales Martínez¹⁵⁰, Pierre Morange¹⁵¹, Clémence Mordacq¹⁰⁵, Guillaume Morelle¹⁵², Stéphane Mouly¹³, Adrián Muñoz-Barrera⁹², Cyril Nafati¹⁵³, João Farelá Neves¹⁵⁴, Lisa F. P. Ng¹⁵⁵

Yeray Novoa Medina¹⁵⁶, Esmeralda Nuñez Cuadros¹⁵⁷, J. Gonzalo Ochoa-Vinyals¹⁵⁸, Zerrin Orbak¹⁵⁹, Mehdi Qualha²⁰, Tayfun Özçelik¹⁶⁰, Qiang Pan Hammarström¹⁶¹, Christophe Parizot¹⁶², Tiffany Pascreau¹⁶², Estela Paz-Artal¹⁶³, Rebeca Pérez de Diego⁸⁵, Aurélien Philippe¹⁶⁴, Quentin Philippot⁷⁸, Laura Planas-Serra¹⁶⁵, Dominique Poin¹⁶⁶, Julien Poissy¹⁶⁷, Géraldine Poncelet⁴², Marie Pouletty¹⁶⁸, Paul Quentric¹³⁸, Didier Raoult¹³⁹, Anne-Sophie Rebillat⁶⁸, Ismail Reisli¹⁶⁹, Pilar Ricart¹⁷⁰, Jean-Christophe Richard¹⁷¹, Nadia Rivet²⁸, Jacques G. Rivière¹⁷², Gemma Rocamora Blanchi¹⁵, Carlos Rodrigo¹, Carlos Rodríguez-Gallego¹⁷³, Agustí Rodríguez-Palmero¹⁷⁴, Carolina Soledad Romero¹⁷⁵, Anya Rothenbuhler¹⁷⁶, Flore Rozenberg⁷⁷, María Yolanda Ruiz del Prado⁷⁸, Joan Sabater Riera¹⁵, Oliver Sanchez¹⁷⁹, Silvia Sánchez-Ramón¹⁸⁰, Agatha Schluter¹⁸¹, Matthieu Schmidt¹⁸¹, Cyril E. Schweitzer¹⁸², Francesco Scolari¹⁸³, Anna Sediva¹⁸⁴, Luis M. Seijó¹⁸⁵, Damien Sene¹³, Sevtpat Senoglu¹¹⁴, Mikko R. J. Seppänen¹⁸⁶, Alex Serra Illovis¹⁸⁷, Mohammad Shahrooei⁶², David Smadja¹⁸⁸, Ali Sobh¹⁸⁹, Xavier Solanich Moreno¹⁵, Jordi Solé-Violán¹⁹⁰, Catherine Soler¹⁹¹, Pere Soler-Palacin¹³³, Yuri Stepanovskiy¹⁹², Annabelle Stoclin¹⁹³, Fabio Taccone¹⁴⁵, Yacine Tandjaoui-Lambiotte¹⁹⁴, Jean-Luc Taupin²⁵, Simon J. Tavernier¹⁹⁵, Benjamin Terrier¹⁹⁷, Caroline Thumerelle¹⁰⁵, Gabriele Tomasoni¹⁹⁸, Julie Toubiana⁴⁷, Josep Trenado Alvarez¹⁹⁹, Sophie Trouillet-Assant²⁰⁰, Jesús Troya²⁰¹, Alessandra Tucci²⁰², Matilde Valeria Ursini⁸⁴, Yurdagul Uzunhan²⁰³, Pierre Vabres²⁰⁴, Juan Valencia-Ramos²⁰⁵, Ana Maria Van Den Rym⁸⁵, Isabelle Vandernoot²⁰⁶, Hulya Vatansev²⁰⁷, Valentina Vélaz-Santamaria⁴¹, Sébastien Viel¹⁶⁶, Cédric Vianen²⁰⁸, Marie E. Vilaire⁶⁸, Audrey Vincent³⁴, Guillaume Voiriot²⁰⁹, Fanny Vuotto¹⁰⁵, Alper Yosunkaya⁹¹, Barnaby E. Young¹²³, Fatih Yucel¹⁰, Faiez Zannad²¹¹, Mayana Zatz²⁶, Alexandre Belot^{212*}

¹University Hospital and Research Institute "Germans Trias i Pujol", Badalona, Spain. ²Navarra Health Service Hospital, Pamplona, Spain. ³Division of Pediatric Infectious Diseases, Necmettin Erbakan University, Meram Medical Faculty, Konya, Turkey.

⁴Department of Infectious Diseases, Loghman Hakim Hospital, Shahid Beheshti University of Medical Sciences, Tehran, Iran.

⁵Hospital Nacional Edgardo Rebagliati Martins, Lima, Peru. ⁶Parc Sanitari Sant Joan de Déu, Sant Boi de Llobregat, Barcelona, Spain.

⁷Virology Research Center, National Institutes of Tuberculosis and Lung Diseases, Shahid Beheshti University of Medical Sciences, Tehran, Iran. ⁸Division of Pediatric Infectious Diseases, Faculty of Medicine, Selçuk University, Konya, Turkey. ⁹Intensive Care Unit, Hôpital Européen, Marseille, France. ¹⁰Immunology Department, University Hospital 12 de Octubre, Research Institute imas12, Complutense University, Madrid, Spain. ¹¹Hospital Sant Joan de Déu, Barcelona, Spain. ¹²Department of Biological Immunology, Necker Hospital for Sick Children, APHP and INEM, Paris, France.

¹³Internal Medicine Department, Hôpital Lariboisière, APHP; Université de Paris, Paris, France. ¹⁴Internal Medicine Department, Pitié-Salpêtrière Hospital, Paris, France. ¹⁵Hospital Universitari de Bellvitge, Barcelona, Spain. ¹⁶Division of Clinical Immunology and Allergy, Necmettin Erbakan University, Meram Medical Faculty, Konya, Turkey. ¹⁷Joint Research Unit, Hospices Civils de Lyon-bio Mérieux, Hospices Civils de Lyon, Lyon Sud Hospital, Lyon, France.

¹⁸Hospital Universitario de Tarragona Joan XXIII, Universitat Rovira i Virgili (URV), IISPV, Tarragona, Spain. ¹⁹Private practice, Paris, France. ²⁰Necker Hospital for Sick Children, AP-HP, Paris, France.

²¹Department of Infectious Diseases, CHU de Caen, Caen, France. ²²Consorcio Hospital General Universitario, Valencia, Spain.

²³The Genetics Institute, Tel Aviv Sourasky Medical Center and Sackler Faculty of Medicine, Tel Aviv University, Tel Aviv, Israel.

²⁴Department of Urology, Nephrology, Transplantation, APHP-SU, Sorbonne Université, INSERM U 1082, Paris, France. ²⁵Service de Médecine Intensive-Réanimation et Pneumologie, APHP Hôpital Pitié-Salpêtrière, Paris, France. ²⁶Cruces University Hospital, Bizkaia, Spain. ²⁷Pediatric Immunology and Vaccinology Unit, Geneva University Hospitals and Faculty of Medicine, Geneva, Switzerland. ²⁸Hematology, Georges Pompidou Hospital, APHP, Paris, France. ²⁹Pediatric Infectious Diseases Unit, Instituto de Investigación 12 de Octubre (imas12), Hospital Universitario 12 de Octubre, Madrid, Spain. ³⁰Department of Immunology, Motol University Hospital, 2nd Faculty of Medicine, Charles University, Department of Pediatrics, Thomayer's Hospital, 1st Faculty of Medicine, Charles University, Prague, Czech Republic. ³¹Centro de Investigación Biomédica en Red de Enfermedades Hepáticas y Digestivas (Ciberhd), Hospital de Mataró, Consorcio Sanitari del Maresme, Mataró, Spain. ³²Service de Pneumologie, Hôpital Bichat, APHP, Paris, France. ³³Clinical Immunology Unit, Pediatric Infectious Disease Department, Faculty of Medicine and Pharmacy, Averroes University Hospital, LÍCIA Laboratório d'Immunologie clinique, d'inflammation et d'allergie, Hassani II University, Casablanca, Morocco. ³⁴Endocrinology Unit, APHP Hôpitaux

- Universitaires Paris-Sud, Le Kremlin-Bicêtre, France. ³⁵Department of Children's Diseases and Pediatric Surgery, I.Horbachevsky Ternopil National Medical University, Ternopil, Ukraine. ³⁶Human Genome and Stem-Cell Research Center, University of São Paulo, São Paulo, Brazil. ³⁷Hospital Insular, Las Palmas de Gran Canaria, Spain. ³⁸Division of Critical Care Medicine, Department of Anesthesiology and Reanimation, Konya State Hospital, Konya, Turkey. ³⁹MS Center, Spedali Civili, Brescia, Italy. ⁴⁰Fondazione IRCCS Ca' Granda Ospedale Maggiore Policlinico, Milan, Italy. ⁴¹Bellvitge University Hospital, L'Hospitalet de Llobregat, Barcelona, Spain. ⁴²Hopital Robert Debré, Paris, France. ⁴³Pediatric Immuno-hematology Unit, Necker Enfants Malades Hospital, AP-HP, Paris, France. ⁴⁴Department of Infectious and Tropical Diseases, University of Brescia, ASST Spedali Civili di Brescia, Brescia, Italy. ⁴⁵Doctoral Health Care Center, Canarian Health System, Las Palmas de Gran Canaria, Spain. ⁴⁶Hôpital Foch, Suresnes, France. ⁴⁷Necker Hospital for Sick Children, Paris University, AP-HP, Paris, France. ⁴⁸Pasteur Institute, Paris, France. ⁴⁹McGill University Health Centre, Montreal, Canada. ⁵⁰University Hospital and Research Institute "Germans Trias i Pujol", IrsiCaixa AIDS Research Institute, UVic-UCC, Badalona, Spain. ⁵¹Clinical Biochemistry, Pathology, Paediatric Neurology and Molecular Medicine Departments and Biobank, Institut de Recerca Sant Joan de Déu and CIBERER-ISCIII, Espilugues, Spain. ⁵²Division of Clinical Immunology and Allergy, Department of Internal Medicine, Necmettin Erbakan University, Meram Medical Faculty, Konya, Turkey. ⁵³Department of Infectious Diseases and Clinical Microbiology, Konya Training and Research Hospital, Konya, Turkey. ⁵⁴Hospital Universitari Vall d'Hebron, Barcelona, Spain. ⁵⁵Pitié-Salpêtrière Hospital, Paris, France. ⁵⁶Respiratory Diseases Division, IRCCS Policlinico San Matteo Foundation and University of Pavia, Pavia, Italy. ⁵⁷Fundació Docència i Recerca Mútua Terrassa, Barcelona, Spain. ⁵⁸UNSW Medicine, St Vincent's Clinical School; Department of Thoracic Medicine, St Vincent's Hospital Darlinghurst, Sydney, Australia. ⁵⁹CHU Saint-Pierre, Université Libre de Bruxelles (ULB), Brussels, Belgium. ⁶⁰Pediatric Intensive Care Unit, Robert-Debré University Hospital, APHP, Paris, France. ⁶¹Sorbonne Paris Nord, Hôpital Jean Verdier, APHP, Bondy, France. ⁶²Specialized Immunology Laboratory of Dr. Shahrooei, Sina Medical Complex, Ahvaz, Iran. ⁶³Centre de génétique humaine, CHU Besançon, Besançon, France. ⁶⁴Sorbonne Université Médecine and APHP Sorbonne Université site Pitié-Salpêtrière, Paris, France. ⁶⁵Department of Internal Medicine, Fondazione IRCCS Policlinico San Matteo, University of Pavia, Pavia, Italy. ⁶⁶Intensive Care Unit, Georges Pompidou Hospital, APHP, Paris, France. ⁶⁷Department of Pneumology, AZ Delta, Roeselare, Belgium. ⁶⁸Institut Jérôme Lejeune, Paris, France. ⁶⁹Department of Microbiology and Immunology, Faculty of Medicine, Mansoura University, Mansoura, Egypt. ⁷⁰Department of Chest, Faculty of Medicine, Mansoura University, Mansoura, Egypt. ⁷¹Department of Medical Biochemistry and Molecular Biology, Faculty of Medicine, Mansoura University, Mansoura, Egypt. ⁷²Faculty of Medicine, Division of Pediatric Infectious Diseases, Selcuk University, Konya, Turkey. ⁷³Division of Pediatric Infectious Diseases, Ondokuz Mayıs University, Samsun, Turkey. ⁷⁴Necmettin Erbakan University, Meram Medical Faculty, Division of Pediatric Allergy and Immunology, Konya, Turkey. ⁷⁵Centre Hospitalier Fleury, Bourg-en-Bresse, France. ⁷⁶Division of Clinical Immunology and Allergy, Department of Internal Medicine, Necmettin Erbakan University, Meram Medical Faculty, Konya, Turkey. ⁷⁷Centre de Génétique, CHU Dijon, Dijon, France. ⁷⁸APHP Tenon Hospital, Paris, France. ⁷⁹Sorbonne Universités, UPMC University of Paris, Paris, France. ⁸⁰Department of Clinical Immunology, Hospital Clínico San Carlos, Madrid, Spain. ⁸¹Genomics Division, Instituto Tecnológico y de Energías Renovables (ITER), Santa Cruz de Tenerife, Spain; CIBER de Enfermedades Respiratorias, Instituto de Salud Carlos III, Madrid, Spain; Research Unit, Hospital Universitario N.S. de Candelaria, Santa Cruz de Tenerife, Spain; Instituto de Tecnologías Biomédicas (ITB), Universidad de La Laguna, San Cristóbal de La Laguna, Spain. ⁸²CHU Limoges and Inserm CIC 1435 & UMR 1092, Limoges, France. ⁸³Infectious Diseases Unit, Department of Pediatrics, Hospital Sant Joan de Déu, Barcelona, Spain; Institut de Recerca Sant Joan de Déu, Spain; Universitat de Barcelona (UB), Barcelona, Spain. ⁸⁴Institute of Genetics and Biophysics 'Adriano Buzzati-Traverso', IGB-CNR, Naples, Italy. ⁸⁵Laboratory of Immunogenetics of Human Diseases, IdiPAZ Institute for Health Research, La Paz Hospital, Madrid, Spain. ⁸⁶Hematology, APHP, Hôpital Européen Georges Pompidou and Inserm UMR-S1140, Paris, France. ⁸⁷Hospital General Universitario and Instituto de Investigación Sanitaria "Gregorio Marañón", Madrid, Spain. ⁸⁸Bégin military Hospital, Bégin, France. ⁸⁹Pediatric Intensive Care Unit, Hospital Sant Joan de Déu, Barcelona, Spain. ⁹⁰Department of Internal Medicine, Hôpital Erasme, Université Libre de Bruxelles, Brussels, Belgium. ⁹¹Division of Critical Care Medicine, Department of Anesthesiology and Reanimation, Necmettin Erbakan University, Meram Medical Faculty, Konya, Turkey. ⁹²Genomics Division, Instituto Tecnológico y de Energías Renovables (ITER), Santa Cruz de Tenerife, Spain. ⁹³Assistance Publique Hôpitaux de Paris, Paris, France. ⁹⁴Division of Allergy and Immunology, Necmettin Erbakan University, Meram Medical Faculty, Konya, Turkey. ⁹⁵CNAG-CRG, Centre for Genomic Regulation (CRG), Barcelona Institute of Science and Technology (BIST); Universitat Pompeu Fabra (UPF), Barcelona, Spain. ⁹⁶Department of Internal Medicine, National Reference Center for Rare Systemic Autoimmune Diseases, AP-HP, APHP-CUP, Hôpital Cochin, Paris, France. ⁹⁷Ghent University Hospital, Ghent, Belgium. ⁹⁸Sharjah Institute of Medical Research, College of Medicine, University of Sharjah, Sharjah, United Arab Emirates. ⁹⁹Department of Biosciences and Nutrition, SE14183, Huddinge, Karolinska Institutet, Stockholm, Sweden. ¹⁰⁰Pediatric Infectious Diseases Unit, Bakirkoy Dr. Sadi Konuk Training and Research Hospital, University of Health Sciences, Istanbul, Turkey. ¹⁰¹Department of Immunology, Hospital Universitario de Gran Canaria Dr. Negrín, Canarian Health System, Las Palmas de Gran Canaria, Spain. ¹⁰²Intensive Care Unit, Marqués de Valdecilla Hospital, Santander, Spain. ¹⁰³Hospital del Mar, Parc de Salut Mar, Barcelona, Spain. ¹⁰⁴Intensive Care Unit, APHM, Marseille, France. ¹⁰⁵CHU Lille, Lille, France. ¹⁰⁶Department of Pediatrics, Columbia University, New York, NY, USA. ¹⁰⁷Centre Hospitalier Intercommunal Poissy Saint Germain en Laye, Poissy, France. ¹⁰⁸Fundació Docència i Recerca Mútua Terrassa, Barcelona, Spain. ¹⁰⁹Hospital Sant Joan de Déu, Kids Corona Platform, Barcelona, Spain. ¹¹⁰Selcuk University, Faculty of Medicine, Chest Diseases Department, Konya, Turkey. ¹¹¹Division of Allergy and Immunology, Balikesir Ataturk City Hospital, Balikesir, Turkey. ¹¹²Division of Critical Care Medicine, Selcuk University, Faculty of Medicine, Konya, Turkey. ¹¹³Division of Pediatric Infectious Diseases, Prof. Dr. Cemil Tascioglu City Hospital, Istanbul, Turkey. ¹¹⁴Departments of Infectious Diseases and Clinical Microbiology, Bakirkoy Dr. Sadi Konuk Training and Research Hospital, University of Health Sciences, Istanbul, Turkey. ¹¹⁵Meram Medical Faculty, Necmettin Erbakan University, Meram Medical Faculty, Konya, Turkey. ¹¹⁶Health Sciences University, Umraniye Education and Research Hospital, Istanbul, Turkey. ¹¹⁷Department of Immunology, 2nd Faculty of Medicine, Charles University and University Hospital in Motol, Prague, Czech Republic. ¹¹⁸Central Clinical Hospital of Ministry of the Interior and Administration in Warsaw, Warsaw, Poland. ¹¹⁹Oncobiologie Génétique Bioinformatique, PC Bio, CHU Besançon, Besançon, France. ¹²⁰Paediatric Infectious Disease Unit, Hospital Authority Infectious Disease Center, Princess Margaret Hospital, Hong Kong (Special Administrative Region), China. ¹²¹Aix Marseille Univ, IRD, MEPHI, IHU Méditerranée Infection, Marseille, France. ¹²²Department of Paediatrics and Adolescent Medicine, The University of Hong Kong, Hong Kong, China. ¹²³National Centre for Infectious Diseases, Singapore. ¹²⁴Hospital Universitario Reina Sofía, Cordoba, Spain. ¹²⁵Imperial College, London, UK. ¹²⁶Endocrinology and diabetes for children, AP-HP, Bicêtre Paris-Saclay Hospital, Le Kremlin-Bicêtre, France. ¹²⁷Neurology Unit, APHP Pitié-Salpêtrière Hospital, Paris University, Paris, France. ¹²⁸Intensive Care Unit, APHP Pitié-Salpêtrière Hospital, Paris University, Paris, France. ¹²⁹National Centre for Infectious Diseases; Tan Tock Seng Hospital; Yong Loo Lin School of Medicine; Lee Kong Chian School of Medicine, Singapore. ¹³⁰Department of Clinical Immunology and Infectious Diseases, National Research Institute of Tuberculosis and Lung Diseases, Shahid Beheshti University of Medical Sciences, Tehran, Iran. ¹³¹Clinical Tuberculosis and Epidemiology Research Center, National Research Institute of Tuberculosis and Lung Diseases (NRITLD), Shahid Beheshti University of Medical Sciences, Tehran, Iran. ¹³²Hospital Sant Joan de Déu and University of Barcelona, Barcelona, Spain. ¹³³Pediatric Infectious Diseases and Immunodeficiencies Unit, Hospital Universitari Vall d'Hebron, Vall d'Hebron Research Institute, Vall d'Hebron Barcelona Hospital Campus, Universitat Autònoma de Barcelona (UAB), Barcelona, Spain. ¹³⁴Hospital Universitari Mútua de Terrassa, Universitat de Barcelona, Barcelona, Spain. ¹³⁵IrsiCaixa AIDS Research Institute, ICREA, UVic-UCC, Research Institute "Germans Trias i Pujol", Badalona, Spain. ¹³⁶Department of Laboratory, Cruces University Hospital, Barakaldo, Bizkaia, Spain. ¹³⁷University of New South Wales, Darlinghurst, NSW, Australia. ¹³⁸APHP Pitié-Salpêtrière Hospital, Paris, France. ¹³⁹Aix-Marseille University, APHM, Marseille, France. ¹⁴⁰Robert Debré Hospital, Paris, France. ¹⁴¹APHP Cochin Hospital, Paris, France. ¹⁴²Necmettin Erbakan University Meram Faculty of Medicine Department of Pediatric Infectious Diseases, Konya, Turkey. ¹⁴³University Hospitals Leuven, Leuven, Belgium. ¹⁴⁴Hospices Civils de Lyon, Hôpital de la Croix-Rousse, Lyon, France. ¹⁴⁵Hôpital Erasme, Brussels, Belgium. ¹⁴⁶CH Gonesse, Gonesse, France. ¹⁴⁷Vascular Medicine, Georges Pompidou Hospital, APHP, Paris, France. ¹⁴⁸Division of Pulmonary and Critical Care, University of Miami, Miami, FL, USA. ¹⁴⁹Guanarteme Health Care Center, Canarian Health System, Las Palmas de Gran Canaria, Spain. ¹⁵⁰Regional University Hospital of Málaga, Málaga, Spain. ¹⁵¹Aix-Marseille Université, Marseille, France. ¹⁵²Department of General Paediatrics, Hôpital Bicêtre, AP-HP, University of Paris Saclay, Le Kremlin-Bicêtre, France. ¹⁵³CHU de La Timone, Marseille, France. ¹⁵⁴Centro Hospitalar Universitário de Lisboa Central, Lisbon, Portugal. ¹⁵⁵Infectious Diseases Horizontal Technology Centre, A*STAR; Singapore Immunology Network, A*STAR, Singapore. ¹⁵⁶Department of Pediatrics, Complejo Hospitalario Universitario Insular-Materno Infantil, Canarian Health System, Las Palmas de Gran Canaria, Spain. ¹⁵⁷Regional University Hospital of Málaga, Málaga, Spain. ¹⁵⁸Hospital Universitario Marqués de Valdecilla, Santander, Spain. ¹⁵⁹Ataturk University Medical Faculty, Erzurum, Turkey. ¹⁶⁰Bilkent University, Department of Molecular Biology and Genetics, Ankara, Turkey. ¹⁶¹Department of Laboratory Medicine, Karolinska Institutet, SE14186, Stockholm, Sweden. ¹⁶²L'Hôpital Foch, Suresnes, France. ¹⁶³Department of Immunology, Hospital Universitario 12 de Octubre, Instituto de Investigación Sanitaria Hospital 12 de Octubre (imas12), Madrid, Spain. ¹⁶⁴APHP Hôpitaux Universitaires Paris-Sud, Le Kremlin-Bicêtre, France. ¹⁶⁵Neuro-metabolic Diseases Laboratory, IDIBELL-Hospital Duran i Reynals, Barcelona; CIBERER U759, ISCIII, Madrid, Spain. ¹⁶⁶Hospices Civils de Lyon, Lyon, France. ¹⁶⁷Université de Lille, Inserm U1285, CHU Lille, Paris, France. ¹⁶⁸Department of General Pediatrics, University Hospital Robert Debré, APHP, Paris, France. ¹⁶⁹Necmettin Erbakan University, Konya, Turkey. ¹⁷⁰Germans Trias i Pujol Hospital, Badalona, Spain. ¹⁷¹Medical Intensive Care Unit, Hôpital de la Croix-Rousse, Hospices Civils de Lyon, Lyon, France. ¹⁷²Pediatric Infectious Diseases and Immunodeficiencies Unit, Hospital Universitari Vall d'Hebron, Vall d'Hebron Research Institute, Vall d'Hebron Barcelona Hospital Campus, Barcelona, Spain. ¹⁷³Department of Immunology, Hospital Universitario de Gran Canaria Dr. Negrín, Canarian Health System, Las Palmas de Gran Canaria, Spain; University Fernando Pessoa Canarias, Las Palmas de Gran Canaria, Spain. ¹⁷⁴Neurometabolic Diseases Laboratory, IDIBELL-Hospital Duran i Reynals, Barcelona, Spain. ¹⁷⁵Consorcio Hospital General Universitario, Valencia, Spain. ¹⁷⁶APHP Hôpitaux Universitaires Paris-Sud, Paris, France. ¹⁷⁷Virology Unit, Université de Paris, Cochin Hospital, APHP, Paris, France. ¹⁷⁸Hospital San Pedro, Logroño, Spain. ¹⁷⁹Respiratory medicine, Georges Pompidou Hospital, APHP, Paris, France. ¹⁸⁰Department of Immunology, Hospital Clínico San Carlos, Madrid, Spain. ¹⁸¹Service de Médecine Intensive Réanimation, Institut de Cardiologie, Hôpital Pitié-Salpêtrière, Paris, France. ¹⁸²CHRU de Nancy, Hôpital d'Enfants, Vandoeuvre, France. ¹⁸³Chair of Nephrology, University of Brescia, Brescia, Italy. ¹⁸⁴Department of Immunology, 2nd Faculty of Medicine, Charles University and Motol University Hospital, Prague, Czech Republic. ¹⁸⁵Clínica Universidad de Navarra, Madrid, Spain. ¹⁸⁶HUS Helsinki University Hospital, Children and Adolescents, Rare Disease Center, and Inflammation Center, Adult Immunodeficiency Unit, Majakka, Helsinki, Finland. ¹⁸⁷Fundació Docència i Recerca Mútua Terrassa, Terrassa, Spain. ¹⁸⁸Hôpital Européen Georges Pompidou, Paris, France. ¹⁸⁹Department of Pediatrics, Faculty of Medicine, Mansoura University, Mansoura, Egypt. ¹⁹⁰Critical Care Unit, Hospital Universitario de Gran Canaria Dr. Negrín, Canarian Health System, Las Palmas de Gran Canaria, Spain. ¹⁹¹CHU de Saint Etienne, Saint-Priest-en-Jarez, France. ¹⁹²Shupky National Medical Academy for Postgraduate Education, Kiev, Ukraine. ¹⁹³Gustave Roussy Cancer Campus, Villejuif, France. ¹⁹⁴Intensive Care Unit, Avicenne Hospital, APHP, Bobigny, France. ¹⁹⁵Laboratory of Immunology and Histocompatibility, Saint-Louis Hospital, Paris University, Paris, France. ¹⁹⁶Department of Internal Diseases and Pediatrics, Primary Immune Deficiency Research Laboratory, Centre for Primary Immunodeficiency Ghent, Jeffrey Modell Diagnosis and Research Centre, Ghent University Hospital, Ghent, Belgium. ¹⁹⁷Department of Internal Medicine, Université de Paris, INSERM, U970, PARCC, F-75015, Paris, France. ¹⁹⁸First Division of Anesthesiology and Critical Care Medicine, University of Brescia, ASST Spedali Civili di Brescia, Brescia, Italy. ¹⁹⁹Intensive Care Department, Hospital Universitari Mútua Terrassa, Universitat Barcelona, Terrassa, Spain. ²⁰⁰Hospices Civils de Lyon, Lyon Sud Hospital, Lyon, France. ²⁰¹Infanta Leonor University Hospital, Madrid, Spain. ²⁰²Hematology Department, ASST Spedali Civili di Brescia, Brescia, Italy. ²⁰³Pneumologie, Hôpital Avicenne, APHP, INSERM U1272, Université Sorbonne Paris Nord, Bobigny, France. ²⁰⁴Dermatology Unit, Laboratoire GAD, INSERM UMR1231 LNC, Université de Bourgogne, Dijon, France. ²⁰⁵University Hospital of Burgos, Burgos, Spain. ²⁰⁶Center of Human Genetics, Hôpital Erasme, Université Libre de Bruxelles, Brussels, Belgium. ²⁰⁷Department of Chest Diseases, Necmettin Erbakan University,

Meram Medical Faculty, Konya, Turkey. ²⁰⁸CHU de Caen, Caen, France. ²⁰⁹Sorbonne Université, Service de Médecine Intensive Réanimation, Hôpital Tenon, Assistance Publique-Hôpitaux de Paris, Paris, France. ²¹⁰General Intensive Care Unit, Konya Training and Research Hospital, Konya, Turkey. ²¹¹CHU de Nancy, Nancy, France. ²¹²University of Lyon, CIRI, INSERM U1111, National Referee Centre RAISE, Pediatric Rheumatology, HFME, Hospices Civils de Lyon, Lyon, France. *Leader of the COVID-Clinicians group.

COVID-STORM Clinicians Giuseppe Foti¹, Giacomo Bellani¹, Giuseppe Citerio¹, Ernesto Contro¹, Alberto Pesci², Maria Grazia Valsecchi³, Marina Cazzaniga⁴

¹Department of Emergency, Anesthesia and Intensive Care, School of Medicine and Surgery, University of Milano-Bicocca, San Gerardo Hospital, Monza, Italy. ²Department of Pneumology, School of Medicine and Surgery, University of Milano-Bicocca, San Gerardo Hospital, Monza, Italy. ³Center of Bioinformatics and Biostatistics, School of Medicine and Surgery, University of Milano-Bicocca, San Gerardo Hospital, Monza, Italy. ⁴Phase I Research Center, School of Medicine and Surgery, University of Milano-Bicocca, San Gerardo Hospital, Monza, Italy.

Imagine COVID Group Christine Bole-Feyso¹, Stanislas Lyonnet^{1*}, Cécile Masson¹, Patrick Nitschke¹, Aurore Pouliet¹, Yoann Schmitt¹, Frederic Tores¹, Mohammed Zarhrate¹

¹Imagine Institute, Université de Paris, INSERM UMR 1163, Paris, France. *Leader of the Imagine COVID Group.

French COVID Cohort Study Group Laurent Abel¹, Claire Andrejak², François Angoulvant³, Delphine Bachelet⁴, Romain Basmaci⁵, Sylvie Behillini⁶, Marine Beluze⁷, Dehbia Benkerrouf⁸, Krishna Bhavsar⁴, François Bompard⁹, Lila Bouadma⁴, Maude Bouscambert¹⁰, Mireille Caralp¹¹, Minerva Cervantes-Gonzalez¹², Anissa Chair⁴, Alexandra Coelho¹³, Camille Couffignal⁴, Sandrine Couffin-Cadiegues¹⁴, Eric D'ortenzio¹², Charlene Da Silveira⁴, Marie-Pierre Debray⁴, Dominique Deplanque¹⁵, Diane Descamps¹⁶, Mathilde Desvallees¹⁷, Alpha Diallo¹⁸, Alphonsine Diout¹³, Céline Dorival⁸, François Dubos¹⁹, Xavier Duval⁴, Philippine Eloy⁴, Vincent V. E. Enouf²⁰, Hélène Esperou²¹, Marina Esposito-Farese⁴, Manuel Etienne²², Nadia Ettalhoui⁴, Nathalie Gault⁴, Alexandre Gaymar¹⁰, Jade Ghosn⁴, Tristan Gigante²³, Isabelle Gorenne⁴, Jérémie Guedj²⁴, Aurélie Hocht¹³, Isabelle Hoffmann⁴, Salma Jaafoura²¹, Ouifia Kafif⁴, Florentia Kaguelidou²⁵, Sabina Kali⁴, Antoine Khalil⁴, Coralie Khan¹⁷, Cédric Laouénan⁴, Samira Laribi⁴, Minh Le⁴, Quentin Le Hingrat⁴, Soizic Le Mestre¹⁸, Hervé Le Nagard²⁴, François-Xavier Lescuré⁴, Yves Lévy²⁶, Claire Levy-Marchal²⁷, Bruno Lina¹⁰, Guillaume Lings²⁴, Jean Christophe Lucet⁴, Denis Malvy²⁸, Marina Lambert¹³, France Mentré⁴, Noémie Mercier¹⁸, Amina Meziane⁸, Hugo Mouquet²⁰, Jimmy Mullaert⁴, Nadège Neant²⁴, Marion Noret²⁹, Justine Pages³⁰, Aurélie Papadopoulos²¹, Christelle Paul¹⁸, Nathan Peiffer-Smadja⁴, Ventislava Petrov-Sanchez³¹, Gilles Peytavin⁴, Olivier Picone³¹, Oriane Puéchal¹², Manuel Rosa-Calatrava¹⁰, Bénédicte Rossignol²³, Patrick Rossignol³², Carine Roy⁴, Marion Schneider⁴, Caroline Semaille¹², Nassima Si Mohammed⁴, Lysa Tagheret⁴, Coralie Tardivon⁴, Marie-Capucine Teller⁴, François Téoulé⁸, Olivier Terrier¹⁰, Jean-François Timsit⁴, Théo Treoux⁴, Christelle Tual³³, Sarah Tubiana⁴, Sylvie van der Werf³⁴, Noémie Vanel³⁵, Aurélie Veislinger³³, Benoît Visseaux¹⁶, Aurélie Wiedemann²⁶, Yazdan Yazdanpanah³⁶

¹Inserm UMR 1163, Paris, France. ²CHU Amiens, Amiens, France. ³Hôpital Necker, Paris, France. ⁴Hôpital Bichat, Paris, France. ⁵Hôpital Louis Mourrier, Colombes, France. ⁶Institut Pasteur, Paris, France. ⁷F-CRIN Partners Platform, AP-HP, Université de Paris, Paris, France. ⁸Inserm UMR 1136, Paris, France. ⁹Drugs for Neglected Diseases Initiative, Geneva, Switzerland. ¹⁰Inserm UMR 1111, Lyon, France. ¹¹Inserm Transfert, Paris, France. ¹²REACTing, Paris, France. ¹³Inserm UMR 1018, Paris, France. ¹⁴Inserm, Pôle Recherche Clinique, France. ¹⁵CIC 1403 Inserm-CHU Lille, Paris, France. ¹⁶Université de Paris, IAME, INSERM UMR 1137, AP-HP, University Hospital Bichat Claude Bernard, Virology, F-75018 Paris, France. ¹⁷Inserm UMR 1219, Bordeaux, France. ¹⁸ANRS, Paris, France. ¹⁹CHU Lille, Lille, France. ²⁰Pasteur Institute, Paris, France. ²¹Inserm sponsor, Paris, France. ²²Rouen - SMIT, France. ²³FCRIN INI-CRCT, Nancy, France. ²⁴Inserm UMR 1137, Paris, France. ²⁵Centre d'Investigation Clinique, Inserm CIC1426, Hôpital Robert Debré, Paris, France. ²⁶Inserm UMR 955, Créteil, France; Vaccine Research Institute (VRI), Paris, France. ²⁷F-CRIN INI-CRCT, Paris, France.

²⁸Bordeaux - SMIT, France. ²⁹RENARCI, Annecy, France. ³⁰Hôpital Robert Debré, Paris, France. ³¹Colombes - Louis Mourier - Gynécologie, Paris, France. ³²University of Lorraine, Plurithematic Clinical Investigation Centre Inserm CIC-P: 1433, Inserm U1116, CHRU Nancy Hopitaux de Brabois, F-CRIN INI-CRCT; (Cardiovascular and Renal Clinical Trialists), Nancy, France. ³³Inserm CIC-1414, Rennes, France. ³⁴Institut Pasteur, UMR 3569 CNRS, Université de Paris, Paris, France. ³⁵Hôpital la timone, Marseille, France. ³⁶Paris - Bichat - SMIT, France.

The Milieu Intérieur Consortium Laurent Abel¹, Andres Alcover², Hugues Aschard², Kalla Astrom³, Philippe Bousso², Pierre Bruhns², Ana Cumano², Caroline Demangel², Ludovic Deriano², James Di Santo², Françoise Dromer², Gérard Eberl², Jost Enninga², Jacques Fellay⁴, Ivo Gomperts-Boneca², Milena Hasan², Serge Herberg², Olivier Lantz⁶, Hugo Mouquet², Etienne Patin², Sandra Pellegrini², Stanislas Pol², Antonio Rausell⁸, Lars Rogge², Anavaj Sakuntabhai², Olivier Schwartz², Benno Schwickowski², Spencer Shorte², Frédéric Tangy², Antoine Toubert², Mathilde Tournier¹⁰, Marie-Noëlle Ungeheuer², Matthew L. Albert^{11*}, Darragh Duffy^{2*}, Lluís Quintana-Murci^{2*}

¹INSERM U1163, University of Paris, Imagine Institute, Paris, France. ²Pasteur Institute, Paris, France. ³Lund University, Lund, Sweden. ⁴EPFL, Lausanne, Switzerland. ⁵Université Paris 13, Paris, France. ⁶Curie Institute, Paris, France. ⁷Cochin Hospital, Paris, France. ⁸INSERM UMR 1163 – Institut Imagine, Paris, France. ⁹Hôpital Saint-Louis, Paris, France. ¹⁰Sorbonne Paris Nord University, Inserm U1153, Inrae U1125, Cnam, Nutritional Epidemiology Research Team (EREN), Bobigny, France. ¹¹In Sitro, San Francisco, CA, USA. *Co-coordinators of The Milieu Intérieur Consortium. Additional information can be found at: www.milieuinterieur.fr/en.

CoV-Contact Cohort Loubna Alavoine¹, Karine K. A. Amat², Sylvie Behillini³, Julia Bielicki⁴, Patricia Bruining⁵, Charles Burdet⁶, Eric Caumes⁷, Charlotte Charpentier⁸, Bruno Coignard⁹, Yolande Costa¹, Sandrine Couffin-Cadiegues¹⁰, Florence Diamond⁸, Aline Dechanet¹¹, Christelle Delmas¹⁰, Diane Descamps⁸, Xavier Duval¹, Jean-Luc Ecobichon¹, Vincent Enouf³, Hélène Espérou¹⁰, Wahiba Frezouls¹, Nadhira Houhou¹, Emilia Ilic-Habensuss¹, Ouifia Kafif¹, John Kikoin¹¹, Quentin Le Hingrat⁸, David Lebeaux²², Anne Leclercq³, Jonathan Lecauch¹, Sophie Letrou¹, Bruno Lina¹³, Jean-Christophe Lucet⁴, Denis Malvy¹⁵, Pauline Manchon¹¹, Milica Mandic¹, Mohamed Meghadecha¹⁶, Justina Motiejunaite¹⁷, Mariama Nouroudine¹, Valentine Piquard¹¹, Andrea Postolache¹¹, Caroline Quintin¹, Jade Rexach¹, Layidé Roufai¹⁰, Zaven Terzian¹¹, Michael Thy¹⁸, Sarah Tubiana⁴, Sylvie van der Werf³⁴, Valérie Vignati¹, Benoît Visseaux⁸, Yazdan Yazdanpanah¹⁴

¹Centre d'Investigation Clinique, Inserm CIC 1425, Hôpital Bichat Claude Bernard, APHP, Paris, France. ²IMEA Fondation Léon M¹Ba, Paris, France. ³Institut Pasteur, UMR 3569 CNRS, Université de Paris, Paris, France. ⁴University of Basel Children's Hospital, Basel, Switzerland. ⁵Julius Center for Health Sciences and Primary Care, University Medical Center Utrecht, Utrecht, Netherlands. ⁶Université de Paris, IAME, Inserm UMR 1137, F-75018, Paris, France. ⁷Hôpital Bichat Claude Bernard, APHP, Paris, France. ⁸Hôpital Pitié Salpêtrière, APHP, Paris, France. ⁹Université de Paris, IAME, INSERM UMR 1137, AP-HP, University Hospital Bichat Claude Bernard, Virology, F-75018 Paris, France. ¹⁰Santé Publique France, Saint Maurice, France. ¹¹Pole Recherche Clinique, Inserm, Paris, France. ¹²Hôpital Bichat Claude Bernard, APHP, Paris, France. ¹³APHP, Paris, France. ¹⁴Virpath Laboratory, International Center of Research in Infectology, Lyon University, INSERM U1111, CNRS UMR 5308, ENS, UCBL, Lyon, France. ¹⁵IAME Inserm UMR 1138, Hôpital Bichat Claude Bernard, APHP, Paris, France. ¹⁶Service des Maladies Infectieuses et Tropicales, Groupe Pellegrin, Place Amélie-Raba-Léon, Bordeaux, France. ¹⁷Hôpital Hotel Dieu, APHP, Paris, France. ¹⁸Service des explorations fonctionnelles, Hôpital Bichat - Claude Bernard, APHP, Paris, France. ¹⁹Center for Clinical Investigation, Assistance Publique-Hôpitaux de Paris, Bichat-Claude Bernard University Hospital, Paris, France.

Amsterdam UMC Covid-19 Biobank Michiel van Agtmael¹, Anna Geke Algera², Frank van Baarle², Diane Bax³, Martijn Beudel⁴, Harm Jan Bogaard⁵, Marije Bomers¹, Lieuwke Bos², Michela Botta², Justin de Brabander⁶, Godelieve Bree⁶, Matthijs C. Brouwer⁴, Sanne de Bruin⁷, Marianna Bugiani⁸, Esther Bulle², Osoul Chouchane¹, Alex Cloberty³, Paul Elbers², Lucas Fleuren², Suzanne Geerlings¹, Bart Geerts⁸, Theo Geijtenbeek⁹, Armand Girbes², Bram Goorhuis¹, Martin P. Grobusch¹, Florianne Hafkamp¹, Laura Hagens², Jorg Hamann¹⁰, Vanessa Harris¹, Robert Hemke¹¹, Sabine M. Hermans¹,

Leo Heunks², Markus W. Hollmann⁸, Janneke Horn², Joppe W. Hovius¹, Menno D. de Jong¹², Rutger Koning⁴, Niels van Mourik¹, Jeanine Nellen¹, Frederique Paulus², Edgar Peters¹, Tom van der Pol¹, Benedikt Preckel⁸, Jan M. Prins¹, Jorinde Raasveld², Tom Reijnders¹, Michiel Schinkel¹, Marcus J. Schultz², Alex Schuurman¹³, Kim Sigaloff¹, Marry Smit², Cornelis S. Stijns¹, Willemke Stijlma², Charlotte Teunissen¹⁴, Patrick Thorat², Anissa Tsonas², Marc van der Valk¹, Denise Veelo⁸, Alexander P. J. Vlaar¹⁵, Heder de Vries², Michèle van Vugt¹, W. Joost Wiersinga¹, Dorien Wouters¹⁶, A. H. (Koos) Zwiderman¹⁷, Diederik van de Beek^{18*}

¹Department of Infectious Diseases, Amsterdam UMC, Amsterdam, Netherlands. ²Department of Intensive Care, Amsterdam UMC, Amsterdam, Netherlands. ³Experimental Immunology, Amsterdam UMC, Amsterdam, Netherlands. ⁴Department of Neurology, Amsterdam UMC, Amsterdam Neuroscience, Amsterdam, Netherlands. ⁵Department of Pulmonology, Amsterdam UMC, Amsterdam, Netherlands. ⁶Department of Infectious Diseases, Amsterdam UMC, Amsterdam, Netherlands. ⁷Department of Pathology, Amsterdam UMC, Amsterdam, Netherlands. ⁸Department of Anesthesiology, Amsterdam UMC, Amsterdam, Netherlands. ⁹Department of Experimental Immunology, Amsterdam UMC, Amsterdam, Netherlands. ¹⁰Amsterdam UMC, Netherlands Biobank Core Facility, Amsterdam UMC, Amsterdam, Netherlands. ¹¹Department of Radiology, Amsterdam UMC, Amsterdam, Netherlands. ¹²Department of Medical Microbiology, Amsterdam UMC, Amsterdam, Netherlands. ¹³Department of Internal Medicine, Amsterdam UMC, Amsterdam, Netherlands. ¹⁴Neurochemical Laboratory, Amsterdam UMC, Amsterdam, Netherlands. ¹⁵Department of Intensive Care, Amsterdam UMC, Amsterdam, Netherlands. ¹⁶Department of Clinical Chemistry, Amsterdam UMC, Amsterdam, Netherlands. ¹⁷Department of Clinical Epidemiology, Biostatistics and Bioinformatics, Amsterdam UMC, Amsterdam, Netherlands. ¹⁸Department of Neurology, Amsterdam UMC, Amsterdam, Netherlands. *Leader of the AMC consortium.

COVID Human Genetic Effort Laurent Abel¹, Alessandro Aiuti², Saleh Al Muhsen³, Fahd Al-Mulla⁴, Mark S. Anderson⁵, Andrés Augusto Arias⁶, Hagit Baris Feldman⁷, Dusan Bogunovic⁸, Alexandre Bolze⁹, Anastasiia Bondarenko¹⁰, Ahmed A. Boustifha¹¹, Petter Brodin¹², Yenan Bryceson¹², Carlos D. Bustamante¹³, Manish Butte¹⁴, Giorgio Casari¹⁵, Samya Chakravarty¹⁶, John Christodoulou¹⁷, Elizabeth Cirulli¹⁸, Antonio Condino-Neto¹⁸, Megan A. Cooper¹⁹, Clifton L. Dalgard²⁰, Joseph L. deRisi²¹, Murkesh Desai²², Beth A. Droleat²³, Sara Espinosa²⁴, Jacques Fellay²⁵, Carlos Flores²⁶, Jose Luis Franco²⁷, Peter K. Gregersen²⁸, Filomene Haerynck²⁹, David Hagin³⁰, Rabi Halwani³¹, Jim Heath³², Sarah E. Henriksen³³, Elena Hsieh³⁴, Kohsuke Imai³⁵, Yuval Itan³⁶, Timokratas Kamiratos³⁶, Kai Kisand³⁷, Cheng-Lung Ku³⁸, Yu-Lung Lai³⁹, Yun Ling⁴⁰, Carrie L. Lucas⁴¹, Tom Maniatis⁴², Davoud Mansouri⁴³, Laszlo Marodi⁴⁴, Isabelle Meyts⁴⁵, Joshua D. Milner⁴⁶, Kristina Mironska⁴⁷, Trine Mogensen⁴⁸, Tomohiro Morio⁴⁹, Lisa F. P. Ng⁵⁰, Luigi D. Notarangelo⁵¹, Giuseppe Novelli⁵², Antonio Novelli⁵³, Cliona O'Farrelly⁵⁴, Satoshi Okada⁵⁵, Tayfun Ozcelik⁵⁶, Rebecca Perez de Diego⁵⁷, Anna M. Planas⁵⁸, Carolina Prando⁵⁹, Aurora Pujol⁶⁰, Lluís Quintana-Murci⁶¹, Laurent Renia⁶², Alessandra Renier⁶³, Carlos Rodriguez-Gallego⁶⁴, Vanessa Sancho-Shimizu⁶⁵, Vijay Sankaran⁶⁶, Kelly Schiabor Barrett⁹, Mohammed Shahrooei⁶⁷, Andrew Snow⁶⁸, Pere Soler-Palacin⁶⁹, Andrés N. Spaan⁷⁰, Stuart Tangye⁷¹, Stuart Turvey⁷², Furkan Uddin⁷³, Mohammed J. Uddin⁷⁴, Diederik van de Beek⁷⁵, Sara E. Vazquez⁷⁶, Donald C. Vinh⁷⁷, Horst von Bernuth⁷⁸, Nicole Washington⁹, Pawel Zawadzki⁷⁹, Helen C. Su^{31*}, Jean-Laurent Casanova^{80*}

¹INSERM U1163, University of Paris, Imagine Institute, Paris, France. ²San Raffaele Telethon Institute for Gene Therapy, IRCCS Ospedale San Raffaele, Milan, Italy. ³King Saud University, Riyadh, Saudi Arabia. ⁴Dasman Diabetes Institute, Department of Genetics and Bioinformatics, Dasman, Kuwait. ⁵University of California, San Francisco, San Francisco, CA, USA. ⁶Universidad de Antioquia, Group of Primary Immunodeficiencies, Antioquia, Colombia. ⁷The Genetics Institute, Tel Aviv Sourasky Medical Center and Sackler Faculty of Medicine, Tel Aviv University, Tel Aviv, Israel. ⁸Icahn School of Medicine at Mount Sinai, New York, NY, USA. ⁹Helix, San Mateo, CA, USA. ¹⁰Shupky National Medical Academy for Postgraduate Education, Kiev, Ukraine. ¹¹Clinical Immunology Unit, Pediatric Infectious Disease Department, Faculty of Medicine and Pharmacy, Averroes University Hospital, LICIA Laboratoire d'immunologie clinique, d'inflammation et d'allergie, Hassann li University, Casablanca, Morocco. ¹²Karolinska Institute, Stockholm, Sweden. ¹³Stanford University, Stanford, CA, USA. ¹⁴University of California, Los Angeles, CA, USA. ¹⁵Medical

Genetics, IRCCS Ospedale San Raffaele, Milan, Italy. ¹⁶Department of Pediatrics and Children's Healthcare of Atlanta, Emory University, Atlanta, GA, USA. ¹⁷Murdoch Children's Research Institute, Victoria, Australia. ¹⁸University of São Paulo, São Paulo, Brazil. ¹⁹Washington University School of Medicine, St. Louis, MO, USA. ²⁰The American Genome Center; Uniformed Services University of the Health Sciences, Bethesda, MD, USA. ²¹University of California San Francisco; Chan Zuckerberg Biohub, San Francisco, CA, USA. ²²Bai Jerbai Wadia Hospital for Children, Mumbai, India. ²³School of Medicine and Public Health, University of Wisconsin, Madison, WI, USA. ²⁴Instituto Nacional de Pediatría (National Institute of Pediatrics), Mexico City, Mexico. ²⁵Swiss Federal Institute of Technology Lausanne, Lausanne, Switzerland. ²⁶Research Unit, Hospital Universitario Nuestra Señora de Candelaria, Canarian Health System, Santa Cruz de Tenerife, Spain. ²⁷University of Antioquia, Medellín, Colombia. ²⁸Feinstein Institute for Medical Research, Northwell Health USA, Manhasset, NY, USA. ²⁹Department of Paediatric Immunology and Pulmonology, Centre for Primary Immunodeficiency Ghent (CPiG), PID Research Laboratory, Jeffrey Modell Diagnosis and Research Centre, Ghent University Hospital, Edegem, Belgium. ³⁰The Genetics Institute Tel Aviv Sourasky Medical Center, Tel Aviv, Israel. ³¹Sharjah Institute of Medical Research, College of Medicine, University of Sharjah, Sharjah, United Arab Emirates. ³²Institute for Systems Biology, Seattle, WA, USA. ³³Children's Hospital of Philadelphia, Philadelphia, PA, USA. ³⁴Anschutz Medical Campus, Aurora, CO, USA. ³⁵Riken, Tokyo, Japan. ³⁶Hellenic Pasteur Institute, Athens, Greece. ³⁷University of Tartu, Tartu, Estonia. ³⁸Chang Gung University, Taoyuan County, Taiwan. ³⁹The University of Hong Kong, Hong Kong, China. ⁴⁰Shanghai Public Health

Clinical Center, Fudan University, Shanghai, China. ⁴¹Yale School of Medicine, New Haven, CT, USA. ⁴²New York Genome Center, New York, NY, USA. ⁴³Shahid Beheshti University of Medical Sciences, Tehran, Iran. ⁴⁴Semmelweis University Budapest, Budapest, Hungary. ⁴⁵KU Leuven, Department of Immunology, Microbiology and Transplantation, Leuven, Belgium. ⁴⁶Columbia University Medical Center, New York, NY, USA. ⁴⁷University Clinic for Children's Diseases, Skopje, North Macedonia. ⁴⁸Aarhus University, Aarhus, Denmark. ⁴⁹Tokyo Medical & Dental University Hospital, Tokyo, Japan. ⁵⁰Singapore Immunology Network, Singapore. ⁵¹National Institute of Allergy and Infectious Diseases, National Institutes of Health, Bethesda, MD, USA. ⁵²Department of Biomedicine and Prevention, University of Rome "Tor Vergata," Rome, Italy. ⁵³Bambino Gesù Children's Hospital, Rome, Italy. ⁵⁴Trinity College, Dublin, Ireland. ⁵⁵Hiroshima University, Hiroshima, Japan. ⁵⁶Bilkent University, Ankara, Turkey. ⁵⁷Laboratory of Immunogenetics of Human Diseases, Innate Immunity Group, IdiPAZ Institute for Health Research, La Paz Hospital, Madrid, Spain. ⁵⁸IBB-CSIC, IDIBAPS, Barcelona, Spain. ⁵⁹Faculdades Pequeno Príncipe e Instituto de Pesquisa Pelé Pequeno Príncipe, Curitiba, Brazil. ⁶⁰Neurometabolic Diseases Laboratory, IDIBELL - Hospital Duran I Reynals; Catalan Institution for Research and Advanced Studies (ICREA); CIBERER U759, ISCIII Madrid Spain, Barcelona, Spain. ⁶¹Institut Pasteur (CNRS UMR2000) and Collège de France, Paris, France. ⁶²Infectious Diseases Horizontal Technology Center and Singapore Immunology Network, Agency for Science Technology (A*STAR), Singapore. ⁶³Medical Genetics, University of Siena, Italy; Genetica Medica, Azienda Ospedaliero-Universitaria Senese, GEN-COVID Multicenter Study, Italy. ⁶⁴Hospital Universitario de Gran Canaria Dr Negrín, Canarian Health

System, Canary Islands, Spain. ⁶⁵Imperial College London, London, UK. ⁶⁶Boston Children's Hospital, Harvard Medical School, Boston, MA, USA. ⁶⁷Saeed Pathobiology and Genetic Laboratory, Tehran, Iran. ⁶⁸Uniformed Services University of the Health Sciences (USUHS), Bethesda, MD, USA. ⁶⁹Hospital Universitari Vall d'Hebron, Barcelona, Spain. ⁷⁰University Medical Center Utrecht, Amsterdam, Netherlands. ⁷¹Garvan Institute of Medical Research, Sydney, Australia. ⁷²The University of British Columbia, Vancouver, Canada. ⁷³Holy Family Red Crescent Medical College; Centre for Precision Therapeutics, NeuroGen Children's Healthcare; Genetics and Genomic Medicine Centre, NeuroGen Children's Healthcare, Dhaka, Bangladesh. ⁷⁴Mohammed Bin Rashid University of Medicine and Health Sciences, College of Medicine, Dubai, United Arab Emirates; The Centre for Applied Genomics, Department of Genetics and Genome Biology, The Hospital for Sick Children, Toronto, Ontario, Canada. ⁷⁵Amsterdam UMC, University of Amsterdam, Department of Neurology, Amsterdam Neuroscience, Amsterdam, Netherlands. ⁷⁶University of California, San Francisco, San Francisco, CA, USA. ⁷⁷McGill University Health Centre, Montreal, Canada. ⁷⁸Charité - Berlin University Hospital Center, Berlin, Germany. ⁷⁹Molecular Biophysics Division, Faculty of Physics, A. Mickiewicz University, Uniwersytetu Poznańskiego 2, Poznań, Poland. ⁸⁰The Rockefeller University, Howard Hughes Medical Institute, Necker Hospital, New York, NY, USA. *Leaders of the COVID Human Genetic Effort.

22 June 2020; accepted 16 September 2020
Published online 24 September 2020
10.1126/science.abd4585

RESEARCH ARTICLE SUMMARY

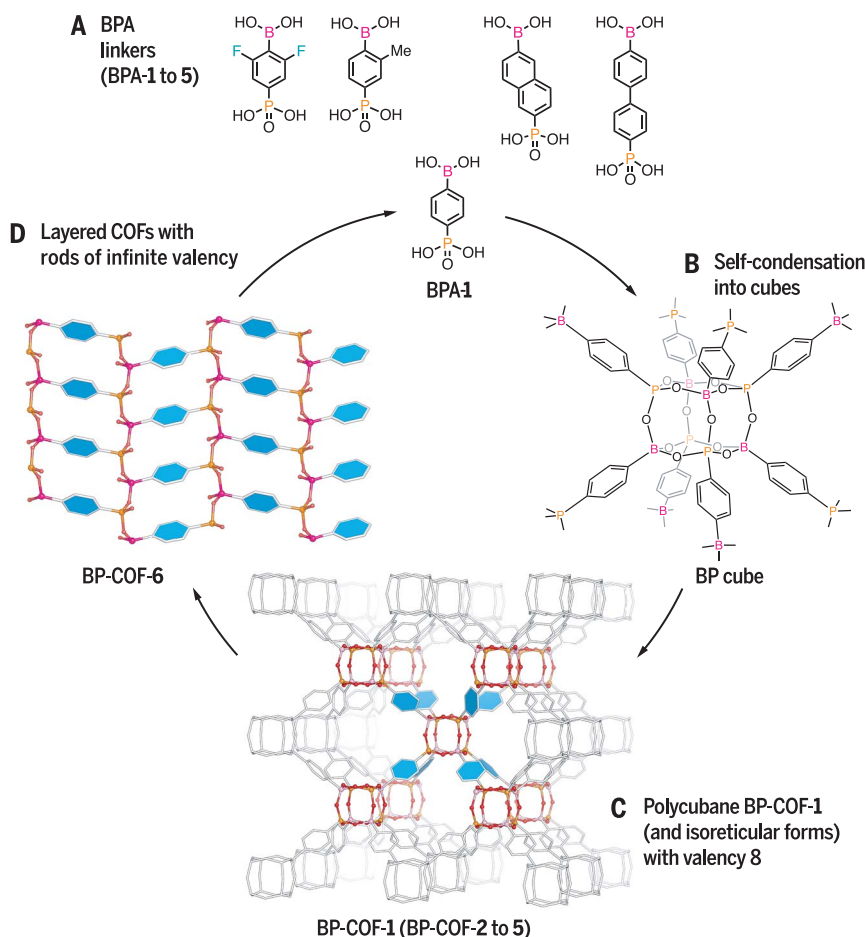
FRAMEWORK MATERIALS

Design of higher valency in covalent organic frameworks

Cornelius Gropp, Tianqiong Ma, Nikita Hanikel, Omar M. Yaghi*

INTRODUCTION: Valency is the connectivity of building units in reticular frameworks. Although metal-organic frameworks (MOFs) are known to have valencies of 3 to 24, covalent organic frameworks (COFs) are limited to the lower valencies of 3 and 4, principally owing to the heavy reliance of organic chemistry on sp^2 and sp^3 hybridization. We show that the diversity of COFs can be increased by finding new ways of linking simple organic molecules into building units of higher and even infinite valencies.

RATIONALE: Now, COFs are made by connecting preformed trigonal-planar, square-planar, and tetrahedral organic building units with linkages of low valency. Our strategy is to implement higher valency in COFs by designing molecules capable of forming higher-valency linkages through clustering. This is difficult to achieve by conventional organic methods. We therefore relied on the isoelectronic replacement of carbon-group elements by boron and phosphorus and demonstrated the feasibility of this chemistry by using borophosphonate



Design of higher valency in COFs from single organic linkers. (A) BPA linkers (BPA-1 to 5) combine a boronic and a phosphonic acid functionality in a single molecule. (B and C) Self-condensation of BPA-1 (B) afforded BP cubes of valency 8 (C) and their reticulated polycubane BP-COF-1. Isorecticular forms (BP-COF-2 to 5) demonstrated the versatility of this chemistry. (D) Upon addition of acid, BP-COF-1 rearranged into the layered BP-COF-6, which exhibits rods of infinite valency.

for the silicate cube motif. We designed simple organic BPA linkers (BPA-1 to 5) based on boron and phosphorus, which self-condensed into cubic units and polycubane COFs of valency 8. The versatility of this chemistry was further exploited by cleaving the cubes in the polycubane COFs, leading to structures with rod units of infinite valency.

RESULTS: The BPA-1 linker combines a boronic acid and a phosphonic acid functionality in a single molecule, which was converted into the boron-phosphorus (BP) cube of a reticulated polycubane BP-COF-1. Specifically, eight BPA-1 linkers self-condensed to form the BP cube with the elimination of eight water molecules per cube. The crystallization of BP-COF-1 was realized through microscopic reversibility: The polarized B-O-P linkage can dynamically form and break at the B-O bond. This constituted new chemistry whereby simple linkers converged into frameworks composed of higher-valency clusters. The versatility of this strategy was demonstrated by the successful crystallization of isorecticular polycubane structures, BP-COF-2 to 5 from the BPA-2 to 5 linkers. This series of functionalized and expanded polycubane structures exhibited permanent porosity. We found that upon addition of acid to BP-COF-1, eight B-O bonds per cube were cleaved and rearranged into BP-COF-6, which exhibits rods of infinite valency. The structure of BP-COF-6 was obtained from single-crystal x-ray diffraction, making it one of the few COFs grown as large crystals. It revealed infinite B-O-P rods linked by phenyl units to form layers, which in the crystal were joined by interstitial water molecules acting to stabilize an otherwise unusual rod-within-layer arrangement.

CONCLUSION: The chemistry of BPA linkers and their demonstrated ability to form cubes and higher-valency structures expand the scope of COFs. In essence, BPA linkers were indispensable in making linkages in the form of cubes and rods of higher valency and their corresponding extended BP-COF structures, thereby opening opportunities for the diversification of COFs through clustering of organic molecules based on sp^2 and sp^3 -hybridized atoms. The extension of this approach to COFs containing combinations of different shapes promises to uncover what we anticipate is a large, untapped structure space. ■

The list of author affiliations is available in the full article online.

*Corresponding author. Email: yaghi@berkeley.edu
Cite this article as C. Gropp et al., *Science* 370, eabd6406 (2020). DOI: 10.1126/science.abd6406

READ THE FULL ARTICLE AT
<https://doi.org/10.1126/science.abd6406>

RESEARCH ARTICLE

FRAMEWORK MATERIALS

Design of higher valency in covalent organic frameworks

Cornelius Gropp^{1,2}, Tianqiong Ma^{1,2}, Nikita Hanikel^{1,2}, Omar M. Yaghi^{1,2*}

The valency (connectivity) of building units in covalent organic frameworks (COFs) has been primarily 3 and 4, corresponding to triangles and squares or tetrahedrons, respectively. We report a strategy for making COFs with valency 8 (cubes) and “infinity” (rods). The linker 1,4-boronophenylphosphonic acid—designed to have boron and phosphorus as an isoelectronic combination of carbon-group elements—was condensed into a porous, polycubane structure (BP-COF-1) formulated as $(-B_4P_4O_{12}-)(-C_6H_4-)_4$. It was characterized by x-ray powder diffraction techniques, which revealed cubes linked with phenyls. The isorecticular forms (BP-COF-2 to 5) were similarly prepared and characterized. Large single crystals of a constitutionally isomeric COF (BP-COF-6), composed of rod units, were also synthesized using the same strategy, thus propelling COF chemistry into a new valency regime.

The development of metal-organic frameworks (MOFs) and covalent organic frameworks (COFs) through reticular chemistry has extended metal-complex and organic chemistries to infinite two- and three-dimensional (2D and 3D) forms (1–6). The extensive diversity and multiplicity of MOFs are fueled by the variety of valency (connectivity) imparted by their building units. These range from 3 to 24 for discrete units and “infinity” for 1D rods; all are multimetallic entities that, when linked with organics, lead to a vast MOF structure space (7). By contrast, the building units in COFs, with few exceptions (8), have been entirely based on the valency of 3 and 4, and there are no reports of any infinite dimensionality components linked with organics. This more limited scope of COF chemistry is evidenced by only 18 different structure types (topologies) reported for COFs (1, 9) versus more than 2000 for MOFs (10, 11). Thus, to increase the valency and dimensionality of building units in COFs, there is an interest in finding ways to overcome limitations imposed by the trigonal-planar (sp^2), square-planar (sp^2), and tetrahedral (sp^3) hybridization of organic building units (Fig. 1A).

Isoelectronic replacement as a synthetic strategy to afford higher valency in COFs

Here, we show how an isoelectronic combination of carbon group elements, based on boron and phosphorus that have low valency, can form COFs composed of higher-valency cube and infinite 1D building units (Fig. 1A). We designed a simple organic molecule—borophosphonic acid, BPA-1—that combined

B and P to make expanded polycubane COFs (Fig. 1B) as well as a COF containing B–O–P rods linked by phenyls. The alternative strategy of using two discrete molecules, each with a different functionality, is commonly practiced in COF chemistry and leads to lower-valency structures. Accordingly, the use of phenyldiboronic acid (BA) and phenyldiphosphonic acid (PA) (Fig. 1B) was unsuccessful, because BA self-condenses into boroxine-linked extended structures that have a valency of 3 (3). We report how our strategy of using a single linker bearing the two different functionalities needed for making the desired B–O–P linkages addresses this problem.

Specifically, we designed linkers BPA-1 to 5 and successfully reticulated them into a 3D COF (BP-COF-1), its functionalized forms (BP-COF-2 and 3), and its expanded forms (BP-COF-4 and 5), all having cubic units and valency of 8 (Fig. 1, B and C). We further elaborated this strategy beyond cubes to show their rearrangement into infinite B–O–P rods linked by organics. The ability to control the reticulation of a single organic linker containing an isoelectronic combination of elements into entities of higher valency and infinite dimensionality adds to the complexity and scope of COFs.

There are two potential strategies to achieve higher valency in COFs. Either a building unit of the desired valency could be made a priori and reticulated, or a designed linker could itself be reticulated to make such a unit in situ. The former is the current conceptual basis of COF chemistry and has led to several structures of valency 6 (8). However, this approach requires arduous, multistep syntheses to obtain the building units in a form amenable to COF reactions and, ultimately, crystallization (12). In general, this strategy has not been successful in making crystalline structures of di-

verse constituents, as often observed for linking the silicate cube with organics (Fig. 1D) (13).

We instead developed the in situ strategy using the cube motif for making higher-valency COFs. We reasoned that by replacing the Si with its isoelectronic B and P combination, the resulting polarization would allow for the microscopic reversibility and ultimately lead to the desired crystalline COFs (Fig. 1D). The polarized B–O–P linkage can break and form at the O–B bond into the trigonal boronic acid with a vacant p orbital and the corresponding phosphonic acid (Fig. 1D). Both functionalities are readily accessible by synthetic chemistry, but so far, their dynamic covalent bonds have not been explored in reticular chemistry (14). Given that BP cube is known as a discrete molecule (15, 16), we targeted the synthesis of the BPA organic linkers and expected that their self-condensation would yield the desired expanded polycubane BP-COFs (Fig. 1B).

Polycubane COFs from linkers containing B and P

BPA-1 was prepared in two steps from commercially available starting materials and was air stable (section S1 of the supplementary materials). BPA-linkers of varying lengths and functionalities were readily accessed by analogous routes in two to three steps, as demonstrated by the synthesis of BPA-2 to 5 (Fig. 1C; section S1). The synthesis of BP-COF-1 is based on the molecular dehydration reaction, in which eight BPA-1 linkers converge to form the cubic borophosphonate with the elimination of eight water molecules per cube (Fig. 1D). Because the dynamic covalent chemistry for the reversible assembly of BP-type molecules has not been previously explored, we screened various reaction conditions for the condensation of these BPA linkers and used modulators to control the reversibility and thus the periodicity of the reticulated products.

Optimized reaction conditions for this series of COFs were exemplified by the synthesis of BP-COF-1 and involved dissolving BPA-1 (20.0 mg, 0.1 mmol) with methylphosphonic acid as modulator (2.5 equiv) in dimethylsulfoxide (0.2 ml) and toluene (0.8 ml). This mixture, containing the dissolved solids but exhibiting solvent phase separation, was sealed in a Pyrex tube and heated at 120°C for 72 hours. BP-COF-1 was isolated and solvent-exchanged with tetrahydrofuran and methanol, then activated under dynamic vacuum to give the crystalline compound as a white powder in 48% yield (section S1).

The atomic composition of BP-COF-1 was determined by elemental and inductively coupled plasma analyses and found to correspond to $C_6H_6BO_4P$ within the standard experimental error (section S1). H_2O was replaced by methylphosphonic acid when used as a modulator

¹Department of Chemistry, University of California–Berkeley, Berkeley, CA 94720, USA. ²Kavli Energy Nanoscience Institute at UC Berkeley, Berkeley, CA 94720, USA.

*Corresponding author. Email: yaghi@berkeley.edu

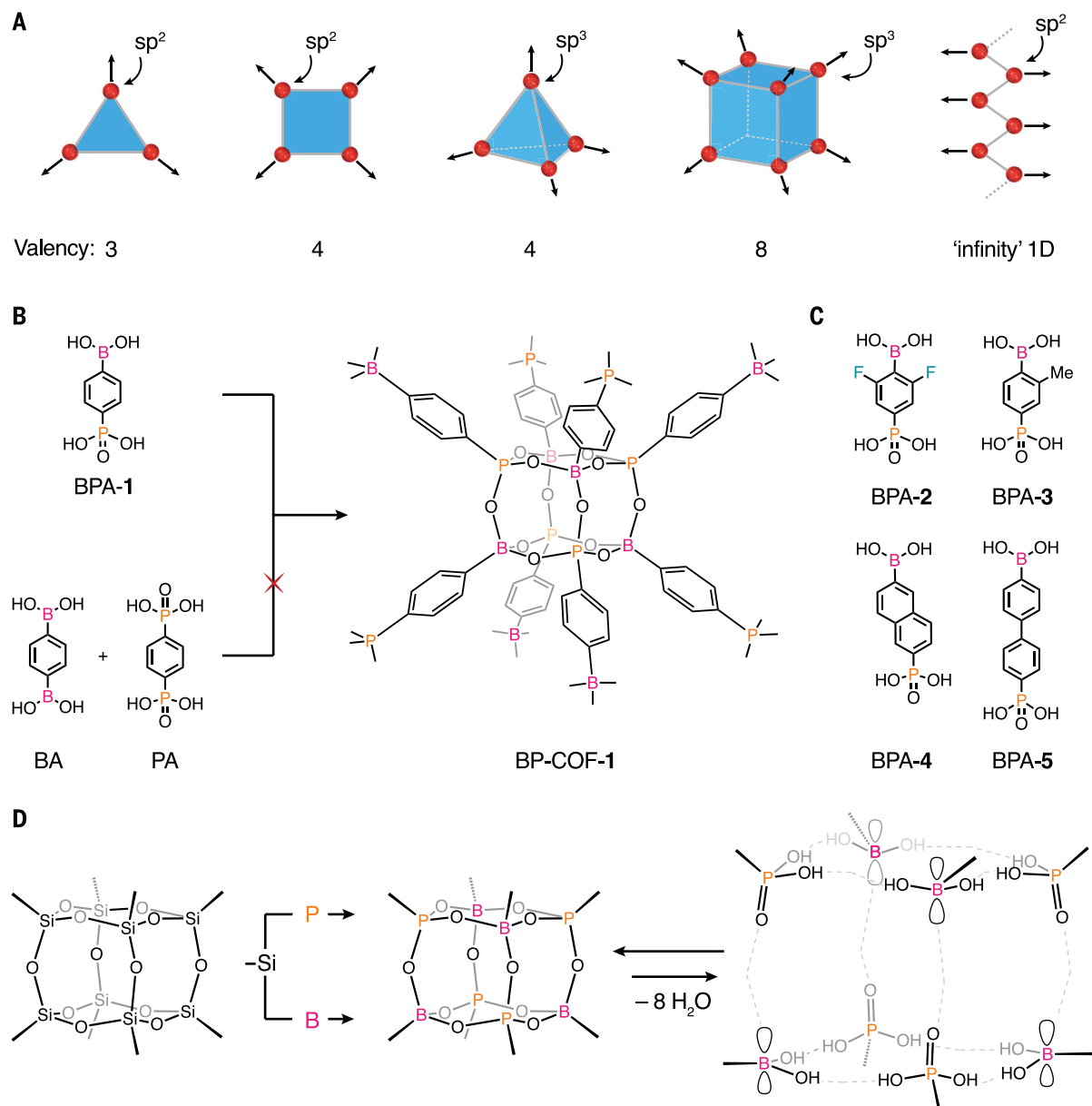


Fig. 1. Higher valency in COFs and synthetic strategy for polycubanes. (A) Building units of valency 3 and 4 are currently used in the design and synthesis of 3D COFs; cubes with valency of 8 and infinite 1D rods have not been reported. (B) Reticulation of a linker designed to hold two functionalities (BPA-1) affords BP-COF-1 with valency of 8; the alternative strategy involving BA and PA gives instead COFs of lower valency. (C) Linkers with different functionalities (BPA-2 and 3) and lengths (BPA-4 and 5) were prepared and used to make the corresponding COFs. (D) Isoelectronic replacement as a conceptual basis for creating reversible in situ formation of the cubic units.

(section S1). The constitution of BP-COF-1 was corroborated by solution-state nuclear magnetic resonance (NMR) of its acid-digested form, which, as expected, gave back the original BPA-1 linker (figs. S2 and S3). Thermogravimetric analysis done under both N_2 and air atmosphere indicated that the framework has a thermal stability of up to 500°C with a weight loss of 36%, corresponding to water and the hydrocarbon linker (section S4). The residual compound after combustion was identified as boronphosphate (BPO_4), confirmed by its powder x-ray diffraction (PXRD) pattern,

and the observed weight loss matched the proportion of carbon and hydrogen present in the compound and found in the elemental analysis (section S5).

The PXRD analysis confirmed the crystallinity of BP-COF-1 and revealed no diffraction peaks that could be attributed to residual starting material or reaction additives (Fig. 2A and fig. S49). Scanning electron microscopy (SEM) micrographs of the BP-COF-1 crystallites indicated a single morphological phase with a homogeneous distribution of crystal sizes of ~ 300 to 400 nm (Fig. 2B). The forma-

tion of the BP cube structure in BP-COF-1 was supported with characteristic resonances in the Fourier-transformed infrared (FT-IR) and ^{11}B , ^{31}P , and ^{13}C solid-state NMR spectra.

A molecular analog of a borophosphonate cube was prepared and served as a model compound (section S1) (17). Diagnostic signals in the FT-IR and NMR spectra of the BP-COF-1 coincided with those we measured for the model system and were distinct from the BPA-1 starting material. The absorption bands between 3000 to 3500 cm^{-1} observed for the $\nu(\text{OH})$ of the $\text{PO}(\text{OH})_2$ and $\text{B}(\text{OH})_3$ groups were

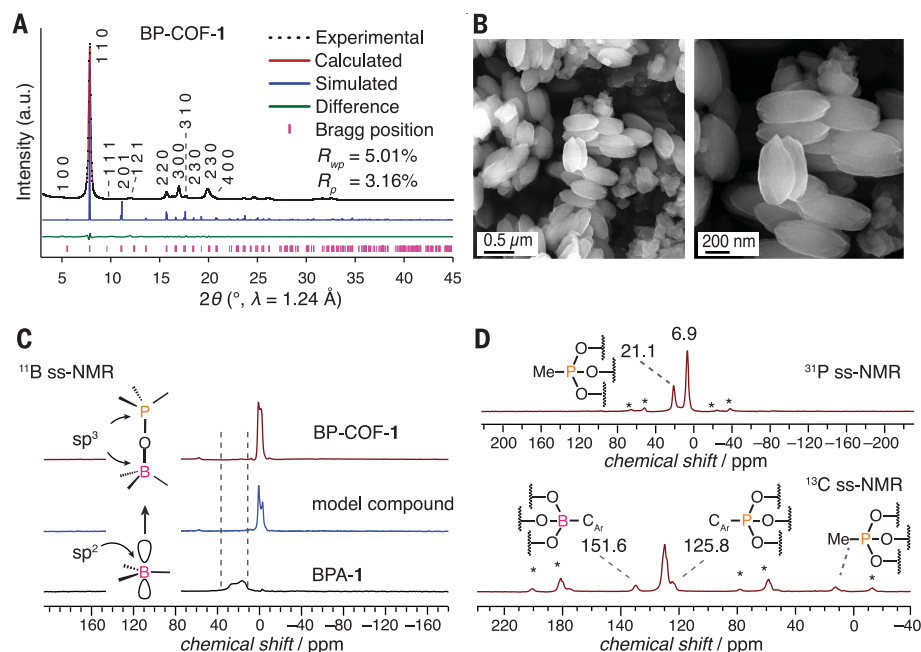


Fig. 2. Structural and molecular characterization of 3D cubic BP-COF-1. (A) Structural refinement of BP-COF-1 from PXRD data analysis displaying the indexed experimental pattern (black), Pawley fitting (red), and the simulated pattern obtained from the modeled structure (blue). a.u., arbitrary units. (B) SEM micrographs of BP-COF-1. (C) Overlay of the ^{11}B solid-state (ss) NMR spectra of BP-COF-1, a molecular borophosphonate model compound, and BPA-1. (D) ^{31}P and ^{13}C NMR spectra of BP-COF-1. Me, methyl.

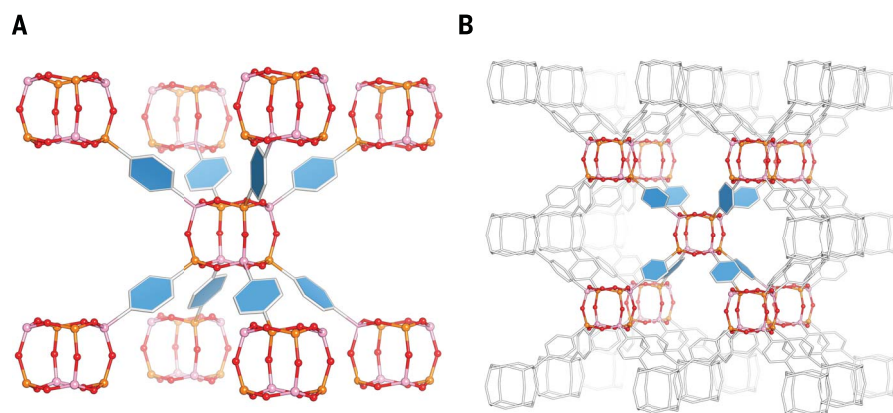


Fig. 3. Crystal structure of BP-COF-1. (A and B) Crystals of BP-COF-1 have cubes linked to eight phenyl units bridging to other such cubes (A) to make a 3D extended polycubane COF (B) (bcu; P222) with valency of 8. C, gray; B, pink; P, orange; O, red. Hydrogens are omitted for clarity.

absent, indicating a complete reaction and the condensation of these groups to make the COF (fig. S7). Strong absorption bands at 1210, 1140, and 1050 cm^{-1} assigned to the $\nu(\text{B}-\text{O}-\text{P})$ of the cubic BP-COF-1 are comparable within $<5\text{ cm}^{-1}$ to vibrational bands found in the model system and molecular reference structures (figs. S5 and S7) (18).

Magic angle spinning (MAS) solid-state NMR spectroscopy of the ^{11}B , ^{31}P , and ^{13}C nuclei was performed to further validate the formation and connectivity of the cubic units (Fig. 2, C and D). The second-order quadrupolar NMR

line shape of the ^{11}B nucleus is a sensitive probe to substantiate the conversion of the trigonal-planar boron site of the starting material (in BPA-1) into the tetrahedral boron site of the product (BP-COF-1) (19). Comparison of the experimental second-order quadrupolar line shapes of the ^{11}B NMR resonances of the starting material BPA-1 and the model system with BP-COF-1 supported the presence of tetrahedral boron sites in both products (Fig. 2C and section S6). The single resonance in the ^{11}B NMR spectrum of BP-COF-1 indicated negligible defect sites within the crystallites.

The ^{31}P spectrum of BP-COF-1 displayed two discrete peaks, a major resonance at 6.9 parts per million (ppm) and a minor one at 21.1 ppm, indicating two distinct P sites. The latter resonance was assigned to residual modulator molecules, methylphosphonates, located at the terminal site of the crystallites. The ^{13}C cross-polarization MAS NMR spectrum displayed discrete resonances in the aromatic region between 151.6 and 125.8 ppm (Fig. 2D). We assigned the resonance at 151.6 ppm to the downfield-shifted carbon bonded to the tetrahedral boron and the peak at 125.8 ppm to the carbon connected to the phosphorus. The relative shifts match well with the ones observed for the molecular model compound, further supporting the formation of the cube units in the COF (section S6) (17, 18).

The crystal structure of BP-COF-1 was obtained by PXRD analysis of its microcrystalline powder. For BP-COF-1, linking of the borophosphonate cubes with eight benzene bridges affords a cubic extended structure based on the body-centered cubic (bcu) topology (Fig. 3 and fig. S55). The distance between the centers of adjacent cubes was 11.128 Å , which includes a distance of 6.228 Å between B and P on adjacent cubes, being bridged by the phenyl units (section S8). A structural model based on a bcu arrangement was built in the P222 space group with the optimized unit cell parameters of $a = 12.800\text{ Å}$, $b = 12.915\text{ Å}$, and $c = 12.798\text{ Å}$. The corresponding simulated PXRD pattern was in good agreement with the experimentally obtained data (Fig. 2A). Pawley refinement of the experimental PXRD pattern yielded the refined unit cell parameters of $a = 12.39(5)\text{ Å}$, $b = 12.52(3)\text{ Å}$, and $c = 12.93(5)\text{ Å}$, with the unweighted reliability factor (R_p) = 5.01% and the weighted reliability factor (wR_p) = 3.16%, and the final structure was obtained by geometry optimization. The corresponding crystal structure has $\text{B}_4\text{P}_4\text{O}_{12}$ cubes each covalently linked to eight phenyl units, acting as bridges to other such linked cubes to give an overall reticular formula of $(-\text{B}_4\text{P}_4\text{O}_{12}-)(-\text{C}_6\text{H}_4-)_4$ for the extended 3D polycubane porous structure of BP-COF-1 (Fig. 3).

The N_2 adsorption analysis of BP-COF-1 demonstrated permanent porosity and a Type I behavior (section S10). The Brunauer-Emmett-Teller (BET) area was calculated to be $519\text{ m}^2\text{ g}^{-1}$, corresponding to $\sim 82\%$ of the theoretically accessible surface area based on the crystal structure (section S11). This result was validated by argon adsorption analysis at 87 K (fig. S63). The pore size distribution, estimated from the N_2 isotherm by a density functional theory (DFT) calculation, indicated a pore diameter of 6.0 Å (section S11), which is in good agreement with the theoretical van der Waals distance of 5.8 Å obtained from the crystal structure. Importantly, H_2 isotherms

at 77 and 87 K for BP-COF-1 also demonstrated the accessibility of the cubic unit for gas sorbates. The experimental gravimetric uptake of H₂ at 1 atm and 77 K measured 11.6 mg g⁻¹ (volumetric uptake 130 cm³ g⁻¹ at 1 atm; fig. S65). The heat of adsorption (Q_{st}) was ~8.8 kJ mol⁻¹, indicating stronger sorbate-framework interactions than comparable boroxine-linked 2D and 3D COFs (20). We attributed the stronger interactions to the polarized nature of the pore environment replete with accessible B–O–P edges of the cubes that make up the structure of BP-COF-1, an aspect that also points to the effectiveness of placing lower-valency atoms into constructs of higher valency within COFs.

Isorecticular forms of polycubane COFs

We extended the approach of having a single linker converge into a high-valency building unit to the synthesis and structure of functionalized and expanded versions of BP-COF-1 by introducing functional groups into BPA-1 to make BPA-2 and 3, as well as expanding the linkers to BPA-4 and 5 (Fig. 1C). The corresponding COFs (BP-COF-2 to 5) were synthesized and characterized as demonstrated for BP-COF-1; they followed the expected pattern of isorectification (21) and exhibited similar spectroscopic and x-ray evidence (sections S3 and S6 to S8). In particular, the expanded isorecticular series (BP-COF-1, 4, and 5) showed a shift to higher *d*-spacing in the PXRD, corresponding to the change in length of the organic units and its impact on the unit cell dimensions (Fig. 4A). A gradual shift of the patterns toward smaller 2θ values was observed (Fig. 4B), in agreement with the increase in linker length measured from B to P of 6.2, 8.4, and 10.5 Å for the phenyl, naphthyl, and biphenyl, which are BPA-1, 4, and 5, respectively (Fig. 4B). Based on our success with these cubic COFs, we anticipate other linkers, such as the tetrahedral form of BPA and combinations based on other shapes, to give a wide range of higher-valency structures (22).

Single crystals of a constitutionally isomeric COF with rod units of infinite valency

In an effort to further explore the condensation reaction of BPA-1 into structures with building units beyond cubes, we investigated the use of reaction additives, such as acids and bases. Under similar reaction conditions used for the synthesis of BP-COF-1, but in the presence of 20 μ l of aqueous HCl_{conc.}, we obtained a new crystalline phase, BP-COF-6, as confirmed by PXRD (fig. S50). Single crystals of 50 μ m with well-defined, uniform block-shaped morphology were obtained and examined by single-crystal x-ray diffraction techniques (Fig. 5). BP-COF-6 crystallized in the *Pc* space group with unit cell parameters of $a = 5.4728(16)$ Å, $b = 4.3774(12)$ Å, $c = 14.285(4)$ Å, and $\beta = 95.402(7)^\circ$ and a unit

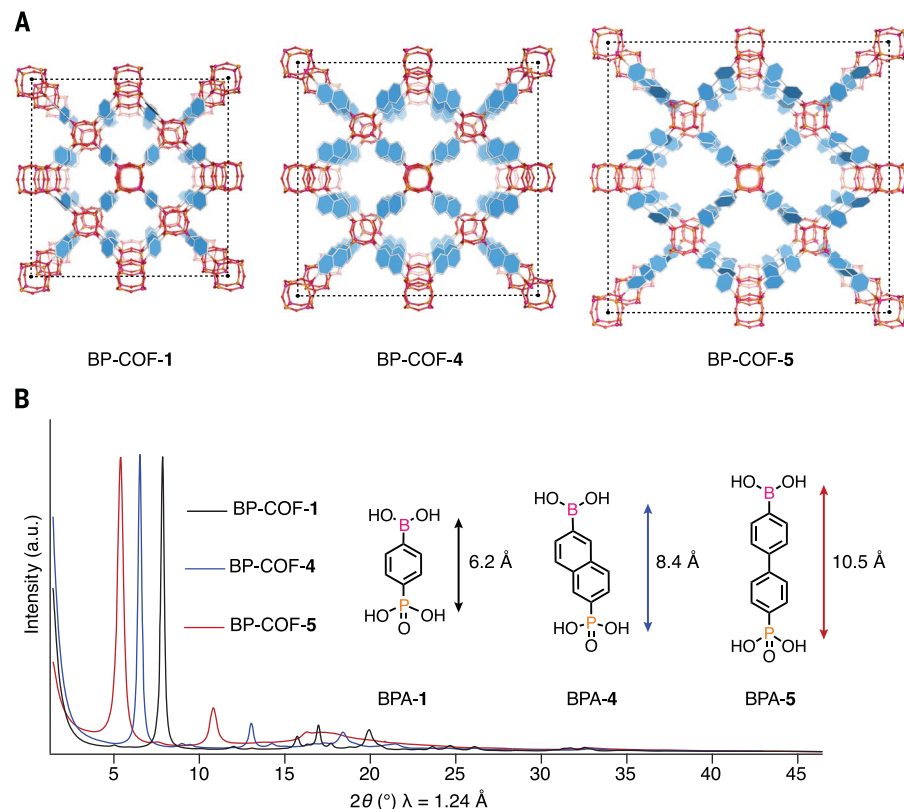


Fig. 4. Isorecticular expansion of BP-COFs. (A) Isorecticular series (BP-COF-1, 4, and 5) demonstrates the generalizability of the in situ approach. Expansion of the unit cell is illustrated by black dotted lines. (B) With increasing length of the BPA linkers, a shift of the highest intensity PXRD peak (110) toward lower 2θ ($^\circ$) was observed. C, gray; B, pink; P, orange; O, red. Hydrogens are omitted for clarity.

cell volume of 340.71(16) Å³ (Fig. 5 and table S2). Structure analysis showed that the cubic borophosphonates were replaced by infinite 1D B–O–P rods of alternating tetrahedral boron and phosphorus building units. The B–O–P bond lengths within the 1D rod were 1.47(3) Å (B–O) and 1.54(1) Å (P–O). These 1D rods were connected by phenyls that had interlayer spacings of 5.47 Å (measured from phenyl to phenyl). This distance exceeded π – π -stacking distances because of the water molecule connecting the layers through hydrogen bonding (H bonding). The layers were stacked along the *a* axis and followed a honeycomb pattern (hcb). The B–O–P rods were oriented along the *b* axis with the uncondensed P=O groups unidirectionally aligned along the $-a$ axis. The O...O distances of 2.58 and 2.60 Å between the P=O and the oxygen at the boron indicated strong hydrogen bonds, most likely stemming from interstitial water molecules strongly bound to the boron and enforcing the tetrahedral geometry (Fig. 5).

The P–O distances of 1.46(2) Å support a P=O double-bond character, and the B–O distance of 1.60(4) Å supports a strong dative bonding of the water molecule donating electron density into the empty p orbital of the boron. This

H-bonding sequence connected the extended 2D layers of BP-COF-6, whose framework was formulated as (–BPO₄–)(–C₆H₄–). This structure motif of B–O–P rods linked by organics led to infinite valency COFs. In the context of single crystals of COFs, there have been several studies of solving crystal structures using electron diffraction (23, 24); however, the single-crystal x-ray structure of BP-COF-6 is one of only a few reported in COF chemistry (25, 26).

Discussion: Rearrangement of polycubane COFs into rod COFs

Elemental analysis, solution NMR of the acid-digested sample, and thermogravimetric analysis of BP-COF-6 confirmed that this compound had identical elemental composition to BP-COF-1 and that they were constitutional isomers (sections S1 and S2). We found that cubic BP-COF-1 could be fully interconverted into the rod BP-COF-6 in the presence of 20 μ l of aqueous HCl_{conc.} (Fig. 6), as evidenced by PXRD (section S1 and fig. S54). We suggest that the strongly bonded, interstitial water molecule at the center of the H bonding between the layers of BP-COF-6 results from hydrolysis (bond breaking) after addition of acid, followed by condensation producing water as a by-product,

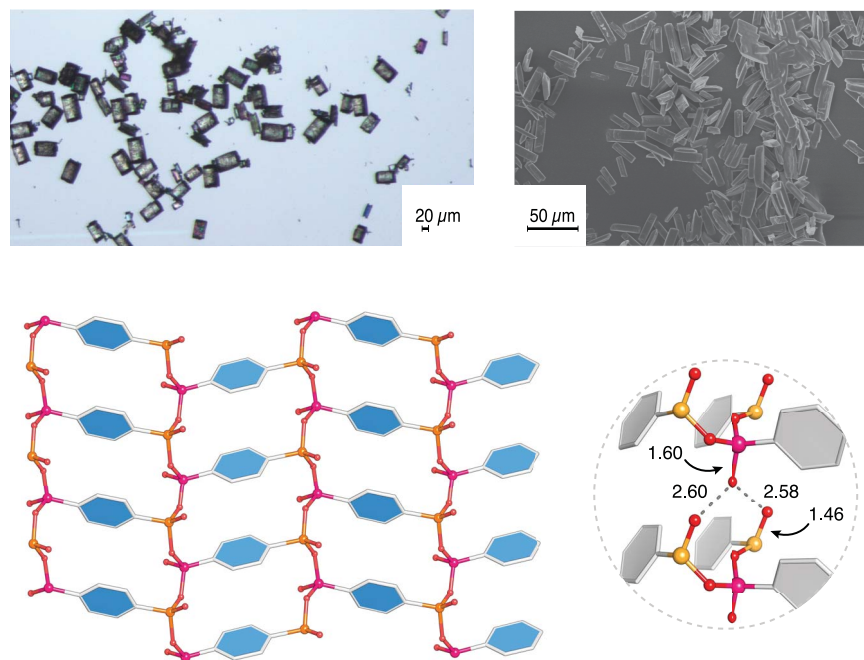


Fig. 5. Single-crystal x-ray diffraction structure of BP-COF-6, which has units of infinite valency.

Optical microscope (top left) and SEM (top right) images of BP-COF-6. A layer in the single-crystal x-ray structure of BP-COF-6 (bottom left). Local H-bonding interactions between the layers are indicated in O...O distances between O on P and B and are given in Å (bottom right). C, gray; B, pink; P, orange; O, red. Hydrogens on the phenyl units and the tightly bound water ligands bound to B atoms are omitted for clarity.

facilitating this clean transformation. Thus, the interconversion potentially follows a breaking of the B–O bonds in the horizontal B–O–P linkages of the cube, keeping the vertical ones untouched and thereby producing B–O–P–phenyl “chains” following the 1, 2, 3, ... sequence (Fig. 6A). Thus, BP-COF-1 can be viewed as being composed of a collection of such chains, which, owing to the bond breaking, are now liberated to slide toward each other in pairs (1, 2, 3, ... and 1', 2', 3', ...; Fig. 6A) and form the B–O–P rod arrangement (1, 1', 2, 2', 3, 3', ...; Fig. 6B) poised for condensation, to ultimately give the rod BP-COF-6 (Fig. 6C). That the P=O bonds remaining after B–O bond breaking all pointed in the same direction supported our model of how this rearrangement took place. The tightly bound water molecules at the boron may very well be playing a stabilizing role in trapping the rod units in BP-COF-6, especially because such rods were previously unknown. This type of rearrangement is distinct in the chemistry of B and P and is a result of the polarized B–O–P linkage, which, on the basis of this report, promises rich chemistry.

Materials and methods

Full experimental details and characterization of BPA-1 to 5 and BP-COF-1 to 6 are pro-

vided in sections S1 to 13 of the supplementary materials.

Synthesis of BP-COF-1

A Pyrex tube measuring 10 mm by 8 mm [outside diameter (od) by inside diameter (id)] was loaded with BPA-1 (20 mg, 0.10 mmol), methylphosphonic acid (24 mg, 0.25 mmol), 0.2 ml of dimethyl sulfoxide (DMSO), and 0.8 ml of toluene. The tube was flash frozen at 77 K under liquid N₂, evacuated to an internal pressure of 100 mtorr, and flame-sealed to a length of 15 cm, approximately. The tube was placed in an oven at 120°C for 72 hours, yielding a white solid. The solvent was removed, and the residual solid was immersed once in 5 ml of tetrahydrofuran and three times in 5 ml of methanol over 24 hours. The solid was activated under dynamic vacuum, first at 25°C for 5 hours and then at 150°C for 6 hours. BP-COF-1 (6.9 mg, 48%) was obtained as a white powder.

Synthesis of BP-COF-6

A Pyrex tube measuring 10 mm by 8 mm (od by id) was loaded with BPA-1 (10 mg, 0.05 mmol), 20 μl of HCl_{conc.}, 0.2 ml of DMSO, and 0.8 ml of toluene. The tube was sealed and placed in an oven at 120°C for 5 days, yielding a white solid. The solvent was removed, and the residual solid was immersed once in 5 ml of tetrahydrofuran

and three times in 5 ml of methanol over 48 hours. The solid was then activated under dynamic vacuum, first at 25°C for 5 hours and then at 150°C for 6 hours. BP-COF-6 (5.0 mg, 60%) was obtained as a white powder.

Conversion of BP-COF-1 into BP-COF-6

A Pyrex tube measuring 10 mm by 8 mm (od by id) was loaded with BP-COF-1 (10 mg, 0.05 mmol), 20 μl of HCl_{conc.}, 0.2 ml of DMSO, and 0.8 ml of toluene. The tube was sealed and placed in an oven at 120°C for 72 hours, yielding a white solid. The solvent was removed, and the residual solid was immersed once in 5 ml of tetrahydrofuran and three times in 5 ml of methanol over 24 hours. The solid was then activated under dynamic vacuum, first at 25°C for 5 hours and then at 150°C for 6 hours. BP-COF-6 was obtained as a pure phase, as confirmed by PXRD.

PXRD

PXRD patterns of BP-COF-1 to 6 were acquired on an in-house Bruker D8 Advance equipped with a Ni filter CuKα ($\lambda = 1.5406$ Å) or on the beamline 7.3.3 at the Advanced Light Source with a Pilatus 2M detector ($\lambda = 1.2389$ Å). For in-house measurements, the samples were mounted on zero-background sample holders and leveled with a glass plate. Some samples were grinded in an agata mortar before analysis. Data were collected between 3° and 50° or 60° with a step width of 0.01 and a total data collection time of 4 to 5 hours. For beamline measurements, powder samples were packed in quartz capillaries and put into a helium atmosphere for measurement in transmission geometry. Silver behenate was used for calibration. The Nika package for IGOR Pro (Wavemetrics) was used to reduce the acquired 2D raw data to a 1D profile (27). Refinements were conducted with the Material Studio (version 4.0, Accelrys, San Diego, CA) (28).

Single-crystal x-ray diffraction

A colorless block-shaped crystal of BP-COF-6 was measured at the beamline 12.2.1 at the Advanced Light Source using a radiation wavelength of $\lambda = 0.7288$ Å. The crystal was mounted on a MiTeGen Kapton loop and submerged in a 100-K nitrogen cryostream for the measurement. The data reduction was carried out with APEXII (29) software packages. The structure solution and refinement were carried out using the SHELX algorithms (30) in Olex2 (31). Crystal data and details of the structure refinement are given in table S1 and in the provided cif file (data S1). Mercury was used for structural visualization (32).

Low-pressure gas sorption

Low-pressure argon, N₂, and H₂ adsorption isotherm measurements of BP-COF-1 to 6 were carried out on a Micromeritics 3-Flex or an

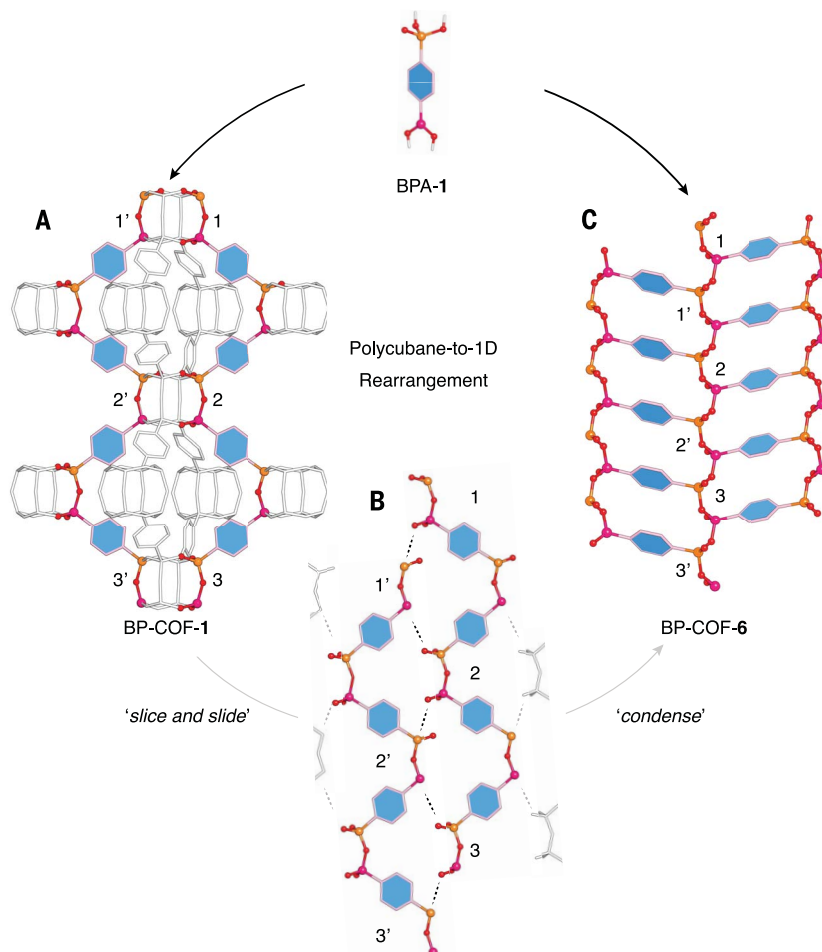


Fig. 6. Polycubane-to-1D rearrangement of BP-COF-1 to BP-COF-6. (A to C) Suggested mechanism for the interconversion of the cubic BP-COF-1 into the layered BP-COF-6 through a “slice-and-slide”-type rearrangement and condensation. C, gray; B, pink; P, orange; O, red. Hydrogens are omitted for clarity.

ASAP 2420 surface area analyzer. A liquid N₂ bath was used for measurements at 77 K. A liquid argon bath was used for measurements at 87 K. Ultrahigh-purity-grade N₂, argon, H₂, and He (99.999% purity) were used throughout adsorption experiments. Solvent-accessible surface areas were calculated with Material Studio (version 4.0, Accelrys, San Diego, CA) (28) using a N₂- or argon-sized probe molecule (of diameters 3.68 and 3.96 Å, respectively) and a grid interval of 0.25 Å (33). The pore size was calculated with MicroActive (version 5.01) (34) from the N₂ or argon isotherms by applying a DFT type, slit geometry, 2D-NLDFT, N₂-Carbon Finite Pores, As=4 Model for nitrogen isotherms, and a DFT type, slit geometry, AR-DFT Model for argon isotherms. The theoretical van der Waals distance was deduced from the model by measuring the heavy atom van der Waals distances. Experimental BET areas were calculated from the respective isotherms with data from the low-pressure range ($P/P_0 \leq 0.1$; see section S10), with pressure points as low as $10^{-7} P/P_0$. The correlation coefficients

and positive C values are given in section S10 for each BET calculation.

REFERENCES AND NOTES

- O. M. Yaghi, M. J. Kalmutzki, C. S. Diercks, *Introduction to Reticular Chemistry: Metal-Organic Frameworks and Covalent Organic Frameworks* (Wiley, 2019).
- O. M. Yaghi et al., Reticular synthesis and the design of new materials. *Nature* **423**, 705–714 (2003). doi: [10.1038/nature01650](https://doi.org/10.1038/nature01650); pmid: [12802325](https://pubmed.ncbi.nlm.nih.gov/12802325/)
- A. P. Côté et al., Porous, crystalline, covalent organic frameworks. *Science* **310**, 1166–1170 (2005). doi: [10.1126/science.1120411](https://doi.org/10.1126/science.1120411); pmid: [16293756](https://pubmed.ncbi.nlm.nih.gov/16293756/)
- H. M. El-Kaderi et al., Designed synthesis of 3D covalent organic frameworks. *Science* **316**, 268–272 (2007). doi: [10.1126/science.1139915](https://doi.org/10.1126/science.1139915); pmid: [17431178](https://pubmed.ncbi.nlm.nih.gov/17431178/)
- K. Geng et al., Covalent organic frameworks: Design, synthesis, and functions. *Chem. Rev.* **120**, 8814–8933 (2020). doi: [10.1021/acs.chemrev.9b00550](https://doi.org/10.1021/acs.chemrev.9b00550); pmid: [31967791](https://pubmed.ncbi.nlm.nih.gov/31967791/)
- C. S. Diercks, O. M. Yaghi, The atom, the molecule, and the covalent organic framework. *Science* **355**, eaal1585 (2017). doi: [10.1126/science.aal1585](https://doi.org/10.1126/science.aal1585); pmid: [28254887](https://pubmed.ncbi.nlm.nih.gov/28254887/)
- M. J. Kalmutzki, N. Hanikel, O. M. Yaghi, Secondary building units as the turning point in the development of the reticular chemistry of MOFs. *Sci. Adv.* **4**, eaat9180 (2018). doi: [10.1126/sciadv.aat9180](https://doi.org/10.1126/sciadv.aat9180); pmid: [30310868](https://pubmed.ncbi.nlm.nih.gov/30310868/)
- S. Dalapati et al., Rational design of crystalline supermicroporous covalent organic frameworks with triangular topologies. *Nat. Commun.* **6**, 7786 (2015). doi: [10.1038/ncomms8786](https://doi.org/10.1038/ncomms8786); pmid: [26178865](https://pubmed.ncbi.nlm.nih.gov/26178865/)

- X. Guan, F. Chen, Q. Fang, S. Qiu, Design and applications of three dimensional covalent organic frameworks. *Chem. Soc. Rev.* **49**, 1357–1384 (2020). doi: [10.1039/C9CS00911F](https://doi.org/10.1039/C9CS00911F); pmid: [32067000](https://pubmed.ncbi.nlm.nih.gov/32067000/)
- E. V. Alexandrov, V. A. Blatov, A. V. Kochetkov, D. M. Proserpio, Underlying nets in three-periodic coordination polymers: Topology, taxonomy and prediction from a computer-aided analysis of the Cambridge Structural Database. *CrystEngComm* **13**, 3947–3958 (2011). doi: [10.1039/c0ce00636j](https://doi.org/10.1039/c0ce00636j)
- V. A. Blatov, A. P. Shevchenko, D. M. Proserpio, Applied topological analysis of crystal structures with the program package ToposPro. *Cryst. Growth Des.* **14**, 3576–3586 (2014). doi: [10.1021/cg500498k](https://doi.org/10.1021/cg500498k)
- J. Jiang, Y. Zhao, O. M. Yaghi, Covalent chemistry beyond molecules. *J. Am. Chem. Soc.* **138**, 3255–3265 (2016). doi: [10.1021/jacs.5b10666](https://doi.org/10.1021/jacs.5b10666); pmid: [26863450](https://pubmed.ncbi.nlm.nih.gov/26863450/)
- W. Chaikittisilp, A. Sugawara, A. Shimojima, T. Okubo, Hybrid porous materials with high surface area derived from bromophenylethynyl-functionalized cubic siloxane-based building units. *Chem. Eur. J.* **16**, 6006–6014 (2010). doi: [10.1002/chem.201000249](https://doi.org/10.1002/chem.201000249); pmid: [20391584](https://pubmed.ncbi.nlm.nih.gov/20391584/)
- S. J. Rowan, S. J. Cantrill, G. R. L. Cousins, J. K. M. Sanders, J. F. Stoddart, Dynamic covalent chemistry. *Angew. Chem. Int. Ed.* **41**, 898–952 (2002). doi: [10.1002/1521-3773\(20020315\)41:6<898::AID-ANIE898>3.0.CO;2-E](https://doi.org/10.1002/1521-3773(20020315)41:6<898::AID-ANIE898>3.0.CO;2-E); pmid: [12491278](https://pubmed.ncbi.nlm.nih.gov/12491278/)
- M. G. Walawalkar, R. Murugavel, H. W. Roesky, H.-G. Schmidt, The first molecular borophosphonate cage: Synthesis, spectroscopy, and single-crystal x-ray structure. *Organometallics* **16**, 516–518 (1997). doi: [10.1021/om960995n](https://doi.org/10.1021/om960995n)
- K. Diemert, U. Englert, W. Kuchert, F. Sandt, A cage molecule with a cubanoid P₄B₄ framework: tBu₄P₄Ph₄B₄O₁₂—A structural analogue of the isovalence electronic organosilasesquioxanes R₆Si₆O₁₂. *Angew. Chem. Int. Ed.* **36**, 241–243 (1997). doi: [10.1002/anie.199702411](https://doi.org/10.1002/anie.199702411)
- J. Tönnemann et al., Borophosphonate cages: Easily accessible and constitutionally dynamic heterocubane scaffolds. *Chem. Eur. J.* **18**, 9939–9945 (2012). doi: [10.1002/chem.201201287](https://doi.org/10.1002/chem.201201287); pmid: [22764094](https://pubmed.ncbi.nlm.nih.gov/22764094/)
- M. G. Walawalkar, R. Murugavel, H. W. Roesky, H.-G. Schmidt, Syntheses, spectroscopy, structures, and reactivity of neutral cubic group 13 molecular phosphonates. *Inorg. Chem.* **36**, 4202–4207 (1997). doi: [10.1021/ic970346j](https://doi.org/10.1021/ic970346j)
- H. Höpfl, The tetrahedral character of the boron atom newly defined—A useful tool to evaluate the N→B bond. *J. Organomet. Chem.* **581**, 129–149 (1999). doi: [10.1016/S0022-328X\(99\)00053-4](https://doi.org/10.1016/S0022-328X(99)00053-4)
- H. Furukawa, O. M. Yaghi, Storage of hydrogen, methane, and carbon dioxide in highly porous covalent organic frameworks for clean energy applications. *J. Am. Chem. Soc.* **131**, 8875–8883 (2009). doi: [10.1021/ja9015765](https://doi.org/10.1021/ja9015765); pmid: [19496589](https://pubmed.ncbi.nlm.nih.gov/19496589/)
- M. Eddaoudi et al., Systematic design of pore size and functionality in isorecticular MOFs and their application in methane storage. *Science* **295**, 469–472 (2002). doi: [10.1126/science.1067208](https://doi.org/10.1126/science.1067208); pmid: [11799235](https://pubmed.ncbi.nlm.nih.gov/11799235/)
- RCSR, The reticular chemistry structure resource; <http://rcsr.net> [accessed 26 June 2020].
- Y.-B. Zhang et al., Single-crystal structure of a covalent organic framework. *J. Am. Chem. Soc.* **135**, 16336–16339 (2013). doi: [10.1021/ja409033p](https://doi.org/10.1021/ja409033p); pmid: [24143961](https://pubmed.ncbi.nlm.nih.gov/24143961/)
- A. M. Evans et al., Seeded growth of single-crystal two-dimensional covalent organic frameworks. *Science* **361**, 52–57 (2018). doi: [10.1126/science.aar7883](https://doi.org/10.1126/science.aar7883); pmid: [29930093](https://pubmed.ncbi.nlm.nih.gov/29930093/)
- T. Ma et al., Single-crystal x-ray diffraction structures of covalent organic frameworks. *Science* **361**, 48–52 (2018). doi: [10.1126/science.aat7679](https://doi.org/10.1126/science.aat7679); pmid: [29976818](https://pubmed.ncbi.nlm.nih.gov/29976818/)
- L. Liang et al., Non-interpenetrated single-crystal covalent organic frameworks. *Angew. Chem. Int. Ed.* **59**, 17991–17995 (2020). doi: [10.1002/anie.202007230](https://doi.org/10.1002/anie.202007230); pmid: [32648325](https://pubmed.ncbi.nlm.nih.gov/32648325/)
- J. Ilavsky, Nika: Software for two-dimensional data reduction. *J. Appl. Cryst.* **45**, 324–328 (2012). doi: [10.1107/S0021889812004037](https://doi.org/10.1107/S0021889812004037)
- Dassault Systèmes, BIOVIA Materials Studio 2017 (Waltham, MA, 2016).
- Bruker AXS Inc., APEX2 (Madison, WI, 2010).
- G. M. Sheldrick, A short history of SHELX. *Acta Crystallogr. A* **64**, 112–122 (2008). doi: [10.1107/S0108767307043930](https://doi.org/10.1107/S0108767307043930); pmid: [18156677](https://pubmed.ncbi.nlm.nih.gov/18156677/)
- O. V. Dolomanov, L. J. Bourhis, R. J. Gildea, J. A. K. Howard, H. Puschmann, OLEX2: A complete structure solution, refinement and analysis program. *J. Appl. Cryst.* **42**, 339–341 (2009). doi: [10.1107/S0021889808042726](https://doi.org/10.1107/S0021889808042726)
- C. F. Macrae et al., Mercury: Visualization and analysis of crystal structures. *J. Appl. Cryst.* **39**, 453–457 (2006). doi: [10.1107/S002188980600731X](https://doi.org/10.1107/S002188980600731X)

33. T. Düren, F. Millange, G. Férey, K. S. Walton, R. Q. Snurr, Calculating geometric surface areas as a characterization tool for metal–organic frameworks. *J. Phys. Chem. C* **111**, 15350–15356 (2007). doi: [10.1021/jp074723h](https://doi.org/10.1021/jp074723h)
34. Micromeritics Instrument Corporation, MicroActive, version 5.01 (Norcross, GA, 2018).

ACKNOWLEDGMENTS

We thank T. Zeng and Y.-B. Zhang for support from the SPST Analytical Instrumentation Center (no. SPST-AIC10112914) at ShanghaiTech University for solid-state NMR measurement during the COVID-19 lockdown. C.G. thanks P. Waller and T. Osborn Popp for discussions in the early stages of the project and H. Lyu, X. Pei, and H. L. Nguyen for advice during the entire project. T.M. and N.H. thank X. Pei for helpful discussions on structure refinements. C.G., T.M., N.H., and O.M.Y. thank C. Zhu for acquiring PXRD data on beamline 7.3.3 of the Advanced Light Source.

Funding: We acknowledge the College of Chemistry Nuclear Magnetic Resonance Facility for resources and staff assistance, where instruments are partially supported by NIH S10OD024998. This research used beamline 7.3.3 and resources of beamline

12.2.1 at the Advanced Light Source, which are U.S. Department of Energy, Office of Science User Facilities, under contract no. DE-AC02-05CH11231. C.G., a Leopoldina postdoctoral fellow of the German National Academy of Science (LPDS 2019-02), acknowledges the receipt of a fellowship of the Swiss National Science Foundation (P2EZP2-184380). N.H. thanks the Studienstiftung des deutschen Volkes and acknowledges receipt of the KAVLI ENSI Philomathia Graduate Student Fellowship. O.M.Y. acknowledges support and collaboration as part of the UC Berkeley–KACST Joint Center of Excellence for Nanomaterials for Clean Energy Applications, King Abdulaziz City for Science and Technology, Riyadh 11442, Saudi Arabia. C.G. and O.M.Y. intend to file a patent application on the reported work. **Author contributions:** C.G. and O.M.Y. conceived the idea and led the project. C.G. synthesized BPA-**1** to **5** and BP-COF-**1** to **5** and conducted the spectroscopic (IR and NMR), thermal gravimetric analysis, and elemental analysis characterizations. T.M. conducted the synthesis of BP-COF-**6** and carried out all PXRD refinements and structural modeling. T.M. and N.H. solved the single-crystal x-ray crystal structure of BP-COF-**6**. N.H. conducted sorption experiments. C.G., T.M., N.H., and O.M.Y. interpreted the results, and C.G., T.M., and O.M.Y. wrote the manuscript. **Competing**

interests: None declared. **Data and materials availability:**

Synthetic procedures, spectroscopic (IR and NMR), thermal gravimetric analysis, and x-ray diffraction data reported in this manuscript are present in the main text or in the supplementary materials. Unit cell parameters and atomic positions of BP-COF-**1** to **5** are provided as xyz files (data S2). The crystallographic data are tabulated in the supplementary materials and archived at the Cambridge Crystallographic Data Centre under reference number CCDC 2013495.

SUPPLEMENTARY MATERIALS

science.sciencemag.org/content/370/6515/eabd6406/suppl/DC1

Materials and Methods

Supplementary Text

Figs. S1 to S122

Tables S1 to S3

References (35–38)

Data S1 and S2

2 July 2020; accepted 3 September 2020

10.1126/science.abd6406

RESEARCH ARTICLE SUMMARY

GEOCHEMISTRY

Deep abiotic weathering of pyrite

Xin Gu*, Peter J. Heaney, Fabio D. A. Aarão Reis, Susan L. Brantley

INTRODUCTION: Oxidative weathering of pyrite, the most abundant sulfide mineral in Earth's crust, is coupled to the biogeochemical cycles of sulfur, oxygen, carbon, and iron. Pyrite oxidation is key to these cycles because of its high reactivity with oxygen. Before the Great Oxidation Event (GOE), atmospheric oxygen concentrations were low on early Earth and pyrite was exposed at Earth's surface, allowing erosion into sediments that were preserved in river deposits. Today, it oxidizes at depth in most rocks and is often not exposed at the land surface. To understand pyrite weathering through geologic time, researchers extrapolate the reaction kinetics based on studies from the laboratory or in acid mine drainage. Such work has emphasized the important role of microorganisms in catalyzing pyrite oxidation. But to interpret the oxidation rates of pyrite on early Earth requires knowledge of the rate-limiting step of the oxidation as it occurs naturally in rocks.

RATIONALE: We investigated the oxidation of pyrite in micrometer-sized grains, in centimeter-sized rock fragments, and in meter-scale boreholes at a small, well-studied catchment in a critical-zone observatory. Our goal was to determine the reaction mechanism of pyrite

weathering in rocks as it occurs today. The slow-eroding catchment is underlain by shale, the most common rock type exposed on Earth. We determined weathering profiles of pyrite through chemical and microscopic analysis.

RESULTS: At the ridgelines of the shale watershed, most pyrite oxidation occurs within a 1-m-thick reaction zone ~16 m below land surface, just above the depth of water table fluctuation. This is the reaction front at the borehole scale. Only limited oxidation occurs in halos around a few fractures at deeper depths. Above the depth where pyrite is 100% oxidized in all boreholes, rock fracture density and porosity are generally higher than below. However, the narrow parts of pore openings called pore throats remain small enough in oxidizing shale to limit access of microorganisms to the pyrite surface. During oxidation, iron oxides pseudomorphically replace the pyrite grains. High-resolution transmission electron microscopy (TEM) reveals that the oxidation front at grain scale is defined by a sharp interface between pyrite and an iron (oxyhydr)oxide (Fh) that is either ferrihydrite or ferroxhyte. This Fh then transforms into a banded structure of iron oxides that ultimately alter to goethite in

outer layers. This complex oxidative transformation progresses inward from fractures when observed at clast scale.

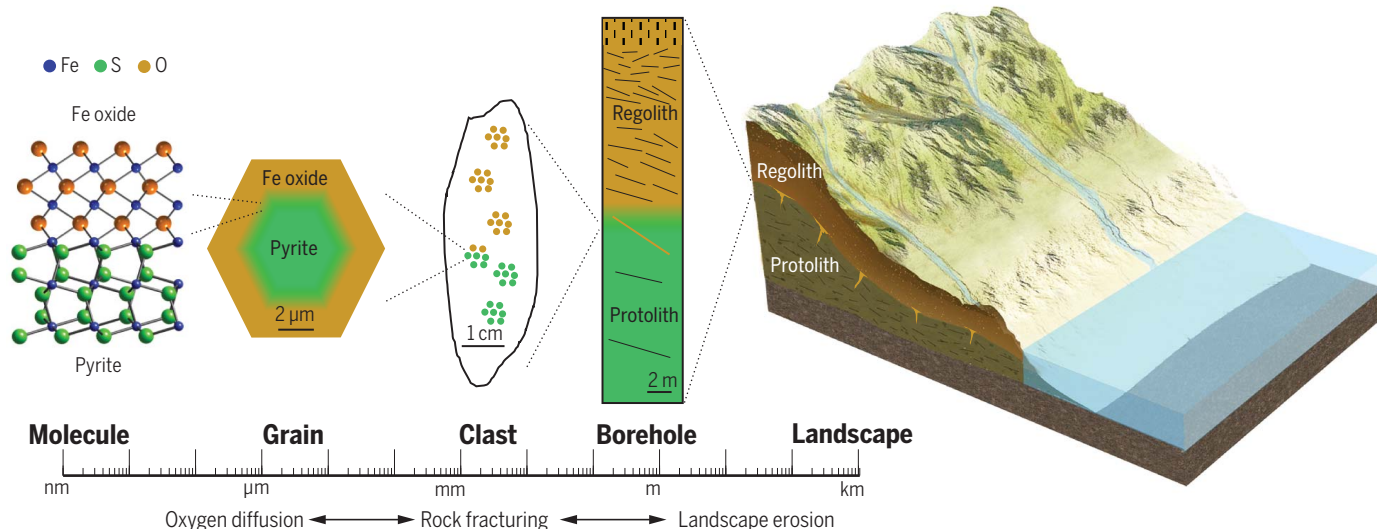
CONCLUSION: Under today's atmosphere, pyrite oxidation, rate-limited by diffusion of oxygen at the grain scale, is regulated by fracturing at clast scale. As pyrite is oxidized at borehole scale before reaching the land surface in most landscapes today, the oxidation rate is controlled by the movement of pyrite upward, which is in turn limited by the rate of erosion. Comparisons of shale landscapes with different erosion rates reveal that fracture spacing varies with erosion rate, so this suggests that fracture spacing may couple the landscape-scale to grain-scale rates. Microbial acceleration of oxidation globally today is unlikely in low-porosity rocks because pyrite oxidation usually occurs at depth, where pore throats limit access, as observed here for shales. Before the GOE, the rate of pyrite oxidation was instead controlled by the slower reaction kinetics in the presence of lower atmospheric oxygen concentrations. At that time, therefore, pyrite was exposed at the land surface, where microbial interaction could have accelerated the oxidation and acidified the landscape, as suggested by others. Our work highlights the importance of fracturing and erosion in addition to atmospheric oxygen as a control on the reactivity of this ubiquitous iron sulfide. ■

The list of author affiliations is available in the full article online.

*Corresponding author. Email: xug102@psu.edu

Cite this article as X. Gu *et al.*, *Science* **370**, eabb8092 (2020). DOI: 10.1126/science.abb8092

S READ THE FULL ARTICLE AT
<https://doi.org/10.1126/science.abb8092>



Schematic depiction of oxidative weathering of pyrite in rocks buried at meters depth. Pyrite oxidation was studied from the molecular (TEM) scale of the pyrite-Fe oxide interface through clast and borehole scales to extrapolate to landscapes. The rate of oxidation of pyrite, limited at grain scale by oxygen diffusion through the shale matrix, is regulated at larger scales by fracturing and erosion.

RESEARCH ARTICLE

GEOCHEMISTRY

Deep abiotic weathering of pyrite

Xin Gu^{1*}, Peter J. Heaney¹, Fabio D. A. Aarão Reis², Susan L. Brantley^{1,3}

Pyrite is a ubiquitous iron sulfide mineral that is oxidized by trace oxygen. The mineral has been largely absent from global sediments since the rise in oxygen concentration in Earth's early atmosphere. We analyzed weathering in shale, the most common rock exposed at Earth's surface, with chemical and microscopic analysis. By looking across scales from 10^{-9} to 10^2 meters, we determined the factors that control pyrite oxidation. Under the atmosphere today, pyrite oxidation is rate-limited by diffusion of oxygen to the grain surface and regulated by large-scale erosion and clast-scale fracturing. We determined that neither iron- nor sulfur-oxidizing microorganisms control global pyrite weathering fluxes despite their ability to catalyze the reaction. This multiscale picture emphasizes that fracturing and erosion are as important as atmospheric oxygen in limiting pyrite reactivity over Earth's history.

Pyrrite is an extremely reactive, abundant sulfide in Earth's crust, and its oxidation is an important regulator of biogeochemical processes (1). Oxidative weathering of pyrite (OWP) is coupled to the global budgets of four of the most common redox-active elements on Earth: sulfur, oxygen, carbon, and iron (2–6). OWP releases ~45% of the world's freshwater flux of sulfur to the ocean (7), controls reactivity of iron in some groundwaters (8, 9), draws oxygen out of the atmosphere (10), and couples with the carbon cycle (11, 12).

OWP is particularly important to our understanding of Earth's dynamic oxygenation history (13, 14). For example, the presence or absence of detrital pyrite in preserved sediments reflects the intensity of terrestrial OWP and can therefore be a record of oxygen in the early atmosphere (2, 15, 16). In addition, when terrestrial OWP increased during the Great Oxidation Event (GOE) at ~2.5 billion years (Gyr) ago, it likely generated acid that in turn affected the balance of some nutrients and trace metals in the ocean (17, 18). Overall, OWP is an important process in the negative feedback that may promote the stabilization of oxygen partial pressure (pO_2) in the atmosphere (19, 20).

Explanations of OWP in Earth's past rely on extrapolations of pyrite oxidation kinetics to low pO_2 and on assumptions that the rate of OWP is proportional to pO_2 (19, 20). This latter assumption is key because extrapolation implicitly requires knowledge of rate-limiting steps. If the mechanism changes, this extrapolation is no longer valid. Previous

research on pyrite reactivity focused on oxidation in the laboratory [e.g., (21–23)] or in acid mine drainage (24, 25). In acid mine drainage, the rate-limiting step is oxidation of aqueous Fe(II) to Fe(III) because Fe(III) is a more efficient oxidant than O_2 in acidic conditions (21, 22, 24). In addition, under acidic or circumneutral pH, OWP can be accelerated by more than one order of magnitude by some iron- and sulfur-oxidizing microorganisms living on or near the mineral surface (26–28).

Owing to the high concentration of O_2 in the modern atmosphere and high reactivity of pyrite, OWP today is suggested to be limited by erosion (2) rather than interfacial reaction. This idea is supported by observations showing that the flux of OWP-generated sulfate is proportional to the rate of erosion in some catchments (29, 30). In addition, several researchers have documented cases where pyrite oxidizes to a depth of meters in pyrite-rich black shales (31–34), pyrite-poor shales (30, 35–38), and crystalline rocks (39).

Although pyrite has been documented in isolated occurrences to oxidize at meters to tens of meters below the land surface, the controls on deep reactivity are still poorly understood (40). We do not know if microorganisms facilitate oxidation reactions at these depths, whether the reaction is oxidant-limited, and how these controls may have changed through time. To answer these questions, we integrated observations from pyrite grains to rock fragments to boreholes in a shale watershed (Fig. 1). Using images and analyses from 10^{-9} to 10^2 m, we explore the implications of multiscale reactivity for the global oxygen and sulfur cycles (3–5).

We study shales because they are the most common rock exposed on Earth and because they are pyrite-containing but low in porosity, like most exposed igneous and metamorphic rocks (2, 11). Our focus is a watershed where erosional and hydrological processes

are well studied (41). This watershed (Shale Hills, Pennsylvania, USA) is slow-eroding but can nonetheless elucidate global OWP because it exhibits some of the same features of OWP observed in shales experiencing some of the highest rainfall and erosion rates in the world (30).

Pyrite measured in boreholes

At Shale Hills, layers of weathered material (regolith) overlie the parent shale (protolith). Regolith consists of a thin soil (0.2 to 3 m) above tens of meters of weathered and fractured rock (15 to 22 m thick). The protolith, a gray Silurian shale, contains trace sulfur in the form of pyrite (30). Pyrite occurs as both single euhedral crystals and raspberry-like clusters of euhedral crystals (framboids) disseminated in a clay + quartz matrix. When considered from the perspective of the land surface, regolith forms as protolith is moved up and through the weathering zone while topsoil is removed by erosion. The cumulative effect is recorded over time in regolith as elemental depth profiles, which extend from the most highly weathered material at land surface to protolith at depth (42, 43). We examined weathering profiles in material recovered from boreholes under a ridge and a valley (fig. S1).

Like other shales (31–35, 38), the earliest alterations observed at Shale Hills are fracturing, dissolution of carbonate, and OWP (30, 36, 37). During OWP, iron oxides replace iron sulfide while retaining the external shape. This phenomenon is called pseudomorphism and is exemplified by octahedral Fe (oxyhydr)oxide microcrystals within framboids (Fig. 2). The Fe oxide phases evolved as the pseudomorphs moved upward through the zone of oxidation. We performed transmission electron microscopy (TEM) on samples at different depths and found that ferrihydrite or ferroxhyte (Fh) formed initially at the interface with the oxidizing pyrite (Fig. 3) but then was later replaced over time by goethite.

Under the south ridge at Shale Hills (fig. S1), OWP initiates 16 m below the land surface (mbls), defining the distance that oxidation has advanced into the subsurface. We identify this distance, L_b , as the thickness of oxidized regolith. We use subscript b to indicate borehole scale (meters) as a contrast to the centimeter scale of a clast (c) or micrometer scale of a grain (g). Pyrite has completely oxidized throughout the layer of thickness L_b , except in the bottom ~1-m-thick depth interval (l_b) located about 1.5 to 3.5 m above the water table, where oxidation and formation of pseudomorphs are ongoing (Fig. 1A and fig. S2). We determined the change in fractional extent of oxidation versus depth across l_b . We identify l_b as the reaction front (Fig. 1A) because pyrite abundance varies generally from deep to shallow as the extent of oxidation varies from 0

¹Department of Geosciences, The Pennsylvania State University, University Park, PA 16802, USA. ²Instituto de Física, Universidade Federal Fluminense, Avenida Litorânea s/n, 24210-340 Niterói, RJ, Brazil. ³Earth and Environmental Systems Institute, The Pennsylvania State University, University Park, PA 16802, USA.

*Corresponding author. Email: xug102@psu.edu

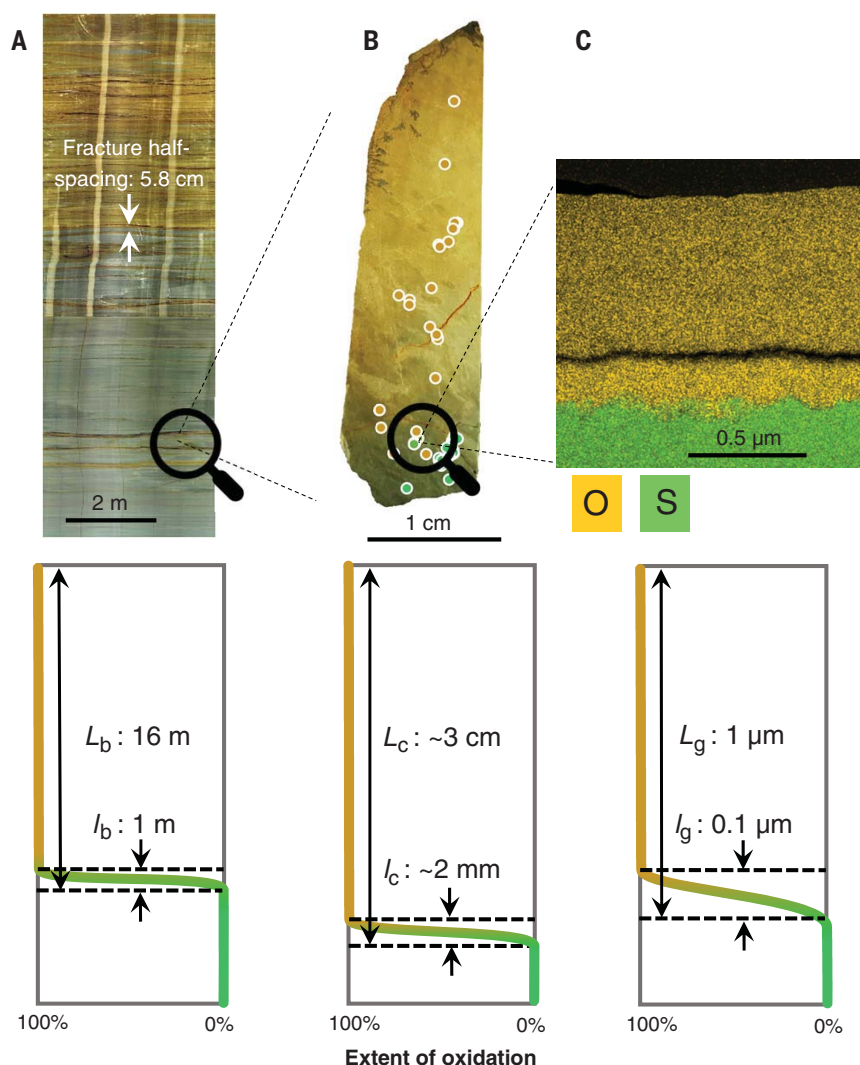


Fig. 1. Images and schematic depth profiles showing extent of pyrite oxidation at borehole (subscript b), clast (c), and grain (g) scales. (A) Optical downhole televiewer image of a drilled core showing depth to rock containing unaltered pyrite, i.e., oxidation advance distance (L_b) and depth interval across which pyrite is oxidizing (the thickness of reaction front, l_b) for borehole CZMW8 under south ridge of Shale Hills. **(B)** Optical image of a partially oxidized shale clast formed as a fragment between fractures from the depth shown in (A) (borehole CZMW8, ~25.5 mbls). The small white circles show the locations of pyrite and Fe oxides pseudomorphs. Distance from fracture into unaltered center of fragment, i.e., oxidation advance distance (L_c), is shown with the thickness of oxidation front (l_c). Extent of oxidation was determined by sulfur concentrations in pyrite and oxide framboids (see Fig. 2), semiquantified from EDS. **(C)** Elemental map (STEM-EDS) of a partially oxidized pyrite grain (green: sulfur; brown: oxygen) collected from the weathered clast as in (B). Thickness of the oxidized rim (L_g , i.e., the oxidation advance distance) and thickness of oxidation front (l_g) for a partially oxidized pyrite grain. Colors vary with extent of oxidation from green (unoxidized) to orange (oxidized). Dark horizontal line is a zone with high porosity. Extent of oxidation was calculated from the mass transfer coefficient τ_{py} as described in materials and methods (0% oxidation for $\tau_{py} = 0$ to 100% for $\tau_{py} = -1$).

to 100%. We also observed that the advance distance of oxidation at the clast scale (L_c) is a few centimeters with a reaction front thickness $l_c \sim 2 \text{ mm}$ (Fig. 1B), and the advance distance of oxidation at the grain scale (L_g) is $\sim 1 \text{ μm}$ with $l_g \sim 0.1 \text{ μm}$ (Fig. 1C). The magnitudes of L and l at all these scales vary with location of borehole in the landscape, depth of clast

in the oxidation front, and distance of pyrite grain from the fractured edge of a clast.

As erosion exhumes the shale, porosity grows through dissolution and fracturing (fig. S2). The average fracture density measured by downhole televiewer increases from 3.9 ± 3.0 fractures per meter below the OWP front to 8.7 ± 3.2 fractures per meter (spacing of $5.8 \pm 2.5 \text{ cm}$)

above the front (measured under the south ridge, fig. S2). The effective porosity (porosity that is open to fluid flow) that we measured by mercury intrusion also increases from $1.6 \pm 0.5\%$ of the protolith to $4.5 \pm 0.3\%$ of the weathered rock across the front (table S1). The increase in porosity cannot be explained by oxidation of the trace pyrite (~ 0.2 to $0.3 \text{ wt } \%$ in protolith). However, as previously documented (30, 44), porosity growth can be largely accounted for by dissolution of chlorite, the most abundant iron-containing clay (13 to 17 wt % in protolith). At the same depth that pyrite becomes $\sim 100\%$ oxidized, dissolution of chlorite begins (30, 37, 44). Under the valley, we observed similar increases in porosity, fracture density, and degree of chlorite dissolution above the depth that OWP reaches 100% (fig. S3) (44).

Although porosity increases upward, the width of pore throats in regolith under the south ridge does not grow larger than 10 to 20 nm as weathering proceeds (30). These throats, the narrow parts of pore openings, are important because they are the most restrictive with respect to access of fluids (45) and microorganisms (46). By contrast, pore throats under the valley at some depths grow larger than 400 nm (table S1). The reason for this larger size is that the sedimentary strata under the valley initially contain more abundant carbonate minerals than under the ridgelines, and the dissolution of these minerals leaves less-constricted pore throats.

Pyrite weathering in shale fragments

Although we emphasize that most of the OWP occurs in a meter-wide reaction zone under ridgelines, the regolith-protolith interface is not a Euclidean plane but rather a highly rough interface shaped by faults and fractures. This geometry has also been suggested for other low-porosity rocks (39, 47). In our study site, for example, OWP is observed around a few fractures beneath the water table under the ridges (44). In one example from an oxidized halo around a fracture, we again observed pyrite + Fe oxides in pseudomorphs (Fig. 2) where oxidation of pyrite is 100% complete at the fracture and decreases to undetectable levels $\sim 3 \text{ cm}$ away. This documents the distance that oxidation advanced from the fracture into the clast, L_c (Fig. 2). The width of the reaction front across which pyrite is 100% oxidized at that scale, l_c , is constrained by observation to be $\sim 2 \text{ mm}$ (Fig. 1B).

We inferred from these observations that, as erosion removes topsoil at the land surface and shale moves closer to the land surface over geologic time, new fractures form and rock fragments or clasts between fractures oxidize progressively inward from their fractured surfaces (fig. S4).

Pyrite weathering in single grains

We measured the oxidation advance distance L_g in grains within partially pseudomorphed

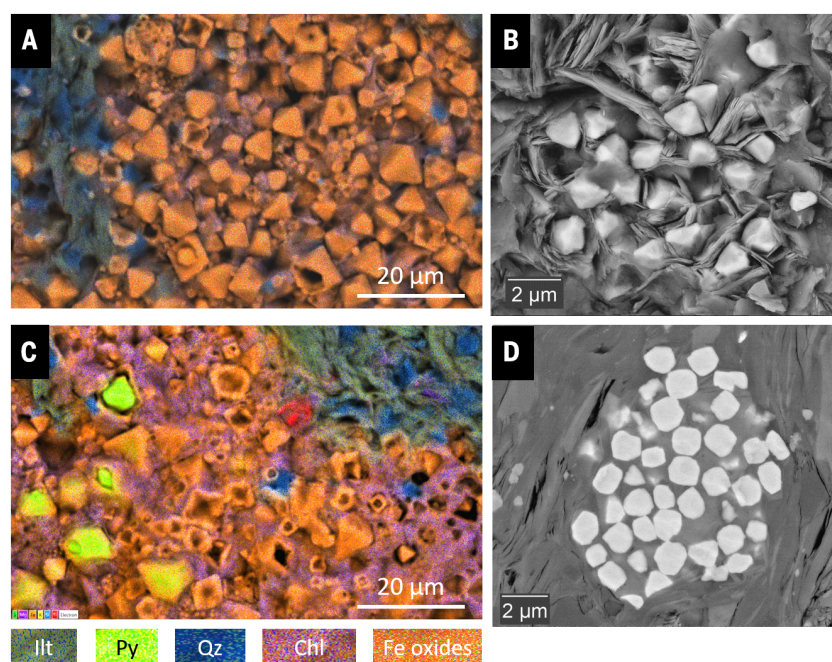


Fig. 2. Photomicrographs of oxidizing pyrite and its pseudomorphs within one rock fragment shown in Fig. 1B. (A) X-ray elemental map (SEM-EDS) of framboidal and euhedral Fe oxide pseudomorphs after pyrite. (B) Back-scattered SEM image of Fe oxide framboid formed in situ in shale as pseudomorph. (C) X-ray elemental map (SEM-EDS) of partially oxidized pyrite. (D) Back-scattered SEM image of unaltered framboidal pyrite on an ion-milled section of deep unaltered bedrock. Chl: chlorite; Ill: illite; Py: pyrite; Qz: quartz.

framboids (Fig. 3). Grains ($\sim 5 \mu\text{m}$ in radius) exhibit pyrite cores surrounded by rims of Fe oxides. The sulfur in the crystalline and nonporous pyrite core of grains is progressively replaced by oxygen to form Fh across a sharp interface (Fig. 3B). No sulfate mineral phases are present because sulfur and oxygen are never observed together. Therefore, the concentration profiles of sulfur and oxygen are reciprocal (Fig. 3B and fig. S5). For one specific grain, the depth of penetration of oxidation, L_{g} , is $\sim 1 \mu\text{m}$ and reaction front thickness, l_{g} , is $\sim 0.1 \mu\text{m}$ (Fig. 3).

Microscopic characterization reveals that Fh transforms to goethite (Gth) within a complex banded structure that follows the sequence pyrite-Fh-Gth-Fh-Gth (Fig. 3B). As we discovered using high-resolution TEM (HRTEM), unoxidized pyrite is surrounded by a very thin layer (10 to 20 nm) of Fh (Fig. 3C). This first transformation to Fh is consistent with laboratory observations that Fh-like iron oxide patches grow pseudomorphically on pyrite surfaces when in contact with O_2 (48–50). Selected area electron diffraction (SAED) and HRTEM show that Fh in turn is enveloped by poorly crystalline Gth with a thickness of $\sim 0.1 \mu\text{m}$ (Fig. 3, C and D, and fig. S6). We infer that Gth was formed directly from Fh because it is the more thermodynamically stable phase (51). This inference is consistent with laboratory observations that the initial oxidation products of pyrite are $\text{Fe}(\text{OH})_3$ (ferrihydrite)

followed by transformation to $\text{FeO}(\text{OH})$ (Gth) + H_2O , or $\text{FeO}(\text{OH})$ (feroxyhyte) followed by transformation to $\text{FeO}(\text{OH})$ (Gth) (51). The Fh-Gth sequence repeats in the outer layer ($\sim 0.9 \mu\text{m}$ in thickness), which is separated from the inner Fh-Gth sequence by a zone with low porosity, which is observed in the back-scattered electron micrograph as a dark zone (Fig. 3B).

This layering offers some insights into the reaction mechanism. Ferrihydrite or feroxyhyte precipitates at near neutral or slightly acidic pH (52, 53). This observation is important because it implies that the H_2SO_4 released during OWP does not drive pH far below neutral. We believe that the released acidity was likely consumed locally by dissolution of other minerals. Consistent with this inference, energy-dispersive x-ray spectra (EDS) of the Fe oxide layers reveal the presence of Si and Al (fig. S5). Because we observed chlorite dissolution initiating near OWP in several boreholes (44), we attribute the Si and Al to H_2SO_4 -driven dissolution of local chlorite (Fig. 3A). Incorporation of silica into Fh also retards the transformation to Gth (54).

The mechanism of oxidation is abiotic

Our observations are distinct from observations for weathering minerals of any composition in that we reported reaction fronts and weathering advance distances across scales from 10^{-9} to 10^2 m , constraining the rate-limiting

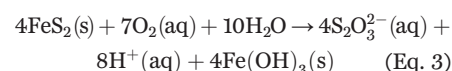
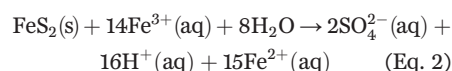
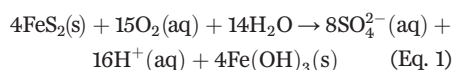
steps and reaction mechanisms. Furthermore, these results can probably be generalized because OWP occurs in rock at depth in very similar ways in other watersheds eroding at much faster rates in other climates (30–35, 38).

The rate of OWP at Shale Hills is limited by diffusion of oxygen through shale matrix rather than chemical reaction. At the landscape scale, the rate is limited by movement of pyrite into the weathering zone, as dictated by the rate of erosion (42, 55). Below the water table, we observed OWP only in halos around fractures (e.g., under the ridge) or where porosity is high because of carbonate dissolution under the valley (44). If transport of oxygen was not slow below the water table, then OWP would be extensive throughout the saturated zone. These observations point toward rate limitation at the clast scale by transport of oxygen, which is in turn limited by the formation of fractures and pores.

Oxidation is also not homogeneous at the grain scale (Fig. 3), suggesting that OWP is limited by transport of reactants or products through matrix to the grain surface. Transport cannot occur by advection at this scale because permeability, effective porosity, and total porosity are low in the shale matrix: In the protolith, these values are ~ 0.25 nanodarcy (56), $1.6 \pm 0.5\%$ (30), and $4.9 \pm 0.4\%$ (30), respectively. For most relatively unfractured low-porosity shales, reactants move by diffusion (57).

The observation that the rate-limiting step at the grain scale is diffusion through shale matrix is consistent with the pseudomorphic nature of the transformation and the sharp interface between pyrite and Fe oxide (Fig. 3A). Pseudomorphism is known to occur for some interfacial dissolution and reprecipitation reactions when the processes are slow and accompanied by small changes in volume (58, 59). We calculated the transformation from Py to Fh to yield a 14% volume decrease (assuming Fe is immobile). This volume decrease could also contribute to the porosity, which is apparent as darker zones in the banded layers (Fig. 3B).

To constrain the mechanism, we consider three possible stoichiometries of OWP:



$\text{Fe}(\text{III})$ is the oxidant when aqueous $\text{Fe}(\text{III})$ is stable at the interface. In that case, the process is controlled by oxidation-reduction cycling

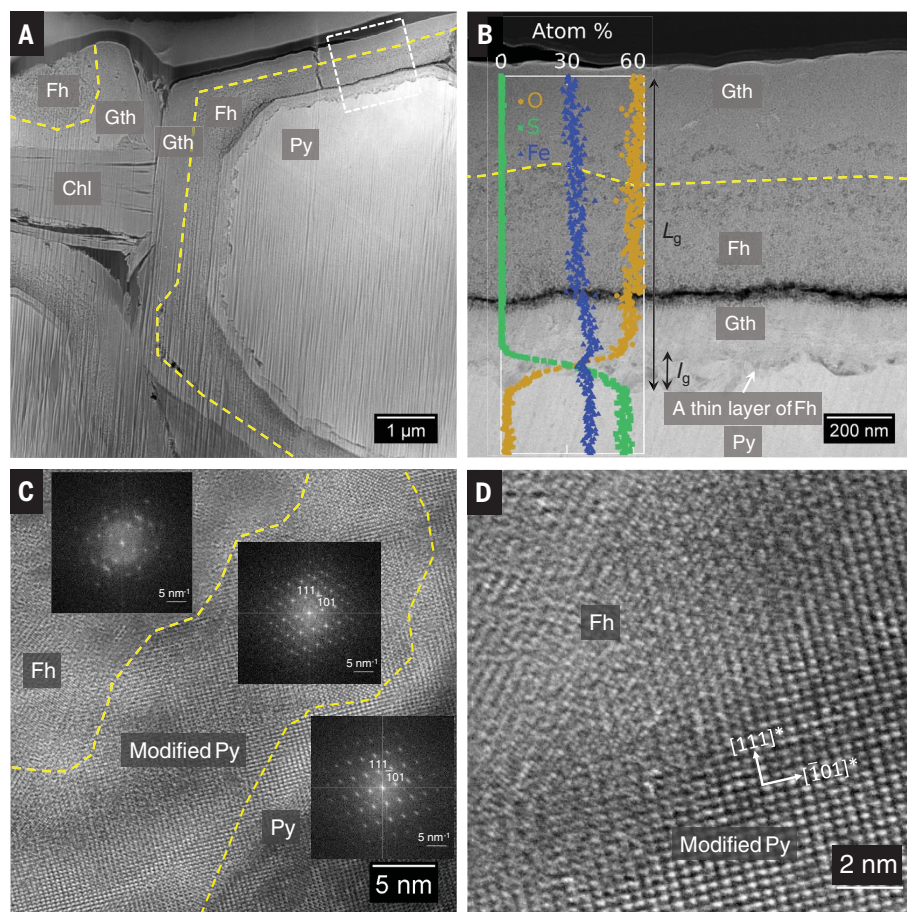


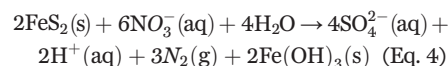
Fig. 3. Pyrite oxidation at grain scale. (A) Scanning TEM (STEM, HAADF mode) on a partially pseudomorphed pyrite grain identified using SEM-EDS (Fig. 2C) and then prepared by FIB. The dark gray rims are Fe oxides, and lighter gray core is pyrite. (B) STEM image showing the pyrite-Fe oxide interface [zoom-in view of the dashed box in (A)]. The colored lines show the elemental variations (normalized atomic percentage) versus distance, extracted from the line scan on the section. Mineral phases were identified from elemental composition (EDS) and electron diffraction. (C) HRTEM image showing the pyrite-Fe oxide interface with an inset showing a FFT of the modified pyrite region. (D) Zoomed-in view of modified Py-Fh interface. Chl: chlorite; Fh: ferrihydrite or feroxyhyte; Gth: goethite; Py: pyrite.

of Fe(II)-Fe(III) and can be accelerated by Fe-oxidizing microorganisms (26, 28). However, the smallest bacteria reported in the subsurface are ~200 nm in nominal diameter (60), larger than the measured pore throats under the ridges (10 to 20 nm, table S1). Therefore, microorganisms are not likely to access the pyrite surface to accelerate the reactions. Alternatively, if thiosulfate formed as in (3), it could diffuse through the matrix out to the fractures and if sulfur-oxidizing microorganisms fit in the large fractures, then OWP could be mediated by thiosulfate-oxidizing organisms. This mechanism is also unlikely, however, because as a highly unstable molecule, thiosulfate is always observed at extremely low concentrations (26, 28). Thus, OWP in this deep, low-porosity rock was not microbially catalyzed.

The mechanism is thus abiotic and is limited by diffusion with respect to either reactants or products. Neither diffusion of H^+ nor

Fe(III) is likely limiting the rate given the circumneutral or slightly acidic pH near the Py-Fh interface. The lack of a sulfur-containing phase near the oxidized pyrite (Fig. 1C and fig. S5) also suggests that outward diffusion of sulfur species is not rate-limiting. Thus, inward diffusion of the oxidant must limit the rate.

At the near-neutral pH of the interface, aqueous Fe(III) is extremely low in concentration, and the oxidant is likely to be O_2 or nitrate. The latter oxidant may oxidize pyrite in nature but only if microorganisms participate. For example, sulfur-oxidizing, nitrate-reducing microorganisms are thought to accelerate OWP if they live directly on pyrite (67):



But nitrate as an oxidant is extremely unlikely because very little nitrate is observed in

pore fluids at Shale Hills (62). We therefore conclude that OWP is abiotic and rate-limited by diffusion of oxygen through the shale matrix.

Toward a multiscale model

Our observations show that oxygen, brought beneath the water table in fractures, diffuses into the matrix and oxidizes the pyrite. Microorganisms could be involved, but only to a very minor extent and only if they live in fractures rather than matrix or in a limited depth range under the valley where pore throats grow larger than micrometers (table S1). Above the water table, 100% of the pyrite oxidizes because the porosity is larger, the spacing between fractures is smaller (fig. S2), the fraction of air in the pores is higher, and the diffusion of oxygen is faster (63). Beneath the water table, OWP is restricted to a few larger, connected fracture zones under the ridge or to depth ranges where dissolution of carbonates has interconnected porosity under the valley (44). These arguments are consistent with simulations of weathering that show that a weathering front can locate either above or below the water table (64, 65).

For the ridge boreholes where the OWP reaction front thickness l_b is ~1 m (Fig. 1), a simple one-dimensional model based on water moving downward and rock moving upward is applicable. The average residence time t_b for shale fragments crossing upward through the reaction front equals l_b divided by the measured erosion rate of $0.02 \pm 0.01 \text{ m kyr}^{-1}$ (66): 50 ± 30 thousand years (kyr). That is, fragments of shale (i.e., clasts) move up through the front over a period of 50 kyr while oxygen diffuses in from the fragment surface to oxidize the pyrite in the interior (fig. S4). At the point of exit from the top of the front after 50 kyr, each clast has become totally oxidized. At that point, the average distance that oxidation advances inward from each fracture, L_c , equals half the average fracture spacing d_f (i.e., inverse of the fracture density, fig. S4).

The residence time during which each fragment crosses the front, 50 kyr, constrains the diffusion-limited oxidation rate of pyrite within each upward-transiting fragment, allowing parameterization of a diffusion model based on fracture spacing. We developed and corroborated such a model against published properties of shale and oxidation rates of pyrite (67). The most important model parameter is the effective diffusivity, D_e , which is smaller than aqueous diffusivity because of the low effective porosity (ϕ) and tortuous pore pathways in the shale matrix (68). The most common empirical equation for D_e is Archie's law, where it varies as ϕ^m , m being the cementation exponent. Using the constraint on D_e from the diffusion model (where shale fragments completely oxidize within 50 kyr) and this empirical equation, we discover that the exponent m constrained by our observations equals

literature values for shale (67). To further corroborate the diffusion model (67), we also calculated the average grain-scale oxidation rate of pyrite in the field of $\sim 10^{-14}$ mol m $^{-2}$ s $^{-1}$. This value is four orders of magnitude smaller than pyrite oxidation measured in the laboratory in well-stirred, slightly acidic water (23). This observation is consistent with rate limitation by diffusion in the field but interfacial reaction in the laboratory.

Global implications

Our observations yield global implications for pyrite oxidation. For example, in some of the fastest-eroding locations on Earth, shales erode 10 to 100 times faster than at Shale Hills but still become 100% pyrite-oxidized beneath the land surface (30). Even in those fast-weathering shales, pyrite pseudomorphically transforms to oxide minerals (30). As shown by theoretical models of weathering (10, 42, 55), this observation implies that erosion limits the rate of OWP at the borehole scale rather than the kinetics of chemical reaction. In fact, by using reasonable parameters for average global pyrite contents and erosion rates, the calculated sulfate release rate for Shale Hills, 2.5 ± 1.4 mmol sulfur m $^{-2}$ year $^{-1}$, straightforwardly extrapolates to the total global riverine sulfate flux from OWP, 1.5 ± 0.5 Tmol sulfur year $^{-1}$ (67).

But to understand global implications over geological time, we also need to understand the mechanisms by which the rate of OWP at clast and grain scales varies proportionally with erosion rate. The answer appears to be that the climate, tectonic, or other drivers that accelerate the rates of erosion also promote increased fracturing (69). This in turn decreases the relevant clast size created between fractures (perhaps also increasing porosity within clasts) and thus accelerates OWP (30). This fits our proposed model (fig. S4) in which the advance of oxidation across each shale fragment between fractures is proportional to the square root of the residence time it takes for the fragment itself to cross the oxidation front. To fully oxidize pyrite in fragments, the fracture half-spacing must be less than the advance distance of oxidation as the clast crosses the reaction front at the borehole scale. A simple equation (eq. S10) predicts the critical fracture spacing that results in total oxidation of pyrite before it is exposed at the land surface and presents the spacing as a function of residence time of shale fragments in the weathering zone, effective porosity of shale matrix, pyrite abundance in protolith, and concentration of dissolved oxygen in fractures.

We used m calculated from Shale Hills for three shales (30) for which we know that pyrite is oxidized before exposure at the land surface to determine the critical fracture spacing calculated from eq. S10 (Fig. 4). The measured fracture spacing and effective porosity for each

of the shales plotted on the figure (symbols) show that fracture spacing is smaller than the critical spacing needed for 100% of the pyrite to be oxidized at the land surface under the present-day atmospheric level (PAL) of oxygen. The curves also show that the effect of fracture spacing is much stronger than that of porosity. These observations emphasize that the most convincing explanation for how OWP can be maintained proportional to erosion is that fracture spacing decreases to shorten the diffusion distance of oxygen as the erosion rate increases.

We can also explore conditions other than those on Earth today. For example, when the atmospheric oxygen concentration was less than 10^{-5} times PAL, OWP was apparently slow enough that pyrite was retained in alluvial sediments, implying that pyrite was exposed at the land surface [e.g., (15, 16)]. Curves plotted for dissolved oxygen equilibrated with $PO_2 = 10^{-5}$ PAL (Fig. 4) clearly show that even highly fractured rocks like those in fast-eroding Taiwan today would still retain pyrite up to the land surface at that time. This observation is consistent with a rate-limiting step for OWP before the GOE that was not erosion but rather the oxidation reaction at the mineral grain surface. Before the GOE, pyrite absence or presence in sediments would have been a function of atmospheric oxygen content, but once the atmospheric oxygen rose high enough to overcome chemical reaction limitation, OWP was limited by erosion and fracturing as it is today. Therefore, the key time scale for detrital pyrite preservation in alluvial sediments before the GOE is that of pyrite oxidation during transport from source to deposition as explored by Johnson *et al.* (2014) (16), but after the GOE the key time scale is the residence time as clasts transit up through the oxidation zone in the subsurface. This emphasizes that the rate of erosion coupled to fracturing in the subsurface is as important as atmospheric oxygen concentration in controlling the presence or absence of pyrite in alluvial material. Rock uplift and fracturing history, which has varied over geologic time (70), therefore must be considered in determining ancient atmospheric oxygen content through analyses of pyrite and models of weathering.

Our observations also emphasize that iron and sulfur-oxidizing microorganisms do not play a dominant role today in OWP globally. This may explain why landscapes of acidification are generally limited to mined regions where pyrite-containing rock is artificially exposed. The only way microorganisms could play an important role, given that they need to grow directly on or near pyrite (26–28), is for pyrite to be exposed in rock where microorganisms can enter pores. However, pyrite would have been present at the land surface during the late Archean even for very low erosion rates

(see Fig. 4). This lends credence to the possibility that an early period of acidification at 2.48 Gyr ago was caused by chemolithoautotrophic bacteria colonizing the land surface where, unlike today, pyrite was exposed (18, 71). More attention to estimating erosion rates and mechanics of subsurface fracturing is needed to understand limits on C, O, S, and Fe cycles globally.

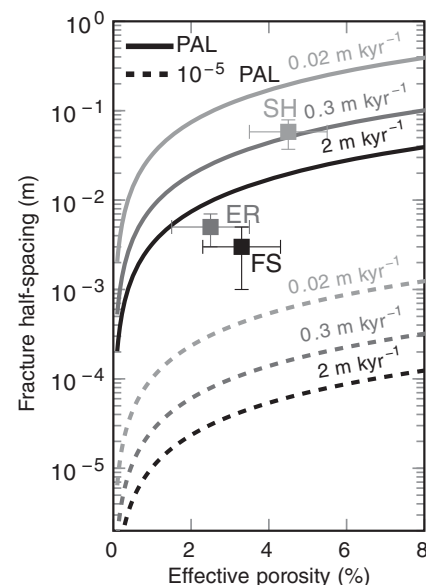


Fig. 4. Model curves showing the critical values of fracture half-spacing and effective porosity for pyrite to completely oxidize (symbols plot below curve) or to remain unoxidized at Earth's surface (symbols plot above curve) for two values of atmospheric oxygen. Squares show fracture half-spacing and effective porosity measured from depth at three watersheds (SH: Shale Hills at Pennsylvania; ER: Eel River at California; FS: Fushan at Taiwan) with different erosion rates. Darker symbols and curves indicate faster erosion rates as labeled: FS (2 m kyr $^{-1}$) > ER (0.3 m kyr $^{-1}$) > SH (0.02 m kyr $^{-1}$). Solid and dashed curves were calculated for oxygen at present atmospheric levels (PAL) or levels from before the GOE (10^{-5} PAL), respectively. Consistent with today's lack of exposed pyrite at land surface in all three watersheds and sulfate release rates for the watersheds that are proportional to erosion rate (30), symbols all plot below the corresponding contour for PAL (erosion-limited oxidation). But all points plot above estimates based on 10^{-5} PAL (dashed lines), suggesting the likelihood of land surface exposure of pyrite before the GOE (reaction-limited oxidation). Parameters estimated from Shale Hills were applied to the other watersheds as described in the text. Error bars show the range of erosion rates (horizontal) and fracture half-spacing (vertical). The contours of different values of erosion rates (darker for higher erosion rate) are calculated using eq. S10 for a 10-m-thick oxidized regolith.

Materials and methods

Geological setting

The Shale Hills catchment (40.6668° N, 77.9028° W) at Susquehanna Shale Hills Critical Zone Observatory (SSHCZO) is a V-shaped 0.08 km² catchment located in the headwaters of the Shaver's Creek watershed in the central Susquehanna River Basin, Pennsylvania, USA (fig. S1). The climate at SSHCZO is characterized as humid continental, with warm to hot summers and cold winters (mean annual air temperature of 10°C), with well-distributed precipitation throughout the year (mean annual precipitation of 107 cm). Vegetative cover is dominated by northern hardwoods with interspersed conifers consisting of oak (*Quercus spp.*), hickory (*Carya spp.*), pine (*Pinus spp.*), hemlock (*Tsuga canadensis*), and red maple (*Acer rubrum*). The short-term erosion rate (0.01 to 0.025 mm year⁻¹) determined from meteoric ¹⁰Be in this catchment (66) is comparable to the long-term erosion rates determined by low-temperature thermochronometry (72) across the Valley and Ridge province, in the Appalachian Mountain region. Both rates are close to the soil production rate (0.015 to 0.065 mm year⁻¹) determined over the 10³- to 10⁴-year time scale from uranium disequilibrium isotopes (73). This similarity implies that the landscape is close to an approximate steady-state geomorphological shape, i.e., that erosion roughly balances soil production. This site is underlain by the Silurian-aged Rose Hill Formation, which consists primarily of shale with minor interbedded carbonate-rich and sandstone layers (37, 74). The shale under the catchment varies from carbonate-rich near the outlet to poor through the rest of the catchment. Carbonate layers in the dipping (and probably folded) shale intersect boreholes under the ridges at tens of meters below land surface but at ~2 mbls under the valley. Although most carbonate at depth under the valley was present in the original shale, some calcite precipitated near the surface (<3 mbls) shows incorporation of C from organic carbon in soil, which is isotopically more depleted (44).

Boreholes

A 7.6-cm-diameter borehole (CZMW8) was drilled to 30.8-m depth under the south ridge of the catchment by HQ wireline coring, and core materials were recovered. Above depths of ~15.5 m, fractured rock fragments with lengths smaller than 10 cm were recovered (recovery: 17 to 40%). Below ~15.5 m, more continuous core materials were recovered (recovery: 45 to 90%) with the exception of the highly fractured zone from 24.7 to 26.2 m (recovery: 21%).

A 7.6-cm-diameter borehole (CZMW10) was drilled to 35-m depth under the valley near the outlet of the catchment by air rotary drilling. Rock fragments and rock powder were sampled during drilling at ~0.8-m intervals. The

unconsolidated material in the top 3 m of the borehole was sampled using a Geoprobe. The groundwater levels of these two boreholes are continuously measured every 30 min using a pressure transducer after well completion (75).

The borehole geophysical logs collected in both borehole CZMW8 and CZMW10 include a three-arm caliper, natural gamma, optical televiwer, acoustic televiwer, full wave-form sonic, bulk density, neutron porosity, fluid temperature, fluid conductivity, and normal resistivity. The logs of the 3-arm caliper and optical televiwer were collected in several other boreholes under the ridge (CZMW5, CZMW6, CZMW7) and under the valley as well (boreholes: CZMW1, CZMW2, CZMW3, CZMW4, Lynch). The fracture density was estimated by counting numbers of fractures per 0.5 m on optical and acoustic borehole images.

Bulk chemistry and mineralogy

Two types of samples were collected for analysis: (i) bulk samples (>100 g each), collected and homogenized over 0.3- to 0.8-m depth intervals; and (ii) centimeter-sized rock fragments that could be separated, on occasion, from the bulk samples. Rock fragments analyzed and discussed in this paper were collected near the depth where almost all of the pyrite becomes depleted (the pyrite oxidation front), or from the fractured zones (3 to 20 g for each sample). Bulk solid-state elemental compositions were determined by lithium metaborate fusion followed by inductively coupled plasma-atomic emission spectroscopy (ICP-AES; Perkin-Elmer Optima 5300DV ICP-AES) at the Penn State Laboratory for Isotopes and Metals in the Environment (LIME). Loss on ignition was determined by ashing the pulverized samples (initial mass ~1 g) at 900°C for 1 hour. Concentrations of total carbon and sulfur were determined on pulverized samples with a combustion-infrared carbon/sulfur determinator (LECO SC632). Bulk compositions are reported on an "as received" basis.

The loss or gain of component *j* during weathering was quantified as the mass transfer coefficient τ_j (76, 77):

$$\tau_j = \frac{C_{j,w}C_{i,p}}{C_{j,p}C_{i,w}} - 1$$

Here, $C_{j,w}$ and $C_{j,p}$ are the concentrations of a mobile element or mineral of interest (*j*) in protolith (*p*) or weathered material (*w*). When $\tau = 0$, element *j* is neither enriched nor depleted with respect to immobile element *i* in protolith; when $\tau < 0$, the element has been lost relative to *i* in protolith; and when $\tau > 0$, the element has been added to the profile relative to the protolith. In this study, the protolith is defined as the zone that shows no pyrite or carbonate depletion and titanium (Ti)

is chosen as the immobile element because it is mostly present in an insoluble mineral (30). The fraction of a mobile element lost from the protolith is a minimum estimate because no element is totally immobile (78). The extent of oxidation was calculated as $-\tau_{py}$.

X-ray diffraction was conducted on a PANalytical Empyrean X-Ray Diffractometer (PANalytical Ltd., Netherlands) at 45 kV and 40 mA using Cu *K* α radiation with a 1/2° divergence and receiving slits. Diffraction profiles were collected from 5° to 70° 2 θ at a rate of 4° min⁻¹. The degree of vermiculitization of chlorite was semiquantitatively estimated through the relative intensities of the (002) reflection at ~7.1 Å and (001) reflection at 14.1 to 14.3 Å of chlorite (79).

SEM

Eleven centimeter-sized rock fragments from different depths were selected for microstructure analysis at the Material Characterization Laboratory of the Pennsylvania State University. All fragments were cut into thin sections (~2 mm thick) using a low-speed diamond saw, polished with sandpaper (600 grid) and later diamond pastes (6 µm and 0.25 µm). Thin sections from each depth were imaged by scanning electron microscope (SEM). Selected sections were further polished by an ion beam milling instrument (Leica EM TIC 3X) to reveal the internal structure. Before imaging, the sections were coated with carbon (~8 nm thick) to reduce surface charging. The sections were imaged at low magnification (<10,000×) using an Environmental SEM (FEI Quanta 250) in backscattered electron mode with an accelerating voltage of 10 to 15 kV. Selected areas were investigated by EDS on the SEM using an Oxford EDS detector with an accelerating voltage of 15 to 20 kV to ensure a minimum dead time of 15%. The sections were imaged at high magnification (>10,000×) using a field-emission SEM (FEI Nova NanoSEM 630) with an accelerating voltage of 8 to 10 kV, landing energy of 4 to 5 kV using a vCD detector.

TEM

Specimens for transmission electron microscopy (TEM) were prepared by focused ion beam (FIB) milling on specific sites (e.g., pyrite-Fe oxide interface pre-identified by SEM-EDS) with the FEI Helios NanoLab 660 DualBeam system. A protective carbon layer was deposited on the region in the shape of a bar and then milling was performed using gallium ions at 30 keV. The specimen was lifted out, attached to a TEM grid and thinned to electron transparency. The FIB specimen was then analyzed on a Talos F200X scanning/transmission electron microscope (S/TEM) or a FEI Titan3 dual aberration corrected S/TEM, both operated at 200 kV and equipped with a SuperX EDS system. Both high angle annular dark field

(HAADF) STEM imaging and HRTEM were completed. Selected areas were examined by SAED and EDS mapping. Electron diffraction patterns were also extracted through fast Fourier transform (FFT) analysis on selected area of HRTEM images using image processing software Fiji (80). The ion mill curtaining in Fig. 3A is removed by a stripe filtering plugin in Fiji (81).

REFERENCES AND NOTES

- Dickard, G. W. Luther 3rd, Chemistry of iron sulfides. *Chem. Rev.* **107**, 514–562 (2007). doi: [10.1021/cr0503658](https://doi.org/10.1021/cr0503658); pmid: [17261073](https://pubmed.ncbi.nlm.nih.gov/17261073/)
- H. D. Holland, The chemistry of the atmosphere and oceans (John Wiley & Sons, NY, 1978).
- L. R. Kump, R. M. Garrels, Modeling atmospheric O₂ in the global sedimentary redox cycle. *Am. J. Sci.* **286**, 337–360 (1986). doi: [10.2475/ajs.286.5.337](https://doi.org/10.2475/ajs.286.5.337)
- R. A. Berner, D. E. Canfield, A new model for atmospheric oxygen over Phanerozoic time. *Am. J. Sci.* **289**, 333–361 (1989). doi: [10.2475/ajs.289.4.333](https://doi.org/10.2475/ajs.289.4.333); pmid: [11539776](https://pubmed.ncbi.nlm.nih.gov/11539776/)
- R. A. Berner, GEOCARBSULF: A combined model for Phanerozoic atmospheric O₂ and CO₂. *Geochim. Cosmochim. Acta* **70**, 5653–5664 (2006). doi: [10.1016/j.gca.2005.11.032](https://doi.org/10.1016/j.gca.2005.11.032)
- R. Raiswell, D. E. Canfield, The iron biogeochemical cycle past and present. *Geochim. Perspect.* **1**, 1–220 (2012). doi: [10.7185/geochempersp.1.1](https://doi.org/10.7185/geochempersp.1.1)
- A. Burke *et al.*, Sulfur isotopes in rivers: Insights into global weathering budgets, pyrite oxidation, and the modern sulfur cycle. *Earth Planet. Sci. Lett.* **496**, 168–177 (2018). doi: [10.1016/j.epsl.2018.05.022](https://doi.org/10.1016/j.epsl.2018.05.022)
- D. R. Lovley, Microbial Fe(III) reduction in subsurface environments. *FEMS Microbiol. Rev.* **20**, 305–313 (1997). doi: [10.1111/j.1574-6976.1997.tb00316.x](https://doi.org/10.1111/j.1574-6976.1997.tb00316.x)
- H. Prommer, P. J. Stuyfzand, Identification of temperature-dependent water quality changes during a deep well injection experiment in a pyritic aquifer. *Environ. Sci. Technol.* **39**, 2200–2209 (2005). doi: [10.1021/es0486768](https://doi.org/10.1021/es0486768); pmid: [15871255](https://pubmed.ncbi.nlm.nih.gov/15871255/)
- E. W. Bolton, R. A. Berner, S. T. Petsch, The weathering of sedimentary organic matter as a control on atmospheric O₂. II. Theoretical modeling. *Am. J. Sci.* **306**, 575–615 (2006). doi: [10.2475/08.2006.01](https://doi.org/10.2475/08.2006.01)
- A. Lerman, L. L. Wu, F. T. Mackenzie, CO₂ and H₂SO₄ consumption in weathering and material transport to the ocean, and their role in the global carbon balance. *Mar. Chem.* **106**, 326–350 (2007). doi: [10.1016/j.marchem.2006.04.004](https://doi.org/10.1016/j.marchem.2006.04.004)
- M. A. Torres, A. J. West, G. Li, Sulphide oxidation and carbonate dissolution as a source of CO₂ over geological timescales. *Nature* **507**, 346–349 (2014). doi: [10.1038/nature13030](https://doi.org/10.1038/nature13030); pmid: [24646998](https://pubmed.ncbi.nlm.nih.gov/24646998/)
- D. E. Canfield, The early history of atmospheric oxygen: Homage to Robert A. Garrels. *Annu. Rev. Earth Planet. Sci.* **33**, 1–36 (2005). doi: [10.1146/annurev.earth.33.092203.122711](https://doi.org/10.1146/annurev.earth.33.092203.122711)
- T. W. Lyons, C. T. Reinhard, N. J. Planavsky, The rise of oxygen in Earth's early ocean and atmosphere. *Nature* **506**, 307–315 (2014). doi: [10.1038/nature13068](https://doi.org/10.1038/nature13068); pmid: [24553238](https://pubmed.ncbi.nlm.nih.gov/24553238/)
- B. Rasmussen, R. Buick, Redox state of the Archean atmosphere: Evidence from detrital heavy minerals in ca. 3250–2750 Ma sandstones from the Pilbara Craton, Australia. *Geology* **27**, 115–118 (1999). doi: [10.1130/0091-7613\(1999\)027<0115:RSOTAA>2.3.CO;2](https://doi.org/10.1130/0091-7613(1999)027<0115:RSOTAA>2.3.CO;2)
- J. E. Johnson, A. Gerpheide, M. P. Lamb, W. W. Fischer, O₂ constraints from Paleoproterozoic detrital pyrite and uraninite. *Geol. Soc. Am. Bull.* **126**, 813–830 (2014). doi: [10.1130/B309491](https://doi.org/10.1130/B309491)
- A. Bekker, H. D. Holland, Oxygen overshoot and recovery during the early Paleoproterozoic. *Earth Planet. Sci. Lett.* **317**, 295–304 (2012). doi: [10.1016/j.epsl.2011.12.012](https://doi.org/10.1016/j.epsl.2011.12.012)
- K. O. Konhauser *et al.*, Aerobic bacterial pyrite oxidation and acid rock drainage during the Great Oxidation Event. *Nature* **478**, 369–373 (2011). doi: [10.1038/nature10511](https://doi.org/10.1038/nature10511); pmid: [22012395](https://pubmed.ncbi.nlm.nih.gov/22012395/)
- D. E. Canfield, Oxygen: A four billion year history (Princeton University Press, 2014).
- S. J. Daines, B. J. W. Mills, T. M. Lenton, Atmospheric oxygen regulation at low Proterozoic levels by incomplete oxidative weathering of sedimentary organic carbon. *Nat. Commun.* **8**, 14379 (2017). doi: [10.1038/ncomms14379](https://doi.org/10.1038/ncomms14379); pmid: [28148950](https://pubmed.ncbi.nlm.nih.gov/28148950/)
- C. O. Moses, D. Kirk Nordstrom, J. S. Herman, A. L. Mills, Aqueous pyrite oxidation by dissolved-oxygen and by ferric iron. *Geochim. Cosmochim. Acta* **51**, 1561–1571 (1987). doi: [10.1016/0016-7037\(87\)90337-1](https://doi.org/10.1016/0016-7037(87)90337-1)
- M. A. Williamson, J. D. Rimstidt, The kinetics and electrochemical rate-determining step of aqueous pyrite oxidation. *Geochim. Cosmochim. Acta* **58**, 5443–5454 (1994). doi: [10.1016/0016-7037\(94\)90241-0](https://doi.org/10.1016/0016-7037(94)90241-0)
- A. C. Johnson *et al.*, Experimental determination of pyrite and molybdenite oxidation kinetics at nanomolar oxygen concentrations. *Geochim. Cosmochim. Acta* **249**, 160–172 (2019). doi: [10.1016/j.gca.2019.01.022](https://doi.org/10.1016/j.gca.2019.01.022)
- P. C. Singer, W. Stumm, Acidic mine drainage: The rate-determining step. *Science* **167**, 1121–1123 (1970). doi: [10.1126/science.167.3921.1121](https://doi.org/10.1126/science.167.3921.1121); pmid: [17829406](https://pubmed.ncbi.nlm.nih.gov/17829406/)
- D. W. Blowes, C. J. Ptacek, J. L. Jambor, C. G. Weisener, The geochemistry of acid mine drainage, in *Treatise on Geochemistry*. Vol. 9. *Environmental Geochemistry* B. Sherwood Lollar (Ed.) (Elsevier, Toronto, 2003), pp. 149–204.
- W. Sand, T. Gerke, R. Hallmann, A. Schippers, Sulfur chemistry, biofilm, and the (in)direct attack mechanism – a critical evaluation of bacterial leaching. *Appl. Microbiol. Biotechnol.* **43**, 961–966 (1995). doi: [10.1007/BF00166909](https://doi.org/10.1007/BF00166909)
- M. Gleisner, R. B. Herbert Jr., P. C. Frogner Kockum, Pyrite oxidation by Acidithiobacillus ferrooxidans at various concentrations of dissolved oxygen. *Chem. Geol.* **225**, 16–29 (2006). doi: [10.1016/j.chemgeo.2005.07.020](https://doi.org/10.1016/j.chemgeo.2005.07.020)
- E. Percak-Dennett *et al.*, Microbial acceleration of aerobic pyrite oxidation at circumneutral pH. *Geobiology* **15**, 690–703 (2017). doi: [10.1111/gbi.12241](https://doi.org/10.1111/gbi.12241); pmid: [28452176](https://pubmed.ncbi.nlm.nih.gov/28452176/)
- D. Calsmels, J. Gaillardet, A. Brenot, C. France-Lanord, Sustained sulfide oxidation by physical erosion processes in the Mackenzie River basin: Climatic perspectives. *Geology* **35**, 1003–1006 (2007). doi: [10.1130/G24132A.1](https://doi.org/10.1130/G24132A.1)
- X. Gu *et al.*, Chemical reactions, porosity, and microfracturing in shale during weathering: The effect of erosion rate. *Geochim. Cosmochim. Acta* **269**, 63–100 (2020). doi: [10.1016/j.gca.2019.09.044](https://doi.org/10.1016/j.gca.2019.09.044)
- R. Littke, U. Klusmann, B. Krooss, D. Leythaeuser, Quantification of loss of calcite, pyrite, and organic matter due to weathering of Torcian black shales and effects on kerogen and bitumen characteristics. *Geochim. Cosmochim. Acta* **55**, 3369–3378 (1991). doi: [10.1016/0016-7037\(91\)90494-P](https://doi.org/10.1016/0016-7037(91)90494-P)
- R. A. Wildman *et al.*, The weathering of sedimentary organic matter as a control on atmospheric O₂: I. Analysis of a black shale. *Am. J. Sci.* **304**, 234–249 (2004). doi: [10.2475/ajs.304.3.234](https://doi.org/10.2475/ajs.304.3.234)
- L. X. Jin *et al.*, Evolution of porosity and geochemistry in Marcellus Formation black shale during weathering. *Chem. Geol.* **356**, 50–63 (2013). doi: [10.1016/j.chemgeo.2013.07.012](https://doi.org/10.1016/j.chemgeo.2013.07.012)
- J. Wan *et al.*, Predicting sedimentary bedrock subsurface weathering fronts and weathering rates. *Sci. Rep.* **9**, 17198 (2019). doi: [10.1038/s41598-019-53205-2](https://doi.org/10.1038/s41598-019-53205-2); pmid: [31748585](https://pubmed.ncbi.nlm.nih.gov/31748585/)
- M. Chigira, T. Oyama, Mechanism and effect of chemical weathering of sedimentary rocks. *Eng. Geol.* **55**, 3–14 (2000). doi: [10.1016/S0013-7952\(99\)00102-7](https://doi.org/10.1016/S0013-7952(99)00102-7)
- S. L. Brantley, M. E. Holleran, L. X. Jin, E. Bazilevskaya, Probing deep weathering in the Shale Hills Critical Zone Observatory, Pennsylvania (USA): The hypothesis of nested chemical reaction fronts in the subsurface. *Earth Surf. Process. Landf.* **38**, 1280–1298 (2013). doi: [10.1002/esp.3415](https://doi.org/10.1002/esp.3415)
- P. L. Sullivan *et al.*, Oxidative dissolution under the channel leads geomorphological evolution at the Shale Hills catchment. *Am. J. Sci.* **316**, 981–1026 (2016). doi: [10.2475/10.2016.02](https://doi.org/10.2475/10.2016.02)
- C. Lerouge *et al.*, A deep alteration and oxidation profile in a shallow clay aquitard: Example of the Tégulines Clay, East Paris Basin, France. *Geofluids* **2018**, 1606753 (2018). doi: [10.1155/2018/1606753](https://doi.org/10.1155/2018/1606753)
- H. Drake, E.-L. Tullborg, A. B. MacKenzie, Detecting the near-surface redox front in crystalline bedrock using fracture mineral distribution, geochemistry and U-series disequilibrium. *Appl. Geochem.* **24**, 1023–1039 (2009). doi: [10.1016/j.apgeochem.2009.03.004](https://doi.org/10.1016/j.apgeochem.2009.03.004)
- S. L. Brantley, M. Lebedeva, E. Bazilevskaya, Relating weathering fronts for acid neutralization and oxidation to pCO₂ and pO₂, in *Treatise on Geochemistry*, J. Farquhar, J. Kasting, D. Canfield, Eds. (Elsevier, ed. 2, 2013), vol. 6, pp. 327–352.
- S. L. Brantley *et al.*, Susquehanna Shale Hills Critical Zone Observatory: Shale Hills in the context of Shaver's Creek watershed. *Vados Zone J.* **17**, 180092 (2018). doi: [10.2136/vzj2018.04.0092](https://doi.org/10.2136/vzj2018.04.0092)
- M. I. Lebedeva, R. C. Fletcher, S. L. Brantley, A mathematical model for steady-state regolith production at constant erosion rate. *Earth Surf. Process. Landf.* **35**, 508–524 (2010). doi: [10.1002/esp.1954](https://doi.org/10.1002/esp.1954)
- C. S. Riebe, W. J. Hahn, S. L. Brantley, Controls on deep critical zone architecture: A historical review and four testable hypotheses. *Earth Surf. Process. Landf.* **42**, 128–156 (2017). doi: [10.1002/esp.4052](https://doi.org/10.1002/esp.4052)
- X. Gu *et al.*, Seismic refraction tracks porosity generation and possible CO₂ production at depth under a headwater catchment. *Proc. Natl. Acad. Sci. U.S.A.* **117**, 18991–18997 (2020). pmid: [32719121](https://pubmed.ncbi.nlm.nih.gov/32719121/)
- A. H. Thompson, A. J. Katz, C. E. Krohn, The microgeometry and transport properties of sedimentary rock. *Adv. Phys.* **36**, 625–694 (1987). doi: [10.1080/00018738700101062](https://doi.org/10.1080/00018738700101062)
- J. K. Fredrickson *et al.*, Pore-size constraints on the activity and survival of subsurface bacteria in a late Cretaceous shale-sandstone sequence, northwestern New Mexico. *Geomicrobiol. J.* **14**, 183–202 (1997). doi: [10.1080/01490459709378043](https://doi.org/10.1080/01490459709378043)
- A. Navarre-Stichler, S. L. Brantley, Basalt weathering across scales. *Earth Planet. Sci. Lett.* **261**, 321–334 (2007). doi: [10.1016/j.epsl.2007.07.010](https://doi.org/10.1016/j.epsl.2007.07.010)
- C. M. Eggleston, J.-J. Ehrhardt, W. Stumm, Surface structural controls on pyrite oxidation kinetics. An XPS-UPS, STM, and modeling study. *Am. Mineral.* **81**, 1036–1056 (1996). doi: [10.2138/am-1996-9-1002](https://doi.org/10.2138/am-1996-9-1002)
- K. M. Rosso, U. Becker, M. F. Hochella, The interaction of pyrite 100 surfaces with O₂ and H₂O: Fundamental oxidation mechanisms. *Am. Mineral.* **84**, 1549–1561 (1999). doi: [10.2138/am-1999-1008](https://doi.org/10.2138/am-1999-1008)
- C. Mahoney, C. März, J. Buckman, T. Wagner, V.-O. Blanco-Velandia, Pyrite oxidation in shales: Implications for palaeo-redox proxies based on geochemical and SEM-EDX evidence. *Sediment. Geol.* **389**, 186–199 (2019). doi: [10.1016/j.sedgeo.2019.06.006](https://doi.org/10.1016/j.sedgeo.2019.06.006)
- R. M. Cornell, U. Schwertmann, *The Iron Oxides: Structure, Properties, Reactions, Occurrence, and Uses* (VCH, 1996).
- F. V. Chukhrov *et al.*, Feroxyhyte, a new modification of FeOOH. *Int. Geol. Rev.* **19**, 873–890 (1977). doi: [10.1080/00206817709471086](https://doi.org/10.1080/00206817709471086)
- J. L. Jambor, J. E. Dutrizac, Occurrence and constitution of natural and synthetic ferrihydrite, a widespread iron oxyhydroxide. *Chem. Rev.* **98**, 2549–2586 (1998). doi: [10.1021/cr970105t](https://doi.org/10.1021/cr970105t); pmid: [11848971](https://pubmed.ncbi.nlm.nih.gov/11848971/)
- R. M. Cornell, R. Giovanoli, P. W. Schindler, Effect of silicate species on the transformation of ferrihydrite into goethite and hematite in alkaline media. *Clays Clay Miner.* **35**, 21–28 (1987). doi: [10.1346/CCMN.1987.0350103](https://doi.org/10.1346/CCMN.1987.0350103)
- A. J. West, A. Galy, M. Bickle, Tectonic and climatic controls on silicate weathering. *Earth Planet. Sci. Lett.* **235**, 211–228 (2005). doi: [10.1016/j.epsl.2005.03.020](https://doi.org/10.1016/j.epsl.2005.03.020)
- B. W. Kuntz, S. Rubin, B. Berkowitz, K. Singha, Quantifying solute transport at the Shale Hills Critical Zone Observatory. *Vados Zone J.* **10**, 843–857 (2011). doi: [10.2136/vzj2010.0130](https://doi.org/10.2136/vzj2010.0130)
- P. M. Jardine *et al.*, Quantifying diffusive mass transfer in fractured shale bedrock. *Water Resour. Res.* **35**, 2015–2030 (1999). doi: [10.1029/1999WR900043](https://doi.org/10.1029/1999WR900043)
- A. Putnis, Mineral Replacement Reactions. *Rev. Mineral. Geochem.* **70**, 87–124 (2009). doi: [10.2138/rmg.2009.70.3](https://doi.org/10.2138/rmg.2009.70.3)
- R. Hellmann *et al.*, Unifying natural and laboratory chemical weathering with interfacial dissolution–reprecipitation: A study based on the nanometer-scale chemistry of fluid-silicate interfaces. *Chem. Geol.* **294–295**, 203–216 (2012). doi: [10.1016/j.chemgeo.2011.12.002](https://doi.org/10.1016/j.chemgeo.2011.12.002)
- B. Luef *et al.*, Diverse uncultivated ultra-small bacterial cells in groundwater. *Nat. Commun.* **6**, 6372 (2015). doi: [10.1038/ncomms7372](https://doi.org/10.1038/ncomms7372); pmid: [25721682](https://pubmed.ncbi.nlm.nih.gov/25721682/)
- J. Bosch, K. Y. Lee, G. Jordan, K. W. Kim, R. U. Meckenstock, Anaerobic, nitrate-dependent oxidation of pyrite nanoparticles by Thiobacillus denitrificans. *Environ. Sci. Technol.* **46**, 2095–2101 (2012). doi: [10.1021/es2022329](https://doi.org/10.1021/es2022329); pmid: [22142180](https://pubmed.ncbi.nlm.nih.gov/22142180/)
- J. N. Weitzman, J. P. Kaye, Nitrogen budget and topographic controls on nitrous oxide in a shale-based watershed. *J. Geophys. Res. Biogeosci.* **123**, 1888–1908 (2019). doi: [10.1029/2017JG004344](https://doi.org/10.1029/2017JG004344)
- F. Callebaut, D. Gabriels, W. Minjauw, M. D. E. Boodt, Redox potential, oxygen diffusion rate, and soil gas composition in relation to water table level in two soils. *Soil Sci.* **134**, 149–156 (1982). doi: [10.1097/00010694-198209000-00001](https://doi.org/10.1097/00010694-198209000-00001)
- M. I. Lebedeva, S. L. Brantley, Relating the depth of the water table to the depth of weathering. *Earth Surf. Process. Landf.* **45**, 2167–2178 (2020). doi: [10.1002/esp.4873](https://doi.org/10.1002/esp.4873)
- Y. Kanzaki, S. L. Brantley, L. R. Kump, A numerical examination of the effect of sulfide dissolution on silicate weathering. *Earth Planet. Sci. Lett.* **539**, 116239 (2020). doi: [10.1016/j.epsl.2020.116239](https://doi.org/10.1016/j.epsl.2020.116239)

66. N. West *et al.*, Regolith production and transport at the Susquehanna Shale Hills Critical Zone Observatory, Part 2: Insights from meteoric ^{10}Be . *J. Geophys. Res. Earth Surf.* **118**, 1877–1896 (2013). doi: [10.1002/jgrf.20121](https://doi.org/10.1002/jgrf.20121)
 67. Details about the model are available as supplementary materials.
 68. P. Grathwohl, Diffusion in natural porous media: Contaminant transport, sorption/desorption and dissolution kinetics (Springer, 1998)
 69. P. Molnar, R. S. Anderson, S. P. Anderson, Tectonics, fracturing of rock, and erosion. *J. Geophys. Res. Earth Surf.* **112**, F03014 (2007).
 70. C. Hawkesworth, P. A. Cawood, B. Dhuime, Rates of generation and growth of the continental crust. *Geoscience Frontiers* **10**, 165–173 (2019). doi: [10.1016/j.gsf.2018.02.004](https://doi.org/10.1016/j.gsf.2018.02.004)
 71. E. E. Stüeken, D. C. Catling, R. Buick, Contributions to late Archaean sulphur cycling by life on land. *Nat. Geosci.* **5**, 722–725 (2012). doi: [10.1038/ngeo1585](https://doi.org/10.1038/ngeo1585)
 72. M. K. Roden, D. S. Miller, Apatite fission-track thermochronology of the Pennsylvania Appalachian Basin. *Geomorphology* **2**, 39–51 (1989). doi: [10.1016/0169-555X\(89\)90005-6](https://doi.org/10.1016/0169-555X(89)90005-6)
 73. L. Ma *et al.*, Regolith production and transport in the Susquehanna Shale Hills Critical Zone Observatory, Part 1: Insights from U-series isotopes. *J. Geophys. Res. Earth Surf.* **118**, 722–740 (2013). doi: [10.1002/jgrf.20037](https://doi.org/10.1002/jgrf.20037)
 74. L. X. Jin *et al.*, Mineral weathering and elemental transport during hillslope evolution at the Susquehanna/Shale Hills Critical Zone Observatory. *Geochim. Cosmochim. Acta* **74**, 3669–3691 (2010). doi: [10.1016/j.gca.2010.03.036](https://doi.org/10.1016/j.gca.2010.03.036)
 75. Data are available at http://www.czo.psu.edu/data_time_series.html.
 76. G. H. Brimhall, W. E. Dietrich, Constitutive mass balance relations between chemical-composition, volume, density, porosity, and strain in metasomatic hydrochemical systems: Results on weathering and pedogenesis. *Geochim. Cosmochim. Acta* **51**, 567–587 (1987). doi: [10.1016/0016-7037\(87\)90070-6](https://doi.org/10.1016/0016-7037(87)90070-6)
 77. S. P. Anderson, W. E. Dietrich, G. H. Brimhall Jr., Weathering profiles, mass-balance analysis, and rates of solute loss: Linkages between weathering and erosion in a small, steep catchment. *Geol. Soc. Am. Bull.* **114**, 1143–1158 (2002). doi: [10.1130/0016-7606\(2002\)114<1143:WPMBA>2.0.CO;2](https://doi.org/10.1130/0016-7606(2002)114<1143:WPMBA>2.0.CO;2)
 78. H. Kim, X. Gu, S. L. Brantley, Particle fluxes in groundwater change subsurface shale rock chemistry over geologic time. *Earth Planet. Sci. Lett.* **500**, 180–191 (2018). doi: [10.1016/j.epsl.2018.07.031](https://doi.org/10.1016/j.epsl.2018.07.031)
 79. C. E. Weaver, The distribution and identification of mixed-layer clays in sedimentary rocks. *Clays Clay Miner.* **4**, 385–386 (1955). doi: [10.1346/CCMN.1955.0040143](https://doi.org/10.1346/CCMN.1955.0040143)
 80. J. Schindelin *et al.*, Fiji: An open-source platform for biological-image analysis. *Nat. Methods* **9**, 676–682 (2012). doi: [10.1038/nmeth.2019](https://doi.org/10.1038/nmeth.2019); pmid: [22743772](https://pubmed.ncbi.nlm.nih.gov/22743772/)
 81. B. Münch, P. Tirtik, F. Marone, M. Stampanoni, Stripe and ring artifact removal with combined wavelet–Fourier filtering. *Opt. Express* **17**, 8567–8591 (2009). doi: [10.1364/OE.17.008567](https://doi.org/10.1364/OE.17.008567); pmid: [19434191](https://pubmed.ncbi.nlm.nih.gov/19434191/)
 82. Data are available at www.czo.psu.edu/data_geochemical_geophysical.html.
- ACKNOWLEDGMENTS**
- We thank B. Watson, E. Roden, and M. Lebedeva for insights. The paper benefitted greatly from the reviews provided by A. Johnson, K. Konhauser, and an anonymous reviewer. **Funding:** Financial support was provided by U.S. DOE grant OBES DE-FG02-05ER15675 (S.L.B.), National Science Foundation grants EAR-1239285 and EAR-1331726 (S.L.B.), and EAR-1925903 (P.J.H.). F.D.A.A.R. acknowledges support from Brazilian agencies FAPERJ (E-26/202.881/2018), CAPES (88887.310427/2018-00), and CNPq (304766/2014-3). This research was conducted in Penn State's Stone Valley Forest, which is funded by the Penn State College of Agriculture Sciences, Department of Ecosystem Science and Management, and managed by the staff of the Forestlands Management Office. **Author contributions:** S.L.B. and X.G. conceived and led the project. X.G. collected the samples and conducted measurements. X.G. and P.J.H. interpreted mineralogical data. X.G. and F.D.A.A.R. developed the multiscale model. X.G. and S.L.B. wrote the paper, with input from all authors; **Competing interests:** The authors declare that they have no competing interests. **Data and materials availability:** Data are available in supplementary materials. Borehole logging data are available at the CZO data repository (82).
- SUPPLEMENTARY MATERIALS**
- science.sciencemag.org/content/370/6515/eabb8092/suppl/DC1
 Supplementary Text
 Figs. S1 to S7
 Tables S1 and S2
 References (83–97)
- 20 March 2020; accepted 17 August 2020
 10.1126/science.abb8092

RESEARCH ARTICLE

CORONAVIRUS

De novo design of picomolar SARS-CoV-2 miniprotein inhibitors

Longxing Cao^{1,2}, Inna Goreshnik^{1,2,3}, Brian Coventry^{1,2,3}, James Brett Case⁴, Lauren Miller^{1,2}, Lisa Kozodoy^{1,2}, Rita E. Chen^{4,5}, Lauren Carter^{1,2}, Alexandra C. Walls¹, Young-Jun Park¹, Eva-Maria Strauch⁶, Lance Stewart^{1,2}, Michael S. Diamond^{4,7}, David Veasley¹, David Baker^{1,2,8,*}

Targeting the interaction between the severe acute respiratory syndrome coronavirus 2 (SARS-CoV-2) spike protein and the human angiotensin-converting enzyme 2 (ACE2) receptor is a promising therapeutic strategy. We designed inhibitors using two de novo design approaches. Computer-generated scaffolds were either built around an ACE2 helix that interacts with the spike receptor binding domain (RBD) or docked against the RBD to identify new binding modes, and their amino acid sequences were designed to optimize target binding, folding, and stability. Ten designs bound the RBD, with affinities ranging from 100 picomolar to 10 nanomolar, and blocked SARS-CoV-2 infection of Vero E6 cells with median inhibitory concentration (IC₅₀) values between 24 picomolar and 35 nanomolar. The most potent, with new binding modes, are 56- and 64-residue proteins (IC₅₀ ~ 0.16 nanograms per milliliter). Cryo-electron microscopy structures of these minibinders in complex with the SARS-CoV-2 spike ectodomain trimer with all three RBDs bound are nearly identical to the computational models. These hyperstable minibinders provide starting points for SARS-CoV-2 therapeutics.

Severe acute respiratory syndrome coronavirus 2 (SARS-CoV-2) infection generally begins in the nasal cavity, with virus replicating there for several days before spreading to the lower respiratory tract (1). Delivery of a high concentration of a viral inhibitor into the nose and into the respiratory system generally might therefore provide prophylactic protection and/or therapeutic benefit for treatment of early infection and could be particularly useful for healthcare workers and others coming into frequent contact with infected individuals. A number of monoclonal antibodies are in development as systemic treatments for coronavirus disease 2019 (COVID-19) (2–6), but these proteins are not ideal for intranasal delivery because antibodies are large and often not extremely stable molecules, and the density of binding sites is low (two per 150 KDa antibody); antibody-dependent disease enhancement (7–9) is also a potential issue. High-affinity spike protein binders that block the interaction with the human cellular receptor angiotensin-converting

enzyme 2 (ACE2) (10) with enhanced stability and smaller sizes to maximize the density of inhibitory domains could have advantages over antibodies for direct delivery into the respiratory system through intranasal administration, nebulization, or dry powder aerosol. We found previously that intranasal delivery of small proteins designed to bind tightly to the influenza hemagglutinin can provide both prophylactic and therapeutic protection in rodent models of lethal influenza infection (11).

Design strategy

We set out to design high-affinity protein minibinders to the SARS-CoV-2 spike receptor binding domain (RBD) that compete with ACE2 binding. We explored two strategies: First, we incorporated the α -helix from ACE2, which makes the majority of the interactions with the RBD into small designed proteins that make additional interactions with the RBD to attain higher affinity (Fig. 1A). Second, we designed binders completely from scratch, without relying on known RBD-binding interactions (Fig. 1B). An advantage of the second approach is that the range of possibilities for

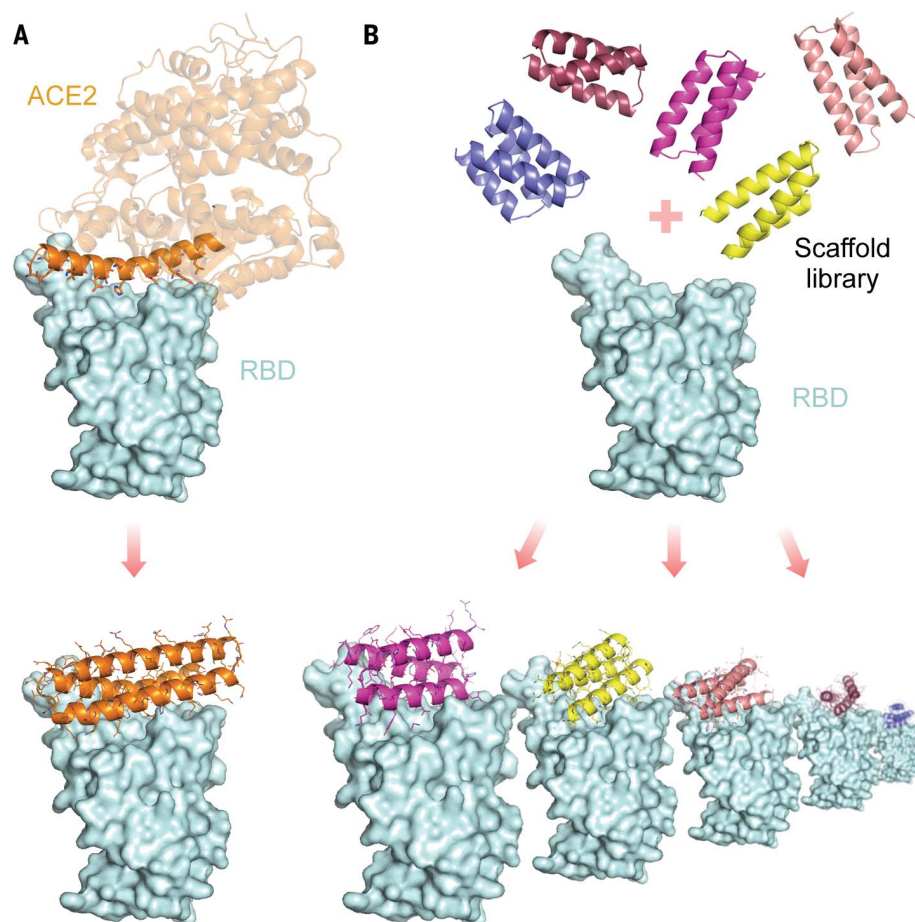


Fig. 1. Overview of the computational design approaches. (A) Design of helical proteins incorporating ACE2 helix. **(B)** Large-scale de novo design of small helical scaffolds (top) followed by RIF docking to identify shape and chemically complementary binding modes.

¹Department of Biochemistry, University of Washington, Seattle, WA 98195, USA. ²Institute for Protein Design, University of Washington, Seattle, WA 98195, USA. ³Molecular Engineering Graduate Program, University of Washington, Seattle, WA 98195, USA. ⁴Department of Medicine, Washington University School of Medicine, St. Louis, MO 63110, USA. ⁵Department of Pathology and Immunology, Washington University School of Medicine, St. Louis, MO 63110, USA. ⁶Department of Pharmaceutical and Biomedical Sciences, University of Georgia, Athens, GA 30602, USA. ⁷The Andrew M. and Jane M. Bursky Center for Human Immunology and Immunotherapy Programs, Washington University School of Medicine, St. Louis, MO 63110, USA. ⁸Howard Hughes Medical Institute, University of Washington, Seattle, WA 98195, USA.

*Corresponding author. Email: dabaker@uw.edu

design is much larger, and so potentially a greater diversity of high-affinity binding modes can be identified. For the first approach, we used the Rosetta blueprint builder to generate minibinders that incorporate the ACE2 helix (human ACE2 residues 23 to 46). For

the second approach, we used rotamer interaction field (RIF) docking (12) with large in silico miniprotein libraries (11) followed by design to generate binders to distinct regions of the RBD surface surrounding the ACE2 binding site (Fig. 1 and fig. S1).

Experimental characterization and optimization

Large pools of designed minibinders (supplementary materials, materials and methods), made by using the first and second approaches, were encoded in long oligonucleotides and

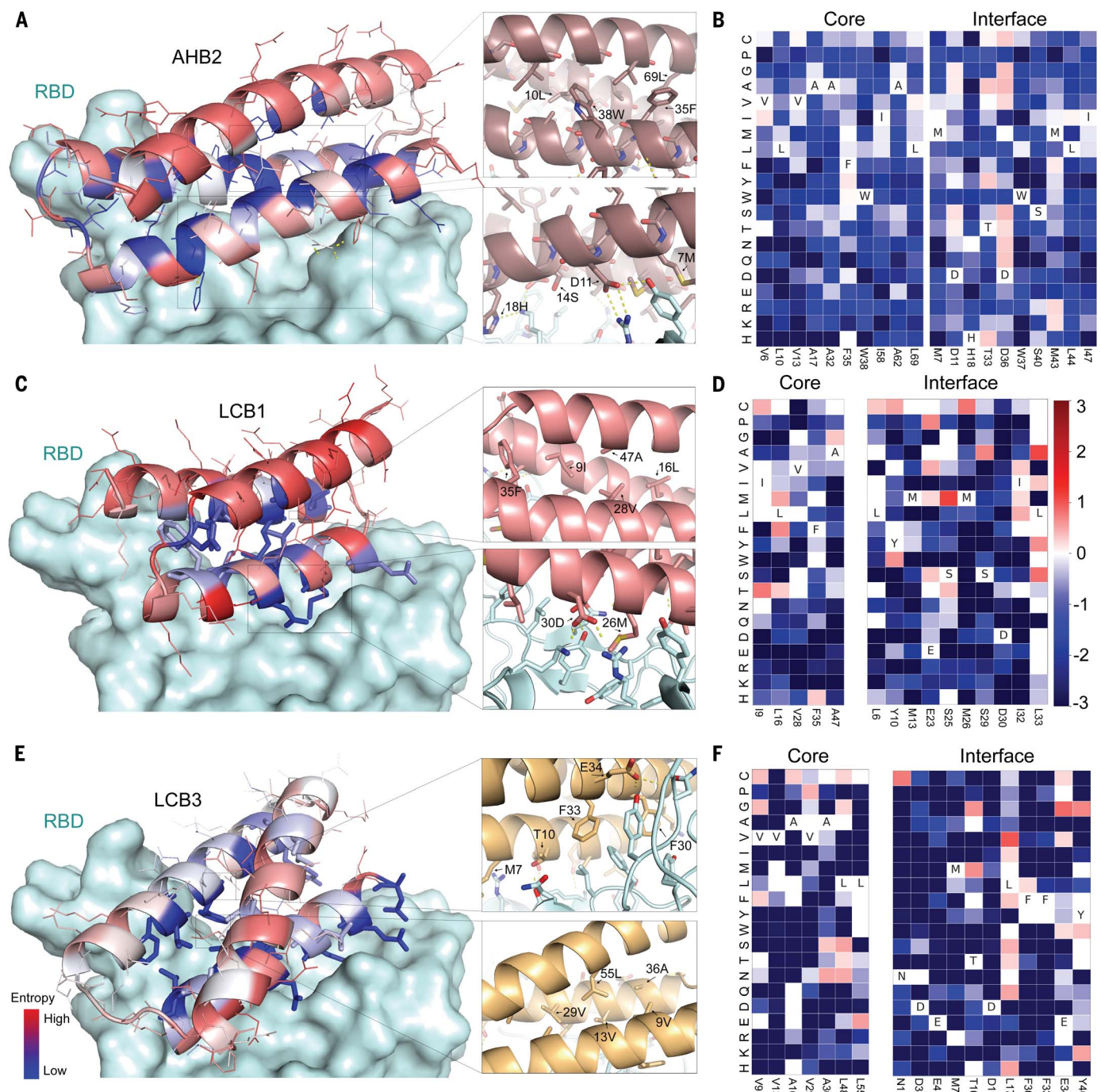


Fig. 2. High-resolution sequence mapping of AHB2, LCB1, and LCB3 before sequence optimization. (A, C, and E) (Left) Designed binding proteins are colored by positional Shannon entropy from site saturation mutagenesis, with blue indicating positions of low entropy (conserved) and red those of high entropy (not conserved). (Right) Zoomed-in views of central regions of the design core and interface with the RBD. (B, D, and F) Heat maps representing RBD-binding enrichment

values for single mutations in the design model core (left) and the designed interface (right). Substitutions that are heavily depleted are shown in blue, and beneficial mutations are shown in red. The depletion of most substitutions in both the binding site and the core suggest that the design models are largely correct, whereas the enriched substitutions suggest routes to improving affinity. Full SSM maps over all positions for AHB2 and all eight de novo designs are provided in figs. S6 and S7.

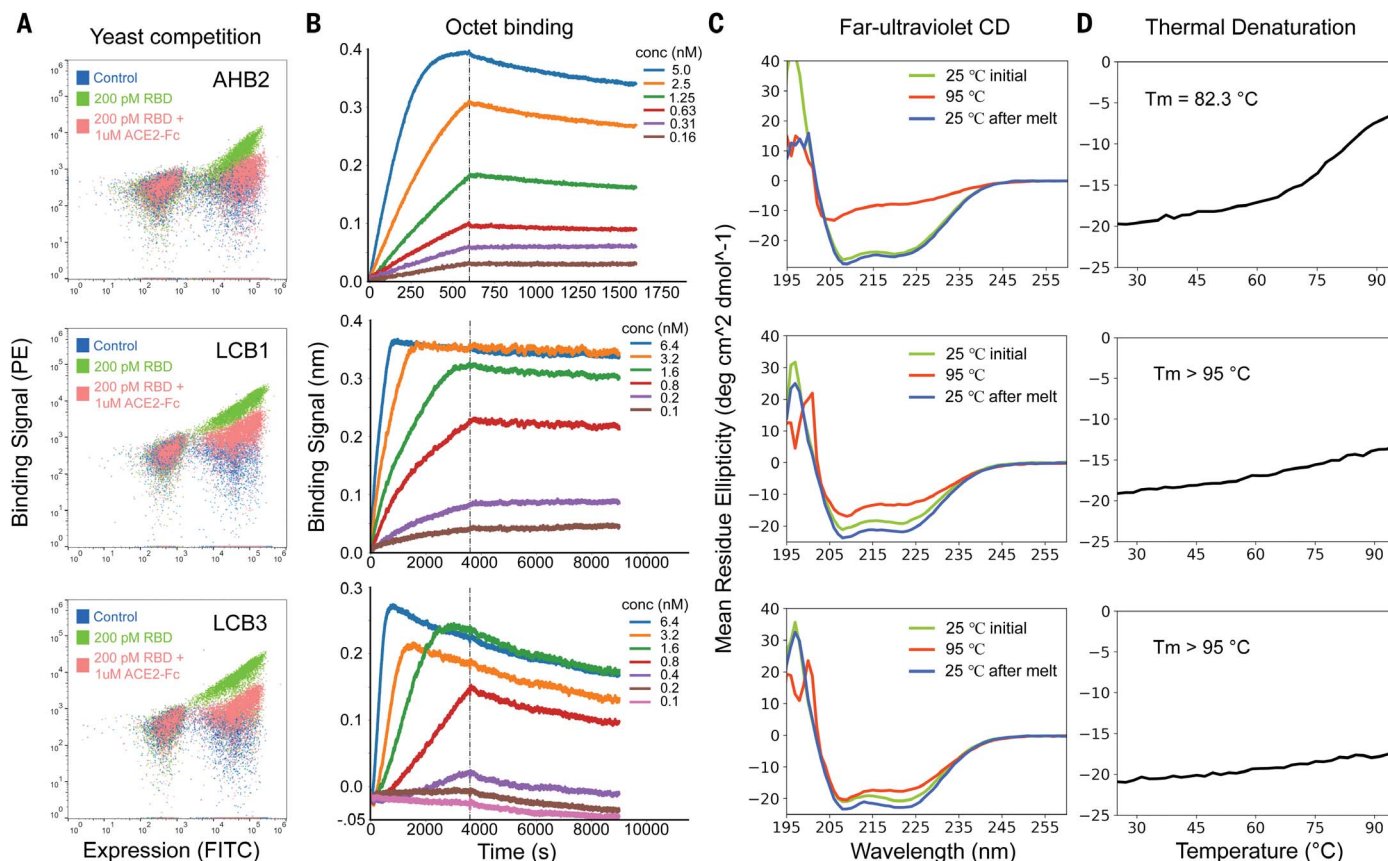


Fig. 3. The optimized designs bind with high affinity to the RBD, compete with ACE2, and are thermostable. (A) ACE2 competes with the designs for binding to the RBD. Yeast cells displaying the indicated design were incubated with 200 pM RBD in the presence or absence of 1 μ M ACE2, and RBD binding to cells (y axis) was monitored with flow cytometry. **(B)** Binding of purified miniproteins to the RBD monitored with BLI. For LCB1 and LCB3,

dissociation constants (K_d) could not be accurately estimated because of a lack of instrument sensitivity and long equilibration times below 200 pM. **(C)** Circular dichroism spectra at different temperatures and **(D)** CD signal at 222-nm wavelength, as a function of temperature. The fully de novo designs LCB1 and LCB3 are more stable than the ACE2 scaffolded helix design AHB2.

screened for binding to fluorescently tagged RBD displayed on the surface of yeast cells. Deep sequencing identified three ACE2 helix scaffolded designs (“approach 1”), and 105 de novo interface designs (“approach 2”) that were enriched after fluorescence-activated cell sorting (FACS) for RBD binding. All three ACE2-scaffolded designs and 12 of the de novo designs were expressed in *Escherichia coli* and purified. One of the ACE2-scaffolded designs and 11 of the 12 de novo designs were soluble and bound RBD with affinities ranging from 100 nM to 2 μ M in biolayer interferometry (BLI) experiments (figs. S2, A, C, and E; and S3). Affinity maturation of the ACE2-scaffolded design by means of polymerase chain reaction (PCR) mutagenesis led to a variant, AHB1, which bound RBD with an affinity of \sim 1 nM (fig. S4) and blocked binding of ACE2 to the RBD (fig. S5A), which is consistent with the design model, but had low thermostability (fig. S4, C and D). We generated 10 additional designs incorporating the binding helix hairpin of AHB1 and found that one bound the RBD and was thermostable (fig. S2, B, D, and F).

For 50 of the minibinders made by using approach 2, and the second-generation ACE2 helix scaffolded design, we generated site saturation mutagenesis libraries (SSMs) in which every residue in each design was substituted with each of the 20 amino acids one at a time. Deep sequencing before and after FACS sorting for RBD binding revealed that residues at the binding interface and protein core were largely conserved for 40 out of the 50 approach 2 minibinders and for the ACE2 helix scaffolded design (Fig. 2 and figs. S6 and S7). For most of these minibinders, a small number of substitutions were enriched in the FACS sorting; combinatorial libraries incorporating these substitutions were constructed for the ACE2-based design and the eight highest-affinity approach 2 designs and again screened for binding to the RBD at concentrations down to 20 pM. Each library converged on a small number of closely related sequences; one of these was selected for each design, AHB2 or LCB1-LCB8, and found to bind the RBD with high affinity on the yeast surface in a manner competed with by ACE2 (Fig. 3 and fig. S8).

AHB2 and LCB1-LCB8 were expressed and purified from *E. coli*, and binding to the RBD assessed with BLI. For seven of the designs, the dissociation constant (K_d) values ranged from 1 to 20 nM (Fig. 3, fig. S8, and table S2), and for two (LCB1 and LCB3), the K_d values were below 1 nM, which is too strong to measure reliably with this technique (Fig. 3). On the surface of yeast cells, LCB1 and LCB3 showed binding signals at 5 pM of RBD after protease (trypsin and chymotrypsin) treatment (fig. S9). Circular dichroism spectra of the purified minibinders were consistent with the design models, and the melting temperatures for most were greater than 90°C (Fig. 3 and fig. S8). The designs retained full binding activity after 14 days at room temperature (fig. S10). AHB1 and -2 and LCB3 also bound to the SARS-CoV RBD (in addition to the SARS-CoV-2 RBD), but with lower affinity (fig. S11); we anticipate that the binding affinities achieved for SARS-CoV-2 could be readily obtained for other coronavirus spike proteins if these were directly targeted for design.

Fig. 4. Cryo-EM characterization of the LCB1 and LCB3 minibinders in complex with SARS-CoV-2 spike protein.

(A) Molecular surface representation of LCB1 bound to the SARS-CoV-2 spike ectodomain trimer viewed along two orthogonal axes (left, side view; right, top view)

(B) Superimposition of the computational design model (silver) and refined cryo-EM structure (magenta) of LCB1 (using the map obtained through local refinement) bound to the RBD (cyan).

(C and D) Zoomed-in views of computational model (silver) of LCB1/RBD complex overlaid on the cryo-EM structure (cyan for RBD and pink for LCB1), showing selected interacting side chains.

(E) Molecular surface representation of LCB3 bound to the SARS-CoV-2 spike ectodomain trimer viewed from the side and top of the spike trimer.

(F) Superimposition of the computational design model (silver) and refined cryo-EM structure (pink) of LCB3 (using the map obtained through local refinement) bound to the RBD (cyan).

(G and H) Zoomed-in view of the interactions between LCB3 (pink) and the SARS-CoV-2 RBD (cyan), showing selected interacting side chains. In (A) and (E), each spike protomer is colored distinctly (cyan, pink, and yellow). For (B) and (F), the RBDs were superimposed to evaluate the binding pose deviations between designed models and refined structure of each minibinder.

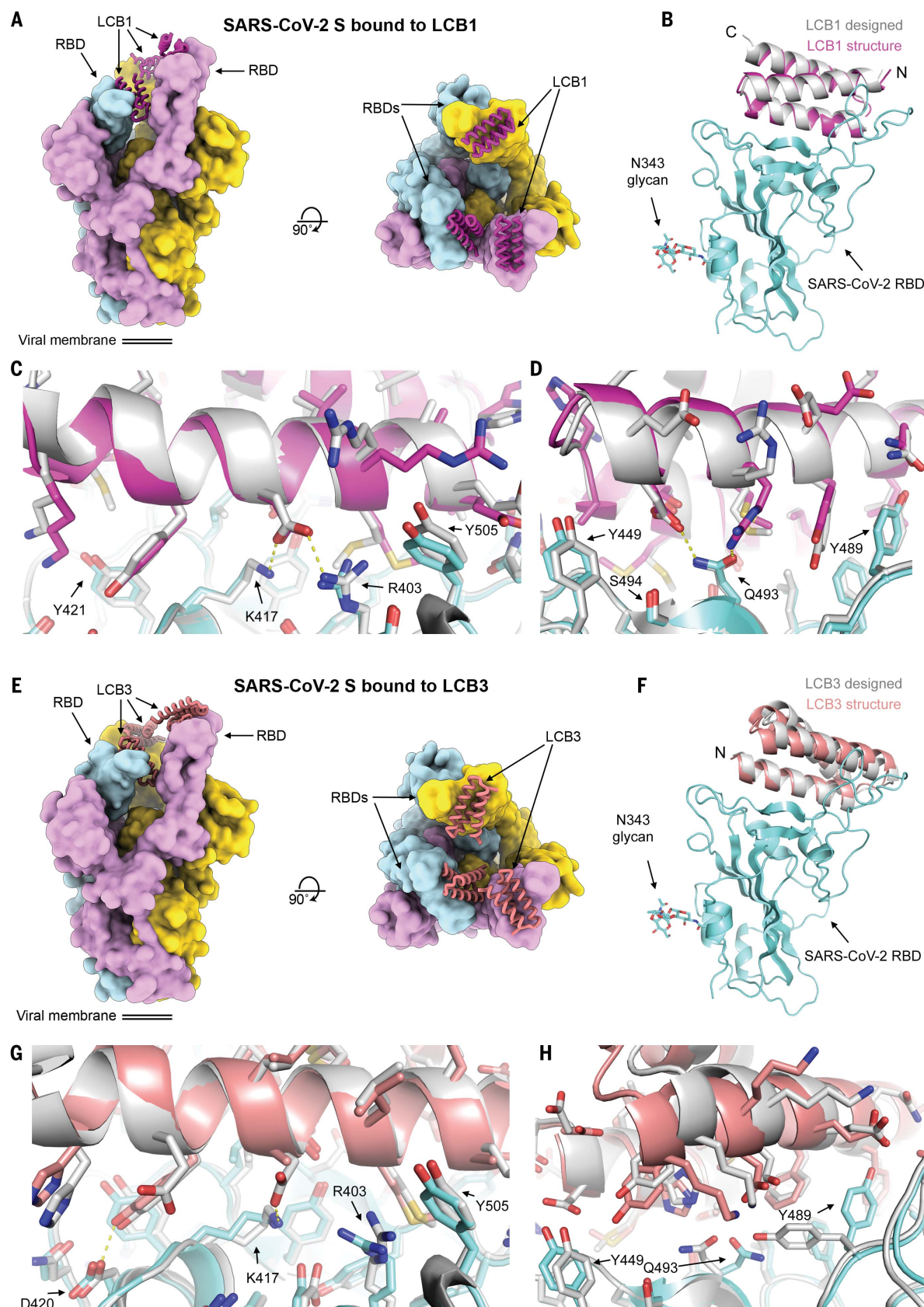
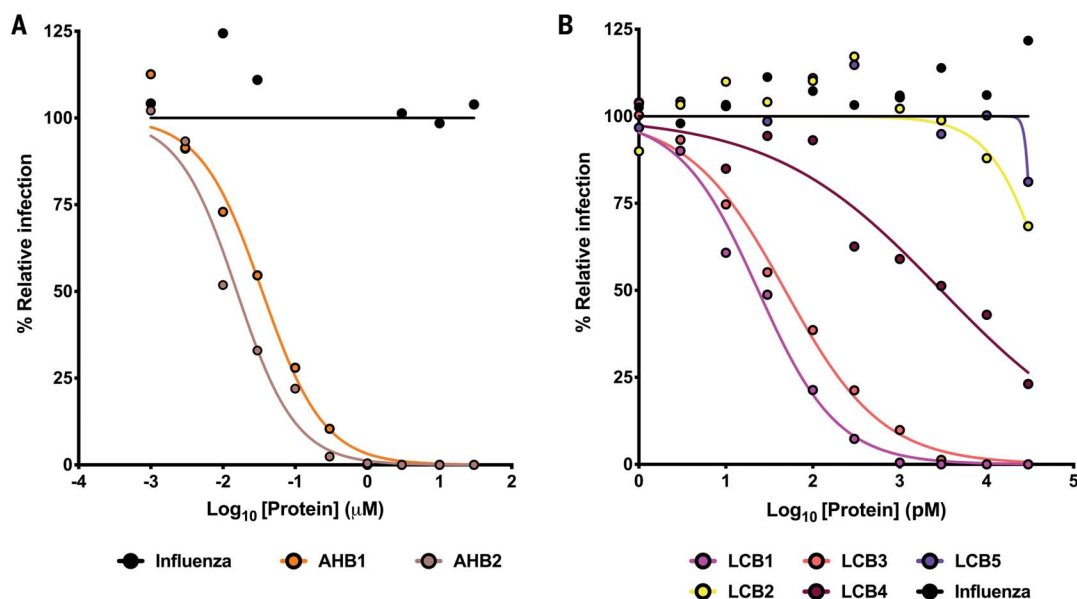


Fig. 5. Neutralization of live virus by designed miniprotein inhibitors. (A and B) Neutralization activity of (A) AHB1 and AHB2 or (B) LCB1-5 were measured with a focus reduction neutralization test. Indicated concentrations of minibinders were incubated with 100 FFU of authentic SARS-CoV-2 and subsequently transferred onto Vero E6 monolayers. AHB1, AHB2, LCB1, and LCB3 potentially neutralize SARS-CoV-2, with median effective concentration (EC_{50}) values <50 nM (AHB1 and AHB2) or <50 pM (LCB1 and LCB3). Data are representative of two independent experiments, each performed in technical duplicate.



Cryo-electron microscopy structure determination

We characterized the structures of LCB1 and LCB3 in complex with the SARS-CoV-2 spike ectodomain trimer by cryo-electron microscopy (cryo-EM) at 2.7 and 3.1 Å resolution, respectively, and found that the minibinders bind stoichiometrically to the three RBDs within the spike trimer (Fig. 4, A and E, and figs. S12 and S13). Although the spike predominantly harbored two open RBDs for both complexes, we identified a subset of particles with three RBDs open for the LCB3 complex (Fig. 4, A and E, and figs. S12 and S13). We improved the resolvability of the RBD/LCB1 and RBD/LCB3 densities by using focused classification and local refinement yielding maps at 3.1 and 3.5 Å resolution, which enabled visualization of the interactions formed by each minibinder with the RBD (Fig. 4, B and F, and figs. S12 and S13).

LCB1 and LCB3 dock with opposite orientations in the crevice formed by the RBD receptor-binding motif through extensive shape complementary interfaces with numerous electrostatic interactions mediated by two out of the three minibinder α -helices (Fig. 4, B to D and F to H). Similar to ACE2, the LCB1 and LCB3 binding sites are buried in the closed S conformational state and require opening of at least two RBDs to allow simultaneous recognition of the three binding sites (Fig. 4, A and E). Both LCB1 and LCB3 form multiple hydrogen bonds and salt bridges with the RBD with buried surface areas of ~1 000 and ~800 Å², respectively (Fig. 4, C, D, G, and H), which is consistent with the subnanomolar affinities of these inhibitors. As designed, the binding sites for LCB1 and LCB3 overlap with that of ACE2 (fig. S14 and table S1) and hence

should compete for binding to the RBD and inhibit viral attachment to the host cell surface.

Superimposition of the designed LCB1/RBD or LCB3/RBD models to the corresponding cryo-EM structures, using the RBD as reference, show that the overall binding modes closely match the design models with backbone $C\alpha$ root mean square deviation of 1.27 and 1.9 Å for LCB1 and LCB3, respectively (Fig. 4, B and F), and that the primarily polar sidechain-sidechain interactions across the binding interfaces present in the computational design models are largely recapitulated in the corresponding cryo-EM structures (Fig. 4, C, D, G, and H). These data show that the computational design method can have quite high accuracy. The structure comparisons in Fig. 4, C, D, G, and H are to the original design models; the substitutions that increased binding affinity are quite subtle and have very little effect on backbone geometry.

Virus neutralization

We investigated the capacity of AHB1, AHB2, and LCB1 to -5 to prevent the infection of cells by bona fide SARS-CoV-2. Varying concentrations of minibinders were incubated with 100 focus-forming units (FFU) of SARS-CoV-2 and then added to Vero E6 monolayers. AHB1 and AHB2 strongly neutralized SARS-CoV-2 (IC_{50} of 35 and 15.5 nM, respectively), whereas a control influenza minibinder showed no neutralization activity (Fig. 5A). Next, we tested the approach 2–designed minibinders LCB1 to LCB5. We observed even more potent neutralization of SARS-CoV-2 by LCB1 and LCB3 with IC_{50} values of 23.54 and 48.1 pM, respectively, within a factor of three of the most potent anti-SARS-CoV-2 monoclonal antibody described to date (13; at increased minibinder incubation volumes, IC_{50} values as low as 11 pM

were obtained) (Fig. 5B). On a per mass basis, because of their very small size, the designs are sixfold more potent than the best monoclonal antibodies.

Conclusions

The minibinders designed in this work have potential advantages over antibodies as potential therapeutics. Together, they span a range of binding modes, and in combination, viral mutational escape would be quite unlikely (figs. S1 and S14 and table S1). The retention of activity after extended time at elevated temperatures suggests that they would not require a temperature-controlled supply chain. The designs have only 5% the molecular weight of a full antibody molecule, and hence in an equal mass have 20-fold more potential neutralizing sites, increasing the potential efficacy of a locally administered drug. The cost of goods and the ability to scale to very high production should be lower for the much simpler miniproteins, which do not require expression in mammalian cells for proper folding, unlike antibodies. The small size and high stability should also make them amenable to formulation in a gel for nasal application and to direct delivery into the respiratory system through nebulization or as a dry powder. We will be exploring alternative routes of delivery in the months ahead as we seek to translate the high-potency neutralizing proteins into SARS-CoV2 therapeutics and prophylactics. Immunogenicity is a potential problem with any foreign molecule, but for previously characterized small de novo–designed proteins, little or no immune response has been observed (11, 14), perhaps because the high solubility and stability together with the small size makes presentation on dendritic cells less likely.

Timing is critical in a pandemic outbreak; potent therapeutics are needed in as short a time as possible. We began to design minibinders in January 2020 on the basis of a Rosetta model of the SARS-CoV-2 spike structure and switched to the crystal structures once they became available (4, 15–17). By the end of May 2020, we had identified very potent neutralizers of infectious virus; during this same time, a number of neutralizing monoclonal antibodies were identified. We believe that with continued development, the computational design approach can become much faster. First, as structure prediction methods continue to increase in accuracy, target models suitable for design could be generated within a day of determining the genome sequence of a new pathogen. Second, with continued improvement in computational design methods, it should be possible to streamline the workflow described here, which required screening of large sets of computational designs, followed by experimental optimization, to identify very-high-affinity binders. The very close agreement of the cryo-EM structures of LCB1 and LCB3 with the computational design models suggest that the main challenges to overcome are not in the de novo design of proteins with shape and chemical complementarity to the target surface, but in recognizing the best candidates and identifying a small number of affinity-increasing substitutions. The large amount of data collected in protein-interface design experiments such as those described here should inform the improvement of the detailed atomic models at the core of Rosetta design calculations, as well as complementary machine-learning approaches, to enable even faster in silico design of picomolar inhibitors such as LCB1 and LCB3. With continued methods development, we

believe that it will become possible to generate ultrahigh-affinity, pathogen-neutralizing designs within weeks of obtaining a genome sequence. Preparing against unknown future pandemics is difficult, and such a capability could be an important component of a general response strategy.

REFERENCES AND NOTES

1. Y. J. Hou *et al.*, *Cell* **182**, 429–446.e14 (2020).
2. R. Shi *et al.*, *Nature* **584**, 120–124 (2020).
3. D. Pinto *et al.*, *bioRxiv* 023903 [Preprint] 10 April 2020; <https://doi.org/10.1101/2020.04.07.023903>.
4. J. Lan *et al.*, *Nature* **581**, 215–220 (2020).
5. M. Yuan *et al.*, *Science* **368**, 630–633 (2020).
6. Y. Wu *et al.*, *Science* **368**, 1274–1278 (2020).
7. K. L. Winarski *et al.*, *Proc. Natl. Acad. Sci. U.S.A.* **116**, 15194–15199 (2019).
8. A. Taylor *et al.*, *Immunol. Rev.* **268**, 340–364 (2015).
9. B. S. Graham, *Science* **368**, 945–946 (2020).
10. A. C. Walls *et al.*, *bioRxiv* 956581 [Preprint] 20 February 2020; <https://doi.org/10.1101/2020.02.19.956581>.
11. A. Chevalier *et al.*, *Nature* **550**, 74–79 (2017).
12. J. Dou *et al.*, *Nature* **561**, 485–491 (2018).
13. W. B. Alsoussi *et al.*, *J. Immunol.* **205**, 915–922 (2020).
14. D. A. Silva *et al.*, *Nature* **565**, 186–191 (2019).
15. J. Shang *et al.*, *Nature* **581**, 221–224 (2020).
16. Q. Wang *et al.*, *Cell* **181**, 894–904.e9 (2020).
17. R. Yan *et al.*, *Science* **367**, 1444–1448 (2020).

ACKNOWLEDGMENTS

We thank S. Halabiya for MiSeq (Illumina) support, E. Procko for Fc tagged RBD protein, and K. Van Wormer and A. C. Smith for their tremendous laboratory support during COVID-19. **Funding:** This work was supported by DARPA Synergistic Discovery and Design (SD2) HR0011835403 contract FA8750-17-C-0219 (L. Cao, B.C., and D.B.). The Audacious Project at the Institute for Protein Design (L.K. and L. Car.), funding from E. and W. Schmidt by recommendation of the Schmidt Futures program (L.M. and I.G.), the Open Philanthropy Project Improving Protein Design Fund (B.C. and D.B.), an Azure computing resource gift for COVID-19 research provided by Microsoft (L. Cao and B.C.), the National Institute of General Medical Sciences (R01GM120553 to D.V.), the National Institute of Allergy and Infectious Diseases (HHSN272201700059C to D.V., D.B., and L.S.), a Helen Hay Whitney Foundation postdoctoral fellowship (J.B.C.), a Pew Biomedical Scholars Award (D.V.), an Investigators in the Pathogenesis of Infectious Disease Award from the Burroughs

Wellcome Fund (D.V.), a Fast Grant award (D.V.), and the University of Washington Arnold and Mabel Beckman cryo-EM center. **Author contribution:** L. Cao and D.B. designed the research; L. Cao developed the computational methods for approach 1 and made the designs based on the ACE2 helix; L. Cao and B.C. developed the computational methods for approach 2, and L. Cao made the de novo designs; B.C., L. Cao, and E.M.S. designed the de novo scaffold library; L. Cao, I.G., and L.K. performed the yeast display assays and next-generation sequencing; L. Cao, I.G., L.M., L.K., A.C.W., and L.Car. purified and prepared the proteins; L. Cao, I.G., and L.M. performed the BLI assays; L. Cao and L.M. collected the circular dichroism results; Y.P. and D.V. solved the cryo-EM structures; J.B.C. and R.E.C. performed the SARS-CoV-2 neutralization assay; L.S., M.S.D., D.V., and D.B. supervised the research; L. Cao, J.B.C., Y.-J.P., L.S., D.V., and D.B. wrote the manuscript; all authors discussed the results and commented on the manuscript. **Competing interests:** L. Cao, I.G., B.C., L.M., L.K., and D.B. are coinventors on a provisional patent application that incorporates discoveries described in this manuscript. D.B. is a cofounder of Neoleukin Therapeutics. M.S.D. is a consultant for Inbios, Vir Biotechnology, and NGM Biopharmaceuticals and is on the Scientific Advisory Board of Moderna. D.V. has a sponsored research agreement from Vir Biotechnology. **Data and materials availability:** The design models and design scripts used in the manuscript have been deposited to http://files.ipd.uw.edu/pub/SARS-CoV-2_binder_2020/scripts_models.zip. The cryo-EM maps and atomic models have been deposited at the Electron Microscopy Data Bank and the Protein Data Bank (PDB) with accession codes EMD: 22532 and PDB: 7JZL (SARS-CoV-2 S/LCB1), EMD: 22574 and PDB: 7JZU (SARS-CoV-2 S/LCB1, local refinement), EMD: 22534 (SARS-CoV-2 S/LCB3, 2 RBDs open), EMD: 22533 and PDB: 7JZM (SARS-CoV-2 S/LCB3, local refinement), and EMD: 22535 (SARS-CoV-2 S/LCB3, 3 RBDs open). This work is licensed under a Creative Commons Attribution 4.0 International (CC BY 4.0) license, which permits unrestricted use, distribution, and reproduction in any medium, provided the original work is properly cited. To view a copy of this license, visit <https://creativecommons.org/licenses/by/4.0>. This license does not apply to figures/photos/artwork or other content included in the article that is credited to a third party; obtain authorization from the rights holder before using such material.

SUPPLEMENTARY MATERIALS

science.sciencemag.org/content/370/6515/426/suppl/DC1
Materials and Methods
Figs. S1 to S14
Tables S1 to S3
References (18–39)

24 July 2020; accepted 3 September 2020
Published online 9 September 2020
10.1126/science.abd9909

NEURODEVELOPMENT

Orderly compartmental mapping of premotor inhibition in the developing zebrafish spinal cord

Sandeep Kishore, Eli B. Cadoff, Moneeza A. Agha, David L. McLean*

In vertebrates, faster movements involve the orderly recruitment of different types of spinal motor neurons. However, it is not known how premotor inhibitory circuits are organized to ensure alternating motor output at different movement speeds. We found that different types of commissural inhibitory interneurons in zebrafish form compartmental microcircuits during development that align inhibitory strength and recruitment order. Axonal microcircuits develop first and provide the most potent premotor inhibition during the fastest movements, followed by perisomatic microcircuits, and then dendritic microcircuits that provide the weakest inhibition during the slowest movements. The conversion of a temporal sequence of neuronal development into a spatial pattern of inhibitory connections provides an “ontogenotopic” solution to the problem of shaping spinal motor output at different speeds of movement.

Whether vertebrates are moving quickly or slowly, locomotion requires alternating activity between antagonistic muscle groups distributed along and across the body. We understand a considerable amount about how distinct types of motor neurons develop and generate different speeds of movement (1). However, we know relatively little about the development and organization of inhibitory circuits that ensure that alternating output patterns are matched to speed. This is due to the challenge in linking synaptic connectivity to neuronal identity and recruitment order in most vertebrates. Here, we asked how commissural inhibitory circuits in the zebrafish spinal cord are organized to ensure left-right alternation at different speeds of swimming. Because commissural inhibitory circuits are critical for left-right alternation in all vertebrates, and because the genetic origins of spinal neurons are evolutionarily conserved (2), zebrafish provide an opportunity to more easily reveal shared principles of locomotor network organization.

Zebrafish move through the water using axial muscle contractions that alternate from left to right across the body (3). To aid quick movements, larger motor neurons born during a “primary” wave of neurogenesis are recruited into an active pool that includes more numerous smaller motor neurons born during a “secondary” wave of neurogenesis that are also recruited at slower speeds (4, 5). By free-swimming larval and adult stages, the sequential development of spinal motor neurons has formed a topographic map of recruitment from ventral to dorsal during increases in body bending frequency and thus the speed of locomotion (6, 7). Reciprocal left-right alternation during swimming is maintained by glycinergic commissural inhibitory interneurons (8), which are also topographically

organized on the basis of recruitment order in zebrafish (6). However, it is not known how differential recruitment patterns are translated into alternating motor output at different speeds of locomotion, because patterns of premotor connectivity arising from commissural inhibitory interneurons in zebrafish (or any other vertebrate) have yet to be revealed.

Stronger perisomatic inhibition of larger motor neurons

To assess how the organization of premotor inhibitory inputs depends on movement speed, we first asked whether differences exist in the compartmental distribution of inhibitory synapses among motor neurons recruited at different speeds. We injected Gal4-UAS constructs (table S1) in 1- to 2-cell-stage zebrafish embryos to sparsely label individual primary ($n = 15$) and secondary ($n = 24$) motor neurons with fluorescent reporters (Fig. 1, A and B). We focused on glycinergic synapse distribution using the glycine receptor GlyR α 1 fused with enhanced green fluorescent protein (eGFP) (9). In 4- to 5-day-old larvae, this *in vivo* labeling approach revealed punctate fluorescent signals in the axonic, somatic, and dendritic compartments of both types of motor neurons (Fig. 1C). Axonic puncta were observed up to 45 μ m from the soma/axon boundary (mean \pm SD; 18 ± 10 μ m, $n = 39$). The largest total number of putative inhibitory synapses were observed in the dendrites for both primary and secondary motor neurons (Fig. 1D). However, consistent with the idea that larger (primary) motor neurons require more potent perisomatic inhibition to curtail their activity (10), primaries exhibited higher total numbers of putative inhibitory contacts in both somatic and axonic compartments than secondaries (Fig. 1D). From the transverse perspective, GlyR α 1 puncta decorated the lateral surface of both primary and secondary motor neurons (Fig. 1F), with putative axonic and somatic synapses concentrated more medially than dendritic synapses in both types of motor neurons (Fig. 1G).

Premotor inhibitory neurons target different compartments

Next, to assess the contribution of commissural inhibitory inputs to GlyR α 1 puncta distributions, we focused on dmrt3a-labeled dI6 neurons, which provide a conserved source of commissural inhibition during locomotion (11, 12). We first optimized the GRASP (GFP reconstitution across synaptic partners) approach for use in zebrafish. GRASP relies on the apposition of pre- and postsynaptic membranes at synapses to reconstitute a split GFP molecule (13, 14). Using Gal4-UAS-based approaches (tables S2 and S3), we created a transgenic zebrafish line with all dI6 neurons labeled with pTagRFP and half of a split GFP molecule tethered to the membrane, as well as all motor neurons with mCerulean and the other half of a split GFP molecule (Fig. 2A). The resulting transgenic larvae should have functional GFP at locations where dI6 and motor neurons form putative synapses. This approach revealed GFP puncta medially and laterally, but with a perisomatic bias (Fig. 2B). Consistent with the reconstitution of GFP at synapses, we observed punctate signals at locations where the axons of dI6 interneurons overlapped with the axons, somata, and dendrites of unidentified motor neurons (Fig. 2C). To better link inputs in different compartments to different motor neuron types, we sparsely labeled dI6 neurons and motor neurons ($n = 12$), which confirmed the presence of axonic, somatic, and dendritic GFP signals in both primaries and secondaries (Fig. 2D).

Axonic, somatic, and dendritic inputs to motor neurons could arise from the same neuron or different neurons. To assess how individual dI6 interneurons contributed to compartmentalization, we used a Gal4-UAS approach to sparsely label dI6 neurons with different cytosolic and synaptophysin-tagged fluorescent proteins in a transgenic line that labels motor neurons (Fig. 2, E and F). dI6 neurons could be divided into discrete types based on their morphologies and distribution of synaptic outputs relative to motor neurons. The first type had large-caliber, primarily descending and local axons with synaptophysin puncta concentrated ventrally and medially in close proximity to motor neuron axons (Fig. 2, G and H). These neurons are likely commissural local (CoLo) neurons that provide left-right direction control during fast startle responses in larval and adult fish (15–17). Two other types of dI6 interneurons with symmetrically bifurcating axons could be divided into groups with either medial synaptic output close to motor neuron somata or lateral synaptic output concentrated in the dendritic neuropil (Fig. 2, G and H). These neurons are likely commissural bifurcating longitudinal (CoBL) neurons, which participate in swimming in larval fish (6, 18). Despite differences in subcellular

Department of Neurobiology, Northwestern University, Evanston, IL 60208, USA.

*Corresponding author. Email: david-mclean@northwestern.edu

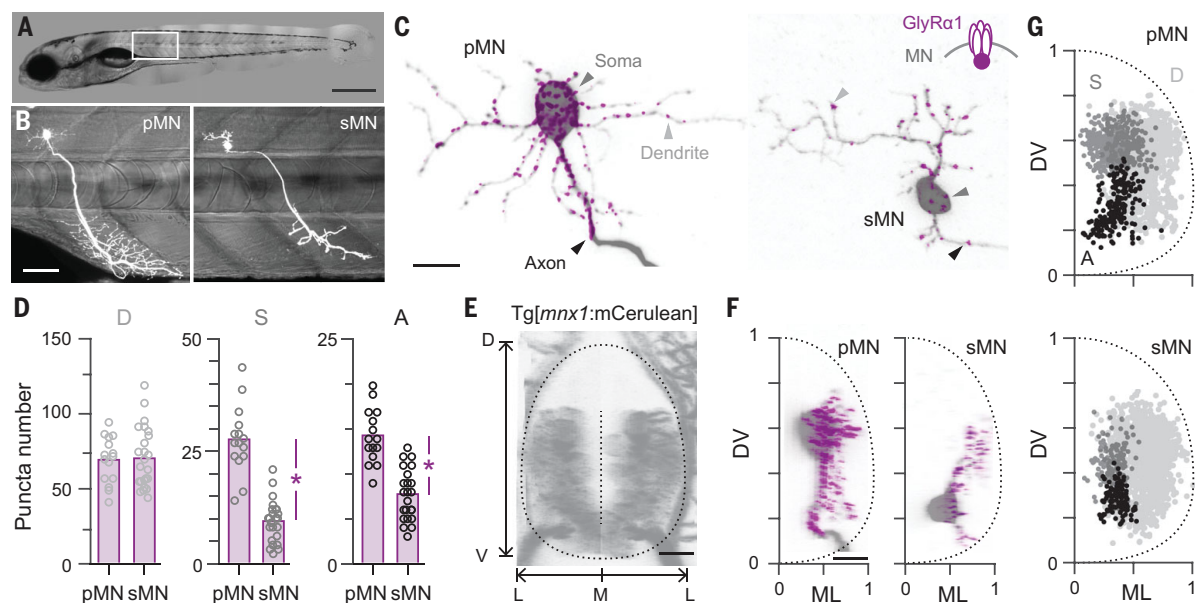


Fig. 1. Differences in glycinergic synapse distribution. (A) Image of a 5-day-old larval zebrafish. Dorsal is up, rostral is left. Boxed region is shown in (B). Scale bar, 0.5 mm. (B) Sparse labeling of a large primary motor neuron (pMN) and a smaller secondary motor neuron (sMN) from different fish. Scale bar, 50 μ m. (C) Confocal images of the distribution of GlyRa1-eGFP in different compartments from neurons shown in (B). Arrowheads [black, gray, and light gray, as used in (G)] indicate different neuronal compartments. Scale bar, 10 μ m. Inset: Schematic of GlyRa1 tagged with eGFP expressed in a motor neuron. (D) Quantification of GlyRa1-eGFP puncta in different compartments (D, dendritic; S, somatic; A, axonic) for pMNs and sMNs. Bars represent mean values. Asterisk indicates significant difference (two-tailed *t* test). D, $t_{(37)} = 0.2$, $P = 0.81$; S, $t_{(37)} = 9.2$, $P < 0.05$; A, $t_{(37)} = 6.8$,

$P < 0.05$; $n = 15$ pMNs and 24 sMNs. (E) Confocal transverse view of the spinal cord of a transgenic larva, *Tg[mnx1:mCherry]*, with motor neurons labeled. Anatomical landmarks are indicated by dotted lines. D, dorsal; V, ventral; M, medial; L, lateral. Scale bar, 10 μ m. (F) Transverse views of neurons in (C) registered to dorsoventral (DV) and mediolateral (ML) landmarks. Here and elsewhere, the 0 to 1 scales are normalized to the ventral (0) and dorsal (1) boundaries of the spinal cord along the y axis, and medial (0) and lateral (1) boundaries along the x axis. Scale bar, 10 μ m. (G) Quantification of the distribution of GlyRa1-eGFP puncta normalized to DV and ML landmarks for pMNs (top; $n = 15$ neurons and 1612 putative synapses) and sMNs (bottom; $n = 24$ neurons and 1478 putative synapses). Axonic contacts (A, black), somatic contacts (S, gray), and dendritic contacts (D, light gray) are indicated.

targeting and axon trajectories, we found no significant difference in the density of synaptophysin puncta related to type, with each averaging one or two synapses along every 10 μ m of axon (Fig. 2I).

dl6 neurons and compartments develop sequentially

Given the topographic pattern of CoBL recruitment (6) and the links between birth order and recruitment order in motor neurons (4, 5), we next asked whether dl6 neuron types are also distinguished by sequence of development. We created a transgenic line that enabled *in vivo* birth-dating using the photoconvertible protein Dendra (19), which changes from green to red in ultraviolet light. Photoconversions performed on day 1 with imaging performed on day 2 ($n = 5$; Fig. 3A) revealed a “primary” wave of dl6 neurons that included large-caliber, axonic dl6-CoLo neurons (Fig. 3B) and a “secondary” wave of unconverted cells numbering ~10 or 20 per segment (Fig. 3C). To see whether dl6 neurons continue to differentiate as the larvae mature to free-swimming stages, we performed photoconversions at day 2 and imaging at day 5 ($n = 6$; Fig. 3D), which revealed a further 20 dl6 neurons added per segment (Fig. 3C). Between day 2 and day 5, motor neuron neurogenesis is largely com-

pleted (5) but dendrites elaborate extensively (20); this suggests that new territories, if not new neurons, are available for innervation by later-developing dl6-CoBLs. Consistent with this idea, there were significant increases in both dl6 neuropil and motor neuron neuropil widths between day 2 and day 5 (Fig. 3, E and F). Contour density analysis of soma positions revealed that later-developing dl6-CoBLs occupy a more dorsal and medial location in the spinal cord (Fig. 3, D and G), which matches the observation that more dorsal CoBLs are recruited at slower speeds (6).

dl6 neuron recruitment matches inhibitory strength

Our observations thus far suggest that distinct types of dl6 neurons emerge in a developmental sequence linking recruitment order and potency of inhibition. To test this idea more directly, we performed electrophysiological recordings from dl6 neurons in current clamp to monitor their spiking activity while simultaneously recording from primary motor neurons on the opposite side of the body in voltage clamp to monitor outward inhibitory currents (Fig. 4, A and B). dl6 neurons were targeted in transgenic lines on the basis of their dorsoventral soma positions; after recording, morphologies were confirmed by either epifluorescence

illumination ($n = 49$) or confocal microscopy ($n = 12$). In a subset of experiments, we also performed photoconversion on day 2 in transgenic fish to further confirm old versus new dl6 neurons for recordings on day 5 ($n = 11$). Primary motor neurons were targeted with differential interference contrast imaging based on size and soma location, and their identity was confirmed by post hoc epifluorescent images (Fig. 4A).

We first assessed differences in recruitment during “fictive” escape responses evoked by a brief electrical stimulus to the tail (21). Like real escapes, fictive escapes involve an initial burst of unilateral motor activity that would rapidly turn the fish away, followed by bilateral rhythmic swimming activity to propel the fish forward, which declines in frequency and speed with time (21). As predicted (15–17), axon-targeting, early-born dl6-CoLo neurons were recruited exclusively during the initial response to the stimulus (Fig. 4B), with firing immediately preceding the short-latency contralateral inhibition that prevents bilateral co-contraction during escape turns (Fig. 4C). dl6-CoBLs were categorized by two types of response. “Faster” dl6-CoBLs were recruited coincident with or just after dl6-CoLos and continued to fire during the period of strong inhibitory drive to contralateral primary motor neurons (Fig. 4,

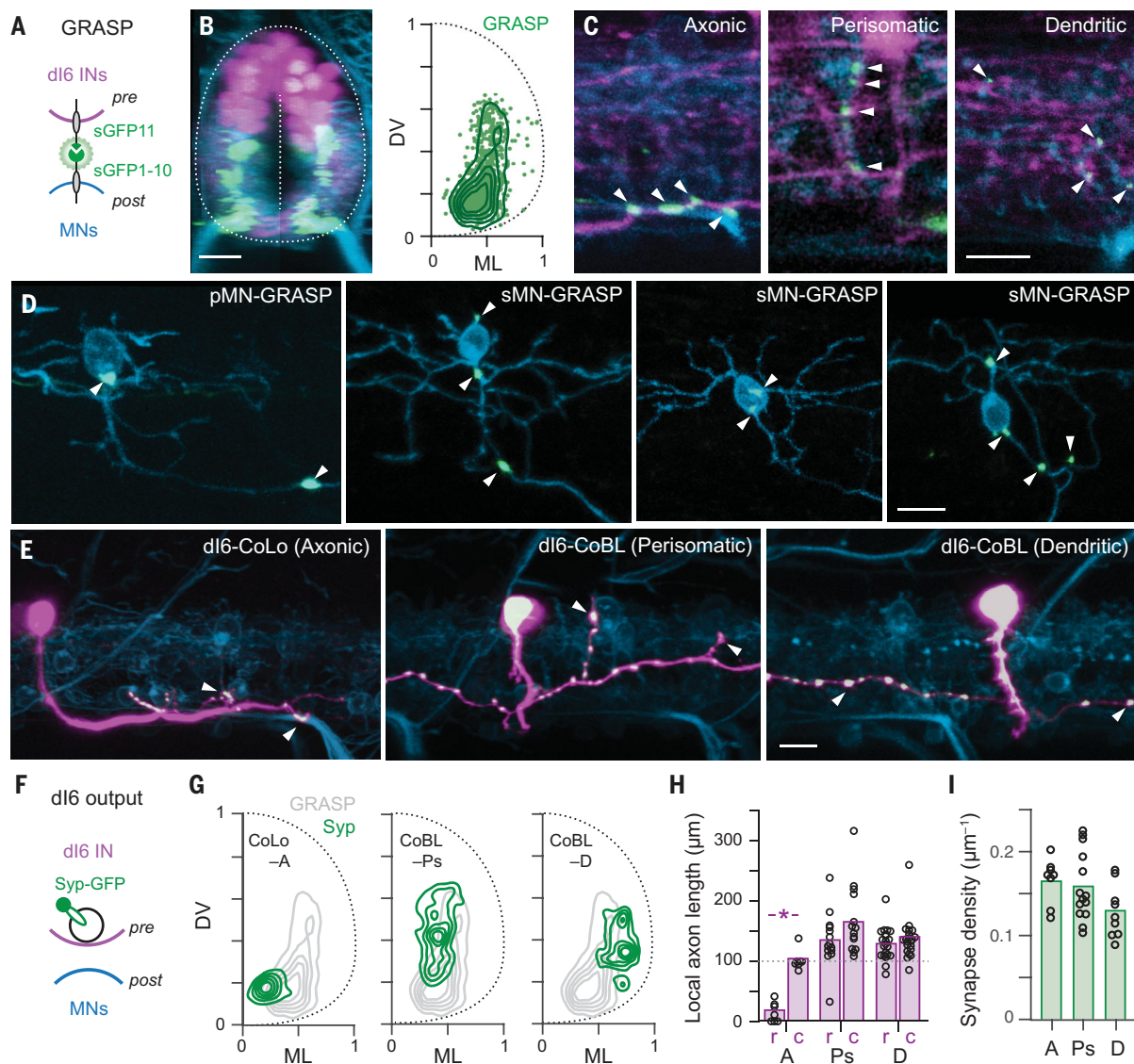


Fig. 2. dl6 neurons target different motor neuron compartments. (A) Schematic illustrating the GRASP method for revealing pre- and postsynaptic connectivity. (B) Left: Transverse view of compound transgenic line labeling all dl6 neurons (pink), all motor neurons (blue), and the resulting GRASP signal (green). Scale bar, 10 μm . Right: Distribution of GRASP puncta (green data points; $n = 15$ fish, 908 GRASP puncta) and a contour density plot (green lines) normalized to anatomical landmarks. (C) Single optical sections of confocal images viewed laterally; white arrowheads indicate GRASP signals in corresponding compartments. Scale bar, 10 μm . (D) GRASP labeling in individual pMN and sMNs (white arrowheads). Motor neurons are sparsely labeled by mCerulean and sGFP1-10; dl6 neurons are sparsely labeled by sGFP11. Scale bar, 10 μm . (E) Lateral views of dl6 neurons sparsely labeled with cytosolic pTagRFP (pink) and synaptophysin-GFP (green);

white indicates colocalization with pTagRFP in the *Tg[mnx1:mCerulean]* motor neuron line (blue). White arrowheads indicate likely connections. Scale bar, 10 μm . (F) Schematic illustrating the procedure to assess dl6 output. (G) Contour density plots of the distribution of synaptophysin puncta for axonic (A, $n = 5$), perisomatic (Ps, $n = 4$), and dendritic (D, $n = 6$) dl6 neurons. (H) Quantification of local commissural axon length measured 100 μm rostral (r) and caudal (c) to the soma for the distinct types of dl6 neurons. Bars represent mean values. Asterisk indicates significant difference (Mann-Whitney U test). Axonic, $U_{(12)} = 0$, $P < 0.05$, $n = 7$; perisomatic, $U_{(26)} = 70$, $P = 0.54$, $n = 14$; dendritic, $U_{(40)} = 186$, $P = 0.79$, $n = 21$. (I) Quantification of synapse density for the distinct types of dl6 neurons. Bars represent mean values. Densities are not significantly different [one-way analysis of variance (ANOVA): $F_{(2,28)} = 2.76$, $P = 0.08$]. Axonic, $n = 8$; perisomatic, $n = 14$; dendritic, $n = 9$.

B and C), which are characterized by higher-frequency swimming (Fig. 4D). Neurons recruited at higher frequencies also had relatively ventral soma positions (Fig. 4E) and lower input resistances (Fig. 4G), consistent with previous work (6). “Faster” dl6-CoBL neurons were also early-born, as indicated by recordings from photoconverted cells (Fig. 4C). Post hoc fills of

“faster” dl6-CoBL neurons also revealed contralateral axons that were concentrated perisomatically (Fig. 4, C and E). “Slower” dl6 CoBLs were never recruited during the initial escape (Fig. 4B) and fired more reliably during later periods of weak inhibitory drive to contralateral primaries (Fig. 4, B and C), which is characterized by lower-frequency swimming (Fig. 4D).

Photoconversions confirmed that slower dl6 CoBLs were born after day 2, and post hoc fills in a different subset of recordings showed that their contralateral axons were concentrated dendritically (Fig. 4, C and E). To assess potential differences in the physiological strength of connectivity, we evoked single spikes in the different types of dl6 neurons

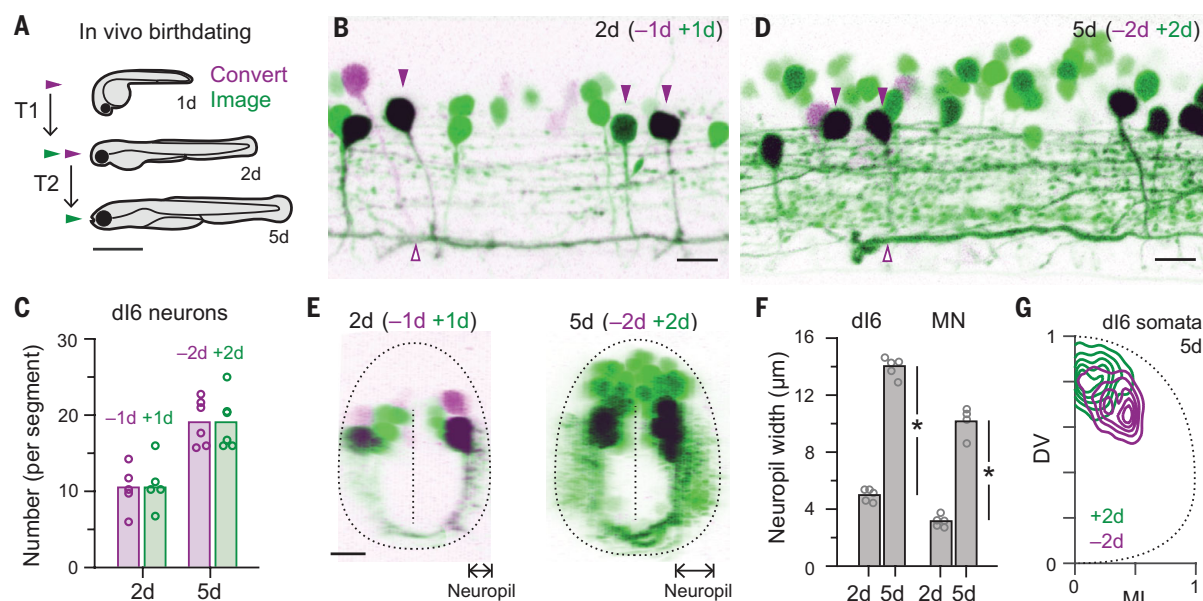


Fig. 3. dl6 neurons emerge in sequence. (A) Schematic illustrating the procedure for using staged photoconversions to determine neuron birthdates in vivo in two time frames (T1, T2). Scale bar, 1 mm. (B) Lateral view of a single spinal segment in *Tg[dmrt3a:Gal4; UAS:Dendra]* embryo at 2 days post-fertilization (dpf). dl6 neurons differentiated on or before 1 dpf (-1d) are purple or black; those that differentiated after 1 dpf (+1d) are green. Solid purple arrowheads mark dl6-CoLo neurons, distinguished by large-caliber axons (open purple arrowhead). Scale bar, 10 μ m. (C) Quantification of the number of old (purple) and new (green) neurons per segment on day 2 (2d) and day 5 (5d) based on staged photoconversions. Data points are from different fish; bars represent mean values. (D) Lateral view of a single spinal segment in *Tg[dmrt3a:Gal4; UAS:Dendra]* larva at 5 dpf. dl6 neurons differentiated on or before day 2 (-2d) are purple or black; those

that differentiated after day 2 (+2d) are green. As in (B), solid purple arrowheads mark dl6-CoLo neurons, and open purple arrowheads point to their large-caliber axons. Scale bar, 10 μ m. (E) Left: Transverse view of *Tg[dmrt3a:Gal4; UAS:Dendra]* embryo at 2 dpf shown in (B). Right: Transverse view of *Tg[dmrt3a:Gal4; UAS:Dendra]* larva at 5 dpf shown in (D). Neuropil width measures are indicated. (F) Quantification of the width of the neuropil on day 2 and day 5 for dl6 neurons and motor neurons (MN). Bars represent mean values. Asterisk indicates significant difference (two-tailed *t* test). dl6 neurons, $t_{(8)} = 24.7$, $P < 0.05$, $n = 5$ (2d and 5d); MNs, $t_{(7)} = 13.7$, $P < 0.05$, $n = 5$ (2d) and $n = 4$ (5d). (G) Contour density plot of the distribution of dl6 neuron somata on day 5 that were born on or before (purple) or after (green) day 2; $n = 5$ larvae, 173 neurons (-2d) and 173 neurons (+2d) measured over ~4 consecutive hemi-segments.

and measured inhibitory postsynaptic currents in primary motor neurons (Fig. 4F). Differences in subcellular distribution of synapses were matched by differences in the amplitude, failure rate, and overall probability of finding a connection (Fig. 4, H to J).

Discussion

Our results show that patterns of development solve the problem of how left-right alternation at different speeds is accomplished by premotor circuits in the zebrafish spinal cord. Inhibitory interneurons that are born early are more likely to synapse onto motor neuron axons, followed by interneurons that innervate motor neuron somata and then interneurons that innervate motor neuron dendrites (Fig. 5). These different synaptic locations are also linked to differences in recruitment order and will have different impacts on spike threshold according to their proximity to the axon initial segment and spike initiation zone: Inputs closer to where spikes are generated will have the most potent inhibition or “veto power” over suprathreshold activity. Differences in inhibitory potency conferred by the subcellular distribution of inhibitory inputs are also

matched by the amplitude of individual inputs and the number of converging ones. The ability of zebrafish to swim quickly is thus wired up before the ability to swim slowly, which matches the emergence of escape behaviors before exploratory ones (22). This pattern ensures that motor neurons receive amounts of inhibition tuned to different speeds of movement. Innervation of motor neurons by axonic and perisomatic dl6 interneurons maintains left-right bending at faster speeds. Dendrite-targeting dl6 interneurons are not active during escape bends or during higher-frequency swimming bends. Dendritic innervation of motor neurons likely provides finer control of motor output at lower speeds (23, 24). Although our focus was on the dl6 population, a similar pattern among other classes of spinal interneurons could help to explain the functional diversity among circuits arising from individual neural progenitors (25).

What distinguishes our work from previous studies in the spinal cord is the conversion of a temporal sequence of neuronal development into a spatial pattern of inhibitory premotor connections that in turn reflects function during locomotion. Efforts to decode the func-

tional logic of spinal circuits based on gene expression patterns, positioning, and time of development (26, 27) will be helped by considering both synaptic partners and subcellular synaptic domains. The wiring pattern we demonstrate here suggests that a common progenitor pool can generate diverse inhibitory circuits by following a simple opportunistic rule: “Form synapses with whatever neuron or neuronal subcompartment is available.” Sequential development along with molecular and spatial cues could also dictate the functional assembly of neuronal circuits more broadly. For example, our discovery of functionally compartmentalized inhibition in the spinal cord resembles the organization of local inhibitory circuits in mammalian cortex and hippocampus, where molecularly and developmentally distinct arrays of GABAergic interneurons targeting different compartments of pyramidal neurons have differential effects on oscillatory activity (28, 29). Thus, the “ontogenotopic” mechanism we reveal here can act in concert with molecular cues to ensure the appropriate assembly of neuronal microcircuits in vertebrates and invertebrates alike (30).

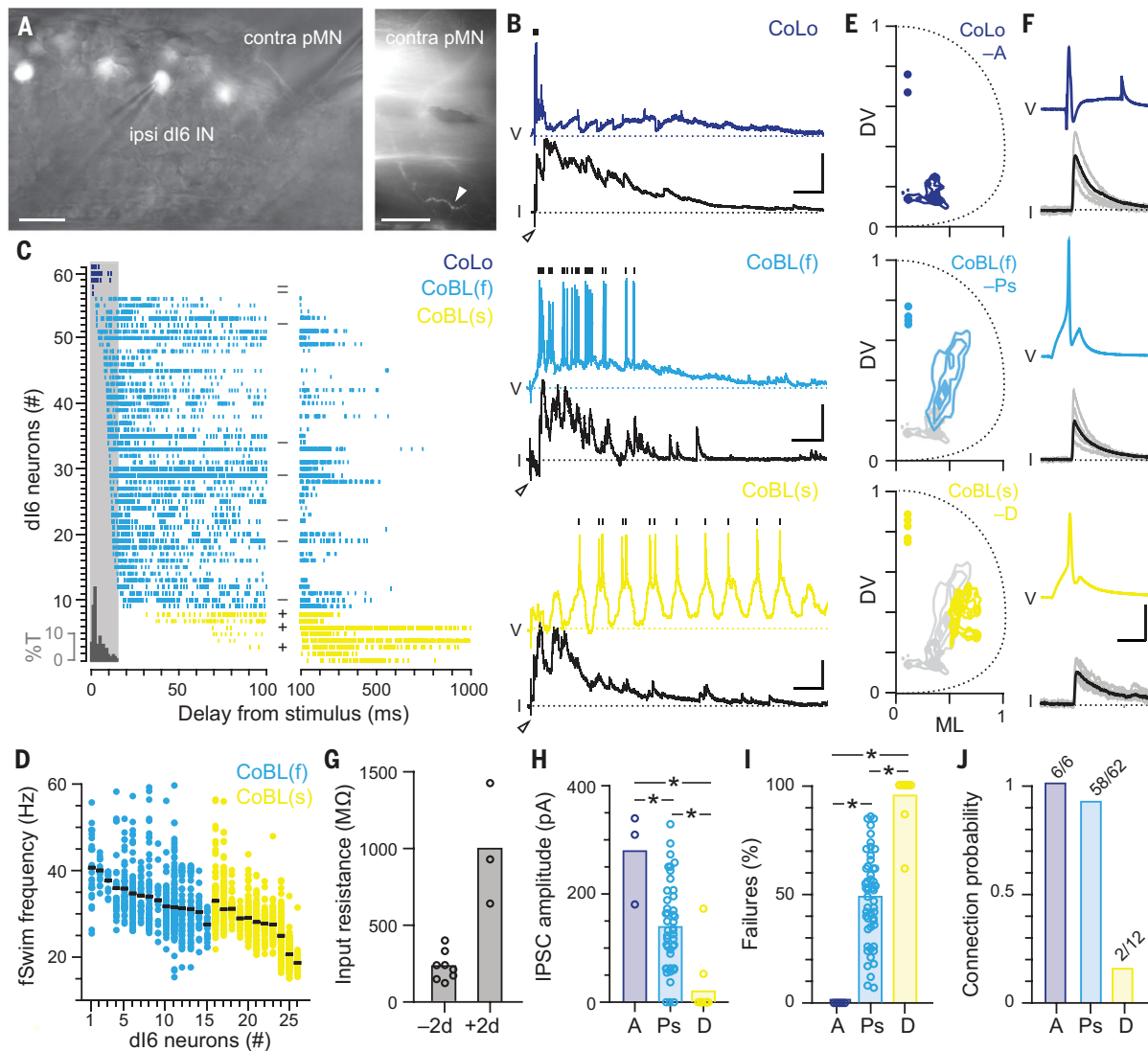


Fig. 4. dl6 recruitment order matches inhibitory strength. (A) Left: Lateral view of a *Tg[dmrt3a:hsGFP]* larva illustrates patch-clamp electrodes targeting a dl6 interneuron (IN) on the ipsilateral side and a pMN on the contralateral side. Scale bar, 10 μ m. Right: Lower-magnification view illustrating the peripheral axon of the contralateral pMN in axial muscle (white arrowhead). Scale bar, 50 μ m. (B) Paired patch-clamp recordings between dl6 neurons and pMNs arranged from top to bottom based on recruitment patterns following the tail stimulus (at open arrowheads). Vertical black lines mark spikes in the dl6 neuron recorded in current clamp. Voltage-clamp recordings from pMNs held at 0 mV (black dotted line) reveal outward inhibitory postsynaptic currents (IPSCs). V, voltage; I, current. Scale bars, dl6-CoLo, 10 mV, 800 pA, 50 ms; faster dl6-CoBL (f), 20 mV, 200 pA, 50 ms; slower dl6-CoBL (s), 10 mV, 200 pA, 50 ms. (C) Spike raster plots normalized to the tail stimulus (time = 0) arranged from top to bottom according to latency and recruitment pattern (CoLos, neurons 57 to 61; faster CoBLs, 9 to 56; slower CoBLs, 1 to 8). Each row represents spiking in multiple fictive swim episodes from the same dl6 neuron. The onset of short-latency IPSCs to motor neurons on the contralateral side is illustrated in the gray histogram and expressed as percentage of total IPSCs (%T). dl6 neurons present on or before (–) and after (+) day 2, as determined from staged photoconversions, are noted in the center of the plot. (D) Quantification of the range of fictive swimming (fSwim) frequencies in a subset of recordings ($n = 26$ of 61) at which faster (f) and slower (s) dl6-CoBL neurons are recruited.

Black lines report mean frequency. (E) Contour density plots of the distribution of axon terminals for axonic CoLos (A, $n = 2$), faster perisomatic CoBLs (Ps, $n = 4$), and slower dendritic CoBLs (D, $n = 5$) defined by their recruitment order. Dots represent the dorsoventral locations of recorded neurons. (F) Current-evoked spikes in dl6 neurons (top traces) and corresponding IPSCs in pMNs (bottom traces). Solid lines are averages; gray lines represent individual sweeps. Current steps (not shown) are 5 ms in duration for the CoBLs and 10 ms for the CoLo. Scale bar, 20 mV, 200 pA, 5 ms. (G) Quantification of input resistance of dl6 neurons born before (–2d) and after (+2d) 2 dpf. (H) Quantification of mean IPSC amplitude for the different types of dl6 neurons. Bars represent mean values. Asterisk indicates significant difference [Kruskal-Wallis ANOVA ($H_{(2)} = 23.9$, $P < 0.05$, $n = 66$) followed by Mann-Whitney U tests with Bonferroni corrections]. A ($n = 3$) versus Ps ($n = 51$), $U_{(52)} = 138$, $P < 0.05$; A ($n = 3$) versus D ($n = 12$), $U_{(13)} = 36$, $P < 0.05$; Ps ($n = 51$) versus D ($n = 12$), $U_{(61)} = 56$, $P < 0.05$]. (I) Quantification of failure rate for the different types of dl6 neurons. Bars represent mean values. Asterisk indicates significant difference [Kruskal-Wallis ANOVA ($H_{(2)} = 35.6$, $P < 0.05$, $n = 74$) followed by Mann-Whitney U tests with Bonferroni corrections]. A ($n = 6$) versus Ps ($n = 56$), $U_{(60)} = 0$, $P < 0.05$; A ($n = 6$) versus D ($n = 12$), $U_{(16)} = 0$, $P < 0.05$; Ps ($n = 56$) versus D ($n = 12$), $U_{(66)} = 633$, $P < 0.05$]. (J) Quantification of probability of forming a connection with a primary motor neuron for the different types of dl6 neurons. Numbers of connected pairs out of total number of recordings are noted above each bar.

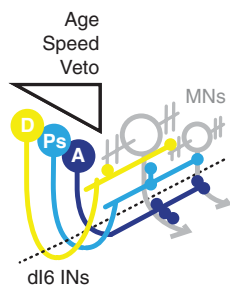


Fig. 5. Summary schematic. Commissural dl6 inhibitory neurons (dl6 INs) emerge in a developmental sequence that matches their age, the swimming speed at which they are recruited, and their ability to “veto” or silence the output of motor neurons (MNs) based on proximity to the spike initiation zone in the axon. This pattern of inhibition bridges motor neuron types, with more dense perisomatic innervation in larger MNs. Dotted line is the midline of the spinal cord. Yellow, dendritic (D); light blue, perisomatic (Ps); dark blue, axonic (A).

REFERENCES AND NOTES

1. J. S. Dasen, *Curr. Opin. Neurobiol.* **42**, 25–32 (2017).
2. M. Goulding, S. Bourane, L. Garcia-Campmany, A. Dalet, S. Koch, *Curr. Opin. Neurobiol.* **26**, 161–166 (2014).
3. J. R. Fetcho, *Brain Behav. Evol.* **40**, 82–97 (1992).
4. S. Kishore, M. W. Bagnall, D. L. McLean, *J. Neurosci.* **34**, 14046–14054 (2014).
5. P. Z. Myers, J. S. Eisen, M. Westerfield, *J. Neurosci.* **6**, 2278–2289 (1986).
6. D. L. McLean, J. Fan, S. Higashijima, M. E. Hale, J. R. Fetcho, *Nature* **446**, 71–75 (2007).
7. J. P. Gabriel *et al.*, *Nat. Neurosci.* **14**, 93–99 (2011).
8. N. Dale, O. P. Ottersen, A. Roberts, J. Storm-Mathisen, *Nature* **324**, 255–257 (1986).
9. D. M. Chow, K. A. Zuchowski, J. R. Fetcho, *Curr. Biol.* **27**, 1173–1183 (2017).
10. H. R. Lüscher, P. Ruenzel, E. Henneman, *Nature* **282**, 859–861 (1979).
11. L. S. Andersson *et al.*, *Nature* **488**, 642–646 (2012).
12. C. Satou *et al.*, *Cell Rep.* **30**, 3036–3050.e4 (2020).
13. E. H. Feinberg *et al.*, *Neuron* **57**, 353–363 (2008).
14. L. J. Macpherson *et al.*, *Nat. Commun.* **6**, 10024 (2015).
15. C. Satou *et al.*, *J. Neurosci.* **29**, 6780–6793 (2009).
16. J. C. Liao, J. R. Fetcho, *J. Neurosci.* **28**, 12982–12992 (2008).
17. J. R. Fetcho, D. S. Faber, *J. Neurosci.* **8**, 4192–4213 (1988).
18. M. E. Hale, D. A. Ritter, J. R. Fetcho, *J. Comp. Neurol.* **437**, 1–16 (2001).
19. N. G. Gurskaya *et al.*, *Nat. Biotechnol.* **24**, 461–465 (2006).
20. S. Kishore, J. R. Fetcho, *Nat. Commun.* **4**, 2086 (2013).
21. D. L. McLean, M. A. Masino, I. Y. Koh, W. B. Lindquist, J. R. Fetcho, *Nat. Neurosci.* **11**, 1419–1429 (2008).
22. M. Jay, D. L. McLean, *Curr. Opin. Physiol.* **8**, 188–192 (2019).
23. R. E. Fyffe, *J. Neurophysiol.* **65**, 1134–1149 (1991).
24. S. Ryglewski *et al.*, *Proc. Natl. Acad. Sci. U.S.A.* **111**, 18049–18054 (2014).
25. M. I. Gabitto *et al.*, *Cell* **165**, 220–233 (2016).
26. M. Tripodi, S. Arber, *Curr. Opin. Neurobiol.* **22**, 615–623 (2012).
27. S. Gosgnach *et al.*, *J. Neurosci.* **37**, 10835–10841 (2017).
28. Z. J. Huang, G. Di Cristo, F. Ango, *Nat. Rev. Neurosci.* **8**, 673–686 (2007).
29. R. C. Bandler, C. Mayer, G. Fishell, *Curr. Opin. Neurobiol.* **42**, 17–24 (2017).
30. J. R. Sanes, S. L. Zipursky, *Cell* **181**, 1434–1435 (2020).

ACKNOWLEDGMENTS

We thank E. Szuter and R. Gocker for fish care, and A. Miri, M. Gallio, C. Chiu, and M. Jay for feedback on the manuscript.

Funding: Supported by NIH grants R01 NS067299 and U19 NS104653. **Author contributions:** Conceptualization, S.K., D.L.M.; methodology, S.K., D.L.M.; validation, D.L.M.; formal analysis, S.K., D.L.M.; investigation, S.K., E.B.C., M.A.A.; writing, S.K., D.L.M.; visualization, S.K., D.L.M.; supervision, D.L.M. **Competing interests:** The authors declare no competing interests. **Data and materials availability:** All data are available in the manuscript or the supplementary materials. Materials requests can be made to D.L.M.

SUPPLEMENTARY MATERIALS

science.sciencemag.org/content/370/6515/431/suppl/DC1
Materials and Methods
Tables S1 to S3
References (31–46)
MDAR Reproducibility Checklist

[View/request a protocol for this paper from Bio-protocol.](#)

26 February 2020; accepted 18 August 2020
10.1126/science.abb4608

REPORT

POLYMER CHEMISTRY

Polyethylene upcycling to long-chain alkylaromatics by tandem hydrogenolysis/aromatization

Fan Zhang^{1*}, Manhao Zeng^{2*}, Ryan D. Yappert³, Jiakai Sun², Yu-Hsuan Lee², Anne M. LaPointe⁴, Baron Peters³, Mahdi M. Abu-Omar^{1,2}, Susannah L. Scott^{1,2†}

The current scale of plastics production and the accompanying waste disposal problems represent a largely untapped opportunity for chemical upcycling. Tandem catalytic conversion by platinum supported on γ -alumina converts various polyethylene grades in high yields (up to 80 weight percent) to low-molecular-weight liquid/wax products, in the absence of added solvent or molecular hydrogen, with little production of light gases. The major components are valuable long-chain alkylaromatics and alkyl naphthenes (average $\sim C_{30}$, dispersity $\bar{D} = 1.1$). Coupling exothermic hydrogenolysis with endothermic aromatization renders the overall transformation thermodynamically accessible despite the moderate reaction temperature of 280°C. This approach demonstrates how waste polyolefins can be a viable feedstock for the generation of molecular hydrocarbon products.

Over the past 70 years, global production of synthetic, petroleum-based plastics has risen sharply, from less than 2 million tonnes in 1950 to 380 million tonnes in 2015 (1). Production is projected to double again within the next 20 years (2). Plastics have become indispensable in many facets of modern life, enhancing the security of our food and health care systems, the performance of textiles, the versatility of consumer electronics, and the energy efficiency of transportation. About 40% of these plastics are destined for short-term use, and most (>90% in the United States) are not recycled (1). The vast bulk of this plastic waste ends up in landfills or is incinerated. However, the embodied energy that can be recovered by combustion is far less than that used in the original manufacturing of the plastic (3). Furthermore, a substantial fraction of the waste is mismanaged, ending up in rivers and oceans where its chemical inertness leads to extremely slow degradation and visible accumulation in the natural environment (4, 5).

Efforts to develop closed-loop life cycles for synthetic plastics by relying on collection, separation, and mechanical recycling have had limited success. The inferior properties of the recycled materials, relative to virgin plastics, contribute to the economic challenges of the “downcycling” model (6). New types of polymers that degrade rapidly in the environment

are being investigated (7), although such materials do not currently have either the physical properties or the cost structure to displace existing commodity plastics. Degradable plastics can also contaminate recycling streams and may encourage single-use product design. Depolymerization (also known as chemical or feedstock recycling) can recover the original monomer subunits, repolymerization of which yields materials with properties identical to those of the original plastic (8). However, this strategy requires prohibitive amounts of energy for polyolefins such as polyethylene (PE) and polypropylene (PP). Controlled partial depolymerization could convert post-consumer waste plastics directly into more valuable chemicals (“upcycling”), although few such processes have yet been developed.

High- and low-density polyethylenes (HDPE and LDPE) currently represent the largest fraction (36% by mass) of all plastic waste (1). Their depolymerization by pyrolysis at temperatures above 400°C, with or without a catalyst, generates complex, low-value mixtures of gas, liquid hydrocarbons, and char (9, 10). Somewhat more selective disassembly can be achieved at lower temperatures via catalytic hydrogenolysis (11, 12) or tandem catalytic alkane metathesis (13), but the low-value alkane products are unlikely to recoup the costs of recovery, separation, and processing using large amounts of a co-reactant (H_2 or liquid alkanes, respectively).

Aromatics are more attractive target products from partial depolymerization. The conventional process for making aromatics is naphtha reforming. This energy-intensive process generates a mixture known as BTX (benzene-toluene-xylenes) at 500° to 600°C (14). In a subsequent step with a large environ-

mental footprint, BTX is alkylated to give linear alkylbenzenes (LABs, used for making surfactants). The most widely used processes require linear olefins (typically, C_{10} to C_{16}) and liquid HF or $AlCl_3$ -HCl as the acid catalyst (15). Manufacturing the BTX by aromatization of shale gas-derived light alkanes requires harsher reaction conditions (propane, 550° to 700°C; ethane, 600° to 800°C; methane, 900° to 1000°C) (16), and the catalysts tend to deactivate rapidly. New zeolite-based catalysts can transform either methanol (17) or syngas (18) into BTX aromatics at lower temperatures, 300° to 400°C. Biomass-based routes include oxidative coupling of ethanol to aromatic alcohols and aldehydes (19), hydrogenolysis/hydrodeoxygenation of bio-oils or lignin to give propylbenzene (20), and Diels-Alder reactions of carbohydrate-derived furanics to give *p*-xylene (21). However, slow rates, low yields, and high H_2 requirements make these processes expensive to operate, and none are practiced commercially. BTX is also formed in the catalytic pyrolysis of PE at 400° to 600°C, although deactivation of the zeolite catalysts by coking is severe (22). The yields are moderate (up to 50 wt %), and large amounts of low-value gases (C_1 to C_5 , > 50 wt %) are formed. Conventional and proposed routes to BTX and linear alkylaromatics are compared in Fig. 1.

Here, we report a one-pot, low-temperature catalytic method to convert various grades of PE directly to liquid alkylaromatics over a simple heterogeneous catalyst. In a proof-of-concept experiment, a low-molecular-weight PE (0.118 g, $M_w = 3.5 \times 10^3 \text{ g mol}^{-1}$, $\bar{D} = 1.90$) was combined with Pt/ γ - Al_2O_3 (0.200 g, containing 1.5 wt % Pt dispersed as ~ 1 -nm nanoparticles; fig. S1, A and B) in an unstirred mini-autoclave (internal volume 10 ml) without solvent or added H_2 (Fig. 2A). After 24 hours at 280° (± 5)°C, the liquid/wax products (80% by mass) were recovered for characterization by dissolving in hot $CHCl_3$ (Fig. 2B, experiment 1). According to gel permeation chromatography with refractive index detection (GPC-RI), most of the PE underwent a decrease in M_w by nearly a factor of 10, to 430 g mol^{-1} , as well as the expected (23) decrease in dispersity (to $\bar{D} = 1.31$). On the basis of their orange color and the appearance of 1H nuclear magnetic resonance (NMR) signals in the region 6.5 to 9.0 ppm (fig. S2), these hydrocarbons appear to have substantial aromatic content. The $CHCl_3$ -insoluble solids include a small amount of organic residue (~ 5 wt %) in addition to the catalyst. The former includes unreacted polymer and large oligomers (including less soluble alkylaromatics), as judged by infrared and 1H NMR spectroscopy (figs. S3 and S4). The missing mass (~ 15 wt %) is presumably volatile hydrocarbons and gases, which were not collected in this exploratory

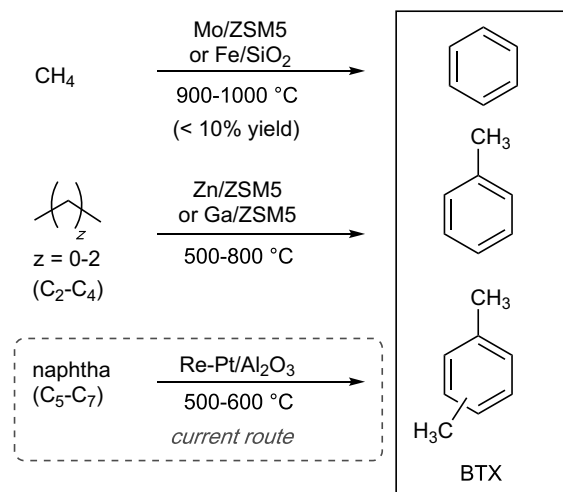
¹Department of Chemical Engineering, University of California, Santa Barbara, CA 93106, USA. ²Department of Chemistry and Biochemistry, University of California, Santa Barbara, CA 93106, USA. ³Department of Chemical Engineering, University of Illinois, Urbana-Champaign, IL 61801, USA. ⁴Department of Chemistry and Chemical Biology, Cornell University, Ithaca, NY 14853, USA.

*These authors contributed equally to this work.

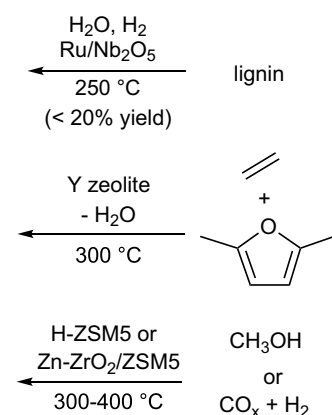
†Corresponding author. Email: sscott@ucsb.edu

A Routes to benzene-toluene-xylenes (BTX) aromatics

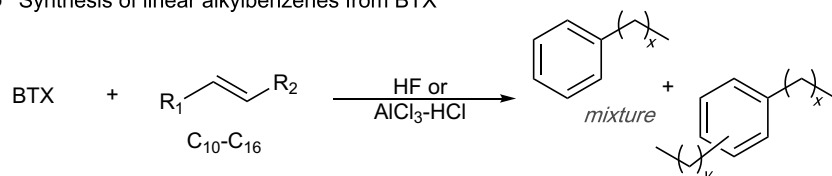
higher temperature routes



lower temperature routes



B Synthesis of linear alkylbenzenes from BTX



C One-pot synthesis of linear dialkylbenzenes from PE (this work)

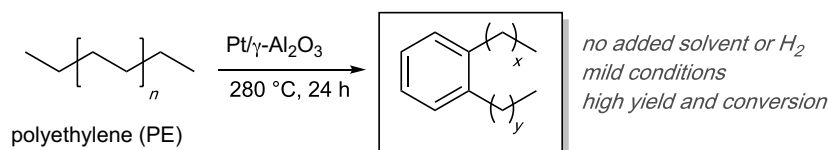


Fig. 1. Routes to alkylbenzenes. (A to C) Current and proposed routes to BTX (A) and the current downstream transformation of BTX to linear alkylbenzenes (B) are compared to the one-pot tandem process from polyethylene (C) reported here.

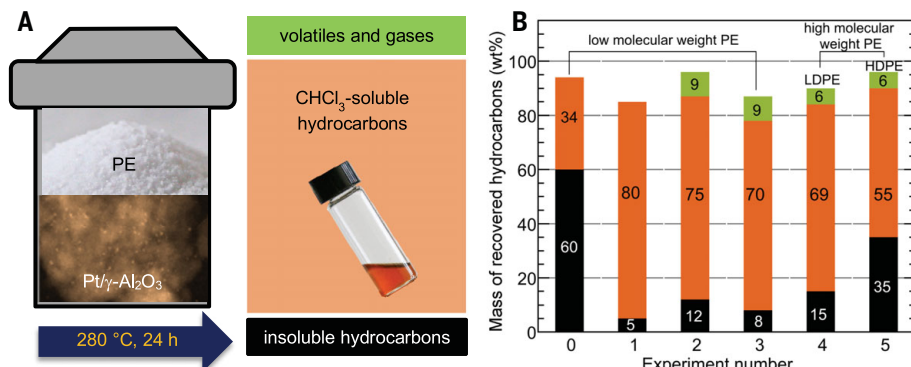


Fig. 2. Solvent-free conversion of various types of polyethylene. (A) Schematic of reactor and product fractions, with photographs of the powdered polymer and liquid products, as well as a transmission electron micrograph of the catalyst. (B) Hydrocarbon distributions after 24 hours at 280 °C. Reactions of a low-molecular-weight PE ($M_w = 3.52 \times 10^3 \text{ g mol}^{-1}$, $\bar{D} = 1.90$) in an unstirred mini-autoclave reactor: (0) catalyzed by γ-Al₂O₃ (no gas recovery); (1) catalyzed by Pt/γ-Al₂O₃ (no gas recovery); (2) catalyzed by Pt/γ-Al₂O₃ (with gas recovery). Reactions catalyzed by Pt/γ-Al₂O₃ in a stirred autoclave reactor with gas recovery: (3) low-molecular-weight PE; (4) LDPE bag ($M_w = 9.45 \times 10^4 \text{ g mol}^{-1}$, $\bar{D} = 7.37$); (5) HDPE bottle cap ($M_w = 5.35 \times 10^4 \text{ g mol}^{-1}$, $\bar{D} = 3.61$).

experiment. In a control experiment conducted without the catalyst under the same reaction conditions, the PE showed no appreciable decrease in M_w . A second control experiment using the same amount of γ-Al₂O₃ but without Pt resulted mostly in a CHCl₃-insoluble residue (~60 wt %) and a much lower yield of soluble hydrocarbon products (34 wt %), with a smaller decrease in molecular weight ($M_w = 1421 \text{ g mol}^{-1}$, $\bar{D} = 1.85$) and negligible aromatic content (Fig. 2B, experiment 0).

To obtain a more complete mass balance and to characterize the volatile reaction products, the exploratory experiment was repeated in a mini-autoclave equipped with a gas port. The recovered gases represent a small fraction of the original polymer mass (9 wt %). They include H₂ (0.2 mg, quantified by GC-TCD) and light hydrocarbons (C₁ to C₈, 9.8 mg, quantified by GC-FID) (figs. S5 and S6). The latter were primarily methane, ethane and propane, with minor amounts of *n*-hexane, cyclohexane, methylcyclopentane, benzene, and *n*-heptane. Additional volatile hydrocarbons (C₇ to C₁₁, 1.5 mg) were recovered by distillation from the autoclave at 150 °C. Their major component was toluene (47 wt %). Together, the light hydrocarbons, the CHCl₃-soluble liquids/waxes (89 mg) and the insoluble organic residue (14 mg) represent an overall mass balance of 96% (Fig. 2B, experiment 2).

When the reaction was conducted in a larger, stirred autoclave (internal volume 90 ml), most of the PE (70 wt %) was converted at 280 °C to high-boiling liquids/waxes (Fig. 2B, experiment 3). In this case, the waxes (24 wt %, $M_w = 723 \text{ g mol}^{-1}$, $\bar{D} = 1.34$) separated spontaneously from the liquids (46 wt %, $M_w = 520 \text{ g mol}^{-1}$, $\bar{D} = 1.12$) inside the reactor. GPC analysis of the liquid fraction using both RI and ultraviolet (UV) detection gave similar results (Fig. 3A), demonstrating that the UV-active (i.e., aromatic) chromophores were evenly distributed across the molecular weight range. The ¹³C NMR spectrum contains signals in the aromatic region (120 to 150 ppm), most corresponding to unsubstituted ring carbons (Fig. 3B). The ¹H NMR spectrum shows that most aromatic protons are associated with benzene rings (6.5 to 7.4 ppm), with fewer bonded to fused aromatic rings such as naphthalenes (7.4 to 9.0 ppm) (24). There is no evidence for olefins or dienes (4.5 to 6.5 ppm; fig. S8A).

The high yield of liquid alkylaromatics was particularly promising; such compounds find widespread application as surfactants, lubricants, refrigeration fluids, and insulating oils (25), and their manufacture from waste polyethylene could displace fossil fuel-based routes. The ¹H NMR spectrum reveals more information about the alkyl substituents (fig. S8A). Protons associated with an aliphatic carbon

directly bonded to an aromatic ring (C_a) resonate in the region 2 to 4 ppm. The overall ratio $H_a/H_{\text{aromatic}} = 1.1$ indicates that the major species are, on average, dialkylaromatics (figs. S7 and S8A). This finding is consistent with a previous report in which dialkylbenzenes were the major products of catalytic aromatization of lighter n -alkanes (C_6 to C_{12}) (26), and with their proposed mechanism of formation by dehydrocyclization of polyethylene (Fig. 4). Combining this information with the overall fraction of aromatic protons (0.037) and the average carbon number (C_{34} for this experiment, based on the M_n value determined by GPC), we estimate the overall alkylaromatic selectivity in the liquid fraction to be $57 (\pm 5)$ mol %, of which ~ 40 mol % is monoaromatic (table S3, experiment 3). Using the aromatic carbon fraction (0.10 accord-

ing to ^{13}C NMR; fig. S8B) instead results in a similar estimate for the alkylaromatic selectivity, $52 (\pm 4)$ mol %. Furthermore, many of the alkyl substituents are unbranched at the C_a position, judging by the intense ^1H signals at 2.35 to 2.85 ppm. The paraffinic $-\text{CH}_2/-\text{CH}_3$ ratio, 7.5, suggests that each alkyl substituent possesses, on average, < 1 branch point.

Individual molecular components in the liquid fraction were identified using field desorption-mass spectrometry (FD-MS; fig. S9). Each mass series shows a log-normal distribution with a maximum intensity at $\sim C_{30}$ (fig. S10). The most abundant products are the alkylbenzene series ($14n - 6$, ~ 22 mol %), as shown in Fig. 3C. Saturated alkanes and alkyl-naphthalenes share the same mass profile ($14n + 2$, 20 mol %) and are the next most abundant group, with smaller amounts of alkyl-

tetralins ($14n - 8$, 16 mol %) and alkyl-naphthalenes (i.e., alkylcycloalkanes; $14n$, 17 mol %). Alkyl-naphthalenes presumably arise by further dehydrocyclization of alkylbenzenes (Fig. 4) (27). Minor aromatic products include polyaromatics such as alkylanthracenes and alkylphenanthrenes ($14n - 4$, 7 mol %) and their partially hydrogenated analogs ($14n - 10$, 8 mol %). According to FD-MS, the selectivity for monoaromatic products (including both alkylbenzenes and alkyltetralins) is ~ 40 mol %, consistent with the ^1H NMR analysis described above. The alkyl-naphthalene products, which have intrinsic value as solvents and hydrogen donors (28), could be further dehydrogenated to alkylaromatics by active control of the partial pressure of H_2 in the reactor. The total yield of cyclic products (both alkylaromatics and alkyl-naphthalenes) in the liquid products is 88 mol % (table S4).

When the reaction time was extended from 24 to 36 hours at 280°C , similar products were formed (table S3, experiment S1), although the molecular weight distributions of both liquid and wax fractions shifted to slightly lower values (fig. S11) and the dispersity decreased further (to $D = 1.06$). At the same time, the alkylaromatic selectivity increased (24 hours, 52 and 71 mol %, respectively, in the liquid and wax fractions; 36 hours, 70 and 88 mol %, respectively) (table S3). Alkylaromatic yields were also strongly temperature-dependent. After 24 hours at a lower temperature (250°C), the CHCl_3 -soluble hydrocarbons (13 wt %) showed a smaller extent of depolymerization ($M_w = 1.8 \times 10^3 \text{ g mol}^{-1}$, $D = 2.11$) and negligible aromatic content; most PE was simply not converted. At a higher reaction temperature (330°C), the polymer was largely converted in 24 hours; however, the major products (77 wt %) were gases and volatile hydrocarbons. The yield of CHCl_3 -soluble hydrocarbons was low (~ 10 wt %), although the overall yield of aromatics was higher ($H_{\text{aromatic}}/H_{\text{total}} = 0.38$), with more

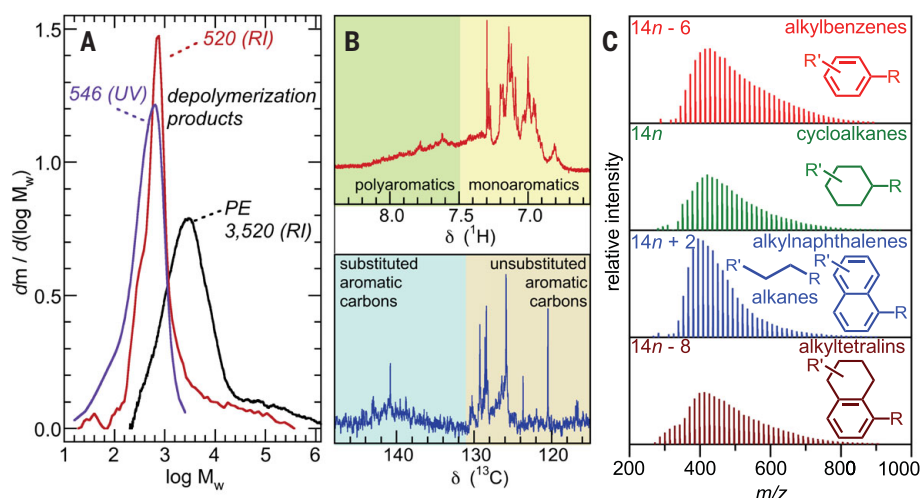
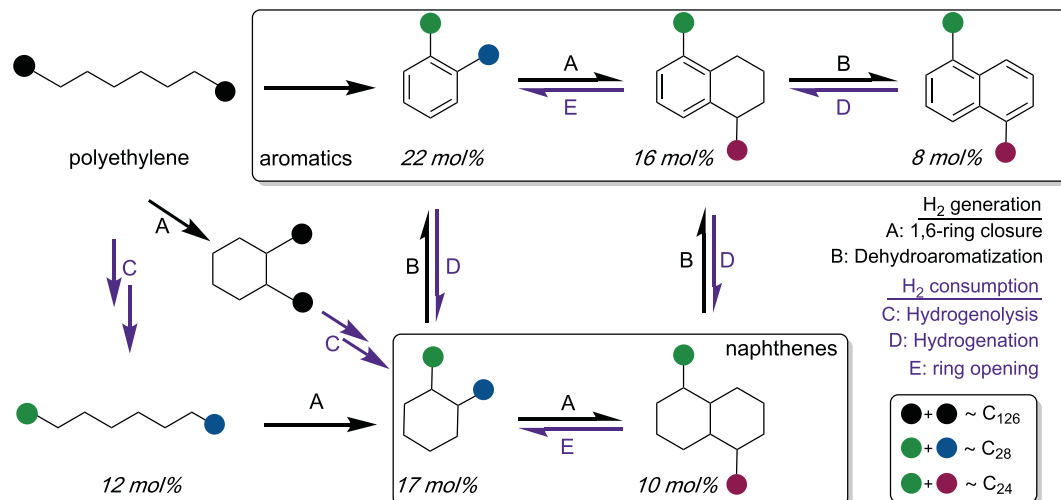


Fig. 3. Analysis of the liquid hydrocarbon fraction from the solvent-free catalytic conversion of polyethylene. Sample had $M_w = 3.52 \times 10^3 \text{ g mol}^{-1}$ and was heated for 24 hours at 280°C (Fig. 2B, experiment 3). (A) GPC analysis, conducted using both RI and UV detectors. (B) ^1H and ^{13}C NMR spectra, recorded in deuterated TCE. (C) FD-MS analysis.

Fig. 4. Overall PE conversion to alkylaromatics and alkyl-naphthalenes, and proposed mechanism of tandem polyethylene hydrogenolysis/aromatization via dehydrocyclization. Yields of each product were estimated using a combination of ^1H NMR and FD-MS analysis (see supplementary materials and tables S2 and S4).



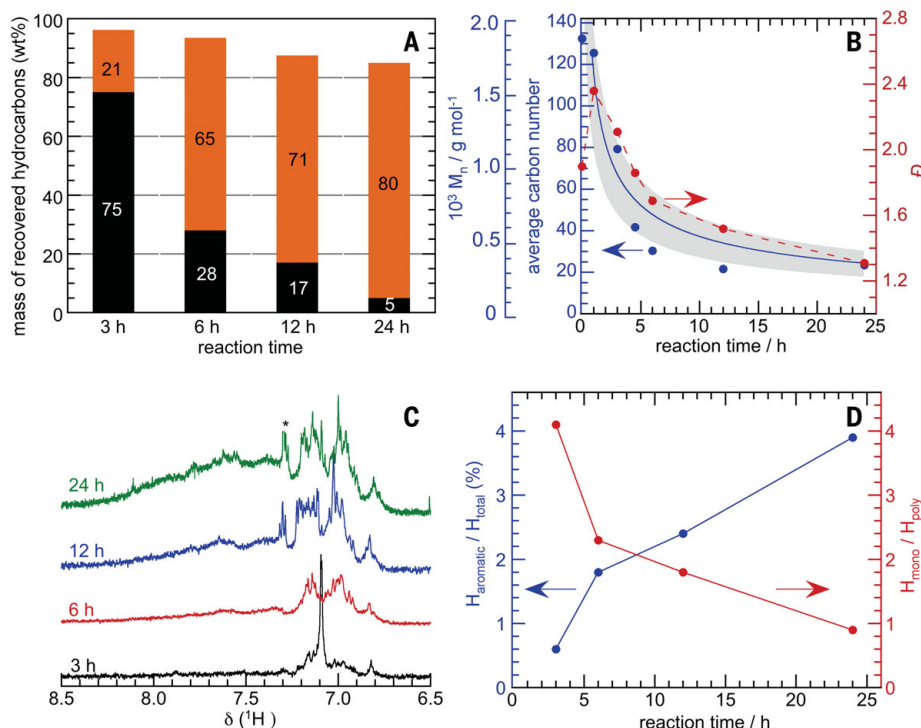


Fig. 5. Time course of the solvent-free disassembly of polyethylene ($M_n = 1.85 \times 10^3$ g mol⁻¹; $\bar{D} = 1.90$) catalyzed by Pt/ γ -Al₂O₃ in an unstirred mini-autoclave reactor at 280°C. **(A)** Evolution of major product fractions (orange, CHCl₃-soluble liquids/waxes; black, insoluble hydrocarbons). **(B)** Overall molecular weight (M_n , blue) and dispersity (\bar{D} , red) for all non-gas hydrocarbons. The red dashed line is present only to guide the eye. The curve fit (solid blue line) shows the refinement of Eq. 3 to the M_n data. Initial conditions: total carbon $n_C = 8.4$ mmol; number of polymer chains $N_0 = 68$ μ mol; total Pt $m_{Pt} = 3 \times 10^{-3}$ g; selectivity for aromatization versus hydrogenolysis, $s = 1/2$ (eq. S22). The shaded region indicates the 95% confidence bands for the model fit. Each independent measurement, which may diverge from the fit because of measurement error, has a 95% confidence interval that represents the mean of many measurements. The set of confidence intervals at all reaction times represents the confidence bands in which the true fit, given the form in Eq. 3, lies. Because the fit and its confidence bands predict the mean of many measurements at a given reaction time, individual measurements can lie outside these bands. **(C)** Time course of the ¹H NMR spectra of the liquid/wax fraction in the aromatic region. The asterisk indicates a truncated residual solvent signal. **(D)** The fraction of aromatic protons and the ratio of mono- to polyaromatic protons.

polyaromatics ($H_{mono}/H_{poly} = 0.25$). The optimum temperature for alkylbenzene formation is therefore 250°C < T < 330°C.

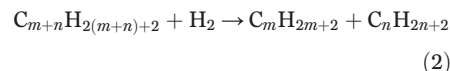
The time course of PE depolymerization was studied at 280°C (table S5, experiments 1a to 1g). A short induction period, lasting about 1 hour, corresponds in large part to the time required for thermal equilibration of the reactor (~0.75 hours). After this time, the liquid hydrocarbon fraction increased (Fig. 5A) as M_n decreased, eventually approaching a plateau at 315 g mol⁻¹ after ~6 hours (Fig. 5B). The dispersity \bar{D} increased initially from 1.94 to 2.36, then decreased to stabilize at 1.31. The alkylaromatic yield also changed appreciably over the course of the reaction. After 3 hours, aromatic protons represented <1% of all protons, mainly associated with alkylbenzenes (Fig. 5, C and D). At longer reaction times, the aromatic fraction and the yield of alkylnaphthalenes increased (table S5).

We also assessed the thermodynamics of n -alkane aromatization. The temperature-needed to achieve appreciable aromatic yields for this endothermic reaction (Eq. 1) decreases as the molecular weight increases (29).



Nonetheless, direct PE conversion to aromatics appears to require particularly mild conditions relative to the much higher operating temperatures generally required for making BTX from molecular n -alkanes (Fig. 1). Thermodynamic values for converting linear PE chains to alkylaromatics at 280°C in 1 atm H₂, estimated using Benson group contributions for long-chain n -alkanes (30), are $\Delta H_1^\circ = 246$ kJ/mol and $\Delta G_1^\circ = 31$ kJ/mol. Thus, aromatization alone is indeed disfavored. However, the reaction occurs in tandem with hydrogenation of a suitable hydrogen acceptor. In solvent-

less PE depolymerization, the PE chains themselves serve as an internal hydrogen sink (Fig. 4). Using Benson group contributions again, the estimated thermodynamic values for C-C bond hydrogenolysis (Eq. 2) are $\Delta H_2^\circ = -49$ kJ/mol and $\Delta G_2^\circ = -74$ kJ/mol.



Consequently, aromatization becomes favorable at 280°C ($\Delta G^\circ = 0$) when even 10% of the H₂ generated is consumed in PE hydrogenolysis.

On the basis of alkylaromatic yield, the aromatization in experiment 2 of Fig. 2B generated 0.50 mmol H₂. More than 90% of this H₂ (0.47 mmol) was consumed in reducing the molecular weight of the polymer via hydrogenolysis, making the tandem process thermodynamically favorable. However, the residual H₂ found in the reactor headspace at the end of the reaction (0.11 mmol) exceeds the expected value (0.03 mmol). Therefore, a significant amount of H₂ is generated in other reactions, such as PE dehydrocyclization to give cycloalkanes and tetralins. Both were observed by FD-MS (see above). Indeed, their yields are higher than the thermodynamic predictions, which favor aromatics. We observed that some of these more saturated compounds condense outside the autoclave's heated zone where the catalyst is located, thereby preventing their further dehydrogenation.

To explore whether polyethylene is necessary to produce long-chain alkylaromatics by tandem catalytic hydrogenolysis/aromatization, we investigated the reaction of n -C₃₀H₆₂ under the same conditions (table S6, experiments S2 and S3). Compared to PE, the n -C₃₀H₆₂ chains experience only half as much hydrogenolysis (consuming just 0.25 mmol H₂ according to fig. S12), as expected on the basis of the chain length dependence of hydrogenolysis kinetics (31). Molecules in the liquid products have an average chain length of C₂₀, with low alkylaromatic content (~10 mol %). Because hydrogenolysis and aromatization occur in tandem, they must occur together. Consequently, the formation of alkylaromatics is greatly enhanced by the use of polyethylene as a feedstock.

Although there are far too many individual reactions and products to formulate a precise kinetic model, a simplified model captures the main features of the tandem reaction. We assume that the Pt surface is covered with molten PE and/or PE-derived hydrocarbons at all times, and that the hydrogenolysis turnover frequency is constant on sites not occupied by aromatic hydrocarbons. As the latter form, they adsorb more strongly than alkanes (32), occupying active sites and reducing the hydrogenolysis rate accordingly. We also assume that hydrogenolysis is random (i.e., all aliphatic C-C

bonds are equally likely to be cleaved) (33). The sole adjustable parameter, k/K , is the ratio of the rate constant for hydrogenolysis (k) and the equilibrium constant for competitive adsorption of aromatics and aliphatic chains (K) (eq. S14). Equation 3 predicts the evolution of the average chain length as a function of the reaction time, initial total carbon amount n_C , and total platinum mass m_{Pt} .

$$\ln \left[1 - \frac{3}{M_n(t)} + \frac{3}{M_n(0)} \right] + \left[\frac{3}{M_n(t)} - \frac{3}{M_n(0)} \right] = - \frac{k}{K} \frac{m_{Pt}}{n_C} t \quad (3)$$

The curve fit of Eq. 3 to an experimental data-set is shown in Fig. 5B, starting with the data point at $t = 1$ hour (i.e., after the induction period caused by reactor heating). Assuming a preferential binding for aromatics of $K = 3.2 \times 10^6$ (32), the hydrogenolysis rate constant k is estimated to be $6.4 \times 10^2 \text{ mol}_{C-C} \text{ bonds hour}^{-1} \text{ g}_{Pt}^{-1}$ at 280°C .

The stability of the Pt/ γ - Al_2O_3 catalyst was investigated by conducting three consecutive 6-hour reactions (to ensure much less than full conversion), with regeneration of the recovered catalyst between each experiment (see supplementary materials). The liquid/wax yield decreased by 15 wt % in the second run but stabilized in the third run (table S6, experiments S4 to S6, and fig. S13). The activity decrease between the first and second runs was comparable to the decrease in the active Pt surface area measured by CO chemisorption, with no notable change between the second and third runs (table S6, experiments S4 to S6). Thus, the intrinsic activity of the catalyst (turnover frequency) appears to be unchanged. The average carbon number of the liquid/wax product increased between the first and second 6-hour runs (as expected because of the lower extent of depolymerization), then stabilized in the third run. Transmission electron microscopy analysis of a catalyst used for 24 hours and regenerated by calcination showed that the Pt nanoparticles increased in size slightly, from 0.8 to 1.2 nm (fig. S1, C and D). In a preliminary scale-up attempt, the amount of PE was increased by nearly a factor of 10 (to 1.1 g) while maintaining the same PE:Pt ratio and reaction conditions. After 24 hours, 0.56 g of a liquid product ($M_w = 483 \text{ g mol}^{-1}$, $D = 1.29$) with 27 mol % aromatic content was obtained (table S6, experiment S7).

To investigate how a tandem catalytic process could be deployed to convert waste polyethylene without large energy input, we also performed solvent-free depolymerization of two different commercial grades of PE: an LDPE plastic bag ($M_w = 9.45 \times 10^4 \text{ g mol}^{-1}$, $D = 7.37$) and an HDPE water-bottle cap ($M_w = 5.35 \times$

10^4 g mol^{-1} , $D = 3.61$). These higher-molecular-weight polymers behaved similarly to the low-molecular-weight polyethylene, giving liquid/wax products with an average carbon number of ~ 30 . After 24 hours at 280°C , the overall liquid yields were 69 and 55 wt % for LDPE and HDPE, respectively (Fig. 2B, experiments 4 and 5), with alkylaromatic selectivities of ~ 44 and 50 mol % (table S3, experiments 4 and 5). Thus, the extent of depolymerization is slightly lower in the same reaction time. For these higher-molecular-weight polyethylenes, the batch process generates its own highly viscous solvent as depolymerization proceeds. Recycling some of the alkylaromatic liquids to serve as solvent for the next batch may accelerate the reaction by facilitating mass and heat transport. The similar results for three very different plastics (including two commercial-grade samples of LDPE and HDPE) suggest that density, degree of branching, and common processing impurities are not major issues.

Shorter residence times should also improve the selectivity for monoaromatic hydrocarbons relative to naphthalenes, etc., and suppress the already low gas yields even further. Alkylbenzene selectivity may be further improved by active control of the partial pressure of H_2 , which must be high enough to promote PE hydrogenolysis but low enough to suppress aromatic hydrogenation. Catalyst improvements in these directions will be necessary to make the tandem reaction compatible with continuous processing and, ultimately, economically viable. The alkylbenzenes with their linear side chains could be sulfonated to produce biodegradable surfactants, which are interesting as higher-value chemical products. This type of commodity polymer upcycling can result in displacement of fossil carbon-based feedstocks, while simultaneously incentivizing better management of plastic waste and recovering considerable material value that can be recirculated into the global economy.

REFERENCES AND NOTES

- R. Geyer, J. R. Jambeck, K. L. Law, *Sci. Adv.* **3**, e1700782 (2017).
- L. Lebreton, A. Andrady, *Palgrave Commun.* **5**, 6 (2019).
- O. Eriksson, G. Finnveden, *Energy Environ. Sci.* **2**, 907–914 (2009).
- J. R. Jambeck et al., *Science* **347**, 768–771 (2015).
- A. Chamas et al., *ACS Sustain. Chem. Eng.* **8**, 3494–3511 (2020).
- A. Rahimi, J. M. Garcia, *Nat. Rev. Chem.* **1**, 0046 (2017).
- Y. Zhu, C. Romain, C. K. Williams, *Nature* **540**, 354–362 (2016).
- I. Vollmer et al., *Angew. Chem. Int. Ed.* **59**, 15402–15423 (2020).
- I. A. Ignatyev, W. Thielemans, B. Vander Beke, *ChemSusChem* **7**, 1579–1593 (2014).
- S. D. Anuar Sharuddin, F. Abrisa, W. M. A. Wan Daud, M. K. Aroua, *Energy Convers. Manage.* **115**, 308–326 (2016).
- V. Dufaud, J. M. Basset, *Angew. Chem. Int. Ed.* **37**, 806–810 (1998).
- G. Celik et al., *ACS Cent. Sci.* **5**, 1795–1803 (2019).
- X. Jia, C. Qin, T. Friedberger, Z. Guan, Z. Huang, *Sci. Adv.* **2**, e1501591 (2016).

- M. R. Rahimpour, M. Jafari, D. Iranshahi, *Appl. Energy* **109**, 79–93 (2013).
- C. Perego, P. Ingallina, *Catal. Today* **73**, 3–22 (2002).
- S. R. Kanitkar, J. J. Spivey, in *Natural Gas Processing from Midstream to Downstream*, N. O. Elbasher, M. M. El-Halwagi, I. G. Economou, K. R. Hall, Eds. (Wiley, 2019), pp. 379–401.
- I. Yarulina, A. D. Chowdhury, F. Meirer, B. M. Weckhuysen, J. Gascon, *Nat. Catal.* **1**, 398–411 (2018).
- K. Cheng et al., *Chem* **3**, 334–347 (2017).
- Q. N. Wang et al., *ACS Catal.* **9**, 7204–7216 (2019).
- A. Maneffa, P. Priece, J. A. Lopez-Sanchez, *ChemSusChem* **9**, 2736–2748 (2016).
- C. L. Williams et al., *ACS Catal.* **2**, 935–939 (2012).
- G. Lopez, M. Artetxe, M. Amutio, J. Bilbao, M. Olazar, *Renew. Sustain. Energy Rev.* **73**, 346–368 (2017).
- A. Inaba, T. Kashiwagi, *Macromolecules* **19**, 2412–2419 (1986).
- B. Behera, S. S. Ray, I. Singh, in *Fluid Catalytic Cracking VII: Materials, Methods and Process Innovations*, M. L. Occelli, Ed. (Elsevier, 2007), pp. 163–200.
- S. Luo, S. C. Ho, M. M. Wu, in *Synthetics, Mineral Oils, and Bio-Based Lubricants: Chemistry and Technology*, L. R. Rudnick, Ed. (CRC Press, 2020), pp. 161–180.
- R. Ahuja et al., *Nat. Chem.* **3**, 167–171 (2011).
- H. B. Mostad, T. U. Riis, O. H. Ellestad, *Appl. Catal.* **63**, 345–364 (1990).
- Q. L. Zhu, Q. Xu, *Energy Environ. Sci.* **8**, 478–512 (2015).
- S. Pradhan et al., *Chem. Sci.* **3**, 2958–2964 (2012).
- S. E. Stein, R. L. Brown, “Structures and Properties Group Additivity Model,” in NIST Chemistry WebBook, NIST Standard Reference Database Number 69, P. J. Linstrom, W. G. Mallard, Eds.; <https://doi.org/10.18434/T4D303>.
- D. W. Flaherty, E. Iglesia, *J. Am. Chem. Soc.* **135**, 18586–18599 (2013).
- C. Xu, Y. L. Tsai, B. E. Koel, *J. Phys. Chem.* **98**, 585–593 (1994).
- J. L. Carter, J. A. Cusumano, J. H. Sinfelt, *J. Catal.* **20**, 223–229 (1971).
- F. Zhang, M. Zeng, R. D. Yappert, J. Sun, Y.-H. Lee, A. M. LaPointe, B. Peters, M. M. Abu-Omar, S. L. Scott, Data deposited in the Dryad repository: <https://doi.org/10.25349/D9ZG6B>.

ACKNOWLEDGMENTS

We thank D. Uchenik and S. Walker for their assistance in FD-MS and NMR experiment setup and data collection. **Funding:** Supported by award DE-AC-02-07CH11358 from the U.S. Department of Energy, Office of Basic Energy Sciences, Division of Chemical Sciences, Geosciences, and Biosciences, as a subcontract from Ames Laboratory. Some experiments were performed using the MRL Shared Experimental Facilities, supported by the MRSEC Program of the NSF under award DMR 1720256, a member of the NSF-funded Materials Research Facilities Network (www.mrfln.org). **Author contributions:** F.Z., M.Z., and S.L.S. designed the experiments and wrote the manuscript. F.Z. and M.Z. were assisted by J.S. and Y.-H.L. in performing experiments and analyzing data. R.D.Y. performed the modeling and assisted with data analysis. A.M.L. analyzed molecular weights. A.M.L., B.P., and M.M.A.-O. provided experimental and theoretical guidance and edited the manuscript. **Competing interests:** F.Z., M.Z., M.M.A.-O., and S.L.S. are inventors on U.S. patent application 63/052,277 (UC Santa Barbara, filed 7/15/2020) partially based on this work. All other authors declare that they have no competing interests. **Data and materials availability:** Data supporting the findings of this study are presented in the paper and the supplementary materials. Additional raw data related to this paper (DSC, FD-MS, GC-FID, GC-TCD, GPS, NMR, computational model fits) are available in the Dryad repository (34).

SUPPLEMENTARY MATERIALS

science.sciencemag.org/content/370/6515/437/suppl/DC1
Materials and Methods
Figs. S1 to S16
Tables S1 to S7
References (35–39)

29 April 2020; accepted 18 August 2020
10.1126/science.abc5441

NANOMATERIALS

Supertwisted spirals of layered materials enabled by growth on non-Euclidean surfaces

Yuzhou Zhao¹, Chenyu Zhang², Daniel D. Kohler¹, Jason M. Scheeler¹, John C. Wright¹, Paul M. Voyles², Song Jin^{1*}

Euclidean geometry is the fundamental mathematical framework of classical crystallography. Traditionally, layered materials are grown on flat substrates; growing Euclidean crystals on non-Euclidean surfaces has rarely been studied. We present a general model describing the growth of layered materials with screw-dislocation spirals on non-Euclidean surfaces and show that it leads to continuously twisted multilayer superstructures. This model is experimentally demonstrated by growing supertwisted spirals of tungsten disulfide (WS₂) and tungsten diselenide (WSe₂) draped over nanoparticles near the centers of spirals. Microscopic structural analysis shows that the crystal lattice twist is consistent with the geometric twist of the layers, leading to moiré superlattices between the atomic layers.

Two-dimensional (2D) van der Waals (vdW) layered materials offer an ideal platform for creating artificial structures with new properties by vertically stacking different layers (1–3). Tuning the twist angles between stacked bilayers results in the formation of moiré patterns and the manipulation of electronic states, leading to observations of quantum phenomena, including unconventional superconductivity (4), moiré excitons (5–8), and tunable Mott insulators (9, 10). Twisted structures have been fabricated by elaborate mechanical stacking of different layers in a one-off and low-throughput fashion (3–10). Beyond twisted bilayers, recent theoretical studies also suggest interesting phenomena in continuously twisted multilayer structures that are termed “3D twistronics” (11–13). Even though the Eshelby twist (14) was recently demonstrated on screw-dislocated nanowires of layered germanium(II) sulfide (15, 16), the amount of twist per layer is quite minute for large-area 2D structures because the Eshelby twist angle is inversely proportional to the lateral cross-sectional area. A different approach is thus desired to directly grow twisted 2D materials and control the interlayer twisting.

Euclidean space provides the mathematical framework for classical crystallography (17). Basic concepts such as crystal lattice and symmetry operations are defined in Euclidean space, which shape our understanding of the physical world in which we live. Intuitively, flat substrates with Euclidean surfaces are used in the growth and mechanical stacking of 2D materials. By contrast, non-Euclidean spaces refer to curved geometrical spaces

where the parallel postulate is false (18) and the geometric transformations originally defined in Euclidean geometry, such as translation and rotation, have different consequences. Because translational symmetry is the central symmetry of crystal lattice, those differences could influence the crystal growth process in non-Euclidean spaces, resulting in exotic new structures. Here, we propose a growth model of screw-dislocated spirals of 2D materials on non-Euclidean surfaces that predicts continuously twisted superstructures in which the large and variable twist angle is exclusively determined by the shape of the non-Euclidean surface and experimentally demonstrate this model on metal dichalcogenides (MX₂).

2D materials typically grow through a layer-by-layer growth mechanism to yield aligned crystal layers. However, owing to the weak vdW interaction between layers, layer-by-layer growth can infrequently generate a small fraction of randomly twisted layers as by-products (19, 20), but the theoretical basis for controlling the twisting from one layer to the next during direct growth is lacking. By contrast, the screw dislocation-driven growth mechanism creates “new layers” by propagating the self-perpetuating growth steps generated by screw dislocations (21–23). Screw dislocation is a line defect that shears part of the crystal lattice along a specific direction. In layered materials, the shear typically happens along the out-of-plane direction and connects layers into one continuous layer, like in a parking ramp (movie S1). When its stress effect [i.e., Eshelby twist (14)] is negligible, an ideal screw dislocation preserves the orientation of each layer owing to the global translational symmetry of the crystal. This generates an aligned spiral shape of edges that are all parallel (Fig. 1A). Such a shape has been observed in many 2D materials such as hexagonal spirals in graphene and hexagonal boron nitride (24, 25)

as well as in triangular or hexagonal spirals in metal chalcogenides, such as WSe₂ (22), MoS₂ (26), WS₂ (27), and Bi₂Se₃ (28).

Geometry provides a fundamental reason behind the aligned shapes of crystals even in the presence of screw dislocations: The translational symmetry of crystal lattice follows Euclidean geometry. This dictates two basic geometric properties for the shape of a single crystal: First, the angle between two adjacent edges is fixed by their crystallographic indices (17), and second, the sum of the measures of the exterior angles is 360° for any convex polygon formed by edges in Euclidean geometry (18). These properties can explain the fact that screw-dislocated MX₂ often grow in triangular spiral shapes with aligned edges (Fig. 1A₁ and fig. S1A) (22, 26, 27). The threefold crystal structure of monolayer MX₂ causes its equilateral triangular shape (29) and the 120° exterior angles. Even when a screw dislocation is introduced, the translational symmetry of the crystal is still mostly conserved. In the normal spiral shape, for each period of three consecutive edges, the sum of the exterior angles is 120° + 120° + 120° = 360°, which means that the new and old edges must be parallel. In a typical crystal growth process, the Euclidean geometry of flat substrates matches the Euclidean nature of lattice; as a result, all layer edges are aligned in these dislocated spirals.

By contrast, the sum of the measures of the exterior angles of a polygon is not 360° in non-Euclidean geometry (18). Because such a property is not compatible with the Euclidean nature of crystals, tiling Euclidean crystal lattices in non-Euclidean spaces leads to new consequences. We specifically consider growing 2D vdW crystals on conical surfaces, because conical surfaces are “developable surfaces” that are locally isometric to plane, which means that they can be flattened onto a plane without distortion (30). Conversely, one can bend and fold a plane into a cone without distortion: As illustrated in Fig. 1B, one must shear half of the plane along the radius and overlap a sector defined by an angle of α . Unfolding the cone surface then results in a circular sector with the angle of 360° – α , which means that on the cone surface, the angle measure of any “full circle” containing the apex is a constant 360° – α and thus the sum of the measures of the exterior angles of any polygon surrounding the apex is also 360° – α . The geometry of the conical surface is non-Euclidean in the sense that it has a singularity at its apex (30), which changes the rules of angles on the conical surfaces and influences the translational and rotational operations. If one tries to draw a simple triangular spiral on such a surface by drawing edges by the angles, for every period, the new edge will twist by an angle of α relative to the edge in the last period (Fig. 1A₂), owing to the non-Euclidean geometry of the cone surface.

¹Department of Chemistry, University of Wisconsin–Madison, Madison, WI 53706, USA. ²Department of Materials Science and Engineering, University of Wisconsin–Madison, Madison, WI 53706, USA.

*Corresponding author. Email: jin@chem.wisc.edu

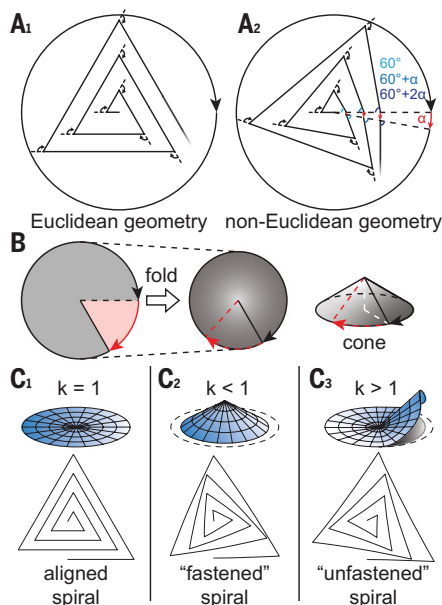


Fig. 1. Triangular dislocation spiral on Euclidean and non-Euclidean surfaces illustrating the twisting process. (A₁) For a triangular spiral on a Euclidean surface, at each vertex, the edge direction changes 120°; thus, after three vertices, it turns 360°, which makes the edge parallel to its original orientation. (A₂) For a triangular spiral on an unfolded non-Euclidean cone surface, after every three vertices, the edge goes across the dashed line once, so it needs to turn an extra angle of α to keep itself straight. (B) A cone can be folded from a circle by cutting along the radius and folding with an angle. (C₁) Euclidean surface ($k = 1$) and a corresponding aligned spiral with no twist. (C₂) Non-Euclidean cone surface ($k < 1$) and a corresponding fastened spiral with a positive twist, which forms a right-handed twisting superstructure. (C₃) Non-Euclidean hyperbolic cone surface ($k > 1$) and a corresponding unfastened spiral with a negative twist, which forms a left-handed twisting superstructure. In (C), all screw dislocations are right-handed, and k is defined as the ratio between the angular period of the specific surface to the period of a Euclidean circle.

When a vdW crystal grows on such cone surfaces, it needs to maintain the angles between the edges as required by its Euclidean lattice. Meanwhile, it will also be bent following the curvature of the cone. Therefore, a 2D vdW crystal with a screw dislocation will grow into a supertwisted spiral shape, with a consistent twist angle of α between each successive layer (Fig. 1A₂ and fig. S1B). Because the twist originates from the geometric mismatch between the non-Euclidean surface and Euclidean lattice, we name this phenomenon “non-Euclidean twist” and refer to the resulting twisted multi-layered structures as “twisted superstructures” or “supertwisted spirals” (versus minute Eshelby twists) in the following discussion.

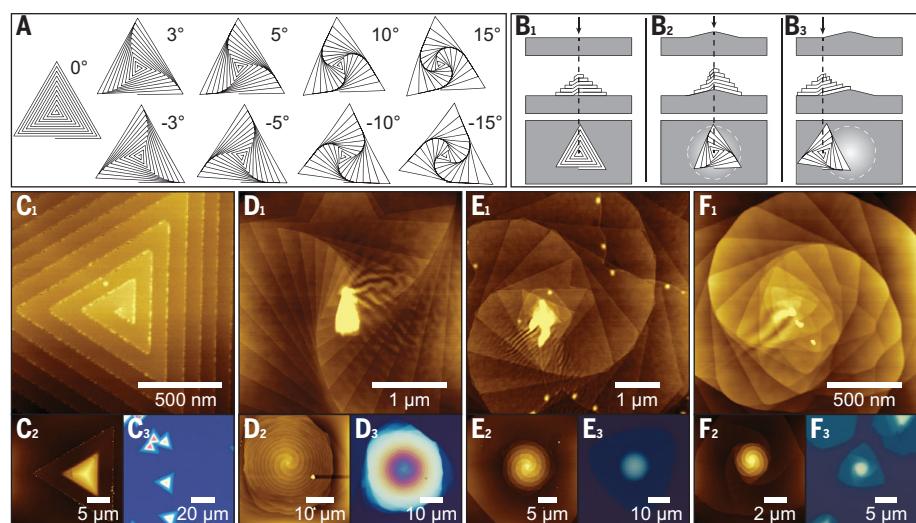


Fig. 2. Simulation and experimental demonstration of supertwisted spirals on non-Euclidean surfaces.

(A) Simulated superstructures of triangular dislocation spirals with increasing positive or negative twist angles. (B₁) A flat substrate surface yields aligned spirals. (B₂) A protruded substrate where the center of the screw dislocation sits on top of a protrusion results in a fastened supertwisted spiral. (B₃) A protruded substrate where the center of the screw dislocation sits on the edge of a protrusion leads to an unfastened supertwisted spiral. (C) AFM (C₁ and C₂) and optical (C₃) images of aligned WS₂ spirals grown on flat SiO₂/Si substrate. (D to F) AFM (D₁, D₂, E₁, E₂, F₁, and F₂) and optical (D₃, E₃, and F₃) images of representative WS₂ supertwisted spirals with various twist angles grown around WO_x particles on SiO₂/Si substrates.

We can further describe the shape of these supertwisted spirals using a simple analytic geometry method. We can define two polar coordinates: (i) on the cone surface ($r_{c.s.}$, $\theta_{c.s.}$), and (ii) on the top-down projection of the cone surface ($r_{proj.}$, $\theta_{proj.}$). Therefore, the cone surface can be mapped to the projection by

$$\begin{cases} r_{proj.} = kr_{c.s.} \\ \theta_{proj.} = \frac{\theta_{c.s.}}{k} \end{cases}$$

where $k = 1 - \alpha/2\pi$ is the ratio between the angle of a “full circle” enclosing the cone center to the angle of a full Euclidean circle (2π , 360°). When $k = 1$, the surface is flat (Euclidean), resulting in an aligned spiral (Fig. 1C₁), as discussed above. When $k < 1$, the surface is a cone, with its angular period ($2\pi - \alpha$) less than the lattice period (2π). Therefore, each full lattice period carries an extra angle of α over into the total twist angle (fig. S2B). Thus, a cone surface transforms an aligned spiral into a “fastened” spiral (Fig. 1C₂; the perspective view is shown in fig. S1B₂), like a fastened spiral torsion spring (movie S2). When $k > 1$, the surface is a developable “hyperbolic cone” surface (31) (Fig. 1C₃). Because the lattice period (2π) is smaller than the angular period of such surface ($2\pi - \alpha$, where α is negative) and cannot fill up space, an extra angle $-\alpha$ needs to be taken from the next lattice period (fig. S2C). Thus, a developable hyperbolic cone surface transforms an aligned spiral into an “unfastened” spiral (Fig. 1C₃), like an unfastened spiral torsion spring (movie S3). In all three cases, α (either zero, positive, or

negative) is the twist angle between successive layers. (See fig. S2 and associated discussion for our suggestion on naming different handedness levels of supertwisted spirals.)

Therefore, screw dislocations and non-Euclidean surfaces cooperate to create twisted superstructures of vdW crystals: First, the weak vdW interaction allows “movement” between layers; second, screw dislocations continuously generate “new layers” and maintain their relative orientations to the old ones (22); and third, the mismatched angular periods between non-Euclidean surfaces and Euclidean lattices provides an extra lattice twist (α) for every successive period in a continuous and consistent way. Using the equations derived above, we simulate the shapes of a series of twisted superstructures of right-handed screw-dislocation spirals with increasing positive or negative twist angles (Fig. 2A and fig. S3). We constrain the boundaries of layers so that the upper layers cannot go over the lower-layer edges. The envelopes of the twisting edges can be mathematically proven to be Archimedean curves. Even though the supertwisted spiral shapes with opposite twist angles appear very similar, they are not mirror images of each other, because they all have right-handed screw dislocations (and different substrate geometries). This non-Euclidean twist mechanism is also completely different from the lattice Eshelby twist mechanism for nanowires of vdW materials (15, 16). In the Eshelby twist mechanism, the direction of the lattice twist is always the same as the screw dislocations, and

the twist angle (α) is determined by $\alpha = b/\pi r^2$, where b is the magnitude of screw dislocation and r is the nanowire radius, so that the twist angle is rather minimal at large radii (14). The non-Euclidean twist, however, can have either the same or opposite direction as that of a screw dislocation, which is determined by the type of non-Euclidean substrate surface (Fig. 1, C_2 and C_3). Moreover, the twist angle can be tunable over a wide range and is exclusively determined by substrate geometry in theory, regardless of the size of the 2D crystals, which allows them to scale up to any lateral dimension.

Although the non-Euclidean twist mechanism is mathematically illustrated on an infinitely large cone or developable hyperbolic cone surfaces, practically we can realize it on a flat substrate modified with suitable geometric features, on which only the center of a layered crystal spiral is affected by the non-Euclidean twist to continuously generate supertwisted layers. Once the initial orientation of a layer is set by its nucleus, the layer continues to grow along the same direction owing to the translational symmetry of the crystal lattice. Figure 2B shows three possible situations: (i) A flat substrate surface yields an aligned spiral without any twist (Fig. 2B₁), (ii) a protruded substrate where the center of a screw dislocation sits on the center of a protrusion results in a fastened supertwisted spiral (Fig. 2B₂), and (iii) a protruded substrate where the center of a screw dislocation sits on the edge of a protrusion leads to an unfastened supertwisted spiral (Fig. 2B₃).

We have experimentally demonstrated the growth of such supertwisted spirals of WS₂ and WSe₂ on SiO₂/Si substrates (Fig. 2, D to F, and figs. S4 and S5) using a water vapor-assisted chemical vapor transport growth, with MX₂ as precursors and water vapor as the transport reagent (see methods for details) (32). As a comparison, Fig. 2C shows “normal” aligned triangular spirals with parallel edges. Such parallel edges rule out the Eshelby twist mechanism as the cause of twisted superstructures in these large pyramid-shaped spirals. The key to achieving non-Euclidean twists is to introduce protrusions onto substrates, as discussed above (Fig. 2, B₂ and B₃). Therefore, we drop-cast SiO₂ (200-nm diameter) or WO₃ (<100-nm diameter) nanoparticles onto SiO₂/Si substrates before the growth reactions (figs. S6 to S8). Intentional introduction of nanoparticles results in a proliferation of supertwisted spirals on typical growth substrates even though not every object is twisted. We also found that the reaction can spontaneously produce some WO_x particle side products (32, 33) that can occasionally serve as the protrusions leading to the spontaneous growth of supertwisted spirals (figs. S9 and S10), but this process is much less

reproducible. Because the formation mechanism is generally the same, we will ignore the difference between SiO₂, WO₃, and spontaneous formation in the subsequent discussion and only focus on understanding the geometric features of these supertwisted spirals.

Under an optical microscope, unlike the simple triangular shapes of aligned spirals (Fig. 2C₃), the supertwisted spirals display circular or spiral shapes (Fig. 2, D₃, E₃, and F₃) that help us to rapidly spot them when the synthesis yield is low. The circular shape consists of three Archimedean spiral curves that result from the envelope curves of the three sets of edges (Fig. 2, D₂ and D₃), which is a good indication of the twisted superstructures. Detailed atomic force microscopy (AFM) imaging on the centers of these representative objects (Fig. 2, D₁, E₁, and F₁) reveals stacks of layers continuously twisting with a consistent

twist angle from one layer to the next. Such a twist angle increases from Fig. 2, C to F, resembling the simulations shown in Fig. 2A. In fig. S4, a collection of 30 examples of supertwisted spirals of WS₂ or WSe₂ are characterized by optical microscopy and AFM, although not every object can be easily resolved with a simple structure model. Their specific morphologies vary with the different twist angles, the number of screw dislocations, and the stacking orders of MX₂ layers (figs. S3 and S11). Notably, Fig. 2, D₁, E₁, and F₁, as well as all AFM images in fig. S4, invariably reveals some particles, protrusions, or abnormality near the centers of the superstructures.

We further verify the proposed non-Euclidean twist mechanism by examining the protrusion near the center and studying the relationship between the angles of edges and the layer numbers using a representative supertwisted WS₂ spiral grown on top of a SiO₂ particle (Fig. 3). The overall superstructure displays three sets of right-handed Archimedean spirals. The protrusion caused by the SiO₂ particle in the center is about 120 nm in height and 500 nm in diameter (Fig. 3A), forming a cone shape owing to the deformation of SiO₂ nanoparticles at the growth temperature around 1000°C (fig. S6; see cross-sectional scanning electron microscopy images in fig. S7). The wrinkles around the center (Fig. 3B) are formed as a result of the curvature difference when the WS₂ layers transit from the protrusion to the flat substrate. Despite these wrinkles, the orientations of all WS₂ layers are well preserved away from the center, likely owing to the strain tolerance of 2D crystal growth (34). The twisted layer edges can be better visualized with AFM phase contrast (Fig. 3B), which clearly reveals a right-handed screw dislocation. In Fig. 3C, all edges revealed by the AFM phase image are highlighted with colored dashed lines, and their angles are plotted as a function of layer number from the bottom of the spiral to the top of the spiral in Fig. 3E. We found an approximately linear relationship between the angle and layer number for all three “Archimedean arms,” and linear fittings yielded an average twist of 14.9° per layer. The simulated supertwisted spiral using a 15° twist angle (Fig. 3D) matches the experimental morphology (Fig. 3C) very well. A similar twist angle analysis was carried out on a more complex supertwisted spiral of bilayers (fig. S12).

Furthermore, we carried out scanning transmission electron microscopy (STEM) analysis on a relatively thin and simple twisted WS₂ superstructure (Fig. 4) to characterize the moiré patterns expected in these twisted superstructures. (An idealized schematic illustration is shown in fig. S13.) Low-resolution high-angle annular dark-field (HAADF) imaging of the whole structure reveals the layer edges (Fig. 4A). A 4D STEM dataset collected on each layer

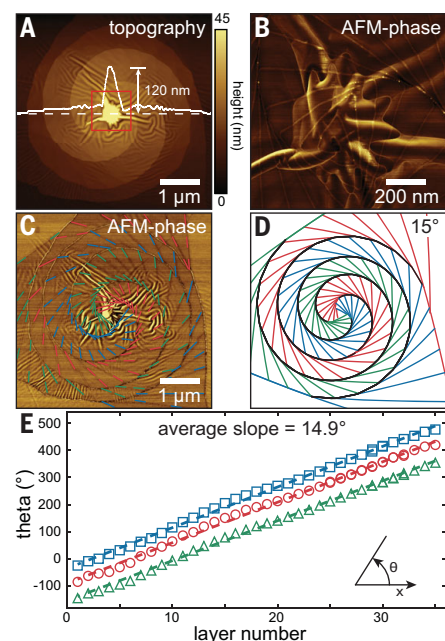


Fig. 3. Twist-angle evolution of a supertwisted WS₂ spiral. (A) Topography of a representative supertwisted spiral. The height profile along the horizontal dashed line reveals the height and width of the protrusion feature at the center. (B) Phase image collected from the red boxed area in (A) reveals wrinkles and layer edges at the spiral core. (C) Phase image corresponding to (A) with all the edges highlighted by colored dashed lines. (D) A supertwisted spiral simulated with a 15° twist angle with its edges highlighted. (E) Scatter plot of the evolving edge angles in (C) as a function of layer number counted from the bottom of the spiral to the top of the spiral. The least-squares linear fittings of each edge set (dashed lines) yield an average slope of 14.9° per layer. The colors of the data points correspond to the colors in (C).

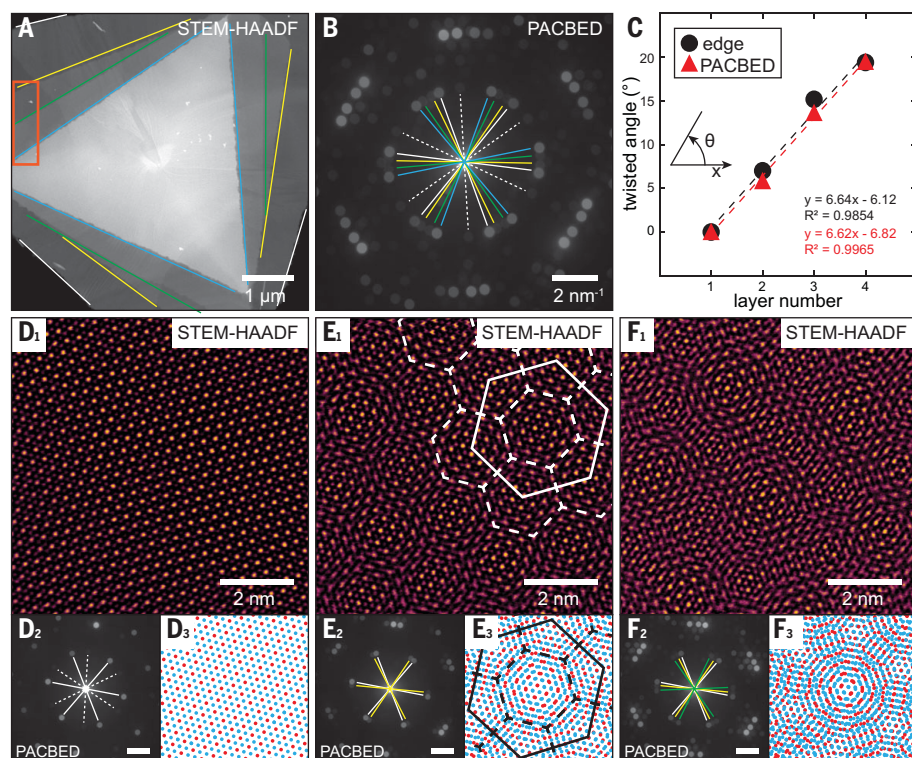


Fig. 4. STEM characterization of a non-Euclidean twisted superstructure. (A) HAADF image of a supertwisted WS_2 plate with edges of different layers highlighted by different colors. (B) Overall PACBED collected from the red boxed region in (A). The orientation of a specific layer can be measured by measuring the angle of a pair of diffraction disks from that layer. (C) Twist angles measured by morphology and diffraction as functions of the layer number, showing highly correlated linear relationships. The lattice angles are measured from six sets of diffraction disks, whereas the morphological twist angles are measured from three edges. R^2 , coefficient of determination of linear regression. (D₁, E₁, and F₁) High-resolution HAADF images collected from the one-, two-, and three-layer areas in the red rectangular region in (A). The images were high-pass filtered for better visualization. (D₂, E₂, and F₂) PACBED collected from areas corresponding to (D₁, E₁, and F₁). Scale bars are 2 nm^{-1} . (D₃, E₃, and F₃) Simulated moiré patterns corresponding to (D₁, E₁, and F₁) using WS_2 models (W atoms, red dots; S atoms, blue dots).

(Fig. 4B) shows the position-averaged convergent beam electron diffraction (PACBED) pattern from the acquisition region, with lines marking diffraction spots attributed to each layer (fig. S14). Lattice twist angles are measured from the diffraction spots in Fig. 4B and plotted in Fig. 4C together with the morphological twist angle measured from Fig. 4A, showing that they match well. The twist angles increase linearly with the layer numbers at an average of 6.6° per layer. Atomic resolution HAADF images (Fig. 4, D₁, E₁, and F₁) acquired from the one-, two-, and three-layer regions show clear moiré patterns. The corresponding PACBED patterns from the same regions with a different layer number (Fig. 4, D₂, E₂, and F₂) clearly show different sets of diffraction disks from different layers. We also constructed the expected moiré patterns by overlapping multiple WS_2 models (Fig. 4, D₃, E₃, and F₃) with lattice rotations determined from diffractions, which match the observation well. Characterization of a more complicated superstructure (fig. S15) leads to similar findings. In addition,

we also performed preliminary reflection spectroscopy and second-harmonic generation imaging to examine the inversion symmetry in supertwisted spirals (fig. S16).

We show how to generate continuously twisted superstructures of layered vdW materials by combining screw-dislocation spirals with non-Euclidean surfaces. By using nanoparticles as protrusions on flat substrates, we can introduce non-Euclidean surfaces to the growth process and experimentally demonstrate the direct growth of supertwisted spirals of WS_2 and WSe_2 materials with a wide range of twist angles and observed moiré patterns in STEM. More precise control of twist angles could be realized using nanofabricated substrates in the future.

REFERENCES AND NOTES

- K. S. Novoselov, A. Mishchenko, A. Carvalho, A. H. Castro Neto, *Science* **353**, aac9439 (2016).
- Y. Liu, Y. Huang, X. Duan, *Nature* **567**, 323–333 (2019).
- F. Liu et al., *Science* **367**, 903–906 (2020).
- Y. Cao et al., *Nature* **556**, 43–50 (2018).
- K. L. Seyler et al., *Nature* **567**, 66–70 (2019).
- K. Tran et al., *Nature* **567**, 71–75 (2019).

- C. Jin et al., *Nature* **567**, 76–80 (2019).
- E. M. Alexeev et al., *Nature* **567**, 81–86 (2019).
- Y. Cao et al., *Nature* **556**, 80–84 (2018).
- G. Chen et al., *Nat. Phys.* **15**, 237–241 (2019).
- F. Wu, R.-X. Zhang, S. Das Sarma, *Phys. Rev. Research* **2**, 022010 (2020).
- E. Khalaf, A. J. Kruchkov, G. Tarnopolsky, A. Vishwanath, *Phys. Rev. B* **100**, 085109 (2019).
- T. Cea, N. R. Walet, F. Guinea, *Nano Lett.* **19**, 8683–8689 (2019).
- M. J. Bierman, Y. K. A. Lau, A. V. Kvit, A. L. Schmitt, S. Jin, *Science* **320**, 1060–1063 (2008).
- Y. Liu et al., *Nature* **570**, 358–362 (2019).
- P. Sutter, S. Wimer, E. Sutter, *Nature* **570**, 354–357 (2019).
- C. Giacomazzo et al., *Fundamentals of Crystallography*, C. Giacomazzo, Ed. (Oxford Univ. Press, ed. 2, 2002).
- M. J. Greenberg, *Euclidean and Non-Euclidean Geometries: Development and History* (Macmillan Learning, 2007).
- K. Liu et al., *Nat. Commun.* **5**, 4966 (2014).
- C.-C. Lu et al., *ACS Nano* **7**, 2587–2594 (2013).
- F. Meng, S. A. Morin, A. Forticaux, S. Jin, *Acc. Chem. Res.* **46**, 1616–1626 (2013).
- M. J. Shearer et al., *J. Am. Chem. Soc.* **139**, 3496–3504 (2017).
- S. A. Morin, A. Forticaux, M. J. Bierman, S. Jin, *Nano Lett.* **11**, 4449–4455 (2011).
- R. Y. Tay et al., *Chem. Mater.* **30**, 6858–6866 (2018).
- H. J. Park et al., *Nano Lett.* **19**, 4229–4236 (2019).
- L. Zhang et al., *Nano Lett.* **14**, 6418–6423 (2014).
- X. Fan et al., *Nano Lett.* **18**, 3885–3892 (2018).
- A. Zhuang et al., *Angew. Chem. Int. Ed.* **53**, 6425–6429 (2014).
- J. Dong, L. Zhang, F. Ding, *Adv. Mater.* **31**, e1801583 (2019).
- S. Izumiya, M. C. Romero Fuster, M. A. S. Ruas, F. Tari, *Differential Geometry from a Singularity Theory Viewpoint* (World Scientific, 2014), p. 384.
- S. M. Farmer, C. R. Calladine, *Int. J. Mech. Sci.* **47**, 509–520 (2005).
- Y. Zhao, S. Jin, *ACS Materials Lett.* **2**, 42–48 (2020).
- P. K. Sahoo, S. Memaran, Y. Xin, L. Balicas, H. R. Gutiérrez, *Nature* **553**, 63–67 (2018).
- K. Wang et al., *Sci. Adv.* **5**, eaav4028 (2019).
- Z. Yuzhou, Yuzhou-Zhao/super-twisted-spirals: Super twisted spirals. Zenodo (2020); <http://doi.org/10.5281/zenodo.3967881>.
- Y. Zhao, C. Zhang, P. M. Voyles, S. Jin, Supertwisted spirals of layered materials enabled by growth on non-Euclidean surfaces. Materials Data Facility (2020); <http://doi.org/10.18126/M8UGYRK1>.

ACKNOWLEDGMENTS

We thank B. Wang for helpful suggestions regarding the discussion of geometry. **Funding:** This research is support by the U.S. Department of Energy, Office of Basic Energy Sciences, Division of Materials Science and Engineering, under award DE-FG02-09ER46664 to S.J., J.C.W., Y.Z., D.D.K., and J.M.S. P.M.V. and C.Z. were supported by the U.S. Department of Energy, Office of Basic Energy Sciences, Division of Materials Science and Engineering, under award DE-FG02-08ER46547. We acknowledge the facilities supported by the UW-Madison Materials Research Science and Engineering Center (DMR-1720415). **Author contributions:** Y.Z. and S.J. conceived the idea and designed the experiments. Y.Z. performed the simulation, synthesis, AFM characterizations, STEM sample preparation, and data analysis. C.Z. and P.M.V. performed the focused ion beam milling, STEM characterizations, and analysis. D.D.K., J.M.S., and J.C.W. performed spectroscopy measurement and analysis. Y.Z. and S.J. wrote the paper with input from all authors. **Competing interests:** The authors declare no competing interests. **Data and materials availability:** All data are available in the main text or the supplementary materials. Computer codes for simulating supertwisted spiral shapes are available at Zenodo (35). 4D STEM data and averaged PACBED data are available through the Materials Data Facility (36).

SUPPLEMENTARY MATERIALS

science.sciencemag.org/content/370/6515/442/suppl/DC1
 Materials and Methods
 Figs. S1 to S16
 References (37–41)
 Movies S1 to S3

8 May 2020; accepted 2 September 2020
 10.1126/science.abc4284

ATMOSPHERIC OXYGEN

Triple iron isotope constraints on the role of ocean iron sinks in early atmospheric oxygenation

Andy W. Heard^{1*}, Nicolas Dauphas¹, Romain Guilbaud², Olivier J. Rouxel³, Ian B. Butler⁴, Nicole X. Nie^{1,5}, Andrey Bekker^{6,7}

The role that iron played in the oxygenation of Earth's surface is equivocal. Iron could have consumed molecular oxygen when Fe³⁺-oxyhydroxides formed in the oceans, or it could have promoted atmospheric oxidation by means of pyrite burial. Through high-precision iron isotopic measurements of Archean-Paleoproterozoic sediments and laboratory grown pyrites, we show that the triple iron isotopic composition of Neoproterozoic-Paleoproterozoic pyrites requires both extensive marine iron oxidation and sulfide-limited pyritization. Using an isotopic fractionation model informed by these data, we constrain the relative sizes of sedimentary Fe³⁺-oxyhydroxide and pyrite sinks for Neoproterozoic marine iron. We show that pyrite burial could have resulted in molecular oxygen export exceeding local Fe²⁺ oxidation sinks, thereby contributing to early episodes of transient oxygenation of Archean surface environments.

Irreversible changes to oxic and euxinic sedimentary iron sinks during the Archean and Paleoproterozoic eras were intimately linked with the oxygenation of Earth's atmosphere during the Great Oxygenation Event (GOE) beginning around 2.43 billion years ago (Ga) (1, 2). Early oxygenation coincided with enhanced sedimentary burial of iron sulfide (pyrite), driven by a greater availability of sulfate resulting from enhanced

volcanic outgassing and/or continental sulfide weathering (3–5). Through the pyrite iron sink, enhanced volcanic SO₂ fluxes in the Neoproterozoic could have indirectly induced the release of oxygen by means of microbial reduction of volcanically derived sulfate and the sequestration of sulfide in sedimentary pyrite (6–8). Meanwhile, iron could have acted as a net sink of oxygen produced during oxygenic photosynthesis, provided that Fe²⁺ dissolved in the oceans was not sequestered in sediments as pyrite but rather as Fe³⁺-oxyhydroxides. It is presently unknown whether the balance of iron oxyhydroxide and pyrite sinks in certain marine sediments resulted in the net production or removal of oxygen in the period leading to the GOE.

Sedimentary Fe isotopic records show large shifts across the GOE (9, 10) (Fig. 1A) that reflect evolution of the Fe, S, and O cycles through the Archean and Paleoproterozoic (11). Pre-GOE pyrites can have ⁵⁶Fe/⁵⁴Fe ratios that

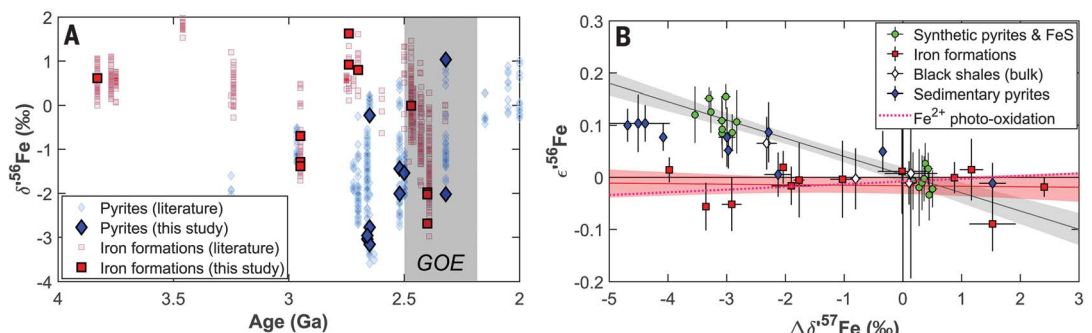
are shifted by up to –3.5 per mil (‰) relative to most terrestrial rocks—a degree of fractionation rarely seen in the post-GOE rock record (9). The interpretation of these pyrite Fe isotopic compositions is not straightforward because they could be controlled by several things: (i) the size of oxidizing iron sinks that removed isotopically heavy Fe³⁺-oxyhydroxides, leaving an isotopically light dissolved Fe²⁺ pool from which pyrite formed (9, 10); (ii) microbial dissimilatory Fe³⁺ reduction (DIR) that preferentially releases an isotopically light Fe²⁺ pool (12, 13); and/or (iii) a kinetic isotope effect (KIE) accompanying partial pyrite precipitation, which produces isotopically light pyrite (14, 15). The relative importance of these processes remains debated (9–18), and this uncertainty has hindered quantitative interpretation of the ancient iron cycle. Consequently, Fe isotope records have not yet constrained the degree to which Fe removal on highly productive continental margins was a net sink or source for early O₂ (8).

Here, we report triple Fe isotopic ratio measurements that allow us to remove ambiguities in interpretations of the pre-GOE iron cycle. This approach relies on our discovery that the main isotopic fractionation processes implicated in the formation of pre-GOE pyrites follow distinct isotopic mass fractionation laws (MFLs), which describe how different isotopic ratios of the same element covary (19, 20). To resolve MFLs, measurement of Fe isotopic ratios must be at higher precision than is typically reported in analysis of ancient sediments. This approach has been used in igneous geochemistry to show that Fe isotopic variations in magmatic olivine followed a kinetic MFL for diffusive transport (21) and in aqueous ultraviolet (UV) photo-oxidation experiments to investigate pathways to the deposition of iron formations (IFs) (22). Measurements of

Origins Laboratory, Department of the Geophysical Sciences and Enrico Fermi Institute, The University of Chicago, Chicago, IL 60637, USA. ²Géosciences Environnement Toulouse, CNRS, UMR5563, 31400 Toulouse, France. ³Unité Géosciences Marines, IFREMER, Plouzané 29280, France. ⁴School of Geosciences, University of Edinburgh, Grant Institute, Edinburgh EH9 3JW, UK. ⁵Earth and Planets Laboratory, Carnegie Institution for Science, Washington, DC 20015, USA. ⁶Department of Earth and Planetary Sciences, University of California, Riverside, CA 92521, USA. ⁷Department of Geology, University of Johannesburg, Johannesburg 2006, South Africa. *Corresponding author. Email: andyheard@uchicago.edu

Fig. 1. Iron isotope systematics of pre-GOE sediments and synthetic pyrites and FeS produced in laboratory experiments. (A) $\delta^{56}\text{Fe}$ (relative to IRMM-014) values of IFs and pyrites analyzed in this study, plotted against their age [published IF and pyrite data compiled in (11) are also plotted for reference].

(B) Triple Fe isotopic systematics for IFs, pyrites, and black shales in $\epsilon^{56}\text{Fe}$ versus $\Delta\delta^{57}\text{Fe}$ space. $\Delta\delta^{57}\text{Fe}$ values are reported as differences from IRMM-014 and the starting material for the natural samples and the synthetic pyrites, respectively. Error bars and shaded areas are 95% confidence intervals. The slopes of endmember MFLs associated with iron-redox processes (red line and red shaded area) and KIEs during pyritization (black line and gray shaded area) are constrained through analysis of isotopically light, Mn-rich IFs and laboratory pyrites precipitated through the H₂S pathway (14, 27, 40), respectively. The slope of the IF MFL agrees well with the theoretical high-temperature equilibrium limit law [defined by the horizontal axis, (20)] and an experimentally determined MFL for Fe²⁺ oxidation [determined by means of UV photo-oxidation (22)], which implies control by Fe²⁺-Fe³⁺ equilibrium. Synthetic pyrite and FeS define a kinetic MFL for sulfide precipitation. Pre-GOE pyrites fall in an intermediate space between iron oxidation and pyritization endmembers.



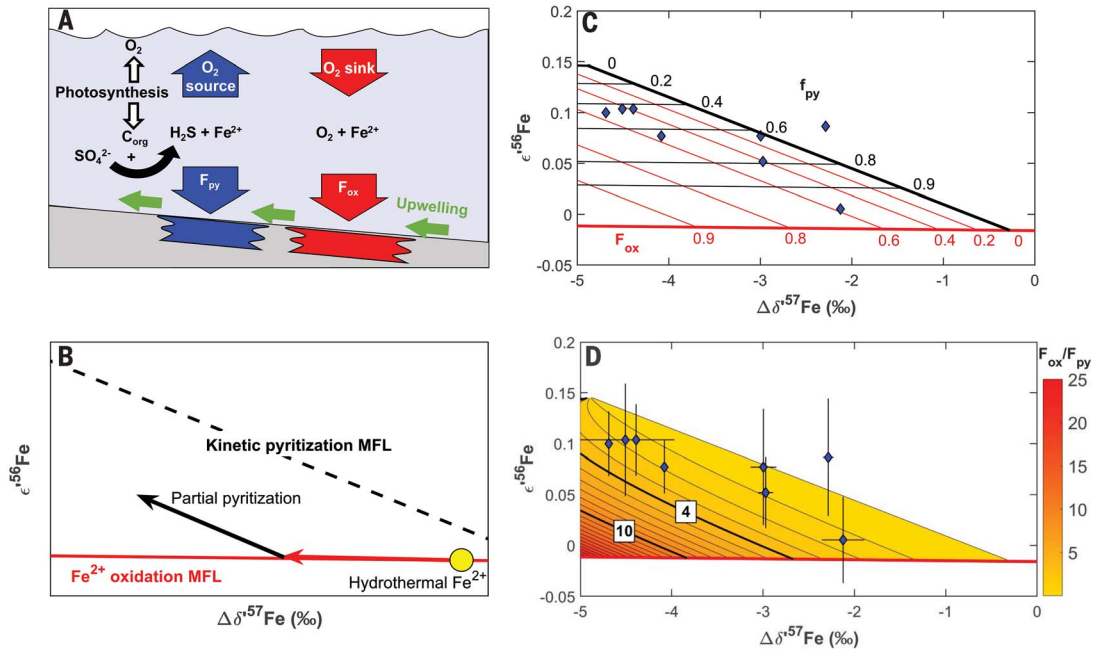


Fig. 2. Interpretation of triple Fe isotope compositions of isotopically light pyrites. (A) Schematic representation of the Fe sinks (F_{ox} and F_{py}), and their inferred links to O₂ cycling in the pre-GOE oceans. (B) Triple Fe isotopic interpretation of the two-step process involved in pyrite formation. Iron with starting composition resembling hydrothermal fluids (yellow circle; $\Delta\delta^{57}\text{Fe} = -0.3\text{‰}$ relative to IRMM-014 with $\epsilon^{56}\text{Fe}$ on the empirical MFL defined by IFs) is oxidized, which drives residual Fe²⁺ to lighter $\delta^{57}\text{Fe}$ compositions along the Fe²⁺ oxidation MFL. Partial pyrite precipitation from this residual Fe²⁺ subsequently causes fractionation along the kinetic pyritization MFL. The approach is detailed in fig. S5 with mathematical derivations provided in the supplementary materials (27). (C) Pyrite data and contours for F_{ox} and f_{py} in triple Fe isotopic space. Both Fe²⁺ oxidation and pyritization are modeled with

Rayleigh distillations. Iron isotopic fractionation during iron oxidation is assumed to reflect the composition of residual dissolved Fe²⁺ experiencing fractional removal of Fe³⁺-oxyhydroxide upon upwelling into oxidizing near surface waters. Iron isotopic fractionation during pyritization is assumed to reflect the composition of the cumulative product, as we analyzed relatively large pyrite nodules (27). The fraction of total upwelled Fe deposited as pyrite is calculated as $F_{\text{py}} = f_{\text{py}} \times (1 - F_{\text{ox}})$. (D) Pyrite data and contours of $F_{\text{ox}}/F_{\text{py}}$ (relative size of oxyhydroxide and pyrite sedimentary Fe sinks). Bold contours at 4 and 10 indicate thresholds for net O₂ source behavior for volcanic H₂S/SO₂ inputs ratios of 1 (7) and 0 (8), respectively. In (B) to (D), $\Delta\delta^{57}\text{Fe}$ values are reported as differences from IRMM-014.

this type, to a comparable or higher precision, are used more frequently in cosmochemistry to resolve nucleosynthetic anomalies in meteorite samples (23–26). For a given MFL, the ratio of $^{56}\text{Fe}/^{54}\text{Fe}$ to that of $^{57}\text{Fe}/^{54}\text{Fe}$ defines the slope

$$\theta^{56/57} = \Delta\delta^{56}\text{Fe}/\Delta\delta^{57}\text{Fe}$$

where $\Delta\delta^x\text{Fe}$ is a change in $\delta^x\text{Fe}$ —where $\delta^x\text{Fe}(\text{‰}) = 1000 \ln[(^x\text{Fe}/^{54}\text{Fe})_{\text{sample}}/(^x\text{Fe}/^{54}\text{Fe})_{\text{IRMM-014}}]$ —imparted by physical, chemical, or biological processes. The $\Delta\delta^x\text{Fe}$ for natural samples is taken as the difference from the bulk silicate Earth, which is approximated by IRMM-014 (20, 22, 23, 26). As discussed below, we also ran pyrite synthesis experiments, and there the $\Delta\delta^x\text{Fe}$ value is taken as the difference from the starting material for each experiment. Isotopic trends that follow a given MFL are, by definition, mass dependent. Apparent departures ($\epsilon^{56}\text{Fe}$) from an arbitrary reference MFL (20, 23, 27), which we choose here to be the high-temperature equilibrium limit law with $\theta^{56/57} = (1/53.939 - 1/55.935)/(1/53.939 - 1/56.935) = 0.678$, are defined as

$$\epsilon^{56}\text{Fe} = (\Delta\delta^{56}\text{Fe} - 0.678 \times \Delta\delta^{57}\text{Fe}) \times 10$$

In $\epsilon^{56}\text{Fe}$ versus $\Delta\delta^{57}\text{Fe}$ space, MFLs form straight lines, whose slopes can be related to $\theta^{56/57}$ through

$$\epsilon^{56}\text{Fe} = 10 \times (\theta^{56/57} - 0.678) \times \Delta\delta^{57}\text{Fe}$$

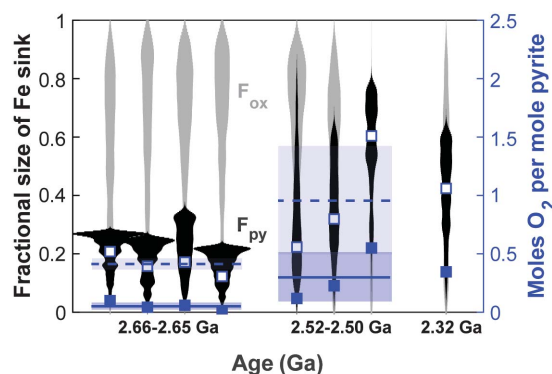
To establish the values of $\theta^{56/57}$ corresponding to two endmember hypotheses that have been put forward to explain the $\delta^{56}\text{Fe}$ pyrite record (9, 10, 14), we measured two sets of samples.

First, we measured a suite of IF samples that show a large range in $\delta^{56}\text{Fe}$ values, including low $\delta^{56}\text{Fe}$ values that most likely reflect precipitation from an iron pool that had experienced extensive iron oxidation (28) (table S1). These samples are well suited to characterize the MFL that is expected if sedimentary pyrite formed from a distilled pool of Fe²⁺ enriched in light Fe isotopes (low $\delta^{56}\text{Fe}$) by precipitation of heavy (high $\delta^{56}\text{Fe}$) Fe³⁺-oxyhydroxides.

Second, we measured experimental products of pyrite synthesis through the FeS-H₂S

pathway (fig. S2 and table S2), which produced pyrite that is isotopically lighter by as much as -2.4‰ in $\delta^{56}\text{Fe}$ relative to the initial FeS pool (fig. S2) (27). In these experiments, we precipitated pyrite in anoxic conditions from an FeS precursor (27), following previously established protocols (14, 27, 29). The experiment yielded a pyrite precipitate and a residual FeS phase that were separated with a calibrated sequential extraction (14), which enabled us to measure the isotopic fractionation between the reactant and product (fig. S2). This fractionation represents a unidirectional KIE associated with pyrite precipitation because, once formed, pyrite is highly insoluble and does not readily exchange with iron in solution. These pyrite samples represent a cumulative product reservoir rather than an instantaneous precipitate, but any deviations from an intrinsic Fe isotope MFL caused by cumulative effects are unresolvable within analytical uncertainties (27). Therefore, these experimental run products are well suited to characterize the MFL that is expected if sedimentary pyrite formation imparted a KIE on Fe isotopes.

Fig. 3. F_{ox} and F_{py} and molar O_2 yield estimates from a Monte Carlo error propagation. Violin plots for probability densities of fractional size of Fe sink (gray, F_{ox} ; black, F_{py}) determined from propagation of errors on the $\epsilon^{56}Fe$ and $\Delta\delta^{57}Fe$ values for each measured pyrite and the errors on the slopes of the MFLs (27). Blue filled and open squares indicate estimated molar O_2 yields per mole of pyrite buried for individual samples using H_2S/SO_2 input ratios of 1 (7) and 0 (8), respectively. Blue solid and dashed lines and shaded areas indicate mean molar O_2 yields for H_2S/SO_2 input ratios of 1 (7) and 0 (8), respectively, and 95% confidence intervals for pyrites in two age bins.



The IFs formed in the oceans after varying degrees of partial Fe^{2+} oxidation define a slope of $\theta^{56/57}_{ox} = 0.6779 \pm 0.0006$ (95% confidence interval) for the oxidizing iron sink, which agrees with iron photo-oxidation experiments (22) and is consistent with the view that equilibrium isotope exchange dominates during Fe^{2+} oxidation (20, 22). The pyrite-precipitation experiments involving a KIE gave $\theta^{56/57}_{KIE} = 0.6743 \pm 0.0005$ (95% confidence interval). Triple Fe isotopic slopes for the two endmember scenarios are measurably distinct (Fig. 1B). Thus, we can use these slopes to address what caused Fe isotopic variations in pre-GOE sedimentary pyrites.

We analyzed a suite of pre-GOE Neoproterozoic-Paleoproterozoic (2.66 to 2.32 Ga) pyrites with depleted $\delta^{56}Fe$ values (as low as -3.1‰) and four black shales from the same formations (Fig. 1A and table S1). The pyrites and shales fall in an intermediate space on the triple Fe isotopic diagram between the endmember MFLs for Fe oxidation and pyrite precipitation (Fig. 1B). We do not interpret this data array as following a single MFL because the pyrite and shale samples come from several distinct formations, and each sample requires contributions from more than one fractionation process (with distinct MFLs). More likely, pre-GOE pyrite and shale $\delta^{56}Fe$ values record a two-step process: partial marine Fe^{2+} oxidation during upwelling of Fe^{2+} -rich deep waters (9) and subsequent kinetic fractionation during partial, sulfide-limited pyrite formation from the remaining Fe^{2+} reservoir (14, 15, 30). In this model, Fe-oxyhydroxide and pyrite sinks sequestered iron upwelling from deep oceans lacking a discrete redoxcline that allowed progressive partial Fe^{2+} oxidation toward black shale depositional settings (Fig. 2A and fig. S7) (10, 27, 31). The loss of such depleted $\delta^{56}Fe_{py}$ values after the GOE, which incidentally would prevent us from resolving MFLs for younger samples, indicates that prevailing conditions

of sulfide limitation and progressive partial Fe oxidation were diminished after the biogeochemical overturn that took place during the GOE (11).

The pyrite samples that we analyzed are nodular—deforming sedimentary laminations around them—and must have formed in the sediment during early diagenesis. They most likely inherited their Fe isotopic compositions from pyrite precipitated in porewater near the sediment-seawater interface, but in some cases dissolution-reprecipitation has eradicated their primary textural features and caused recrystallization into massive forms. In situ work on Archean pyrites suggests that these secondary texture-altering processes do not eradicate primary sedimentary Fe isotopic signatures (18). A major source of iron to porewaters would have been downward diffusion of overlying Fe^{2+} -rich seawater into the sediments (9). The crux of the debate is whether pyrite simply inherited the Fe isotopic composition of seawater, which was by far the largest exchangeable Fe reservoir, or whether some kinetic isotopic fractionation was expressed if pyritization was incomplete because of limited sulfide supply. The triple Fe isotopic measurements reported here indicate that the latter case was true for the low $\delta^{56}Fe$ pre-GOE pyrites that we studied.

For any isotopically light pyrite sample, we can estimate contributions to the $\delta^{56}Fe$ value from prior oxidation of the Fe^{2+} pool and the KIE during pyritization. To do so, we first calculate contributions of Fe-oxidation to $\delta^{56}Fe$ values of the water mass ($\delta^{56}Fe_w$) from which pyrite formed, from intercepts of the kinetic pyritization MFL passing through individual data points with the oxidation MFL (Fig. 2B). We then determine the Fe isotopic fractionation imparted by pyritization by taking the difference in $\delta^{56}Fe$ values between those of pyrite and $\delta^{56}Fe_w$ (Fig. 2B and fig. S5) (27).

Our approach assumes that partial iron oxidation and pyritization were the main drivers of $\delta^{56}Fe$ variations in sedimentary pyrite. However, it is conceivable that some pore-water or marine Fe^{2+} was sourced from DIR (12, 13, 32), a microbial metabolism that seems to have been active since at least 3.2 Ga (18). This represents a source of uncertainty in our model. Experiments to date suggest that the isotopic fractionation during DIR reflects equilibration of Fe^{2+} and Fe^{3+} after the reduction step (33), and therefore we expect that it would fall into the same class of redox equilibrium processes that define the Fe^{2+} oxidation MFL. Thus, the observed departure of natural pyrite from this MFL implies that, regardless of the potential role of DIR, a KIE during pyritization is also required to explain pre-GOE $\delta^{56}Fe_{py}$ values.

The fraction of Fe^{3+} -oxyhydroxide removed to give the $\delta^{56}Fe_w$ value on the intercept (F_{ox} = fraction of Fe in oxyhydroxide sink out of total Fe upwelled) and the fraction of pyrite removed from that remaining Fe^{2+} pool (f_{py} = fraction of Fe in pyrite out of Fe remaining after Fe removal to the oxyhydroxide sink) were calculated under Rayleigh fractionation conditions (Fig. 2, fig. S5, and table S5). The setting that we envision is progressive Fe^{2+} oxidation as Fe^{2+} -rich deep waters are upwelled toward more oxidizing photic zone conditions (9, 10) (fig. S7). We also explored a one-dimensional dispersion-reaction steady-state model for water column Fe^{2+} oxidation, and find that our conclusions using Rayleigh distillation are robust (27, 34). We treated pyrite as a cumulative product of pyritization (27). The fraction of upwelled Fe sequestered in the sedimentary pyrite sink is $F_{py} = f_{py} \times (1 - F_{ox})$. In Fig. 2D, we plot contours of constant F_{ox}/F_{py} , which show that $\epsilon^{56}Fe$ measurements are diagnostic of the relative size of the oxyhydroxide and pyrite iron sinks.

To fully propagate the effect of uncertainties in sample measurements and $\theta^{56/57}$ values for the endmember processes on uncertainties in F_{ox} , f_{py} , and F_{py} , we used a Monte Carlo simulation (Fig. 3). Estimates for F_{py} span 10 to 80% of the upwelled iron pool (within a 95% confidence interval) for the low $\delta^{56}Fe$ pyrites that we studied. With initial pre-GOE deep-water [Fe^{2+}] concentration of $\sim 50 \mu M$ (1), the pyrite sink could have removed 5 to 40 μM of dissolved iron. This requires ~ 10 to 80 μM of seawater-dissolved sulfate to be microbially reduced to sulfide, which is ~ 0.04 to 0.3% of the modern seawater sulfate concentration of 28 mM but is within recent estimates for Archean seawater sulfate based on S isotope modeling (35, 36). For the ~ 2.65 Ga Jeerinah and Lokammona formations, we infer that as little as 10% of iron upwelled onto the shelf was deposited as pyrite (Fig. 2C, Fig. 3, and fig. S6) (27).

When volcanic SO_2 is the primary sulfur source, burial of reduced sulfur in pyrite represents a net oxidation of Earth's surface (6–8) (Fig. 2A). For example, the reaction $2\text{SO}_2 + \text{H}_2\text{O} + \text{Fe}^{2+} \rightarrow \text{FeS}_2 + 2\text{H}^+ + 2.5\text{O}_2$ —describing the net effect of SO_2 photolysis and hydrolysis, cyanobacterial photosynthesis, microbial sulfate reduction, and pyrite precipitation—indicates that pyrite burial can indirectly drive net O_2 export to the atmosphere-ocean system (8). The reaction provides a maximum estimate for O_2 export during pyrite burial for several reasons: (i) A more reduced original sulfur source, such as volcanic H_2S or sulfate from the oxidative weathering of sulfides, would weaken the net oxidative effect of pyrite burial. (ii) Other types of primary productivity—such as anoxygenic photoferrotrophy, which oxidizes Fe^{2+} directly—could have contributed organic matter for sulfate reduction, but only cyanobacterial activity would have produced O_2 . A more realistic estimate for the volcanic $\text{H}_2\text{S}/\text{SO}_2$ emission ratio at ~ 1 (7) would result in a net 1 mol O_2 yield per mole of pyrite buried.

To oxygenate the atmosphere by means of pyrite burial, the produced O_2 would also need to overcome O_2 buffers in the ocean, primarily the upwelled Fe^{2+} flux (Fig. 2A). Oxygen-driven Fe^{2+} oxidation consumes 0.25 mol of O_2 per mole of Fe^{3+} buried, so net O_2 sources and sinks will be balanced when $F_{\text{ox}}/F_{\text{py}}$ is 4 and 10 for volcanic $\text{H}_2\text{S}/\text{SO}_2$ emission ratios of 1 (7) and 0 (8), respectively. Depending on $F_{\text{ox}}/F_{\text{py}}$ ratios, iron deposition on productive continental margins could have been a net source or sink for O_2 in the atmosphere-ocean system. Triple Fe isotopic systematics are diagnostic of $F_{\text{ox}}/F_{\text{py}}$ ratios (Fig. 2D). Pre-GOE pyrite data all fall above the $F_{\text{ox}}/F_{\text{py}} = 4$ contour, and the $F_{\text{ox}}/F_{\text{py}} = 10$ contour is outside of the error bar on pyrite $\epsilon^{56}\text{Fe}$ values. We can therefore rule out net O_2 sink-like behavior for the case where SO_2 dominated Neoproterozoic volcanic emissions. Even with a conservative volcanic $\text{H}_2\text{S}/\text{SO}_2$ ratio of 1 (7), our data support a net O_2 source in Neoproterozoic pyrite-forming environments, particularly after 2.52 Ga (Fig. 2D and Fig. 3). The inference that the oxic sink did not overwhelm local oxygen sources associated with pyrite deposition also holds if F_{ox} is calculated using a one-dimensional dispersion-reaction model (27, 34). Average results from Monte Carlo simulations imply that even in the cases where we find the smallest F_{py} and largest F_{ox} , in ~ 2.65 Ga Jeerinah and Lokamonna formation pyrites, some O_2 could have been exported to the atmosphere-ocean system during pyrite burial after exhausting local Fe^{2+} oxidation sinks. We focused on the lowest $\delta^{56}\text{Fe}$ pyrites because these give us the most leverage to characterize MFLs. Pre-GOE pyrites, although displaying much more negative $\delta^{56}\text{Fe}$ values (average of $\sim -2\text{‰}$) than post-GOE pyrites (Fig. 1A), span a range of values. The more-

typical pre-GOE pyrites could have formed from a seawater reservoir that did not experience such protracted Fe^{2+} oxidation (9, 10) or may reflect higher degrees of pyritization. The amount of oxygen produced in such settings (moles of O_2 generated per mole of pyrite buried) would have been higher than the values calculated here for the isotopically lightest pyrites. Therefore, the conclusion that iron oxide burial did not locally buffer O_2 generated by pyrite burial in the Neoproterozoic is robust.

The triple Fe isotopic proxy provides insights into the iron cycle in Earth's early oceans. Before the GOE, large and probably fluctuating hydrothermal iron fluxes to the oceans (31) were removed to two sedimentary sinks (Fig. 2A and fig. S7) (27). The major sink was Fe^{3+} -oxyhydroxides that were deposited from upwelling water masses in the oceans that lacked a discrete redoxcline and allowed protracted partial iron oxidation (9, 10). The second iron sink was on highly productive continental margins, where the deposition of pyrite-rich sediments was generally sulfide limited because of a small marine sulfate pool. Small relative changes in iron removal to these oxyhydroxide and sulfide sinks potentially led to perturbations in the net O_2 supply to the atmosphere-ocean system that fueled shallow-marine oxygen oases (37, 38) and helped prime the Earth system for whiffs of atmospheric O_2 in the runup to the GOE (39).

REFERENCES AND NOTES

- H. D. Holland, *The Chemical Evolution of the Atmosphere and Oceans* (Princeton Univ. Press, 1984).
- A. P. Gumsley et al., *Proc. Natl. Acad. Sci. U.S.A.* **114**, 1811–1816 (2017).
- C. T. Scott et al., *Geology* **39**, 119–122 (2011).
- C. T. Reinhard, R. Raiswell, C. Scott, A. D. Anbar, T. W. Lyons, *Science* **326**, 713–716 (2009).
- E. E. Stüeken, D. C. Catling, R. Buick, *Nat. Geosci.* **5**, 722–725 (2012).
- L. R. Kump, M. E. Barley, *Nature* **448**, 1033–1036 (2007).
- F. Gaillard, B. Scaillet, N. T. Arndt, *Nature* **478**, 229–232 (2011).
- S. L. Olson et al., *Earth Planet. Sci. Lett.* **506**, 417–427 (2019).
- O. J. Rouxel, A. Bekker, K. J. Edwards, *Science* **307**, 1088–1091 (2005).
- N. Planavsky et al., *Geochim. Cosmochim. Acta* **80**, 158–169 (2012).
- A. W. Heard, N. Dauphas, *Geology* **48**, 358–362 (2020).
- B. L. Beard et al., *Science* **285**, 1889–1892 (1999).
- C. Archer, D. Vance, *Geology* **34**, 153–156 (2006).
- R. Guilbaud, I. B. Butler, R. M. Ellam, *Science* **332**, 1548–1551 (2011).
- J. M. Rolison et al., *Earth Planet. Sci. Lett.* **488**, 1–13 (2018).
- N. Dauphas, S. G. John, O. Rouxel, *Rev. Mineral. Geochem.* **82**, 415–510 (2017).
- J. Marin-Carbonne et al., *Earth Planet. Sci. Lett.* **392**, 67–79 (2014).
- J. Marin-Carbonne et al., *Geobiology* **18**, 306–325 (2020).
- E. D. Young, A. Galy, H. Nagahara, *Geochim. Cosmochim. Acta* **66**, 1095–1104 (2002).
- N. Dauphas, E. A. Schauble, *Annu. Rev. Earth Planet. Sci.* **44**, 709–783 (2016).

- A. J. McCoy-West, J. G. Fitton, M.-L. Pons, E. C. Inglis, H. M. Williams, *Geochim. Cosmochim. Acta* **238**, 542–562 (2018).
- N. X. Nie, N. Dauphas, R. C. Greenwood, *Earth Planet. Sci. Lett.* **458**, 179–191 (2017).
- N. Dauphas et al., *Astrophys. J.* **686**, 560–569 (2008).
- M. Schiller, M. Bizzarro, J. Siebert, *Sci. Adv.* **6**, eaay7604 (2020).
- H. Tang, N. Dauphas, *Earth Planet. Sci. Lett.* **359–360**, 248–263 (2012).
- H. Tang, N. Dauphas, P. R. Craddock, “High precision iron isotopic analyses of meteorites and terrestrial rocks: ^{56}Fe distribution and mass fractionation laws,” LPS id. 1903, paper presented at the 40th Lunar and Planetary Science Conference, The Woodlands, Texas, 23 to 27 March 2009.
- Materials and methods are available as supplementary materials online.
- H. Tsikos, A. Matthews, Y. Erel, J. M. Moore, *Earth Planet. Sci. Lett.* **298**, 125–134 (2010).
- D. Rickard, *Geochim. Cosmochim. Acta* **61**, 115–134 (1997).
- O. J. Rouxel, A. Bekker, K. J. Edwards, *Science* **311**, 177 (2006).
- A. Bekker et al., *Econ. Geol.* **105**, 467–508 (2010).
- S. Severmann, T. W. Lyons, A. Anbar, J. McManus, G. Gordon, *Geology* **36**, 487–490 (2008).
- H. A. Crosby, E. E. Roden, C. M. Johnson, B. L. Beard, *Geobiology* **5**, 169–189 (2007).
- A. D. Czaja et al., *Geochim. Cosmochim. Acta* **86**, 118–137 (2012).
- J. W. Jamieson, B. A. Wing, J. Farquhar, M. D. Hannington, *Nat. Geosci.* **6**, 61–64 (2013).
- S. A. Crowe et al., *Science* **346**, 735–739 (2014).
- S. L. Olson, L. R. Kump, J. F. Kasting, *Chem. Geol.* **362**, 35–43 (2013).
- C. M. Ostrander et al., *Nat. Geosci.* **12**, 186–191 (2019).
- A. D. Anbar et al., *Science* **317**, 1903–1906 (2007).
- D. Rickard, G. W. Luther 3rd, *Chem. Rev.* **107**, 514–562 (2007).
- A. W. Heard, N. Dauphas, Archean-Paleoproterozoic pyrite and iron formation Fe isotope and sedimentary S isotope records, version 1.0, Interdisciplinary Earth Data Alliance (IEDA) (2019); <https://doi.org/10.1594/IEDA/111446>.

ACKNOWLEDGMENTS

Discussions with S. Olson, J. Waldbauer, S. Aarons, and S. Holo were appreciated. N. Brauser and A. Davis are thanked for comments on the clarity of the manuscript. We thank A. Olinto, J. Passolano, D. DeYoung, J. Eason, M. Grosse, F. Ciesla, K. Mormann, J. Hanchar, S. Lippert, R. Klain, C. Garza, V. Gavin, S. Bandyk, A. Peralta, C. Kielch, T. Indelli, T. Hopp, and M. Andrews and the UJAMAA Construction team for renovating our laboratory infrastructure and supporting its operation. **Funding:** This work was funded by NASA grants 80NSSC17K0744 to N.D. and A.W.H. (Habitable Worlds), 359NNX17AE86G to N.D. (LARS), NNX17AE87G and 80NSSC20K0821 to N.D. (Emerging Worlds), and NSF grant EAR-2001098 to N.D. (CESDI). A.W.H. was supported by an Eckhardt Scholarship from the University of Chicago. Participation by A.B. was supported by NSERC Discovery and Acceleration grants. **Author contributions:** A.W.H., N.D., and N.X.N. initiated the study. O.J.R. and A.B. provided samples. A.W.H., R.G., and I.B.B. performed the pyrite synthesis experiments. A.W.H. and N.X.N. measured iron isotopic compositions. A.W.H. and N.D. performed modeling. All authors contributed to interpretation of results. A.W.H., N.D., and A.B. wrote the first draft of the manuscript, which was subsequently edited with input from all authors. **Competing interests:** The authors declare that they have no competing interests. **Data and materials availability:** All original data are reported in the tables in the supplementary materials. The literature iron isotope data presented in Fig. 1A are compiled in the EarthChem Library (41).

SUPPLEMENTARY MATERIALS

science.sciencemag.org/content/370/6515/446/suppl/DC1
Materials and Methods
Supplementary Text
Figs. S1 to S10
Tables S1 to S5
References (42–66)

18 October 2019; accepted 3 September 2020
10.1126/science.aaz8821

STRUCTURAL BIOLOGY

Structural basis of nucleosome-dependent cGAS inhibition

Joshua A. Boyer^{1*}, Cathy J. Spangler^{1*}, Joshua D. Strauss^{1*}, Andrew P. Cesmat², Pengda Liu^{1,3}, Robert K. McGinty^{1,2,3†}, Qi Zhang^{1,3†}

Cyclic guanosine monophosphate (GMP)–adenosine monophosphate (AMP) synthase (cGAS) recognizes cytosolic foreign or damaged DNA to activate the innate immune response to infection, inflammatory diseases, and cancer. By contrast, cGAS reactivity against self-DNA in the nucleus is suppressed by chromatin tethering. We report a 3.3-angstrom-resolution cryo–electron microscopy structure of cGAS in complex with the nucleosome core particle. The structure reveals that cGAS uses two conserved arginines to anchor to the nucleosome acidic patch. The nucleosome-binding interface exclusively occupies the strong double-stranded DNA (dsDNA)–binding surface on cGAS and sterically prevents cGAS from oligomerizing into the functionally active 2:2 cGAS–dsDNA state. These findings provide a structural basis for how cGAS maintains an inhibited state in the nucleus and further exemplify the role of the nucleosome in regulating diverse nuclear protein functions.

A fundamental host defense mechanism is to detect and respond to nucleic acids from bacterial and viral pathogens and damaged cellular DNA (1, 2). In the mammalian innate immune system, cyclic guanosine monophosphate (GMP)–adenosine monophosphate (AMP) synthase (cGAS) and stimulator of interferon genes (STING) mediate a major pathway in response to cytosolic DNA

fragments that derive from pathogens or from cellular DNA damage caused by inflammatory diseases and cancer (3). In the cytoplasm, cGAS is activated by recognizing and binding double-stranded DNA (dsDNA) in a sequence-independent manner, resulting in the synthesis of a second messenger, 2′–3′ cyclic GMP–AMP (cGAMP), which features both noncanonical (2′–5′) and canonical (3′–5′) phosphodiester

linkages (4, 5). STING, an endoplasmic reticulum membrane protein, binds cGAMP and triggers a signaling cascade to activate inflammatory responses, including the induction of type I interferons (6–8). Although it was discovered as a cytosolic dsDNA sensor, cGAS has since been shown to be enriched in the nucleus (9–13). Despite being surrounded with endogenous genomic DNA, nuclear cGAS activity is suppressed through tethering to chromatin (9), and the nucleosome, the fundamental unit of the genome, has been shown to competitively suppress the enzymatic activity of cGAS (12). Such suppression is critical to prevent unnecessary triggering of immune responses.

To understand the molecular mechanism through which nucleosome-bound cGAS maintains its resting, inhibited state, we used cryo–electron microscopy (cryo-EM) to solve the

¹Department of Biochemistry and Biophysics, School of Medicine, University of North Carolina at Chapel Hill, Chapel Hill, NC, USA. ²Division of Chemical Biology and Medicinal Chemistry, Eshelman School of Pharmacy, University of North Carolina at Chapel Hill, Chapel Hill, NC, USA. ³Lineberger Comprehensive Cancer Center, School of Medicine, University of North Carolina at Chapel Hill, Chapel Hill, NC, USA.

*These authors contributed equally to this work.

†Corresponding author. Email: rmcginty@email.unc.edu (R.K.M.); zhangqi@unc.edu (Q.Z.)

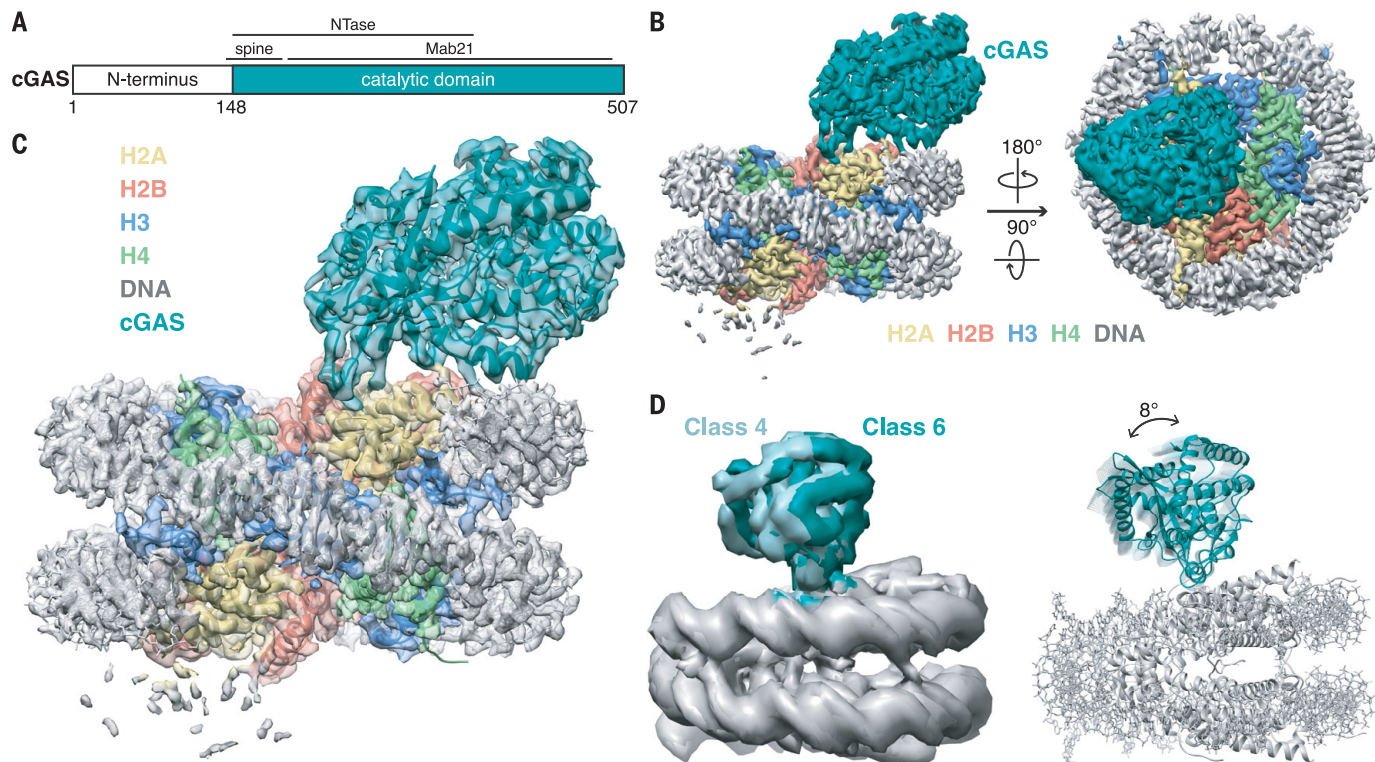


Fig. 1. Overall structure of nucleosome-bound cGAS. (A) Schematic of the mouse cGAS primary structure colored by domains. NTase, nucleotidyltransferase. (B) Side and top views of the composite cryo-EM density map of the cGAS-NCP complex. cGAS, H2A, H2B, H3, H4, and DNA are colored teal, yellow, red, blue, green, and gray, respectively.

(C) Transparent composite cryo-EM density map overlaid onto an atomic model of the cGAS-NCP complex. (D) Overlay of 3D subclasses (left) and structural representations that depict the hinge motion of cGAS relative to the nucleosome (right) created by morphing between cGAS structures docked into class 4 and class 6 maps.

structure of the mouse cGAS catalytic domain bound to the nucleosome core particle (NCP) (Fig. 1 and movie S1). Mouse cGAS is composed of an unstructured N terminus (amino acid residues 1 to 147) and a highly structured,

bilobate C terminus (amino acid residues 148 to 507) (Fig. 1A) (4). The positively charged N terminus plays a role in enhancing the cGAS-DNA phase transition to promote cGAMP production (14). The C terminus comprises

the nucleotidyltransferase catalytic domain and the Mab21 dsDNA recognition domain, where an α -helical spine (amino acid residues 148 to 183) bridges the two cGAS C-terminal lobes (15–21). Because the disordered N-terminal

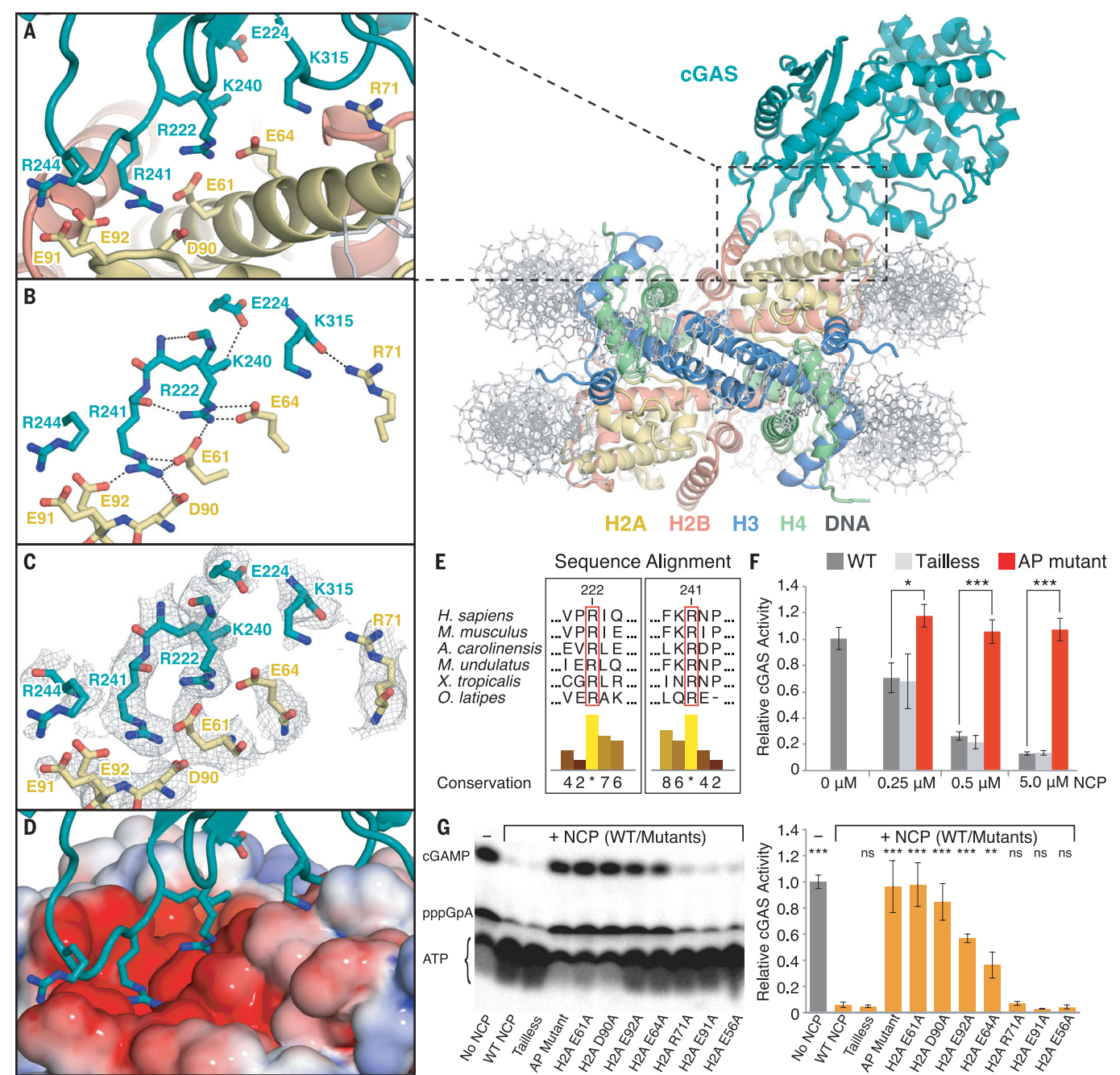


Fig. 2. Interactions between cGAS and the nucleosome core particle.

(A) Close-up view of the binding interface of the cGAS-NCP complex. (B) Close-up view of the hydrogen bond network between cGAS residues (teal) and histone H2A residues (yellow). (C) Close-up view of the binding interface with a composite map overlaid. (D) Identical view of cGAS interacting with the nucleosome acidic patch as highlighted with the electrostatic potential surface, where positive is shown in blue and negative is shown in red. (E) Conservation of the arginine anchors R222 and R241 of cGAS across vertebrates. Numerical and histogram representations of the conservation score are shown; asterisks

denote complete identity conservation (www.jalview.org/). (F) Quantification of nucleosome-dependent inhibition of cGAS activity. WT, wild-type; AP, acidic patch. (G) Quantification of the inhibitory effect of individual nucleosome acidic patch residues on cGAS activity (0.5 μ M cGAS: 5 μ M dsDNA) in the presence of 5 μ M NCP mutants. ATP, pppGpA, and cGAMP are substrate, intermediate, and product, respectively. Average relative cGAS activities from three replicates are plotted with SDs represented as error bars (mean \pm SD). ns, $P > 0.05$; * $P < 0.05$; ** $P < 0.01$; and *** $P < 0.001$ for statistical differences between WT and mutant NCPs.

region of cGAS is not required for nuclear tethering (9), we expressed and purified the catalytic domain of mouse cGAS, referred to simply as “cGAS” hereafter, for structural and enzymatic studies. We assembled the cGAS-NCP complex by mixing cGAS with recombinant human NCP in a 3:1 ratio and isolated the resulting 2:1 cGAS-NCP complex by gel filtration chromatography (fig. S1). The purified cGAS-NCP complex was used to prepare

specimens for cryo-EM single-particle analysis. The complex was stable during grid preparation, allowing us to collect images in a native state without cross-linking.

A total of 2100 movies were recorded on a Talos Arctica 200-kV microscope equipped with a Gatan K3 direct electron detector. After iterative rounds of two-dimensional (2D) classification, initial 3D classification of 433,445 particles revealed a heterogeneous mixture of 2:1 (class 4;

27%) and 1:1 (class 1; 21%) cGAS-NCP complexes (fig. S2). Independent 3D refinements of the 2:1 and 1:1 classes gave initial EM density maps at 4.35-Å resolution for both stoichiometries. Through Bayesian particle polishing, iterative contrast transfer function refinement, and 3D reclassification, the resolution of the 1:1 complex map was improved to 3.41 Å with 70,790 particles, and the resolution of the 2:1 complex map was improved

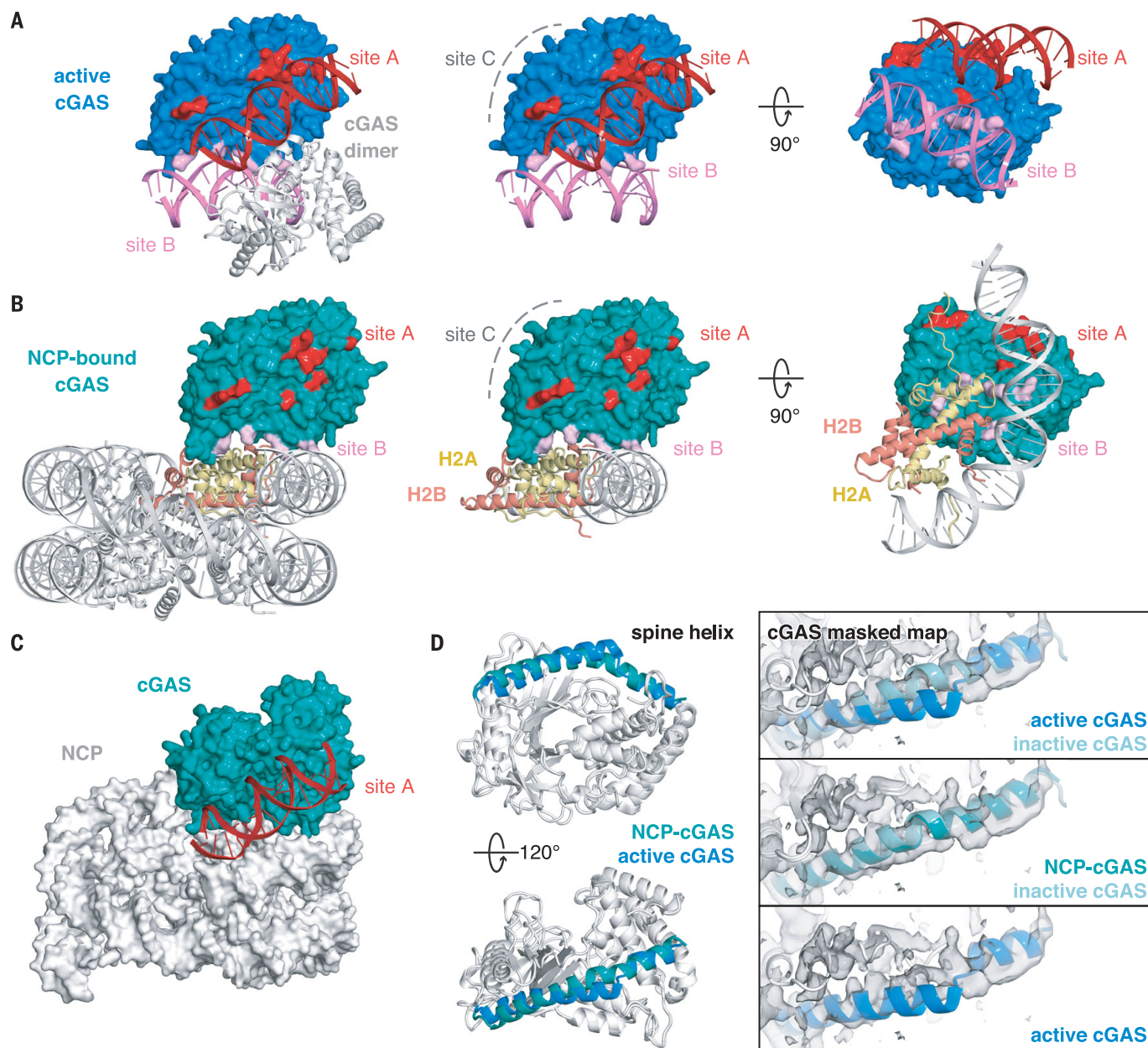


Fig. 3. Mechanism of nucleosome-dependent inhibition of cGAS activity.

(A) Structure of the functionally active 2:2 cGAS-DNA complex (PDBID: 4LEZ). DNA-binding sites A, B, and C are highlighted in red, pink, and gray, respectively. Middle and right panels depict side and bottom views of cGAS-DNA interactions for one cGAS monomer, respectively. (B) Structure of the cGAS-NCP complex with cGAS DNA-binding sites A, B, and C highlighted in red, pink, and gray, respectively. cGAS-interacting H2A and H2B chains are highlighted in yellow and

red, respectively. Middle and right panels show side and bottom views of cGAS-NCP interactions, respectively. (C) Overlay of active cGAS-site A DNA structure onto NCP-cGAS; dsDNA is shown in red. (D) Side and top views of overlay between NCP-bound and active cGAS structures with the spine helix highlighted in teal and blue, respectively. Right panels show overlays of spine helices onto the 3.9-Å resolution 1:1 cGAS_{mask}-NCP map. Inactive, apo-cGAS was obtained from PDBID 4K8V.

to 3.30 Å with 45,587 particles. To maximize the overall resolution at the cGAS-NCP-binding interface, we combined all 116,377 particles from the 1:1 and 2:1 cGAS-NCP reconstructions and refined the final map to an overall resolution of 3.26 Å. In this reconstruction, high-resolution structural features are visible throughout the nucleosome and into the nucleosome-interacting face of cGAS (Fig. 1, B and C, and figs. S2 to S4). By contrast, regions of the reconstructed map corresponding to parts of cGAS that are farther from the nucleosome interface are less well resolved, suggesting conformational heterogeneity or structural dynamics. Multibody refinement using cGAS and nucleosome masks revealed a rigid-body rotation of cGAS hinging from the nucleosome interface (fig. S2 and movie S2). To improve cGAS visualization, we performed an additional 3D classification restricted to local angular searches. This 3D classification recapitulated our earlier observations of a mixture of 1:1 and 2:1 complexes, and further revealed several distinct cGAS conformations relative to the nucleosome (e.g., classes 3, 4, and 6) (Fig. 1D and fig. S2). Subsequent refinement of the most populated class (class 6; 38%) with a mask enveloping cGAS resulted in the 3.9-Å-resolution 1:1 cGAS_{mask}-NCP reconstruction with clear density for all regions of cGAS and noticeable blurring of nucleosome density (figs. S2 and S3).

To generate an atomic model of the 1:1 cGAS-NCP complex, we docked a high-resolution crystal structure of the apo mouse cGAS catalytic domain (15) and a cryo-EM structure of the NCP (22) into the 3.26-Å-resolution 1:1 cGAS-NCP map and performed iterative manual model building and real space refinement. Because of the low signal-to-noise ratio in the map regions corresponding to cGAS residues far away from the nucleosome interface, reference model restraints were applied during refinement to preserve model quality. Additionally, to minimize over-refinement into the full map, the resultant model was refined against one sharpened, masked half-map, leading to a final model that showed excellent correlation to both the sharpened, masked full map and the other sharpened, masked half-map (Fig. 1C, fig. S3, table S1, and movie S1). The model also correlated well with the 3.9-Å map reconstructed using a cGAS mask. Therefore, we prepared a composite map from the 3.26-Å sharpened map and the 3.9-Å cGAS masked map to best represent our 1:1 complex (Fig. 1C and fig. S4). Through docking and real space refinement, a structure was solved using the 3.30-Å-resolution 2:1 cGAS-NCP map that is nearly identical to the 1:1 complex (figs. S3 and S5 and table S1).

The high-resolution complex structure clearly reveals how cGAS binds the nucleosome. An

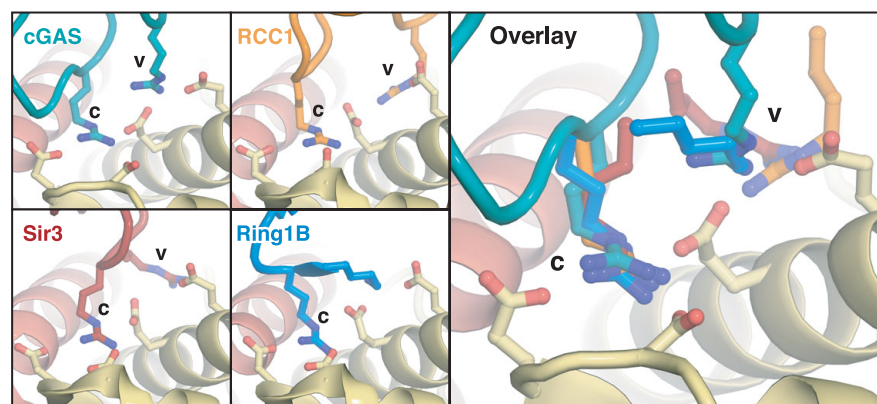


Fig. 4. Arginine anchors bind the nucleosome acidic patch. Identical views of canonical (c) and variant (v) arginine anchors used by cGAS (c: R241, v: R222) and the nucleosome-binding proteins RCC1 (PDBID: 3MVD), Sir3 (PDBID: 3TU4), and Ring1B (PDBID: 4R8P). Parts of the Ring1B structure not shown to allow visualization of the arginine anchor.

intricate set of interactions is formed between two cGAS arginines (R222 and R241) and four acidic patch residues (E61, E64, D90, and E92) in histone H2A (Fig. 2, A to D). cGAS R222 and R241 reside in spatially adjacent loops with conformations stabilized by an interloop hydrogen-bonding network and direct side-chain interactions with histones. R222 forms three intermolecular hydrogen bonds with H2A E61 and E64, as well as two intramolecular hydrogen bonds with backbone atoms of cGAS K240 and R241 in the adjacent loop. cGAS K240 in turn also forms a hydrogen bond with E224. R241, in addition to interacting with R222, inserts its side chain into the cavity surrounded by H2A E61, D90, and E92, and is completely encapsulated with four intermolecular hydrogen bonds. In addition to this major contact site, the backbone of cGAS K315 is hydrogen bonded with the side chain of H2A R71 (Fig. 2, A and B). Together, these interactions create two pivot points that provide a structural basis for the observed hinge motions of cGAS relative to the nucleosome surface (Fig. 1D).

This structure provides molecular mechanisms to explain biochemical and cellular data that identified a role for nuclear tethering in cGAS inactivation (9). For example, based on the structure, all cGAS mutations that showed no or mild effects in changing nuclear localization and tethering, including K335E, K395M/K399M, ΔH378–C393, K382A, E211A/D213A, R244E, and loop242–247 (IPRGNP to SGSGSG) (9), are not expected to perturb the cGAS-NCP interactions (fig. S6). Although cGAS R244 is positioned adjacent to H2A E91, neither side chain is well resolved in our reconstructions, thus providing no evidence of a stable interaction, which is consistent with the mild effects of R244E mutation in perturbing nuclear tethering (fig. S4). By contrast, the R222E and R241E mutants, which charge-reverse the two arginines of cGAS that are key for anchoring to

the nucleosome, exhibit the most deleterious effects in abolishing nuclear tethering. Moreover, the K240E mutation also abolishes nuclear tethering of cGAS, suggesting that the observed intramolecular interactions with R222 and E224 are important in stabilizing the local conformation of the anchoring residues of cGAS for NCP binding. The K240E mutation could also have a repulsive effect by sandwiching an additional negatively charged side chain between H2A E61 and E64 on the acidic patch below and cGAS E224 above. Despite cGAS being one of the most rapidly evolved genes with substantial sequence variations (23, 24), both R222 and R241 are completely conserved in cGAS across all vertebrates (Fig. 2E) (9). Although R222 also participates in dsDNA binding to activate cGAMP synthesis, the R241E mutation does not impair DNA-dependent cGAMP synthesis by cGAS (17, 18). The lack of a functional role for R241 in cGAS enzymatic activity suggests that the evolutionary conservation of R241 may largely be to preserve interactions with the nucleosome acidic patch. This interaction ensures that cGAS is suppressed when encountering endogenous chromatinized DNA either in the nucleus or in the cytosol during processes such as mitosis and apoptosis. Sequence and structural alignments between cGAS and nuclear Mab21L1/L2 proteins further suggest that the arginine anchors may be evolutionarily conserved in other nuclear Mab21 family proteins that potentially interact with the nucleosome for their functions (fig. S7) (25, 26).

Beyond these mutational analyses of cGAS localization and function, it was reported that the nucleosome can competitively suppress DNA-dependent cGAS activity (12). Moreover, mutating acidic patch residues within H2A-H2B abolishes binding of histone dimers to cGAS in pull-down assays (12). To verify that cGAS binding to the acidic patch results in the observed competitive suppression of DNA-

dependent activity, we performed cGAS enzymatic assays with titration of nucleosome as a competitor (Fig. 2F and fig. S8). We clearly observed that the nucleosome outcompeted dsDNA and exhibited a dose-dependent inhibition of cGAMP synthesis; by contrast, comprehensive mutation of the acidic patch (H2A E61A, E64S, N68A, D72S, N89A, D90A, and E91S) completely abolished the ability of the nucleosome to suppress cGAS activity. To further dissect the role of individual acidic patch residues in cGAS inactivation, we performed thorough site-directed mutagenesis of H2A paired with enzymatic and binding assays (Fig. 2G and fig. S9). Single-point mutations of H2A E61A and D90A, the two residues located at the core of the interactions with cGAS R222 and R241, completely abolished the ability of the nucleosome to bind cGAS and suppress its enzymatic activity. Mutant nucleosomes containing H2A E92A and E64A exhibited weaker binding affinities than the wild-type, resulting in partial suppression of cGAS activity. By contrast, nucleosomes assembled with H2A R71A or E91A showed cGAS inhibition comparable to both wild-type and negative control H2A E56A-mutated nucleosomes. Altogether, these results not only strengthen the evidence for a critical role of the nucleosome acidic patch in interacting with cGAS R222 and R241, but also suggest that the observed H2A R71-cGAS K315 interaction is dispensable for the nucleosome-mediated cGAS inactivation. It is well known that histone tails play an important role in nucleosome dynamics and recruitment of proteins to chromatin loci (27). Therefore, we further investigated whether histone tails may also contribute to the regulation of cGAS. However, we observed no changes in the inhibitory function nor binding of the nucleosome upon deleting N-terminal tails from all four histones, suggesting that in the absence of any histone modifications, the nucleosome acidic patch plays the dominant role in sequestering cGAS in its resting, inhibited nuclear state.

How does the nucleosome inhibit cGAS activity? To activate enzymatic synthesis of cGAMP, cGAS needs to oligomerize into the functionally active 2:2 cGAS-DNA state, where each cGAS interacts with two dsDNA helices through two distinct DNA-binding sites (site A and site B) (Fig. 3A) (17, 18). Site A contains 10 residues (K151, R158, K160, R161, K162, S165, K180, K184, K372, and K395), which not only contribute to most of the buried surface area between cGAS and dsDNA, but also form the site that induces bending of the spine helix to allosterically transform the catalytic pocket to an active conformation. By contrast, site B, which consists of only six residues (R222, K240, K315, K323, K335, and R342), has a higher binding affinity for dsDNA than does site A

(17). An additional dsDNA-binding site C that is critical for DNA-induced activity and liquid-phase condensation of human cGAS was identified, but is much less conserved in mouse cGAS (residues 247 to 291 and 408 to 421) (27). The nucleosome exclusively occupies site B on the cGAS surface through binding to the H2A-H2B dimer and proximity to nucleosomal DNA while leaving sites A and C completely exposed (Fig. 3B). Indeed, overlaying the DNA-bound cGAS structure (17) onto the cGAS-NCP structure shows that dsDNA can still be recognized by cGAS at site A without colliding with the nucleosome, even accounting for the observed cGAS conformational heterogeneity (Fig. 3C and fig. S10). However, the nucleosome sterically prevents cGAS from oligomerizing into its functionally active 2:2 cGAS-DNA state. Furthermore, the nucleosome-bound cGAS adopts an overall conformation that is essentially identical to the DNA-free inactive state, with a root mean square deviation (RMSD) of 0.7 Å over all backbone atoms, but is distinct from the active conformation (an RMSD of 2.3 Å over all backbone atoms), where DNA binding alters the N-terminal spine helix, repositions the activation loop, and opens the entrance to the catalytic pocket (Fig. 3D) (15–20). Together, these findings show how the nucleosome uses its histone surface, rather than DNA, to recognize and maintain cGAS in the resting, inhibited state.

It has become increasingly clear that the nucleosome plays essential roles in regulating nuclear protein functions, and the acidic patch has emerged as a key hot spot for interactions (28, 29). Arginine residues in nucleosome-interacting proteins called arginine anchors bind to the acidic patch in canonical and variant locations. cGAS uses one canonical arginine anchor (R241) that interacts with H2A E61, D90, and E92 in a nearly identical conformation as that observed for other nucleosome-binding proteins, including RCC1, Sir3, and Ring1B (30–32) (Fig. 4). An additional variant-type arginine anchor in cGAS (R222) interacts with similar H2A residues (E61 and E64) as other nucleosome-binding proteins (33) but exhibits a distinct conformation (Fig. 4). Overall, our structure establishes the molecular mechanism governing nucleosome-mediated inhibition of nuclear cGAS and further expands the paradigm of nucleosome acidic patch recognition by proteins involved in diverse nuclear processes.

REFERENCES AND NOTES

- R. Barbalat, S. E. Ewald, M. L. Mouchess, G. M. Barton, *Annu. Rev. Immunol.* **29**, 185–214 (2011).
- J. Wu, Z. J. Chen, *Annu. Rev. Immunol.* **32**, 461–488 (2014).
- A. Ablasser, Z. J. Chen, *Science* **363**, eaat8657 (2019).
- L. Sun, J. Wu, F. Du, X. Chen, Z. J. Chen, *Science* **339**, 786–791 (2013).
- J. Wu et al., *Science* **339**, 826–830 (2013).
- H. Ishikawa, G. N. Barber, *Nature* **455**, 674–678 (2008).
- B. Zhong et al., *Immunity* **29**, 538–550 (2008).
- D. L. Burdette et al., *Nature* **478**, 515–518 (2011).
- H. E. Volkman, S. Cambier, E. E. Gray, D. B. Stetson, *eLife* **8**, e47491 (2019).
- H. Liu et al., *Nature* **563**, 131–136 (2018).
- M. Gentili et al., *Cell Rep.* **26**, 2377–2393.e13 (2019).
- C. Zierhut et al., *Cell* **178**, 302–315.e23 (2019).
- H. Jiang et al., *EMBO J.* **38**, e102718 (2019).
- M. Du, Z. J. Chen, *Science* **361**, 704–709 (2018).
- P. Gao et al., *Cell* **153**, 1094–1107 (2013).
- F. Civril et al., *Nature* **498**, 332–337 (2013).
- X. Li et al., *Immunity* **39**, 1019–1031 (2013).
- X. Zhang et al., *Cell Rep.* **6**, 421–430 (2014).
- L. Andreeva et al., *Nature* **549**, 394–398 (2017).
- W. Zhou et al., *Cell* **174**, 300–311.e11 (2018).
- W. Xie et al., *Proc. Natl. Acad. Sci. U.S.A.* **116**, 11946–11955 (2019).
- S. Bilokapic, M. Strauss, M. Halic, *Nat. Commun.* **9**, 1330 (2018).
- X. Wu et al., *Nucleic Acids Res.* **42**, 8243–8257 (2014).
- D. C. Hancks, M. K. Hartley, C. Hagan, N. L. Clark, N. C. Elde, *PLOS Genet.* **11**, e1005203 (2015).
- M. Mariani et al., *Hum. Mol. Genet.* **8**, 2397–2406 (1999).
- C. C. de Oliveira Mann, R. Kiefersauer, G. Witte, K. P. Hopfner, *Sci. Rep.* **6**, 27498 (2016).
- B. Fierz, M. G. Poirier, *Annu. Rev. Biophys.* **48**, 321–345 (2019).
- A. A. Kalashnikova, M. E. Porter-Goff, U. M. Muthurajan, K. Luger, J. C. Hansen, *J. R. Soc. Interface* **10**, 20121022 (2013).
- R. K. McGinty, S. Tan, *Curr. Opin. Struct. Biol.* **37**, 54–61 (2016).
- R. D. Makde, J. R. England, H. P. Yennawar, S. Tan, *Nature* **467**, 562–566 (2010).
- K. J. Armache, J. D. Garlick, D. Canzio, G. J. Narlikar, R. E. Kingston, *Science* **334**, 977–982 (2011).
- R. K. McGinty, R. C. Henrici, S. Tan, *Nature* **514**, 591–596 (2014).
- C. J. Anderson et al., *Cell Rep.* **26**, 1681–1690.e5 (2019).

ACKNOWLEDGMENTS

Single particle cryo-EM data were collected at the University of North Carolina at Chapel Hill School of Medicine Cryo-Electron Microscopy Facility, which is partially supported by NIH P30CA016086 and is part of the Molecular Microscopy Consortium of the University of North Carolina at Chapel Hill, Duke University, and the NIEHS. We thank M. Kesimer (University of North Carolina at Chapel Hill) for SEC-MALS assistance and members of the Zhang and McGinty laboratories for critical comments. **Funding:** This work is supported by start-up funds and a Jefferson Pilot Fellowship from the University of North Carolina at Chapel Hill to Q.Z., NIH grant no. 1R35GM133498 and Searle Scholars and Pew-Stewart Scholars awards to R.K.M., NIH grant no. R21CA234979 to P.L., and grant no. F99CA253730 to C.J.S. **Author contributions:** Q.Z. and R.K.M. supervised the studies. Q.Z., J.A.B., R.K.M., and C.J.S. conceived the study and designed the experiments. J.A.B. prepared samples, grids, and performed in vitro functional assays. C.J.S. processed the cryo-EM data and performed in vitro functional assays. J.D.S. performed screening and collected the cryo-EM data. A.P.C. and P.L. contributed reagents. R.K.M. built and refined the atomic model with assistance from C.J.S. and Q.Z. Q.Z., J.A.B., R.K.M., and C.J.S. wrote the manuscript with contributions from all coauthors. **Competing interests:** The authors declare no competing interests. **Data and materials availability:** Cryo-EM maps have been deposited in the Electron Microscopy Data Bank under accession codes EMD-22408 (1:1 cGAS-nucleosome complex), EMD-22409 (2:1 cGAS-nucleosome complex), and EMD-22413 (1:1 cGAS_{mask}-nucleosome complex). Atomic coordinates of the 1:1 and 2:1 cGAS-nucleosome complexes have been deposited in the Protein Data Bank with accession codes 7J09 and 7J0A, respectively. All materials in this study are available upon request.

SUPPLEMENTARY MATERIALS

science.sciencemag.org/content/370/6515/450/suppl/DC1
Materials and Methods

Figs. S1 to S10

Table S1

References (34–44)

Movies S1 and S2

MDAR Reproducibility Checklist

[View/request a protocol for this paper from Bio-protocol.](#)

29 May 2020; accepted 28 August 2020

Published online 10 September 2020

10.1126/science.abd0609

STRUCTURAL BIOLOGY

Structural basis for the inhibition of cGAS by nucleosomes

Tomoya Kujirai^{1*}, Christian Zierhut^{2*†}, Yoshimasa Takizawa¹, Ryan Kim², Lumi Negishi¹, Nobuki Uruma^{1,3}, Seiya Hirai^{1,4}, Hironori Funabiki^{2‡}, Hitoshi Kurumizaka^{1,3,4‡}

The cyclic guanosine monophosphate–adenosine monophosphate synthase (cGAS) senses invasion of pathogenic DNA and stimulates inflammatory signaling, autophagy, and apoptosis. Organization of host DNA into nucleosomes was proposed to limit cGAS autoinduction, but the underlying mechanism was unknown. Here, we report the structural basis for this inhibition. In the cryo-electron microscopy structure of the human cGAS–nucleosome core particle (NCP) complex, two cGAS monomers bridge two NCPs by binding the acidic patch of the histone H2A–H2B dimer and nucleosomal DNA. In this configuration, all three known cGAS DNA binding sites, required for cGAS activation, are repurposed or become inaccessible, and cGAS dimerization, another prerequisite for activation, is inhibited. Mutating key residues linking cGAS and the acidic patch alleviates nucleosomal inhibition. This study establishes a structural framework for why cGAS is silenced on chromatinized self-DNA.

The cyclic guanosine monophosphate–adenosine monophosphate (GMP-AMP) synthase (cGAS)–stimulator of interferon genes (STING) pathway senses pathogenic DNA and activates the innate immune system during infections, cancer, and autoimmune diseases (1, 2). DNA sensing is achieved by three distinct DNA binding surfaces on cGAS (sites A, B, and C) (3). DNA allosterically activates cGAS to synthesize cyclic GMP-AMP (cGAMP) (3–6), which then associates with STING (6–11), promoting autophagy, inflammation, senescence, or apoptosis (8, 9, 12). A central question is how cGAS avoids activation by self-DNA. Although the nuclear envelope may limit cGAS from accessing chromosomes (1, 2), cGAS signaling is attenuated even when cGAS is forced into the nucleus (13). After mitotic nuclear envelope disassembly, cGAS rapidly associates with chromosomes (14, 15), but signaling is largely suppressed (15, 16). Furthermore, although cGAS activation is not observed under normal growth, some cGAS may nonetheless be present within the nucleus (17, 18). cGAS mutations that weaken nuclear tethering of cGAS constitutively activate it without the need for exogenous DNA (18), but the structural basis of nuclear tethering and cGAS inhibition remains unclear.

Isolated chromatin (19) or reconstituted nucleosomes (15) can bind cGAS, but these stimulate cGAMP synthesis less effectively than naked DNA (15, 19, 20). Furthermore, cGAS has higher affinity for reconstituted nucleosomes than for DNA, and nucleosomes competitively inhibit DNA-dependent cGAS activation (15), suggesting that nucleosome binding underlies the inefficient cGAS activation by chromosomes. To monitor nucleosome-dependent suppression under physiological conditions, we used interphase *Xenopus* egg extracts, where exogenously added DNA efficiently assembles into functional chromatin (Fig. 1, A and B) (21). When chromatin formation was prevented by depleting histones H3 and H4 from the extract (21), exogenously added DNA stimulated cGAMP production

after cGAS addition (Fig. 1, A and B). In mock-depleted control extracts, after nucleosome assembly, cGAS activity was severely impaired (Fig. 1, A and B, and fig. S1), indicating that chromatin inhibits cGAS under physiological conditions.

To reveal the mechanism underlying the nucleosome-mediated suppression of cGAS activation, we determined the cryo-electron microscopy (cryo-EM) structure of the complex formed between nucleosome core particles (NCPs) and human cGAS lacking the unstructured N terminus. This construct was chosen because the N terminus induces aggregation and liquid-liquid phase separation, which would interfere with structural analysis (22). Native gel electrophoresis confirmed that, similar to nucleosomes with linker DNA, cGAS binds to NCPs with higher affinity than to naked DNA (Fig. 1C). Cryo-EM visualization of these cGAS–NCP complexes showed that most of the NCP-like particles are bridged by cGAS-like particles to form stacks (fig. S2). To obtain higher-resolution EM maps, we used GraFix (23). Two major complexes (1 and 2) were isolated and subjected to cryo-EM analysis (fig. S3, A and B). Similar to unfixed samples, most NCP-like particles formed multimers, where cGAS-like particles were seen between NCPs (fig. S3, C and D). Consistent with their gel migration, complex 1 and complex 2 were predominantly composed of two and three NCPs, respectively (fig. S3, C and D). We consider this multimeric configuration to represent the major organization of the cGAS–NCP complex, and we subsequently focused on complex 1, because of its simpler organization (figs. S4 to S6 and table S1). The large majority (86%) of particles in complex 1 that were processed for three-dimensional classification contained

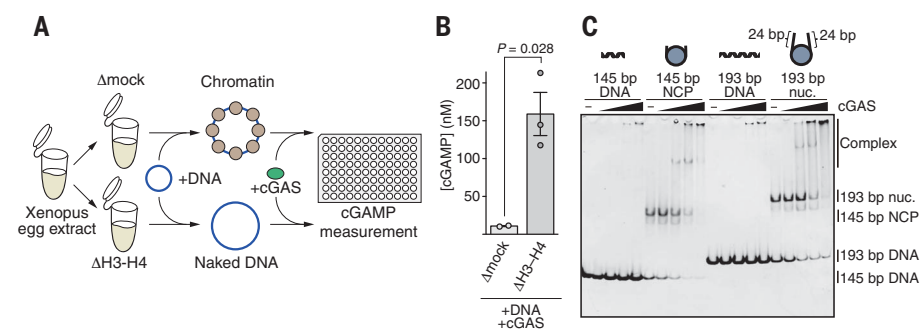


Fig. 1. cGAS-mediated cGAMP synthesis is inhibited by nucleosomes under physiological conditions.

(A) cGAMP synthesis by cGAS in *Xenopus* egg extracts. Interphase extracts depleted for histones H3 and H4 (ΔH3-H4) or mock-depleted with unspecific antibodies (Δmock) were incubated with exogenously added plasmid DNA and cGAS. After incubation, samples were taken for Western blotting and cGAMP detection by enzyme-linked immunosorbent assay. (B) Averages (bars) and SEM (error bars) for the indicated extract types. *P* value derived with unpaired *t* test. (C) cGAS–nucleosome binding assay. Increasing amounts of cGAS were mixed with either 145 base-pair (bp) DNA, the nucleosome core particle (NCP) containing 145 bp DNA (no linker DNA), 193 bp DNA, or the nucleosome (nuc.) containing 193 bp DNA (24 bp linker DNA). The indicated species were separated by nondenaturing polyacrylamide gel electrophoresis and visualized with ethidium bromide staining. The result was reproduced in another independent experiment.

¹Laboratory of Chromatin Structure and Function, Institute for Quantitative Biosciences, The University of Tokyo, 1-1-1 Yayoi, Bunkyo-ku, Tokyo 113-0032, Japan. ²Laboratory of Chromosome and Cell Biology, The Rockefeller University, New York, NY 10065, USA. ³Graduate School of Advanced Science and Engineering, Waseda University, 2-2 Wakamatsu-cho, Shinjuku-ku, Tokyo 162-8480, Japan. ⁴Department of Biological Sciences, Graduate School of Science, The University of Tokyo, 1-1-1 Yayoi, Bunkyo-ku, Tokyo 113-0032, Japan.

*These authors contributed equally to this work.

†Present address: Division of Cancer Biology, The Institute of Cancer Research, London SW3 6JB, UK.

‡Corresponding author. Email: funabih@rockefeller.edu (H.F.); kurumizaka@iqb.u-tokyo.ac.jp (H.K.)

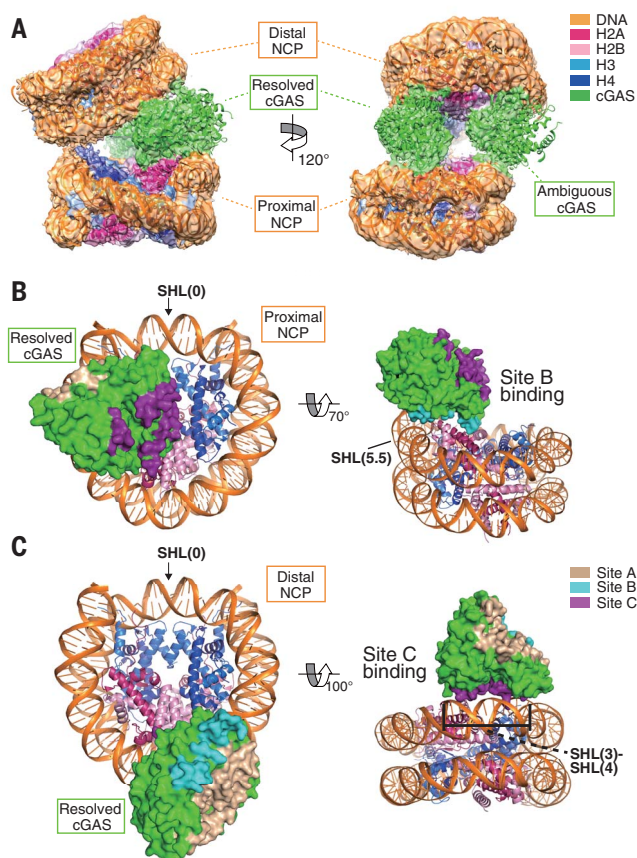


Fig. 2. Cryo-EM structure of the cGAS-nucleosome complex. (A) Cryo-EM density of the cGAS-nucleosome complex with fitted structural model. (B) cGAS DNA binding site B (cyan) binds the proximal nucleosome through contacts with DNA at SHL5.5 and with the H2A-H2B dimer. (C) cGAS DNA binding site C (purple) binds the distal nucleosome at SHL3 and SHL4. DNA binding site A (beige) does not interact with DNA or histones.

two nucleosomes (fig. S4B). Although some of these classes contained one cGAS protomer between two NCPs, suggesting some variability in the possible arrangements, the highest resolution was obtained in the class that contained two cGAS protomers between the two NCPs (fig. S4B).

In the cGAS-NCP complex structure with 3.9-Å resolution (fig. S5), two cGAS monomers bind two NCPs, forming a sandwich-like structure in which the NCPs are intimately associated (Fig. 2A). One cGAS molecule fits well into the cryo-EM map, but the cryo-EM map for the other cGAS molecule is more ambiguous (fig. S6A). A 3.3-Å resolution structure of the resolved cGAS-NCP was generated by a focused refinement after subtraction of the ambiguous cGAS-NCP (figs. S4 and S5). Although resolution of the catalytic pocket is not high enough to assess its local conformation (fig. S5, D and E), it is clear that this cGAS monomer binds to the proximal NCP at the acidic patch on the H2A-H2B histone dimer surface and DNA around superhelical

location (SHL) 5.5 (proximal NCP, Fig. 2B); by binding DNA around SHL3 and SHL4 in the other NCP (distal NCP), this cGAS protomer also bridges the two NCPs (Fig. 2, A and C). The ambiguous cGAS monomer may bind to similar NCP surfaces, because cryo-EM densities were observed around nearly symmetric NCP regions (fig. S6C). The ambiguity of this cGAS monomer may reflect its flexibility. Below, we focus our analysis on interactions between the resolved cGAS and the two NCPs.

In previous crystal structures of the cGAS dimer-DNA complex, two cGAS protomers sandwich two DNA fragments, with each cGAS protomer binding one DNA fragment with site A and the other with site B, both of which are essential for cGAS activation (3, 4, 6, 24–27) (fig. S7). Site C contributes to cGAS activation by promoting DNA-mediated oligomerization (3) (fig. S7). Within the cGAS-DNA complex, cGAS dimerization is also important for catalytic activation (4). However, direct interaction of the two cGAS protomers in the cGAS-NCP complex is prevented by

steric hindrance (fig. S8). Furthermore, the configuration of each cGAS DNA binding site is reorganized in the context of NCP binding in a manner that is incompatible with binding to exogenous DNA.

Although site A is solvent-exposed in the cGAS-NCP complex and does not contact nucleosomal DNA (Fig. 3A, left panel), it is inaccessible to exogenous DNA owing to steric clashes with the proximal NCP (Fig. 3A, right panel). The lack of interactions at site A in the NCP complex is consistent with our previous findings that site A mutations do not affect the affinity of cGAS for mononucleosomes nor cGAS association with mitotic chromosomes (15).

Site B is repurposed, with a loop segment binding histones rather than DNA (Fig. 2B). Rather than binding DNA, R236, K254, and R255 of the loop directly bind to the acidic patch of the proximal NCP (Fig. 3B), a hotspot for chromatin interactors (28). The side-chain density of cGAS R255 is clearly visible, revealing that R255 interacts with residues E61, D90, and E92 of histone H2A (Fig. 3B), forming a classic arginine anchor such as that found in Kaposi's sarcoma LANA (latency-associated nuclear antigen) peptide (fig. S9). As previously indicated (18), this loop is conserved among vertebrate cGAS homologs (fig. S10) but not in the RNA-activated cGAS paralog OAS1 (2'-5'-oligoadenylate synthase 1) (figs. S10 and S11). In addition, an α helix within site B (residues 346 to 355) is located near the DNA around SHL5.5 of the proximal NCP. K347 and K350 within this α helix may interact with the major groove and the backbone of the nucleosomal DNA, respectively (Fig. 3C). The main-chain moieties of several other site B residues, K327, S328, S329, and L354, are located close to R71 of histone H2A and may stabilize the cGAS-NCP interaction (Fig. 3D). Altogether, key residues of site B that are essential for DNA-mediated cGAS activation (3, 5, 25–27) are blocked by the NCP in the cGAS-NCP complex.

cGAS DNA binding site C (fig. S7) binds DNA of the distal NCP in the cGAS-NCP complex (Fig. 2C). Residues 273 to 290 of an α helix within site C are located near nucleosomal DNA around SHL3 (Fig. 3E). In this α helix, the basic residues R281, K282, and K285 may interact with the DNA backbone (Fig. 3E). The KRKR loop (K299, R300, K301, and R302) (3) may also interact with nucleosomal DNA around SHL3 (Fig. 3E). K427, K428, and H429, which form the KKH loop (3), may interact with nucleosomal DNA around SHL4 (Fig. 3F). In this context, site C cannot access DNA in trans outside of the complex. This potentially suppresses liquid-liquid phase separation-mediated enrichment of cGAS to nucleosome-free DNA within chromatin (3, 22). Gel shift analysis shows that although cGAS mutated at these site C basic residues can bind NCPs to

Fig. 3. cGAS-nucleosome interactions. (A) Close-up view of cGAS DNA binding site A in the complex (left). The human cGAS-DNA structure [light gray; Protein Data Bank (PDB) ID 6CT9] and the cGAS-nucleosome structure were superimposed by aligning cGAS (right). Binding of exogenous DNA to site A would cause steric clash with nucleosomal DNA. (B to D) Interactions between the nucleosome and cGAS DNA binding site B. Close-up views of the cGAS residues (B) R236, K254, and R255; (C) K347 and K350; and (D) L354, K327, S328, and S329 are shown. The focused refined EM-density map after subtraction of the ambiguous cGAS-distal nucleosome (see Materials and Methods section of the supplementary materials) was used for representations. Single-letter abbreviations for the amino acid residues are as follows: A, Ala; D, Asp; E, Glu; H, His; K, Lys; L, Leu; R, Arg; and S, Ser. (E and F) Interactions between the nucleosome and cGAS DNA binding site C. Close-up views of (E) the cGAS α helix region containing R281, K282, and K285 and the KRKR loop containing K299, R300, K301, and R302; and (F) the KKH loop containing K427, K428, and H429 are shown. The EM-density map of the overall structure of the cGAS-nucleosome complex was used for representation. cGAS DNA binding sites are colored as in Fig. 2.

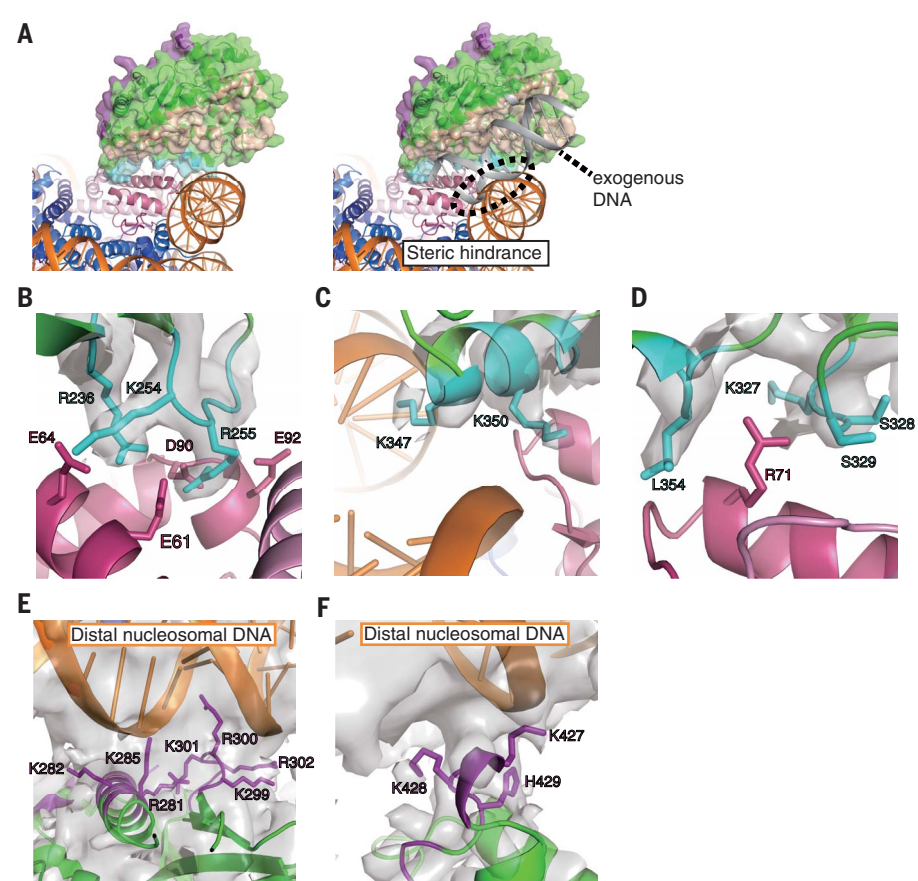
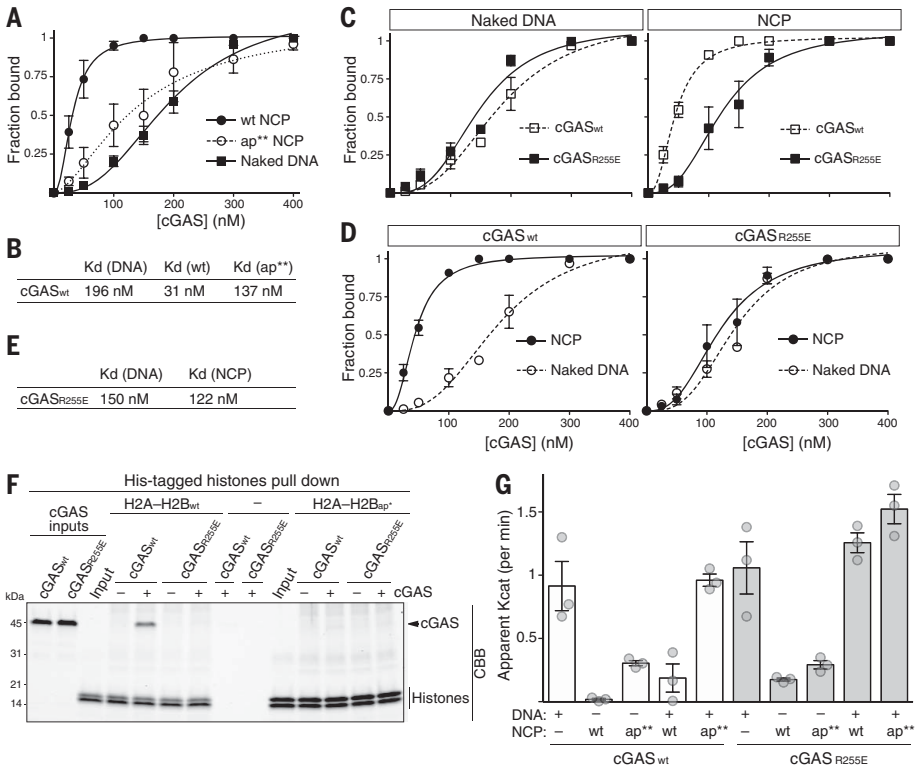


Fig. 4. The acidic patch on the nucleosome and R255 of cGAS are required for high-affinity association between nucleosomes and cGAS and for competitive inhibition of cGAS by nucleosomes. (A and B) Quantitative gel shift analysis of the binding affinity between cGAS and naked DNA or the indicated nucleosomes (wt, wild type; ap**, acidic patch mutated). See fig. S13A for example gels. Data represent mean and SEM of four independent experiments. 145 bp naked DNA or NCPs containing 145 bp of DNA were used. (C to E) Quantitative gel shift analysis of the binding affinity between naked DNA or wt nucleosomes and the indicated cGAS. Note that (C) and (D) are different representations of the same experiments. See fig. S13C for example gels. Data represent mean and SEM of three independent experiments. 145 bp naked DNA or NCPs containing 145 bp of DNA were used. (F) Analysis of the interaction between cGAS (wt or R255E) and either wt hexahistidine (His_6)-tagged H2A-H2B dimers or acidic patch mutated (ap*) His_6 -H2A-H2B dimers. cGAS, histones, and talon beads were mixed, incubated, and collected on a magnet. After washing, bound proteins were separated by gel electrophoresis and visualized with Coomassie brilliant blue (CBB). Equal fractions of inputs and pull-downs were loaded. Results were confirmed in two additional independent experiments. (G) Quantifications of catalytic activity of the indicated cGAS version with naked DNA, wt NCPs, or acidic patch mutated (ap**) NCPs in vitro. Averages (bars) and SEM (error bars) of three experiments (dots) are shown. Naked DNA and NCPs were 145 bp and used at 230 nM each.



form complexes with discrete sizes, it cannot form large multimers (fig. S12), suggesting that site C is required for cGAS to generate NCP stacks.

To confirm our interpretations of NCP-dependent suppression of cGAS activity, we focused on site B interactions with the acidic patch of the NCP (Fig. 3B), as site C mutations inactivate human cGAS (3). Mutating the acidic patch [ap** H2A: Glu⁵⁶→Thr (E56T), E61T, E64T, D90S, E91T, and E92T; and ap** H2B: E105T and E113T] abrogated the high-affinity interaction between cGAS and the NCP (Fig. 4, A and B, and fig. S13A). R255 of cGAS site B, which binds the acidic patch (Fig. 3B), is highly conserved in vertebrates but is predicted not to be involved in DNA binding (18) (fig. S10). In cells, mutating R255 and the equivalent R241 of mouse cGAS to glutamic acid was reported to weaken the tight nuclear tethering of cGAS (18). To test whether R255 is critical for NCP binding, we prepared mutant human cGAS, in which R255 was replaced by glutamic acid (cGAS_{R255E}, fig. S13B). Consistent with our structure model, NCP binding of cGAS_{R255E} was decreased, whereas DNA binding was largely unaffected (Fig. 4, B to E, and fig. S13C). Unlike wild-type cGAS that binds NCPs with higher affinity than naked DNA, cGAS_{R255E} did not show such preference (Fig. 4, B to E). Furthermore, although wild-type cGAS bound to H2A-H2B dimers, this interaction was not observed for cGAS_{R255E} (Fig. 4F). Similarly, as we showed previously (15), acidic patch mutations in H2A and H2B (ap* H2A: E56A, E61A, E64A, D90A, E91A, and E92A; and ap* H2B: E113A) also interfere with cGAS interaction (Fig. 4F). These data indicate that the interaction between R255 of cGAS and the nucleosome acidic patch is crucial for specific binding of cGAS to nucleosomes.

To test whether this interaction is important for inhibition of DNA-dependent cGAS activation, we monitored how naked DNA, wild-type NCPs, or ap** NCPs stimulate cGAMP production by wild-type cGAS or cGAS_{R255E}. In contrast to the almost complete inhibition of cGAMP production by wild-type NCPs with wild-type cGAS, using either cGAS_{R255E} or ap** NCPs increased cGAMP production (Fig. 4G and figs. S14 and S15), supporting the importance of interactions between cGAS and the acidic patch for cGAS inhibition. However, this did not lead to full activation of cGAS (Fig. 4G and fig. S14), likely because of the conformation of nucleosomal DNA, which may not be optimal for cGAS activation. On naked DNA, cGAS makes many contacts with the backbone of more than a full turn of DNA, which is in a straight conformation (3, 4, 24–27) (fig. S7). In contrast, the curvature of DNA wrapped around the histone octamer may interfere with the structural changes in cGAS

required for full catalytic activity (example shown in fig. S16).

The significance of the cGAS-acidic patch interactions for cGAS inhibition was better illustrated when competitive inhibition of naked DNA-stimulated cGAMP production was assessed (Fig. 4G, combinations of DNA and wild-type or ap** NCPs). Whereas wild-type NCPs were able to competitively inhibit wild-type cGAS activation by an equal amount of naked DNA, ap** NCPs lost this inhibitory activity (Fig. 4G, left). In contrast, cGAS_{R255E} was refractory to inhibition by even wild-type NCPs (Fig. 4G, right). Moreover, whereas wild-type cGAS is suppressed by NCPs with or without the linker DNA, cGAS_{R255E} is activated by NCPs with linker DNA but not by NCPs without linker DNA (fig. S17). These findings predict that cGAS_{R255E}, which cannot be competitively inhibited by NCPs, is activated by nucleosome-free segments of genomic DNA in cells. Indeed, in HeLa cells expressing cGAS_{R255E}, high basal levels of cGAMP have been observed (18). Altogether, these structural, biochemical, and cellular analyses support the importance of the interaction between cGAS site B and the nucleosome acidic patch in competitive inhibition of DNA-dependent cGAS activation.

The competitive inhibition by nucleosomes can explain how stimulation of cGAS by chromosomal self-DNA can be prevented, despite the presence of nucleosome-free regions. Our analysis indicates that NCPs can competitively inhibit cGAS activation by at least four mechanisms (fig. S18). First, DNA binding at site A is prevented by steric clashes with the proximal NCP. Second, site B is occupied by the acidic patch of the proximal NCP and therefore is inaccessible to exogenous DNA. Third, cGAS dimerization is prevented by steric clashes with the proximal NCP. Fourth, the formation of tandem cGAS-NCP chains via sites B and C prevents cGAS-DNA oligomerization, which is required for full activation (3, 4). However, the fourth mechanism may be species specific, because several site C basic residues that are predicted to contact nucleosomal DNA, such as those in the KRKR and KKH loops, are not highly conserved (3) (fig. S10). As human and mouse cGAS exhibit different enzymatic, DNA-length sensitivity, and phase-separation characteristics (3, 22), chromatin inhibition of cGAS may also be modified species-specifically. It is likely that diverse mechanisms, such as the expression of H2A variants that lack the acidic patch, regulate the nucleosome-dependent suppression of cGAS.

REFERENCES AND NOTES

1. A. Ablasser, Z. J. Chen, *Science* **363**, eaat8657 (2019).
2. M. Motwani, S. Pesiridis, K. A. Fitzgerald, *Nat. Rev. Genet.* **20**, 657–674 (2019).
3. W. Xie et al., *Proc. Natl. Acad. Sci. U.S.A.* **116**, 11946–11955 (2019).

4. X. Li et al., *Immunity* **39**, 1019–1031 (2013).
5. R. M. Hooy, J. Sohn, *eLife* **7**, e39984 (2018).
6. P. Gao et al., *Cell* **153**, 1094–1107 (2013).
7. H. Ishikawa, G. N. Barber, *Nature* **455**, 674–678 (2008).
8. L. Sun, J. Wu, F. Du, X. Chen, Z. J. Chen, *Science* **339**, 786–791 (2013).
9. J. Wu et al., *Science* **339**, 826–830 (2013).
10. A. Ablasser et al., *Nature* **498**, 380–384 (2013).
11. K. Kato, H. Omura, R. Ishitani, O. Nureki, *Annu. Rev. Biochem.* **86**, 541–566 (2017).
12. H. Ishikawa, Z. Ma, G. N. Barber, *Nature* **461**, 788–792 (2009).
13. M. Gentili et al., *Cell Rep.* **26**, 2377–2393.e13 (2019).
14. H. Yang, H. Wang, J. Ren, Q. Chen, Z. J. Chen, *Proc. Natl. Acad. Sci. U.S.A.* **114**, E4612–E4620 (2017).
15. C. Zierhut et al., *Cell* **178**, 302–315.e23 (2019).
16. L. Zhong et al., *Cell Discov.* **6**, 26 (2020).
17. H. Jiang et al., *EMBO J.* **38**, e102718 (2019).
18. H. E. Volkman, S. Cambier, E. E. Gray, D. B. Stetson, *eLife* **8**, e47491 (2019).
19. K. J. Mackenzie et al., *Nature* **548**, 461–465 (2017).
20. X. Lahaye et al., *Cell* **175**, 488–501.e22 (2018).
21. C. Zierhut, C. Jenness, H. Kimura, H. Funabiki, *Nat. Struct. Mol. Biol.* **21**, 617–625 (2014).
22. M. Du, Z. J. Chen, *Science* **361**, 704–709 (2018).
23. B. Kastner et al., *Nat. Methods* **5**, 53–55 (2008).
24. F. Cviril et al., *Nature* **498**, 322–337 (2013).
25. X. Zhang et al., *Cell Rep.* **6**, 421–430 (2014).
26. L. Andreeva et al., *Nature* **549**, 394–398 (2017).
27. W. Zhou et al., *Cell* **174**, 300–311.e11 (2018).
28. A. A. Kalashnikova, M. E. Porter-Goff, U. M. Muthurajan, K. Luger, J. C. Hansen, *J. R. Soc. Interface* **10**, 20121022 (2013).

ACKNOWLEDGMENTS

We thank Y. Iikura and J. Kato (University of Tokyo) for their assistance and Y. Arimura for helpful discussions and comments on the manuscript. We also thank M. Kikkawa for cryo-EM data collection. **Funding:** This work was supported in part by JSPS KAKENHI grants JP17H01408 (to H.K.), JP18H05534 (to H.K.), JP19K06522 (to Y.T.), and JP20K15711 (to T.K.); JST CREST grant JPMJCR16G1 (to T.K. and H.K.); the Platform Project for Supporting Drug Discovery and Life Science Research (BINDS) from AMED under grants JP20am0101076 (to H.K.) and JP20am01011150004 (to M. Kikkawa); JST ERATO grant JPMJER1901 (to H.K.); and National Institutes of Health grant R35GM132111 (to H.F.). **Author contributions:** C.Z., R.K., T.K., and N.U. purified cGAS proteins. T.K. and S.H. prepared the cGAS-nucleosome complex. C.Z., R.K., T.K., S.H., and L.N. performed biochemical analyses. T.K. and Y.T. performed the cryo-EM analysis. T.K., C.Z., H.F., and H.K. conceived of and designed the work. T.K., C.Z., R.K., H.F., and H.K. wrote the paper. H.F. and H.K. guided and supervised all of the work. All of the authors discussed the results and commented on the manuscript. **Competing interests:** The authors declare no competing interests. H.F. is affiliated with the Graduate School of Medical Sciences, Weill Cornell Medicine, and the Cell Biology Program of the Sloan Kettering Institute. **Data and materials availability:** The cryo-EM reconstructions and atomic model of the cGAS-nucleosome complex have been deposited in the Electron Microscopy Data Bank and the Protein Data Bank under accession code EMD-30267 and PDB ID 7COM. All data and materials are available from the corresponding authors upon request.

SUPPLEMENTARY MATERIALS

science.sciencemag.org/content/370/6515/455/suppl/DC1
Materials and Methods
Figs. S1 to S18
Table S1
References (29–47)
MDAR Reproducibility Checklist

[View/request a protocol for this paper from Bio-protocol.](#)

27 May 2020; accepted 28 August 2020
Published online 10 September 2020
10.1126/science.abd0237

DISPLAY TECHNOLOGY

Metasurface-driven OLED displays beyond 10,000 pixels per inch

Won-Jae Joo^{1*}, Jisoo Kyoung^{1†}, Majid Esfandypour², Sung-Hoon Lee¹, Hyun Koo¹, Sunjin Song¹, Young-Nam Kwon¹, Seok Ho Song³, Jun Cheol Bae¹, Ara Jo¹, Myong-Jong Kwon¹, Sung Hyun Han¹, Sung-Han Kim¹, Sungwoo Hwang¹, Mark L. Brongersma^{2*}

Optical metasurfaces are starting to find their way into integrated devices, where they can enhance and control the emission, modulation, dynamic shaping, and detection of light waves. In this study, we show that the architecture of organic light-emitting diode (OLED) displays can be completely reenvisioned through the introduction of nanopatterned metasurface mirrors. In the resulting meta-OLED displays, different metasurface patterns define red, green, and blue pixels and ensure optimized extraction of these colors from organic, white light emitters. This new architecture facilitates the creation of devices at the ultrahigh pixel densities (>10,000 pixels per inch) required in emerging display applications (for instance, augmented reality) that use scalable nanoimprint lithography. The fabricated pixels also offer twice the luminescence efficiency and superior color purity relative to standard color-filtered white OLEDs.

The Fabry-Pérot (FP) cavity is a very simple but versatile optical component that consists of two opposing mirrors (1, 2). This optical element has a distinctive ability to transmit light or build up optical energy at selected wavelengths that meet a specific resonance condition. Their behavior is often characterized by a quality factor (*Q* factor) that quantifies the rate of energy loss from the cavity (2). Higher *Q* factors facilitate stronger light-matter interaction with materials placed in the cavity, at the cost of a reduced spectral bandwidth of operation. The reflectivity of the mirrors plays a key role in determining the cavity *Q* factor, and different choices can be made on the basis of the intended application (3, 4). For instance, single-frequency laser resonators leverage highly-reflective distributed Brag reflectors to benefit from a high *Q* factor (>10,000) (4). On the other hand, OLED microcavities tend to feature lower *Q* factors (<10) to achieve enhanced light extraction across the broader emission bands of organic molecules. Lower-quality Ag mirrors suffice for this purpose (5). The cavity length, typically taken as the distance between the mirrors, plays an equally important role in the cavity dynamics, as it determines the resonant frequency. However, the effective cavity length can be modified by controlling the reflection phase of the mirrors. Recent work indicates that the reflection phase of metallic mirrors can be altered through nanostructuring (6–10), which enables the tuning of cavity resonances

(11–13). We further show that a judicious design of meta-mirrors opens entirely new possibilities, such as engineering the free spectral range of the cavity. In this work, we leverage these physics concepts to achieve a breakthrough in OLED display technology.

Two different types of OLEDs have successfully been commercialized in mid-size mobile devices and large-scale televisions. First, red, green, and blue (RGB) OLEDs are mostly used in mobile displays and boast a superior device performance by taking full advantage of beneficial cavity effects (14, 15). In such OLEDs, FP cavities are used to minimize the undesired coupling of emitted photons to waveguided modes and to narrow the intrinsic emission spectrum of the emitting organics by capitalizing on the Purcell effect. The current fabrication approach for creating separated RGB subpixels relies on material depositions through a fine-metal mask (FMM), which presents serious practical challenges to display scaling (16). It does not allow downscaling of the pixel size because of shadowing effects in the deposition and also precludes upscaling of the overall display size owing to sagging of large-area FMMs. To circumvent these problems, large-display manufacturers have begun to use white OLEDs with color filters, and this technology is currently dominating the TV markets (17). This is not an ideal solution, however, as the large optical loss (>70%) caused by the color filters renders displays more power-hungry and accelerates device degradation (e.g., burn-in phenomenon). These factors greatly hamper the application of white OLEDs in high-brightness augmented reality displays (18, 19). To satisfy the ever-increasing demand for ultrahigh pixel density in next-generation displays, a fundamentally new device architecture and fabrication approach is clearly needed.

Here we propose a novel OLED device design (Fig. 1A) with spatially varying metaphotonic FP cavities (i.e., a meta-OLED), which can benefit from microcavity effects without relying on FMM-based fabrication (16–19). We show that the emission spectrum of meta-OLED pixels is widely tunable and can cover the entire visible spectrum through precise design of nanopatterns on the Ag reflector to form metamirrors. We also demonstrate improvements in the luminance efficiency and color purity resulting from optimized microcavity effects. Finally, we experimentally verify the pixel scalability of meta-OLEDs for use in ultrahigh-density display applications.

The resonance condition for an OLED microcavity can be written as

$$\varphi_{\lambda, \text{top}} + 4\pi \cdot \frac{nL_{\text{cavity}}}{\lambda} + \varphi_{\lambda, \text{bottom}} = 2(m+1)\pi$$

where $\varphi_{\lambda, \text{top}}$ and $\varphi_{\lambda, \text{bottom}}$ are the reflection phases at the top and bottom metal mirrors, respectively; λ is the resonance wavelength; n is an averaged refractive index; L_{cavity} is the physical length of the cavity; and m is the resonance order (20). The reflection phase of a highly conductive metallic mirror is close to π , and the length of a FP cavity with metallic mirrors is simply proportional to the distance between the reflective surfaces. As a consequence, the side-by-side RGB pixels in conventional OLED displays have different optimal thicknesses, as depicted in fig. S1. By using nanostructured mirrors in our meta-OLED (Fig. 1A), we can decouple the physical cavity length from the effective optical cavity length by capitalizing on the broad tunability of the reflection phase of these metasurface mirrors. The ability to tune this phase across a full 2π distance enables us to achieve resonance for the RGB pixels at a perfectly constant physical mirror spacing (fig. S2). To fully prove the meta-OLED concept, we show how to create such pixels by spatially varying the nanopillar arrangement. We start by making 300- μm -by-300- μm pixels in which we arrange 80-nm-high nanopillars on a square lattice with pitches varying from 180 to 380 nm (Fig. 1B). To investigate whether the color tuning is very sensitive to the pillar diameter, we fabricate such arrays with pillars of 80-, 100-, and 120-nm diameter. We then build the OLED structure with the RGB emitters and charge-transport layers on top of the mirrors (materials and methods). The development of cost-effective fabrication routes for nanostructured RGB pixels that offer scalability from the wafer scale to the square-meter scale is of critical importance for the success of our meta-OLED technology. In this work, we explored the possibility of using a nanoimprint process to create metamirrors (figs. S3 and S4). Scanning electron microscopy (SEM)

¹Samsung Advanced Institute of Technology, Samsung Electronics, Suwon, 16678, Korea. ²Geballe Laboratory for Advanced Materials, Stanford University, Stanford, CA 94305, USA. ³Department of Physics, Hanyang University, Seoul, 04763, Korea.

*Corresponding author. Email: wj.joo@samsung.com (W.-J.J.); brongersma@stanford.edu (M.L.B.) †Present address: Department of Physics, Dankook University, Cheonan-si, Chungnam, 31116, Korea.

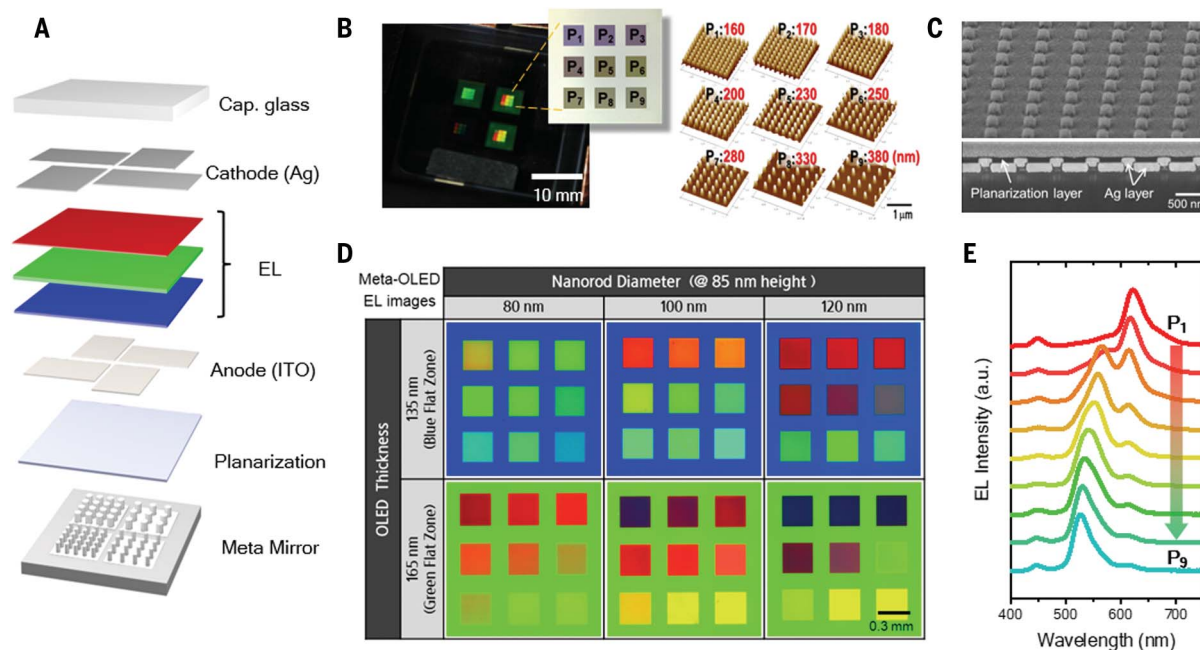


Fig. 1. EL characteristics of meta-OLED pixels. (A) Schematic diagram of our meta-OLED design with a metasurface mirror. ITO, indium tin oxide. (B) (Left) Photo of a meta-OLED test cell that consists of four sections and is driven at 3 V. The inset shows an optical microscopy (OM) image of three-by-three metamirrors with different pitches (P_1 to P_9). (Right) Atomic force microscopy images of the metamirrors show the nanopillar arrays with different pitches ($P_1 = 160$ nm to $P_9 = 380$ nm) and a constant diameter (80 nm) and height (80 nm). (C) SEM images of a bird's-eye view (top) and a cross-sectional view (bottom) of the Ag metamirror fabricated by nanoimprint lithography. (D) OM images (three-by-three layout) of a

meta-OLED biased at 3 V. The emission color of the meta-OLED can be tuned widely by controlling the reflection phase of each metamirror. In the three-by-three layout, each metamirror has an area of $300\ \mu\text{m}$ by $300\ \mu\text{m}$. Nanopillar diameters are 80, 100, and 120 nm. Total OLED thicknesses determining the background color at the flat mirror area are 135 and 165 nm for blue and green, respectively. (E) EL spectra showing continuous spectral tuning of the emission with pillar pitch. For these measurements, larger ($600\ \mu\text{m}$ by $600\ \mu\text{m}$) pixels were created to achieve high signal-to-noise spectra. The pillar height and diameter were kept constant at 80 and 100 nm, respectively, and the OLED thickness was 135 nm. a.u., arbitrary units.

images of fabricated metamirrors are shown in Fig. 1C.

Figure 1D shows high-spatial resolution electroluminescence (EL) images of three-pixel-by-three-pixel arrays with different metamirror designs. In the upper panels, the blue background is an area with a smooth metallic reflector (i.e., no pillars). The total thickness of the broadband emissive OLED stack is 135 nm physically and 240 nm optically, considering the refractive indices of the stacked organic layers and the indium tin oxide anode. This was intentionally set to satisfy the resonant condition for blue emission at $\lambda = 450$ nm. All of the metamirror pixels show a uniform color and intensity, highlighting the quality and uniformity of the nanopatterning. The nanopillars increase the reflection phase, and increasingly dense arrays are needed to achieve resonance at longer wavelengths (fig. S5). Figure 1E shows how we can continuously redshift the emission peaks by increasing the pillar density. The pixels with larger pillar diameters clearly offer stronger color tuning with pitch. The larger-diameter pillars produce smaller gap spacings (at the same pitch), and the higher degree of tunability can therefore be linked to the higher sensitivity of the mode index of gap plasmons to the gap size for the smaller gaps. In Fig. 1D, the lower (green background) panels have identical meta-

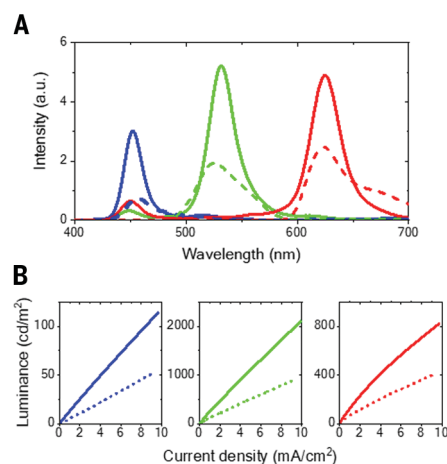
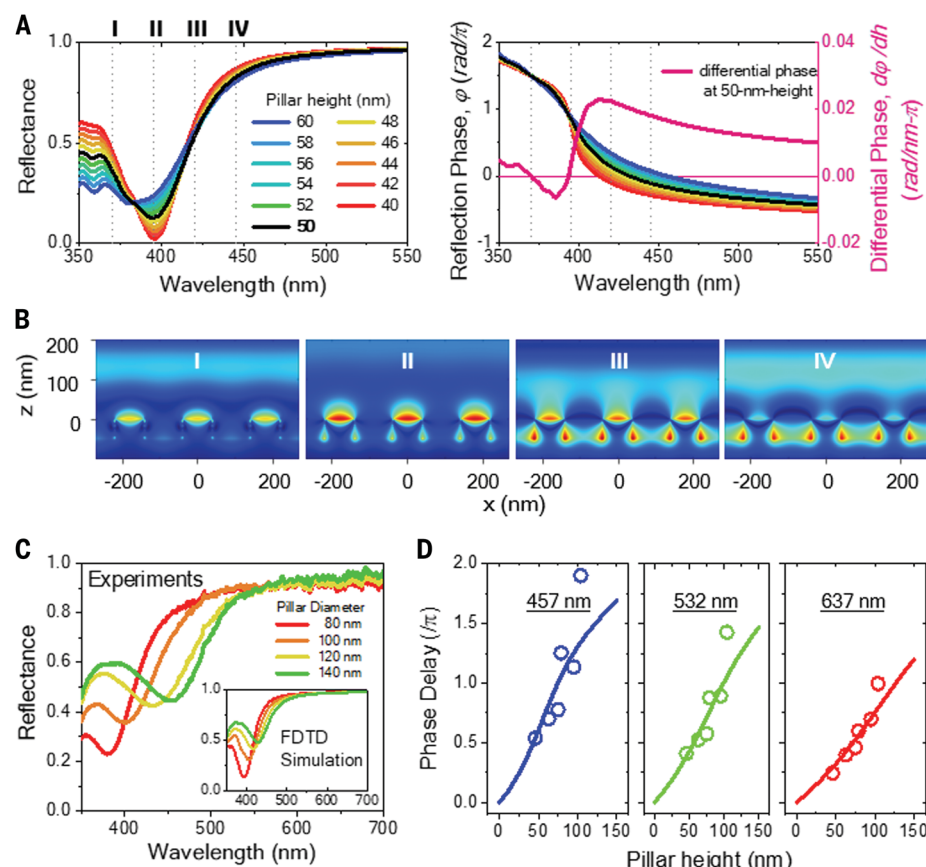


Fig. 2. Comparison in EL performances between meta-OLEDs (solid curves) and color-filtered white OLEDs (dashed curves). (A) EL spectra of OLEDs driven at $3\ \text{mA}/\text{cm}^2$. Hybrid-type RGB meta-OLED pixels are applied with a flat Ag mirror for the blue spectrum and with metamirrors for the green and red spectra. White-OLED parts are all identical. (B) Luminance as a function of the current density. The slope indicates the luminance efficiency.

mirrors as in the upper row, but the resonance wavelength of the flat region is shifted into the green region (520 nm) by increasing the thickness of the hole-transport layer. Compared with the emission wavelengths of the upper panels, those of the lower panels exhibit an overall redshift, and the red pixels “reset” to blue by operating on the next resonance order m . These studies clearly indicate that appropriate combinations of the OLED device stack and metamirror designs can be taken to create any desired color across the visible spectrum.

We compare the device performance of our meta-OLED to that of color-filtered white OLEDs (Fig. 2). To ensure a fair comparison, all devices have an identical white-OLED stack and are driven at the same current density ($3\ \text{mA}/\text{cm}^2$). The emission spectra of the color-filtered OLEDs were obtained by convolving the measured white spectrum with the spectral response of known color filters (fig. S6). The solid curves show spectra taken from the meta-OLED devices. The blue spectrum is taken from a pixel with a flat mirror, whereas the

Fig. 3. Reflectance behavior of metamirrors comprised of a rectangular array of cylindrical nanopillars. (A) FDTD simulations of the spectral reflectance and reflection phase for metamirrors with a nanopillar diameter (d) of 80 nm, a pitch (p) of 180 nm, and heights (h) varying from 40 to 60 nm. The resonance wavelength λ_r is 395 nm. Differential phase ($\delta\phi/\delta h$) indicates the phase change with a 1-nm increase in pillar height. (B) Magnetic field (H_y) distributions incident on the 50-nm-high metamirror in (A). The incident wavelengths for panels I to IV are 370, 395, 420, and 445 nm, respectively. As the wavelength of the incident light becomes longer than λ_r , the confined mode gradually moves into the gap between the nanopillars (III and IV). (C) Measured reflectance spectra of the metamirrors with four different nanopillar diameters ($h = 50$ nm, spacing = 100 nm). The inset shows the FDTD simulation result. (D) Dependence of the phase delay on the nanopillar height at RGB wavelengths for metamirrors with 80-nm-diameter pillars. The open circles (or solid curves) indicate the measured (or FDTD-simulated) values.



green and red spectra are obtained from pixels with differently designed metamirrors (fig. S7). This hybrid combination of FP cavities and metacavities is favorable for RGB pixilation of meta-OLED displays. The emission from the meta-OLED pixels (solid curves) is about twice as high as, and spectrally narrower than, the emission from the color-filtered white OLED pixels (dashed curves in Fig. 2A). These benefits are derived from the Purcell effect, by which the radiative decay rate and angular radiation properties of emitters can be controlled by tailoring their local environment (21, 22). We can selectively activate one RGB dopant at a time by having its emission satisfy the resonance condition, and this results in the observed enhancement of internal quantum efficiency (fig. S8). Because the metamirrors offer greater design freedom of the cavity and the placement of emitter layers, the coupling of emitters to the desired FP modes can be optimized, and losses to undesired waveguide modes reduced. Figure 2B shows that increases of internal quantum efficiency and outcoupling efficiency work in tandem to produce a higher luminance efficiency, as measured with a standard spectroradiometer (SR-3AR, Topcon). This low-numerical aperture measurement is favored in microdisplay applications, which require smaller divergence emission for higher coupling efficiency into headset combiners.

Further improvements in desirable Purcell enhancements and device performance can be obtained by controlling the orientation of the emitting molecules and by optimization of the metamirror reflectivity (fig. S9). The full width at half maximum (FWHM) for R, G, and B pixels, which reflects the color purity of a display, is accordingly narrowed from 44, 49, and 28 nm in the color-filter method to 32, 28, and 19 nm in meta-OLEDs. The narrow optical bandwidth of meta-OLEDs can reach ~90% color agreement with the BT2020 recommendation, which outlines the most rigorous color gamut standard to date for ultrahigh-definition television (23).

Next, we discuss our design considerations for the metamirrors. To demonstrate the benefits of the meta-OLED concept over the use of white OLEDs with color filters, we need to satisfy two key requirements: The metamirrors must afford broad tunability of the reflection phase across the visible wavelength range and must offer high reflectance (>90%) to ensure high luminance efficiency and color purity (14, 15). Previous studies in the radio frequency and visible spectral ranges have shown that high-impedance metasurface mirrors can offer such desirable traits (9, 11, 24). These devices have been created by patterning a metal surface with grooves, dimples, or pillars. To illustrate the optical properties of such

metamirrors, we first discuss finite-difference time-domain (FDTD) simulations of the spectral reflectance and reflection phase for a rectangular array of nanopillars with a diameter of 80 nm, a pitch of 180 nm, and a height varying from 40 to 60 nm (Fig. 3A). These simulations show a pronounced resonance dip in the reflectivity spectrum at 395 nm. Field plots show that at shorter wavelengths (370 nm), plasmons are excited just on top of the pillar surface (Fig. 3B, panel I), and the reflection phase only weakly depends on pillar height (Fig. 3A, red curve). On resonance, we can also see a clear excitation of gap plasmons that live between the pillars (Fig. 3B, panel II). The excitation of the gap modes provides an effective route to tune the reflection phase with pillar height. Whereas the reflectivity is low exactly on resonance, it rapidly increases to acceptable values as the illumination wavelength increases (Fig. 3A). An effective tuning of the reflection phase with pillar height is also observed on the long-wavelength side of the resonance, making this a desirable operating regime (Fig. 3B, panels III and IV).

To verify the reflection behavior, we create two sets of metamirrors with reflection properties modified by varying either the nanopillar height or diameter. The prepared metamirrors have rectangular lattices with 100-nm gaps.

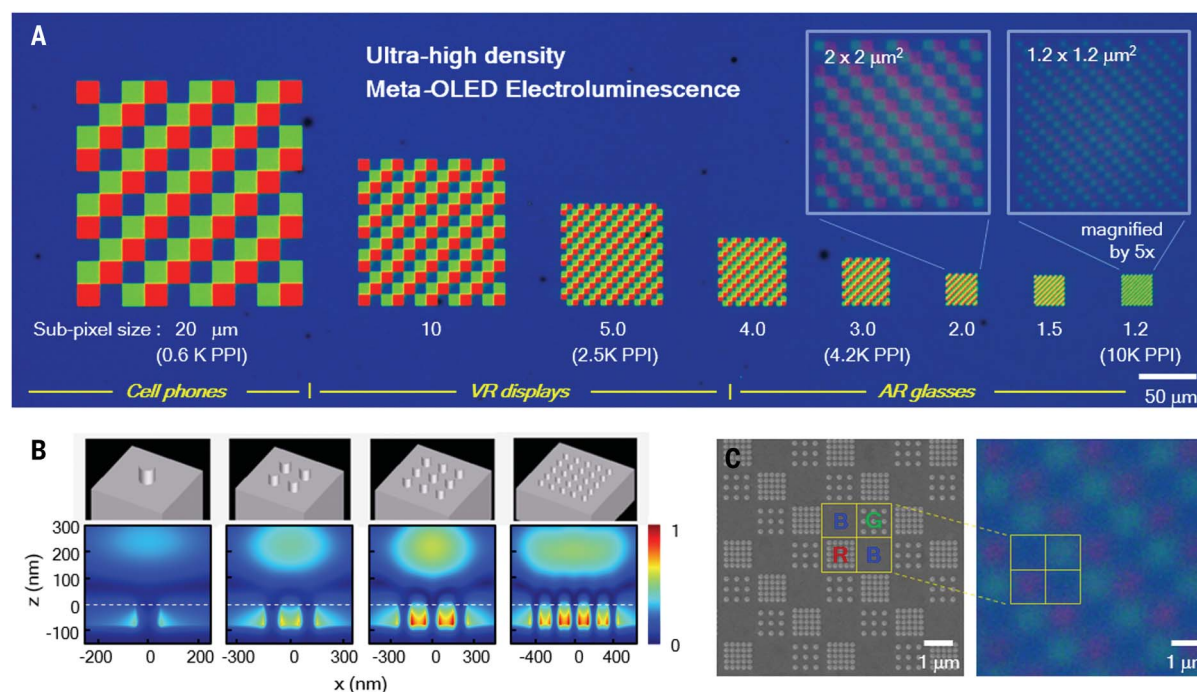


Fig. 4. Ultrahigh density, RGB-pixelated meta-OLEDs. (A) EL images of the interlaced RGB meta-OLEDs designed to determine the pixel-scaling limit for meta-OLEDs. The interlaced RGB pixels are seen in (C). The nanopillars in the green and red metamirrors have identical diameters (100 nm) and heights (80 nm) but different pitches of 340 and 200 nm, respectively. The insets show the fivefold magnifications of 2.0- and 1.2- μm subpixels. Pixel density is

calculated under the consideration of a BGRB arrangement. VR, virtual reality; AR, augmented reality. (B) FDTD-simulated H_y -field distribution ($\lambda = 620$ nm) on the critically downscaled red metamirrors. (C) SEM image and its corresponding EL image of 1.2- μm subpixel pattern. The yellow box indicates a BGRB pixel. The green subpixel has dimensions of only three nanopillars by three nanopillars.

First, we measured the dependence of their spectral reflectance on the diameter by using 50-nm-high nanopillars (Fig. 3C). As the diameter increases from 80 to 140 nm, the resonance dip in the reflection spectrum shifts toward longer wavelengths and the resonance absorption decreases, in agreement with FDTD simulations (Fig. 3C, inset). The redshift makes intuitive sense when we realize that the dense forest of nanopillars serves as an anisotropic effective medium with a high effective index for light waves propagating along the pillar direction. Physically, this high index is derived from the high mode index of the gap plasmons that can be excited in the gaps between the pillars. The metamaterial mirrors with 80-nm-diameter pillars provide a very high reflectance across the visible spectrum. Next, the height-dependence of the reflection phase is determined for metamirrors with 80-nm-diameter pillars (Fig. 3D). The achievable reflection phases of prepared metamirrors were directly measured by using a Michelson interferometer and lasers with emission wavelengths close to the RGB colors of the display (fig. S10). The measurements are consistent with the FDTD simulations (solid lines). We find that for all RGB wavelengths, the reflection phase increases quasi-linearly with the pillar height, as expected for a Gires-Tournois cavity structure (i.e., an asymmetric FP cavity with one non-

transmissive mirror) (25). We observe the largest phase changes in the blue region (457 nm) near the resonant peak, and the phase change is somewhat reduced for the longer green (532 nm) and red (637 nm) wavelengths. We find that a pillar height of 80 nm can provide sufficient tuning of the reflection phase at all wavelengths to allow device designs with a constant cavity thickness. The effective cavity lengths can simply be tuned by changing the local nanopillar pitch and diameter at a constant pillar height. Consistent with theory, our results show that the effective index of the nanopillar medium (including mode index of gap plasmons) rapidly increases with decreasing nanopillar pitch. A lower pillar density thus results in a lower effective index and a reduced effective cavity length.

Finally, the pixel scalability of meta-OLEDs is experimentally evaluated with interlaced RGB cavities. For ease of fabrication, green and red metamirrors were designed with only 80-nm-high nanopillars. This design enables us to engrave the green and red metamirrors in a nanoimprint lithography master mold in a single photolithography step without having to consider overlay errors.

The RGB subpixels were square in shape, with alternating RGB patterns, and have been reduced in size from mobile display levels

[400 pixels per inch (PPI)] to ultrahigh density μ -displays (10,000 PPI). Figure 4A shows EL images of the RGB pixelated meta-OLEDs taken with a conventional optical microscope. In large subpixels (e.g., 10 and 20 μm), the clear RGB colors validate that the phase tuning of metamirrors is appropriately achieved. Surprisingly, even with downscaling of the subpixel size to 2.0 and 1.2 μm , no appreciable color distortion or luminance reduction was observed in the metacavity pixels. They appear somewhat blurry, owing to the resolution limit of optical microscopy (OM) (Fig. 4C, right). FDTD simulations also support the possibility of realizing wavelength-scale, pixelated meta-OLEDs (Fig. 4B and fig. S11). For the metamirror of the red cavity, the strong gap resonance appears in arrays with dimensions of at least three nanopillars by three nanopillars and behaves similarly to those of infinite periodic arrays. Small differences in reflection phase that result from critically reducing the number of pillars in a pixel can be accounted for with a subtle redesign of the pillar geometry. According to FDTD simulations, the two-by-two (or three-by-three) nanopillar arrays for green (or red) pixels are at the downscaling limit of meta-OLEDs and are truly at the wavelength scale (~ 0.7 μm). Previously, a metasurface color printing was demonstrated at the optical diffraction limit

(250 nm by 250 nm); in agreement with our simulation results, this work showed that a two-by-two array of four nanodisks is the minimum pixel unit (26). In this case, the 1.2- μm -subpixel displays correspond to a pixel density of 10,000 PPI in an RGBG arrangement and to 15,000 PPI in a pentile-type arrangement (two subpixels in a pixel) (27).

To date, FMMs and color filters have played an important role in the development of OLED displays and have been key to the commercial success of these applications. However, the next generation of microdisplays for augmented reality applications require substantially higher luminance ($>10,000\text{ cd/m}^2$) and pixel density ($>5000\text{ PPI}$) than the displays in current products, such as mobile phones or televisions (18). To satisfy all of these requirements, OLEDs must now overcome technical limits, the low pixel density associated with FMMs, and the low luminance efficiency resulting from the use of absorptive color filters. We have demonstrated that the presented metaphotonic technology offers new possibilities for implementing highly efficient RGB pixels in OLEDs without relying on FMMs and color filters. Our approach can deliver a twofold increase in luminescence efficiency and a higher color purity than color-filtered white-light OLEDs and an ultrahigh pixel density of 10,000 PPI. The role of metamirrors can be expanded to solve other intrinsic problems with conventional microcavities. By engineering the wavelength-dependent phase response of the metamirror, we can artificially manipulate the free spectral range of the cavity, which can then be

used to suppress the undesired blue sideband (third-order blue) in the red pixel (second-order red), enabling further improvements in color purity (figs. S12 and S13). Typical angular color shifts of conventional microcavity OLEDs can also be markedly reduced by engineering the angle dependence of the metamirror reflection phase (28) (figs. S13 and S14). Given the myriad of advantages demonstrated in this study, we expect metaphotonic OLEDs to emerge as the leading technology for the next generation of microdisplays and to become one of the most practical applications of metaphotonic technology (29).

REFERENCES AND NOTES

1. A. Perot, C. Fabry, *Astrophys. J.* **9**, 87–115 (1899).
2. J. Barnes, *Science* **30**, 29–30 (1909).
3. E. F. Schubert et al., *Science* **265**, 943–945 (1994).
4. N. Jukam, *Nat. Photonics* **13**, 823–825 (2019).
5. R. Meerheim, R. Nitsche, K. Leo, *Appl. Phys. Lett.* **93**, 043310 (2008).
6. R. Ameling, D. Dregely, H. Giessen, *Opt. Lett.* **36**, 2218–2220 (2011).
7. A. M. Shaltout, J. Kim, A. Boltasseva, V. M. Shalae, A. V. Kildishev, *Nat. Commun.* **9**, 2673 (2018).
8. J. Flannery, R. Al Maruf, T. Yoon, M. Bajcsy, *ACS Photonics* **5**, 337–341 (2018).
9. M. Esfandyarpour, E. C. Garnett, Y. Cui, M. D. McGehee, M. L. Brongersma, *Nat. Nanotechnol.* **9**, 542–547 (2014).
10. V. A. Fedotov, A. V. Rogacheva, N. I. Zheludev, P. L. Mladyonov, S. L. Prosvirnin, *Appl. Phys. Lett.* **88**, 091119 (2006).
11. M. Esfandyarpour, A. G. Curto, P. G. Kik, N. Engheta, M. L. Brongersma, *Nat. Commun.* **9**, 3224 (2018).
12. N. Yu, F. Capasso, *Nat. Mater.* **13**, 139–150 (2014).
13. Y.-W. Huang et al., *Nano Lett.* **16**, 5319–5325 (2016).
14. C. Xiang, W. Koo, F. So, H. Sasabe, J. Kido, *Light Sci. Appl.* **2**, e74 (2013).
15. M. Wang, J. Lin, Y.-C. Hsiao, X. Liu, B. Hu, *Nat. Commun.* **10**, 1614 (2019).
16. C.-W. Han et al., *SID Symp. Dig. Tech. Pap.* **45**, 770–773 (2014).

17. H.-J. Kim et al., *J. Disp. Technol.* **12**, 526–531 (2016).
18. A. Ghosh et al., *SID Symp. Dig. Tech. Pap.* **47**, 837–840 (2016).
19. W. Song et al., *SID Symp. Dig. Tech. Pap.* **50**, 46–49 (2019).
20. B. E. A. Saleh, M. C. Teich, in *Fundamentals of Photonics* (Wiley, ed. 2, 2019), pp. 436–446.
21. H. Cho et al., *Opt. Express* **27**, 11057–11068 (2019).
22. S. Hofmann, M. Thomschke, B. Lüssem, K. Leo, *Opt. Express* **19** (Suppl 6), A1250–A1264 (2011).
23. E. Jang, Y. Kim, Y.-H. Won, H. Jang, S.-M. Choi, *ACS Energy Lett.* **5**, 1316–1327 (2020).
24. D. Sievenpiper, L. Zhang, R. F. J. Broas, N. G. Alexopolous, E. Yablonovitch, *IEEE Trans. Microw. Theory Tech.* **47**, 2059–2074 (1999).
25. S. I. Maslovski, M. G. Silveirinha, *Phys. Rev. B* **80**, 245101 (2009).
26. K. Kumar et al., *Nat. Nanotechnol.* **7**, 557–561 (2012).
27. J.-H. Lee, K.-R. Kim, C.-S. Kim, in *Proceedings of the 2017 IEEE International Symposium on Circuits and Systems (ISCAS)* (IEEE, 2017), doi:10.1109/ISCAS.2017.8050386.
28. K.-T. Lee, S. Y. Han, Z. Li, H. W. Baac, H. J. Park, *Sci. Rep.* **9**, 14917 (2019).
29. G. Tan et al., *Opt. Express* **25**, 33629–33642 (2017).

ACKNOWLEDGMENTS

Funding: No funding. **Author contributions:** W.-J.J., M.L.B., and S.H.S.: conceptualization and writing. J.K., M.E., and S.S.: software. S.-H.L., H.K., J.C.B., A.J., M.-J.K., S.H.H., and Y.-N.K.: validation. S.-H.K. and S.H.: writing and supervision. **Competing interests:** W.-J.J., M.L.B., and M.E. are inventors on a patent application related to this work filed by Samsung Electronics Co. Ltd. (U.S. 10615372, 4 April 2020). The authors declare no other competing interests. **Data and materials availability:** All data needed to evaluate the conclusions in the paper are present in the paper and/or the supplementary materials.

SUPPLEMENTARY MATERIALS

science.sciencemag.org/content/370/6515/459/suppl/DC1
Materials and Methods
Supplementary Text
Figs. S1 to S14
References

18 May 2020; accepted 7 September 2020
10.1126/science.abc8530

DEVELOPMENTAL BIOLOGY

Lineage analysis reveals an endodermal contribution to the vertebrate pituitary

Peter Fabian¹, Kuo-Chang Tseng¹, Joanna Smeeton^{1,2}, Joseph J. Lancman³, P. Duc Si Dong^{3,4}, Robert Cerny⁵, J. Gage Crump^{1*}

Vertebrate sensory organs arise from epithelial thickenings called placodes. Along with neural crest cells, cranial placodes are considered ectodermal novelties that drove evolution of the vertebrate head. The anterior-most placode generates the endocrine lobe [adenohypophysis (ADH)] of the pituitary, a master gland controlling growth, metabolism, and reproduction. In addition to known ectodermal contributions, we use lineage tracing and time-lapse imaging in zebrafish to identify an endodermal contribution to the ADH. Single-cell RNA sequencing of the adult pituitary reveals similar competency of endodermal and ectodermal epithelia to generate all endocrine cell types. Further, endoderm can generate a rudimentary ADH-like structure in the near absence of ectodermal contributions. The fish condition supports the vertebrate pituitary arising through interactions of an ancestral endoderm-derived proto-pituitary with newly evolved placodal ectoderm.

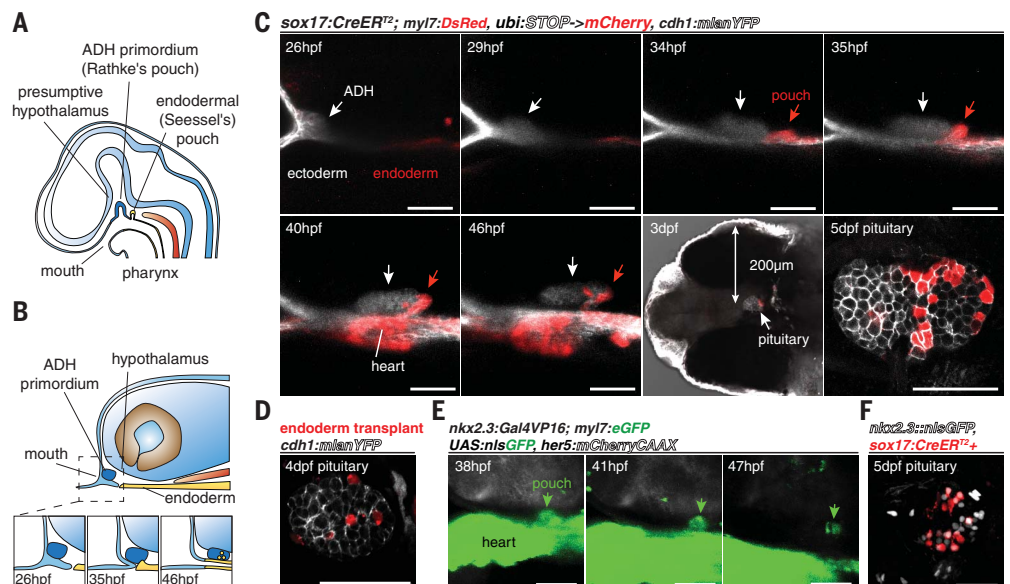
Along with the olfactory, lens, and otic placodes, the adenohypophysis (ADH) is thought to derive exclusively from head ectoderm (1, 2). Whereas the ADH generates the endocrine portion of the pituitary, the neural portion arises from the ventral hypothalamus. During embryogenesis, an epithelial invagination of the ectoderm called Rathke's pouch (3) is induced by the ventral brain and contributes to a single ADH placode. Just posterior to Rathke's pouch lies

Seessel's pouch (4), an outpocketing of the anterior-most endoderm whose function has long remained a mystery (Fig. 1A). Older histological studies had postulated contributions of Seessel's pouch to head structures, including the ADH in birds and mammals (5–8), yet definitive evidence had been lacking. Using lineage tracing, time-lapse imaging, and single-cell RNA sequencing (scRNAseq) in zebrafish, we demonstrate substantial contribution of endoderm-derived cells to the ADH

primordium and all the resultant endocrine cell types of the adult pituitary.

To characterize ADH development, we performed time-lapse imaging in conjunction with three independent approaches to label endoderm-derived cells. Starting at 24 hours postfertilization (hpf), frontal-view time-lapse recordings of a ubiquitous enhanced green fluorescent protein (eGFP) line (*ubi:loxP-eGFP-STOP-loxP-mCherry*) revealed invagination of the ADH placode at the front of the head, consistent with formation of Rathke's pouch in other vertebrates (movie S1). We next labeled early endoderm by treating *sox17:CreER^{T2}; ubi:loxP-eGFP-STOP-loxP-mCherry* fish (9) with 4-OH-tamoxifen (4OHT) during gastrulation (4 to 6 hpf). Confocal imaging confirmed 4OHT-dependent Cre-mediated excision of the *loxP-eGFP-loxP* cassette to drive mCherry expression only in endoderm (fig. S1, A and B). Time-lapse microscopy from 36 to 49 hpf revealed a small group of mCherry⁺ cells budding dorsally from the anterior-most pharyngeal endoderm to join the ADH (fig. S2A and movie S2). To image endodermal morphogenesis in relation to earlier placode development, we performed time-lapse microscopy from 26 to 46 hpf in 4OHT-treated *sox17:CreER^{T2}; ubi:loxP-STOP-loxP-mCherry* fish carrying a *cdh1:mlanYFP* transgene to label epithelial cell membranes (Fig. 1, B and C, and movies S3 and S4). The ectodermal

Fig. 1. Time-lapse analysis of endodermal contributions to the ADH. (A) During embryogenesis, the ectodermal Rathke's pouch is induced by the hypothalamus and lies adjacent to the endodermal Seessel's pouch. (B) Schematic of endoderm-lineage contribution to the ADH. (C) Representative images from time-lapse recording of 4OHT-treated *sox17:CreER^{T2}; ubi:loxP-STOP-loxP-mCherry; cdh1:mlanYFP* fish show invagination and posterior transit of ectodermal ADH and formation of an endodermal pouch that detaches from the pharynx and fuses to the ADH. Ventral imaging after lower-jaw dissection reveals the deep location of the pituitary, which is imaged at high resolution at 5 dpf. (D) Confocal section shows endodermal contributions to pituitary. (E) Labeling by an *nkx2.3:Gal4VP16* transgene shows similar endodermal pouching and incorporation into the posterior portion of the ADH. The hypothalamus is visualized by *her5:mCherryCAAX* (white). (F) At 5 dpf, co-localization of *sox17:CreER^{T2}-* and *nkx2.3:Gal4VP16*-labeled cells is observed in the pituitary. *myl7* transgenes label the heart in (C) (red) and (E) (green). Scale bars, 50 μ m.



¹Department of Stem Cell Biology and Regenerative Medicine, Eli and Edythe Broad CIRM Center for Regenerative Medicine and Stem Cell Research, W.M. Keck School of Medicine, University of Southern California, Los Angeles, CA 90033, USA. ²Columbia Stem Cell Initiative, Department of Rehabilitation and Regenerative Medicine, and Department of Genetics and Development, Columbia University Irving Medical Center, New York, NY 10032, USA. ³Human Genetics Program, Sanford Burnham Prebys Medical Discovery Institute, La Jolla, CA 92037, USA. ⁴Graduate School of Biomedical Sciences, Sanford Burnham Prebys Medical Discovery Institute, La Jolla, CA 92037, USA. ⁵Department of Zoology, Charles University, Prague, Czech Republic.

*Corresponding author. Email: gcrump@usc.edu

placode is initially separate from the more posterior endoderm. As the placode moves inward, an endodermal bud projects dorsally from the anterior-most endoderm, fuses with the posterior portion of the placode, and detaches from the pharynx. Compared with no labeling in six of six dimethyl sulfoxide (DMSO)-treated controls, 4OHT treatment labeled $11 \pm 4\%$ of pituitary cells by 5 days postfertilization (dpf) ($N = 5$) versus $56 \pm 19\%$ of cells in pouches ($N = 5$), a fully endoderm-derived structure (fig. S1C and movie S5). Adjusting for incomplete conversion efficiency, our results indicate ~20% endodermal contribution to the zebrafish ADH.

We also used blastula-stage transplantation of rhodamine-labeled endodermal precursors into *cdh1:mlanYFP* hosts to confirm ADH contributions. Consistent with labeling by genetic recombination, time-lapse recordings from 29 to 40 hpf revealed budding, detachment, and fusion of the anterior-most endoderm with the ectodermal placode, with $8 \pm 5\%$ contribution to the pituitary by 4 dpf ($N = 5$) (Fig. 1D; fig. S2, B to D; and movies S6 and S7). In a third technique, we used an endoderm-specific *nkx2.3:Gal4VP16* transgene (10) to drive *UAS:nlsGFP* expression and observed similar budding, detachment, and fusion of endoderm to the posterior portion of the ADH (Fig. 1E and movie S8), with $14 \pm 6\%$ pituitary contribution in

nkx2.3:Gal4VP16; UAS:NfsB-mCherry; cdh1:mlanYFP fish at 3 dpf ($N = 5$) (fig. S3 and movie S9). In all approaches, time-lapse imaging revealed contribution of endodermal cells to the same posterior region of the ADH, and $25.0 \pm 18\%$ of *nkx2.3:Gal4VP16; UAS:nlsGFP* cells were co-labeled by *sox17:CreER^{T2}; ubi:loxP-STOP-loxP-mCherry* ($N = 5$) (Fig. 1F and movie S10).

We next investigated the fate of endoderm-derived cells in the pituitary. Analysis of 4OHT-treated *sox17:CreER^{T2}; ubi:loxP-STOP-loxP-mCherry* or endoderm transplant fish revealed extensive intermixing of endodermal and ectodermal cells throughout the 6-month adult pituitary, with no contribution in six of six DMSO-treated controls (figs. S1B and S5). RNA in situ hybridization in 4OHT-treated *sox17:CreER^{T2}; ubi:loxP-STOP-loxP-mCherry* fish revealed mCherry+ endoderm-lineage cells expressing markers of corticotropes and melanotropes (*pomca*) and somatotropes (*gh1*) in the embryonic (3 dpf) and adult (6-month) pituitaries (Fig. 2, A to F). After near complete ablation of Rathke's pouch ectoderm, using a previously validated *pitx3* morpholino (11), we observed an ADH-like structure composed of, in some cases, >95% *sox17:CreER^{T2}*-labeled endodermal cells. This ADH-like structure was properly positioned between the trabeculae and under the hypothalamus and expressed

the epithelial marker *cdh1:mlanYFP* and hormone-encoding gene *gh1* ($N = 14$) but not *pomca* ($N = 23$) [potentially owing to direct regulation of *Pomc* by Pitx proteins (12)] (Fig. 2, G to I). Whereas endodermal cell contribution increased from 10.3 ± 3.3 ($N = 6$) to 15.5 ± 5.1 ($N = 11$) ($P = 0.01$ two-tailed *t* test) upon ectoderm ablation, indicating some compensatory growth, ADH-like structures were significantly smaller (39 ± 5 cells in *pitx3*-MO versus 113 ± 10 cells in control, $P = 10^{-9}$ two-tailed *t* test) (fig. S4), with corresponding decreases in *gh1*+ cells (1.9 ± 1.8 *pitx3*-MO, 17.5 ± 3.4 control, $P = 10^{-5}$ two-tailed *t* test). Reciprocally, endoderm is dispensable for endocrine differentiation, as we observed similar numbers of *pomca*+ cells in the pituitaries of wild types and *sox32* mutants that completely lack endoderm (13) (22 ± 4 , $N = 6$ wild types versus 18 ± 2 , $N = 3$ mutants, $P = 0.085$ two-tailed *t* test) (Fig. 2I). Thus, endoderm has equal competence to ectoderm in forming endocrine cell types and generating a rudimentary ADH-like structure but requires interactions with placodal ectoderm for proper size and maturation of the pituitary.

To determine the full potential of endoderm-derived cells in the mature pituitary, we performed scRNAseq of adult pituitaries from 4OHT-treated *sox17:CreER^{T2}; ubi:loxP-eGFP-loxP-mCherry* fish or those with transplanted *ubi:loxP-eGFP-STOP-loxP-mCherry* (eGFP+)

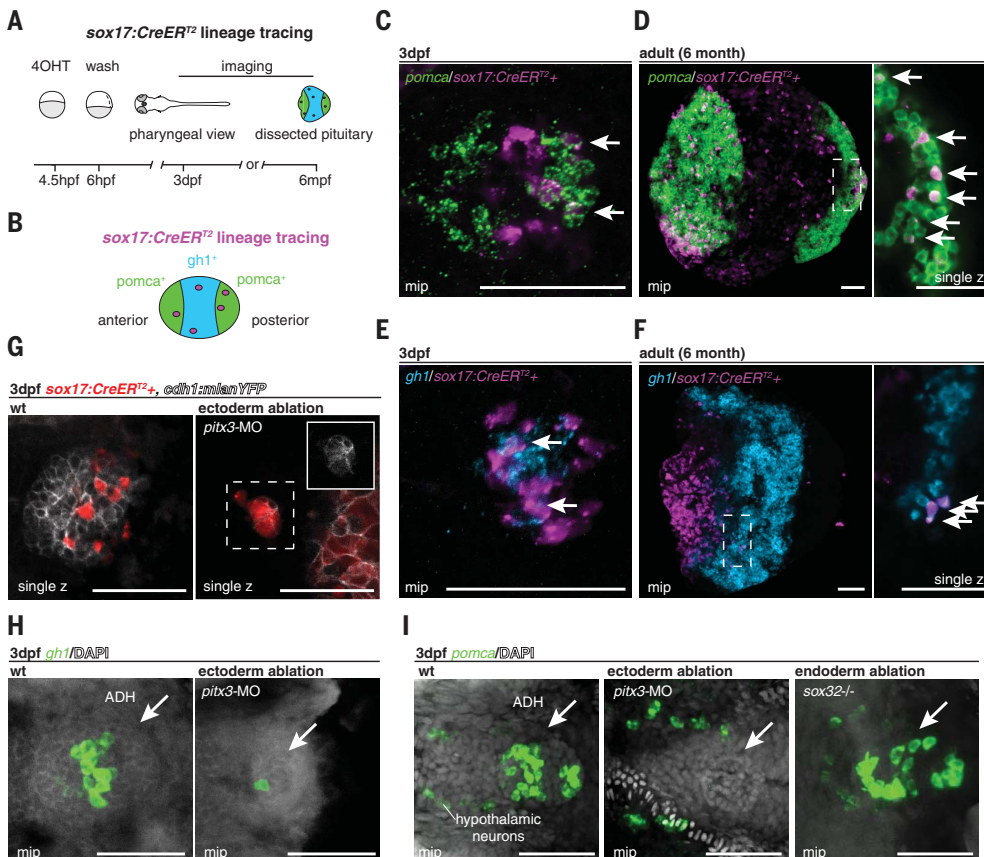


Fig. 2. Endodermal contributions to hormone-producing cells of the pituitary.

(A) Schematic of endoderm-lineage labeling followed by imaging of the stained larval and adult pituitary gland. (B) Schematic of the three anterior-posterior domains of the pituitary. (C to F) Confocal imaging of endoderm-lineage cells (anti-mCherry antibody, magenta) with RNA in situ hybridization for *pomca* (C and D) or *gh1* (E and F). Arrows designate double-positive cells. (G) After genetic ablation of ectodermal precursors by *pitx3*-MO injection, endodermal cells (red, *sox17:CreER^{T2}; ubi:loxP-STOP-loxP-mCherry* treated with 4OHT at 4 hpf) generate a reduced ADH-like structure that expresses *cdh1:mlanYFP* (white, insert). (H) Ectoderm ablation by *pitx3*-MO injection results in a reduced ADH-like structure that expresses *gh1* (green). (I) Expression of *pomca* is lost in *pitx3*-MO embryos lacking ectodermal contributions but not in *sox32* mutants lacking endoderm; hypothalamic neuron expression of *pomca* is unaffected in both cases. Arrows indicate ADH and nuclei are visualized by DAPI (white). Scale bars, 50 μ m. DAPI, 4',6-diamidino-2-phenylindole; mip, maximum intensity projection; wt, wild type.

endoderm. Barcoded cDNA libraries were prepared from fluorescence-activated cell-sorted live cells by using the 10X Genomics Chromium platform, followed by Illumina next-generation sequencing. After filtering for quality, we obtained data for 19,028 cells (average 1139 genes per cell) from two *sox17:CreER^{T2}* experiments (4634 and 6520 cells) and one transplantation experiment (7874 cells). Using Louvain clustering, we identified 10 cell clusters: 6 classical pituitary endocrine cell populations [corticotropes (*pomca*+/

tbx19), melanotropes (*pomca*+/*pax7a*), gonadotropes (*fshb*+/*lhb*), somatotropes (*pou1f1*+/*gh1*), lactotropes (*pou1f1*+/*prl*), and thyrotropes (*pou1f1*+/*tshb*)], 1 fish-specific endocrine population [somatolactotropes (*pou1f1*+/*smtla*+/*smtlb*)], 2 potential progenitor clusters (*isl1*+/*cga* and *prop1*+/*her6*), and a small cluster with characteristics of endothelial cells (*flila*+/*kdr1*+/*plvapa*), pituicytes (*cyp26b1*), and immune cells (*cd74a*+/*cd74b*+/*pfn1*+/*apoc1*+/*ccr9a*, potentially macrophages) (Fig. 3 and figs. S5 to S12). The presence of all tetrapod

hormone-releasing subtypes (14) in zebrafish supports evolutionary conservation of the pituitary across vertebrates, and common expression of *pou1f1* suggests that fish-specific somatolactotropes share a lineage with somatotropes, lactotropes, and thyrotropes. To identify endoderm-derived cells, we queried the scRNAseq data for expression of *mCherry* (*sox17:CreER^{T2}* tracing) or *eGFP* (endoderm transplantation) (Fig. 4 and figs. S7 to S12). We observed endodermal contributions to all major endocrine cell types and their

Fig. 3. Single-cell analysis of the zebrafish pituitary. (A) UMAP visualization shows the unsupervised clustering of the aggregate of three scRNAseq experiments, revealing 10 major clusters of pituitary cells present in zebrafish. (B) Dot-plot shows the percentage (pct. exp.) and average expression (avg. exp.) of cluster marker genes. (C) UMAP visualization of cluster marker genes. max, maximum; min, minimum; UMAP, Uniform Manifold Approximation and Projection.

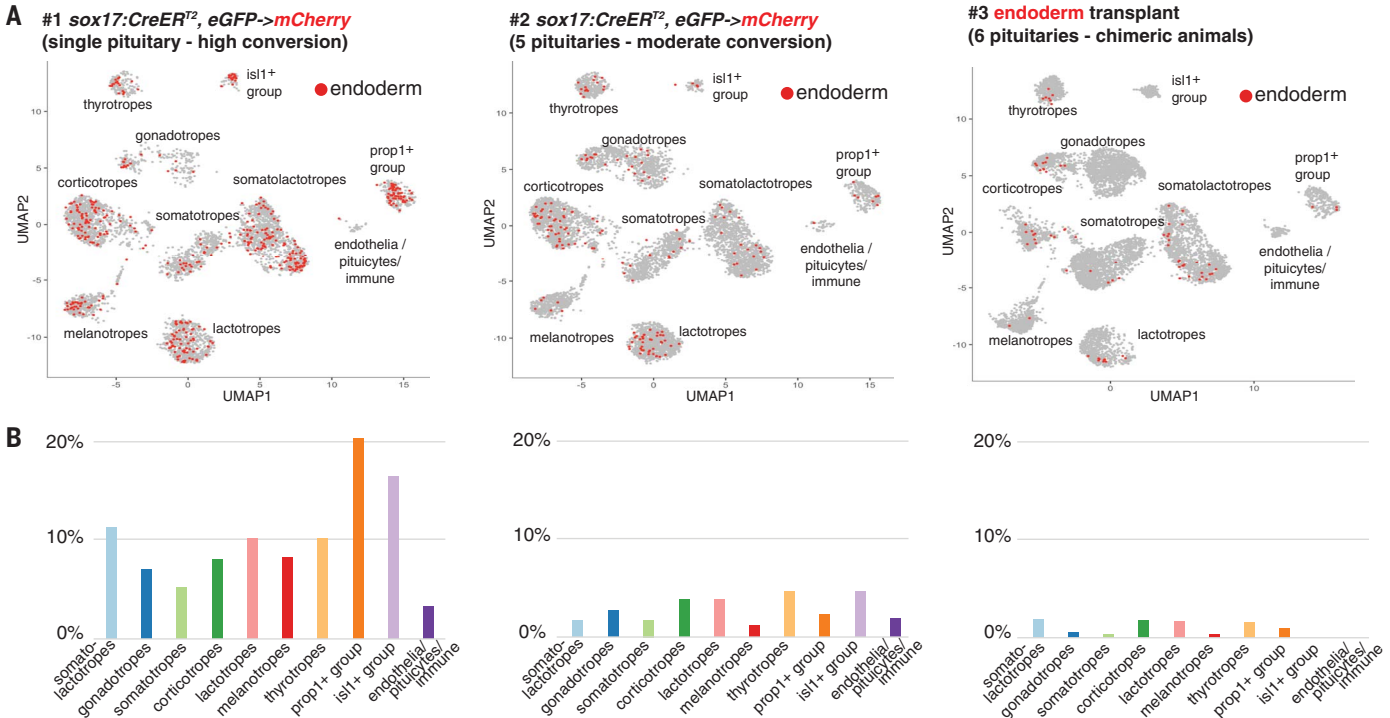
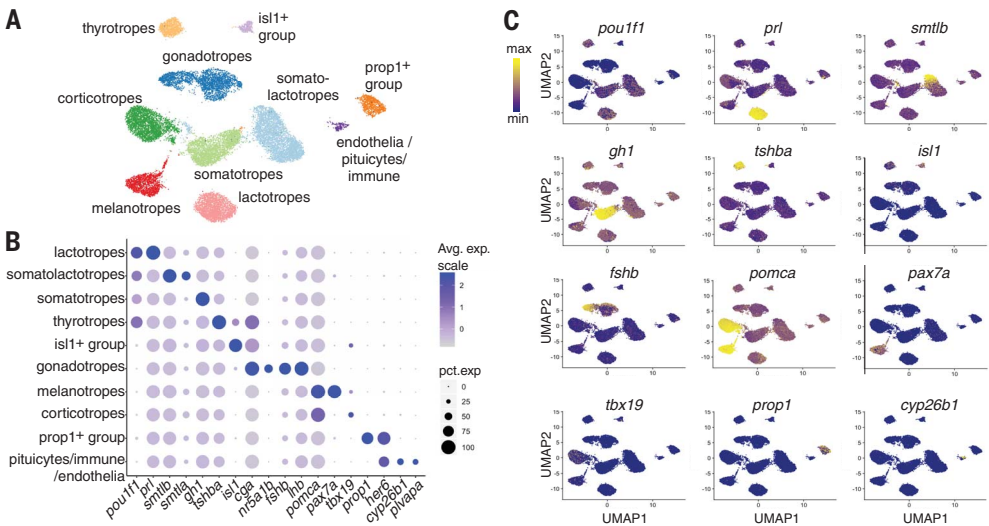


Fig. 4. Single-cell analysis reveals endodermal contributions to all endocrine cell types of the adult pituitary. (A) Endoderm marker gene expression in each of the three independent scRNAseq experiments. (B) Bar graphs show percentage contribution of endoderm-lineage cells to each cell cluster.

progenitors in three independent experiments (except for the *isl1+* group in transplants). Endodermal contributions to endocrine cells ranged from 5 to 11% for the high conversion *sox17:CreER^{T2}* pituitary, 1.3 to 4.5% for five pooled moderate conversion *sox17:CreER^{T2}* pituitaries, and 0.3 to 1.9% for six pooled transplant pituitaries. By contrast, we observed only a single *mCherry*⁺ cell contributing to the rare endothelia-pituitocyte-immune cluster for each *sox17:CreER^{T2}* experiment and no contribution for the transplant experiment, with re-clustering revealing these as immune cells (fig. S12). Consistent with a lack of contribution to endothelial cells, *sox17:CreER^{T2}* labeling did not overlap with an endothelial-specific *flila:eGFP* transgene in five of five larval (6 dpf) and two of two adult (5 months) pituitaries (fig. S13 and movie S11). Endodermal contributions to endocrine cells are underestimates given incomplete *sox17:CreER^{T2}* conversion and transplant efficiency, as well as substantial transcript dropout for *mCherry* (predicted 51 to 55% of cells) and *eGFP* (predicted 60% of cells) (fig. S7). Despite their initial contribution to the posterior portion of the embryonic ADH, these studies reveal that endodermal cells substantially intermix with ectodermal cells and can generate all endocrine cell types of the adult pituitary. The endoderm contributes to a number of other endocrine glands (e.g., pancreas, thyroid, and parathyroid), and hence, contributions to the pituitary may reflect a broader endocrine potential of the endoderm than previously appreciated.

Our findings of a dual epithelial origin of the zebrafish pituitary help resolve a long-standing controversy regarding the evolutionary and embryonic origins of the vertebrate pituitary. In the nonvertebrate chordate, amphioxus, the endoderm-derived pre-oral pit (Hatschek's diverticulum) lies adjacent to the central nervous system and expresses placodal genes (*Pitx1*, *Lhx3*, *Six1/2*, and *Eya1*) (15, 16) and the pituitary-specific transcription factor *Pou1f1* (17). Although nonvertebrate chordates

lack the defining hormone-encoding genes of vertebrate pituitary cells, it has been suggested that the vertebrate pituitary arose through modifications of an endoderm-derived structure in ancestral chordates (2). Although the pituitary has been considered a strictly ectodermal structure, including in jawless vertebrates such as hagfish (18), older histological studies had suggested endodermal contributions to the hagfish ADH (19), and transient contact of endoderm-derived Seessel's pouch and ectoderm-derived Rathke's pouch has been observed in embryos of chick (5, 8), rabbit (5), rat (6), and dog (7). In zebrafish, our high-resolution time-lapse imaging allowed us to definitively determine that endoderm-derived cells of Seessel's pouch detach and fuse with the ectodermal Rathke's pouch, followed by intermixing in the ADH primordium and resultant pituitary. It will be interesting to determine the extent to which the reported associations of Seessel's pouch endoderm and Rathke's pouch ectoderm in other vertebrates result in dual epithelial contributions to the pituitary.

We propose that endodermal contributions to the zebrafish pituitary may represent the vestiges of the embryonic structure giving rise to the endoderm-derived pituitary-like organ in ancestral chordates. As in nonvertebrate chordates, endoderm can form a rudimentary ADH-like structure in the near absence of ectodermal contributions in zebrafish. In the early vertebrate lineage, new interactions of endoderm with placodal ectoderm and likely also the ventral hypothalamus may have promoted endocrine differentiation in an equally competent endodermal and ectodermal epithelial field. Analogous contributions of endodermal cells to classically considered ectodermal structures has been shown for teeth in amphibians (20) and external epithelial head structures in basal fishes (21), revealing extensive interchangeability of ectodermal and endodermal epithelia in generating diverse cranial organs.

REFERENCES AND NOTES

1. C. Gans, R. G. Northcutt, *Science* **220**, 268–273 (1983).
2. G. Schlosser, *Int. J. Dev. Biol.* **61**, 633–648 (2017).
3. M. H. Rathke, *Arch. Anat. Physiol. Wiss. Med.* **5**, 482–485 (1838).
4. A. Seessel, *Arch. Anat. Physiol.* **1**, 449–467 (1877).
5. W. J. Atwell, *Anat. Rec.* **10**, 19–38 (1915).
6. A. C. Bruni, *Internat. Monstsch. f. Anat. u. Physiol.* **31**, 129–237 (1994).
7. J. Nusbaum, *Anat. Anz.* **12**, 161–168 (1896).
8. G. St. Remy, *C.R. de la Societe de Biologie* **47**, 423–425 (1895).
9. D. Hockman et al., *eLife* **6**, e21231 (2017).
10. C. P. Choe et al., *Dev. Cell* **24**, 296–309 (2013).
11. S. Dutta et al., *Development* **132**, 1579–1590 (2005).
12. T. Lamourie et al., *Genes Dev.* **10**, 1284–1295 (1996).
13. T. Dickmeis et al., *Genes Dev.* **15**, 1487–1492 (2001).
14. L. Y. M. Cheung et al., *Endocrinology* **159**, 3910–3924 (2018).
15. Z. Kozmik et al., *Dev. Biol.* **306**, 143–159 (2007).
16. V. Soukup et al., *Evodevo* **6**, 5 (2015).
17. S. Candiani, N. D. Holland, D. Oliveri, M. Parodi, M. Pestarino, *Brain Res. Bull.* **75**, 324–330 (2008).
18. Y. Oisi, K. G. Ota, S. Kuraku, S. Fujimoto, S. Kuratani, *Nature* **493**, 175–180 (2013).
19. A. Gorbman, *Am. Zool.* **23**, 639–654 (1983).
20. V. Soukup, H. H. Epperlein, I. Horáček, R. Cerný, *Nature* **455**, 795–798 (2008).
21. M. Minarik et al., *Nature* **547**, 209 (2017).

ACKNOWLEDGMENTS

We thank M. Matsutani and J. DeKoeper Crump for fish care; N. Nelson and C. Arata for library preparation; J. Boyd at the USC Stem Cell Flow Cytometry Core; the high-performance computing core at USC; D. Ruble at the CHLA Sequencing Core; J. Eberhart, M. Swartz, and J. Everson for *sox32* mutant embryos; and C. Kimmel for curiosity about Seessel's pouch in zebrafish. **Funding:** This work was supported by NIH R35DE027550 to J.G.C.; NIH K99DE027218 to J.S.; W. M. Keck Foundation, NIH U01DK105541, and NIH DP2 DK098092 to P.D.S.D.; and GACR project 19-18634S to R.C. **Author contributions:** P.F., R.C., and J.G.C. conceived the project. P.F. performed all zebrafish experiments. P.F., J.S., and K.-C.T. performed scRNAseq. J.J.L. and P.D.S.D. contributed *sox17:CreER^{T2}* fish. P.F. and J.G.C. wrote the manuscript and performed data interpretation, with input from J.S., K.-C.T., and R.C. **Competing interests:** The authors declare no competing interests. **Data and materials availability:** All datasets generated from this study are available in the Gene Expression Omnibus repository under accession number GSE148591.

SUPPLEMENTARY MATERIALS

science.sciencemag.org/content/370/6515/463/suppl/DC1
Materials and Methods
Figs. S1 to S13
References (22–29)
MDAR Reproducibility Checklist
Movies S1 to S11

6 December 2019; accepted 4 September 2020
10.1126/science.aba4767

MICROBIOTA

Proximal colon-derived O-glycosylated mucus encapsulates and modulates the microbiota

Kirk Bergstrom^{1,2,*}, Xindi Shan^{1†}, David Casero³, Albert Batushansky⁴, Venu Lagishetty⁵, Jonathan P. Jacobs⁶, Christopher Hoover¹, Yuji Kondo¹, Bojing Shao¹, Liang Gao¹, Wesley Zandberg⁷, Benjamin Noyovitz⁷, J. Michael McDaniel¹, Deanna L. Gibson², Sepideh Pakpour⁸, Negin Kazemian⁸, Samuel McGee¹, Courtney W. Houchen⁹, Chinthapally V. Rao⁹, Timothy M. Griffin^{4,10}, Justin L. Sonnenburg¹¹, Rodger P. McEver^{1,10}, Jonathan Braun³, Lijun Xia^{1,10,*}

Colon mucus segregates the intestinal microbiota from host tissues, but how it organizes to function throughout the colon is unclear. In mice, we found that colon mucus consists of two distinct O-glycosylated entities of Muc2: a major form produced by the proximal colon, which encapsulates the fecal material including the microbiota, and a minor form derived from the distal colon, which adheres to the major form. The microbiota directs its own encapsulation by inducing Muc2 production from proximal colon goblet cells. In turn, O-glycans on proximal colon-derived Muc2 modulate the structure and function of the microbiota as well as transcription in the colon mucosa. Our work shows how proximal colon control of mucin production is an important element in the regulation of host-microbiota symbiosis.

In mammals, the colon houses a dense and diverse commensal microbiota, which has an impact on both health and disease (1–4). The colon mucus system modulates host-commensal symbiosis (5–10). Mucus is primarily a large polymeric network of Mucin-2 in mice and humans (Muc2 or MUC2, respectively), which is heavily O-glycosylated (11, 12). An established model is that colon mucus is primarily produced by goblet cells in the distal colon to initially form a single nonmobile inner mucus layer, tightly attached to the epithelium, which segregates microbiota from the colon mucosa (5, 13). The inner mucus layer subsequently becomes a loose mobile outer layer where microbiota reside (13, 14). However, how the mucus system forms and functions along the whole colon is unclear.

To address this question, we developed a whole-colon imaging method to analyze the origin and composition of mouse colonic mucus via sections of wild-type “colon coils” labeled with anti-Muc2 antibody, *Maackia amurensis* lectin II (MALII, recognizing α 2,3-linked sialylated and sulfated glycans) (15), and the general bacterial probe EUB338 (Fig. 1A and fig. S1, A to C) (16). We discovered that MALII was negative in most proximal colon goblet cells but was strongly positive in distal colon goblet cells (Fig. 1, A and B). In contrast, MALII was negative in the mucus layers throughout the colon, except in a previously

undescribed minor portion of the inner layer closest to the distal colon mucosal surface (fig. S2A). This suggests that (i) luminal mucus is mainly derived from the proximal colon, a finding supported by increased size and number of goblet cells and higher *Muc2* expression in the proximal versus distal colon (Fig. 1C and fig. S2B); and (ii) the inner layer consists of two distinct entities of Muc2 from the proximal or distal colon goblet cells. Notably, we found that MALII primarily marked sulfated O-glycans on Muc2 (fig. S3). Transcriptome analysis of healthy proximal versus distal colon revealed a significant difference in their gene expression profiles (>1000 genes, including *Muc2*) even among similar cell types including goblet cells. Collectively, these data underscore the functional uniqueness of these two colon regions (fig. S1D).

Whole-colon imaging showed that the luminal mucus layers were attached to bacteria-dense fecal pellets to create “bacteria-sparse” zones between pellets (Fig. 1, D to F, and fig. S2C) (16). This was confirmed by colonizing mice with a green fluorescent protein (GFP)-tagged gut symbiont, *Bacteroides thetaiotaomicron* (*B. theta*^{GFP}) (17), which was only found inside mucus-coated fecal pellets (fig. S4). These data indicate that proximal colon-derived mucus encapsulates bacteria in fecal pellets, which supports the idea that the mucus can associate with fecal pellets (18, 19). We found

that the mucus structure and segregating functions on freshly excreted fecal pellets and on fecal pellets in situ within their corresponding colon tissues were identical (Fig. 1, G and H, and fig. S5D) (16). [A mucus barrier layer was also detected on fecal surfaces of healthy primates (baboons) and humans (fig. S6).] These findings in mice were validated using unfixed (fig. S5) or unprocessed (fig. S2D) pellet-containing colon tissues and excreted pellets, excluding fixation artifacts.

Further analysis of the formation of the mucus coating revealed a stepwise establishment of the fecal-associated mucus layers, with a Muc2⁺MALII[−] layer associating with feces first in the proximal colon, followed by addition of a Muc2⁺MALII⁺ layer in the distal colon coinciding with appearance of Muc2⁺MALII⁺ goblet cells (fig. S7). The Muc2⁺MALII⁺ layer likely forms after compression as the fecal mass pushes it against the mucosal wall (fig. S8). Intact fecal mucus could be successfully extracted, and glycomics analysis further confirmed its similarity to proximal colon- versus distal colon-derived mucus (fig. S9 and table S1) (16). The mucus phenotype was reproduced in different inbred and outbred strains of mice of both sexes at different ages (fig. S10, A to E), as well as in rats (fig. S10, F and G). On the basis of these findings, we redefine the mucus system to reflect its origin, biochemical structures, and function (fig. S10H): The colon mucus system consists of a proximal colon-derived mucus “niche” and “barrier” layer, the latter composed of a proximal colon-derived “b1 layer” and a distal colon-derived “b2 layer” (Fig. 1H and fig. S10H).

We then asked how the b1 and b2 mucus barrier layers contribute to host-microbiota interactions in the colon. More than 80% of the mouse colon mucin mass is derived from ubiquitously expressed core 1-derived and proximal colon-expressed core 3-derived complex mucin-type O-glycans (20, 21). To determine the contribution of these O-glycans from different colon regions to overall mucus function, we generated mice lacking both types of O-glycans preferentially in the proximal colon (TM-DKO^{prox}), in the distal colon (TM-IEC *C1galt1*^{−/−}) (20), and in both the proximal and distal colon (TM-DKO) (Fig. 2A and fig. S11) (16). Analysis of mucus barrier status in tissues and fecal pellets showed significantly reduced mucus thickness in distal colons of TM-DKO^{prox} versus wild-type

¹Cardiovascular Biology Research Program, Oklahoma Medical Research Foundation, Oklahoma City, OK 73104, USA. ²Department of Biology, University of British Columbia, Okanagan Campus, Kelowna, British Columbia V1V 1V7, Canada. ³Inflammatory Bowel and Immunobiology Institute, Cedars Sinai Medical Center, Los Angeles, CA 90048, USA. ⁴Aging and Metabolism Research Program, Oklahoma Medical Research Foundation, Oklahoma City, OK 73104, USA. ⁵Vatche and Tamar Manoukian Division of Digestive Diseases, Department of Medicine, David Geffen School of Medicine at UCLA, Los Angeles, CA 90095, USA. ⁶Division of Gastroenterology, Hepatology and Parenteral Nutrition, VA Greater Los Angeles Healthcare System, Los Angeles, CA 90025, USA. ⁷Department of Chemistry, University of British Columbia, Okanagan Campus, Kelowna, British Columbia V1V 1V7, Canada. ⁸School of Engineering, University of British Columbia, Okanagan Campus, Kelowna, British Columbia V1V 1V7, Canada. ⁹Department of Internal Medicine, University of Oklahoma Health Sciences Center, Oklahoma City, OK 73104, USA. ¹⁰Department of Biochemistry and Molecular Biology, University of Oklahoma Health Sciences Center, Oklahoma City, OK 73104, USA. ¹¹Department of Microbiology and Immunology, Stanford University School of Medicine, Stanford, CA 94305, USA.

*Corresponding author. Email: lijun-xia@omrf.org (L.X.); kirk.bergstrom@ubc.ca (K.B.)

†These authors contributed equally to this work.

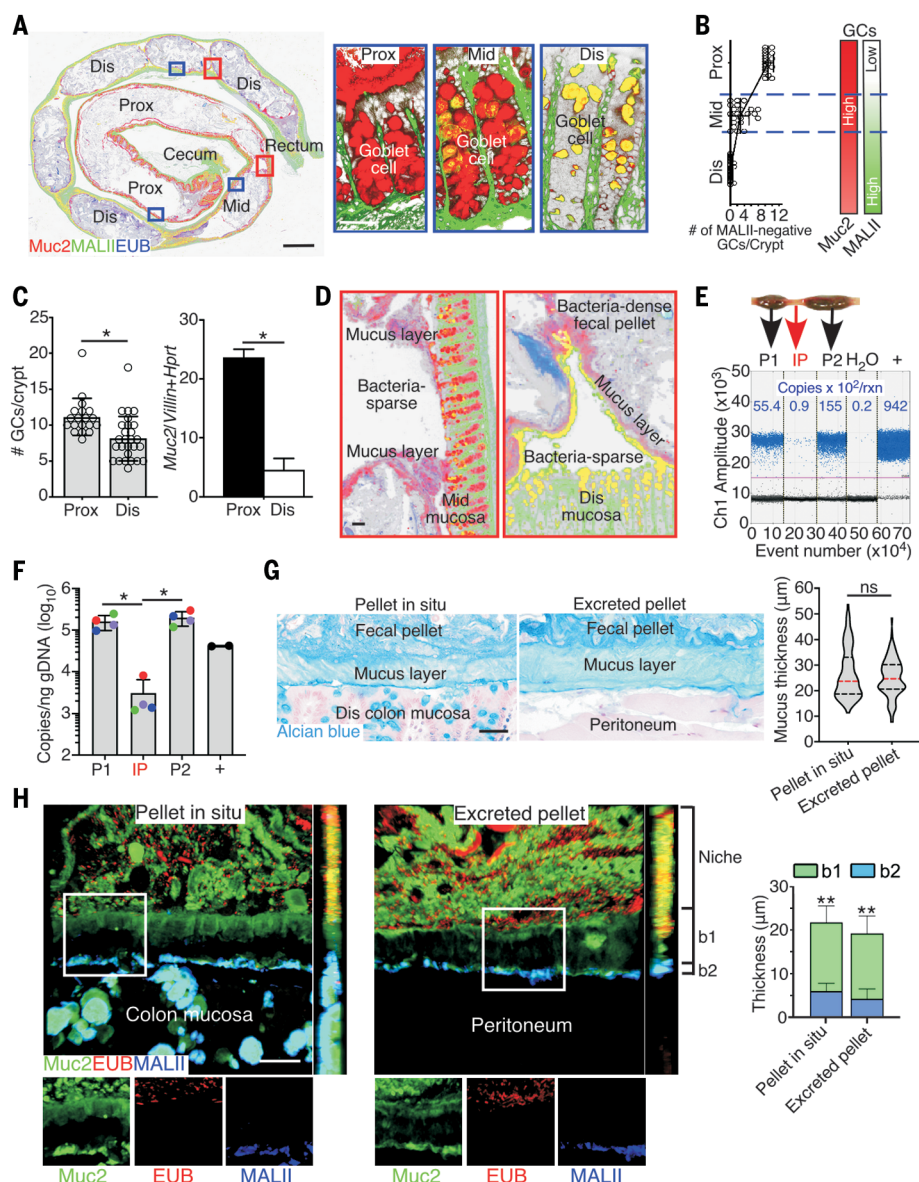


Fig. 1. Proximal colon-derived mucus encapsulates microbiota-containing fecal pellets. (A) Tiled immunofluorescent image of a longitudinal Carnoy's fixed paraffin-embedded (CFPE) wild-type whole colon coil section (left) with goblet cells highlighted (blue-boxed images, right). Prox, Mid, and Dis denote proximal, middle, and distal colon, respectively. (B) Left: Enumeration of Muc2⁺MALII[−] goblet cell numbers (GCs) in different colon regions. Right: Schematic GC Muc2 and MALII expression profile. (C) Left: Number of GCs per crypt. Right: Muc2 expression in colon epithelium [quantitative polymerase chain reaction (qPCR) normalized to Villin and Hprt]. (D) Magnified images of red boxed areas in (A). (E) Representative droplet digital PCR (ddPCR) scatterplot of the bacterial 16S rRNA gene of samples from wild-type distal colon with (P) or without pellets (inter-pellet, IP). H₂O, negative control; +, positive control. (F) Mean ddPCR 16S rRNA copy number among replicates. Each point represents one animal; each color denotes the same animal. (G) Left: Alcian blue-stained sections of tissues and feces. Right: Violin plot of median mucus thickness (median, red; quartiles, black). (H) Top left: Z-stacked confocal images of cross sections of colon with pellet or an excreted pellet wrapped in peritoneum; the narrow image at right shows the corresponding y/z plane. Bottom left: Single-colored images of white-boxed regions. Right: Thickness of the mucus layers. Scale bars, 4 mm [(A), left]; 20 μm [(A), right, (D), (G), and (H)]. Results are representative of two (C) or three [(A), (B), (G), and (H)] independent experiments each with $n = 4$ or 5 mice per experiment, or $n = 4$ mice pooled from two independent extractions [(E) and (F)]. Data are means \pm SD [(B), (C), (F), and (H)]. * $P < 0.05$, ** $P < 0.01$ [two-tailed unpaired t test in (C), left, and (F); Mann-Whitney test in (C), right, (F), and versus b2 layer in (H)]; ns, not significant.

mice (Fig. 2A), characterized by loss of the b1 layer, whereas the b2 layer remained relatively intact (Fig. 2B). In contrast, wild-type mice had both b1 and b2 layers, TM-IEC *C1galt1*^{−/−} mice had only a visible b1 layer, and TM-DKO lacked both (Fig. 2B). Loss of the b1 layer, but not the b2 layer, also significantly reduced the overall distance of the microbes to the mucosal tissue (Fig. 2B, lower panel). These results indicate that proximal colon-derived O-glycans form the b1 layer critical for segregating the microbiota from the host tissue.

To confirm that fecal pellets were encapsulated by proximal O-glycosylated mucus, we performed complementary analyses, which demonstrated that (i) the mucus coating of excreted pellets was diminished in TM-DKO^{prox} mice (Fig. 2C) as a result of rapid degradation of proximally secreted mucus (Fig. 2D); (ii) colonized *B. theta*^{GFP} was not encapsulated in TM-DKO^{prox} mice (fig. S12); (iii) the b1 and b2 layers were rescued on mucus-deficient fecal pellets transplanted into the proximal colon of wild-type but not TM-DKO mice (fig. S13); (iv) gavaged fluorescent beads were sequestered in the mucus-coated pellets within the colon of wild-type but not mutant mice (fig. S14, A to D); and (v) there was increased expression of *16S rRNA* within the inter-pellet tissues of TM-DKO^{prox} and TM-DKO mice relative to the wild type (fig. S14, E to G). The defective mucus coating was also observed in the native state (fig. S14, H and I). Physiopathologically, defective mucus encapsulation of fecal pellets in TM-DKO^{prox} mice was associated with increased susceptibility to spontaneous colitis (Fig. 2E) as well as acute intestinal injury (fig. S15), although disease severity was worst in TM-DKO mice, indicating that both b1 and b2 layers contribute to mucosal homeostasis. As expected, TM-IEC *C1galt1*^{−/−} mice developed disease as a result of their impaired mucus barrier function (Fig. 2, C and E, and fig. S16) (21). Notably, *Il10*^{−/−} mice, an alternative model of microbiota-dependent colitis (22), had an impaired b1 layer, associated with altered proximal colon homeostasis and increased distal mucosal microbial intrusion, despite an intact b2 layer (fig. S17). Collectively, our data show that the proximal colon is essential in producing the O-glycosylated mucus that encapsulates the microbiota, limiting it from interacting with the mucosa and causing disease as it migrates distally (fig. S16).

To determine whether the microbiota influenced its own encapsulation by O-glycosylated mucus, we compared the mucus system in microbiota-replete or -deficient hosts. The fecal mucus coating in germ-free (GF) fecal pellets was marginal relative to specific pathogen-free (SPF) fecal pellets (fig. S18), which suggests that the microbiota promotes its encapsulation via

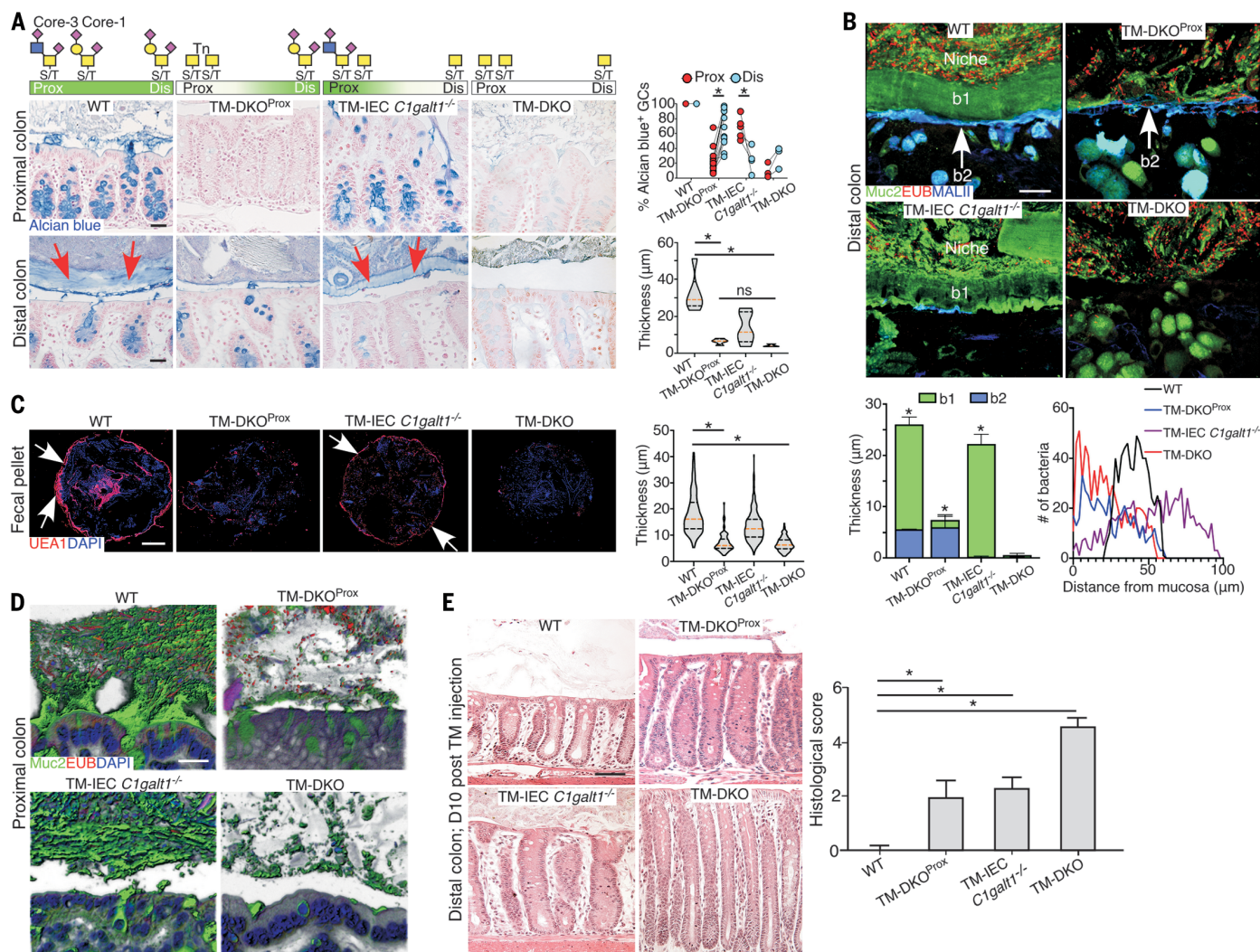


Fig. 2. Proximal colon-derived mucin-type O-glycans govern the composition and function of the mucus barrier. (A) Top left: Diagrams depicting simplified forms of core 1- or core 3-derived O-glycans or Tn antigen (GalNAc) in the different colon regions of mouse lines used for results below. Bottom left: Representative images of colon sections stained with Alcian blue. Arrows denote the mucus barrier layer. Top right: Proportion of Alcian blue⁺ goblet cells in different colon regions. Bottom right: Violin plot of median mucus thickness in distal colons. (B) Top: Z-stack confocal images of colon sections; b1, b2, and niche identify the different sublayers of the mucus. Bottom left: Mean mucus thickness in distal colons. Bottom right: Histogram showing frequency distribution of individual bacterial distances to the top of the distal mucosa surface shown at the top. (C) Left: Confocal tiling images of cross sections

of fecal pellets stained with the lectin UEA1. Arrows mark the mucus layer. Right: Violin plot of mucus thickness of the entire mucus layer surrounding the fecal pellet represented at left. (D) Blended Z-stack confocal images of proximal colon cross sections. (E) Left: Representative images of hematoxylin and eosin-stained colon cross sections. Right: Graph of histologic colitis scores. TM, tamoxifen. Scale bars, 20 μm [(A), (B), and (D)], 500 μm (C), 50 μm (E). Results are representative of three independent experiments, each with $n = 3$ to 5 mice per group. Data are means \pm SD [(B) and (E)] or median (red) and quartiles (black) [(A) and (C)]. * $P < 0.05$ [two-tailed Mann-Whitney test in (A), top right; Kruskal-Wallis test with Dunn's multiple-comparisons posttest in (A), bottom right, and (C); one-way analysis of variance (ANOVA) with Tukey's or Dunnett's multiple-comparisons posttest in (B) and (E), respectively].

mucus production. Comparison of mucus formation in GF versus conventionalized littermates (ExGF), and in SPF mice versus their littermates treated with broad-spectrum antibiotics (SPF^{Abx}) (Fig. 3A) indicated that ExGF mice [day 21 after conventionalization (D21)] had a robust mucus layer similar to that of SPF mice (Fig. 3A). By contrast, SPF^{Abx} mice, like GF mice, had a poorly formed mucus layer, which was restored when the microbiota was reconstituted (SPF^{Recon}) (Fig. 3A). Longitudinal analysis of the fecal mucus coating in ExGF

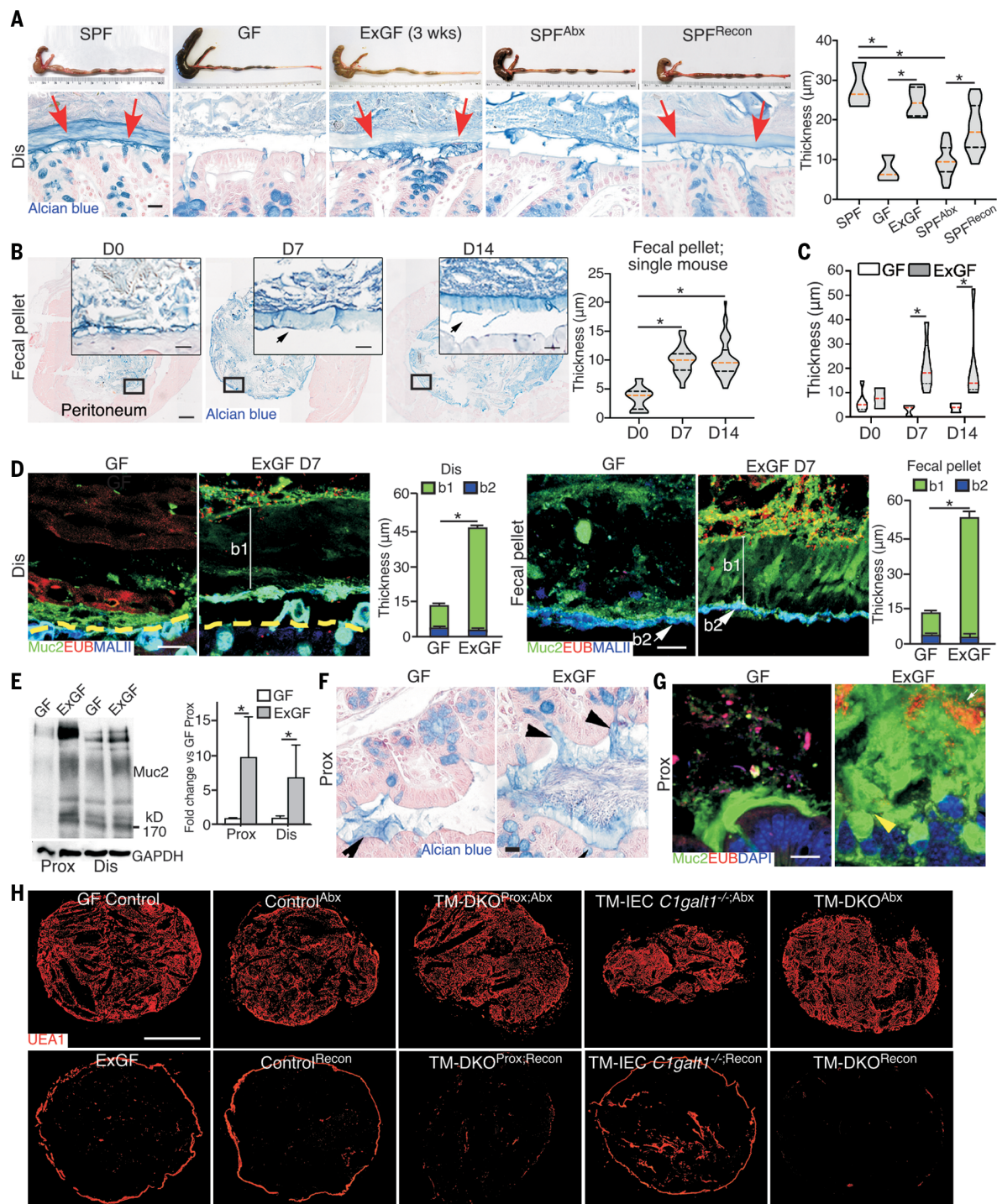
mice before and after conventionalization showed that the encapsulation was formed by D7 (Fig. 3, B and C). This result was reproduced in ExGF mice mono-associated with *B. theta*^{GFP} (fig. S19), indicating that a complex microbiota is not required for microbiota-induced formation of fecal-associated O-glycosylated mucus.

We further probed whether and how microbiota regulate proximal colon goblet cell function. The microbiota induced formation of the b1, but not the b2, mucus barrier layer in tis-

sues and on fecal pellets in ExGF (Fig. 3D) and SPF^{Recon} mice (fig. S20A). This correlated with higher Muc2 expression and secretion in proximal colons of colonized (ExGF, SPF^{Recon}) versus microbiota-deficient littermates, as shown by Western blot (Fig. 3E and fig. S20C), Muc2 staining (Fig. 3F and fig. S20, B, D, and E), and glycan metabolic labeling (fig. S21). We further noted that the secretory response segregated the microbiota away from the tissue (Fig. 3G and fig. S20, D and E) and was independent of inflammasome signaling (fig. S21B), a known

Fig. 3. The microbiota directs its own encapsulation by inducing Muc2 production in the proximal colon.

(A) Gross picture of colon (top left) and Alcian blue-stained mucus and goblet cells in colon sections (bottom left) of mice with and without a complex microbiota. Arrows mark mucus barrier layer. Right: Violin plot of median mucus barrier layer thickness in distal colon sections.



(B) Left: Formation of the fecal mucus barrier over time in ExGF mice. Images show Alcian blue-stained excreted fecal sections. Insets show magnified images of mucus layer (arrows). Right: Violin plot of median mucus barrier layer thickness of excreted feces from multiple GF and ExGF mice. (C) Violin plot of median mucus barrier layer thickness of excreted feces from multiple GF and ExGF mice. (D) Confocal Z-stack images of distal colon (left) and excreted fecal pellet sections (right). Arrows denote the b2 layer; white line spans the thickness of the b1 layer; yellow dashed line denotes mucosal surface. Graphs of b1 and b2 layer thickness are at the right of each group of images. (E) Left: Western blot of tissue Muc2. Right: Densitometry of Muc2 signal. GAPDH, loading control. (F) Alcian blue-stained GF and ExGF colon sections. Arrowheads mark mucus secretion. (G) Confocal Z-stack images of GF and ExGF colon sections. Arrowheads, secreted mucus. (H) Tiled confocal images of excreted fecal pellet sections from mice before or after inoculation with a complex microbiota. Scale bars, 10 μ m [insets in (B)], 20 μ m [(A), (D), (F), and (G)],

500 μ m (B), 1000 μ m (H). Results are representative of three independent experiments, each with $n = 3$ to 5 mice per group. Data are median (red) and quartiles (black) [(A) to (C)] or means \pm SD [(D) and (E)]. * $P < 0.05$ [Kruskal-Wallis test with Dunn's multiple-comparisons posttest in (A), versus D0 in (B), and versus GF b1 layer in (D); two-tailed Mann-Whitney test in (C); one-way ANOVA with Tukey's multiple-comparisons posttest (E)].

modulator of goblet cell secretory responses (23). Fecal mucus screening revealed that the microbe-induced encapsulation was observed only in mouse lines with complex O-glycosylation pathways retained in the prox-

imal colon epithelium (i.e., ExGF, SPF^{Recon}, and TM-IEC *C1galt1*^{-/-;Recon}) (Fig. 3H). These studies indicate that the microbiota specifically induces the b1 mucus barrier layer by inducing Muc2 expression and secretion in

proximal colon goblet cells, leading to microbiota encapsulation.

To determine the impact of the microbe-induced encapsulation of fecal pellets by proximal colon-derived O-glycosylated mucus

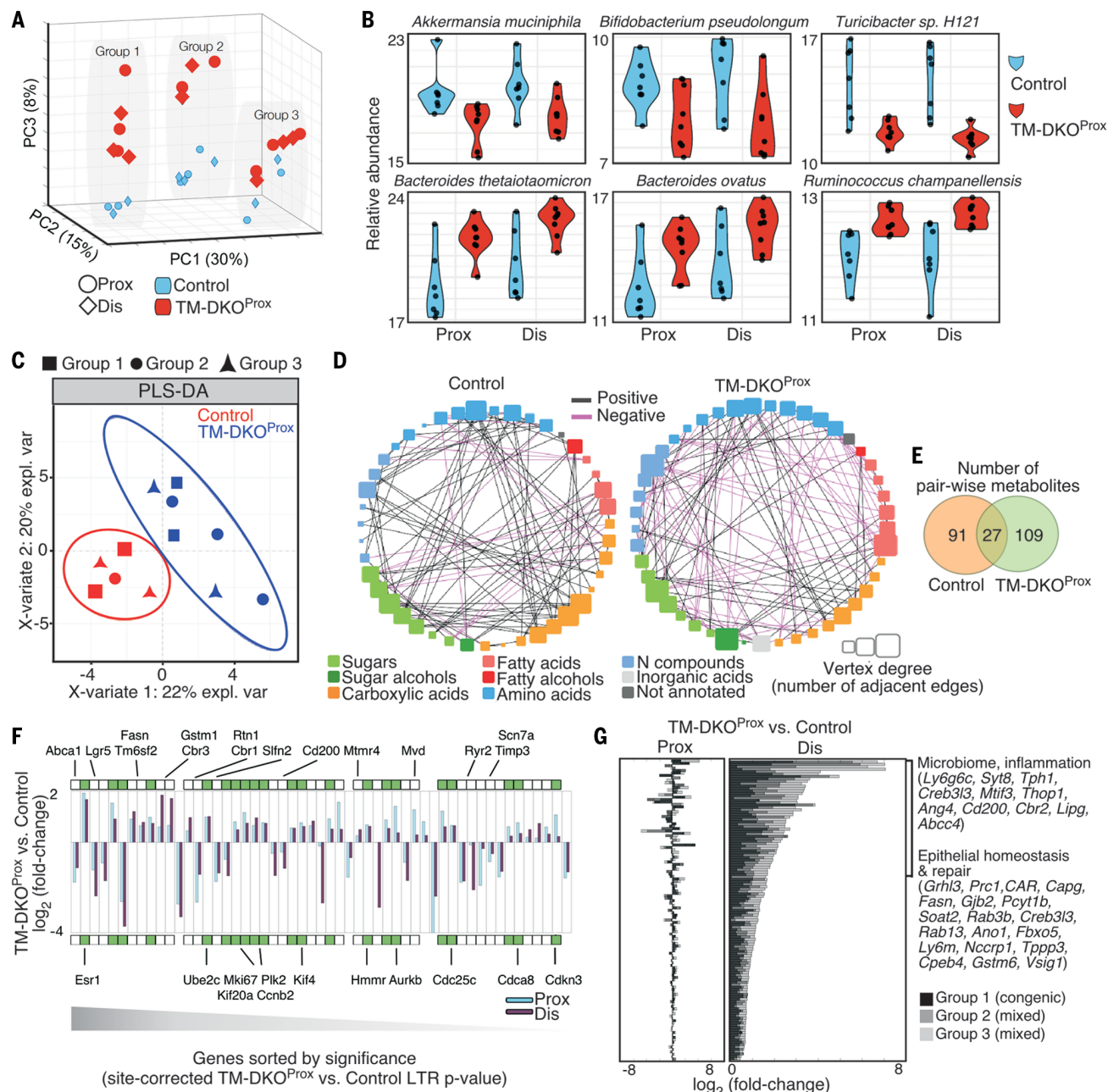


Fig. 4. Loss of O-glycans in the proximal colon alters microbiota community structure and the host mucosal transcriptome throughout the colon.

(A) Principal components analysis (PCA) of species-level counts. The first three principal components (PC1, PC2, PC3) and percent of variance explained are shown; $n = 5$ mice per group. All mice received tamoxifen injections of the same dose, lot, and time point (16). (B) Relative abundance for selected taxa showing the highest PC3 loadings in (A); the y axis represents variance-stabilized data computed from species-level counts (Bracken classifier). (C) Partial least-squares discriminant analysis (PLS-DA) of microbial metabolites. (D) Metabolite correlation networks between control ($n = 5$) and TM-DKO^{Prox} ($n = 5$). (E) Venn diagram of pairwise-

correlated metabolites. (F) Gene expression changes common to proximal and distal samples [left to right (LTR)-adjusted $P < 0.01$; only group 1 is shown for clarity]. Bars show relative (fold) changes in TM-DKO^{Prox} versus Control. Boxes mark genes expressed in colon epithelium; those specifically annotated in cell cycle and proliferation pathways (hypergeometric enrichment $P < 10^{-12}$) are highlighted in green. The gray gradient highlights P values in decreasing significance. (G) TM-DKO^{Prox} versus control gene expression changes specific to distal samples. Bar plots show gene expression \log_2 -transformed fold change (FC) in each group of mice (black and gray bars) for both proximal and distal colon; shown at right are selected top-ranked genes by global fold change, grouped by their molecular function.

on the microbial ecosystem and host responses, we performed system-level analyses of the microbiota composition, metabolic output, and host transcriptome in TM-DKO^{Prox} mice and their control littermates (three independent

groups) with a normalized community (fig. S22, A and B) (16). Analysis of microbiota composition by taxonomic classification and quantitation of shotgun metagenomics from proximal and distal lumen contents (table S2) showed

that, beyond group-specific features (PC1/2; Fig. 4A), there were differences between TM-DKO^{Prox} communities versus littermate controls common to all groups (PC3; Fig. 4A and fig. S22D), independent of colon region and

α -diversity (fig. S22C). Among taxa reduced in TM-DKO^{Prox} versus control were *Akkermansia muciniphila*, a known mucin forager (24), *Turicibacter* sp. H121, and *Bifidobacterium pseudolongum* (Fig. 4B); among taxa increased were *Ruminococcus champanellensis* and members of genus *Bacteroides* (Fig. 4B and fig. S22D). Peak-to-trough analysis (25) on metagenomes of *A. muciniphila* and *B. thetaiotaomicron* indicated a contribution of proximally derived O-glycosylated mucins to microbial replication rates (fig. S23A).

Metabolic profiling (table S3) (16) of proximal fecal content from control and TM-DKO^{Prox} groups revealed that these community shifts were concomitant with an altered metabolic landscape (fig. S23, B and C) independent of cage effects (Fig. 4C). Correlation-based network analysis of intermetabolite relationships showed 3 times as many negative correlations and only 27 correlated metabolic pairs found in common between the pooled control and TM-DKO^{Prox} groups (Fig. 4, D and E, and table S4) (16). Among 50 unique primary metabolites detected in both groups, three were consistently observed only in TM-DKO^{Prox} mice: 3-hydroxybutyric acid, 2-oxoglutarate, and glucose-6-phosphate (fig. S23C).

Finally, despite intergroup variability (Fig. 4A), host transcriptomics in all groups of mice (table S5) revealed that proximal O-glycan loss led to systemic changes (in both proximal and distal regions) in a set of 53 genes, including many related to cell cycle and epithelial homeostasis (Fig. 4F and figs. S24 and S25) (16). Additionally, a set of 147 genes involved in the interaction between the microbiome and inflammation were up-regulated exclusively in distal colon of TM-DKO^{Prox} mice, whereas the same genes were only marginally or inconsistently regulated in the proximal colon (Fig. 4G)

(16). Collectively, these results imply that the proximal colon O-glycans are sufficient to affect the mucosal ecosystem by altering (i) community structure by forging a growth-promoting or regulatory microenvironment for commensals, (ii) community function by altering metabolic output, and (iii) transcriptional homeostasis locally and in distal sites.

Our data indicate that the proximal colon-derived O-glycan-rich mucus forms both the niche and a primary barrier that encapsulates fecal materials and provides an enclosed ecosystem for microbiota (fig. S26). This model represents a major revision of the current mucus system model, which describes a mucus layer locally produced and attached to the distal colon tissue. The fecal-associated mucus provides new insights into microbiota metabolism and composition, and it may lead to noninvasive strategies such as fecal mucus screening for disease diagnosis.

REFERENCES AND NOTES

1. L. V. Blanton, M. J. Barratt, M. R. Charbonneau, T. Ahmed, J. I. Gordon, *Science* **352**, 1533 (2016).
2. T. Gensollen, S. S. Iyer, D. L. Kasper, R. S. Blumberg, *Science* **352**, 539–544 (2016).
3. E. Y. Hsiao et al., *Cell* **155**, 1451–1463 (2013).
4. J. Lloyd-Price et al., *Nature* **569**, 655–662 (2019).
5. G. C. Hansson, *Annu. Rev. Biochem.* **89**, 769–793 (2020).
6. E. C. Martens, M. Neumann, M. S. Desai, *Nat. Rev. Microbiol.* **16**, 457–470 (2018).
7. C. Tropini, K. A. Earle, K. C. Huang, J. L. Sonnenburg, *Cell Host Microbe* **21**, 433–442 (2017).
8. G. P. Donaldson, S. M. Lee, S. K. Mazmanian, *Nat. Rev. Microbiol.* **14**, 20–32 (2016).
9. B. Chassaing, A. T. Gewirtz, *Cell. Mol. Gastroenterol. Hepatol.* **7**, 157–160 (2018).
10. M. Van der Sluis et al., *Gastroenterology* **131**, 117–129 (2006).
11. A. Allen, D. A. Hutton, J. P. Pearson, *Int. J. Biochem. Cell Biol.* **30**, 797–801 (1998).
12. M. R. Kudelka, T. Ju, J. Heimburg-Molinaro, R. D. Cummings, *Adv. Cancer Res.* **126**, 53–135 (2015).
13. M. E. Johansson et al., *Proc. Natl. Acad. Sci. U.S.A.* **105**, 15064–15069 (2008).
14. H. Li et al., *Nat. Commun.* **6**, 8292 (2015).

15. C. Geisler, D. L. Jarvis, *Glycobiology* **21**, 988–993 (2011).
16. See supplementary materials.
17. W. R. Whitaker, E. S. Shepherd, J. L. Sonnenburg, *Cell* **169**, 538–546.e12 (2017).
18. J. B. J. Kamphuis, M. Mercier-Bonin, H. Eutamène, V. Theodorou, *Sci. Rep.* **7**, 8527 (2017).
19. A. Swidsinski, V. Loening-Baucke, H. Verstraelen, S. Osowska, Y. Doerffel, *Gastroenterology* **135**, 568–579 (2008).
20. K. Bergstrom et al., *Mucosal Immunol.* **10**, 91–103 (2017).
21. J. Fu et al., *J. Clin. Invest.* **121**, 1657–1666 (2011).
22. S. Rakoff-Nahoum, L. Hao, R. Medzhitov, *Immunity* **25**, 319–329 (2006).
23. G. M. Birchenough, E. E. Nyström, M. E. Johansson, G. C. Hansson, *Science* **352**, 1535–1542 (2016).
24. N. Ottman, S. Y. Geerlings, S. Aalvink, W. M. de Vos, C. Belzer, *Best Pract. Res. Clin. Gastroenterol.* **31**, 637–642 (2017).
25. T. Korem et al., *Science* **349**, 1101–1106 (2015).

ACKNOWLEDGMENTS

We thank G. Hansson and R. Newberry for reagents and mice; P. Kincade for critical comments; and R. Banks, M. Hart, M. Rheault, J. Gibon, and A. Norris for technical support. **Funding:** Supported by NIH grants R01DK085691 and GM103441, the Oklahoma Center for Adult Stem Cell Research, and the Stephenson Cancer Center of the University of Oklahoma. **Author contributions:** L.X. and K.B. conceived and designed the experiments, interpreted data, and wrote the manuscript; K.B., X.S., D.C., A.B., V.L., J.P.J., B.S., L.G., Y.K., C.H., W.Z., B.N., S.M., J.M.M., D.L.G., S.P., and N.K. performed experiments and analyzed data; and J.B., D.C., A.B., J.L.S., C.W.H., C.V.R., T.M.G., and R.P.M. commented on the project and contributed to the manuscript preparation. **Competing interests:** The authors have declared that no conflict of interest exists. **Data and materials availability:** All sequencing data have been deposited in Gene Expression Omnibus (GSE133257) and Short Read Archive (PRJNA657953). All other data are available in the manuscript or supplementary materials.

SUPPLEMENTARY MATERIALS

science.sciencemag.org/content/370/6515/467/suppl/DC1
Materials and Methods
Supplementary Text
Figs. S1 to S26
Tables S1 to S6
References (26–81)
MDAR Reproducibility Checklist

[View/request a protocol for this paper from Bio-protocol.](#)

15 July 2019; resubmitted 10 July 2020
Accepted 4 September 2020
10.1126/science.aay7367

SOCIALITY

Social selectivity in aging wild chimpanzees

Alexandra G. Rosati^{1*}, Lindsey Hagberg², Drew K. Enigk³, Emily Otali⁴, Melissa Emery Thompson³, Martin N. Muller³, Richard W. Wrangham², Zarin P. Machanda^{5*}

Humans prioritize close, positive relationships during aging, and socioemotional selectivity theory proposes that this shift causally depends on capacities for thinking about personal future time horizons. To examine this theory, we tested for key elements of human social aging in longitudinal data on wild chimpanzees. Aging male chimpanzees have more mutual friendships characterized by high, equitable investment, whereas younger males have more one-sided relationships. Older males are more likely to be alone, but they also socialize more with important social partners. Further, males show a relative shift from more agonistic interactions to more positive, affiliative interactions over their life span. Our findings indicate that social selectivity can emerge in the absence of complex future-oriented cognition, and they provide an evolutionary context for patterns of social aging in humans.

Social bonds have adaptive consequences over the life span; strong social support enhances health, longevity, and biological fitness (1, 2). In humans, old age is characterized by increasing selectivity for positive, meaningful social interactions, manifesting as a cluster of behavioral and cognitive features we call the human social aging phenotype. First, older adults across societies have smaller yet more emotionally fulfilling social networks than do younger adults, owing to an increasing focus on existing close relationships rather than new relationships (3–6). Second, older adults exhibit a positivity bias, showing greater attention to and memory for positive versus negative socioemotional information and reduced engagement in tension and conflicts (7–9). The origin of this social aging pattern is therefore a central issue both for evolutionary perspectives on the life course and for promoting well-being in old age.

Socioemotional selectivity theory, which argues that the central process generating life-span shifts in sociality is an explicit sense of future personal time and mortality (10, 11), has emerged as the most influential explanation for the human social aging phenotype. The core idea is that when individuals perceive the future as expansive (as in youth) they prioritize building new relationships and interacting with many partners, whereas when time is perceived as short (as in old age) people focus on existing, important social ties. In support of this view, older adults perceive a more limited future than younger adults; people who anticipate curtailed time horizons,

because of an illness diagnosis, natural disaster, or a geographic move, generally exhibit preferences similar to those of older adults; and experimental manipulation of future time perspective shifts socioemotional biases (9, 11–13). However, some evidence indicates that changes in socioemotional goals can be independent of future time perspective (14, 15). Thus, the role of shortened time perspectives in social selectivity during aging is currently unclear.

Here, we use a comparative approach to provide a test of the origins of human social aging patterns. Socioemotional selectivity theory proposes that changes in social goals and behavior during aging are causally dependent on an awareness of shortened personal time horizons. However, there is no evidence that any other species are aware of their own future mortality or can imagine far-off future experiences in this rich way. Some nonhumans do engage in forms of future-oriented planning, but only in short-term food acquisition contexts, such as saving a tool to access food hours or days later, and some of these instances may actually recruit lower-level cognitive mechanisms (16, 17). Even verbal young children show limitations in future-oriented cognition and can struggle to imagine their future selves (18). Accordingly, if this kind of subjective future time perspective is causally necessary to generate the human social aging phenotype, then other animals should not show these characteristic shifts.

An alternative possibility is that the human social aging phenotype is mediated by proximate mechanisms that are more widely shared across species. Cost-benefit trade-offs about whether to be social and with whom to socialize are critical for many animals. As aging imposes new constraints due to declines in physical condition, immunological health, and social status (19–22), older individuals might need to adjust their social choices. Accordingly, socioemotional selectivity in humans could represent an adaptive response where older adults focus on important social relationships

that provide benefits and avoid interactions that may have negative consequences. If so, other animals might also show social selectivity without necessarily possessing sophisticated future-oriented cognition like humans.

We test these alternatives by examining whether the key characteristics of the human social aging phenotype are shared with wild chimpanzees (*Pan troglodytes*). Chimpanzees are an ideal comparand because they are one of humans' two closest living relatives; have long life spans of 50 to 60 years in the wild; and form flexible, long-term social bonds. They have a high degree of choice about who to interact with owing to their large fission-fusion societies, which comprise temporary and fluid subgroups ("parties") that can range from one chimpanzee to almost an entire community. Our data come from Kibale National Park, Uganda, where we have documented social interactions in a community of wild chimpanzees on a near-daily basis for more than 20 years, providing longitudinal observations that are unparalleled in human research.

Using 78,000 hours of observations made between 1995 and 2016, we analyzed the social interactions of 21 male chimpanzees ranging in age from 15 (when males are physically mature and enter the adult hierarchy) to 58 years, with an average of 10.6 years of data per individual and 141.6 observation days per year. We examined males because they exhibit stronger bonds and more frequent social interactions than females, who are relatively asocial (23, 24). We used mixed models to test the importance of age in the longitudinal data. We always controlled for an individual's dominance rank, which has a pervasive effect on chimpanzee social interactions and declines in old age (19, 25). Few males had adult maternal brothers, so we did not account for kinship, but we did control for other predictors such as year or female presence, when appropriate for the social metric (see supplementary materials).

We first examined whether older chimpanzees focused their social interactions on important partners, a key signature of the human social aging phenotype. To characterize relationships, we used a spatial proximity metric indexing the time that pairs of individuals spend near each other. Close proximity is an important marker of affiliation in primates, as it is a prerequisite for other cooperative interactions, such as grooming, and signals social comfort (1). We indexed social preferences by examining how often two individuals were within 5 m of each other when in the same party. We then categorized male-male dyads as "mutual friends" (both showed a preference for sitting near the other, above their individual average rates of association), "one-sided friends" (one individual showed this preference, but their partner did not), or "nonfriends" (neither individual preferred to associate with

¹Departments of Psychology and Anthropology, University of Michigan, Ann Arbor, MI, USA. ²Department of Human Evolutionary Biology, Harvard University, Cambridge, MA, USA. ³Department of Anthropology, University of New Mexico, Albuquerque, NM, USA. ⁴Kibale Chimpanzee Project, Makerere University Biological Field Station, Kibale National Park, Uganda. ⁵Departments of Anthropology and Biology, Tufts University, Medford, MA, USA.

*Corresponding author. Email: rosati@umich.edu (A.G.R.); zarin.machanda@tufts.edu (Z.P.M.)

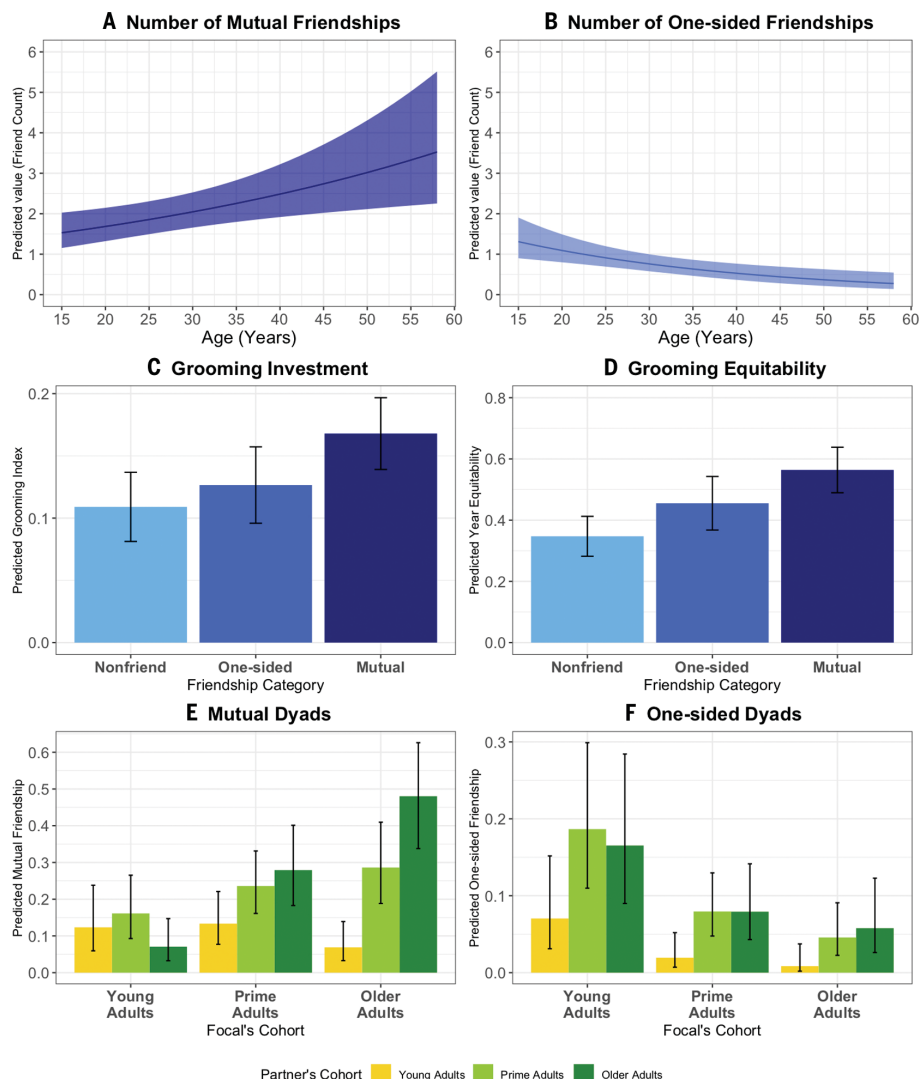


Fig. 1. Friendships in aging chimpanzees. (A and B) Older males had more mutual friendships, whereas younger males had more one-sided friendships. (C and D) Chimpanzees invested more and had more equitable grooming patterns with mutual friends. (E and F) Older males (35+ years) were mutual friends with peers and were attractive partners for younger males' (15 to 20 years) and prime-aged males' (20 to 35 years) one-sided friendships. Ribbons and error bars indicate 95% confidence interval (CI) estimates.

the other). Thus, mutual friendships are reciprocated, whereas one-sided friendships are not. We found that the number of mutual friends increased with age [$\chi^2 = 6.89$, degrees of freedom (df) = 1, $P < 0.01$] (Fig. 1A), whereas one-sided friendships declined ($\chi^2 = 9.76$, df = 1, $P < 0.005$) (Fig. 1B). For example, 15-year-olds had an average of 2.1 one-sided friends and 0.9 mutual friends, whereas 40-year-olds had 0.6 one-sided friends and 3.0 mutual friends. Age and dominance had independent effects on relationships (see supplementary materials); higher rank and older age both predicted more mutual friendships but fewer one-sided friendships.

To test whether mutual friendships were high-value bonds like those prioritized by older humans, we then examined grooming, a prin-

icipal form of primate social investment (1). We first assessed whether mutual friends were more likely to groom each other and found that chimpanzees of all ages engaged in more total grooming with mutual friends than with one-sided or nonfriends ($\chi^2 = 94.38$, df = 2, $P < 0.0001$; $P < 0.0001$ for significant pairwise comparisons) (Fig. 1C), with similar results for grooming given and received (see supplementary materials). Second, mutual friends engaged in longer grooming bouts ($\chi^2 = 25.03$, df = 2, $P < 0.0001$; $P < 0.05$ for significant pairwise comparisons). Third, mutual friends had more equitable patterns of grooming, both within bouts of grooming ($\chi^2 = 38.23$, df = 2, $P < 0.0001$) and across the year ($\chi^2 = 58.13$, df = 2, $P < 0.0001$) (Fig. 1D). Using this dyadic data, we further found that

mutual friendships were more common among dyads of older males than dyads of prime-aged or younger males, but one-sided friendships were driven by younger males seeking out prime-aged and older partners (see Fig. 1, E and F, and supplementary materials). Thus, chimpanzees invested more, and invested more equitably, in mutual relationships than one-sided ones, and older adults had more mutual friendships than younger adults did.

Older human adults have smaller and more selective social networks, so we next examined how chimpanzee gregariousness changed with age. We assessed the likelihood that an individual was observed alone and found that although males were rarely alone (<1% of observation time), solitariness did increase with age ($\chi^2 = 4.51$, df = 1, $P < 0.05$). Yet when chimpanzees did socialize, age predicted an increased likelihood that they were in a party that included at least one other adult male, as opposed to only females or juveniles ($\chi^2 = 15.73$, df = 1, $P < 0.0001$) (Fig. 2A). Moreover, older males were observed in larger male parties ($\chi^2 = 19.50$, df = 1, $P < 0.0001$) and were more likely to be in close proximity of another adult male ($\chi^2 = 18.02$, df = 1, $P < 0.0001$) (Fig. 2B). For example, 15-year-olds were found in parties averaging 5.8 other males and were physically near another male in 36.6% of observations. In contrast, 40-year-olds were found in parties with 6.6 other males and in proximity to another male in 53.7% of observations. Thus, older males showed some declines in their overall tendency to be gregarious but were more likely to be in parties with and sit near important social partners when they did choose to socialize.

Our final set of analyses tested whether chimpanzees exhibit an increasing positivity bias, the other key component of the human social aging phenotype. We examined the overall rate at which individual male chimpanzees groomed all others in the community (as an index of positive social interaction) versus the rate at which they gave aggression to all others (as an index of negative interactions; comprising both directed aggression, where the individual targets another individual by hitting, biting, or chasing, and nondirected aggressive displays without specific targets). We found that whereas grooming remained fairly constant across the life span, aggression decreased with age ($\chi^2 = 69.09$, df = 1, $P < 0.0001$; $P < 0.0005$ for comparisons of age slopes) (Fig. 2C). Grooming and aggression received from others showed similar patterns (see supplementary materials). Chimpanzees therefore show a behavioral shift from relatively more negative interactions to more positive ones during aging, analogous to the human positivity bias.

Overall, our data provide the first evidence for social selectivity during aging in non-humans. We found that older chimpanzees, like

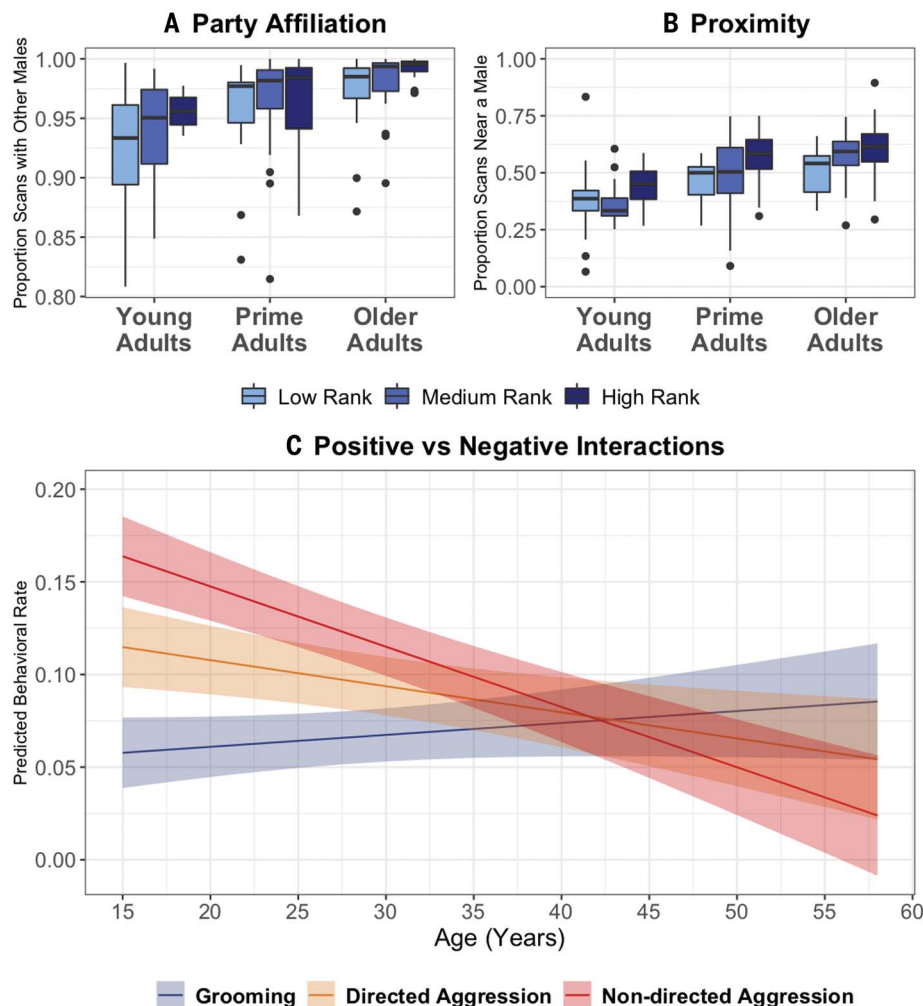


Fig. 2. Gregariousness and positivity bias in aging chimpanzees. Older males were more likely than not to be observed (A) in parties with other males and (B) sitting in proximity to those males. (C) While both directed aggression (with specific targets) and nondirected aggression (displays) declined with age, grooming remained fairly constant. Ribbons indicate 95% CI estimates.

humans, prioritized high-quality relationships; whereas younger adults had more asymmetrical friendships characterized by reduced investment, older adults exhibited more mutual friendships characterized by high, equitable investment. Second, older chimpanzees were more likely to be observed alone but tended to socialize more with important partners by joining parties with other males, joining larger male parties, and sitting in close proximity to other males. Finally, chimpanzees exhibited an increasing positivity bias with age, showing consistent grooming but reductions in aggression across the life span. These patterns were notably independent of dominance rank; despite their falling status, older males were more likely to be mutual friends with each other and were targets of the one-sided advances of younger males. Together, our data indicate that chimpanzees demonstrate key behavioral signatures of the human social aging

phenotype, showing that increasing social selectivity can occur in the absence of a rich future time perspective.

These data support the view that senescence drives fundamental shifts in the costs and benefits of social interactions across species. Yet although many species face new constraints during aging, chimpanzees and humans show a response to these constraints that is not universal. In particular, several other primate species exhibit social withdrawal during aging—reducing social interactions overall without focusing on important partners—as well as a negativity bias characterized by declines in affiliation but steady rates of aggression (26–32). Why do aging chimpanzees and humans instead show social selectivity and a positivity bias? We propose that optimal social responses to aging depend on a species' social organization and life history. The relationships of many species are primarily based on kinship,

and senescence makes it difficult to form new relationships as close relatives die. Consequently, social withdrawal may be a common pattern. Yet social relationships are flexible, can occur outside of kinship, and last many years in long-lived humans and chimpanzees (23, 24). Thus, strongly established relationships may be more reliable for older chimpanzees than for other primates. This may be especially important for species with relatively low reproductive skew like chimpanzees, as older individuals can still obtain fitness benefits via cooperative alliances despite changes in health and social status (19–22).

A second question concerns the specific proximate mechanisms underpinning social selectivity in chimpanzees. Socioemotional selectivity theory proposes that the human social aging phenotype causally depends on an explicit sense of the self in time, but given that other animals have constrained future-oriented cognition (16, 17), other proximate mechanisms must play a role in nonhumans. In some primates, age-related shifts in social behavior have been proposed to stem from declining capacities to cope with stress (32), yet older chimpanzees do not exhibit major increases in sensitivity to either energetic or social stressors despite higher overall glucocorticoids (22). An alternative possibility is that chimpanzee social aging patterns are driven by shifts in emotional reactivity, given that an increasing capacity for emotional regulation is a feature of human aging (8, 14). Thus, a key question is whether older chimpanzees also exhibit shifts in affective processes, such as a less reactive temperament or lower rates of reactive aggression.

Our findings demonstrate how data from long-lived, socially flexible animals are crucial for disentangling the proximate and ultimate causes of human social aging patterns. In addition to testing how different species respond to the constraints of aging, comparative data can inform our understanding of the evolution of social roles. In other long-lived mammals such as cetaceans and elephants, older individuals serve as stores of ecological knowledge that benefit groupmates (33). This indicates that a prolonged life course can shape adaptive strategies for information processing and suggests that the social aging phenotype characteristic of chimpanzees and humans may be due in part to the social knowledge that long-lived, socially flexible species can acquire. Indeed, older adult humans exhibit greater crystallized intelligence and skillfulness at reasoning about social conflicts (34). Similarly, older chimpanzees might acquire social knowledge over their life span that makes them attractive social partners despite falling dominance status. In sum, although humans exhibit extraordinary cognitive features that allow for complex reasoning about the future, commonalities

in social aging between humans and other animals are key to understanding the evolution and function of these mechanisms.

REFERENCES AND NOTES

1. J. B. Silk, *Science* **317**, 1347–1351 (2007).
2. N. Snyder-Mackler *et al.*, *Science* **368**, eaax9553 (2020).
3. J. E. Lansford, A. M. Sherman, T. C. Antonucci, *Psychol. Aging* **13**, 544–552 (1998).
4. L. L. Carstensen, *Psychol. Aging* **7**, 331–338 (1992).
5. C. Wrzus, M. Hänel, J. Wagner, F. J. Neyer, *Psychol. Bull.* **139**, 53–80 (2013).
6. T. English, L. L. Carstensen, *Int. J. Behav. Dev.* **38**, 195–202 (2014).
7. A. E. Reed, L. Chan, J. A. Mikels, *Psychol. Aging* **29**, 1–15 (2014).
8. S. T. Charles, L. L. Carstensen, *Annu. Rev. Psychol.* **61**, 383–409 (2010).
9. M. Mather, L. L. Carstensen, *Trends Cogn. Sci.* **9**, 496–502 (2005).
10. L. L. Carstensen, *Science* **312**, 1913–1915 (2006).
11. L. L. Carstensen, D. M. Isaacowitz, S. T. Charles, *Am. Psychol.* **54**, 165–181 (1999).
12. H. H. Fung, L. L. Carstensen, A. M. Lutz, *Psychol. Aging* **14**, 595–604 (1999).
13. S. J. Barber, P. C. Oritz, B. Martins, M. Sakaki, M. Mather, *Mem. Cognit.* **44**, 869–882 (2016).
14. D. Grün, N. Sharifian, Q. Chu, *Psychol. Aging* **31**, 583–593 (2016).
15. H. H. Fung, D. M. Isaacowitz, *Psychol. Aging* **31**, 553–557 (2016).
16. N. J. Mulcahy, J. Call, *Science* **312**, 1038–1040 (2006).
17. C. R. Raby, N. S. Clayton, *Behav. Processes* **80**, 314–324 (2009).
18. C. M. Atance, *Child Dev. Perspect.* **9**, 178–182 (2015).
19. D. P. Watts, *Behaviour* **155**, 969–1009 (2018).
20. M. Emery Thompson *et al.*, *R. Soc. Open Sci.* **5**, 180840 (2018).
21. M. E. Thompson *et al.*, *Philos. Trans. R. Soc. London Ser. B* **375**, 20190607 (2020).
22. M. Emery Thompson *et al.*, *Proc. Natl. Acad. Sci. U.S.A.* **117**, 8424–8430 (2020).
23. Z. P. Machanda, I. C. Gilby, R. W. Wrangham, *Int. J. Primatol.* **34**, 917–938 (2013).
24. K. E. Langergraber, J. C. Mitani, L. Vigilant, *Proc. Natl. Acad. Sci. U.S.A.* **104**, 7786–7790 (2007).
25. M. Hasegawa, N. Kutsukake, *Behav. Ecol. Sociobiol.* **69**, 89–99 (2015).
26. L. Almeling, K. Hammerschmidt, H. Sennhenn-Reulen, A. M. Freund, J. Fischer, *Curr. Biol.* **26**, 1744–1749 (2016).
27. L. J. N. Brent, A. Ruiz-Lambides, M. L. Platt, *Proc. Biol. Sci.* **284**, 20170515 (2017).
28. G. Schino, M. Pinzaglia, *Am. J. Primatol.* **80**, e22746 (2018).
29. M. Nakamichi, *Primates* **25**, 192–203 (1984).
30. J.-L. Picq, *Folia Primatol.* **59**, 217–220 (1992).
31. A. G. Rosati, A. M. Arre, M. L. Platt, L. R. Santos, *Behav. Ecol. Sociobiol.* **72**, 163 (2018).
32. L. Almeling, H. Sennhenn-Reulen, K. Hammerschmidt, A. M. Freund, J. Fischer, *Am. J. Primatol.* **79**, e22711 (2017).
33. D. P. Croft, L. J. N. Brent, D. W. Franks, M. A. Cant, *Trends Ecol. Evol.* **30**, 407–416 (2015).
34. I. Grossmann *et al.*, *Proc. Natl. Acad. Sci. U.S.A.* **107**, 7246–7250 (2010).
35. A. Rosati *et al.*, Social selectivity in aging wild chimpanzees, Version 2, Dryad (2020); <https://doi.org/10.5061/dryad.j3tx95xbx>.

ACKNOWLEDGMENTS

We thank F. Warneken and T. Antonucci for feedback and C. Powell at CSCAR for statistical advice. **Funding:** NIH-R01AG04395, NSF-1926653, NSF-1926737, NSF-1926352, NSF-1355014, NSF-9807448, NSF-0416125, NSF GRFP DGE-0237002, Sloan Foundation FG-2019-12054, and long-term support from the Leakey Foundation and UNM. **Author contributions:** A.G.R. and Z.P.M. conceived of the project. All authors performed the research A.G.R. and Z.P.M. analyzed the data. A.G.R. and Z.P.M. wrote the paper with input from all authors. **Competing interests:** The authors declare no competing interests. **Data and materials availability:** All data are available at the Dryad Digital Repository (35).

SUPPLEMENTARY MATERIALS

science.sciencemag.org/content/370/6515/473/suppl/DC1
Materials and Methods
Figs. S1 to S3
Tables S1 to S5
References (36–41)

19 October 2019; accepted 25 August 2020
10.1126/science.aaz9129

ADAPTATION

Experimental evolution makes microbes more cooperative with their local host genotype

Rebecca T. Batstone^{1,2*}, Anna M. O'Brien^{1,3}, Tia L. Harrison¹, Megan E. Frederickson^{1,4,5}

Advances in microbiome science require a better understanding of how beneficial microbes adapt to hosts. We tested whether hosts select for more-cooperative microbial strains with a year-long evolution experiment and a cross-inoculation experiment designed to explore how nitrogen-fixing bacteria (rhizobia) adapt to legumes. We paired the bacterium *Ensifer meliloti* with one of five *Medicago truncatula* genotypes that vary in how strongly they “choose” bacterial symbionts. Independent of host choice, *E. meliloti* rapidly adapted to its local host genotype, and derived microbes were more beneficial when they shared evolutionary history with their host. This local adaptation was mostly limited to the symbiosis plasmids, with mutations in putative signaling genes. Thus, cooperation depends on the match between partner genotypes and increases as bacteria adapt to their local host.

Host-associated microbiota are often beneficial, but we have a limited understanding of adaptation between partners in these mutualisms, especially at the genomic level. Mutualisms are sometimes viewed as reciprocal parasitism, potentially resulting in antagonistic coevolution that maintains genetic variation within populations. However, recent work has questioned the prevalence of fitness conflict in mutualisms (1), and concordant fitness interests between part-

ners should lead to evolutionary stasis, reducing genetic variation in mutualistic traits like partner quality (2, 3).

Poor-quality microbes could be “cheaters” that increase their own fitness at their host’s expense (4). However, hosts often “choose” their microbiota (5) and preferentially associate with or reward more-cooperative microbes, selecting against would-be cheaters (6, 7). Such partner choice can be adaptive (8, 9) but is also paradoxical: If choosy hosts select high-quality symbionts, variation in symbiont quality should decrease, reducing the selective advantage of partner choice (10). Still, many hosts are choosy and many symbionts are not very beneficial (4, 11), making the persistence of ineffective microbes perplexing.

Ineffective microbes might simply be mismatched with their host. A high-quality microbe on one host genotype may be a low-quality microbe on another. Such genotype-by-genotype

(GxG) interactions for symbiont quality are common, maintain variation in the benefits symbionts provide to hosts (3, 12), and are a prerequisite for coevolution (13, 14). Local adaptation, whereby partners from the same site outperform partners from different sites, can generate GxG interactions and occurs in mutualisms (12, 15), but it is not ubiquitous (16). Furthermore, the genetic mechanisms underlying local adaptation or GxG interactions remain largely unknown.

Legume-rhizobium interactions are economically and ecologically important and a model for studying mutualisms. Legumes trade carbon for nitrogen fixed by rhizobia, which they house in root nodules (17). Rhizobia have rapid generation times, can be cultured, and can acquire mutations through horizontal gene transfer (18). Rhizobia are also amenable to genome-wide association studies (GWASs) that can identify genomic variants associated with phenotypes (19). Adapting these approaches, Burghardt *et al.* (20) found stronger selection on rhizobia in hosts than on rhizobia free-living in soil.

Here, we resequenced and cross-inoculated rhizobia after they evolved on one of five host genotypes that vary in choosiness to test whether choosier hosts select for more cooperative symbionts or whether rhizobia adapt to their local host genotype. We used two rhizobia strains that differ in host benefits: ineffective nitrogen fixer *Ensifer meliloti* strain Sm1021 (referred to here as Em1021) and effective nitrogen fixer *E. meliloti* strain WSM1022 (Em1022) (9, 17). We paired both strains with one of five inbred lines of *Medicago truncatula*: Line 270 is indiscriminate, whereas the others all prefer Em1022 to Em1021, with line 267 almost exclusively partnering with Em1022 in

¹Department of Ecology & Evolutionary Biology, University of Toronto, Toronto, ON M5S 3B2, Canada. ²Carl R. Woese Institute for Genomic Biology, University of Illinois, Urbana, IL 61801, USA. ³Department of Mechanical & Industrial Engineering, University of Toronto, Toronto, ON M5S 3G8, Canada. ⁴Centre for the Analysis of Genome Evolution & Function, University of Toronto, Toronto, ON M5S 3B2, Canada. ⁵Radcliffe Institute for Advanced Study, Harvard University, Cambridge, MA 02138, USA.

*Corresponding author. Email: rtbats98@illinois.edu

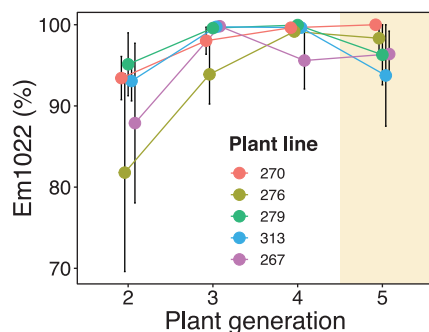


Fig. 1. High-quality microbial partner spread nearly to fixation in all treatment groups. The percentage (mean \pm 1 SE) of the effective N-fixing strain (Em1022) across plant generations in the evolution experiment was calculated from soil samples for generations 2 to 4, and nodules were dissected from plants in generation 5 (shaded in light orange). Colors indicate *M. truncatula* genotypes. All plants were initially inoculated with 33% Em1022.

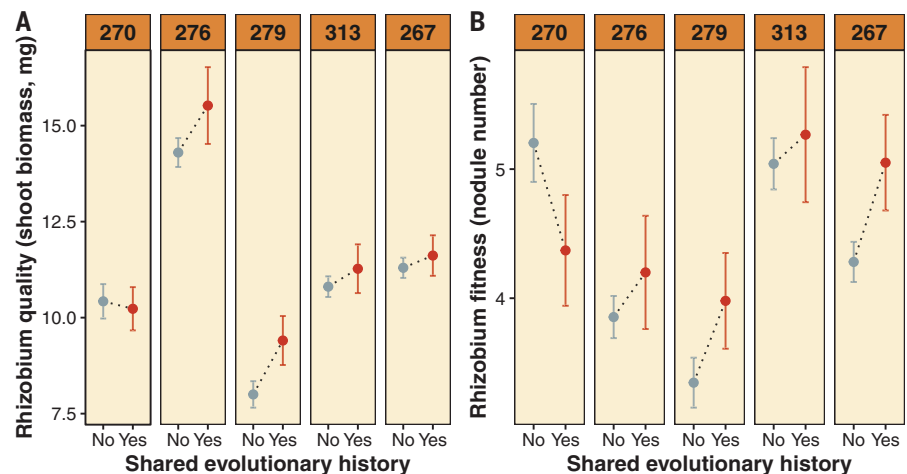


Fig. 2. Bacteria adapt to their local host genotype. (A and B) Mean \pm 1 SE shoot biomass (A) and nodule number (B) for all combinations of 40 derived bacterial isolates from the evolution experiment and five plant genotypes (numbered across top). Bacteria share evolutionary history with the host genotype they evolved on during the evolution experiment.

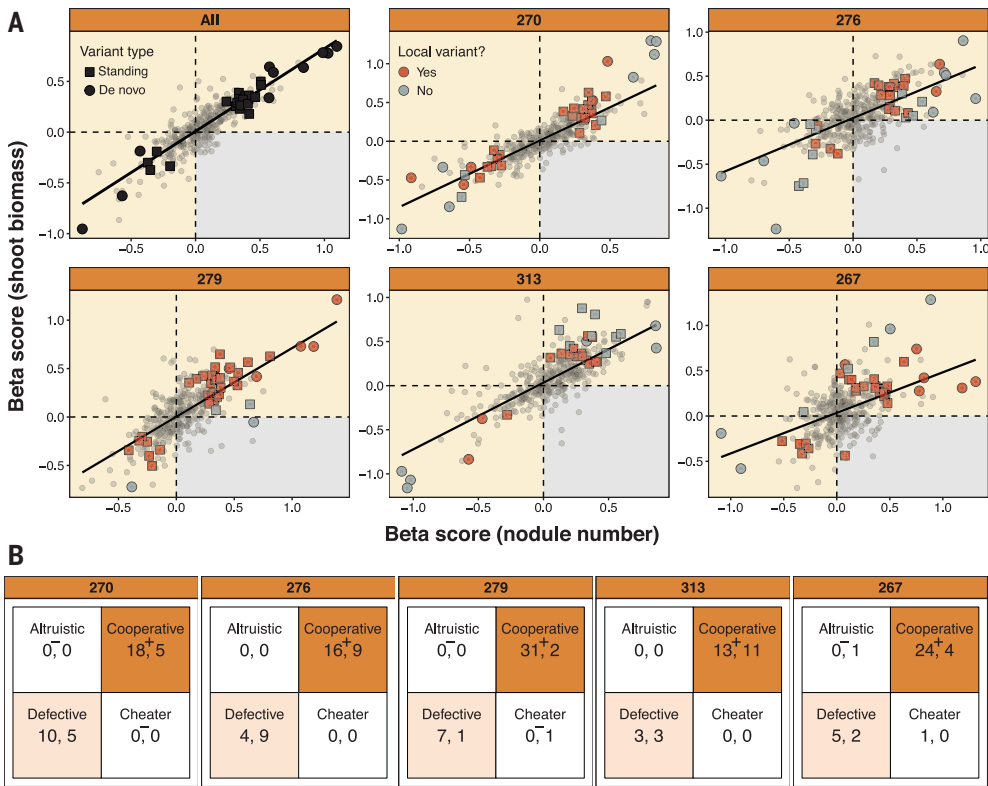


Fig. 3. Most of the significant genomic variants were cooperative and local. (A) GWAS beta scores for symbiont quality (shoot biomass) and fitness (nodule number) for the 363 variants (points) among the 40 derived isolates, averaged over all plant lines or for each host genotype separately. Larger symbols are variants with one or more statistically significant effects (squares indicate segregating in the ancestor; circles indicate de novo). For the panels showing each host genotype, red symbol color indicates that variants evolved in individual host environments and gray symbol color indicates that they did not. The region shaded in gray defines cheater variants. (B) Counts of significant variants in each host environment. (Category definitions are provided in the text.) Numbers before commas indicate local variants, and numbers after commas indicate variants that evolved in a different host environment. Plus (+) or minus (−) symbols indicate categories with more or fewer variants, respectively, than the null expectation. Orange shading indicates a high number of total variants relative to the other three quadrants; light red shading indicates a moderate number of variants relative to the other three quadrants.

past experiments (9, 17). After a year-long evolution experiment spanning five plant generations, we isolated “derived” rhizobia from nodules and compared them to the original “ancestral” strains.

Even though Em1021 started with a twofold advantage (17), it became nearly extinct on all host lines (Fig. 1). At the end of the experiment, Em1021 associated with only 15% of plants and occupied only 3% of 336 sampled nodules. In a linear model combining strain frequencies in soil and nodules (17), we found a marginally significant effect of generation ($F_{3,96} = 2.40$, $P = 0.0730$) but no effect of plant line ($F_{4,96} = 0.552$, $P = 0.698$). The effective symbiont, Em1022, outcompeted Em1021 on all hosts regardless of choosiness, indicating that partner choice was not an important selective force.

We assayed Em1022 phenotypes by planting new seeds of the same five plant lines and singly inoculating each with either ancestral Em1022 or 1 of the 40 derived isolates, testing replicates of all possible combinations of host genotypes and isolates (17). We quantified the symbiotic quality of rhizobium isolates by measuring aboveground plant biomass and rhizobium fitness by measuring nodule number. We also sequenced whole genomes of the 40 derived isolates and nine replicates each of the ancestors and conducted GWASs for symbiont quality and fitness both on specific host genotypes and across all plant lines (17).

Variation in the benefits that experimentally evolved bacteria conferred to hosts was largely determined by the matches between rhizobium and host genotypes. Derived and ancestral Em1022 did not differ significantly in symbiont quality or fitness (tables S1A and S2A). However, derived bacteria provided greater benefits to the host genotype they were paired with during the evolution experiment (Fig. 2A), although a few isolates were high- or low-quality symbionts across plant lines (figs. S1 and S2). Derived rhizobia also achieved higher fitness when tested on their local host genotype, with the exception of isolates that evolved on the least choosy host genotype (line 270) (Fig. 2B). Linear mixed models found significantly positive effects of shared evolutionary history on both rhizobium quality and fitness (tables S1B and S2B).

Averaged across all hosts, there was a positive relationship between rhizobia quality and fitness (fig. S3), suggesting that none of the 40 derived strains evolved to cheat and that strong fitness feedback makes cooperation adaptive for rhizobia. Pairwise correlations between the same trait on different hosts were weaker and often not statistically significant (fig. S4), suggesting that microbial quality or fitness on one host poorly predicts quality or fitness on another.

Genomic sequencing of *E. meliloti* isolates uncovered 1330 genetic variants, including 547 de novo mutations (fig. S5A). Most de novo variants (305) were specific to rhizobia derived

on the least choosy host line (line 270); fewer variants (16 to 59) were specific to rhizobia derived on other lines (fig. S5A). After filtering out most singletons and variants in high linkage disequilibrium, reducing our set to 363 variants (fig. S5B), GWASs identified 145 variants significantly associated with rhizobium quality or fitness (referred to as significant variants) in one or more host environments (table S3). These variants were mostly located on two symbiosis plasmids, pSymA and pSymB, which contain genes essential for the symbiotic and free-living phases of the rhizobium life cycle, respectively (21, 22); 62 variants were on pSymA, 68 on pSymB, and only 15 were on the bacterial chromosome.

Beta scores, which represent the strength of association between a genomic variant and a phenotype, were strongly positively correlated between symbiont quality and fitness (Fig. 3A), meaning that genomic variants that increased microbial fitness also increased microbial benefits to plants. Within each host environment, most of the significant variants evolved in isolates paired with that host genotype in the evolution experiment (i.e., local variants; red symbols in Fig. 3A and numbers before commas in Fig. 3B). We categorized variant effects as “cooperative” if beta scores for symbiont quality and fitness were both greater than zero, “defective” if beta scores were both less than zero, “altruistic” if beta scores were positive for symbiont quality but

negative for symbiont fitness, or “cheater” if beta scores were positive for symbiont fitness but negative for symbiont quality. In all five host environments, most of the significant variant effects were cooperative and local (Fig. 3B and table S3).

We used permutations to assess whether this pattern could have occurred by chance by randomly assigning genomes to phenotypes 1000 times and recalculating beta scores (17). There were significantly more local-cooperative associations in all five host environments (Fig. 3B, plus symbols) and significantly fewer local-altruistic and local-cheater associations in some host environments (Fig. 3B, minus symbols) at a 5% false discovery rate. The numbers of associations in other categories (e.g., defective variants) did not differ from null expectations.

Local, cooperative variants were located in genes that putatively encode a calcium-binding protein, a flavin adenine dinucleotide (FAD)-binding oxidoreductase, and two Ti-type conjugative transfer relaxases, among others (table S3). These functions may be related to nodule initiation or rhizobium survival inside nodules (23). Variant effects were often host-specific and generally conditionally beneficial on their local host or deleterious on a nonlocal host (table S3), suggesting selection in local contexts and drift in nonlocal contexts. When variants exhibited significant effects on multiple hosts, they tended to be consistently beneficial or deleterious across hosts; only two variants had significant, opposite-sign effects across hosts, suggesting that trade-offs are rare (table S3). In summary, cooperation evolved more often, and cheating or altruism less often, than expected by chance as bacteria adapted to their local host genotype.

In our evolution experiment, we expected the choosiest host line to most strongly favor the better symbiont, Em1022. However, the ineffective strain, Em1021, went nearly extinct across all plant lines, even on indiscriminate

hosts (Fig. 1), suggesting that this strain is a universally poor competitor. By contrast, Em1022 evolved previously uncharacterized variants that differed in both symbiont quality and fitness. Derived bacteria provided greater host benefits and generally achieved higher fitness on the host genotype with which they shared evolutionary history (Fig. 2), and we detected a significant excess of genomic variants with cooperative effects on local hosts (Fig. 3). These results suggest that local adaptation is a more important evolutionary force shaping microbial cooperation than is partner choice. Furthermore, when microbes are consistently paired with the same host and dispersal is limited, the resulting local adaptation likely leads to more, not less, cooperation. What emerges is a model of adaptation in host-microbe mutualisms: Microbes can rapidly adapt to a particular host genotype through standing or de novo variants that also benefit local hosts but have varying effects on nonlocal host genotypes, maintaining the variation in mutualist quality that we observe in host-associated microbiomes. Our results also imply that transplanting microbiota is more likely to be effective among closely related hosts or that one needs to give sufficient time for microbes to adapt to a new host environment.

REFERENCES AND NOTES

1. M. E. Frederickson, *Trends Ecol. Evol.* **32**, 727–734 (2017).
2. J. L. Sachs, C. J. Essenberg, M. M. Turcotte, *Trends Ecol. Evol.* **26**, 202–209 (2011).
3. K. D. Heath, J. R. Stinchcombe, *Evolution* **68**, 309–317 (2014).
4. J. L. Sachs, M. O. Ehinger, E. L. Simms, *J. Evol. Biol.* **23**, 1075–1089 (2010).
5. K. R. Foster, J. Schluter, K. Z. Coyte, S. Rakoff-Nahoum, *Nature* **548**, 43–51 (2017).
6. E. T. Kiers, R. A. Rousseau, S. A. West, R. F. Denison, *Nature* **425**, 78–81 (2003).
7. K. D. Heath, P. Tiffin, *Evolution* **63**, 652–662 (2009).
8. A. K. Simonsen, J. R. Stinchcombe, *Proc. Biol. Sci.* **281**, 20142036 (2014).
9. R. T. Batstone, E. M. Dutton, D. Wang, M. Yang, M. E. Frederickson, *New Phytol.* **213**, 1850–1861 (2017).
10. K. R. Foster, H. Kokko, *Proc. Biol. Sci.* **273**, 2233–2239 (2006).
11. P. H. Thrall, J. Burdon, M. J. Woods, *J. Appl. Ecol.* **37**, 52–65 (2000).
12. M. A. Rúa et al., *BMC Evol. Biol.* **16**, 122 (2016).
13. K. D. Heath, *Evolution* **64**, 1446–1458 (2010).
14. J. D. Hoeksema, *New Phytol.* **187**, 286–300 (2010).
15. S. S. Porter, M. L. Stanton, K. J. Rice, *PLOS ONE* **6**, e27935 (2011).
16. T. L. Harrison, C. W. Wood, I. L. Borges, J. R. Stinchcombe, *Ecol. Evol.* **7**, 4367–4376 (2017).
17. Materials and methods are available as supplementary materials.
18. P. Remigi, J. Zhu, J. P. W. Young, C. Masson-Boivin, *Trends Microbiol.* **24**, 63–75 (2016).
19. B. Epstein et al., *mSphere* **3**, e00386-18 (2018).
20. L. T. Burghardt et al., *Proc. Natl. Acad. Sci. U.S.A.* **115**, 2425–2430 (2018).
21. F. Galibert et al., *Science* **293**, 668–672 (2001).
22. T. M. Finan et al., *Proc. Natl. Acad. Sci. U.S.A.* **98**, 9889–9894 (2001).
23. K. M. Jones, H. Kobayashi, B. W. Davies, M. E. Taga, G. C. Walker, *Nat. Rev. Microbiol.* **5**, 619–633 (2007).
24. R. Batstone, A. O'Brien, T. Harrison, M. Frederickson, rtbastone/how-rhizobia-evolve: First release of data and code for “Experimental evolution makes microbes more cooperative with their local host genotype,” Zenodo (2020); <https://doi.org/10.5271/zenodo.3981117>.

ACKNOWLEDGMENTS

We thank volunteers J. Li, C. Chen, G. Ferguson, F. Samad-zada, L. Wang, X. Zhang, D. Li, K. Ong, and J. Wong. The Frederickson Lab, especially E. Dutton and J. Laurich, as well as L. Burghardt, J. Lau, J. Stinchcombe, and C. Wood, provided feedback. I. Anreiter assisted with quantitative polymerase chain reactions, and A. Petrie, B. Cole, and C. Bonner managed the greenhouse. **Funding:** We acknowledge funding from an NSERC Discovery Grant and Accelerator Supplement (M.E.F.), Ontario Graduate (R.T.B.) and NSERC (T.L.H.) scholarships, and the University of Toronto. **Author contributions:** R.T.B. and M.E.F. conceived the study and designed experiments; R.T.B. conducted experiments; R.T.B. and M.E.F. analyzed phenotypic data; R.T.B., A.M.O., and T.L.H. conducted bioinformatics; and all authors wrote the manuscript. **Competing interests:** The authors declare no competing interests. **Data and materials availability:** Raw sequence reads have been deposited at NCBI BioProject ID PRJNA512862 (www.ncbi.nlm.nih.gov/bioproject/?term=PRJNA512862). All data and code for analyses are available on Zenodo (24).

SUPPLEMENTARY MATERIALS

science.sciencemag.org/content/370/6515/476/suppl/DC1
Materials and Methods
Figs. S1 to S6
Tables S1 to S4
References (25–60)
MDAR Reproducibility Checklist
13 March 2020; accepted 31 August 2020
10.1126/science.abb7222



UNDERSTANDING DYNAMIC ECOSYSTEMS



SEE INSIDE FOR DETAILS:

President's Address | Registration | Plenary Lectures | Topical Lectures
Scientific Sessions | Career Workshops

Climate Change

Sustainability

Artificial Intelligence

International S&T

Resource Management

Public Engagement

Technology

Diversity

Public Health

Infectious Disease

Innovation

Ecology

Workforce Development

Big Data

Anthropogenic Processes

Microbiome

**The 2021 AAAS Annual Meeting will convene entirely online February 8-11,
with related pre-released materials available starting in late January.**



Dear Science Enthusiast:

It is difficult to believe how much our world has changed since our 2020 AAAS Annual Meeting in February. The theme of the 2021 Annual Meeting, *Understanding Dynamic Ecosystems*, took on a new and unexpected meaning, especially in light of how vital advances in science and technology come together to meet and to overcome the challenges of today's rapidly changing world.

What 2020 has demonstrated is that coming together virtually to highlight and discuss advances and collaborations across the STEM ecosystem is needed now more than ever—so much so that we are radically reducing the registration fee for our scientific program, thanks in part to the generous support of our sponsors. We continue to offer workshops, e-posters, and other complimentary programming.

Just as the rest of the world has adapted to a new normal, so too has your Annual Meeting team. Our new virtual format has transformed many aspects of the meeting, and we extend our gratitude to our attendees, speakers, sponsors, and volunteers for their patience and flexibility.

This February, we hope you will consider sharing your voice with our diverse community of scientists, educators, policymakers, journalists, and many others.

Sincerely,

Claire M. Fraser, Ph.D.

President, AAAS

Chair, 2021 Annual Meeting

Dean's Endowed Professor and Director, Institute for Genome Sciences

University of Maryland School of Medicine



Starting in late January, Look out for the pre-release of meeting content:

- **Hundreds of Scientific Session videos**, highlighting the work of individual panelists will be available to stream.
- **E-poster galleries** will showcase research, including highlights from early career researchers.

Live February 8–11,

- Invited **Topical Lecturers** will be available for Q&A.
- **Scientific Sessions** will convene to discuss how each presenter's work interacts with others' and for Q&A.
- **Public Workshops** will focus on:
 - Advancing your career;
 - Advocating and building alliances;
 - Diversifying and enhancing equity in the scientific enterprise.
- And, of course, leading scientists will address attendees and the public during **Plenary Lectures**.

CONNECT WITH US! #AAASmtg



aaas.org/meetings



[@AAASmeetings](https://twitter.com/AAASmeetings)



[/AAAS.Science](https://www.facebook.com/AAAS.Science)

**Thanks to the generous support of our sponsors,
access to the scientific program for AAAS members
is available at a deeply discounted rate of \$50.**

Not a AAAS Member?

**Now's the time to join. The 2021 Annual Meeting is open
exclusively to members, but we've made joining easier than
ever with new membership options ranging from \$25 to \$225.***

**Simply choose the membership option for you and complete
your meeting registration.**

*Offer valid from November 6, 2020 to February 11, 2021, for new individual members only. There is a limit of one AAAS "Future of Science" T-shirt per membership order. Members with an international shipping address and student members who select a digital subscription are not eligible to receive the T-shirt. Please allow up to ten weeks for delivery of the T-shirt. The AAAS "Future of Science" T-shirt is provided as is, without any guarantees or warranty, and cannot be exchanged or returned.

In association with the product, AAAS makes no warranties of any kind, either express or implied, including but not limited to warranties of merchantability or fitness for a particular purpose. AAAS members are entitled to receive issues published only during their 12-month membership term.



Plenary Lectures



Claire M. Fraser

President, AAAS
University of Maryland School of Medicine

Presented by: **ASU** Arizona State University

Host University



Ruha Benjamin

Princeton University



Anthony S. Fauci

U.S. National Institute of Allergy
and Infectious Diseases



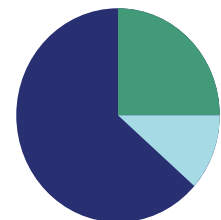
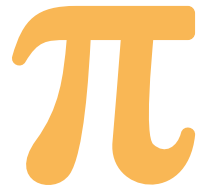
Mary L. Gray

Microsoft Research



Sethuraman Panchathan

National Science Foundation



Topical Lectures

Anne H. Charity Hudley

University of California,
Santa Barbara



Joseph M. DeSimone

Carbon, Inc. and
Stanford University



Ayanna Howard

Georgia Institute
of Technology



Yalidy Matos

Rutgers University

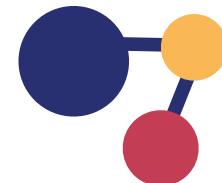


Nalini M. Nadkarni

University of Utah



As of September 30, 2020



Scientific Sessions

2021: A CRITICAL YEAR TO SUPPORT CLIMATE AND BIODIVERSITY

Organized by Andrew Allen, The Royal Society, London, United Kingdom

21ST CENTURY ALCHEMY: TURNING WASTE INTO RESOURCES

Organized by Boyoung Choe, National Research Council of Science and Technology, Sejong, Korea, Republic of (South)

AEROSPACE INDUSTRY: OPPORTUNITIES FOR PHYSICAL AND FUNCTIONAL EXPANSION

Organized by Lynnette D. Madsen, National Science Foundation, Alexandria, VA

AMAZON DEVELOPMENT PATHWAYS TO FOSTER CONSERVATION AND SOCIO-ECONOMIC PROSPERITY

Organized by Jessica Tome Garcia and Lauren Barredo, Sustainable Development Solutions Network, New York, NY

AN EPIDEMIOLOGICAL BLUEPRINT TO UNDERSTAND THE COMPLEX DYNAMICS OF A PANDEMIC

Organized by Marianne Lucien, ETH Zurich, Zurich, Switzerland

APPROPRIATE SCIENTIFIC RESPONSES TO CRISES

Organized by Atsushi Arakawa, Japan Science and Technology Agency, Tokyo, Japan

ARTIFICIAL INTELLIGENCE FOR PHYSICS: EXPERIMENTAL AND THEORETICAL PERSPECTIVES

Organized by Sergei Gleyzer, University of Alabama, Tuscaloosa, AL; Meenakshi Narain, Brown University, Providence, RI

ASTROBIOLOGY AND ORIGINS OF LIFE: FROM CHEMICAL NETWORKS TO LIVING ECOSYSTEMS

Organized by David Baum, University of Wisconsin-Madison, Madison, WI

BACTERIA, KEY PLAYERS IN MANY DIVERSE ECOLOGICAL NETWORKS

Organized by John Beutler, National Cancer Institute, Frederick, MD

BIOLOGICAL INVASIONS IN MOUNTAIN ECOSYSTEMS: RESEARCH AND EDUCATION

Organized by Robert Pal and Beverly Karplus Hartline, Montana Technological University, Butte, MT

BIOSPHERE RESPONSES TO GEOENGINEERING

Organized by Forrest Hoffman, Oak Ridge National Laboratory, Oak Ridge, TN; Cheng-En Yang, University of Tennessee, Knoxville, TN

BRAIN-MACHINE INTERFACES: SCIENCE, IMPACT, AND ETHICS

Organized by Jit Muthuswamy, Arizona State University, Tempe, AZ; Eric Maass, Medtronic RTG, Tempe, AZ

CANNABIDIOL 2021: SCIENCE, SAFETY, AND SOCIETAL ISSUES

Organized by Sol Bobst, ToxSci Advisors LLC, Houston, TX

CLEARING THE AIR: THE CASE FOR LOWERING US PM2.5 STANDARDS

Organized by Marianthi-Anna Kioumourtzoglou and Joan Casey, Columbia University Mailman School of Public Health, New York, NY

COASTAL ECOSYSTEMS: THE RELATIONSHIP BETWEEN COMMUNITY AND ENVIRONMENT

Organized by David Souza, UK Research and Innovation, Swindon, United Kingdom

COASTAL STORM EFFECTS IN THE TIME OF CLIMATE CHANGE

Organized by Ronadh Cox, Williams College, Williamstown, MA

COLLABORATING AT A DISTANCE TO FIGHT COVID-19

Organized by Heather Evans, National Institute of Standards and Technology, Gaithersburg, MD; Marla Dowell, National Institute of Standards and Technology, Boulder, CO

COMPLEX GLYCANS IN CORONAVIRUS BIOLOGY: THE SWEET SECRETS OF A PANDEMIC

Organized by Iain Wilson, Universität für Bodenkultur Wien, Vienna, Austria; Elisa Fadda, Maynooth University, Maynooth, Ireland

COMPUTATIONAL MODELING OF THE OVARY: APPLICATIONS FOR PREDICTIVE TOXICOLOGY

Organized by Karen H. Watanabe, Arizona State University, Phoenix, AZ; Mary B. Zelinski, Oregon National Primate Research Center, Beaverton, OR

COMPUTER SIMULATION MODELING FOR COVID POLICY: GLOBAL PERSPECTIVES

Organized by Abraham Flaxman, Institute for Health Metrics and Evaluation, Seattle, WA

COMPUTING, ARTIFICIAL INTELLIGENCE, AND SOCIETAL IMPACTS: AN INFLECTION POINT

Organized by Daniel A. Reed, University of Utah, Salt Lake City, UT

CONSEQUENCES OF INCARCERATION ON HEALTH INEQUITY AND RACIAL INJUSTICE

Organized by Linda Teplin, Northwestern University, Chicago, IL

CONVERSATIONAL CHALLENGES OF AI TEAMING WITH HUMANS

Organized by Randi Martin, Rice University, Houston, TX

COUPLING EXPERIMENTS AND MODELS IN STUDIES OF THE MICROBIOME

Organized by Mark Alber and Joel Sachs, University of California, Riverside, CA

COVID-19 ACADEMIC SYSTEM STRESS TEST: WINNERS AND LOSERS WHEN SCIENCE MOVES HOME

Organized by Stephanie Pfirman, Arizona State University, Tempe, AZ

CREATING AND IMPROVING PATHWAYS FOR STEM PROFESSIONALS TO ADVISE CONGRESS

Organized by Mike Miesen and Laura Manley, Harvard University, Cambridge, MA

DECONSTRUCTING CANCER CELLS FOR MORE EFFECTIVE TREATMENT

Organized by Matthew Midgley and Emily Mobley, Wellcome Sanger Institute, Cambridge, United Kingdom

DESIGNER MOLECULES: UNDERSTANDING AND UTILIZING THEIR QUANTUM NATURES

Organized by Jens Dilling, TRIUMF, Vancouver, Canada; Ronald Fernando Garcia Ruiz, Massachusetts Institute of Technology, Cambridge, MA

DEVELOPING RESILIENT FOOD SYSTEMS IN A DISASTER-PRONE WORLD

Organized by Nicole Arbour, International Institute for Applied Systems Analysis, Laxenburg, Austria

DIGITAL AND GREEN: INSTRUMENTS FOR DRIVING SOCIO-ECONOMIC RECOVERY

Organized by Vinny Pillay, South African Department of Science and Technology, Pretoria, South Africa

DYNAMICS IN URBAN ECOSYSTEMS AND ENVIRONMENTS: MULTI-DISCIPLINARY PERSPECTIVES

Organized by Qihao Weng, Indiana State University, Terre Haute, IN; Elizabeth A. Wentz, Arizona State University, Tempe, AZ

DYNAMICS OF TROPICAL FORESTS AND THEIR IMPACT ON THE CLIMATE

Organized by Frédéric Achard, European Commission Joint Research Centre, Ispra, Italy

EFFECTS OF SPACE TRAVEL ON THE HUMAN BODY

Organized by David Souza, UK Research and Innovation, Swindon, United Kingdom

EVALUATING THE PROMOTION AND PROTECTION OF THE U.S. BIOECONOMY

Organized by Mary Maxon, Lawrence Berkeley National Laboratory, Emeryville, CA; Jeff Furman, Boston University, MA

EVOLVING POLICY PRIORITIES IN INTERNATIONAL SCIENTIFIC PARTNERSHIPS

Organized by Amanda Vernon, American Academy of Arts and Sciences, Cambridge, MA

EXPLORING MARS: PAST, PRESENT, AND FUTURE

Organized by Matt Shindell, Smithsonian National Air & Space Museum, Washington, DC

EXPLORING TIPPING POINTS IN NATURAL AND SOCIAL SYSTEMS

Organized by Veera Mitzner, Future Earth, Boulder, CO

HOW THINKING ABOUT RELIGION CAN INCREASE RACIAL AND GENDER DIVERSITY IN SCIENCE

Organized by Bethany Boucher, Rice University, Houston, TX

HUMAN IMPACTS ON GLOBAL WILDLIFE AND THEIR HABITATS

Organized by David Souza, UK Research and Innovation, Swindon, United Kingdom

HUMAN NICHE CONSTRUCTION THEORY: A LENS TO ANALYZE ONGOING CLIMATE CHANGE

Organized by Cara Ocobock, University of Notre Dame, IN

INDIGENOUS KNOWLEDGE, SCIENCE, AND ETHICAL FRAMEWORKS FOR COLLABORATION

Organized by Curtis Baxter and Robert O'Malley, American Association for the Advancement of Science, Washington, DC

INEQUITIES IN THE CRIMINAL JUSTICE ECOSYSTEM: POLICING, MONETARY SANCTIONS, JAIL

Organized by William Alex Pridemore, State University of New York at Albany, NY

INSTITUTION, JOURNAL, REPORTER: STRATEGICALLY MITIGATING COVID-19 MISINFORMATION

Organized by Valeria Sabate, American Association for the Advancement of Science, Washington, DC

INSTITUTIONAL RESPONSES TO COVID: THE IMPACT ON UNDERGRADUATE STEM INSTRUCTION

Organized by Charles Henderson, Western Michigan University, Kalamazoo, MI; Michael Feder, American Association for the Advancement of Science, Washington, DC

INTERPRETING PUBLIC OPINION OF SCIENTISTS AND THEIR WORK

Organized by Cary Funk, Pew Research Center, Washington, DC

LANGUAGE DEVELOPMENT AND HEALTH: DEAF CHILDREN DURING QUARANTINE

Organized by Donna Jo Napoli, Swarthmore College, PA

MAPPING AND MODELING MICROBIOMES

Organized by Matthew Sullivan, The Ohio State University, Columbus, OH; Ruth Varner, University of New Hampshire, Durham, NH

MESSENGERS FROM THE COSMOS: RECEIVING GRAVITATIONAL WAVES, PARTICLES, AND LIGHT

Organized by Nancy Levenson, Space Telescope Science Institute, Baltimore, MD; Gabriela Gonzalez, Louisiana State University, Baton Rouge, LA

MICROBIOME AND GUT-BRAIN INTERACTIONS

Organized by Rosa Krajmalnik-Brown, Arizona State University, Tempe, AZ; Sarkis Mazmanian, California Institute of Technology, Pasadena, CA

MITIGATING THE IMPACT OF GLOBAL TICK-BORNE DISEASES

Organized by Timothy Sellati, Global Lyme Alliance, Stamford, CT; Susanna Visser, Centers for Disease Control, Fort Collins, CO

MONARCHS: PUBLIC RESPONSE SEEN THROUGH POLICY, MEDIA, AND CITIZEN SCIENCE

Organized by Bruce Lewenstein and Anurag Agrawal, Cornell University, Ithaca, NY

NEUROSCIENCE FOR ARCHITECTURE: EVIDENCE FOR A NEW BRAIN-BASED SCIENCE OF DESIGN

Organized by Thomas D. Albright, Salk Institute for Biological Studies, La Jolla, CA

OCEANIC RESPONSES TO THE CLIMATE: RECOGNIZING CHANGES AND EXTREMES

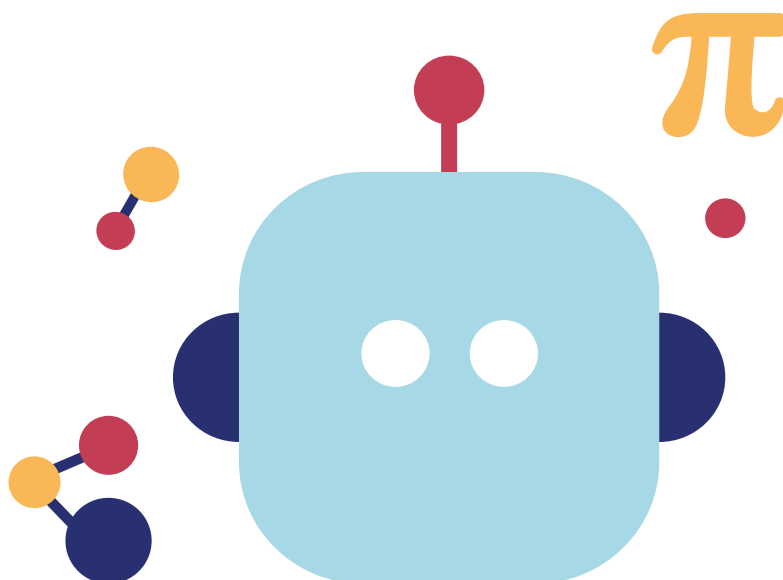
Organized by Lijing Cheng, Chinese Academy of Sciences, Beijing, China

OPEN SCIENCE: ISSUES AND CHALLENGES ACCELERATED BY COVID-19

Organized by Jerry Sheehan, National Institutes of Health, Bethesda, MD; Kazuhiro Hayashi, National Institute of Science and Technology Policy, Tokyo, Japan

OPPORTUNITY AT TIMES OF CHANGE: CATALYZING THE EVOLUTION OF GRADUATE EDUCATION

Organized by Barbara Natalizio, National Postdoctoral Association, Rockville, MD



PHOSPHORUS AND CLIMATE CHANGE: A VICIOUS CIRCLE

Organized by James Elser, University of Montana, Polson, MT; Matt Scholz, Arizona State University, Tempe, AZ

POLYGENIC RISK SCORES: USES AND MISUSES IN HEALTH, RESEARCH, AND SOCIETY

Organized by Sarah Tishkoff, University of Pennsylvania, Philadelphia, PA; Kyle Brothers, University of Louisville, KY

PURSUING ENVIRONMENTAL JUSTICE THROUGH SCIENCE AND RELIGION

Organized by Lilah Sloane-Barrett and Katy Hinman, American Association for the Advancement of Science, Washington, DC

REDUCING WASTE IN THE U.S. SEAFOOD SUPPLY CHAIN

Organized by Lekelia Jenkins, Arizona State University, Tempe, AZ; Dave Love, Johns Hopkins University, Baltimore, MD



RESEARCH AND INNOVATION: ENHANCING COLLABORATIONS BETWEEN ACADEMIA AND INDUSTRY

Organized by Lorne Whitehead and Michele Mossman, University of British Columbia, Vancouver, Canada

RESOLVING LGBTQ DISPARITIES IN STEM REPRESENTATION THROUGH DEMOGRAPHIC DATA

Organized by Rochelle Diamond, National Organization of Gay & Lesbian Scientists & Technical Professionals, Pasadena, CA

RESPONSE OF DIGITAL TECHNOLOGY TO COVID-19 AND CLIMATE CHANGE

Organized by Andrew Allen, The Royal Society, London, United Kingdom

SCALING LOCALIZED MANUFACTURING FOR SUSTAINABILITY AND RESILIENCE

Organized by K.C. Morris, National Institute of Standards and Technology, Gaithersburg, MD; Björn Johansson, Chalmers University of Technology, Gothenburg, Sweden

SCIENCE AND ENGINEERING FOR HUMANITARIAN GOALS

Organized by Lynnette D. Madsen, National Science Foundation, Alexandria, VA

STRENGTHENING COMMUNITIES AND SCIENTIFIC RESEARCH IN ADAPTING TO CLIMATE CHANGE

Organized by Pamela Doughman and Ben Wender, California Energy Commission, Sacramento, CA

STRENGTHENING SUSTAINABILITY PROGRAMS AND CURRICULA IN HIGHER EDUCATION

Organized by Lida Beninson and Emi Kameyama, National Academies of Sciences, Engineering, and Medicine, Washington, DC

THE COVID-19 INFODEMIC: COMBATTING MISINFORMATION DURING GLOBAL CRISES

Organized by Stefan Stieglitz, University of Duisburg-Essen, Duisburg, Germany

THE CRITICAL AND EVOLVING ROLE OF SCIENTIFIC ADVISORY COMMITTEES IN POLICYMAKING

Organized by Michael Fernandez and Erin Heath, American Association for the Advancement of Science, Washington, DC

THE DIGITALIZATION OF HEALTHCARE AND ITS EFFECTS ON ENGAGEMENT AND GOVERNANCE

Organized by Calvin Ho, University of Hong Kong, Hong Kong; Madeleine Murtagh, Newcastle University, Newcastle upon Tyne, United Kingdom

THE DYNAMIC PAST: HOW SCIENCE HELPS GIVE VOICE TO SILENCED STORIES

Organized by Robert O'Malley, American Association for the Advancement of Science, Washington, DC

THE FUTURE OF CITIES: GREEN BUILDINGS AND SUSTAINABLE INFRASTRUCTURE

Organized by David Souza, UK Research and Innovation, Swindon, United Kingdom

THE GUT MICROBIOME: IMPACT FROM EARLY LIFE ON HEALTH AND DISEASE

Organized by Samantha Wynne and Emily Mobley, Wellcome Sanger Institute, Cambridge, United Kingdom

THE IMPACTS OF MOBILE TECHNOLOGY AND REGULATION IN A PANDEMIC

Organized by Katina Michael, Arizona State University, Tempe, AZ; Roba Abbas, University of Wollongong, Australia

THE IMPORTANCE OF BIOLOGICAL COLLECTIONS IN THE FIGHT AGAINST COVID-19

Organized by Keegan Sawyer and Audrey Thevenon, National Academies of Sciences, Engineering, and Medicine, Washington, DC

THE INTERDEPENDENCE OF HUMAN HEALTH AND AQUATIC SOCIAL-ECOLOGICAL SYSTEMS

Organized by Kathryn Fiorella, Cornell University, Ithaca, NY

THE MATHEMATICS OF HOMEOSTASIS AND HEALTH

Organized by Michael Reed, Duke University, Durham, NC

THE PANDEMIC'S SOCIAL ECOSYSTEM: LEARNING NEW PATHS TOWARD KNOWLEDGE AND TRUST

Organized by Jonathan Coopersmith, Texas A&M University, College Station, TX; Lisa Onaga, Max Planck Institute for the History of Science, Berlin, Germany

THE QUANTUM ECOSYSTEM: INNOVATION

Organized by Charles Clark, Joint Quantum Institute, Gaithersburg, MD; Araceli Venegas-Gomez, QURECA, Glasgow, United Kingdom

THE ROLES OF STATISTICS AND DATA SCIENCE IN FIGHT AGAINST COVID-19

Organized by Lei Liu, Washington University in St. Louis, MO

THEY (AND WE) ARE WHAT WE EAT: LINKING DIET AND GUT MICROBIOME TO HUMAN HEALTH

Organized by Farida Mohamedshah, Institute of Food Technologists, Chicago, IL

TIME MATTERS: TRANSIENTS AND DYNAMICS IN THE MANAGEMENT OF ECOSYSTEMS

Organized by Alan Hastings, University of California, Davis, CA; Kim Cuddington, University of Waterloo, Canada

UNDERSTANDING AND ENABLING HUMAN TRAVEL TO THE MOON AND MARS

Organized by Leslie DeChurch, Northwestern University, Winter Park, FL

USING GENOMICS TO TRACK AND DEFEAT COVID-19, MALARIA, AND CHOLERA

Organized by Alison Cranage, Wellcome Sanger Institute, Cambridge, United Kingdom; Emily Mobley, Wellcome Sanger Institute, Cambridge, United Kingdom

USING TECHNOLOGY TO IMPROVE UNDERSTANDING OF CHANGES TO BIODIVERSITY

Organized by Jonas Brunschwig, swissnex Boston, Cambridge, MA; Tiffany Merz-Cheok, University of Zurich, Zurich, Switzerland

WORKSHOPS

Career Workshops

Opportunities to gain advice and strategies from experienced STEM professionals

COMMUNICATING FOR IMPACT: HOW TO SHARE RESEARCH THROUGH THE NEWS MEDIA

Organized by Diana Brazzell, Footnote, Washington, DC

ELEVATING SCIENCE IN A VIRTUAL, WORK-FROM-HOME ENVIRONMENT

Organized by Greg Kunkle, Pacific Northwest National Laboratory, Richland, WA

ENGAGING WITH INSTITUTIONS ABROAD THROUGH THE FULBRIGHT SPECIALIST PROGRAM

Organized by Amirah Nelson, World Learning, Washington, DC

FOSTERING CAREER DEVELOPMENT THROUGH RESEARCH LEARNING EXPERIENCES

Organized by Joan Ferrini-Mundy and Ali Abedi, University of Maine, Orono, ME

HOW TO BUILD AND MANAGE SCIENTIST NETWORKS

Organized by Robin Tim Weis, Office of Science and Technology Austria, Washington, DC

HOW TO CREATE AND DELIVER AN EFFECTIVE WEBINAR

Organized by Dennis Meredith, Independent, Fallbrook, CA

HOW TO CREATE COMPELLING RESEARCH TALKS USING ELEMENTS OF STORY

Organized by Holly Walter Kerby, Wisconsin Institute of Discovery, Madison, WI

INTERNATIONAL DOCTORAL NETWORKS AND RESEARCHERS' MOBILITY FOR EXCELLENT RESEARCH

Organized by Julie Lepretre, European Commission, Brussels, Belgium

JOURNALS, JOURNALS EVERYWHERE, BUT WE SHOULD STOP AND THINK

Organized by Roxanne Bogucka, University of Texas at Austin, TX

MIND THE GAP: BRIDGING THE EXPECTATION GAP BETWEEN RESEARCHERS AND EMPLOYERS

Organized by Mostafa Moonir Shawrav, Marie Curie Alumni Association, Vienna, Austria

MIND THE GAP: ENGAGING SCIENTISTS WITH K-12 EDUCATORS TO ADVANCE STEM EDUCATION

Organized by Kitchka Petrova, National Science Foundation, Alexandria, VA

PREPARING FOR SUSTAINABLE RESEARCH CAREERS INSIDE OR OUTSIDE OF ACADEMIA

Organized by Mostafa Moonir Shawrav and Gabor Kismihok, Marie Curie Alumni Association, Vienna, Austria

REIMAGINING MENTORSHIP VIA AN INTERDISCIPLINARY LEARNING COMMUNITY

Organized by Amanda Diekman, Indiana University, Bloomington, IN

SKILLS FOR RESILIENT RESEARCHERS

Organized by Julie Lepretre, European Commission, Brussels, Belgium

UNIQUE STRATEGIES FOR TEACHING AND LEARNING ABOUT SCIENCE AND TECHNOLOGY POLICY

Organized by Deborah Stine, Science, Technology, and Innovation Policy Analysis & Education, LLC, Pittsburgh, PA

WHAT STORY? THE POWER OF THE PODCAST FOR SCIENCE COMMUNICATION AND YOUR CAREER

Organized by Elaine Devine, Taylor & Francis, Abingdon, United Kingdom

WINNING UNDECIDED HEARTS & MINDS: COMMUNICATING WITH VALUES

Organized by Heather Conklin, Science Communication Journal Club, Oceanside, CA

YOU ARE A LEADER! NAVIGATE YOUR STEM CAREER JOURNEY THROUGH 360 DEGREE LEADERSHIP

Organized by Alaina Levine, Quantum Success Solutions, Tucson, AZ

Advocacy Workshops

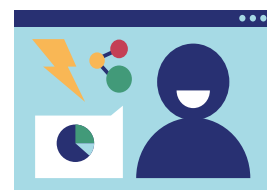
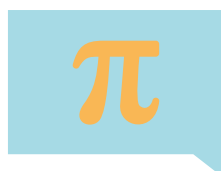
Explore ways of promoting science in your community

BRINGING SCIENCE TO LOCAL POLICY SOLUTIONS: THE LOCAL SCIENCE ENGAGEMENT NETWORK

Organized by Daniel Barry, American Association for the Advancement of Science, Washington, DC

CLIMATE CHANGE CONVERSATIONS: CREATING DIALOGUE ABOUT SOLUTIONS

Organized by Elana Kimbrell, American Association for the Advancement of Science, Washington, DC



COMMUNITY ENGAGEMENT AND OUTREACH FOR STEMM EDUCATORS

Organized by Theresa L. Harris, American Association for the Advancement of Science, Washington, DC

COMMUNITY ENGAGEMENT IN THE TIME OF COVID: SOLUTIONS FOR REMOTE STEM OUTREACH

Organized by Victoria Herrmann, The Arctic Institute, Washington, DC

CONTINUING EFFECTIVE COMMUNITY ENGAGEMENT IN TIMES OF COVID-19

Organized by Latasha Wright, BioBus, Bronx, NY

CREATING SCIENCE-POLICY CAPACITIES AND OPPORTUNITIES THROUGH FELLOW-SHIP PROGRAMS

Organized by Marcella Ohira, Inter-American Institute for Global Change Research, Montevideo, Uruguay

LEGISLATORS IN LAB COATS: HOW TO RUN FOR OFFICE AND CHANGE THE WORLD

Organized by Shaughnessy Naughton, 314 Action, Philadelphia, PA

PATHWAYS FOR EARLY CAREER SCIENTISTS CATALYZING POLICY CHANGE

Organized by Holly Mayton, National Science Policy Network, Virginia Beach, VA

PUT THE BOTTOM LINE UP FRONT TO IMPACT POLICY & IMPROVE YOUR COMMUNICATION

Organized by Jessica Soule, American Association for the Advancement of Science, Washington, DC

SCIENCE COMMUNICATION AS A TOOL FOR TRAINING THE NEXT GENERATION OF INFLUENCERS

Organized by Adriana Bankston, Journal of Science Policy and Governance, Washington, DC

SCIENCE COMMUNICATION ON-LINE PROGRAMME (SCOPE)

Organized by Michelle Paulsen, Northwestern University, Evanston, IL

SCIENTISTS AS CITIZENS: PATHWAYS FOR LOCAL GOVERNMENT ENGAGEMENT

Organized by Rebecca Mandt, Engineers and Scientists Acting Locally, Cambridge, MA

SUCCEEDING AS A SCIENCE LEADER WORKING OUTSIDE ACADEMIA

Organized by Aaron Mertz, The Aspen Institute, New York, NY

Culture, Equity, & Inclusion Workshops

Discover strategies for creating inclusive networks

BUILDING YOUR PROFESSIONAL NETWORKS AS A WOC IN STEM

Organized by Ana Porras, Cornell University, Ithaca, NY

CAREERS IN STEM POLICY: OPPORTUNITIES FOR UNDERREPRESENTED MINORITIES

Organized by Brandy Huderson, National Science Foundation, Alexandria, VA

CONCEPTUALIZING STUDENT DIVERSITY IN THE CLASSROOM

Organized by Stanley Lo, University of California San Diego, La Jolla, CA

ETHICAL EVALUATION OF AI/IS IMPACT ON HUMAN WELL-BEING USING IEEE 7010-2020

Organized by Alice Vo Edwards, The CEO Within LLC, North Las Vegas, NV

INCLUSIVE ONLINE TEACHING: TOWARD MORE IMPACTFUL AND ENGAGED LEARNING

Organized by Leyte Winfield, Spelman College, Atlanta, GA

LEVERAGING OUR PRIVILEGE TO ADDRESS SYSTEMIC BIASES

Organized by Maria-Denise Dearing, University of Utah, Salt Lake City, UT

MOVEMENT-BUILDING IN STEM IN THE MIDST OF THE BLACK LIVES MATTER MOVEMENT.

Organized by Jessica Esquivel, Fermilab, Batavia, IL

NAVIGATING THE TRAINEE-MENTOR RELATIONSHIP AS A STEM TRAINEE WITH A DISABILITY

Organized by Mahadeo Sukhai, Canadian National Institute for the Blind, Kingston, Canada

SCIENCE COMMUNICATION AND ENGAGEMENT WITH RELIGIOUS PUBLICS

Organized by Robert O' Malley, American Association for the Advancement of Science

SCIENCE-DANCE FOR INCLUSIVE COMMUNITY ENGAGEMENT, EDUCATION & SOCIAL CHANGE

Organized by Lewis Hou, Science Ceilidh, Edinburgh, United Kingdom

SOUNDING THE ALARM: ADDRESSING RACISM, COVID-19, AND MENTAL HEALTH IN SCIENCE

Organized by Kerrie Wilkins-Yel, University of Massachusetts Boston, MA

CONNECT WITH US! #AAASmtg



@AAASmeetings



/AAAS.Science

The 2021 AAAS Annual Meeting will convene entirely online, February 8-11, with related prereleased materials available starting in late January.

Please see our website for the most up-to-date program information:

aaas.org/meetings

Registration will be available in November!



myIDP:
A career plan customized
for you, by you.

For your career in science, there's only one

Science

Features in myIDP include:

- Exercises to help you examine your skills, interests, and values.
- A list of 20 scientific career paths with a prediction of which ones best fit your skills and interests.
- A tool for setting strategic goals for the coming year, with optional reminders to keep you on track.
- Articles and resources to guide you through the process.
- Options to save materials online and print them for further review and discussion.
- Ability to select which portion of your IDP you wish to share with advisors, mentors, or others.
- A certificate of completion for users that finish myIDP.



Visit the website and start planning today!
myIDP.sciencecareers.org

ScienceCareers In partnership with: AAAS



FACULTY POSITION IN CANCER EPIGENETICS at FOX CHASE CANCER CENTER

The Fox Chase Cancer Center invites applicants for tenure-track faculty positions at the level of assistant professor and associate professor in the **Cancer Epigenetics Institute** and **Cancer Signaling and Epigenetics Program**. While outstanding candidates working in all areas of epigenetics are invited to apply, we are particularly soliciting applications from candidates that are interested in the following areas: **1.** the relationship between higher order genome organization and cancer development, progression and/or resistance; **2.** the role chromatin has in genome stability; **3.** the relationship between cellular signaling, chromatin modulation and cancer; **4.** the relationship between metabolic pathways and epigenetic control; **5.** the role of modified nucleic acids (DNA, RNA) and associated regulation in cancer; **6.** the relationship between immune oncology and epigenetics.

Successful applicants will join a highly interactive institution that is committed to bridging basic discovery to clinical application through collaboration. Fox Chase was among the nation's first institutions to receive Comprehensive Cancer Center designation from the NCI in 1974. There are 119 research faculty that generate \$63.2 million in funding. The research faculty are surrounded by clinical colleagues that provide care for over 105,000 individuals and support >170 clinical trials, of which >60 are investigator-initiated. Two particular highlights of the center are the superb clinical pipeline that facilitates rapid translation of basic science discoveries into the clinic and the world-class core facilities that are easily accessed.

Applicants interested in joining such an environment should have a Ph.D. and/or M.D. degree with an outstanding record of research productivity. The application should contain the following information - a curriculum vitae, a brief (up to two pages) statement of research interests and future goals and a list of three individuals providing letters of recommendation. Please send the application via email to Johnathan Whetstone (Johnathan.Whetstone@fccc.edu), Director, Cancer Epigenetics Institute, Co-Leader, Cancer Signaling and Epigenetics Program, Fox Chase Cancer Center.

Equal Opportunity Employer.

Tenure-track Assistant or Associate Professor of Genetics or Genomics

In anticipation of substantial growth over the next five years, the Department of Human Genetics at the University of Utah School of Medicine (www.genetics.utah.edu) seeks outstanding applicants for one or more tenure-track positions at the level of Assistant or Associate Professor. We seek highly creative scientists who use genetics to investigate fundamental biological problems. We encourage applicants whose research focuses on evolutionary and functional genetics and genomics; human and medical genetics; computational genomics; and research programs using established model or unconventional organisms. As part of a vibrant community of faculty with a strong track record of collaborative mentorship, research, and funding, the Department of Human Genetics lies at the interface between basic and clinical sciences. This creates ample opportunities for interdisciplinary research (e.g., our Center for Genetic Discovery, Transformative Excellence Program in Evolutionary Genetics and Genomics, and Center for Genomic Medicine). As a department, we value diversity and equity, and believe that the best science is done when researchers of diverse backgrounds are integrated and supported in an inclusive manner. We seek faculty who share these values. Our institution is set in a unique geographical landscape that attracts a heterogeneous and productive scientific community. Successful candidates will receive a generous startup package and enjoy a stimulating research environment that places a strong emphasis on innovation and interaction.

Link to apply: <http://utah.peopleadmin.com/postings/108145>


Applicants are asked to submit:

- Curriculum Vitae - CV and 3 most relevant reprints or preprints
- Research statement - Describe your most significant scientific accomplishments, your goals for research as a faculty member, and the qualifications and experience that have prepared you to achieve these goals.
- Teaching statement - Describe your commitment to education, your teaching philosophy, and the courses you might potentially teach.
- Diversity, equity, and inclusion statement - Describe your past and future contributions to diversity, equity, and inclusion through research, teaching, and service.

The University of Utah is an Affirmative Action/Equal Opportunity employer and does not discriminate based upon race, national origin, color, religion, sex, age, sexual orientation, gender identity/expression, status as a person with a disability, genetic information, or Protected Veteran status. Individuals from historically underrepresented groups, such as minorities, women, qualified persons with disabilities and protected veterans are encouraged to apply. Veterans' preference is extended to qualified applicants, upon request and consistent with University policy and Utah state law. Upon request, reasonable accommodations in the application process will be provided to individuals with disabilities. To inquire about the University's nondiscrimination or affirmative action policies or to request disability accommodation, please contact: Director, Office of Equal Opportunity and Affirmative Action, 201 S. Presidents Circle, Rm 135, (801) 581-8365.

The University of Utah values candidates who have experience working in settings with students from diverse backgrounds, and possess a strong commitment to improving access to higher education for historically underrepresented students.

Science Careers

FROM THE JOURNAL SCIENCE 


Confused about
your next career move?



**Download Free Career
Advice Booklets!**

ScienceCareers.org/booklets



A man with short dark hair, wearing a white lab coat over a light blue button-down shirt, and clear safety goggles. He is smiling slightly and looking towards the camera. His arms are crossed, and he is wearing blue nitrile gloves. The background is a blurred laboratory setting with shelves containing various bottles and equipment.

YOU'D SMILE TOO IF YOU JUST ADVANCED YOUR CAREER.



Find your next job at [ScienceCareers.org](https://www.sciencecareers.org)

There's scientific proof that when you're happy with what you do, you're better at what you do. Access career opportunities, see who's hiring and take advantage of our proprietary career-search tools. Get tailored job alerts, post your resume and manage your applications all in one place: [sciencecareers.org](https://www.sciencecareers.org)

ScienceCareers

FROM THE JOURNAL SCIENCE  AAAS



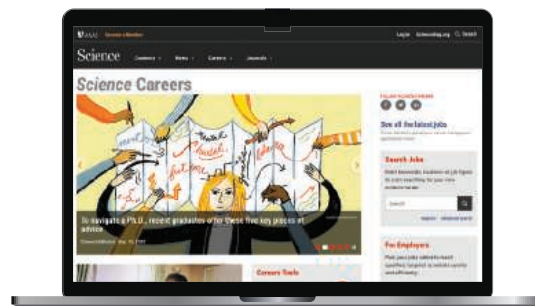
Science Careers helps you advance your career. Learn how !

- Register for a free online account on **ScienceCareers.org**.
- Search hundreds of job postings and find your perfect job.
- Sign up to receive e-mail alerts about job postings that match your criteria.
- Upload your resume into our database and connect with employers.
- Watch one of our many webinars on different career topics such as job searching, networking, and more.
- Download our career booklets, including Career Basics, Careers Beyond the Bench, and Developing Your Skills.
- Complete an interactive, personalized career plan at "my IDP."
- Visit our Employer Profiles to learn more about prospective employers.
- Read relevant career advice articles from our library of thousands.

Visit **ScienceCareers.org**
today — all resources are free

ScienceCareers

FROM THE JOURNAL SCIENCE  AAAS



SCIENCECAREERS.ORG

By Naomi A. Rankin, Matthias I. Gröschel, and Maha R. Farhat

Mentorship at a distance

The year is 2022. It is a warm summer day in Boston, and Naomi, an incoming graduate student, sits in a cafe waiting for two colleagues who have greatly influenced her career—although they’ve never met in person. It was back in 2020 when Naomi, then an undergraduate at Howard University, spent a summer working virtually with Matthias, a postdoc, and Maha, the lab principal investigator, through a Harvard University internship program. Now that the world has managed COVID-19, they are excited to finally meet face-to-face and reflect on that summer experience.

NAOMI: I remember that day in March 2020 when everything seemed to unravel. I was told to evacuate my campus and that classes would be virtual for the indefinite future. While many of my peers’ summer research opportunities were canceled, I was lucky that the Harvard summer internship was scheduled to continue virtually. But I wondered how I would learn a completely new topic and research style from 3000 kilometers and two time zones away. How would I form a relationship with my mentors?

MATTHIAS: Both Maha and I had doubts about the virtual internship format. I had never mentored a student completely remotely, and I knew you had never done this type of research before. I counted on Maha’s experience mentoring students and her optimism that we would make it work.

NAOMI: The biggest challenge for me was not knowing whether I was on track. If we had been working together in person, it would have been easy to casually touch base and get gentle nudges in the right direction when I needed them. But I was too nervous to ask basic questions over video calls and chat, so I relied on trial and error and online tutorials. Then, when I presented my work to you, I was disappointed to learn that the model I had worked on for 2 weeks was completely wrong.

MAHA: I remember that moment well. It became clear then that we needed to reset our expectations and how we communicated. I urged you to use chat liberally and reach out for more frequent short check-ins. As the days rolled on, you seemed to become more at ease asking for help.

NAOMI: It certainly helped that you were present and responsive via telephone calls and chat. I also learned the



**“With a little work,
we formed a lasting bond.”**

importance of making my concerns heard. And when we began to speak more often, I got to see another side of your lives. I never expected to have video calls with Matthias while he was at the playground with his kids!

MATTHIAS: Me neither! Do you remember when my daughter poured water on my laptop? It delayed me terribly in sending over a key figure for your final presentation. I was balancing so much at the time and yet desperately wanted to be there when you needed me.

NAOMI: Yes, that wasn’t the smoothest moment—but ultimately it only strengthened our relationship. Seeing your struggles with working from

home helped me realize that we are all human, navigating through a difficult time together.

MATTHIAS: I enjoyed connecting with you informally; it felt very genuine. It also offered an opportunity to reflect on what kind of mentor I want to be in the “real” world. I hope to carry that forward with me.

MAHA: Losing the connection with mentees was among the hardest aspects of the quarantine for me professionally. Shifting to a more relaxed communication style really helped. It also reinforced my belief that science and scientists should be less aloof and more welcoming, especially to aspiring scientists early in their careers.

NAOMI: The virtual environment made it hard to connect at times—but with a little work, we formed a lasting bond. ■

Naomi Rankin is an undergrad at Howard University. Matthias Gröschel is a postdoc and Maha Farhat an assistant professor at Harvard Medical School. Farhat is also an attending pulmonologist at Massachusetts General Hospital. Send your career story to SciCareerEditor@aaas.org.